Magnetic screening currents and coupling losses induced in superconducting magnets for thermonuclear fusion

Alexandre Louzguiti

UNIVERSITE D'AIX-MARSEILLE

COMMISSARIAT A L'ENERGIE ATOMIQUE

ECOLE DOCTORALE 353

REGION PACA - ASSYSTEM

IUSTI/UMR 7343 - CEA/IRFM

Thèse présentée pour obtenir le grade universitaire de docteur

Discipline : SCIENCES POUR L'INGENIEUR
Spécialité : Energétique

Alexandre LOUZGUITI

Magnetic screening currents and coupling losses induced in superconducting magnets for thermonuclear fusion

Courants d'écrantage magnétique et pertes par couplage induites dans les aimants supraconducteurs pour la fusion thermonucléaire

Soutenue le 01/12/2017 devant le jury :

Marco BRESCHI	University of Bologna	Rapporteur
Pascal TIXADOR	Grenoble INP	Rapporteur
Arend NIJHUIS	University of Twente	Examinateur
Eric SERRE	Aix-Marseille Université	Examinateur
Frédéric TOPIN	Aix-Marseille Université	Directeur de thèse
Louis ZANI	CEA	Encadrant CEA
Jean-Luc DUCHATEAU	CEA	Invité

Toute personne persévérante a d'abord commencé par être obstinée.

A ma mère et mon frère

Acknowledgements

First, I would like to begin by expressing my gratitude to the Commissariat à l'Energie Atomique et aux énergies alternatives (CEA), to the Conseil Régional Provence Alpes Côte d'Azur and to ASSYSTEM for their financial support which has allowed me to be a PhD candidate within the IRFM facilities during three years.

I am also grateful to Dr. Alain BECOULET for having hosted me within the IRFM institute and to Dr. Sylvain BREMOND for having hosted me within the STEP service and for his sincere interest in my work throughout these three years.

I am profoundly indebted to Pr. Pascal TIXADOR and to Dr. Marco BRESCHI for having carefully examined the present manuscript, for their precious remarks and for their thoughtful questions during the defense.

I am also thankful to Pr. Eric SERRE and Dr. Arend NIJHUIS for having accepted to be part of the committee and for their sincere questions and comments during the defense, testifying to their interest in the work presented here.

I would also like to thank Dr. Frédéric TOPIN for having supervised my doctoral project with a lot of interest and enthusiasm despite the appreciable difference in our research themes. I am grateful to him for the fruitful discussions that have always occurred between us in a spirit of openness and mutual respect.

Furthermore, I would like to express my great appreciation to Dr. Louis ZANI for the substantial time he has devoted to me during these three years. His rigor and commitment have enabled me to surpass myself and to push the work I have carried out in this doctoral project even further.

I thank Dr. Daniel CIAZYNSKI for having given me valuable help on the understanding of the physics occurring inside superconducting composites as well as thoughtful guidance on the choice and development of the analytical tools presented in this thesis.

I warmly thank Dr. Bernard TURCK for all our discussions that have been more than beneficial to me. I would also like to sincerely thank him for his enthusiasm and energy that have been really appreciated, especially in hard times when exhaust and lack of lucidity could be felt. His guidance has been one of the keystone to this PhD project.

Many thanks to Dr. Jean-Luc DUCHATEAU for his numerous discussions and advice, not only about the physics involved in the present research, but also about the applied superconductivity and fusion communities; they have enabled me to grasp a broader view of the research in these exciting fields.

Heartfelt thanks go to Mr. Alexandre TORRE for sharing his experience, for his availability and his kindness and for having always left his door open to my problems and questions which have been – I have to admit – numerous, and sometimes quite unexpected. An important part of my understanding of the superconductivity field and associated engineering issues has come from our exchanges.

I wish to thank Dr. Ion TISEANU for having welcomed me with sincere hospitality within his facilities in INFLPR Bucharest on the occasion of a collaboration that has turned out to be truly instructive in several levels. I would also like to thank Mr. Daniel DUMITRU and Dr. Mihail LUNGU for their friendliness and companionship.

I am grateful to Mr. Yann STEPHAN, for the time he has devoted in following up my research, for his real interest in it and for his suggestions that have offered me another perspective on my work.

For their precious help, support and guidance throughout the experiments we have conducted during the PhD project, I wish to profoundly thank Mr. Manuel TENA, Mr. Romain GONCALVES, Mr. Guillaume JIOLAT, Mr. Denis GUIBERT, Mr. Sylvain GIRARD and Mr. Denis ARRANGER. I also thank them for their kindness and for all the good times we have shared during the three years, especially during the morning coffees and the workshops. In addition, even if I have not had the opportunity to carry out an experiment with Mr. Hervé CLOEZ, I would like to thank him for the precious legacy he has left in SPEEDY and JOSEFA facilities.

My grateful thanks are also extended to Dr. Valérie LAMAISON for having hosted me within the GCRY group with such kindness, for her open-mindedness and for her sincere interest in my work.

I am also deeply thankful to Mr. Benoit LACROIX for having taken the time to introduce me to the cryogenics and for all the very good times we have spent together during these three years. These acknowledgments also extend to Mrs. Sylvie NICOLLET and I am grateful to her for all the scientific - and non-scientific - discussions we have shared.

I warmly thank Dr. Patrick HERTOUT for our discussions and his precious advice on analytical and numerical mathematics as well as for his sincere friendliness.

In addition, I would like to express my gratitude to Mr. Jean-François MAHIEU and Mr. Yannick MINEO for their kind help in fixing informatics-related issues and to Mrs. Evelyne POITEVIN and Mrs. Stéphanie SANCHEZ for their availability, their efficiency in any administrative process and their profound kindness.

I also thank Mr. Maxime CHILETTI for his help in the review of this manuscript.

Working within IRFM during three years has been a real pleasure and I would therefore also like to sincerely thank those whose presence, discussions and sharing have been greatly appreciated: Mr. Julien SAID, Mr. Quentin LE COZ, Mr. Yohann BALE, Mr. Adrien FONTAINE, Mr. Christophe ROUX, Mr. Gilles GROS, Mrs. Sylvie GIBERT, Mr. Patrick PROCHET, Mr. Patrick DECOOL, Mr. Jean-Louis MARECHAL, Mrs. Julie JOLY and Mr. Marc GONICHE.

Finally, I am truly grateful to all my colleagues, friends and family who have honored me by attending to the defense and who have provided me with important moral support in doing so. In particular to : Mr. Julien SAID, Mr. Amine BADRY, Mr. Julian MAIRE, Mrs. Hélène GUIGON, Mrs. Amandine NUGUET (and I also thank Mrs. Chantal & Mr. André NUGUET for their long-distance support !), Mr. Bruno LOUZGUITI, Mrs. Pascale RENAUD and Mrs. Inès MEZIANE.

I would like to conclude these acknowledgements by expressing my profound and sincere gratitude to my beloved partner, Inès, for having accepted the numerous sacrifices associated with this intense project, for her help in the everyday life necessities, for her patience, for her moral support and for her sincere faith in me.

Table of Contents

I. Introduction

I.1 General context

In a worldwide context where energy production and exchange take more and more place into the human activity, new sources of energy are continuously under investigation within the global research field, first under the purely scientific aspect, then gradually entering into the field of industrial mass production to become available to a maximum of users.

In this environment, aside to the conventional energy sources (coal, oil and fission for the most active ones) and among the new means of energy production (e.g. photovoltaic), the concept of power generation issued from fusion physical mechanism has emerged during the 1950's as a possible component of a future energy mix. The fusion use for civil energy production purpose is intended to be established through the exploitation of plasma magnetic confinement and principally aims at developing the tokamak-type installations.

The tokamak approach bears two main advantages: relying on quasi-infinite resources on earth (derived from hydrogen fueling for plasma) and carrying marginal risks of uncontrolled and accidental dissemination endangering populations (derived from spontaneous plasma extinction tendency).

On the other hand substantial challenges remain ahead and should also be considered in the tokamak strategy. Indeed the control of fusion plasma burning requires high level of technicality and experience given the high number of parameters to be mastered to reach steady-state regimes plasma.

Among these critical components is the magnetic system, keystone of the plasma control (see details below). Since several decades the international community has installed and operated many fusion installations throughout the world, mainly tokamaks such as TFR (FR), Tore Supra/WEST (FR), FT (IT), ASDEX (DE), TEXTOR (DE), COMPASS (CZ), MAST (UK), JET (UK), TCV (CH), Alcator (US), PLT (US), DIII-D (US), TFTR (US), T3 (RU), T10 (RU), SST1 (IN), EAST (CN), KSTAR (KR) but also other type of machines like stellarators such as ST (US), W7-X (DE) or heliotrons such as LHD (JP). Some of those tokamaks are shown in Figure 1.

Figure 1 : Images of some major tokamaks. Left: JET -- Middle: Tore Supra/West – right: EAST

The above list includes tokamaks currently in operation; most of them have mainly scientific scopes dedicated to a broad range of thematics, from plasma physics experiments to sub-components development (first wall, divertor, diagnostics, heating sources, current drive etc…).

The next generation of tokamaks is more and more oriented on the demonstration of energy production capacities:

- JT-60SA will be operated in Japan around 2020 and is substantially devoted to investigations on long plasma pulses relevant to future fusion reactor (DEMO)
- ITER will be operated in France around 2025 and is principally oriented towards demonstrating the operability of long pulses of D-T nuclear plasma

Those two large tokamaks are illustrated in Figure 2.

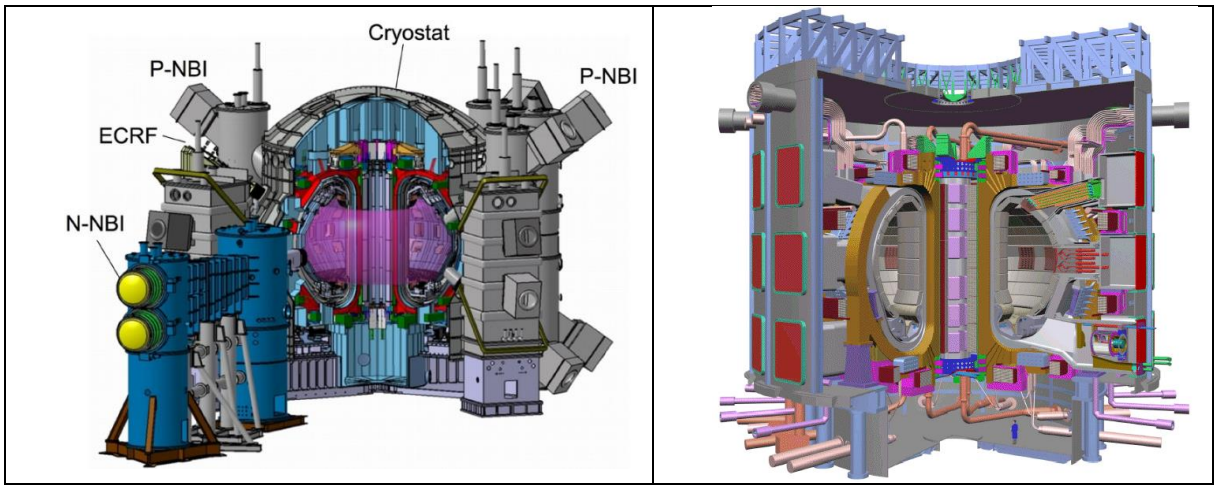

Figure 2 : Left: JT-60SA – right: ITER

The magnet system being a key component of a tokamak it is important to ensure its reliability during operation and therefore to consolidate the best technical and scientific knowledge on it. Another noticeable point to be considered is that magnet system is a major cost driver for the whole tokamak (about 1/3 of construction investment) and that knowledge mastering is also a component of machine merit in this regard.

I.2 Fusion and tokamak

While fission is based on the principle of heavy nuclei splitting into smaller nuclei, fusion is based on the merging of two light nuclei into a heavier one.

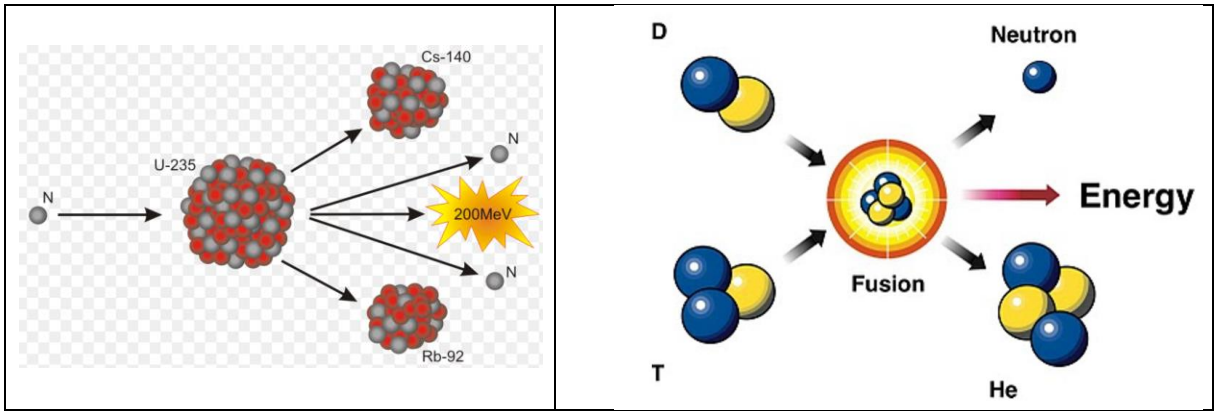

Figure 3 : Left: fission reaction – right: fusion reaction

Both reactions result into creation of energy through a neutron generation, and are therefore compatible with energy production strategy.

While in fission the reaction is self-generated by chain reaction, in the case of fusion the reaction is not self-maintained as demanding conditions must be established and sustained to allow the fusion between the two nuclei. As an example the coulomb repulsion barrier must be overpassed to allow the particles to interact, in a medium where density and temperature must therefore be sufficiently high to trigger the reaction. Typically the order of magnitude of the plasma core temperature in its reaction state is about hundred millions of Kelvin.

The fusion reaction is usually based on Deuterium and Tritium atoms, which are the most facilitating components for the reaction. The most common fusion reactions producing neutrons are

$$^{2}D + {}^{3}T \rightarrow n\ (14.03MeV) + {}^{4}He(3.56MeV)$$
$$^{2}D + {}^{2}D \rightarrow n\ (2.45MeV) + {}^{3}He(0.82MeV)$$

In order to allow continuous burn regime, these reactions must be triggered and confined in a closed volume.

We focus here on the specific closed volume formed in a tokamak configuration. The principle of tokamak was first established in Russia [1] (tokamak being issued from acronym TOroidal naya KAmera MAgnitnaya Katushka or toroidal chamber with magnetic coil) and relies on a torus-shaped plasma confined by a discrete number of coils enclosing it, called Toroidal Field coils or TF coils (see Figure 4). With this configuration, the charged particles moving along those toroidal lines would be subject to a drift due to a magnetic field gradient, and would not finally be confined, preventing the configuration from generating a stable equilibrium. To cancel this effect, the plasma drives a current which adds a poloidal component to the toroidal magnetic field, resulting in helical lines (see Figure 4) that cancel the gradient effect: particles are confined and their trajectories explore both high and low field zones.

The plasma current is induced by transformer effect through the coupling between inner coils (further called in our work Central Solenoid or CS system, visible in Figure 4): the current variation in CS generates by mutual induction a current in the plasma. This current creates the above-mentioned poloidal field component and heats the plasma by Joule effect. The later effect is not sufficient to reach the reaction temperature but contributes to it; it has to be assisted by additional heating systems (e.g. electromagnetic antennas). Once established, the plasma current is maintained by induction with CS.

The described TF and CS systems are further complemented by the system of Poloidal Field (PF) coils which are located on the edge of the TF outer envelope (see Figure 4) and which drive the plasma control by imposing, at each moment of the scenario, the most appropriate plasma magnetic field configuration to maintain the plasma stability. As an example of the PF coils roles, the uppermost PF coil is mainly devoted to plasma initiation (start of plasma expansion).

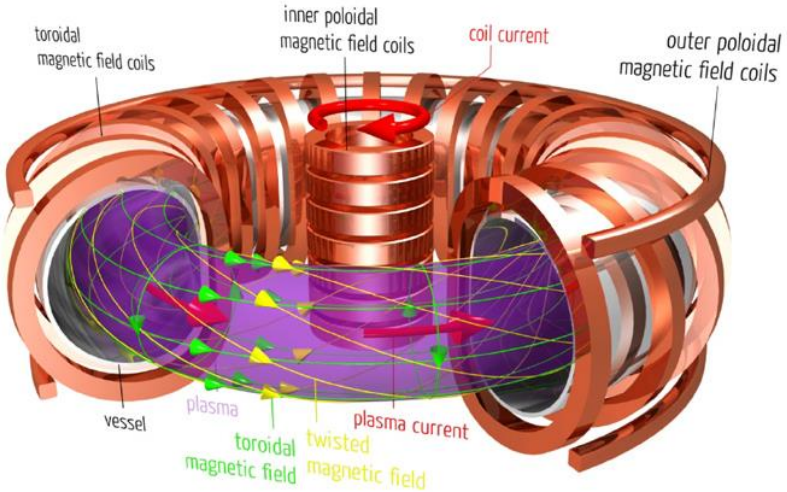

Figure 4 : General magnetic field configuration of a tokamak. The purely toroidal field lines (green) and the twisted field lines (yellow) derived from combination with plasma self-field, are shown. Toroidal Field Coils and Poloidal Field Coils are also shown. Here CS and PF systems are respectively figured by "inner poloidal magnetic field coils" and "outer poloidal magnetic field coils"

We have already stressed at this stage that, among the three systems presented, CS and PF ones are pulsed (i.e. they generate a time varying magnetic field). Since these two systems are major drivers regarding the plasma burn duration and stability (which are crucial for the operation reliability), it is important to note that the robustness of the pulsed magnet system must be ensured in a tokamak. This is a point supporting the rationale of our research work.

I.3 Superconductivity

The superconductivity aspect is a major characteristic of fusion magnets since the ultimate goal of a tokamak is to produce a net electric power; the "balance of plant" aspect is then of central importance. In an illustrative approach, the plasma magnetic field (which drives fusion power) being of substantial amplitude (order of few teslas) and being established in large volumes (e.g. 840 m^3 for ITER), the energy

stored in magnet system is expected to be high. If the magnets were resistive, the electrical power needed to energize them and maintain this configuration would be so high that the global power balance would become negative and therefore hopeless for any economic model.

Superconducting technology is consequently unavoidable in the large scale fusion electricity endeavor and should therefore be considered as a key component for technical and scientific knowledge mastering.

The basic principles of superconductivity are described below together with the particularities attached to the fusion technology.

Superconductivity is characterized by the two main properties of the material when in superconducting state:

1. The zero value of its resistivity inside its volume.
2. The zero value of the magnetic field inside its volume (Meissner effect).

The property evoked at first point (zero resistivity) derives from a specific interaction between electrons and the crystalline network, resulting into a perturbation of their wave function that allows electron pairing and further on their mobility into the crystalline network without interaction with this latter (no collision between them i.e. no Joule effect). We will not enter into details of these considerations that are out of the scope of this work, but as an example the BCS theory [2] well describes the physics underlying this phenomenon.

Note that the present resistive property is not absolute as in reality the superconducting state is valid in a domain limited by upper values of three driving parameters: the temperature, the magnetic field and the current density. An example of superconducting state operational domain limits is illustrated in Figure 5.

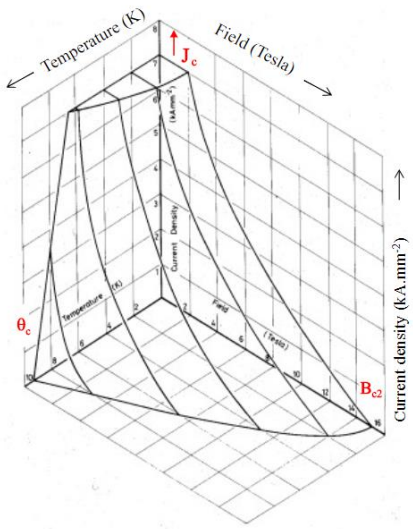

Figure 5 : Critical surface for NbTi material (see [3]). The absolute B and T limit parameters (critical field and critical temperature) are shown in red.

These considerations on limits will not be considered in the present work as attached to the current transport properties in DC regimes, while our scope is to deal with currents induced in AC regimes. However it should be kept in mind that in transient conditions the critical properties are the main drivers for anticipating the stability limits in given conditions. As a matter of fact the AC shielding phenomena will induce local variations of the three above-mentioned parameters and therefore impose (B, T, J) excursions possibly out of the critical surface.

In addition, the property evoked at second point (full expulsion of magnetic field, i.e. Meissner effect) will not be considered in our work since large magnets are using type-II superconductors which are in their mixed state during operation (state in which the Meissner effect does not apply anymore). We will nevertheless consider that our material is always in superconducting state regarding its resistivity.

Furthermore, a point should be made clear: since the supercurrents that shield the superconductor from any magnetic field – i.e. corresponding to the Meissner effect – will not be considered in our work, we will exclusively use the expressions “screening currents” or “shielding currents” throughout the present manuscript to designate the currents induced by a magnetic field variation – i.e. corresponding to Lenz’s law.

In our work the application of superconductivity principles will be implemented in the specific environment of fusion magnets, which embeds specific technology and faces specific operational loads; both will be subject of the next section.

I.4 Fusion magnets: Tokamak operation context and CICC technology

As previously mentioned the magnet system is a major component of a tokamak and therefore was subject to continuous R&D programs aiming at establishing the most adapted design for the present but also future tokamaks. Since the way to power production requires large tokamaks (fusion power exponentially increases with size) the projection lies in heavily energized magnets, i.e. carrying high currents and subject to high mechanical constraints.

As an illustration to the context where the work takes place, we here describe more features on ITER project. ITER (acronym standing for International Tokamak Experimental Reactor) will be the largest tokamak ever built and will be operated at St Paul-lez-Durance near CEA site in France. The reactor will be built and operated in the framework of an international collaboration which has also been involved since several decades in the fusion research program related to all components of a tokamak, including magnets.

The main scope of ITER is to ultimately demonstrate a maintained combustion of a deuterium-tritium plasma over long durations (typically 1000 seconds) and with a net fusion power balance gain (the ratio between extracted and injected energy) situated between 5 and 10.

ITER will be the first machine including and operating the major technologies requested for the exploitation of a commercial fusion reactor: superconductivity, plasma-facing components, tritium breeding components, robotics maintenance and diagnostics.

An illustration of this tokamak can be seen in Figure 6.

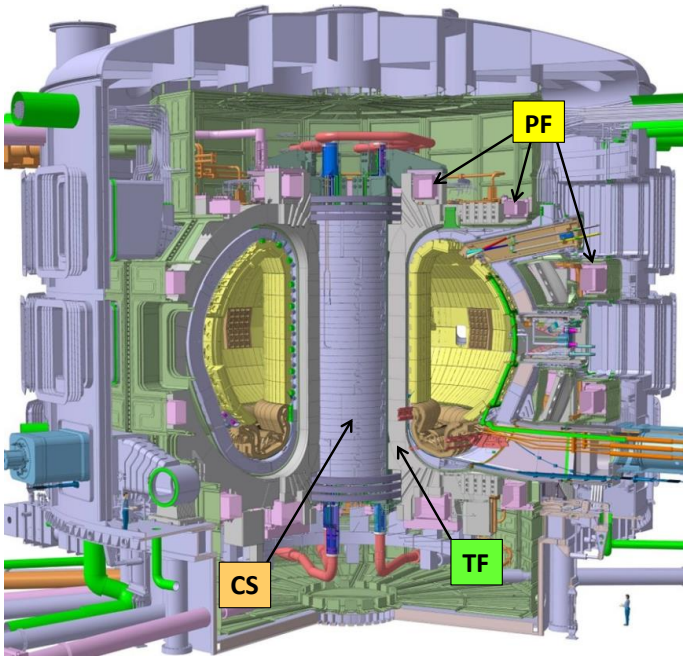

Figure 6 : ITER tokamak 3D cut view. TF, CS and PF magnet systems are indicated.
Three PF coils out of the six are pointed by arrows. Human scale at bottom right figures the machine size.

The ITER magnet system conductors are based on a specific technology: the Cable-In-Conduit Conductor or CICC. This technology is particularly adapted to the main constraints faced by ITER magnets: high currents injected, high magnetic field on conductors and therefore large mechanical loads on conductors.

The CICC concept main features are:

- A cable made up of a large number of strands twisted in multiple stages. The strands can be of different natures (superconducting versus copper) and with different sizes (diameter). A lot of combinations of patterns can be included at each stage (bundles with different number of strands twisted together).

- Some stages can be wrapped into thin metallic sheets to ensure their compaction and increase the inter-stage resistance.

- Cooling channels can be inserted into the cable usually under the form of spirals or tubes. Their role is, when hydraulic lengths are important, to relieve the pressure drop while still keeping the cable cooling capacity.

- An external thick metallic jacket into which the cable is drawn. The role of this jacket is to confine the coolant (helium), ensuring a forced circulation and therefore a more efficient wetting of the superconducting strands. But the jacket mainly serves as structural material for absorbing the high mechanical efforts developed in the coil. It avoids the cable plasticization and the need for delicate technologies such as reinforced strands. On the other hand the external jacket eases the insulation integration into the winding, and knowing that ITER coils can experience high voltages during currents discharge, this point is also beneficial.

An illustration of typical ITER CICCs is shown in Figure 7.

Figure 7 : Two ITER CICC illustrations: (left) view of CS conductor, round cable in square jacket; (right) exploded view of TF Model Coil [4] cable, with wrapped petals and central spiral

The smallest integrated element of the CICC is the superconducting strand. The strand provided for fusion is of composite type, i.e. it is composed of a mix of different metallic alloys integrated with the superconducting material. The metallic part acts as thermal stabilizer, mechanical embedding matrix and possible support for surface treatment (coating).

The two categories of superconducting material located in the strands are:

- The NbTi, alloy composed of Niobium and Titanium, bears the advantage of being insensitive to mechanical strain, and thus is quite adapted for any forming step (twisting, bending etc…) in the magnet manufacturing. The NbTi can be used up to magnetic field of about 11T at temperature of 1.8 K (superfluid helium).
- The Nb_3Sn, alloy composed of Niobium and Tin, can be operated at much higher fields (about 25 T at 4.2 K) and therefore is unavoidable for projects with such requirements (large tokamaks). This material is obtained after a specific heat treatment that triggers the chemical formation of a superconducting phase. The drawback of this material is that, after heat treatment, it bears a sensitivity to mechanical deformation, that directly impacts (reversibly but at a certain point irreversibly) the critical performances. It should therefore in most cases be formed before the heat treatment (always before cabling and mostly before forming) and consequently can require large ovens. The complexity of the fabrication process and the demanding QA steps result in a much higher price of Nb_3Sn compared to NbTi.

In all strands the superconducting material is embedded into a metallic matrix, mostly composed of copper, whose role is to stabilize the superconductor against local perturbations thanks to its heat absorption capacity. In case of quench, it allows to temporarily delay the discharge of the energy stored in the magnet (thanks to the current deviation from superconductor to copper) until the external protection circuit is activated. Finally, it allows a good conduction from coolant to superconducting material and therefore further contributes to its stability. Other metals can also be integrated, serving as resistive barrier or anti-diffusion barrier.

Some views of superconducting strands are shown in Figure 8.

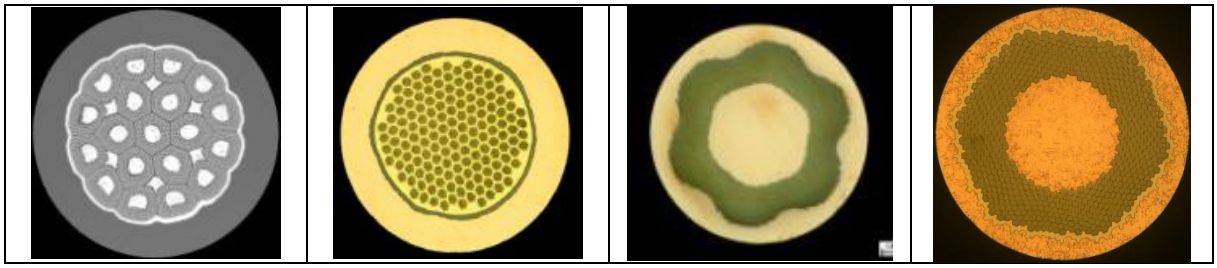

Figure 8 : Different types of superconducting strands for fusion magnets.
From left to right: ITER Nb_3Sn internal tin type; ITER Nb_3Sn bronze route type; ITER NbTi; JT-60SA NbTi

As an example of selected superconducting material, in ITER project the TF and CS coils experiencing about 12-13 T, the Nb_3Sn is chosen. Conversely, the PF coils experiencing about 5-6 T, the NbTi is selected. For JT-60SA project, since the TF system maximum field is about 6 T, NbTi is used.

The strand integration into a CICC follows a specific cabling process: strands are twisted into multiplets (e.g. triplet, including 3 strands), then multiplets are twisted, forming the second stage bundle, next, the second stage bundles are twisted, forming the third stage bundle, and so on. Following this process the cable may contain any number of stages (e.g. 5 stages for ITER). An illustration of cable manufacturing steps can be seen in Figure 9.

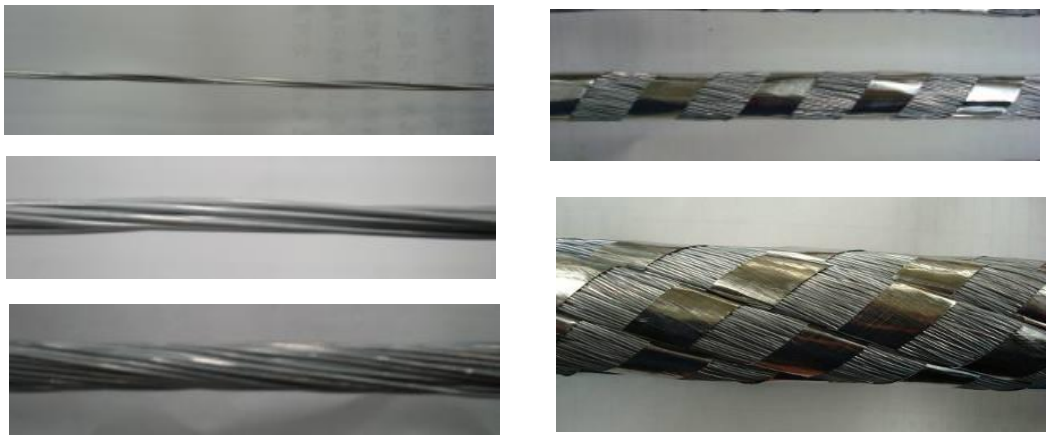

Figure 9 : Examples of successive cabling stages for ITER CICC. Note the addition of wrappings at the 4th stage

Apart from ITER and JT-60SA, the CICC technology has already been integrated in several other tokamaks such as EAST (CN) and KSTAR (KR) and other fusion installations such as W7-X (DE) [5] and LHD (JP) [6]. The tokamak JT-60SA (which stands for "Japanese Tokamak 60 Super Advanced"), which will shortly be operational, also uses CICC technology (see [7]).

Although the CICC technology has been developed for many years in accordance with the fusion magnet needs, it still presents risks which are intrinsic to any superconducting magnet: the appearance of instability possibly leading to a quench, i.e. the rapid transition from superconducting state to resistive state of the whole cable. Given the high values of energy stored in the magnets, the release of this energy remains a serious issue as it can irreversibly induce degradations and lead to underperforming magnets.

Going more in depth into those sources of instabilities while in tokamak operation context, the CICCs can be subject to various load prone to trigger transitions from superconducting to resistive state.

They can be of diverse nature:

- increase of current density (J), that can be due to an uneven distribution of currents inside the cable (e.g. bad connections quality).
- increase of temperature, that can be caused by an external heating source (e.g. thermal shield failure, vacuum loss) or internal one (e.g. current partially entering resistive part of superconducting strand).
- increase of magnetic field, that can be caused by e.g. uneven current distribution leading to local field inhomogeneities.
- decrease of critical properties, that can be due to local damage of superconductor bulk (e.g. caused by superconductor filament fracture due to mechanical load).

In the present work we pay attention to specific instability sources: those coming from the pulsed variations of magnetic field, leading to the establishment of shielding currents in the CICC, triggering both local heating sources and local current density increase.

As a matter of fact, in order to ensure a stable plasma regime, the tokamak operation requires rapid variations of current in the CS and PF systems. As an example, the typical variations of CS and PF are illustrated in Figure 10.

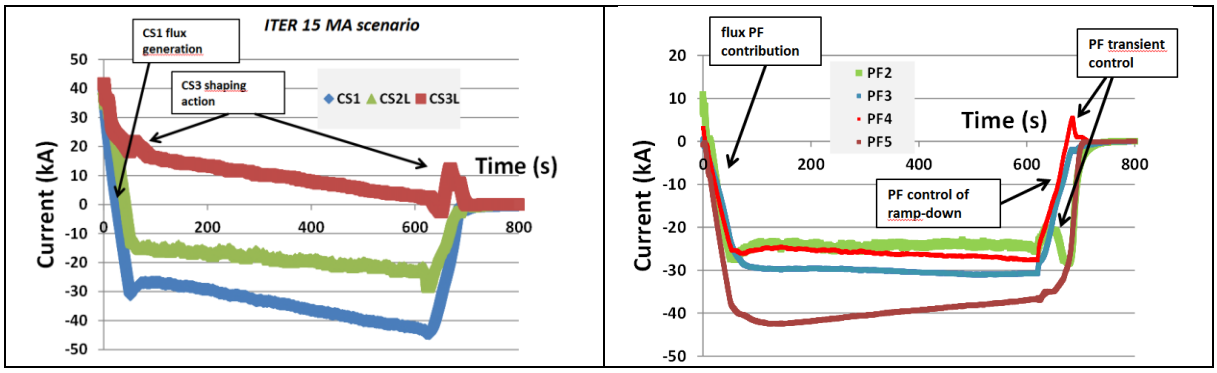

Figure 10 : Examples of ITER transient current variations in CS (left) and PF (right) system. The data refer to ITER baseline 15 MA scenario.

These rapid current variations (and thus those of magnetic field on conductor) being requested to ensure the tokamak operation (e.g. CS breakdown step necessary to initiate the plasma before ramping its current up), it is of high importance to assess that they do not systematically induce conductor instabilities as this would lead to an inoperable tokamak.

It is clearly seen here that the mastering of knowledge about the evaluation of consequences issued from the shielding current and their associated heat loads, stands as an important point regarding the establishment of a secured fusion magnet design.

I.5 Thesis content and associated strategy

During the above-mentioned transient field variations the shielding currents trigger both local heating sources (called AC losses) and local over-currents, impacting the stability limit of the conductor. In our work we consider the only AC losses due to shielding currents flowing in the resistive part, that are called **coupling losses**. However when CICCs are considered, the ab-initio evaluation of those coupling losses is extremely difficult as it combines multiple sources of complexity:

- the coupling currents flow along the strands, but strands trajectories in CICC are difficult to know since the combination of twisting stages and cable compaction makes it almost unpredictable

- the shielding currents redistribute in the volume by crossing between strands and therefore establish inhomogeneous current 3D distribution in a medium whose discontinuous nature adds difficulties for representing the shielding effect

- the coupling currents locally heat and deposit their power through their path inside strands and across resistive connections between strands. These resistive paths being highly dependent on the inter-strand contact physics, which is non-linear and hardly known, severe difficulties are encountered for developing a model

The possible approaches for representing this behavior are of two types: analytical or numerical. Fusion community has attempted to address the item through both ways:

- On one side the numerical approach consists in representing, in the more relevant way possible, the 3D strands (or bundle of strands) network, figuring then its resistive (strands intersections) and inductive (strands mutual coupling) components. The basic equilibrium equations (Maxwell equations) are then applied to define at any moment the current in any part of the network. Summing up the local heat loads one can then deduce the thermal perturbation imposed to the

conductor and can attempt to determine the distance to unstable regimes. The advantage of this approach is that it can be conducted down to the smallest scale, leading to a diagnostic considering the smallest local effects. Furthermore a predictive approach can be attempted since any design can in principle be treated. On the other hand difficulties are also present with this approach, for instance the challenge of relevance when representing a complex system containing a large number of interacting elementary units, or for large size magnets, the heavy model setting process and the demanding CPU time for calculations. In the fusion community EU working groups are involved in such approach, for example using the THELMA [8] or JackPot [9] codes (see further in the document).

- On the other side the analytical approach is relying on the representation of heat load by analytical expressions, dependent on conductor characteristics (e.g. cable time constant, see further) and on the magnetic field variation. The usual approach (the "single time constant" approach) consists in a simplification of the conductor shielding effect using analogies with classical models of transient behavior of superconducting composites. Indeed, in this approach, a single time constant, which is the parameter used to classically characterize the coupling losses at strand scale (see reference books [10], [11]), is used to represent the coupling losses at conductor scale. The single time constant approach then assumes that, although bearing substantial topologic differences, the conductor behaves similarly as a strand. The large majority of analyses on AC losses at the conductor scale follows this method ([12]-[16]). In addition, two models deviate from this "strand-like" analogy. A heuristic one, called MPAS [17], considers that the coupling between the different cabling stages can be represented with several weighted time constants: its ability to represent the experimental reality has been established, but it is not a predictive model as the time constants it considers have to be determined from AC losses measurements at different frequencies. The other one [18] provides analytical formulae of coupling currents and losses inside conductors from its electrical and geometrical features: it is then a predictive model, but it does not take the coupling between the induced currents into account, and therefore its validity domain is restricted to slowly time varying magnetic fields. The advantage of these analytical models lies in their high versatility of integration into simulation tools (e.g. thermo-hydraulic codes); they also consume low CPU resources and thus allow a broad variety of explorations (e.g. different magnetic field variations for MPAS). On the other hand their associated drawback is the macroscopic nature of their parameters and thus their strong dependence on experimental curves (AC losses energy per cycle versus frequency); as a result, their capacity of prediction is strongly limited for cable designs other than already existing ones (except for [18], but whose domain of prediction is restricted to slowly time varying magnetic fields).

The advantages and disadvantages of the already existing approaches are summarized in Table 1. In this table, we have divided the existing approaches in three main categories: analytical, heuristic and numerical. The analytical and heuristic approaches are both based on the use of analytical expressions but our distinction between them lies in their origins. Indeed, we consider as analytical the approaches that have been derived from electromagnetic equations while we consider as heuristic the ones that have been derived from observations of experimental results and/or from the extension of an existing analytical modeling outside of its initial frame. In addition, for better readability of the table, we have chosen to make use of the plus signs to provide a nuanced appreciation of the accuracy of the results obtained by the different methods.

As an example, the first line of Table 1 indicates that the Multistage cable model [18]

- has been derived from electromagnetic equations
- can predict the coupling losses of a CICC from measurements of its electrical and geometrical parameters and well matches the experimental results
- requires very light computation given its analytical and explicit nature
- provides relatively detailed information on the induced coupling currents
- but is not valid for every magnetic regimes encountered in tokamaks (here, the model is not valid for fast transient magnetic regimes)

Table 1

	Valid for every magnetic regimes in tokamaks	Prediction of losses from measured features of CICC	Light computing time	Information on coupling currents
Analytical approach				
Multistage cable model (CEA)	☒	☑++	☑+++	☑++
Heuristic approach				
«$n\tau$» approach (most common) *one time constant*	☒	☒	☑+++	☒
MPAS model (CEA, used at ITER) *several time constants*	☑	☒	☑+++	☒
Numerical approach				
THELMA code (University of Bologna, IT)	☑	☑+++	☒	☑+++
JackPot code (University of Twente, NL)	☑	☑+++	☒	☑+++
Our objective	☑	☑+	☑++	☑+

The purpose of the present work is to develop a model that would somehow stand between [17] and [18], thus trying to initiate a bridge between both approaches while remaining at the same time in the analytical approach category.

The key point of our strategy is to keep using analytical tools to establish a CICC coupling losses model, but which deviates from the single time constant approach and from the MPAS model since we consider the CICC electrical and geometrical features as departure point instead of the experimental AC

losses results. Our strategy is then similar to that of [18], except that our intention is to establish models whose domain of validity is the largest possible, i.e. we aim at covering all possible transient regimes regardless of their dynamics with respect to the system time constants (see Table 1). This is an important objective as we will try to represent the magnetic shielding effects of a cable in tokamak configuration, thus subject to a broad variety of magnetic field regimes (see section I.4).

To achieve this aim, our progress strategy is based on a scale by scale approach:

- First step is conducted at the smallest elementary unit bearing coupling losses: the strand. At **strand scale,** a generalization of the analytical coupling model is conducted, also standing as a toolbox for the larger scales.

- Second step is carried out at cable stage, but with the simplest description of a cable, i.e. an assembly of single bundles. Here too the generalization to any transient regime is targeted. This step as **single stage scale** also stands as toolbox for the next step.

- Third step is still located at cable stage but integrates an additional geometrical complexity, i.e. it considers **two cabling stages** with independent twist pitches. This step allows the improvement of the relevance of the modeling, considering a second degree of detail in the cable architecture.

Along the progress across those different steps, continuous confrontation will be carried out between the results of our analytical approach and those of previously developed models, i.e. the ones presented in Table 1. In addition, throughout this manuscript we have chosen to include the demonstrations leading to our analytical results since our methodology differs from the ones used in the previous models. Our objective is thus not only to present our analytical results, but also to share the methodology that has led us to them.

Nevertheless, being aware that these complex and long analytical demonstrations can make the reader lose the thread of the work presented in this manuscript, their objective and location will be presented schematically in the "methodology" section of each scale (strand, single stage and two cabling stages). In order to further enhance the readability of this document, the objective will be recalled to the reader at the beginning of each demonstration.

II. Superconducting composites

Content: This part is dedicated to the presentation of a general analytical modeling of coupling losses in superconducting composites and its associated algorithm. Experimental work (AC losses measurements) on strands is also presented as well as comparisons with other analytical models.

Associated publications:

- A. Louzguiti, L. Zani, D. Ciazynski, B. Turck, F. Topin, *Development of an Analytical-Oriented Extensive Model for AC Coupling Losses in Multilayer Superconducting Composite*, I.E.E.E. Trans. on App. Superconductivity, Vol. 26, April 2016, Art. No. 4700905. (reference [40])
- A. Louzguiti, L. Zani, D. Ciazynski, B. Turck, F. Topin, *Modélisation analytique de la puissance thermique générée par les courants de couplage à l'intérieur d'un composite supraconducteur*, Actes du Congrès de la Société Française de Thermique (SFT), Mars 2017, 8 p. (reference [41])

II.1 Presentation

II.1.1 Architecture

Superconducting composites are majorly encountered in conductors of large superconducting magnets which are needed in tokamaks or particle accelerators. Although their average diameter is less than a millimeter, they present a specific and quite complex layout.

Composites are cylindrical and made of several superconducting filaments (from a few dozens to several thousands) whose diameter lies in the range of a dozen of microns; these filaments are lightly twisted (usually with a twist pitch lying in the 15-25 mm range) and are located in what is known as the filamentary zone of the composite. In this filamentary zone, we also find a metallic - thus resistive - matrix which fills every space between the filaments.

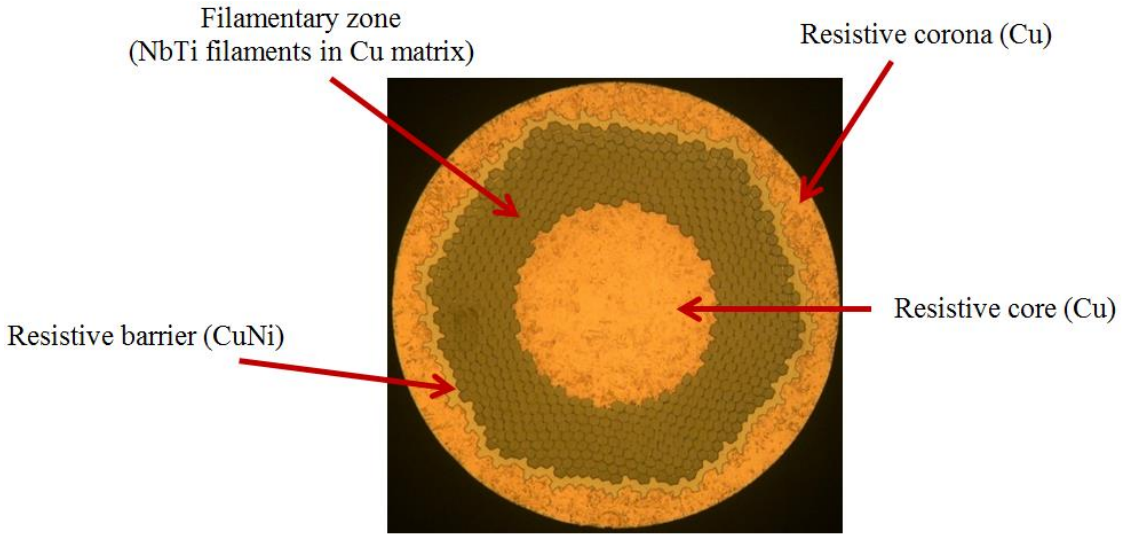

Figure 11 : Detailed architecture of a JT-60SA TF conductor strand (0.81 mm diameter)

In addition to the filamentary zone, composites may also feature a copper core and multiple external resistive layers. The layer located just after the filamentary zone is often called “resistive barrier” as it consists of a more resistive material (e.g. CuNi); its role is to reduce both the intrastrand and interstrand coupling losses [19]. The most outer one(s) are again made of copper. All these layers are visible on Figure 11 and Figure 12.

Filamentary zones of Nb_3Sn composites appear to be slightly different from the ones of NbTi composites as the filaments are gathered in bundles (see Figure 12) instead of being uniformly spread over the zone; this is due to their different fabrication process.

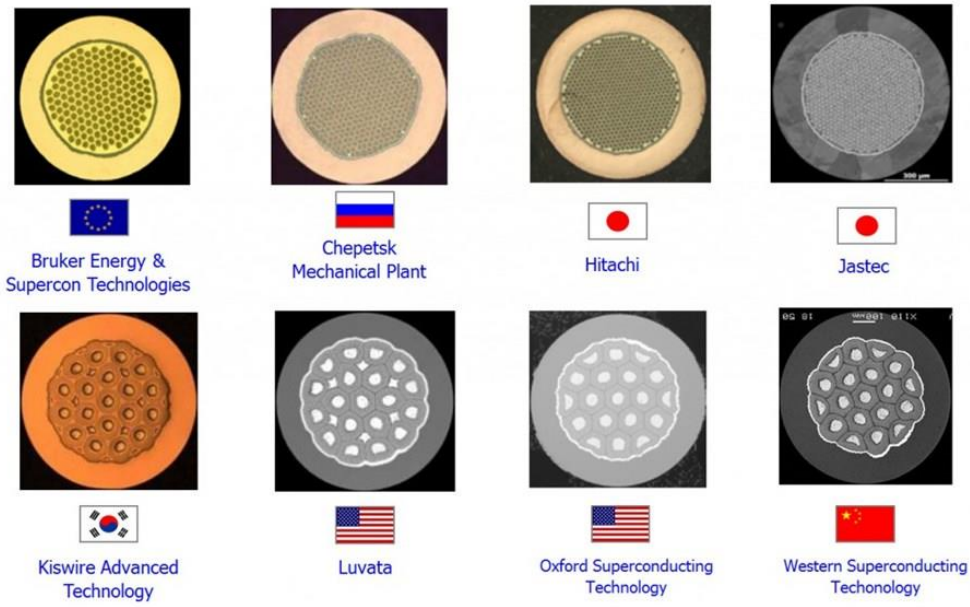

Figure 12 : Examples of different designs of NbTi (above) and Nb_3Sn (below) superconducting composite

The need for these specific types of architectures essentially arises from the necessity to protect the composites against stability issues.

Indeed, instabilities occur when the local temperature in the superconductor exceeds its critical value; the local increase of temperature can be caused by hysteresis losses. Therefore, in order to enhance the protection of the superconductor against instabilities, it is recommended to subdivide the superconductor into several small filaments instead of having one large filament for at least two reasons:

- the hysteresis losses per unit volume of superconductor increase with the filament diameter [10]; therefore the total losses and associated heat are smaller when the superconductor is divided into several small filaments
- for a given volume of superconductor, the total exchange surface – and thus the cooling – is enhanced if the total volume is divided into several small volumes

Furthermore, the omnipresence of copper inside superconducting composites is needed for several reasons. Indeed, thanks to its very good thermal and electrical conductivity, it enhances the stability of the composite by:

- tentatively providing another path for the transport current in case of a local transition; this other path is less resistive than the superconductor in its normal state and thus corresponds to a lower

local Joule heating. The superconducting filament may then have enough time to cool down and recover its superconducting state.
- improving the cooling effect provided by the refrigerating fluid because its thermal conductivity is higher than that of superconductors

Finally, twisting the filaments is an efficient way to reduce the intrastrand coupling losses since the magnetic flux they enclose cancels out every twist pitch; this prevents then the appearance of very strong current loops that would exceed the critical current of the filament and generate very strong ohmic losses at the ends of the composite when subject to an external time varying magnetic field.

II.1.2 State of the art on coupling losses modeling at composite scale

Before presenting a synthetic historical review and discussion of the previous work accomplished on the coupling losses issue at strand scale, we will provide a brief reminder of the different losses generated inside superconducting composites under magnetic AC regimes.

When multifilamentary strands are subject to a time-varying external magnetic field, they develop currents in specific zones to shield themselves from this magnetic variation following Lenz's law. The induced currents are flowing through the different materials present in the composite and are due to magnetic shielding at different scales:

- The superconducting filament develops its own peripheral currents to shield itself from any magnetic variation; the local critical current density Jc is then temporarily outreached in the outer region of the filament which enters into the flux flow regime and thus develops a local resistivity. The excess current density (difference between the local current density and Jc) will decay because of the local resistivity, and the magnetic variation will penetrate deeper into the filament leading also to the penetration of screening currents. Once the local current density has fallen to the local Jc, it persists indefinitely because of the zero resistivity of the superconductor and the filament develops then persistent magnetization currents. The total ohmic losses generated during the transient flux flow regime correspond to the "hysteresis losses"
- The filamentary zone (containing a large number of superconducting filaments embedded in a resistive matrix) develops a supercurrent flowing in its outer edge filaments to shield its enclosed volume. This supercurrent will loop back by crossing the resistive matrix and the resistive layers of the composite : this will generate the so-called "coupling losses"
- All the copper present throughout the composite also participates in the magnetic shielding of the whole composite by carrying other screening currents classically known as eddy currents whose associated ohmic heating are simply named the "eddy currents losses"

As described in the previous section, each of these currents directly threatens the superconductor with a transition into its normal state (flux jump) : first, because of the creation of local heat sources inside (hysteresis losses) and outside (coupling and eddy currents losses) the superconductor, secondly because the induced currents (magnetization and coupling currents) will cumulate with any current already carried by the filament (transport current), thus creating another local heat source if the superconductor enters transitorily into the flux flow regime.

AC losses therefore play a major role in the composite stability, for this reason they have been deeply investigated since the 70's ([20]-[37]).

A complete study both theoretical and experimental [20] has provided an important insight of the behavior of superconducting composites with respect to an external time-varying magnetic field. The derivation of the magnetization of the composite due to currents shielding the superconductor (i.e. magnetization currents) and shielding the entire composite (i.e. coupling currents) is shown together with the calculation of their associated losses: hysteresis losses and an approximation for the coupling losses for composites in coil configuration. The experimental results are in reasonable agreement with the developed theory.

In the same time period, Morgan [21] has improved the coupling losses modeling by giving the complete time-dependent equation of a system composed of two filaments embedded in a copper matrix. For a composite containing a large number of filaments, as it is usually the case, the two-filament approach seems inappropriate and is then replaced by a macroscopic model considering a supercurrent flowing through outer edge filaments and looping back across the resistive matrix. The supercurrent is supposed to have a cosine distribution in the cross section of the composite, i.e. of the form $K = K_0\cos(\theta)$ with θ the radial angle and K_0 the amplitude of the current per unit length; this distribution is legitimated by the fact that it will produce an internal uniform magnetic field in the opposite direction of the applied field. The value of K_0 is then given as a function of the time-variation of the external magnetic field B_a when the supercurrent is not time varying, i.e. when $\dot{K}_0 = 0$ (the overdot notation refers to the time derivative). The external or applied magnetic field B_a is defined as the magnetic field that would exist in the volume of the composite if the composite was removed (or if any shielding effect occurring inside the composite was omitted).

Following this work, Carr [22] and Ries [23] have pushed the modeling of coupling losses one step further by providing the macroscopic behavior of a composite composed of a central filamentary zone and a copper sheath subject to a transverse magnetic field for any time regime. Even though they have derived it with two different approaches, the same homogeneous representation of the filamentary zone is used. In his studies, Carr has summarized the electrical properties of the composite in an effective transverse conductivity for which he has given approximate formulae for the two extreme values of the filament-to-matrix contact resistance [24]. This method provides an efficient way to calculate the coupling currents across the resistive matrix and offers then the possibility to represent the response of the composite at its scale instead of the filament one. His treatment refers to the shielding accomplished by classical resistive conductors together with considerations on the frequency domain of the applied magnetic field and the associated skin depths while the alternative approach provided by Ries makes use of the effective transverse conductivity to promptly derive the relation verified by the internal magnetic field; we will thus here discuss the outcomes of the latter one.

For the sake of simplicity, the notation F will refer to a composite consisting in a filamentary zone only, F/R to composite with a filamentary zone and an outer resistive layer, F/R/R to a composite with a filamentary zone and two outer resistive layers and so on. For example, all composites present on Figure 12 are represented by F/R/R as they are composed of - starting from their center - a filamentary zone, an outer resistive barrier and a copper layer and the layout of the JT-60SA composite on Figure 11 will then be referred to as R/F/R/R (copper core, filamentary zone, resistive barrier and outer copper layer).

For a composite composed of a central filamentary zone only (F) or with an outer copper layer (F/R), the induction B_i inside the filamentary zone is governed by the first-order differential equation

$$B_i + \tau\dot{B}_i = B_a \tag{1}$$

where B_a is the magnitude of the transverse applied magnetic field, $\dot{B}_i$ is the time derivative of B_i and τ is the time constant of the system whose expression is

$$\tau = \frac{\mu_0}{2}\left(\frac{l_p}{2\pi}\right)^2 \frac{1}{\rho_t} \tag{2}$$

with l_p the twist pitch of the filaments and ρ_t the effective transverse resistivity (inverse of the effective transverse conductivity mentioned above).

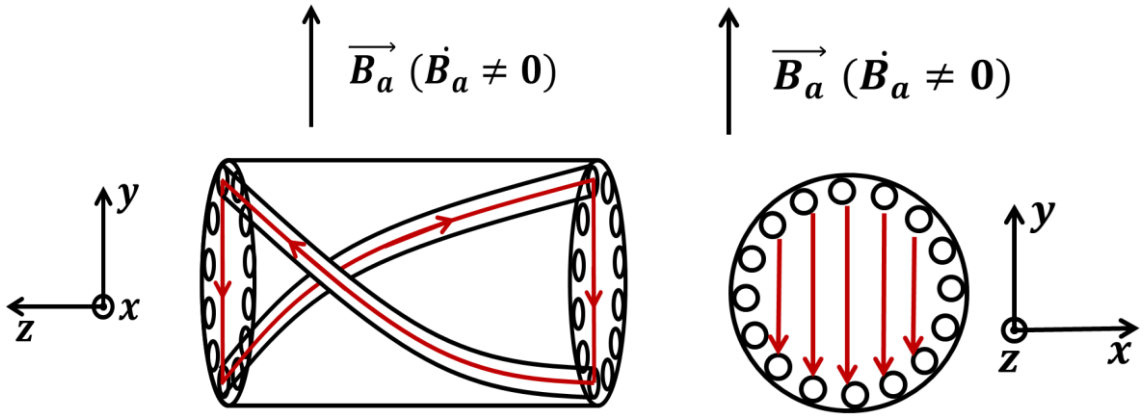

(a) : Longitudinal view (b) : Cross-section view

Figure 13 : Schematic views of coupling currents inside the filamentary zone (only outer edge filaments are represented)

It is interesting to note that equation (1) is valid for both F and F/R, the only difference between them lies in the formula of ρ_t, which in the first case is the effective transverse resistivity of the filamentary zone while in the second one, it is a combination of the effective transverse resistivity of the filamentary zone and of the transverse resistivity of the outer layer. In fact, in the case of F/R, the outer resistive layer is seen as another path for coupling currents flowing in the outer edge filaments to loop back (see Figure 14); therefore the total effective conductivity can be expressed as a weighted sum of the transverse conductivities of the two zones since they are in parallel.

To push this idea further, we can also take a look at composites with a central filamentary zone surrounded by several resistive layers. Turck has made a detailed investigation on this issue [25] and provided the analytical method and formulae enabling the description of the response of composites with layouts ranging from F/R to F/R/R/R to a transverse magnetic field. He has quantitatively shown that a cupronickel barrier surrounding the filamentary zone was significantly reducing the coupling losses. Indeed, the resistivity of the copper sheath being usually lower than the effective matrix resistivity of the filamentary zone, the flow of the coupling currents through the copper sheath can be responsible for a major part of the dissipated energy if the sheath is thick. The local resistance created by the cupronickel barrier enhances the average resistance of the alternative path and thus reduces the coupling losses. For composites with several outer resistive layers, the expression of the time constant of the composite given by equation (2) is still valid provided that the total effective resistivity is computed again with the taking into account of the radii and resistivities of the outer layers.

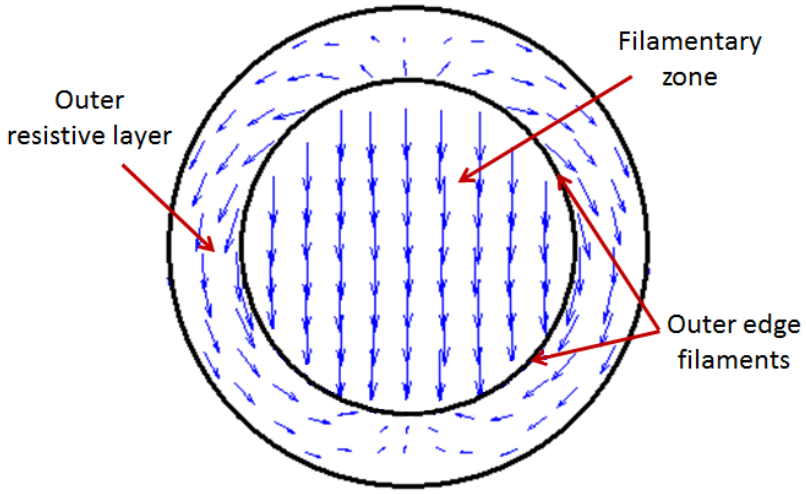

Figure 14 : Coupling currents flowing in the outer edge filaments looping back using the filamentary zone and the outer resistive layer in the case of a F/R composite

The next step is of course to compute the coupling power dissipated in the whole composite. In order to do so, two methods giving the same results can be used.

The first one is simply to integrate the Joule power density $\vec{J}.\vec{E}$ over the whole volume, with $\vec{J}$ the local coupling current density flowing through the resistive parts and $\vec{E}$ the local electric field. The other one is to compute the magnetization M inside the filamentary zone and then to integrate the local density power $-M\dot{B}_i$ over the volume.

Both methods give the following power per unit volume of filamentary zone [10] (see discussion below)

$$P = \frac{n\tau \dot{B}_i{}^2}{\mu_0} \tag{3}$$

with $n = 2$ for a cylindrical composite.

Before going any further, a point should be made clear: for composites consisting in a filamentary zone only (F types), the only part were coupling currents will generate ohmic power is of course the filamentary zone, while for composites of types F/R/…/R (central filamentary zone surrounded by one or several resistive layers) the coupling currents will not only dissipate energy inside the filamentary zone but also in the outer resistive layers. Therefore, one must not misunderstand equation (3) : P corresponds to the power dissipated in the whole composite divided by the volume enclosed by the outer edge filaments (which will often be referred to as "volume of filamentary zone" by abuse of language). This expression has only been chosen for its schematic and simple view.

If we now apply a sinusoidal external magnetic field $B_a = B_p \sin(\omega t)$, with $\omega = 2\pi f$ the angular frequency, using (1) we obtain in complex notations

$$\bar{B}_i = \frac{B_p e^{j\omega t}}{1 + j\omega\tau} \tag{4}$$

Then we can readily give the internal magnetic field amplitude $|\bar{B}_i|$ as

$$|\bar{B}_i| = \frac{B_p}{\sqrt{1 + (\omega\tau)^2}} \tag{5}$$

Using (3), the associated power density P averaged over time (after a time long compared to τ) will then be

$$P = \frac{{B_p}^2}{2\mu_0} \frac{n\tau\omega^2}{1+(\omega\tau)^2} \tag{6}$$

As a matter of fact, we see from equation (5) that the composite will behave as a low-pass filter with regard to the external magnetic field: its low frequency components will penetrate through the composite while its high ones will be completely shielded by the outer edge filaments. This leads to the conclusion that the power dissipated by hysteresis inside the filaments will also depend on the frequency: at high frequencies, the applied transverse field will partly be shielded by the outer edge filaments so that the internal filaments will see a smaller excursion of the magnetic field and thus dissipate less energy.

In addition, equation (6) indicates that the coupling power density P will rise as f^2 in the low frequency domain and will become constant reaching its maximum for frequencies higher than $1/(2\pi\tau)$ as indicated in [22].

As it is widely used within the applied superconductivity community, we can also express the losses in terms of average losses per cycle Q per unit volume (of filamentary zone); this can be done very quickly multiplying P by the period T of the cycle. Using (6), we have

$$Q = \frac{{B_p}^2}{2\mu_0} \frac{2\pi n\tau\omega}{1+(\omega\tau)^2} \tag{7}$$

Of course these considerations and formulae are relevant only to the coupling losses generated by a transverse field and assume that the outer edge filaments are not saturated and that the composite is not carrying any transport current. In case of saturation, we would need to add the penetration losses corresponding to the work done by the variation of the magnetic field in the saturated filaments on the outer edge which is very similar to hysteresis losses in a single filament but at strand scale [23]. Regarding the impact of a transport current on these losses, it has been investigated both theoretically [21],[26] and experimentally [27],[28] but we will not detail its nature here.

From an experimental point of view, Kwasnitza [29] has measured Q vs f curves for a transverse sinusoidal applied magnetic field up to roughly 15Hz for composites featuring different twist pitches - from 5 to 50 mm. He has experimentally highlighted the global dependence of the time constant of the composite as $1/{l_p}^2$ (with l_p the twist pitch of the filaments) as indicated by equation (2), the time constant being here determined by the maximum of each Q vs f curve. The $Q(f=0)$ values deduced from linear fittings of the measured Q vs f curves in the low frequency domain are all equal to the same value which corresponds to the hysteresis losses per cycle.

According to equation (7), the curve of losses per unit volume per cycle Q versus the angular frequency ω of the sinusoidal applied magnetic field (curve referred to as "Q vs f curve" thereafter) will exhibit a maximum at $\omega = 1/\tau$ and its initial slope will be proportional to $n\tau$. In other words, this means that for composite containing only one filamentary zone located at the center of the strand (F/R/…/R types), the time constant τ of the system can be determined using one method or the other.

However a precision is needed on this point. Indeed, let us note B_{react} the reacting magnetic field generated by the supercurrent flowing in the outer edge filament. This field will be proportional to the

previously mentioned K_0 (amplitude of the cosine supercurrent distribution) and, by superposition, we can say that the internal field B_i is the sum of the applied field B_a and of the reacting magnetic field B_{react}, therefore : $B_i = B_a + B_{react}$. Equation (1) states that $B_i + \tau \dot{B}_i = B_a$ so, replacing B_i with $(B_a + B_{react})$, we obtain $B_a + B_{react} + \tau\left(\dot{B}_a + \dot{B}_{react}\right) = B_a$ which leads to

$$B_{react} + \tau \dot{B}_{react} = -\tau \dot{B}_a \quad (8)$$

where the $-\tau \dot{B}_a$ term can be seen as the exciting magnetic field while the $\tau \dot{B}_{react}$ one reflects the self-induction.

It is important to point out the fact that τ is present on both sides of equation (8), but it does not have the same meaning at all. In fact, the τ on the left-hand side reflects the coupling of the supercurrent with itself and therefore really corresponds to the definition of time constant of a system; it refers to the time needed for the induced supercurrent to relax when the applied field B_a is no longer time-varying (i.e. when the exciting magnetic field $-\tau \dot{B}_a$ is zero). Actually it exactly corresponds to the "L/R" time constant of a RL circuit, L being the self-inductance and R the resistance. On the other hand, the τ present on the right-hand side of equation (8) reflects the coupling between the supercurrent and the external source generating the applied field B_a: it therefore does not answer to the definition of time constant of a system, it can alternatively be seen as "M/R" where M is the mutual inductance between the supercurrent and the external source and R the resistance which is here the same as for the RL circuit. The only reason why the τ on both sides of (8) are equal here is because both the field B_{react} created by the supercurrent and the applied field B_a are uniform and oriented along the y-axis in the volume enclosed by the supercurrent: the self-inductance L of the supercurrent and the mutual inductance M between the supercurrent and the external source have then here the same value. It thus explains why it is possible to measure the time constant of a composite in steady-state or slowly time-varying regimes even though the composite cannot express its own time constant in these regimes.

This point is a very important one as today it is not unusual to encounter values of the "$n\tau$" parameter - measured on Q vs f curves of conductors - used to deduce the conductor response for regimes other than steady-state ones. This "$n\tau$" parameter is determined from the initial slope of the measured Q vs f curve by analogy with the F or F/R composite; indeed in the low frequency region, i.e. for $\omega\tau \ll 1$, equation (7) indicates that the Q vs f curve becomes linear with a slope equal to $2\pi^2 {B_p}^2 n\tau/\mu_0$.

As a matter of fact, well before reaching the conductor scale, it could be misleading to use the "$n\tau$" value deduced from the initial slope of the Q vs f curve to extrapolate the response of some composites (e.g. featuring a copper core, as the one displayed on Figure 11) at higher frequencies. Indeed, at the beginning of the 80's, Ciazynski has studied the coupling losses occurring in a R/F/R composite [30] and has shown that the internal induction B_i could not be modeled by equation (1). In reality, in addition to the supercurrent flowing through the outer edge filaments, another supercurrent is flowing in the inner edge filaments; the classical description with a single time constant is therefore no longer valid. To model the behavior of these supercurrents, one has to replace the time constant τ with a two-by-two matrix containing four time coefficients which reflect the electromagnetic coupling (self and mutual) between the supercurrents; the new time constants of this system are the eigenvalues of the previous matrix. Ciazynski has derived the expressions of the four time coefficients and the equation governing the supercurrents for any time regime. He has also expressed the power dissipated by the coupling currents but only for slowly time-varying regimes.

As a consequence, when trying to model the response of the JT-60SA TF conductor strand which is of R/F/R/R type (Cu core, filamentary zone, CuNi barrier and outer Cu layer, see Figure 11) for regimes other than very slowly time-varying ones, we have realized that there was not any analytical solution to

this problem in the literature. This is due to the fact that the design of composites has kept evolving because of the more and more challenging environment strands have to face (e.g. larger superconducting tokamaks) while the analytical modeling of coupling losses has been abandoned in favor of numerical modeling.

Accordingly we have decided to develop a general analytical modeling of coupling losses generated inside composites featuring any number of concentric layers of any nature (filamentary or resistive) in order to

- provide the community with an exhaustive model able to thoroughly describe the magnetic behavior of any cylindrical composite
- open the way for the study of the composites stability thanks to the ability of the model to generate detailed cartographies of the power density with very low CPU consumption
- create a tool able to rationally design superconducting composites with respect to their coupling losses and their magnetic environment

This general analytical model is presented in the next section.

II.2 Development of the Coupling Losses Algorithm for Superconducting Strands

In this section, we will present the analytical model we have used to determine the main physical fields and the coupling losses induced in any axisymmetric composite. The outputs of this model are used to build the Coupling Losses Algorithm for Superconducting Strands (CLASS) which aims at modeling the magnetic response of a composite to any transverse and uniform magnetic excitation.

II.2.1 Methodology

First of all, we will here describe the methodology we have used to model the response of a composite to a time-varying transverse and uniform magnetic field. The nature of this problem could be assimilated to the eddy currents one except that the superconducting parts (filaments) of the composite play a major role and induces strong differences. Indeed, they have a zero electric field in their volume when they are not saturated; therefore they will impose multiple boundary conditions in the composite since each filament will exhibit an equipotential in its whole volume.

In a classical holistic approach of the problem, we would start by considering a conductor of resistivity ρ subject to a time-varying magnetic field and derive the equation governing its behavior. If we apply the curl operator on both sides of Maxwell-Faraday equation $\vec{\nabla} \times \vec{E} = -\dot{\vec{B}}$; we then obtain

$$\vec{\nabla} \times \left(\vec{\nabla} \times \vec{E}\right) = -\vec{\nabla} \times \dot{\vec{B}}$$

which gives, using Maxwell-Ampère equation $\vec{\nabla} \times \vec{B} = \mu_0 \vec{J}$ (the displacement current is considered here to be negligible, see assumption A6 after)

$$\vec{\nabla}\left(\vec{\nabla}.\vec{E}\right) - \vec{\Delta}\vec{E} = -\mu_0\dot{\vec{J}}$$

If we add the local Ohm's law $\vec{E} = \rho\vec{J}$, we now have

$$\vec{\Delta}\vec{J} - \frac{\mu_0}{\rho}\dot{\vec{J}} = \vec{0} \tag{9}$$

Therefore the induced currents are governed by a classical diffusion equation. However due to the presence of the multiple boundary conditions imposed by the superconductor and the complex geometry (helicoids) of the filaments, this approach seems to be too complex to analytically solve the problem.

Consequently we propose an alternative vision based on the determination of the spatial form of the induced currents; this approach will be used in all our analytical studies at each scale of a superconducting cable (from a single composite to any multi-stage bundle).

When a conductor is subject to a time-varying magnetic field B_a, we know that a set of currents will be induced to shield the conductor from this magnetic variation. We can then virtually split the shielding currents; indeed, a part of these currents can be seen as shielding the time-variation of the magnetic field B_a produced by an external source while the other part of the induced currents will try to shield the time-variation of the magnetic field B_{react} produced by all the induced currents (the B_{react} field can then be seen as a kind of self-field).

Our method aims at determining the spatial form of the induced currents using the logical chain displayed on Figure 15: $\dot{\overrightarrow{B_a}}$ creates an electric field $\overrightarrow{E^{(1)}}$ which gives rise to a spatial distribution of currents $\overrightarrow{J^{(1)}}$ which in turn produces a magnetic field $\overrightarrow{B^{(1)}}$. The time-variation of $\overrightarrow{B^{(1)}}$, i.e. $\dot{\overrightarrow{B^{(1)}}}$, creates $\overrightarrow{E^{(2)}}$ which generates a distribution of currents $\overrightarrow{J^{(2)}}$ which in turn produces a magnetic field $\overrightarrow{B^{(2)}}$ and so on.

Let us assume that the spatial distribution of currents $\overrightarrow{J^{(k)}}$ can be modeled using a linearly independent family of N_k spatial functions $\left(f_1^{(k)}, f_2^{(k)}, \dots, f_{N_k}^{(k)}\right)$ and let us call this family $F^{(k)}$, this means that we can write $\overrightarrow{J^{(k)}}$ at every point of space M and at every instant t as

$$\overrightarrow{J^{(k)}}(M,t) = \sum_{i=1}^{n_k} a_i^{(k)}(t) f_i^{(k)}(M)$$

where $\left(a_i^{(k)}\right)_{1\le i\le n_k}$ are functions of time only and $\left(f_i^{(k)}\right)_{1\le i\le n_k}$ are the spatial functions constituting the $F^{(k)}$ linearly independent family.

By definition, the time-variation of $\overrightarrow{J^{(k)}}$, i.e. $\dot{\overrightarrow{J^{(k)}}}$, creates the new distribution $\overrightarrow{J^{(k+1)}}$ which can be modeled using the linearly independent family of spatial functions $F^{(k+1)}$, this means that the time-variation of each element $a_i^{(k)}(t) f_i^{(k)}(M)$ of $\overrightarrow{J^{(k)}}$ will produce a sub-distribution which can be expressed using the spatial functions of $F^{(k+1)}$. Our iterative process then stops as soon as the family $F^{(N)}$ of spatial functions of the distribution $\overrightarrow{J^{(N)}}$ is included in the families $\left(F^{(k)}\right)_{1\le k\le N-1}$ of spatial functions of the previous distributions $\left(\overrightarrow{J^{(k)}}\right)_{1\le k<N}$, i.e. when $F^{(N)} \in \left(F^{(1)} \oplus F^{(2)} \oplus \dots \oplus F^{(N-1)}\right)$.

Indeed, since $F^{(N)}$ is included in the $\left(F^{(k)}\right)_{1\leq k\leq N-1}$ families, we can express $\overrightarrow{J^{(N)}}$ using the spatial functions of the $\left(F^{(k)}\right)_{1\leq k\leq N-1}$ families, i.e. $\overrightarrow{J^{(N)}}$ can be expressed as a linear combination of the $\left(a_i^{(k)}(t)f_i^{(k)}(M)\right)_{1\leq i\leq n_k,1\leq k\leq N-1}$ elements. However, the time-variation of these elements can, by assumption, only produce sub-distributions that can be expressed using the spatial functions of the $\left(F^{(k)}\right)_{1\leq k\leq N}$ families, thus of the $\left(F^{(k)}\right)_{1\leq k\leq N-1}$ families since $F^{(N)}$ is included in the $\left(F^{(k)}\right)_{1\leq k\leq N-1}$ families. We immediately conclude that the $\overrightarrow{J^{(N+1)}}$ distribution generated by $\dot{\overrightarrow{J^{(N+1)}}}$ can be expressed using the spatial functions of the $\left(F^{(k)}\right)_{1\leq k\leq N-1}$ families only. Applying the same logic to any $\overrightarrow{J^{(N+p)}}$ with p a positive integer, we deduce that every $\left(\overrightarrow{J^{(k)}}\right)_{k\geq 1}$ can be expressed using spatial functions of the $\left(F^{(k)}\right)_{1\leq k\leq N-1}$ families only.

When the N^{th} iteration is reached we are then sure to have found all the spatial functions required to model the global distribution of induced currents (in other words, all the spatial modes) and the linearly independent family F of all the spatial functions is $F=\left(F^{(1)}\oplus F^{(2)}\oplus ...\oplus F^{(N-1)}\right)$; this means that the global distribution of induced currents $\vec{J}=\sum_{k=1}^{N}\overrightarrow{J^{(k)}}$ must be of the form

$$\vec{J}(M,t)=\sum_{i=1}^{n_F}a_i(t)f_i(M) \tag{10}$$

where $(a_i)_{1\leq i\leq n_F}$ are functions of time only and $(f_i)_{1\leq i\leq n_F}$ are the n_F spatial functions constituting the linearly independent family F.

Note that there can be cases where N is equal to infinity, meaning that new spatial functions will be involved at each iteration, it is therefore not possible to find them all in a finite number of iterations. However, even in this situation, it may be possible to quickly identify the nature of the spatial functions that will be involved in the next iterations. When this occurs we can also say that we have reached the end of our analytical procedure as soon as we have identified the nature of the functions induced at each new iteration.

This analytical iterative procedure is very useful as it enables us to find the spatial form of the induced currents; it can be seen as another way for solving the Laplacian of equation (9). The main difference between both methods lies in the fact that we only consider the spatial modes that will be excited, while the solving of the Laplacian will disclose all the allowed spatial modes, even those that will not be excited because of the spatial form of the external applied magnetic field.

As a consequence we will always be able to suppose a solution to equation (9) under the form given by (10) which will then simply be reduced to a first-order differential equation in time on the $(a_i)_{1\leq i\leq N_F}$ functions of (10).

It is important to point out that our logical procedure does not correspond to what physically occurs inside a conductor when shielding its volume. As a matter of fact, all distributions $\left(\overrightarrow{J^{(k)}}\right)_{k\geq 1}$ are induced at the same time and our decomposition is a simple view of the mind of the magnetic shielding effect; it therefore does not reflect the order of occurrence of the different shielding effects.

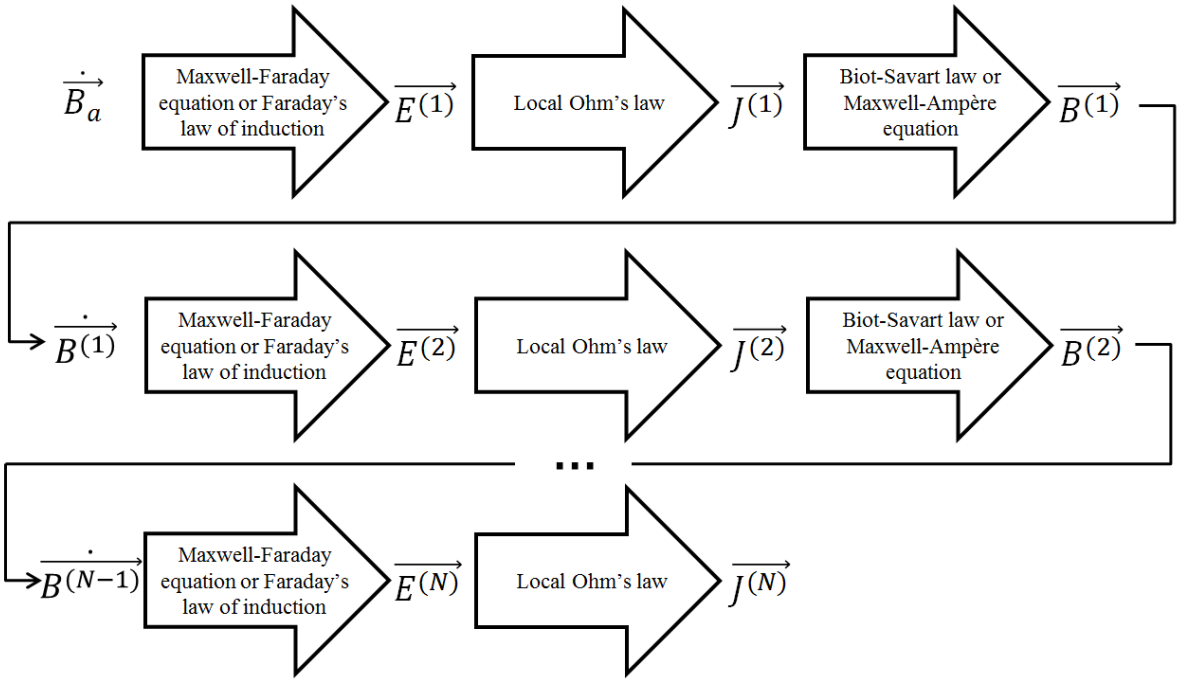

Figure 15 : Logical chain of calculation of induced currents

As a result, when trying to analytically find the spatial form of the induced currents, we will always begin by a study in regimes where all the induced currents are not time-varying.

First because the solution provided by this study can be extended to commonly encountered regimes where the applied magnetic field B_a is slowly time-varying (e.g. when ramp-up time is long compared to the largest time constant of the system) and secondly, because this solution provides the current distribution $\overrightarrow{J_1}$ needed in our logical chain. By abuse of language the regimes where all the induced currents are not time-varying will be referred to as "steady-state regimes" in the following. Note that in these regimes, the applied magnetic field B_a is supposed to be time varying.

We have followed this methodology during the study at composite scale and we present here a schematic summary of the analytical content of this study (as mentioned in section I.5):

- **In section II.2.3 we establish the expression of the electric field due to the time variation of the applied magnetic field $\overrightarrow{B_a}$ and we then deduce the distribution of currents induced in the composite in steady-state regime**
- **In section II.2.4 we express the magnetic field generated by the distribution of current found in steady-state regime (at the end of section II.2.3). We then compute the new distribution of current induced by the time variation of this magnetic field. Finally, we combine these results to those of section II.2.3 to establish the equation of the composite for any time regime**
- **In section II.2.5 we evaluate the shielding made by the outer copper sheath and we discuss the saturation of filaments**
- **In section II.2.6 we compute the power generated by coupling currents as a function of coefficients, previously introduced in section II.2.3**
- **In section II.2.7 we express the currents and the electric and magnetic fields in the composite as a function of the previous coefficients**

❖ **In section II.2.8 we establish the expression of coupling losses as a function of the previous coefficients. We also demonstrate that the coupling losses generated inside complex composites can be expressed as a sum of the coupling losses generated inside simple composites; this result is important and will be used in the study of a two cabling stages conductor**

II.2.2 Assumptions

The main assumptions used in our model are the classical ones:

A1. The system is invariant by translation along the composite axis (z-axis, see Figure 16)

A2. The external magnetic field B_a is assumed transverse (along the y-axis, see Figure 16) and spatially uniform within the composite

A3. The composite does not carry any transport current

A4. The filaments are not saturated, i.e. $\overrightarrow{E_s} = \vec{0}$ in the filaments, with s the longitudinal direction along the filaments. This relation is extended to the whole filamentary zone with the commonly used [10],[23],[25], [30] homogeneous representation presented in [22]

A5. The filaments are lightly twisted, i.e. $\left(\frac{2\pi R}{l_p}\right)^2 \ll 1$ where R is the composite radius and l_p is the twist pitch of the filaments

A6. The time variation of the external magnetic field B_a is slow enough to neglect the displacement current so that $\vec{\nabla}.\vec{\jmath} = 0$ where $\vec{\jmath}$ is the current density inside the composite

A7. The time variation of the external magnetic field B_a is also slow enough to ensure that the copper sheath does not magnetically shield its enclosed volume

The following Maxwell's equation $\vec{\nabla} \times \vec{B} = \mu_0 \vec{\jmath} + \mu_0 \varepsilon_0 \dot{\vec{E}}$ can be reduced to $\vec{\nabla} \times \vec{B} = \mu_0 \vec{\jmath}$ if the displacement current is negligible compared to the current flowing inside the composite (assumption A6). This leads to the following condition:

$$\frac{\mu_0 \varepsilon_0 \left\|\dot{\vec{E}}\right\|}{\mu_0 \left\|\vec{\jmath}\right\|} = \frac{\varepsilon_0 \left\|\dot{\vec{E}}\right\|}{\left\|\vec{\jmath}\right\|} \ll 1$$

Using the complex notations we can write $\left\|\dot{\vec{E}}\right\| \sim \left\|\vec{E}\right\| 2\pi\omega$ with ω the angular frequency. Inside the composite, Ohm's law states that $\vec{E} = \rho\vec{\jmath}$ with ρ the local resistivity, therefore $\frac{\left\|\dot{\vec{E}}\right\|}{\left\|\vec{\jmath}\right\|} \sim \rho\omega$.

The previous condition becomes then $\varepsilon_0 \rho\omega \ll 1$, or alternatively, using $\omega = 2\pi f$

$$f \ll \frac{1}{2\pi\varepsilon_0\rho}$$

If we consider the cupronickel resistivity which is within the $10^{-7}\Omega.m$ range (usually the highest one in the composite), $2\pi\varepsilon_0\rho$ is then within the $10^{-17}s$ range.

Consequently, we can neglect the displacement current as long as

$$f \ll 10^{17}Hz$$

The classical range of frequencies of magnetic variation considered for coupling losses being largely inferior to $10^{17}Hz$, we can legitimately reduce the previous Maxwell's equation to

$$\vec{\nabla} \times \vec{B} = \mu_0 \vec{\jmath}$$

In addition, since mathematically $\vec{\nabla}.(\vec{\nabla} \times \vec{B}) = 0$, we can conclude that $\vec{\nabla}.\vec{J} = 0$; assumption A6 is then justified.

Assumption A7 will be considered later because we first need to introduce some analytical tools to justify it.

In our approach, conversely to the configurations explored in the previous analytical models that were limited in number and/or nature of layers, we allow ourselves to consider any of the possible configurations: composite whose cross-section consists of n circular concentric layers (see Figure 16) either filamentary (i.e. superconducting filaments embedded in a resistive matrix) or purely resistive.

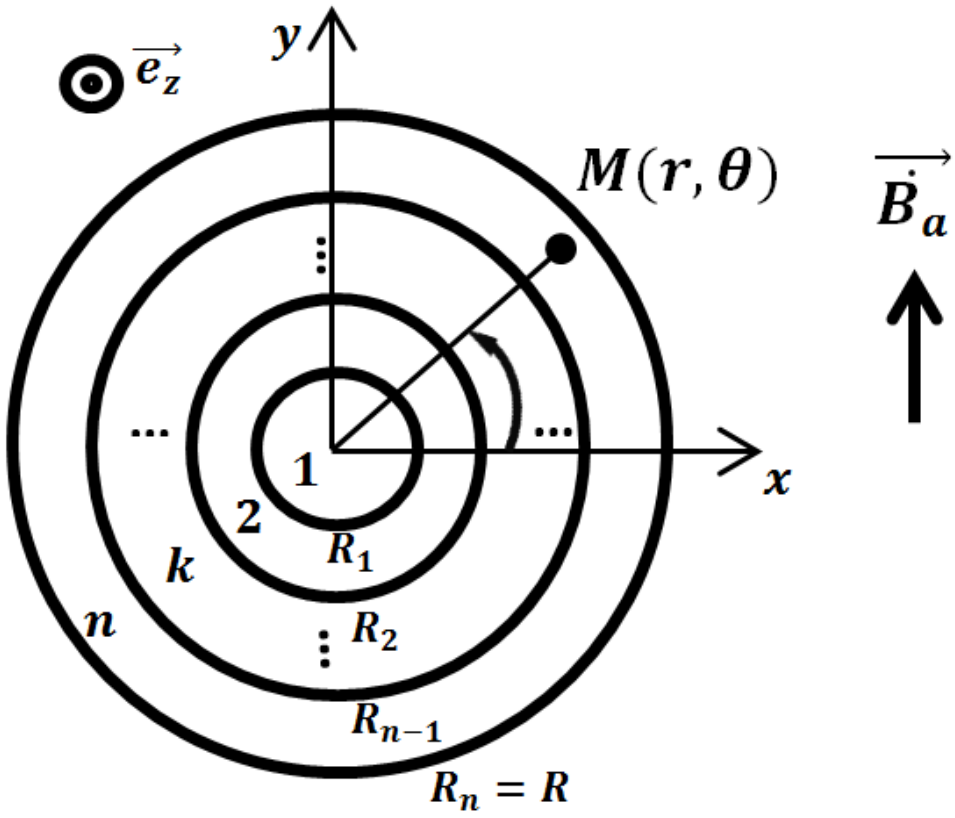

Figure 16 : Scheme showing the generic cross-section geometry of composites considered by our model

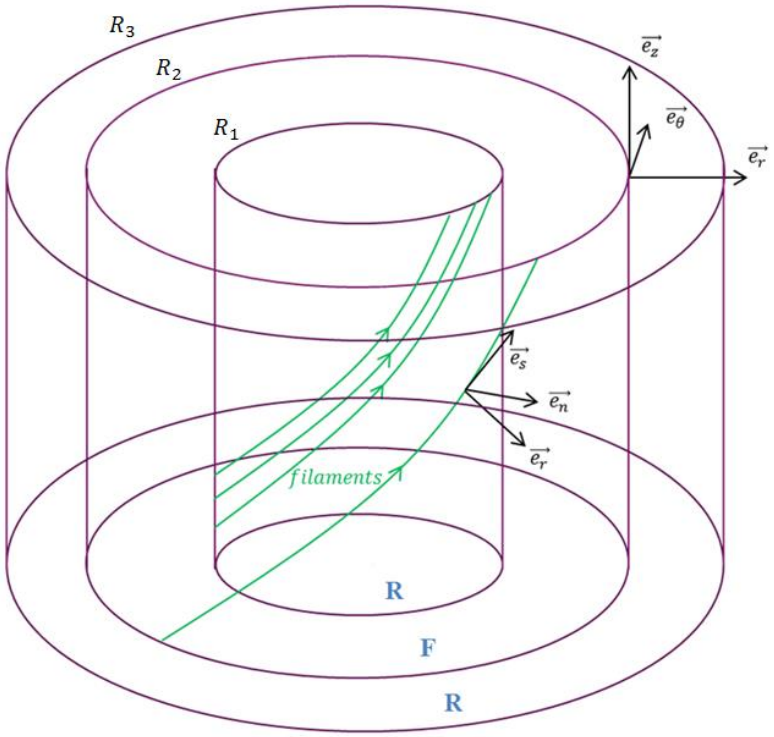

Figure 17 : Scheme showing the trajectories of filaments and their associated local frame $(\vec{e_r}, \vec{e_n}, \vec{e_s})$ inside a R/F/R strand

The trajectory followed by each filament is a helix of radius r and constant pitch l_p, whose center is the center of the composite. The local geometric coordinate system associated to each filament is curvilinear and described by $(\vec{e_r}, \vec{e_n}, \vec{e_s})$ which relates to the cylindrical coordinate system $(\vec{e_r}, \vec{e_\theta}, \vec{e_z})$ as

$$\vec{e_r} = \vec{e_r} \quad (11)$$

$$\vec{e_n} = cos\alpha\ \vec{e_\theta} - sin\alpha\ \vec{e_z} \quad (12)$$

$$\vec{e_s} = sin\alpha\ \vec{e_\theta} + cos\alpha\ \vec{e_z} \quad (13)$$

with α the angle between $\vec{e_z}$ and $\vec{e_s}$

α satisfies then the relation

$$tan\alpha = \frac{2\pi r}{l_p} \quad (14)$$

Since all the filaments are inside the composite we have $r < R$ and thus $tan\alpha < \frac{2\pi R}{l_p}$.

Using assumption A5, we then deduce

$$tan^2\,\alpha \ll 1 \quad (15)$$

II.2.3 Study in steady-state regime

❖ **We will derive here the electric field due to the time variation of the applied magnetic field $\overrightarrow{B_a}$ and we will then deduce the distribution of currents induced in the composite in steady-state regime.**

By superposition, we can express the magnetic field $\vec{B}$ inside the composite as $\vec{B} = \overrightarrow{B_a} + \overrightarrow{B_{react}}$ with $\overrightarrow{B_a}$ the applied magnetic field and $\overrightarrow{B_{react}}$ the reacting magnetic field created by the induced currents flowing through the composite. Since by assumption the induced currents are not time-varying (we recall that the term "steady-state regime" refers to a regime where the induced currents are not time-varying.), neither is the reacting magnetic field, then $\dot{\overrightarrow{B_{react}}} = \vec{0}$ ($\vec{0}$ is the null vector).

As a result, Maxwell-Faraday equation $\vec{\nabla} \times \vec{E} = -\dot{\vec{B}}$ gives here

$$\vec{\nabla} \times \vec{E} = -\dot{\overrightarrow{B_a}} \tag{16}$$

The expression of this equation in cylindrical coordinates (r, θ, z) leads to the following system

$$\frac{\partial E_z}{\partial \theta} = -r\dot{B}_a \sin\theta \tag{17}$$

$$\frac{\partial E_z}{\partial r} = \dot{B}_a \cos\theta \tag{18}$$

$$\frac{\partial (rE_\theta)}{\partial r} = \frac{\partial E_r}{\partial \theta} \tag{19}$$

Equations (17) and (18) give

$$E_z = r\dot{B}_a \cos\theta + E_0$$

with E_0 a constant value (we consider here a steady-state regime).

In a cylinder made of a material of resistivity ρ, this longitudinal electric field would give rise to a longitudinal current $J_z = E_z/\rho$ whose average over the whole volume would be E_0/ρ. According to assumption A3, the average current should be zero; it follows that $E_0 = 0$. By analogy, E_z can then be reduced everywhere in the composite to

$$E_z = r\dot{B}_a \cos\theta \tag{20}$$

In each filamentary zone, the relation $\overrightarrow{E_s} = \vec{0}$ (coming from assumption A4) implies $E_s = 0$ which can be alternatively expressed as $\overrightarrow{E_r}.\overrightarrow{e_s} + \overrightarrow{E_\theta}.\overrightarrow{e_s} + \overrightarrow{E_z}.\overrightarrow{e_s} = 0$. Using equation (13), we then obtain

$$E_\theta sin\alpha + E_z cos\alpha = 0$$

Making use of equation (14), this is equivalent to

$$E_\theta = -\frac{l_p}{2\pi r} E_z \tag{21}$$

which, combined with (20), gives

$$E_\theta = -\frac{l_p}{2\pi}\dot{B}_a \cos\theta \tag{22}$$

Regarding the calculation of E_r, we first need to introduce another equation. According to the homogeneous representation (assumption A4), we can assign an effective transverse resistivity ρ_t to the filamentary zone; this implies $\overrightarrow{E_t} = \rho_t \overrightarrow{J_t}$ with $\overrightarrow{E_t}$ the transverse electric field and $\overrightarrow{J_t}$ the transverse current.

Since $\vec{\nabla}.\vec{J} = 0$ from assumption A6, we have $\vec{\nabla}.\left(\overrightarrow{J_t} + \overrightarrow{J_z}\right) = \vec{\nabla}.\left(\frac{\overrightarrow{E_t}}{\rho_t}\right) = \frac{1}{\rho_t}\vec{\nabla}.\left(\overrightarrow{E_t}\right) = 0$ because of the longitudinal invariance assumed by A1 (i.e. $\frac{\partial}{\partial z} = 0$). This gives the new equation

$$\vec{\nabla}.\overrightarrow{E_t} = 0 \tag{23}$$

In cylindrical coordinates, it can be reformulated as

$$\frac{\partial(rE_r)}{\partial r} + \frac{\partial E_\theta}{\partial \theta} = 0 \tag{24}$$

Together with (19) and (22), we can deduce

$$E_r = -\frac{l_p}{2\pi}\dot{B}_a \sin\theta + \frac{V_0}{r} \tag{25}$$

with V_0 a constant value (we consider here a steady-state regime).

If the considered filamentary zone is central, we can readily conclude that V_0 must be zero in order not to obtain a divergent solution at $r = 0$; in the opposite case, we have to retain this value.

We have now calculated the expression of the transverse electric field in each filamentary zone and therefore now need to study that of each resistive zone.

Using the previously introduced notation $\overrightarrow{E_t}$ and equation (16), we can write $\vec{\nabla} \times \overrightarrow{E_t} = \vec{0}$ since $\overrightarrow{\dot{B}_a}$ is oriented along the y-axis; we can then conclude that there exists a scalar potential V_t such that

$$\overrightarrow{E_t} = -\vec{\nabla}V_t \tag{26}$$

Combining it with (23), it appears that in each resistive zone, V_t satisfies Laplace's equation

$$\Delta V_t = 0 \tag{27}$$

Let us note V_{t_k} the value of V_t in a resistive layer numbered k, since it is solution of (27), its general form must be

$$V_{t_k}(r,\theta) = \sum_{i=-\infty}^{\infty}[a_{k_i}\cos(i\theta) + b_{k_i}\sin(i\theta)]\, R_k(r/R_k)^i,\ a_{k_i} \in \mathbb{R},\ b_{k_i} \in \mathbb{R} \tag{28}$$

Note that the general formulation of V_{t_k} is chosen so that the a_{k_i} and b_{k_i} coefficients have the dimension of an electric field.

Injecting the expression of V_{t_k} into equation (26) yields the general forms of the components of the transverse electric field in each resistive zone

$$\begin{cases} E_{r_k} = -\sum_{i=-\infty, i\neq 0}^{\infty} \left[a_{k_i}\cos(i\theta) + b_{k_i}\sin(i\theta)\right] i(r/R_k)^{i-1} \\ E_{\theta_k} = \sum_{i=-\infty, i\neq 0}^{\infty} \left[a_{k_i}\sin(i\theta) - b_{k_i}\cos(i\theta)\right] i(r/R_k)^{i-1} \end{cases} \quad (29)$$

In order to complete the system, we must add the boundary conditions. First, at each interface between layers, the continuity of the azimuthal component of the transverse electric field E_θ between the layers k and $k+1$ can expressed as

$$E_{\theta_k}(R_k) = E_{\theta_{k+1}}(R_k) \quad (30)$$

Secondly, we have to consider Kirchhoff's current law; its expression depends on the nature of the interface (i.e. resistive/resistive, resistive/filamentary or filamentary/filamentary):

- For an interface of resistive/resistive type, Kirchhoff's current law requires the continuity of the radial component of the current density J_r

$$\frac{E_{r_k}(R_k)}{\rho_{t_k}} = \frac{E_{r_{k+1}}(R_k)}{\rho_{t_{k+1}}} \quad (31)$$

  where ρ_{t_k} is the transverse resistivity of the layer k.

- At an interface of resistive/filamentary or filamentary/filamentary type, Kirchhoff's current law must include the additional current flowing through the filaments located on the boundary so that it becomes

$$\frac{\partial K_{s_k}}{\partial \theta} = \frac{l_p}{2\pi}\left[\frac{E_{r_k}(R_k)}{\rho_{t_k}} - \frac{E_{r_{k+1}}(R_k)}{\rho_{t_{k+1}}}\right] \quad (32)$$

  where K_{s_k} is the surface current (i.e. in $A.m^{-1}$) flowing through all the filaments located at $r = R_k$.

If the composite is composed of at least one filamentary zone and one resistive layer, there will necessarily be an interface of resistive/filamentary type. Assuming layers k and $k+1$ are respectively resistive and filamentary, expressions (22) and (29) and equation (30) implies

$$\begin{cases} b_{k_{-1}} - b_{k_1} = -\frac{l_p}{2\pi}\dot{B}_a \\ a_{k_i} = 0, i \in \mathbb{Z}^* \\ b_{k_i} = 0, i \in \mathbb{Z}^*\backslash\{-1,1\} \end{cases} \quad (33)$$

since $\cos(i\theta)_{i\in\mathbb{N}^*}$ and $\sin(i\theta)_{i\in\mathbb{N}^*}$ are linearly independent families.

Assuming now that layers k and $k+1$ are respectively filamentary and resistive, we obtain

$$\begin{cases} b_{k+1_{-1}}\left(\frac{R_{k+1}}{R_k}\right)^2 - b_{k+1_1} = -\frac{l_p}{2\pi}\dot{B}_a \\ a_{k+1_i} = 0, i \in \mathbb{Z}^* \\ b_{k+1_i} = 0, i \in \mathbb{Z}^*\backslash\{-1,1\} \end{cases} \quad (34)$$

Therefore, in a resistive layer k in contact with a filamentary zone, the transverse electric field components will be of the form

$$\begin{cases} E_{r_k} = -\left[b_{k_{-1}}\left(\frac{R_k}{r}\right)^2 + b_{k_1}\right]\sin(\theta) \\ E_{\theta_k} = \left[b_{k_{-1}}\left(\frac{R_k}{r}\right)^2 - b_{k_1}\right]\cos(\theta) \end{cases} \tag{35}$$

since $b_{k_{-1}}$ and b_{k_1} are the only non-zero coefficients.

If we consider a resistive layer $k+1$ (resp. $k-1$) adjacent to another resistive layer k whose E_{r_k} and E_{θ_k} expressions are described by (35), boundary conditions (30) and (31) ensure that $E_{r_{k+1}}$ (resp. $E_{r_{k-1}}$) and $E_{\theta_{k+1}}$ (resp. $E_{\theta_{k-1}}$) expressions will also have the same form as (35), again because $\cos(i\theta)_{i\in\mathbb{N}^*}$ and $\sin(i\theta)_{i\in\mathbb{N}^*}$ are linearly independent families.

We have thus shown by induction that E_{r_k} and E_{θ_k} expressions in every resistive layer k of the composite will share the same form as (35).

Knowing the general form of the electric field in the resistive layers, we can now deduce from equation (32) that the surface current K_{s_k} flowing through the filaments located at $r = R_k$ (if at least one of the layers k and $k+1$ is filamentary) must be of the form $K_{s_k} = K_{0_k}\cos(\theta)$ because of the expressions of E_r in the filamentary and resistive zones. In addition, the V_0 term present in equation (25) must be zero in order to ensure assumption A3 (no transport current).

From this exhaustive study, we are now able to give the general expressions of E_{r_k}, E_{θ_k} and E_{z_k} in each layer together with those of K_{s_k} for steady-state regimes

$$\begin{cases} E_{r_k} = -\left[E_{0_{2k-1}}\left(\frac{R_k}{r}\right)^2 + E_{0_{2k}}\right]\sin(\theta) \\ E_{\theta_k} = \left[E_{0_{2k-1}}\left(\frac{R_k}{r}\right)^2 - E_{0_{2k}}\right]\cos(\theta) \\ E_{z_k} = r\dot{B}_a\cos\theta \\ K_{s_k} = K_{0_k}\cos(\theta) \end{cases} \tag{36}$$

In order to ease and bring some consistency to the notation we have replaced the $b_{k_{-1}}$ and b_{k_1} coefficients of a layer k respectively with $E_{0_{2k-1}}$ and $E_{0_{2k}}$ since they have the dimension of an electric field ($b_{k+1_{-1}}$ and b_{k+1_1} are thus now noted as $E_{0_{2k+1}}$ and $E_{0_{2k+2}}$ respectively).

We can now produce a short summary of the results achieved so far:

- If the layer k is filamentary, we have

$$\begin{cases} E_{0_{2k-1}} = 0 \\ E_{0_{2k}} = \frac{l_p}{2\pi}\dot{B}_a \end{cases} \tag{37}$$

- For an interface of resistive/resistive type located at $r = R_k$, boundary equations (30) and (31) enable us to write

$$\begin{cases} E_{0_{2k+1}} = \frac{1}{2}\left(\frac{R_k}{R_{k+1}}\right)^2\left(\frac{\rho_{t_{k+1}}}{\rho_{t_k}}+1\right)E_{0_{2k-1}} + \frac{1}{2}\left(\frac{R_k}{R_{k+1}}\right)^2\left(\frac{\rho_{t_{k+1}}}{\rho_{t_k}}-1\right)E_{0_{2k}} \\ E_{0_{2k+2}} = \frac{1}{2}\left(\frac{\rho_{t_{k+1}}}{\rho_{t_k}}-1\right)E_{0_{2k-1}} + \frac{1}{2}\left(\frac{\rho_{t_{k+1}}}{\rho_{t_k}}+1\right)E_{0_{2k}} \end{cases} \quad (38)$$

Or, alternatively

$$\begin{cases} E_{0_{2k-1}} = \frac{1}{2}\left(\frac{R_{k+1}}{R_k}\right)^2\left(\frac{\rho_{t_k}}{\rho_{t_{k+1}}}+1\right)E_{0_{2k+1}} + \frac{1}{2}\left(\frac{\rho_{t_k}}{\rho_{t_{k+1}}}-1\right)E_{0_{2k+2}} \\ E_{0_{2k}} = \frac{1}{2}\left(\frac{R_{k+1}}{R_k}\right)^2\left(\frac{\rho_{t_k}}{\rho_{t_{k+1}}}-1\right)E_{0_{2k+1}} + \frac{1}{2}\left(\frac{\rho_{t_k}}{\rho_{t_{k+1}}}+1\right)E_{0_{2k+2}} \end{cases} \quad (39)$$

- For an interface of resistive/filamentary type located at $r = R_k$ (i.e. layers k and $k+1$ are respectively resistive and filamentary), equation (30) together with expressions (36) and (37) now lead to

$$-E_{0_{2k-1}} + E_{0_{2k}} = \frac{l_p}{2\pi}\dot{B}_a \quad (40)$$

Alternatively, if the layers k and $k+1$ are interchanged, i.e. k is filamentary and $k+1$ is resistive, we have

$$-\left(\frac{R_{k+1}}{R_k}\right)^2 E_{0_{2k+1}} + E_{0_{2k+2}} = \frac{l_p}{2\pi}\dot{B}_a \quad (41)$$

- In order not to obtain a divergent solution at $r = 0$ we can deduce from expression (36) that

$$E_{0_1} = 0 \quad (42)$$

- If the ultimate layer is resistive, the radial current flowing at $r = R$ (i.e. $J_{r_n}(R)$) must be zero as not net current can escape the composite (if the ultimate layer was filamentary, this radial current could flow through the outer edge filaments). Consequently, since $E_{r_n}(R) = \rho_{t_n} J_{r_n}(R)$, we can conclude that $E_{r_n}(R) = 0$, and using (36)

$$E_{0_{2n}} = -E_{0_{2n-1}} \quad (43)$$

- Using equation (32) and the general form of E_{r_k} and K_{s_k} present in (36) we can also express each K_{0_k} (when they exist, i.e. on the edges of a filamentary zone) as a function of the $E_{0_{2k-1}}$, $E_{0_{2k}}$, $E_{0_{2k+1}}$ and $E_{0_{2k+2}}$ coefficients

$$K_{0_k} = \frac{1}{\rho_{t_k}}\frac{l_p}{2\pi}\left[E_{0_{2k-1}} + E_{0_{2k}} - \frac{\rho_{t_k}}{\rho_{t_{k+1}}}\left(\frac{R_{k+1}}{R_k}\right)^2 E_{0_{2k+1}} - \frac{\rho_{t_k}}{\rho_{t_{k+1}}}E_{0_{2k+2}}\right] \quad (44)$$

Note that in case the ultimate zone of the composite is filamentary, we have $J_{r_{n+1}}(R) = E_{r_{n+1}}(R)/\rho_{t_{n+1}} = 0$ (i.e. there is no current flowing outside the composite). Using equation (32) again, we see that equation (44) is also valid for $k = n$ after having removed $E_{0_{2n+1}}$ and $E_{0_{2n+2}}$, i.e.

$$K_{0_n} = \frac{1}{\rho_{t_n}}\frac{l_p}{2\pi}\left[E_{0_{2n-1}} + E_{0_{2n}}\right] \quad (45)$$

We have now derived all the analytical equations required for the determination of every $E_{0_{2k-1}}$ and $E_{0_{2k}}$ coefficients. The method described in Appendix A can then be used to analytically solve the system.

From another perspective which is more suitable for automating the solving procedure with an algorithm, for a composite made of n layers, one can express the whole system as a matrix equation $[A][E_0] = \frac{l_p}{2\pi}\dot{B_a}[Y]$ where $[E_0]$ is the column vector of the $2n-1$ $\left(E_{0_i}\right)_{2\leq i\leq 2n}$ coefficients (since $E_{0_1} = 0$). $[A]$ is a $(2n-1)\times(2n-1)$ square matrix which is automatically built line by line (depending on the nature of each interface and on the positions of the filamentary zones) from equations (30), (31) and (37) with the general expressions given by (36) and $[Y]$ is a column vector whose $2n-1$ components (either 0 or 1) are deduced from equation (37). The method used to automatically build $[A]$ and $[Y]$ is described in Appendix B.

The analytical study of the coupling currents induced in steady-state regimes is now achieved and we know the spatial form of these currents; the first part of our global methodology is then also achieved (first line of Figure 15). We will then make use of this knowledge to push the modeling towards any time-varying regimes following the philosophy depicted in Figure 15.

Again, by abuse of language, the term "time-varying regimes" refers here to regimes where all quantities inherent to the composite - in particular the induced currents - can no longer be considered as constant over time; they occur when the characteristic time for the external magnetic excitation B_a to vary is comparable to or smaller than the largest time constant of the system.

II.2.4 Study in time-varying regime

❖ **We will express here the magnetic field generated by the distribution of current found in steady-state regime (at the end of section II.2.3). We will then compute the new distribution of current induced by the time variation of this magnetic field. Finally, we will combine these results to those of section II.2.3 to establish the equation of the composite for any time regime.**

As mentioned previously, we will make use of the results of our analytical study in steady-state regimes to find the spatial solution of the induced currents in time-varying regimes. To make the link with the logical chain displayed in Figure 15, the electric field found in the previous analytical study in steady-state regimes corresponds to $\overrightarrow{E^{(1)}}$ and the associated distribution of currents to $\overrightarrow{J^{(1)}}$ since they are due to $\overrightarrow{\dot{B_a}}$ only.

In order to follow our logical chain we will now calculate the magnetic field $\overrightarrow{B^{(1)}}$ created by $\overrightarrow{J^{(1)}}$, i.e. created by the distribution of currents induced by $\overrightarrow{\dot{B_a}}$. The distribution of currents $\overrightarrow{J^{(1)}}$ can be subdivided into two sub-distributions : the first one corresponds to the currents flowing through the resistive parts of the composites thus in its cross-section while the second one corresponds to the currents flowing through the superconducting filaments located on the edges of each filamentary zone.

Since the first sub-distribution of currents is exclusively flowing in the cross-section plane of the composite, it will have a tendency to produce a magnetic field oriented along the z-axis while the magnetic time-variation $\overrightarrow{\dot{B_a}}$ produced by an external source is supposed to be along the y-axis; this sub-

distribution will thus not take part in the magnetic shielding of the inside of the composite and will therefore be omitted for this reason in the following.

Consequently we will consider that the magnetic field $\overrightarrow{B^{(1)}}$ is exclusively produced by the second sub-distribution of currents, i.e. the currents flowing through the superconducting filaments located on the edges of each filamentary zone, and we will now focus on its determination assuming that each supercurrent flowing at $r = R_k$ can be seen a surface current of the form $K_{s_k} = K_{0_k}\cos(\theta)$.

Before determining the magnetic field $\overrightarrow{B^{(1)}}$ produced by all the surface currents $\left(K_{s_k}\right)_{1\leq k\leq n}$, we will briefly calculate the magnetic field produced by only one surface current $K_{s_k} = K_{0_k}\cos(\theta)$ located at $r = R_k$.

Maxwell-Ampère equation $\vec{\nabla} \times \vec{B} = \mu_0 \vec{\jmath}$ combined with the relation between the magnetic field $\vec{B}$ and the magnetic vector potential $\vec{A}$, i.e. $\vec{B} = \vec{\nabla} \times \vec{A}$ leads to $\vec{\Delta}\vec{A} = -\mu_0 \vec{\jmath}$ considering the Coulomb gauge, that is to say $\vec{\nabla}.\vec{A} = 0$.

The supercurrent $K_{s_k} = K_{0_k}\cos(\theta)$ flowing through the filaments located at $r = R_k$ is oriented along the s direction (longitudinal direction along the filaments) and can thus be decomposed as $K_{s_k}\overrightarrow{e_s} = K_{\theta_k}\overrightarrow{e_\theta} + K_{z_k}\overrightarrow{e_z}$ with $K_{\theta_k} = K_{0_k}\cos(\theta)\,sin\alpha$ and $K_{z_k} = K_{0_k}\cos(\theta)\,cos\alpha$ using the relation $\overrightarrow{e_s} = sin\alpha\,\overrightarrow{e_\theta} + cos\alpha\,\overrightarrow{e_z}$ given by (13).

From the Biot-Savart law $\vec{A}(M) = \frac{\mu_0}{4\pi}\iint_{P\in S}\frac{K_{s_k}dS}{PM}\overrightarrow{e_s}$, we see that the magnetic vector potential $\vec{A}(M)$ created by the supercurrent $K_{s_k} = K_{0_k}\cos(\theta)$ can also be decomposed as

$$\vec{A}(M) = \frac{\mu_0 K_{0_k} sin\alpha}{4\pi}\iint_{P\in S}\frac{\cos(\theta)\,dS}{PM}\overrightarrow{e_\theta} + \frac{\mu_0 K_{0_k} cos\alpha}{4\pi}\iint_{P\in S}\frac{\cos(\theta)\,dS}{PM}\overrightarrow{e_z} = A_\theta(M)\overrightarrow{e_\theta} + A_z(M)\overrightarrow{e_z}$$

where S is the surface where the supercurrent is flowing.

We then have

$$\frac{A_\theta}{A_z} = tan\alpha \tag{46}$$

Making use of assumption A5 which implies $tan^2\,\alpha \ll 1$, to the first order, we can consider that the azimuthal component A_θ of the magnetic vector potential created by the supercurrent is negligible compared to its axial component A_z. We can then suppose that the magnetic vector potential $\vec{A}$ is reduced to its axial component only: $\vec{A} = A_z\overrightarrow{e_z}$.

Using $\vec{\Delta}\vec{A} = -\mu_0 \vec{\jmath}$, we can deduce that, inside and outside the supercurrent (i.e. respectively for $r < R_k$ and $r > R_k$), A_z satisfies Laplace's equation

$$\Delta A_z = 0 \tag{47}$$

Let us note $A_{z_{int}}$ and $A_{z_{ext}}$ the values of A_z, the magnetic vector potential due to the supercurrent $K_{0_k}\cos(\theta)$ flowing at $r = R_k$, respectively inside and outside the supercurrent. Since $A_{z_{int}}$ and $A_{z_{ext}}$ are solutions of (47), their general form must be

$$\begin{cases} A_{z_{int}}(r,\theta) = \sum_{i=0}^{\infty} [a_{int_i}\cos(i\theta) + b_{int_i}\sin(i\theta)]\, R_k(r/R_k)^i, a_{k_{int\,i}} \in \mathbb{R}, b_{k_{int\,i}} \in \mathbb{R} \\ A_{z_{ext}}(r,\theta) = \sum_{i=-\infty}^{0} [a_{ext_i}\cos(i\theta) + b_{ext_i}\sin(i\theta)]\, R_k(r/R_k)^i, a_{k_{ext\,i}} \in \mathbb{R}, b_{k_{ext\,i}} \in \mathbb{R} \end{cases} \quad (48)$$

Note that a_{int_i} and b_{int_i} are zero for $i < 0$ and that a_{ext_i} and b_{ext_i} are zero for $i > 0$ to avoid any divergence at $r = 0$ and $r \to \infty$. The general formulations of $A_{z_{int}}$ and $A_{z_{ext}}$ are chosen so that the a_{int_i}, a_{ext_i}, b_{int_i} and b_{ext_i} coefficients have the dimension of a magnetic field.

Using $\vec{B} = \vec{\nabla} \times \vec{A}$, we can also give the general formulation of the magnetic field inside and outside the supercurrent using the general expressions given by (48)

$$\begin{cases} B_{r_{int}}(r,\theta) = \sum_{i=1}^{\infty} [-a_{int_i}\sin(i\theta) + b_{int_i}\cos(i\theta)] i (r/R_k)^{i-1} \\ B_{r_{ext}}(r,\theta) = \sum_{i=-\infty}^{-1} [-a_{ext_i}\sin(i\theta) + b_{ext_i}\cos(i\theta)] i (r/R_k)^{i-1} \\ \hline B_{\theta_{int}}(r,\theta) = -\sum_{i=1}^{\infty} [a_{int_i}\cos(i\theta) + b_{int_i}\sin(i\theta)] i (r/R_k)^{i-1} \\ B_{\theta_{ext}}(r,\theta) = -\sum_{i=-\infty}^{-1} [a_{ext_i}\cos(i\theta) + b_{ext_i}\sin(i\theta)] i (r/R_k)^{i-1} \end{cases} \quad (49)$$

In addition, the expressions of the magnetic field must also satisfy the interface conditions at $r = R_k$. On the one hand, the continuity of the component normal to the interface which here corresponds to the radial component of the magnetic field (i.e. B_r), leads to

$$B_{r_{int}}(R_k,\theta) = B_{r_{ext}}(R_k,\theta), \theta \in \mathbb{R} \quad (50)$$

On the other hand, the component tangent to the interface which here corresponds to the azimuthal component of the magnetic field (i.e. B_θ), must satisfy

$$B_{\theta_{ext}}(R_k,\theta) - B_{\theta_{int}}(R_k,\theta) = \mu_0 K_{0_k}\cos(\theta), \theta \in \mathbb{R} \quad (51)$$

Since $\cos(i\theta)_{i\in\mathbb{N}^*}$ and $\sin(i\theta)_{i\in\mathbb{N}^*}$ are linearly independent families, using equation (50), we can deduce that

$$\begin{cases} a_{int_1} = a_{ext_{-1}} \\ b_{int_1} = -b_{ext_{-1}} \end{cases} \quad (52)$$

and from equation (51), that

$$\begin{cases} a_{int_1} + a_{ext_{-1}} = \mu_0 K_{0_k} \\ b_{int_1} = b_{ext_{-1}} \end{cases} \quad (53)$$

The combination of systems (52) and (53) leads to the conclusion that

$$\begin{cases} a_{int_1} = a_{ext_{-1}} = \mu_0 K_{0_k}/2 \\ b_{int_1} = b_{ext_{-1}} = 0 \end{cases} \tag{54}$$

Consequently, using the general expressions given by (48) and (49), we now have

$$\begin{cases} A_{z_{int}}(r,\theta) = \dfrac{\mu_0 K_{0_k}}{2} r\cos(\theta) \\ A_{z_{ext}}(r,\theta) = \dfrac{\mu_0 K_{0_k}}{2} \dfrac{R_k^2}{r}\cos(\theta) \end{cases} \tag{55}$$

And

$$\begin{cases} B_{r_{int}}(r,\theta) = -\dfrac{\mu_0 K_{0_k}}{2}\sin(\theta) \\ B_{r_{ext}}(r,\theta) = -\dfrac{\mu_0 K_{0_k}}{2}\left(\dfrac{R_k}{r}\right)^2 \sin(\theta) \\ B_{\theta_{int}}(r,\theta) = -\dfrac{\mu_0 K_{0_k}}{2}\cos(\theta) \\ B_{\theta_{ext}}(r,\theta) = \dfrac{\mu_0 K_{0_k}}{2}\left(\dfrac{R_k}{r}\right)^2 \cos(\theta) \end{cases} \tag{56}$$

Using system (56), we can also express the x and y components of the magnetic field as

$$\begin{cases} B_{x_{int}}(r,\theta) = 0 \\ B_{x_{ext}}(r,\theta) = -\dfrac{\mu_0 K_{0_k}}{2}\left(\dfrac{R_k}{r}\right)^2 \sin(2\theta) \\ B_{y_{int}}(r,\theta) = -\dfrac{\mu_0 K_{0_k}}{2} \\ B_{y_{ext}}(r,\theta) = \dfrac{\mu_0 K_{0_k}}{2}\left(\dfrac{R_k}{r}\right)^2 \cos(2\theta) \end{cases} \tag{57}$$

We must keep in mind that the components of the magnetic field calculated above are the components of the magnetic field created by a surface current of the form $K_{0_k}\cos(\theta)$ flowing on the surface of the cylinder described by the equation $r = R_k$.

We have here found that the magnetic field inside a cosine distributed surface current $K_0\cos(\theta)$, flowing on the surface of a cylinder, is uniform and oriented along the y-axis; this result is well known, especially in the accelerator community.

For a composite consisting in a filamentary zone only, using equations (37) and (45), the supercurrent flowing through the outer edge filaments is found to be equal to $\frac{1}{\rho_t}\left(\frac{l_p}{2\pi}\right)^2 \dot{B}_a\cos(\theta)$. With the $K_0\cos(\theta)$ notation, this leads to $K_0 = \frac{1}{\rho_t}\left(\frac{l_p}{2\pi}\right)^2 \dot{B}_a$, and therefore, according to equation (57), $B_{y_{int}} = -\frac{\mu_0}{2}\frac{1}{\rho_t}\left(\frac{l_p}{2\pi}\right)^2 \dot{B}_a = -\tau\dot{B}_a$ with τ given by equation (2). If $\dot{B}_a$ is positive, the internal reacting magnetic

field $B_{y_{int}}$ will then be negative, thus trying to shield the interior of the composite; this result is therefore physically consistent and corroborates previous analytical studies.

Furthermore, since a composite can feature multiple surface currents (on the edges of each filamentary zone), we can now express, by superposition, the magnetic vector potential $A_{z_k}^{(1)}$ created by all the surface currents inside a layer k as

$$A_{z_k}^{(1)}(r,\theta) = \frac{\mu_0}{2}\left[\frac{1}{r}\sum_{i=1}^{k-1} K_{0_i} R_i^2 + r\sum_{i=k}^{n} K_{0_i}\right]\cos(\theta) \tag{58}$$

where K_{0_i} is the amplitude of the surface current flowing at $r = R_i$. Note that for an interface of resistive/resistive type, the formula above is still valid replacing the K_{0_i} of the considered interface with zero since there is no filament.

Following our logical chain, we can now compute the axial electric field $E_{z_k}^{(2)}$ generated in each layer k by the time-variation of the surface currents using the following alternative formulation of Maxwell-Faraday equation

$$E_{z_k}^{(2)} = -\dot{A}_{z_k}^{(1)} \tag{59}$$

From equation (21), i.e. $E_\theta = -\frac{l_p}{2\pi r}E_z$, the new azimuthal component of the electric field in a filamentary zone is

$$E_{\theta_k}^{(2)} = \frac{l_p}{2\pi r}\dot{A}_{z_k}^{(1)} \tag{60}$$

In reality, we should also consider the azimuthal component $A_{\theta_k}^{(1)}$ of the magnetic vector potential created by the supercurrents and have $E_{\theta_k}^{(2)} = \frac{l_p}{2\pi r}\dot{A}_{z_k}^{(1)} - \dot{A}_{\theta_k}^{(1)}$ instead of (60). If we note $A_{z_{k_i}}^{(1)}$ and $A_{\theta_{k_i}}^{(1)}$ the contributions of each supercurrent K_{s_i}, we see that

$$E_{\theta_k}^{(2)} = \sum_{i=1}^{n}\left[\frac{l_p}{2\pi r}\dot{A}_{z_{k_i}}^{(1)} - \dot{A}_{\theta_{k_i}}^{(1)}\right]$$

And, according to equation (46), we can calculate the ratio of the second to the first term in the above sum:

$$\frac{\dot{A}_{\theta_{k_i}}^{(1)}}{\frac{l_p}{2\pi r}\dot{A}_{z_{k_i}}^{(1)}} = \frac{2\pi r}{l_p}\frac{\dot{A}_{\theta_{k_i}}^{(1)}}{\dot{A}_{z_{k_i}}^{(1)}} = \frac{2\pi r}{l_p}tan\alpha = tan^2\,\alpha \ll 1$$

since $tan\alpha = \frac{2\pi r}{l_p}$ from equation (14).

Therefore the reduction of the magnetic vector potential $\overrightarrow{A_k^{(1)}}$ created by the supercurrents to its axial component $A_{z_k}^{(1)}$ only is all the more justified since the taking into account of its azimuthal component $A_{\theta_k}^{(1)}$ has a largely negligible effect.

Now, replacing $A_{z_k}^{(1)}$ in equation (60) with its expression given in equation (58), in each filamentary zone we have

$$E_{\theta_k}^{(2)} = \frac{\mu_0}{2}\frac{l_p}{2\pi}\left[\frac{1}{r^2}\sum_{i=1}^{k-1}\dot{K}_{0_i}R_i^2 + \sum_{i=k}^{n}\dot{K}_{0_i}\right]\cos(\theta) \tag{61}$$

It should be noted that expression (61) of $E_{\theta_{react\,k}}$ can be rewritten using the formulation present in (36) i.e.

$$E_{\theta_k}^{(2)} = \left[E_{0_{2k-1}}^{(2)}\left(\frac{R_k}{r}\right)^2 - E_{0_{2k}}^{(2)}\right]\cos(\theta) \tag{62}$$

with, by identification

$$\begin{cases} E_{0_{2k-1}}^{(2)} = \dfrac{\mu_0}{2}\dfrac{l_p}{2\pi}\displaystyle\sum_{i=1}^{k-1}\dot{K}_{0_i}\left(\frac{R_i}{R_k}\right)^2 \\ E_{0_{2k}}^{(2)} = -\dfrac{\mu_0}{2}\dfrac{l_p}{2\pi}\displaystyle\sum_{i=k}^{n}\dot{K}_{0_i} \end{cases} \tag{63}$$

Using the previously introduced notation $\overrightarrow{E_t^{(2)}}$ and Maxwell-Faraday equation $\vec{\nabla}\times\overrightarrow{E^{(2)}} = -\dot{\overrightarrow{B^{(1)}}}$, we can write $\vec{\nabla}\times\overrightarrow{E_t^{(2)}} = \vec{0}$ since we have seen that the magnetic field $\overrightarrow{B^{(1)}}$ produced by the surface currents did not have any axial component (i.e. along the z-axis).

From the considerations presented in our analytical study in steady-state regimes for the calculation of E_{r_k} in the filamentary zones and the expression of $E_{\theta_k}^{(2)}$ given by (61), we can immediately deduce that, in each filamentary zone, $E_{r_k}^{(2)}$ will be given by

$$E_{r_k}^{(2)} = -\left[E_{0_{2k-1}}^{(2)}\left(\frac{R_k}{r}\right)^2 + E_{0_{2k}}^{(2)}\right]\sin(\theta) \tag{64}$$

where $E_{0_{2k-1}}^{(2)}$ and $E_{0_{2k}}^{(2)}$ are also given by (63).

Again using considerations from the study in steady-state regimes, we can also deduce that the expressions of the transverse electric field components ($E_{r_k}^{(2)}$ and $E_{\theta_k}^{(2)}$) in the resistive zones of the composite are also given by

$$\begin{cases} E_{r_k}^{(2)} = -\left[E_{0_{2k-1}}^{(2)}\left(\dfrac{R_k}{r}\right)^2 + E_{0_{2k}}^{(2)}\right]\sin(\theta) \\ E_{\theta_k}^{(2)} = \left[E_{0_{2k-1}}^{(2)}\left(\dfrac{R_k}{r}\right)^2 - E_{0_{2k}}^{(2)}\right]\cos(\theta) \end{cases} \tag{65}$$

Note that here the $E_{0_{2k-1}}^{(2)}$ and $E_{0_{2k}}^{(2)}$ coefficients are not given by (63) because the formulae presented in (63) are only valid for filamentary zones.

Since the electric field $\overrightarrow{E^{(2)}}$ shares the same spatial form as the previous one found for steady-state regimes, we can deduce using Kirchhoff's current law (32) that the new supercurrents will also have the same form as the previous ones, i.e. $K_{s_k}^{(2)} = K_{0_k}^{(2)}\cos(\theta)$.

From these observations and the considerations of section II.2.1 , we can say that we have now reached the end of our logical chain because the new distribution of currents $\overrightarrow{J^{(2)}}$, i.e. the new surface currents $\left(K_{s_k}^{(2)}\right)_{1\leq k\leq n}$, shares the same spatial form as the previous one, i.e. the previous surface currents $\left(K_{s_k}\right)_{1\leq k\leq n}$, found for steady-state regimes.

We are now sure that, for any time-varying regime, the spatial form of the components of the transverse electric field in each layer k (E_{r_k} and E_{θ_k}) and of the supercurrents $\left(K_{s_k}\right)_{1\leq k\leq n}$ will be given by (36), i.e.

$$\begin{cases} E_{r_k} = -\left[E_{0_{2k-1}}\left(\dfrac{R_k}{r}\right)^2 + E_{0_{2k}}\right]\sin(\theta) \\ E_{\theta_k} = \left[E_{0_{2k-1}}\left(\dfrac{R_k}{r}\right)^2 - E_{0_{2k}}\right]\cos(\theta) \\ K_{s_k} = K_{0_k}\cos(\theta) \end{cases} \tag{66}$$

The complete basis of spatial functions enabling the description of the system being established, we can now formulate the global equation of the system as a time-dependent only equation.

Indeed, we now consider that the $E_{0_{2k-1}}$ and $E_{0_{2k}}$ coefficients associated to the transverse electric field in each filamentary zone k are due both to $\dot{B}_a$, i.e. the time-variation of the magnetic field created by an external source, and to the time-variation of the magnetic field created by the surface currents $\left(K_{s_k}\right)_{1\leq k\leq n}$. The contribution of $\dot{B}_a$ in the $E_{0_{2k-1}}$ and $E_{0_{2k}}$ coefficients of each filamentary zone has been given through equations (37) while the contribution of the time-variation of the surface currents $\left(K_{s_k}\right)_{1\leq k\leq n}$ is given by equations (63). Therefore for every filamentary layer k, we can now, by superposition, write

$$\begin{cases} E_{0_{2k-1}} = \dfrac{\mu_0}{2}\dfrac{l_p}{2\pi}\displaystyle\sum_{i=1}^{k-1}\dot{K}_{0_i}\left(\frac{R_i}{R_k}\right)^2 \\ E_{0_{2k}} = \dfrac{l_p}{2\pi}\dot{B}_a - \dfrac{\mu_0}{2}\dfrac{l_p}{2\pi}\displaystyle\sum_{i=k}^{n}\dot{K}_{0_i} \end{cases} \tag{67}$$

which can alternatively be written as

$$\begin{cases} E_{0_{2k-1}} - \dfrac{\mu_0}{2}\dfrac{l_p}{2\pi}\displaystyle\sum_{i=1}^{k-1}\dot{K}_{0_i}\left(\frac{R_i}{R_k}\right)^2 = 0 \\ E_{0_{2k}} + \dfrac{\mu_0}{2}\dfrac{l_p}{2\pi}\displaystyle\sum_{i=k}^{n}\dot{K}_{0_i} = \dfrac{l_p}{2\pi}\dot{B}_a \end{cases} \tag{68}$$

We can also express E_{z_k} in every zone as

$$E_{z_k} = \left[r\left(\dot{B}_a - \frac{\mu_0}{2}\sum_{i=k}^{n}\dot{K}_{0_i}\right) - \frac{1}{r}\frac{\mu_0}{2}\sum_{i=1}^{k-1}\dot{K}_{0_i}{R_i}^2\right]\cos(\theta) \tag{69}$$

superposing the expressions of E_{z_k} given in (36) and obtained by the combination of equations (58) and (59).

In addition, in our study in steady-state regime, we have derived the expressions of the $\left(K_{0_i}\right)_{1\leq i\leq n}$ as functions of the $E_{0_{2k-1}}$ and $E_{0_{2k}}$ coefficients; they are given by equations (44) and (45). We have also seen that the $E_{0_{2k-1}}$ and $E_{0_{2k}}$ coefficients of the resistive zones could be expressed as functions of the $E_{0_{2k-1}}$ and $E_{0_{2k}}$ coefficients of the filamentary zones only and this fact is independent of the regime considered because the coefficients are linked by boundary conditions.

Now let us consider a composite made of n_f filamentary zones and n_{Intf} interfaces between filamentary layers, we know that there will be $2n_f$ $E_{0_{2k-1}}$ and $E_{0_{2k}}$ coefficients (or $2n_f - 1$ if the first layer is filamentary, because E_{0_1} is always zero) for the filamentary zones and n_{Intf} boundary conditions due to the continuity of the azimuthal component E_θ of the electric field between filamentary layers; it is therefore possible to express all the $E_{0_{2k-1}}$ and $E_{0_{2k}}$ coefficients of the filamentary zones as functions of only $2n_f - n_{Intf}$ of these coefficients (or $2n_f - 1 - n_{Intf}$ if the first layer is filamentary). This is not a coincidence, because the number of edges of filamentary zones, thus the number of existing surface currents, is exactly equal to $2n_f - n_{Intf}$ (or $2n_f - 1 - n_{Intf}$ if the first layer is filamentary). We have then shown that the system could be expressed using a set of only $2n_f - n_{Intf}$ (or $2n_f - 1 - n_{Intf}$ if the first layer is filamentary) variables which can be chosen to be either the reduced number of $E_{0_{2k-1}}$ and $E_{0_{2k}}$ coefficients of the filamentary zones or the K_{0_i} amplitudes of surface currents.

Consequently, replacing the time derivatives of the $\left(K_{0_i}\right)_{1\leq i\leq n}$ amplitudes of surface currents in the set of equations (68) for $1 \leq k \leq n$ with their expressions as functions of the time derivatives of the reduced number of $E_{0_{2k-1}}$ and $E_{0_{2k}}$ coefficients of the filamentary zones, the system can be expressed as

$$\left[E_{0_{f\,red}}\right] + \left[T_{f_E}\right]\left[\dot{E}_{0_{f\,red}}\right] = \dot{B}_a\left[Y_{f_E}\right] \tag{70}$$

where $\left[E_{0_{f\,red}}\right]$ is the column vector of the $2n_f - n_{Intf}$ (or $2n_f - 1 - n_{Intf}$ if the first layer is filamentary) reduced number of $E_{0_{2k-1}}$ and $E_{0_{2k}}$ coefficients of the filamentary zones, $\left[T_{f_E}\right]$ is a $2n_f - n_{Intf}$ (or $2n_f - n_{Intf} - 1$) square matrix whose coefficients have the dimension of time and $\left[Y_{f_E}\right]$ is a column vector having the same size as $\left[E_{0_{f\,red}}\right]$ and whose coefficients can be calculated analytically from the previous considerations.

Alternatively, replacing all the $E_{0_{2k-1}}$ and $E_{0_{2k}}$ coefficients present in the set of equations (68) for $1 \leq k \leq n$ with their expressions as functions of the non-zero K_{0_i} amplitudes of surface currents, it is also possible to express the global equation of the system as

$$\left[K_{0_f}\right] + \left[T_{f_K}\right]\left[\dot{K}_{0_f}\right] = \dot{B}_a\left[Y_{f_K}\right] \tag{71}$$

where $\left[K_{0_f}\right]$ is the column vector of the $2n_f - n_{Intf}$ (or $2n_f - 1 - n_{Intf}$ if the first layer is filamentary) non-zero amplitudes of surface currents, $\left[T_{f_K}\right]$ is a $2n_f - n_{Intf}$ (or $2n_f - n_{Intf} - 1$) square matrix whose coefficients have the dimension of time and $\left[Y_{f_K}\right]$ is a column vector having the same size as $\left[K_{0_f}\right]$ and whose coefficients can also be calculated analytically from the previous considerations.

Both formulations have advantages and disadvantages: equation (70) will preferably be chosen for the derivation of coupling losses generated inside the composite while equation (71) has a more enlightening physical meaning. Indeed, it is much easier to understand that the system can be represented with an equation on the surface currents only rather than on some electric field coefficients, because we physically understand that the surface currents are actually trying to shield the composite from the time-variations of the magnetic field created by an external source and that they are linked both electrically (through resistances) and magnetically (through inductances).

It is also interesting to note that $[T_{f_E}]$ and $[T_{f_K}]$ are actually similar matrices and they therefore share the same eigenvalues which physically represent the time constants of the system.

Another important point is that the number of time constants of a composite is therefore always equal to the number of edges of filamentary zones it contains; we are now able to determine the number of time constants of a composite with a short glimpse at its design.

As we have already presented a detailed analytical procedure for the derivation of the equation of the system in our study in steady-state regime, we will simply provide a summary of the new analytical procedure for time-varying regimes:

We express all the $E_{0_{2k-1}}$ and $E_{0_{2k}}$ coefficients of every resistive zone as functions of those of the filamentary zones using equations (38), (39), (42), (43) and (343). If there exist interfaces between filamentary layers, we make use of equation (343) at these interfaces to express one of the $E_{0_{2k-1}}$ and $E_{0_{2k}}$ coefficients of the filamentary zones adjacent to the interfaces as function of the others. We then have a basis for the $E_{0_{2k-1}}$ and $E_{0_{2k}}$ coefficients that we call $\left(E_{0_{f\,red}}\right)$: indeed the $E_{0_{2k-1}}$ and $E_{0_{2k}}$ coefficients of every layer can be expressed as a linear combination of the $E_{0_{2k-1}}$ and $E_{0_{2k}}$ coefficients contained in $\left(E_{0_{f\,red}}\right)$ only. Similarly let us call $\left(K_{0_f}\right)$ the family of the non-zero K_{0_i} amplitudes of surface currents (i.e. those located on the edge of a filamentary zone). The expressions of the amplitudes contained in $\left(K_{0_f}\right)$ being given by equations (44) and (45), we can also express these amplitudes as functions of the $E_{0_{2k-1}}$ and $E_{0_{2k}}$ coefficients of $\left(E_{0_{f\,red}}\right)$ only; these coefficients can reciprocally be expressed as functions of the amplitudes of $\left(K_{0_f}\right)$. Finally from the set of equations (68) for $1 \leq k \leq n$, we only keep those featuring the $E_{0_{2k-1}}$ and $E_{0_{2k}}$ coefficients contained in $\left(E_{0_{f\,red}}\right)$ and then replace the $\dot{K}_{0_i}$ present in the remaining equations with their expressions as functions of the time-derivatives of the coefficients contained in $\left(E_{0_{f\,red}}\right)$ and thus obtain matrix equation (70); indeed the relations between the elements of $\left(\dot{K}_{0_f}\right)$ and $\left(\dot{E}_{0_{f\,red}}\right)$ are the same as the ones between elements of $\left(K_{0_f}\right)$ and $\left(E_{0_{f\,red}}\right)$. In order to obtain matrix equation (71), we start from matrix equation (70) and replace the coefficients contained in $\left(E_{0_{f\,red}}\right)$ with their expressions as functions of the elements of $\left(K_{0_f}\right)$.

In our study in steady-state regime, we have provided the logical tree to build the $[A]$ matrix and the $[Y]$ column vector which are needed to express the equation of the system as in equation (348), i.e. $[A][E_0] = \frac{l_p}{2\pi}\dot{B}_a[Y]$. We will not provide here the logical tree to build the $[T_{f_E}]$, $[T_{f_K}]$ matrices and the $[Y_{f_E}]$, $[Y_{f_K}]$ column vectors of matrix equations (70) and (71) since it would feature too many exceptions, making it quite unattractive.

Alternatively, we have chosen to express the equation of the system as

$$[A][E_0] + \frac{\mu_0}{2}\left(\frac{l_p}{2\pi}\right)^2 \frac{1}{\rho_{t_1}}[B]\left[\dot{E}_0\right] = \frac{l_p}{2\pi}\dot{B}_a[Y] \tag{72}$$

where $[A]$ and $[Y]$ are exactly the same as the ones used in steady-state regime and $[B]$ is another square matrix whose coefficients are dimensionless and whose derivation is shown through Appendix C.

It is important to point out that matrix equation (72) does not have the same size as matrix equations (70) and (71), i.e. $[A]$ and $[B]$ are $2n-1$ square matrices while $\left[T_{f_E}\right]$ and $\left[T_{f_K}\right]$ are $2n_f - n_{Intf}$ (or $2n_f - n_{Intf} - 1$ if the first layer is filamentary) square matrices. This means that the system described by matrix equations (70) and (71) will have $(2n_f - n_{Intf})$ or $(2n_f - n_{Intf} - 1)$ time constants (eigenvalues) while the system described by matrix equation (72) will have $(2n-1)$ time constants; this seems to be physically inconsistent as these three matrix equations are describing the same system. In reality, there will only be $(2n_f - n_{Intf})$ or $(2n_f - n_{Intf} - 1)$ physical time constants (eigenvalues) in matrix equation (72); the other eigenvalues will be artificial and all equal to $\frac{\mu_0}{2}\left(\frac{l_p}{2\pi}\right)^2 \frac{1}{\rho_{t_1}}$. We employ the term "artificial" here because the additional eigenvalues are a consequence of our mathematical manipulation and do not correspond to any physical process occurring inside the strand. In fact, the appearance of these extra eigenvalues is due to the fact that we have duplicated some lines of the $[A]$ matrix into the $[B]$ matrix to render it invertible. Indeed, the continuity equations on E_θ and J_r which are represented by some lines of the $[A]$ matrix are still valid after a derivation with respect to time; we have therefore duplicated these lines into $[B]$ without physically changing the system (the multiplication by $\frac{\mu_0}{2}\left(\frac{l_p}{2\pi}\right)^2 \frac{1}{\rho_{t_1}}$ has no effect since the right-hand terms of continuity equations (343), (344) and (345) are zero). In reality, the extra eigenvalues correspond to the eigenvectors that will always be zero; this explains why they have no incidence on the physical behavior of the composite. As mentioned previously, we have chosen this formulation over matrix equations (70) and (71) as it is much more adequate for the development of a general algorithm.

II.2.5 Discussion about specific assumptions of the model

❖ **We will evaluate here the shielding made by the outer copper sheath and we will discuss the saturation of filaments to establish the domain of validity of the model.**

II.2.5.1 Discussion about shielding by the outer copper sheath

Now that we have completed the derivation of the equations governing any composite with n cylindrical concentric layers either filamentary or purely resistive for a time-varying regime, we can discuss assumption A7 which states that "the time variation of the external magnetic field B_a is slow enough to ensure that the copper sheath does not magnetically shield its enclosed volume".

In order to do so, we will establish a simplified equation governing the currents induced in the copper sheath making use of the results of the previous sections. This simplified approach requires the thickness e of the copper sheath to be small compared to the composite radius R so that these currents can be represented to good approximation by a surface current K_{Cu} located at $r = R - e/2$ as displayed on Figure 18 and flowing in the axial direction (i.e. along the z-axis).

This approach will enable us to give an estimate of the frequency domain in which our model is valid.

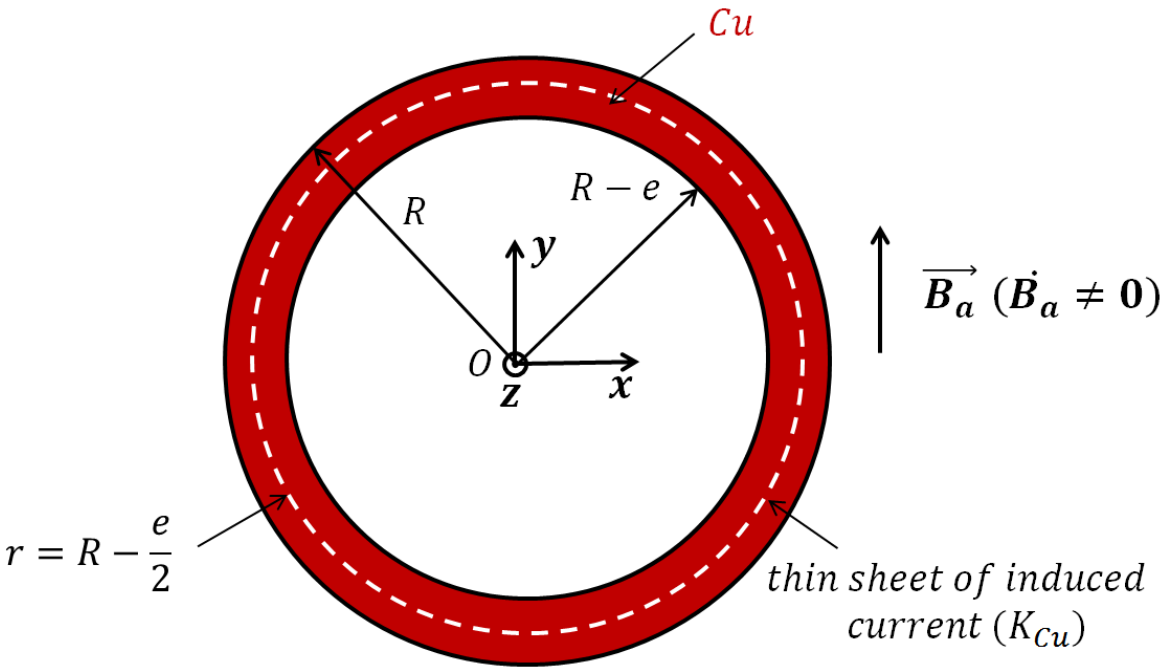

Figure 18 : Scheme of an external copper sheath

If an external time-varying magnetic field B_a is applied to the copper sheath alone, an axial electric field $E_z = r\dot{B}_a \cos(\theta)$ will be created according to equation (20) which in turn will give rise to a local axial current density $J_z = \frac{E_z}{\rho_{Cu}}$ with ρ_{Cu} the copper resistivity. We therefore have

$$J_z = \frac{r\dot{B}_a}{\rho_{Cu}} \cos(\theta) \tag{73}$$

We consider that the distribution of current density J_z can be alternatively seen as flowing through a thin sheet of current K_{Cu} located at $r = R - \frac{e}{2}$, i.e. at the middle of the sheath as indicated on Figure 18. This assumption implies that

$$K_{Cu} = \int_{R-e}^{R} J_z(r)dr \tag{74}$$

Combining equations (73) and (74), we obtain

$$K_{Cu} = \frac{\dot{B}_a}{\rho_{Cu}} \cos(\theta) \int_{R-e}^{R} r dr \simeq \frac{Re\dot{B}_a}{\rho_{Cu}} \cos(\theta) \tag{75}$$

since e is assumed to be small compared to R.

From the previous equation we see that K_{Cu} can also be written as $K_{Cu} = K_{0_{Cu}} \cos(\theta)$ with

$$K_{0_{Cu}} = \frac{Re\dot{B}_a}{\rho_{Cu}} \tag{76}$$

Following our logical chain displayed on Figure 15, we now have to compute the reacting magnetic vector potential $A_z^{(1)}$ created by the sheet of current K_{Cu}. Since K_{Cu} can be written as $K_{0_{Cu}}\cos(\theta)$, we can use equations (55) so that

$$A_z^{(1)} = \begin{cases} \dfrac{\mu_0 K_{0_{Cu}}}{2} r\cos(\theta) \;\; for\, r \le R - \dfrac{e}{2} \\ \dfrac{\mu_0 K_{0_{Cu}}}{2} \dfrac{\left(R-\frac{e}{2}\right)^2}{r}\cos(\theta) \;\; for\, r \ge R - \dfrac{e}{2} \end{cases} \tag{77}$$

Knowing $A_z^{(1)}$, we can now compute the axial electric field $E_z^{(2)}$ generated by the time-variation of the surface current K_{Cu} using the alternative formulation of Maxwell-Faraday equation as we did for the derivation of equation (59)

$$E_z^{(2)} = -\dot{A}_z^{(1)} \tag{78}$$

In addition local Ohm's law indicates that $J_z^{(2)} = \frac{E_z^{(2)}}{\rho_{Cu}}$. Then, making use of equations (74), (77) and (78), the new current sheet $K_{Cu}^{(2)}$ is

$$K_{Cu}^{(2)} = \int_{R-e}^{R} J_z^{(2)}(r)dr = -\frac{\mu_0 \dot{K}_{0_{Cu}}}{2\rho_{Cu}}\cos(\theta)\left[\int_{R-e}^{R-\frac{e}{2}} r dr + \left(R-\frac{e}{2}\right)^2 \int_{R-\frac{e}{2}}^{R} \frac{dr}{r}\right] \tag{79}$$

We can compute and reduce the first term in brackets as follows

$$\int_{R-e}^{R-\frac{e}{2}} r dr = \frac{\left(R-\frac{e}{2}\right)^2 - (R-e)^2}{2} = \frac{Re}{2}\left(1 - \frac{3}{4}\frac{e}{R}\right) \simeq \frac{Re}{2}$$

since we have supposed $\frac{e}{R} \ll 1$

The second term leads to

$$\left(R-\frac{e}{2}\right)^2 \int_{R-\frac{e}{2}}^{R} \frac{dr}{r} = -\left(R-\frac{e}{2}\right)^2 ln\left(1-\frac{e}{2R}\right) \simeq \left(R-\frac{e}{2}\right)^2 \frac{e}{2R} \simeq \frac{Re}{2}$$

using the Taylor series expansion of $ln\left(1-\frac{e}{2R}\right)$ to the first order since $\frac{e}{R} \ll 1$.

From these calculations, we can now simplify equation (79)

$$K_{Cu}^{(2)} = -\frac{\mu_0 Re}{2\rho_{Cu}} \dot{K}_{0_{Cu}} \cos(\theta) \tag{80}$$

We now see that it is also possible to write $K_{Cu}^{(2)}$ as $K_{Cu}^{(2)} = K_{0_{Cu}}^{(2)}\cos(\theta)$ with

$$K_{0_{Cu}}^{(2)} = -\frac{\mu_0 Re}{2\rho_{Cu}} \dot{K}_{0_{Cu}} \tag{81}$$

Since $K_{Cu}^{(2)}$ shares the same spatial form as K_{Cu} we can now legitimately suppose that the currents induced in the copper sheath can be expressed as $K_{Cu} = K_{0_{Cu}} \cos(\theta)$. Then, we can give, by superposition, the equation governing the spatial amplitude $K_{0_{Cu}}$ of the surface current K_{Cu} flowing at $r = R - \frac{e}{2}$ using equations (76) and (81)

$$K_{0_{Cu}} + \frac{\mu_0 Re}{2\rho_{Cu}} \dot{K}_{0_{Cu}} = \frac{Re}{\rho_{Cu}} \dot{B}_a$$

which can be written as

$$K_{0_{Cu}} + \tau_{Cu} \dot{K}_{0_{Cu}} = \frac{2}{\mu_0} \tau_{Cu} \dot{B}_a \tag{82}$$

with

$$\tau_{Cu} = \frac{\mu_0 Re}{2\rho_{Cu}} \tag{83}$$

Note that this formula is fully consistent with the one given in [31].

By superposition, the internal magnetic field B_i in the volume enclosed by the copper sheath, i.e. for $r \leq R - e$ (see Figure 18) will be given by

$$B_i = B_a - \frac{\mu_0 K_{0_{Cu}}}{2}$$

according to equation (57). This is equivalent to

$$K_{0_{Cu}} = \frac{2}{\mu_0} (B_a - B_i)$$

Replacing $K_{0_{Cu}}$ with $\frac{2}{\mu_0}(B_a - B_i)$ in equation (82) and multiplying both sides by $\frac{\mu_0}{2}$ leads to

$$B_i + \tau_{Cu} \dot{B}_i = B_a \tag{84}$$

which is identical to (1).

The condition to ensure that the copper sheath does not magnetically shield its enclosed volume can be expressed as

$$\left| \frac{\dot{B}_i}{\dot{B}_a} \right| \simeq 1$$

We can use the complex notation and equation (84) to write

$$\bar{B}_i = \frac{\bar{B}_a}{(1 + j\omega\tau_{Cu})}$$

In addition, we have

$$\dot{\bar{B}}_i = j\omega\bar{B}_i = j\omega\frac{\bar{B}_a}{(1+j\omega\tau_{Cu})} = \frac{j\omega\bar{B}_a}{(1+j\omega\tau_{Cu})} = \frac{\dot{\bar{B}}_a}{(1+j\omega\tau_{Cu})}$$

which enables us to write

$$\left|\frac{\dot{B}_i}{\dot{B}_a}\right| = \left|\frac{\dot{\bar{B}}_i}{\dot{\bar{B}}_a}\right| = \left|\frac{1}{1+j\omega\tau_{Cu}}\right| = \frac{1}{\sqrt{1+(\omega\tau_{Cu})^2}}$$

The previous condition is then equivalent to

$$\frac{1}{\sqrt{1+(\omega\tau_{Cu})^2}} \simeq 1$$

For $\left|\dot{B}_i\right|$ to not differ from more than 1% from $\left|\dot{B}_a\right|$, we need

$$\frac{1}{\sqrt{1+(\omega\tau_{Cu})^2}} \geq 0.99$$

which leads to

$$\omega\tau_{Cu} \leq \frac{\sqrt{1-0.99^2}}{0.99} \simeq 0.142 \tag{85}$$

To give a relevant estimate of τ_{Cu}, we choose the following parameters which are relevant for several strands used in fusion: $\rho_{Cu} = 2.10^{-10}\Omega.m$, $R = 0.5\,mm$ and $e = R/4$, using (83), we obtain the following value for τ_{Cu}

$$\tau_{Cu} \simeq 0.2\,ms \tag{86}$$

Replacing the angular frequency ω with $2\pi f$ and τ_{Cu} with $0.2\,ms$, condition (85) implies

$$f \leq 113\,Hz \tag{87}$$

Note that this value is not as high as we can expect, and this frequency range could be encountered in tokamaks during ELMs.

We can also easily derive a condition of minimum duration of a rising or falling ramp of B_a to ensure that the magnetic shielding accomplished by the copper sheath is negligible.

First, we can differentiate equation (84) with respect to time in order to obtain

$$\dot{B}_i + \tau_{Cu}\ddot{B}_i = \dot{B}_a \tag{88}$$

We immediately see that equation (88) is in fact the equation of a first-order system and, in the case of a rising (or falling) ramp going from 0 to B_m (or $-B_m$) in a time T_a, we have $\left|\dot{B}_a\right| = B_m/T_a$. We can therefore conclude that a time of $5\tau_{Cu}$ is needed for $\left|\dot{B}_i\right|$ to go from an initial zero value to $\left|\dot{B}_a\right|$; indeed $5\tau_{Cu}$ is the time for $\left|\dot{B}_i\right|$ to reach 99% of its final value, i.e. $\left|\dot{B}_a\right|$, because $1 - e^{-5} \simeq 0.99$.

Considering that the magnetic shielding accomplished by the copper sheath is negligible if it occurs for less than 1% of the total ramp duration T_a, we can write the following condition

$$5\tau_{Cu} \leq \frac{T_a}{100} \tag{89}$$

which, with $\tau_{Cu} = 0.2\ ms$, leads to

$$T_a \geq 0.1\ s \tag{90}$$

The ranges of maximum frequencies and minimum ramp durations found by our simple model where the copper sheath might shield its enclosed volume are seldom the ones experienced by magnets in tokamaks. Some exceptions can be met in very specific cases such as plasma disruption and ELMs, or the rapid breakdown step in CS; in this cases specific analyses should be led.

II.2.5.2 Discussion about the saturation of filaments

Before deriving the formulae needed for the computation of the power dissipated by coupling currents, we also need to give a limit for the validity of assumption A4. Indeed, in order for the superconducting filaments not to be saturated, they must carry a current inferior to their critical current. Let us call λ the proportion of superconductor in a filamentary zone, the maximum local current $I_{loc\ max}$ that an elementary area of length $rd\theta$ and thickness dr can carry is

$$I_{loc\ max} = \lambda J_c r d\theta dr \tag{91}$$

where J_c is the critical current density of the superconducting material.

On another side, the local coupling current I_{loc} carried by the same elementary area is

$$I_{loc} = K_0 \cos(\theta) r d\theta \tag{92}$$

To ensure the validity of assumption A4, we therefore need $|I_{loc}| \leq |I_{loc\ max}|$, i.e.

$$|K_0 \cos(\theta)| \leq \lambda J_c dr \tag{93}$$

using equations (91) and (92).

The most critical case is reached in the midplane for which $\theta = 0$ or $\theta = \frac{\pi}{2}$, i.e. for $|\cos(\theta)| = 1$. Consequently, the maximum surface current amplitude $K_{0_{max}}$ allowed without saturating more than the first ring of filaments is then

$$K_{0_{max}} = \lambda J_c d_f \tag{94}$$

according to condition (93) for $dr = d_f$, with d_f the filaments diameter.

Beyond this limit, we can reasonably consider that the analytical formulae derived in our approach still hold for relatively small values of dr, i.e. when dr does not exceed more than 10% of the filamentary layer thickness.

For an interface of R/F type located at $r = R_k$, condition (94) becomes then

$$K_{0_{max}} = 0.1(R_{k+1} - R_k)\lambda J_c \tag{95}$$

And for an interface of F/R type located at $r = R_k$, condition (94) becomes

$$K_{0_{max}} = 0.1(R_k - R_{k-1})\lambda J_c \tag{96}$$

with $R_{k-1} = 0$ if $k = 1$, i.e. if the filamentary layer is located at the center of the composite.

II.2.6 Power dissipated by coupling currents

❖ **We will compute here the power generated by coupling currents as a function of the E_{0_k} coefficients introduced in section II.2.3 .**

We will first remind the expressions of each component of the electric field in every layer k from equations (66) and (69)

$$\begin{cases} E_{r_k} = -\left[E_{0_{2k-1}}\left(\frac{R_k}{r}\right)^2 + E_{0_{2k}}\right]\sin(\theta) \\ E_{\theta_k} = \left[E_{0_{2k-1}}\left(\frac{R_k}{r}\right)^2 - E_{0_{2k}}\right]\cos(\theta) \\ E_{z_k} = \left[r\left(\dot{B}_a - \frac{\mu_0}{2}\sum_{i=k}^{n}\dot{K}_{0_i}\right) - \frac{1}{r}\frac{\mu_0}{2}\sum_{i=1}^{k-1}\dot{K}_{0_i}{R_i}^2\right]\cos(\theta) \end{cases} \tag{97}$$

To compute the local power density P_k dissipated by coupling currents in each layer k, we use the following formula

$$P_k = \vec{J}_k.\vec{E}_k \tag{98}$$

Decomposing vectors $\vec{J}_k$ and $\vec{E}_k$ in the cylindrical frame $(\overrightarrow{e_r}, \overrightarrow{e_\theta}, \overrightarrow{e_z})$, equation (98) becomes

$$P_k = J_{r_k}E_{r_k} + J_{\theta_k}E_{\theta_k} + J_{z_k}E_{z_k} \tag{99}$$

We have previously assumed $E_{r_k} = \rho_{t_k}J_{r_k}$ and $E_{\theta_k} = \rho_{t_k}J_{r_k}$, where ρ_{t_k} is the effective transverse resistivity of layer k. We can also define ρ_{l_k} as being the effective longitudinal resistivity of each layer k so that we have $E_{z_k} = \rho_{l_k}J_{z_k}$.

Note that in each resistive layer $\rho_{t_k} = \rho_{l_k}$ since metals are isotropic materials. However, in the filamentary zones, the effective transverse and longitudinal resistivities are different from one another, but they are of the same order of magnitude.

As a consequence, in each filamentary zone k, equation (99) leads to

$$P_k = \frac{E_{r_k}^2 + E_{\theta_k}^2}{\rho_{t_k}} + \frac{E_{z_k}^2}{\rho_{l_k}} \tag{100}$$

The ratio of the second to the first term of equation (100) can be majored as follows

$$\frac{\frac{E_{z_k}^2}{\rho_{l_k}}}{\frac{E_{r_k}^2+E_{\theta_k}^2}{\rho_{t_k}}} = \frac{E_{z_k}^2}{E_{r_k}^2+E_{\theta_k}^2}\frac{\rho_{t_k}}{\rho_{l_k}} \leq \frac{E_{z_k}^2}{E_{\theta_k}^2}\frac{\rho_{t_k}}{\rho_{l_k}} \tag{101}$$

Using relation (21), i.e. $E_\theta = -\frac{l_p}{2\pi r}E_z$, valid in each filamentary zone, we can deduce

$$\frac{E_{z_k}^2}{E_{\theta_k}^2}\frac{\rho_{t_k}}{\rho_{l_k}} = \left(\frac{2\pi r}{l_p}\right)^2\frac{\rho_{t_k}}{\rho_{l_k}} \ll 1$$

since $\left(\frac{2\pi r}{l_p}\right)^2 \ll 1$ according to assumption A5 and because ρ_{t_k} and ρ_{l_k} are of the same order of magnitude.

We can therefore reduce equation (101) in each filamentary zone to the following

$$P_k = \frac{E_{r_k}^2+E_{\theta_k}^2}{\rho_{t_k}} \tag{102}$$

On another side, in the resistive zones relation (21), i.e. $E_\theta = -\frac{l_p}{2\pi r}E_z$, is not valid but we can still consider that $E_{z_k}^2 \ll E_{r_k}^2+E_{\theta_k}^2$. Indeed, we can legitimately assume that first, the values of E_θ are of the same order of magnitude in the resistive zones and in the filamentary zones and secondly, that the values of E_z are also of the same order of magnitude in the resistive and filamentary zones. The ratio of $E_{z_k}^2/E_{\theta_k}^2$ being negligible in the filamentary zones, we can deduce that it is also the case in the resistive zones; we can therefore use formula (102) to evaluate the power density dissipated in each layer of the composite.

Replacing E_{r_k} and E_{θ_k} by their expressions given by (97) in formula (102), we obtain

$$P_k(r,\theta) = \frac{\left[E_{0_{2k-1}}\left(\frac{R_k}{r}\right)^2 + E_{0_{2k}}\right]^2\sin^2(\theta) + \left[E_{0_{2k-1}}\left(\frac{R_k}{r}\right)^2 - E_{0_{2k}}\right]^2\cos^2(\theta)}{\rho_{t_k}}$$

which reduces to

$$P_k(r,\theta) = \frac{1}{\rho_{t_k}}\left[{E_{0_{2k-1}}}^2\left(\frac{R_k}{r}\right)^4 + {E_{0_{2k}}}^2 - 2\,E_{0_{2k-1}}\left(\frac{R_k}{r}\right)^2 E_{0_{2k}}\cos(2\theta)\right] \tag{103}$$

The average power density $\bar{P}$ dissipated in a length L of composite is equal to

$$\bar{P} = \frac{1}{\pi R^2 L}\sum_{k=1}^{n}\iiint_{V_k} P_k(r,\theta)\,dV = \frac{1}{\pi R^2 L}\sum_{k=1}^{n}\int_{z=0}^{L}\int_{r=R_{k-1}}^{r=R_k}\int_{\theta=0}^{2\pi} P_k(r,\theta)\,r\,dr\,d\theta\,dz \tag{104}$$

Combining equations (103) and (104), we finally obtain

$$\bar{P} = \frac{1}{\rho_{t_1}}\left(\frac{R_1}{R}\right)^2 {E_{0_2}}^2 + \sum_{k=2}^{n} \frac{1}{\rho_{t_k}}\left(\frac{R_k}{R}\right)^2 \left(\left[\left(\frac{R_k}{R_{k-1}}\right)^2 - 1\right] {E_{0_{2k-1}}}^2 + \left[1 - \left(\frac{R_{k-1}}{R_k}\right)^2\right] {E_{0_{2k}}}^2\right) \qquad (105)$$

Note that the formula of the average power density is not given here per unit volume of filamentary zone as it has been done in (3) but per unit volume of composite.

II.2.7 Calculation of coupling currents and of electric and magnetic fields in the composite

❖ **We will express here the currents and the electric and magnetic fields in the composite as a function of the E_{0_k} coefficients.**

Our main objective here is to produce analytical tools which are able to compute every physical quantity inherent to a composite subject to a transverse time-varying magnetic field as this situation is commonly encountered in large superconducting devices (e.g. tokamaks, particle accelerators, etc.).

However since it is not possible to give an expression of these quantities without the preliminary knowledge of the composite design, we have decided to build a general algorithm (CLASS : Coupling Losses Algorithm for Superconducting Strands) able to compute them using mainly analytical formulae and the electrical and geometrical parameters of the strand. This choice of an analytical oriented algorithm is motivated by the fact that it ensures a very fast and light computation of the composite response to time-varying magnetic field: this is an important point in an environment where heavy computation times are required by other physics (e.g. thermal sciences, mechanics, etc.). It also has the benefit to be easily reproducible since all the formulae required for the calculation of the composite response are explicitly given in this manuscript.

We will now give a review of the expressions of each of the following physical quantities

- the surface current amplitudes $\left(K_{0_k}\right)_{1\leq k\leq n}$ flowing through the edges of the filamentary zones
- the distribution of the electric field $\vec{E}$
- the distribution of the transverse current $\vec{J}$ flowing through the resistive parts of the strand
- the distribution of the magnetic field $\vec{B}$

inside the composite as function of the $\left(E_{0_k}\right)_{2\leq k\leq 2n}$ coefficients and of its electrical (resistivities) and geometrical (radii of each zone and twist pitch of the filaments) parameters only.

The expressions of the surface current amplitudes $\left(K_{0_k}\right)_{1\leq k\leq n}$ has been given in equation (349)

$$[K_0] = \frac{1}{\rho_{t_1}} \frac{l_p}{2\pi} [M][E_0] \qquad (106)$$

where $[M]$ is a $n \times (2n-1)$ matrix whose coefficients can be computed using the procedure given in Figure 79.

The formulae of the transverse components of the electric field $\vec{E}$ in layer k are visible in (97)

$$\begin{cases} E_{r_k} = -\left[E_{0_{2k-1}}\left(\frac{R_k}{r}\right)^2 + E_{0_{2k}}\right]\sin(\theta) \\ E_{\theta_k} = \left[E_{0_{2k-1}}\left(\frac{R_k}{r}\right)^2 - E_{0_{2k}}\right]\cos(\theta) \end{cases} \tag{107}$$

The axial component of the electric field $\vec{E}$ in each layer is also given in (97) but as functions of the surface current amplitudes $\left(K_{0_k}\right)_{1\leq k\leq n}$ i.e.

$$E_{z_k} = \left[r\left(\dot{B}_a - \frac{\mu_0}{2}\sum_{i=k}^{n}\dot{K}_{0_i}\right) - \frac{1}{r}\frac{\mu_0}{2}\sum_{i=1}^{k-1}\dot{K}_{0_i}{R_i}^2\right]\cos(\theta)$$

First, using equations (350) and (352), we can replace the sum terms present in the above expression as follows

$$\begin{cases} \frac{\mu_0}{2}\sum_{i=k}^{n}\dot{K}_{0_i} = \frac{\mu_0}{2}[S]_{2k}\left[\dot{K}_0\right] \\ -\frac{\mu_0}{2}\sum_{i=1}^{k-1}\dot{K}_{0_i}{R_i}^2 = \frac{\mu_0}{2}{R_k}^2[S]_{2k-1}\left[\dot{K}_0\right] \end{cases}$$

where $[S]_{2k-1}$ and $[S]_{2k}$ are the line vectors defined in (351) and (353).

Therefore we now obtain the following expression for E_{z_k}

$$E_{z_k} = \left[r\left(\dot{B}_a - \frac{\mu_0}{2}[S]_{2k}\left[\dot{K}_0\right]\right) + \frac{{R_k}^2}{r}\frac{\mu_0}{2}[S]_{2k-1}\left[\dot{K}_0\right]\right]\cos(\theta)$$

which can be re-expressed as

$$E_{z_k} = r\left[\dot{B}_a + \frac{\mu_0}{2}\left([S]_{2k-1}\left(\frac{R_k}{r}\right)^2 - [S]_{2k}\right)\left[\dot{K}_0\right]\right]\cos(\theta)$$

Secondly, using the time derivative of equation (106), we finally have

$$E_{z_k} = r\left[\dot{B}_a + \frac{\mu_0}{2}\frac{1}{\rho_{t_1}}\frac{l_p}{2\pi}\left([S]_{2k-1}\left(\frac{R_k}{r}\right)^2 - [S]_{2k}\right)[M]\left[\dot{E}_0\right]\right]\cos(\theta) \tag{108}$$

From (107) we can readily derive the transverse components of the current distribution $\vec{J}$ in each layer k as

$$\begin{cases} J_{r_k} = \dfrac{E_{r_k}}{\rho_{t_k}} = -\dfrac{1}{\rho_{t_k}}\left[E_{0_{2k-1}}\left(\dfrac{R_k}{r}\right)^2 + E_{0_{2k}}\right]\sin(\theta) \\ J_{\theta_k} = \dfrac{E_{\theta_k}}{\rho_{t_k}} = \dfrac{1}{\rho_{t_k}}\left[E_{0_{2k-1}}\left(\dfrac{R_k}{r}\right)^2 - E_{0_{2k}}\right]\cos(\theta) \end{cases} \tag{109}$$

Regarding the axial component of $\vec{J}$, we can only give its expression in the resistive zones from (108)

$$J_{z_k} = \frac{E_{z_k}}{\rho_{t_k}} = \frac{1}{\rho_{t_k}} r\left[\dot{B}_a + \frac{\mu_0}{2}\frac{1}{\rho_{t_1}}\frac{l_p}{2\pi}\left([S]_{2k-1}\left(\frac{R_k}{r}\right)^2 - [S]_{2k}\right)[M]\left[\dot{E}_0\right]\right]\cos(\theta) \tag{110}$$

the expressions of J_z in the filamentary zones require the knowledge of their equivalent longitudinal resistivities; they must be consistent with their associated equivalent transverse resistivities.

Finally, to complete this review, we will derive here the expressions of the transverse components of the magnetic field $\vec{B}$.

Since the applied field $\overrightarrow{B_a}$ is oriented along the y-axis, we can deduce that

$$\begin{cases} B_{r_k} = B_a \sin(\theta) \\ B_{\theta_k} = B_a \cos(\theta) \end{cases}$$

Then, from $\vec{B} = \vec{\nabla} \times \vec{\mathrm{A}}$ and expression (58) of the magnetic vector potential generated by the surface currents, we have

$$\begin{cases} B_{r_k} = \dfrac{1}{r}\dfrac{\partial A_{z_k}}{\partial \theta} = -\dfrac{\mu_0}{2}\left[\dfrac{1}{r^2}\displaystyle\sum_{i=1}^{k-1} K_{0_i} R_i^2 + \sum_{i=k}^{n} K_{0_i}\right]\sin(\theta) \\ B_{\theta_k} = -\dfrac{\partial A_{z_k}}{\partial r} = \dfrac{\mu_0}{2}\left[\dfrac{1}{r^2}\displaystyle\sum_{i=1}^{k-1} K_{0_i} R_i^2 - \sum_{i=k}^{n} K_{0_i}\right]\cos(\theta) \end{cases}$$

Now, superposing the two above systems, we can write

$$\begin{cases} B_{r_k} = \left[B_a - \dfrac{\mu_0}{2}\left(\dfrac{1}{r^2}\displaystyle\sum_{i=1}^{k-1} K_{0_i} R_i^2 + \sum_{i=k}^{n} K_{0_i}\right)\right]\sin(\theta) \\ B_{\theta_k} = \left[B_a + \dfrac{\mu_0}{2}\left(\dfrac{1}{r^2}\displaystyle\sum_{i=1}^{k-1} K_{0_i} R_i^2 - \sum_{i=k}^{n} K_{0_i}\right)\right]\cos(\theta) \end{cases}$$

As we did in the derivation of E_{z_k}, we first can replace the sum terms to have

$$\begin{cases} B_{r_k} = \left[B_a + \dfrac{\mu_0}{2}\left([S]_{2k-1}\left(\dfrac{R_k}{r}\right)^2 - [S]_{2k}\right)[K_0]\right]\sin(\theta) \\ B_{\theta_k} = \left[B_a - \dfrac{\mu_0}{2}\left([S]_{2k-1}\left(\dfrac{R_k}{r}\right)^2 + [S]_{2k}\right)[K_0]\right]\cos(\theta) \end{cases}$$

and then replace $[K_0]$ with $\frac{1}{\rho_{t_1}}\frac{l_p}{2\pi}[M][E_0]$ using (106) to finally obtain

$$\begin{cases} B_{r_k} = \left[B_a + \frac{\mu_0}{2}\frac{1}{\rho_{t_1}}\frac{l_p}{2\pi}\left([S]_{2k-1}\left(\frac{R_k}{r}\right)^2 - [S]_{2k}\right)[M][E_0]\right]\sin(\theta) \\ B_{\theta_k} = \left[B_a - \frac{\mu_0}{2}\frac{1}{\rho_{t_1}}\frac{l_p}{2\pi}\left([S]_{2k-1}\left(\frac{R_k}{r}\right)^2 + [S]_{2k}\right)[M][E_0]\right]\cos(\theta) \end{cases} \quad (111)$$

II.2.8 Coupling losses per cycle per unit volume of filamentary zone

❖ **We will establish here the expression of coupling losses as a function of the E_{0_k} coefficients. We will also demonstrate that the coupling losses generated inside complex composites can be expressed as a sum of the coupling losses generated inside simple composites; this result is important and will be used in the study of a two cabling stages conductor in section IV.3 .**

In order to remove any ambiguity, let us clarify what we mean by "volume of filamentary zone" or "volume enclosed by the outer edge filaments". If we note R_f the radius on which the most outer edge filaments are located, here are its values for different designs of composite:

- for an F type composite, $R_f = R_1 = R$, (R always refers to the composite radius)
- for an F/R type composite, $R_f = R_1$
- for an R/F type composite, $R_f = R_2 = R$
- for an R/F/R/R type composite (e.g. JT-60SA TF strand displayed on Figure 11), $R_f = R_2$

The volume that we have called "volume of filamentary zone" or "volume enclosed by the outer edge filaments" throughout the manuscript is in fact the one of a cylinder of radius R_f and length L; this length is not set to any value as the composite geometry is considered to be invariant along its axis according to assumption A1. Therefore the coupling losses per cycle per unit volume of filamentary zone Q correspond to the total energy that has been dissipated over the whole volume of the composite and during a cycle of a periodic magnetic excitation, divided by the volume of the cylinder of radius R_f.

After having clearly defined the notion of "coupling losses per cycle per unit volume of filamentary zone Q", we will now focus on its determination as function of the frequency f of a sinusoidal magnetic excitation. This "Q vs f" curve is usually considered in the community as it gives the full characterization of the frequency response of a composite with regard to any magnetic excitation.

Up to this point, we possess all the elements to produce this curve. Indeed, we have derived the formulae required to compute the coupling losses generated by any magnetic signal inside a composite. Therefore, in order to obtain one point of the "Q vs f" curve, we should simulate the time response of the $\left(E_{0_k}\right)_{2\leq k\leq 2n}$ coefficients to a sinusoidal magnetic signal with a specific frequency using equation (72), deduce the average coupling power density thanks to (105) and compute the associated value of Q. To produce the full curve we should then repeat this process for different values of the frequency of magnetic excitation.

Even though this process can be achieved in a very reasonable time, we propose a faster method leading to an analytical expression of $Q(f)$.

Let us assume that the composite is subject to the following magnetic signal

$$B_a = B_p \sin(\omega t)$$

with $\omega = 2\pi f$, the angular frequency.

We can first start by deriving the classical expression of $Q(\omega)$ for a composite made of a filamentary zone only (F type) given in (7) (with $n = 2$ for a cylindrical composite) i.e.

$$Q(\omega) = \frac{{B_p}^2}{\mu_0} \frac{2\pi\omega\tau}{1 + (\omega\tau)^2}$$

from time equation (1), i.e. $B_i + \tau \dot{B}_i = B_a$, and from expression (3) of coupling power per unit volume of filamentary zone which is

$$P = \frac{2\tau {\dot{B}_i}^2}{\mu_0}$$

Using equation (1), the expression of B_a and the initial condition $B_i(t = 0) = B_a(t = 0) = 0$, we find the following solution for B_i

$$B_i(t) = \frac{B_p}{1 + (\omega\tau)^2} \left[\sin(\omega t) - \omega\tau \cos(\omega t) + \omega\tau e^{-t/\tau}\right]$$

After a time long compared to τ (typically for $t > 5\tau$), we have

$$B_i(t \gg \tau) = \frac{B_p}{1 + (\omega\tau)^2} [\sin(\omega t) - \omega\tau \cos(\omega t)]$$

Therefore

$$\dot{B}_i(t \gg \tau) = \frac{B_p \omega}{1 + (\omega\tau)^2} [\cos(\omega t) + \omega\tau \sin(\omega t)]$$

In the following, the notation $\langle X(t) \rangle$ will always corresponds to $\langle X(t) \rangle = \frac{1}{T} \int_{t_0}^{t_0+T} X(t) dt$.

If we now compute the average of ${\dot{B}_i}^2(t)$ over the time period $T = 1/f$ of the applied magnetic signal, we have

$$\langle {\dot{B}_i}^2(t) \rangle = \left(\frac{B_p \omega}{1 + (\omega\tau)^2}\right)^2 \langle [\cos(\omega t) + \omega\tau \sin(\omega t)]^2 \rangle$$

$$= \left(\frac{B_p \omega}{1 + (\omega\tau)^2}\right)^2 [\langle \cos^2(\omega t) \rangle + (\omega\tau)^2 \langle \sin^2(\omega t) \rangle + 2\omega\tau \langle \sin(\omega t) \cos(\omega t) \rangle]$$

$$= \left(\frac{B_p \omega}{1 + (\omega\tau)^2}\right)^2 \frac{1}{2} [1 + (\omega\tau)^2]$$

$$= \frac{1}{2}\frac{{B_p}^2\omega^2}{1+(\omega\tau)^2}$$

As a consequence, since $Q = \langle P(t)\rangle T$ and $T = \frac{2\pi}{\omega}$, using (3) we have

$$Q(\omega) = \frac{2\tau}{\mu_0}\langle {\dot{B}_i}^2\rangle\, T = \frac{{B_p}^2}{\mu_0}\frac{2\pi\omega\tau}{1+(\omega\tau)^2}$$

Now that we have derived the expression of Q as function of ω for F type composites, we will focus on its determination for other types of composite.

Since we know the expression of the (spatial) average power density $\bar{P}$ dissipated in any composite as function of the $\left(E_{0_k}\right)_{2\le k\le 2n}$ coefficients from (105), we can first begin by rewriting it in the following abbreviated form

$$\bar{P}(t) = \sum_{j=2}^{2n} \beta_j {E_{0_j}}^2(t) \tag{112}$$

with, by identification

$$\begin{cases} \beta_2 = \dfrac{1}{\rho_{t_1}}\left(\dfrac{R_1}{R}\right)^2 \\ \beta_{2j-1} = \dfrac{1}{\rho_{t_j}}\left(\dfrac{R_j}{R}\right)^2\left[\left(\dfrac{R_j}{R_{j-1}}\right)^2 - 1\right] \;\; for\; 2\le j\le n \\ \beta_{2j} = \dfrac{1}{\rho_{t_j}}\left(\dfrac{R_j}{R}\right)^2\left[1-\left(\dfrac{R_{j-1}}{R_j}\right)^2\right] for\; 2\le j\le n \end{cases} \tag{113}$$

From equation (112), it is possible to express the coupling losses per cycle per unit volume of filamentary zone Q as

$$Q(\omega) = \left(\frac{R}{R_f}\right)^2 \langle \bar{P}(t)\rangle T = \frac{2\pi}{\omega}\left(\frac{R}{R_f}\right)^2 \sum_{j=2}^{2n} \beta_j \langle {E_{0_j}}^2(t)\rangle \tag{114}$$

Note that the term $\left(\frac{R}{R_f}\right)^2$ comes from the fact that $\bar{P}$ has been defined per unit volume of composite while Q is defined per unit volume of filamentary zone.

To complete the process, we now need to analytically solve equation (72), i.e.

$$[A][E_0] + \frac{\mu_0}{2}\left(\frac{l_p}{2\pi}\right)^2 \frac{1}{\rho_{t_1}}[B]\left[\dot{E}_0\right] = \frac{l_p}{2\pi}\dot{B}_a[Y]$$

for the time dependence of the $\left(E_{0_k}\right)_{2\le k\le 2n}$ coefficients.

In order to do so, we begin by re-expressing time equation (72) as

$$[E_0] + [\tau]\left[\dot{E}_0\right] = \frac{l_p}{2\pi}\dot{B}_a[A]^{-1}[Y] \tag{115}$$

where $[\tau]$ is a $(2n-1)\times(2n-1)$ matrix whose coefficients have the dimension of time and which is defined as

$$[\tau] = [A]^{-1}[B] \tag{116}$$

Assuming that $[\tau]$ is a diagonalizable matrix, we can express it as

$$[\tau] = [V][\tau_c][V]^{-1} \tag{117}$$

where $[\tau_c]$ is the diagonal matrix containing the eigenvalues of $[\tau]$ and $[V]$ is the matrix containing the eigenvectors of $[\tau]$.

Replacing $[\tau]$ with $[V][\tau_c][V]^{-1}$ in (115) leads to

$$[E_0] + [V][\tau_c][V]^{-1}\left[\dot{E}_0\right] = \frac{l_p}{2\pi}\dot{B}_a[A]^{-1}[Y]$$

The multiplication on each side by $[V]^{-1}$ gives

$$[X] + [\tau_c]\left[\dot{X}\right] = \dot{B}_a[Y_b] \tag{118}$$

with

$$[X] = [V]^{-1}[E_0] \tag{119}$$

and

$$[Y_b] = \frac{l_p}{2\pi}[V]^{-1}[A]^{-1}[Y] \tag{120}$$

Equation (118) can alternatively be written, for $1 \le k \le 2n-1$, as

$$[X]_k + \tau_{c_k}\left[\dot{X}\right]_k = \dot{B}_a[Y_b]_k \tag{121}$$

where $[X]_k$ and $[Y_b]_k$ are respectively the k^{th} component of the column vectors $[X]$ and $[Y_b]$, and $\tau_{c_k} = [\tau_c]_{k\,k}$ is the k^{th} diagonal element of $[\tau_c]$, i.e. the k^{th} eigenvalue of $[\tau]$.

By analogy with the previous resolution of equation (1), we can give the solutions of equations (121) as

$$[X]_k(t) = \frac{[Y_b]_k B_p \omega}{1 + \left(\omega\tau_{c_k}\right)^2}\left[\cos(\omega t) + \omega\tau_{c_k}\sin(\omega t)\right] \tag{122}$$

These solutions are obtained considering the initial conditions $([X]_k(t=0) = 0)_{1\le k\le 2n-1}$ and are valid after a time long compared to the greatest value of $\left(\tau_{c_k}\right)_{1\le k\le 2n-1}$.

Inverting relation (119), we have $[E_0] = [V][X]$ which leads to

$$E_{0_j}(t) = \sum_{k=1}^{2n-1}[V]_{j-1\,k}[X]_k(t) \tag{123}$$

Remember that since E_{0_1} is always zero, the first component of the $[E_0]$ $(2n-1)\times 1$ column vector is E_{0_2} and its j^{th} component is in fact $E_{0_{j-1}}$. To avoid any confusion, we note $[E_0]_j$ the j^{th} component of column vector $[E_0]$ and E_{0_j} the j^{th} coefficient of the $\left(E_{0_j}\right)_{2\leq \mathrm{j}\leq 2n}$; we therefore have $[E_0]_j = E_{0_{j-1}}$.

The combination of equations (122) and (123) enables us to write

$$E_{0_j}{}^2(t) = \left(B_p\omega\right)^2\left[\cos(\omega t)\sum_{k=1}^{2n-1}\frac{[V]_{j-1\,k}[Y_b]_k}{1+\left(\omega\tau_{c_k}\right)^2} + \sin(\omega t)\sum_{k=1}^{2n-1}\omega\tau_{c_k}\frac{[V]_{j-1\,k}[Y_b]_k}{1+\left(\omega\tau_{c_k}\right)^2}\right]^2$$

Thus, the average of $E_{0_j}{}^2(t)$ over one cycle of duration T is

$$\langle E_{0_j}{}^2(t)\rangle = \frac{\left(B_p\omega\right)^2}{2}\left(\left[\sum_{k=1}^{2n-1}\frac{[V]_{j-1\,k}[Y_b]_k}{1+\left(\omega\tau_{c_k}\right)^2}\right]^2 + \left[\sum_{k=1}^{2n-1}\omega\tau_{c_k}\frac{[V]_{j-1\,k}[Y_b]_k}{1+\left(\omega\tau_{c_k}\right)^2}\right]^2\right)$$

since $\langle\cos^2(\omega t)\rangle = \langle\sin^2(\omega t)\rangle = \frac{1}{2}$ and $\langle\cos(\omega t)\sin(\omega t)\rangle = 0$.

This average can be factorized, using $A^2+B^2 = (A-iB)(A+iB)$ with i the imaginary unit, as

$$\langle E_{0_j}{}^2(t)\rangle = \frac{\left(B_p\omega\right)^2}{2}\left[\sum_{k=1}^{2n-1}\frac{[V]_{j-1\,k}[Y_b]_k}{1+\left(\omega\tau_{c_k}\right)^2}\left(1-i\omega\tau_{c_k}\right)\right]\left[\sum_{k=1}^{2n-1}\frac{[V]_{j-1\,k}[Y_b]_k}{1+\left(\omega\tau_{c_k}\right)^2}\left(1+i\omega\tau_{c_k}\right)\right]$$

To make the above expression lighter we will temporarily note the terms appearing in the sums as a_k and b_k respectively, i.e.

$$\begin{cases} a_k = \dfrac{[V]_{j-1\,k}[Y_b]_k}{1+\left(\omega\tau_{c_k}\right)^2}\left(1-i\omega\tau_{c_k}\right) \\ b_k = \dfrac{[V]_{j-1\,k}[Y_b]_k}{1+\left(\omega\tau_{c_k}\right)^2}\left(1+i\omega\tau_{c_k}\right) \end{cases}$$

Thus $\langle E_{0_j}{}^2(t)\rangle$ can be expressed as

$$\langle E_{0_j}{}^2(t)\rangle = \frac{\left(B_p\omega\right)^2}{2}\left[\sum_{k=1}^{2n-1}a_k\right]\left[\sum_{k=1}^{2n-1}b_k\right]$$

In addition, we have

$$\left[\sum_{k=1}^{2n-1}a_k\right]\left[\sum_{k=1}^{2n-1}b_k\right] = \left[\sum_{k=1}^{2n-1}a_k\right]\left[\sum_{l=1}^{2n-1}b_l\right] = \sum_{k=1}^{2n-1}\sum_{l=1}^{2n-1}a_kb_l = \frac{1}{2}\sum_{k=1}^{2n-1}\sum_{l=1}^{2n-1}(a_kb_l + a_lb_k)$$

since summation indices k and l can be interchanged, and

$$a_kb_l + a_lb_k = \frac{[V]_{j-1\,k}[Y_b]_k}{1+\left(\omega\tau_{c_k}\right)^2}\frac{[V]_{j-1\,l}[Y_b]_l}{1+\left(\omega\tau_{c_l}\right)^2}\left[\left(1-i\omega\tau_{c_k}\right)\left(1+i\omega\tau_{c_l}\right) + \left(1-i\omega\tau_{c_l}\right)\left(1+i\omega\tau_{c_k}\right)\right]$$

$$= 2[V]_{j-1\,k}[Y_b]_k[V]_{j-1\,l}[Y_b]_l \frac{1+\omega^2\tau_{c_k}\tau_{c_l}}{\left[1+\left(\omega\tau_{c_k}\right)^2\right]\left[1+\left(\omega\tau_{c_l}\right)^2\right]}$$

Thus

$$\langle {E_0}_j{}^2(t)\rangle = \frac{\left(B_p\omega\right)^2}{2}\sum_{k=1}^{2n-1}\sum_{l=1}^{2n-1}[V]_{j-1\,k}[Y_b]_k[V]_{j-1\,l}[Y_b]_l \frac{1+\omega^2\tau_{c_k}\tau_{c_l}}{\left[1+\left(\omega\tau_{c_k}\right)^2\right]\left[1+\left(\omega\tau_{c_l}\right)^2\right]}$$

Moreover, using a partial fraction decomposition, it appears that

$$\frac{1+\omega^2\tau_{c_k}\tau_{c_l}}{\left[1+\left(\omega\tau_{c_k}\right)^2\right]\left[1+\left(\omega\tau_{c_l}\right)^2\right]} = \frac{1}{\tau_{c_k}+\tau_{c_l}}\left[\frac{\tau_{c_k}}{1+\left(\omega\tau_{c_k}\right)^2}+\frac{\tau_{c_l}}{1+\left(\omega\tau_{c_l}\right)^2}\right]$$

Therefore we can conclude that

$$\langle {E_0}_j{}^2(t)\rangle = \frac{\left(B_p\omega\right)^2}{2}\sum_{k=1}^{2n-1}\sum_{l=1}^{2n-1}\frac{[V]_{j-1\,k}[Y_b]_k[V]_{j-1\,l}[Y_b]_l}{\tau_{c_k}+\tau_{c_l}}\left[\frac{\tau_{c_k}}{1+\left(\omega\tau_{c_k}\right)^2}+\frac{\tau_{c_l}}{1+\left(\omega\tau_{c_l}\right)^2}\right]$$

which reduces to

$$\langle {E_0}_j{}^2(t)\rangle = \left(B_p\omega\right)^2\sum_{k=1}^{2n-1}\sum_{l=1}^{2n-1}\frac{[V]_{j-1\,k}[Y_b]_k[V]_{j-1\,l}[Y_b]_l}{\tau_{c_k}+\tau_{c_l}}\frac{\tau_{c_k}}{1+\left(\omega\tau_{c_k}\right)^2}$$

splitting the previous double sum into two double sums and interchanging k and l in the second one.

Finally, we obtain

$$\langle {E_0}_j{}^2(t)\rangle = \left(B_p\omega\right)^2\sum_{k=1}^{2n-1}\frac{[V]_{j-1\,k}[Y_b]_k\tau_{c_k}}{1+\left(\omega\tau_{c_k}\right)^2}\sum_{l=1}^{2n-1}\frac{[V]_{j-1\,l}[Y_b]_l}{\tau_{c_k}+\tau_{c_l}} \tag{124}$$

The combination of equations (114) and (124) enables us to write

$$Q(\omega) = \frac{2\pi}{\omega}\left(\frac{R}{R_f}\right)^2\sum_{j=2}^{2n}\beta_j\left(B_p\omega\right)^2\sum_{k=1}^{2n-1}\frac{[V]_{j-1\,k}[Y_b]_k\tau_{c_k}}{1+\left(\omega\tau_{c_k}\right)^2}\sum_{l=1}^{2n-1}\frac{[V]_{j-1\,l}[Y_b]_l}{\tau_{c_k}+\tau_{c_l}}$$

which can be re-expressed as

$$Q(\omega) = {B_p}^2\left(\frac{R}{R_f}\right)^2\sum_{k=1}^{2n-1}\left[\sum_{j=1}^{2n-1}\sum_{l=1}^{2n-1}\frac{\beta_{j+1}[V]_{j\,k}[V]_{j\,l}[Y_b]_l[Y_b]_k}{\tau_{c_k}+\tau_{c_l}}\right]\frac{2\pi\omega\tau_{c_k}}{1+\left(\omega\tau_{c_k}\right)^2} \tag{125}$$

We have now derived the analytical expression of $Q(\omega)$ for any composite for any magnetic excitation B_a of the form $B_a = B_p\sin(\omega t)$.

If we take a close look at formula (125) we notice that it is very similar to the formula (7) of $Q(\omega)$ for F type composites, i.e.

$$Q(\omega) = \frac{{B_p}^2}{\mu_0} \frac{2\pi\omega\tau}{1+(\omega\tau)^2}$$

In order to highlight the resemblance between formulae (7) and (125) we will introduce another function $Q_{classical}(\omega,\tau)$ defined as

$$Q_{classical}(\omega,\tau) = \frac{{B_p}^2}{\mu_0} \frac{2\pi\omega\tau}{1+(\omega\tau)^2} \tag{126}$$

which represents the average coupling losses per cycle of magnetic excitation $B_p \sin(\omega t)$ per unit volume of filamentary zone for a composite with only one time constant τ.

Using this new function, it is then possible to formulate equation (125) as

$$Q(\omega) = \sum_{k=1}^{2n-1} \alpha_k Q_{classical}\left(\omega, \tau_{c_k}\right) \tag{127}$$

with

$$\alpha_k = \mu_0 \left(\frac{R}{R_f}\right)^2 \sum_{j=1}^{2n-1} \sum_{l=1}^{2n-1} \frac{\beta_{j+1} [V]_{j\,k} [V]_{j\,l} [Y_b]_l [Y_b]_k}{\tau_{c_k} + \tau_{c_l}} \tag{128}$$

where β is defined in (113), $[V]$ and $[\tau_c]$ are obtained diagonalizing $[\tau]$, and $[Y_b]$ is defined in (120).

Formula (127) is a very meaningful physical result as it clearly indicates that the coupling losses of a complex strand with N multiple time constants can be seen as a cumulation of the coupling losses generated by N elementary strands (i.e. F type strands) having specific effective time constants and effective volumes. Indeed, instead of formula (127), we could write

$$Q(\omega) = \sum_{k=1}^{2n-1} \left(\frac{R_{f_k}}{R_f}\right)^2 Q_{classical}\left(\omega, \tau_{c_k}\right)$$

where R_{f_k} would be defined as $R_{f_k} = R_f \sqrt{\alpha_k}$ and would represent the radius of the effective shielded volume of each elementary strand. In this regard we can straightforwardly realize that the coupling between the screening currents leads to the modification of the shielding accomplished by each screening current if it was isolated; the notion of partial shielding can therefore be observed down to the strand scale.

Furthermore, we have previously mentioned that a strand with n layers did not really have $2n-1$ time constants; the number of time constants it possesses is equal to the number of edges of its filamentary zones. The apparent surplus of time constants in formula (127) seems to be inconsistent with this fact. However we have also mentioned that among the $2n-1$ time constants, some were artificial ones because their presence was due to our modeling. This paradox is solved by the fact that the α_k coefficients associated with the artificial time constants are zero (we will not demonstrate this point here but we have observed it for every design we tested).

Another point is that the sum of the α_k coefficients is equal to 1. In order to demonstrate this, let us consider an F type composite with its outer edge filaments located at $r = R_f$ subject to a step-type variation of the applied magnetic field from 0 to B_s. The energy stored per unit length of strand E_l just after the step is equal to

$$E_l = \frac{{B_s}^2}{\mu_0}\pi {R_f}^2$$

After the step, the currents induced inside the strand will start to decrease until they reach zero; the final energy stored in the strand will then also be zero. The only dissipative phenomena we consider here are coupling losses, therefore we can deduce that the integral over time of the coupling losses per unit length of strand after the step will then be equal to E_l to ensure the conservation of energy.

If we apply the same step change of B_a on a composite with multiple time constants and with the same R_f, the energy stored per unit length of this composite just after the step will also be equal to E_l. Indeed, the change of B_a being instantaneous, the magnetic shielding of the composite will exclusively be accomplished by its outer edge filaments located at $r = R_f$; it is only when the current they carry start to decay that the internal edge filaments (located at $r < R_f$) begin to develop their own screening currents.

Since the coupling losses of a strand with N multiple time constants correspond to the sum of those generated by N F type strands having their outer edge filaments located at $r = R_{f_k}$ $(1 \leq k \leq N)$, we deduce that E_l can also be expressed as

$$E_l = \sum_{k=1}^{N} \frac{{B_s}^2}{\mu_0}\pi {R_{f_k}}^2$$

Consequently, we have

$$\sum_{k=1}^{N} {R_{f_k}}^2 = {R_f}^2$$

which is equivalent to

$$\sum_{k=1}^{N} \left(\frac{R_{f_k}}{R_f}\right)^2 = 1$$

And since $\alpha_k = \left(R_{f_k}/R_f\right)^2$, we have thus demonstrated that

$$\sum_{k=1}^{N} \alpha_k = 1$$

Finally it also important to notice that in a strand with N distinct time constants, the $(\alpha_k)_{1\leq k\leq N}$ depend on the transverse resistivities of the different zones. Indeed the $(\alpha_k)_{1\leq k\leq N}$ are given by formula (128) in which appear the coefficients of β, $[V]$, $[Y_b]$ and the time constants $\left(\tau_{c_k}\right)_{1\leq k\leq N}$; all these parameters depend on the transverse resistivities of the different zones. The only exception is for strands with a single time constant, in this case there will only be one non zero α_k coefficient which must be equal to 1 and therefore does not depend on the transverse resistivities of the different zones.

II.3 Comparisons with literature analytical models

In this section we will show that the formulae derived in our analytical modeling are fully consistent with those issued from previous analytical studies found in the literature.

II.3.1 F type composite

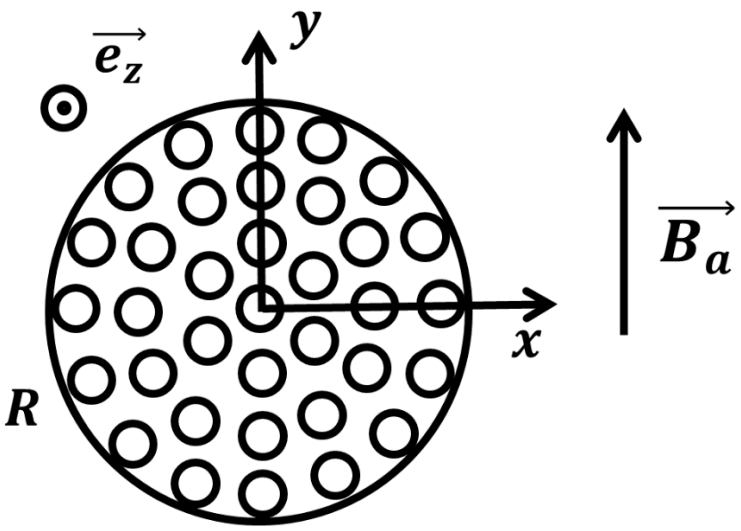

Figure 19 : Scheme of cross-section of F type composite

In the case of a composite consisting in a unique zone of filamentary type (displayed on Figure 19), we can give the equation governing E_{0_2} using equation (72) and the relevant expressions of $[A]$, $[Y]$ and $[B]$ that we have previously derived (i.e. $[A] = [Y] = [B] = 1$)

$$E_{0_2} + \frac{\mu_0}{2}\left(\frac{l_p}{2\pi}\right)^2 \frac{1}{\rho_{t_1}} \dot{E}_{0_2} = \frac{l_p}{2\pi} \dot{B}_a$$

In this case there will be a supercurrent, whose spatial amplitude is $K_{0_1} = \frac{1}{\rho_{t_1}} \frac{l_p}{2\pi} E_{0_2}$, flowing through the superconducting filaments located on the edge of the composite. According to equation (57), we know that this supercurrent will create a reacting magnetic field $\overrightarrow{B_{react}} = -\frac{\mu_0 K_{0_1}}{2} \overrightarrow{e_y}$ inside the composite. By superposition, the total internal magnetic field $\vec{B}_i$ will be given by

$$\vec{B}_i = \overrightarrow{B_a} + \vec{B}_{react} = B_a \overrightarrow{e_y} - \frac{\mu_0 K_{0_1}}{2} \overrightarrow{e_y} = B_i \overrightarrow{e_y}$$

with

$$B_i = B_a - \frac{\mu_0 K_{0_1}}{2}$$

Replacing K_{0_1} with $\frac{1}{\rho_{t_1}}\frac{l_p}{2\pi}E_{0_2}$ in the expression above leads to

$$B_i = B_a - \frac{\mu_0}{2}\frac{1}{\rho_{t_1}}\frac{l_p}{2\pi}E_{0_2}$$

which is equivalent to

$$E_{0_2} = \frac{2}{\mu_0}\rho_{t_1}\frac{2\pi}{l_p}(B_a - B_i)$$

If we now replace E_{0_2} by $\frac{2}{\mu_0}\rho_{t_1}\frac{2\pi}{l_p}(B_a - B_i)$ in the equation on E_{0_2}, we have

$$\frac{2}{\mu_0}\rho_{t_1}\frac{2\pi}{l_p}(B_a - B_i) + \frac{l_p}{2\pi}(\dot{B}_a - \dot{B}_i) = \frac{l_p}{2\pi}\dot{B}_a$$

Multiplying both sides by $\frac{\mu_0}{2}\frac{1}{\rho_{t_1}}\frac{l_p}{2\pi}$, after some manipulations, we finally obtain

$$B_i + \frac{\mu_0}{2}\left(\frac{l_p}{2\pi}\right)^2\frac{1}{\rho_{t_1}}\dot{B}_i = B_a$$

which is exactly the classical equation governing the internal induction inside a composite composed of a filamentary zone only (see equations (1) and (2) in the "state of the art" section).

II.3.2 R/F/R type composite

We will now derive the equations governing R/F/R type composites (see Figure 20) and compare them to those developed by Ciazynski [30].

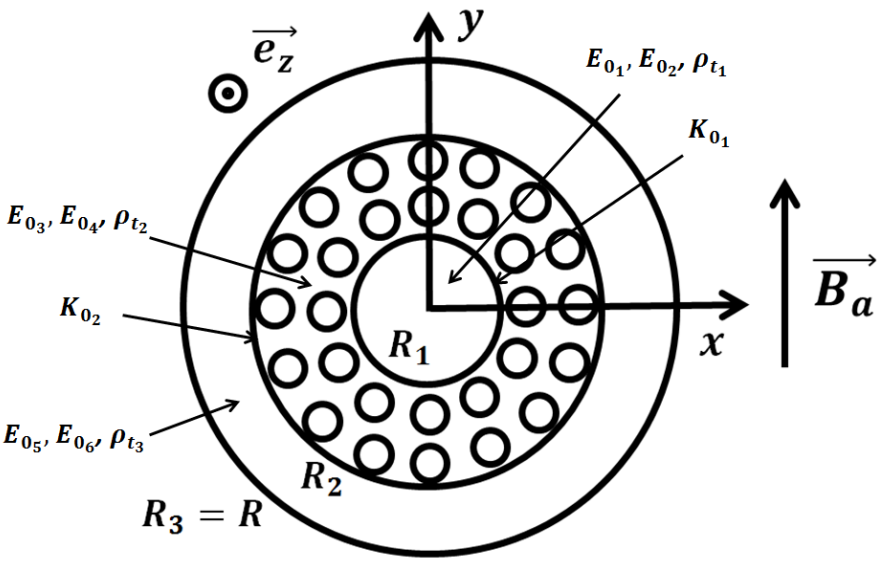

Figure 20 : Scheme of cross-section of R/F/R type composite

For this geometry, we will not use equation (72) as the associated expressions of $[A]$, $[Y]$ and $[B]$ will be quite heavy and not easy to manipulate. We will then start by writing equations (68) for $k = 2$ and $n = 3$ as it is a much more convenient way :

$$\begin{cases} E_{0_3} - \dfrac{\mu_0}{2}\dfrac{l_p}{2\pi}\displaystyle\sum_{i=1}^{1} \dot{K}_{0_i}\left(\dfrac{R_i}{R_2}\right)^2 = 0 \\ E_{0_4} + \dfrac{\mu_0}{2}\dfrac{l_p}{2\pi}\displaystyle\sum_{i=2}^{3} \dot{K}_{0_i} = \dfrac{l_p}{2\pi}\dot{B}_a \end{cases}$$

This leads to

$$\begin{cases} E_{0_3} = \dfrac{\mu_0}{2}\dfrac{l_p}{2\pi}\left(\dfrac{R_1}{R_2}\right)^2 \dot{K}_{0_1} \\ E_{0_4} = -\dfrac{\mu_0}{2}\dfrac{l_p}{2\pi}\dot{K}_{0_2} + \dfrac{l_p}{2\pi}\dot{B}_a \end{cases}$$

given the fact that $K_{0_3} = 0$ since there is no filament at $r = R_3$ in the R/F/R composite (see Figure 20). Using the expressions of K_{0_1} and K_{0_2} as functions of the $\left(E_{0_k}\right)_{2\leq k\leq 6}$ given by (44) for $k = 1$ and $k = 2$, we have

$$\begin{cases} K_{0_1} = \dfrac{l_p}{2\pi}\left[\dfrac{1}{\rho_{t_1}}E_{0_2} - \dfrac{1}{\rho_{t_2}}\left(\dfrac{R_2}{R_1}\right)^2 E_{0_3} - \dfrac{1}{\rho_{t_2}}E_{0_4}\right] \\ K_{0_2} = \dfrac{l_p}{2\pi}\left[\dfrac{1}{\rho_{t_2}}E_{0_3} + \dfrac{1}{\rho_{t_2}}E_{0_4} - \dfrac{1}{\rho_{t_3}}\left(\dfrac{R_3}{R_2}\right)^2 E_{0_5} - \dfrac{1}{\rho_{t_3}}E_{0_6}\right] \end{cases}$$

We also have to consider the two continuity equations of E_θ at $r = R_1$ and $r = R_2$ given by (343) for $k = 1$ and $k = 2$

$$\begin{cases} -E_{0_2} - \left(\dfrac{R_2}{R_1}\right)^2 E_{0_3} + E_{0_4} = 0 \\ E_{0_3} - E_{0_4} - \left(\dfrac{R_3}{R_2}\right)^2 E_{0_5} + E_{0_6} = 0 \end{cases}$$

as well as the boundary condition $E_{r_3}(R_3) = 0$ given by (43)

$$E_{0_6} = -E_{0_5}$$

The combination of these equations enables us to express E_{0_2}, E_{0_5} and E_{0_6} as functions of E_{0_3} and E_{0_4}

$$\begin{cases} E_{0_2} = -\left(\dfrac{R_2}{R_1}\right)^2 E_{0_3} + E_{0_4} \\ E_{0_5} = \dfrac{{R_2}^2}{{R_2}^2 + {R_3}^2}\left(E_{0_3} - E_{0_4}\right) \\ E_{0_6} = \dfrac{{R_2}^2}{{R_2}^2 + {R_3}^2}\left(-E_{0_3} + E_{0_4}\right) \end{cases}$$

Injecting these new relations into the formulae of K_{0_1} and K_{0_2} above leads to

$$\begin{cases} K_{0_1} = \dfrac{1}{\rho_{t_2}} \dfrac{l_p}{2\pi} \left[-\left(\dfrac{R_2}{R_1}\right)^2 \left(\dfrac{\rho_{t_2}}{\rho_{t_1}} + 1\right) E_{0_3} + \left(\dfrac{\rho_{t_2}}{\rho_{t_1}} - 1\right) E_{0_4} \right] \\ K_{0_2} = \dfrac{1}{\rho_{t_2}} \dfrac{l_p}{2\pi} \left[\left(1 - \dfrac{\rho_{t_2}}{\rho_{t_3}} \dfrac{{R_3}^2 - {R_2}^2}{{R_3}^2 + {R_2}^2}\right) E_{0_3} + \left(1 + \dfrac{\rho_{t_2}}{\rho_{t_3}} \dfrac{{R_3}^2 - {R_2}^2}{{R_3}^2 + {R_2}^2}\right) E_{0_4} \right] \end{cases}$$

Finally, replacing E_{0_3} and E_{0_4} with their expressions as functions of $\dot{K}_{0_1}$, $\dot{K}_{0_2}$ and $\dot{B}_a$ in the new formulae of K_{0_1} and K_{0_2}, we obtain

$$\begin{cases} K_{0_1} + \left(\dfrac{\rho_{t_2}}{\rho_{t_1}} + 1\right) \tau_c \dot{K}_{0_1} + \left(\dfrac{\rho_{t_2}}{\rho_{t_1}} - 1\right) \tau_c \dot{K}_{0_2} = \left(\dfrac{\rho_{t_2}}{\rho_{t_1}} - 1\right) \dfrac{2}{\mu_0} \tau_c \dot{B}_a \\ K_{0_2} + \left(\dfrac{R_1}{R_2}\right)^2 \left(\dfrac{\rho_{t_2}}{\rho_{t_3}} \dfrac{{R_3}^2 - {R_2}^2}{{R_3}^2 + {R_2}^2} - 1\right) \tau_c \dot{K}_{0_1} + \left(\dfrac{\rho_{t_2}}{\rho_{t_3}} \dfrac{{R_3}^2 - {R_2}^2}{{R_3}^2 + {R_2}^2} + 1\right) \tau_c \dot{K}_{0_2} = \left(\dfrac{\rho_{t_2}}{\rho_{t_3}} \dfrac{{R_3}^2 - {R_2}^2}{{R_3}^2 + {R_2}^2} + 1\right) \dfrac{2}{\mu_0} \tau_c \dot{B}_a \end{cases}$$

with

$$\tau_c = \frac{\mu_0}{2} \left(\frac{l_p}{2\pi}\right)^2 \frac{1}{\rho_{t_2}}$$

These equations can be turned into the following matrix equation

$$\begin{bmatrix} K_{0_1} \\ K_{0_2} \end{bmatrix} + \begin{bmatrix} \tau_{1\,1} & \tau_{1\,2} \\ \tau_{2\,1} & \tau_{2\,2} \end{bmatrix} \begin{bmatrix} \dot{K}_{0_1} \\ \dot{K}_{0_2} \end{bmatrix} = \frac{2}{\mu_0} \begin{bmatrix} \tau_{ext\,1} \\ \tau_{ext\,2} \end{bmatrix} \dot{B}_a$$

with

$$\begin{cases} \tau_{1\,1} = \left(\dfrac{\rho_{t_2}}{\rho_{t_1}} + 1\right) \tau_c \\ \tau_{1\,2} = \left(\dfrac{\rho_{t_2}}{\rho_{t_1}} - 1\right) \tau_c \\ \tau_{2\,1} = \left(\dfrac{R_1}{R_2}\right)^2 \left(\dfrac{\rho_{t_2}}{\rho_{t_3}} \dfrac{{R_3}^2 - {R_2}^2}{{R_3}^2 + {R_2}^2} - 1\right) \tau_c \\ \tau_{2\,2} = \left(\dfrac{\rho_{t_2}}{\rho_{t_3}} \dfrac{{R_3}^2 - {R_2}^2}{{R_3}^2 + {R_2}^2} + 1\right) \tau_c \end{cases}$$

and

$$\begin{cases} \tau_{ext\,1} = \tau_{1\,2} = \left(\dfrac{\rho_{t_2}}{\rho_{t_1}} - 1\right) \tau_c \\ \tau_{ext\,2} = \tau_{2\,2} = \left(\dfrac{\rho_{t_2}}{\rho_{t_3}} \dfrac{{R_3}^2 - {R_2}^2}{{R_3}^2 + {R_2}^2} + 1\right) \tau_c \end{cases}$$

These results are exactly the same as those found by Ciazynski [30]; our general approach is thus consistent.

It is interesting to note that $\tau_{ext\,1} = \tau_{1\,2}$ and $\tau_{ext\,2} = \tau_{2\,2}$; this means that the coupling between K_{0_1} and $\dot{K}_{0_2}$ is identical to the one between K_{0_1} and $\frac{2}{\mu_0}\dot{B}_a$. Indeed the magnetic field created by the second surface current (i.e. K_{0_2}) in its enclosed volume is perfectly uniform and equal to $-\frac{\mu_0}{2}K_{0_2}$ according to (57); the first surface current (i.e. K_{0_1}) feels then its time-variation it in the exact same way it feels $\dot{B}_a$.

It is also interesting to note that, in case $\rho_{t_1} = \rho_{t_2}$, we have $\tau_{ext\,1} = \tau_{1\,2} = 0$, and the new time equation on the spatial amplitudes of the surface currents K_{0_1} and K_{0_2} becomes

$$\begin{bmatrix} K_{0_1} \\ K_{0_2} \end{bmatrix} + \begin{bmatrix} \tau_{1\,1} & 0 \\ \tau_{2\,1} & \tau_{2\,2} \end{bmatrix} \begin{bmatrix} \dot{K}_{0_1} \\ \dot{K}_{0_2} \end{bmatrix} = \frac{2}{\mu_0} \begin{bmatrix} 0 \\ \tau_{ext\,2} \end{bmatrix} \dot{B}_a$$

Therefore, if the initial value of K_{0_1} is zero, it will remain zero no matter the time variations of B_a. This result makes sense as, in case $\rho_{t_1} = \rho_{t_2}$, the continuity of J_r at $r = R_1$ will always be ensured and thus there would be no need for an axial surface current at $r = R_1$ to balance the radial current flow. Consequently, in case $\rho_{t_1} = \rho_{t_2}$, the time equation can be reduced to

$$K_{0_2} + \tau_{2\,2}\dot{K}_{0_2} = \frac{2}{\mu_0}\tau_{ext\,2}\dot{B}_a$$

and there will only be one time constant equal to $\tau_{2\,2}$.

Furthermore, in steady-state regimes, i.e. when the surface currents are not time-varying ($\dot{K}_{0_1} = \dot{K}_{0_2} = 0$), we have

$$\begin{cases} K_{0_1} = \left(\frac{1}{\rho_{t_1}} - \frac{1}{\rho_{t_2}}\right)\left(\frac{l_p}{2\pi}\right)^2 \dot{B}_a \\ K_{0_2} = \left(\frac{1}{\rho_{t_3}}\frac{{R_3}^2 - {R_2}^2}{{R_3}^2 + {R_2}^2} + \frac{1}{\rho_{t_2}}\right)\left(\frac{l_p}{2\pi}\right)^2 \frac{1}{\rho_{t_2}}\dot{B}_a \end{cases}$$

When $\rho_{t_1} > \rho_{t_2}$, the first surface current is flowing in the opposite direction to the second one. At first sight this seems quite unintuitive; indeed assuming B_a is increasing with time, we expect both surface current amplitudes K_{0_1} and K_{0_2} to be positive in order to screen the strand from the time variation of B_a.

In reality, K_{0_2} will be positive while K_{0_1} will be negative, this can be explained saying that the current induced between any pair of filaments located at $r = R_2$ will use the filaments located at $r = R_1$ to shunt the central zone (of resistivity ρ_{t_1} higher than ρ_{t_2}), i.e. they prefer to temporarily flow through the filaments located at $r = R_1$ to loop back in the second zone rather than directly crossing the central zone.

Therefore, in addition to the currents induced between filaments located at $r = R_1$ - which would give a positive K_{0_1} if they were alone - there exists a surplus of current due to filaments located at $r = R_2$ which can make the global K_{0_1} (corresponding to the superposition of the two contributions) negative if $\rho_{t_1} > \rho_{t_2}$.

The configuration for which the central resistive zone is replaced with a hole allows an easy understanding of this phenomenon. Indeed, in this case the currents induced between two distant filaments located at $r = R_2$ would have no choice but to circulate through the filaments located at $r = R_1$ to loop back. In the configuration featuring a central hole, we would have $\rho_{t_1} \to \infty$, thus $1/\rho_{t_1} = 0$, and $K_{0_1} = -\frac{1}{\rho_{t_2}}\left(\frac{l_p}{2\pi}\right)^2 \dot{B}_a$ which would be negative for a rising ramp of B_a.

Consequently, we can deduce that the part of the induced currents due to the filaments located at $r = R_1$ in the expression of K_{0_1} above, is $\frac{1}{\rho_{t_1}}\left(\frac{l_p}{2\pi}\right)^2 \dot{B}_a$, while the other one (i.e. due to the filaments located at $r = R_2$) is $-\frac{1}{\rho_{t_2}}\left(\frac{l_p}{2\pi}\right)^2 \dot{B}_a$.

II.4 Applications

II.4.1 Simulations of Q vs f curves for F/R and R/F type composites

In order to give a more practical vision of the outputs of our analytical modeling, we have chosen to compute the Q vs f curves of both R/F and F/R type composites (see Figure 21). In order to do this, we will choose the following geometrical parameters for both strands (representative of ITER and JT-60SA strands)

$$\begin{cases} R_2 = R = 0.81/2\ mm = 0.405\ mm \\ R_1 = R/\sqrt{2} \simeq 0.286\ mm \\ l_p = 15\ mm \end{cases}$$

so that the area of the first zone equals that of the second zone, i.e. $\pi {R_1}^2 = \pi\left({R_2}^2 - {R_1}^2\right)$.

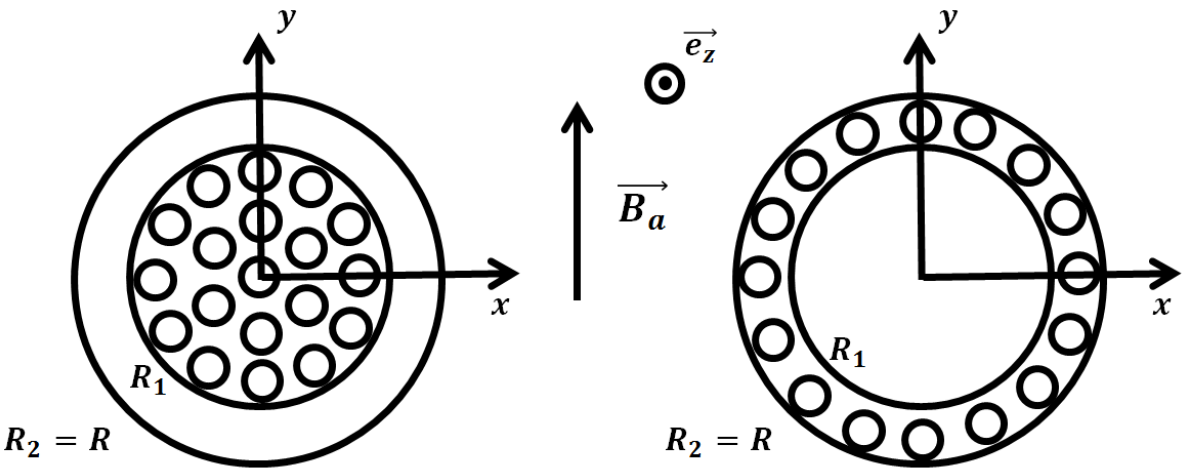

Figure 21 : Schemes of cross-sections of F/R (left) and R/F (right) type composites

We are here interested in the values of the ρ_{t_2}/ρ_{t_1} ratio rather than in the absolute values of ρ_{t_1} and ρ_{t_2}, therefore we will set ρ_{t_1} to the following realistic value (which corresponds to the resistivity of copper with $RRR = 150$ at $T = 4.2K$ and $B = 1T$)

$$\rho_{t_1} = 1.5 \times 10^{-10} \Omega.m$$

We have explored several cases resulting into a total of ten Q vs f curves which correspond to the following values of the ρ_{t_2}/ρ_{t_1} ratio (which covers about 2 orders of magnitude)

$$\rho_{t_2}/\rho_{t_1} = \begin{cases} 1/9 \\ 1/3 \\ 1 \\ 3 \\ 9 \end{cases}$$

We have considered a sinusoidal magnetic excitation $B_a = B_p sin(\omega t)$, with $B_p = 2T$ for both strands; the results for the F/R type strand are displayed in Figure 22 and those of the R/F in Figure 23.

Note that the curves displayed on Figure 22 correspond to coupling losses per cycle per unit volume of strand (they are not per unit volume of filamentary zone).

These curves have been computed using formulae (127) and (128); in the case of the F/R composite they are fully consistent with the formula found in [25], i.e.

$$Q(\omega) = \left(\frac{R_f}{R}\right)^2 \frac{{B_p}^2}{\mu_0} \frac{2\pi\omega\tau}{1 + (\omega\tau)^2}$$

with

$$\tau = \frac{\mu_0}{2}\left(\frac{l_p}{2\pi}\right)^2 \left[\frac{1}{\rho_{t_1}} + \frac{1}{\rho_{t_2}}\left(\frac{{R_2}^2 - {R_1}^2}{{R_2}^2 + {R_1}^2}\right)\right]$$

For each value of the ρ_{t_2}/ρ_{t_1} ratio, we have obtained only one non zero α_k coefficient, equal to 1. This is consistent with our previous discussions since the F/R type composite has only one time constant.

We can also notice that the maximum of the curves are all equal to one another and that they are shifted to the right with increasing ρ_{t_2}/ρ_{t_1} ratio.

From equation (126), we can see that the Q vs f curves corresponding to strands with only one time constant τ reach their maximum for $\omega = 1/\tau$; this maximum does not depend on τ and is equal to

$$Q_{max} = \left(\frac{R_f}{R}\right)^2 \frac{{B_p}^2 \pi}{\mu_0}$$

Note that the $\left(R_f/R\right)^2$ term is needed here to give the coupling losses per cycle per unit volume of strand instead of unit volume of filamentary zone.

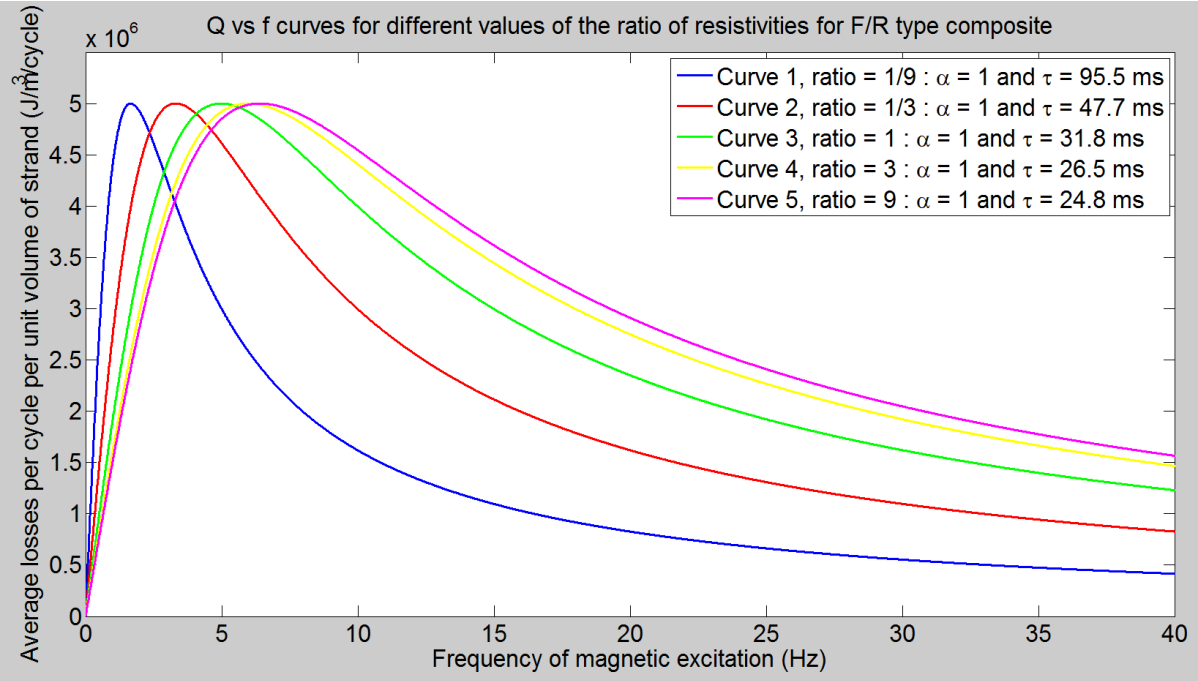

Figure 22 : Q vs f curves of F/R type composite with different values of ρ_{t_2}/ρ_{t_1} for $B_a = B_p sin(\omega t)$, $B_p = 2T$

For an F/R type composite, there is only one time constant τ which is inversely proportional to the total effective transverse resistivity of the strand. This total effective resistivity consists in a combination of the effective transverse resistivity of the filamentary zone and of the transverse resistivity of the outer layer (we have already discussed this point in section II.1.2). When the resistivity of the second zone (R) increases, the total effective transverse resistivity also increases, as a consequence, the time constant τ decreases and the maximum of the Q vs f curve is then shifted to the right. There even exists a limit to the minimum value of τ: it is reached when the resistivity of the second zone (R) is infinitely higher than that of the first layer (F). In this case, the F/R type strand actually corresponds to an F type strand and we obtain $\tau = 23.9\ ms$ using the parameters of our example.

The Q vs f curves displayed on Figure 23 are also coupling losses per cycle per unit volume of strand (not per unit volume of filamentary zone).

These curves have also been computed using formulae (127) and (128) but this time, unlike the case of the F/R type composite, we can see that there are two α_k coefficients per curve (except for the third curve) and that their values are sensitive to the ρ_{t_2}/ρ_{t_1} ratio. This clearly supports our discussion on the dependence of the α_k coefficients on the transverse resistivity of the different zones for strands with more than one time constant.

In addition, conversely to the F/R type composites, we can notice that the maxima of each curve are all different from one another even though they are also shifted to the right with increasing ρ_{t_2}/ρ_{t_1} ratio.

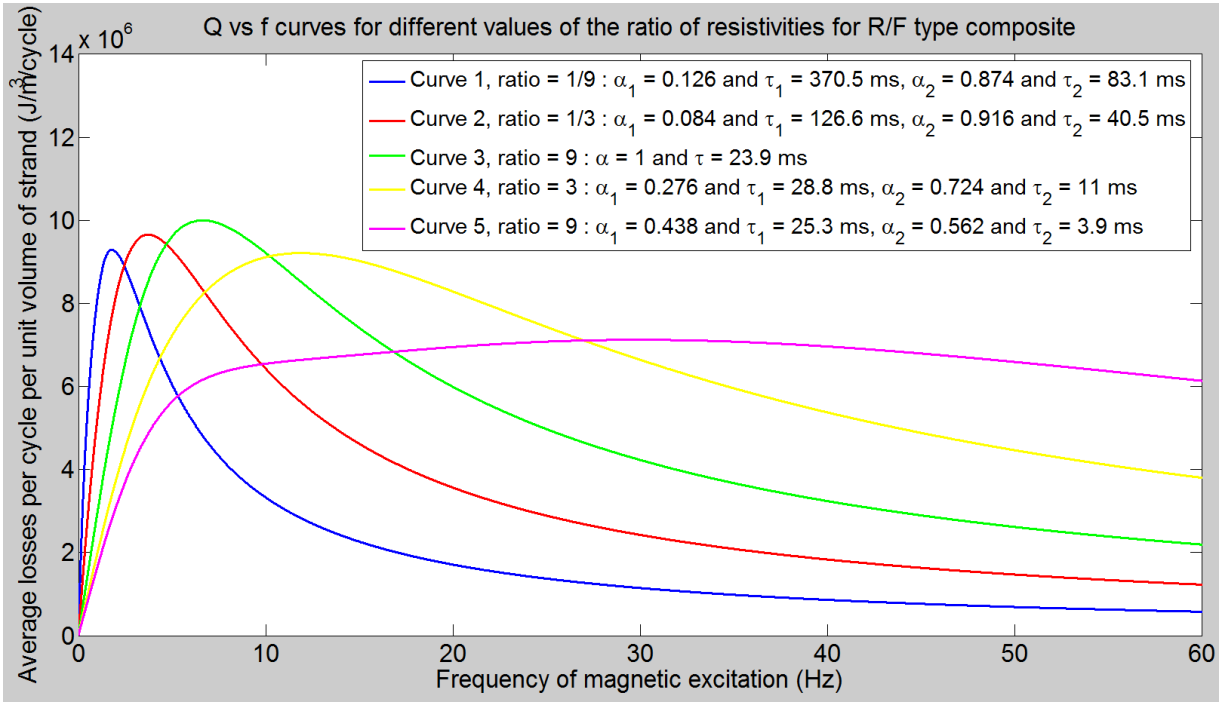

Figure 23 : Q vs f curves of R/F type composite with different values of ρ_{t_2}/ρ_{t_1} for $B_a = B_p sin(\omega t)$, $B_p = 2T$

As a remark, we can see that the third curve is the only one with a single time constant and a single α_k coefficient. This comes from the fact that $\rho_{t_2} = \rho_{t_1}$ for this curve and, in this case, the R/F type composite has no longer two time constants but only one (as previously mentioned in the R/F/R case). As a matter of fact, when $\rho_{t_2} = \rho_{t_1}$, the first surface current normally flowing at $r = R_1$ has not any specific role and both zones are electrically equivalent, so virtually merge. Therefore the composite features only one surface current flowing at $r = R_2$ with only one α_k coefficient equal to 1 and there is only one time constant left.

The fifth curve is interesting as it deviates in shape from the other ones. For this reason we have displayed it on Figure 24 together with its decomposition as a weighted sum of two classical (i.e. single time constants) Q vs f curves, as indicated in formula (127). This means that, in addition to curve 5, we have plotted $\alpha_1 Q_{classical}(\tau_{c_1})$ and $\alpha_2 Q_{classical}(\tau_{c_2})$ such that curve 5 is equal to $\alpha_1 Q_{classical}(\tau_{c_1}) + \alpha_2 Q_{classical}(\tau_{c_2})$. The fact that it deviates in shape from the other curves is majorly due to the fact that the values of its α_1 and α_2 coefficients are close from one another (respectively 0.562 and 0.438) while in the other curves, α_1 predominates. Since the two α_k coefficients are in the same range and the two time constants quite far apart we can observe that the convolution of the two contributions results in a curve with a maximum rather "flat", unlike the curves usually expected from the "single time constant" approach for representing the strand behavior.

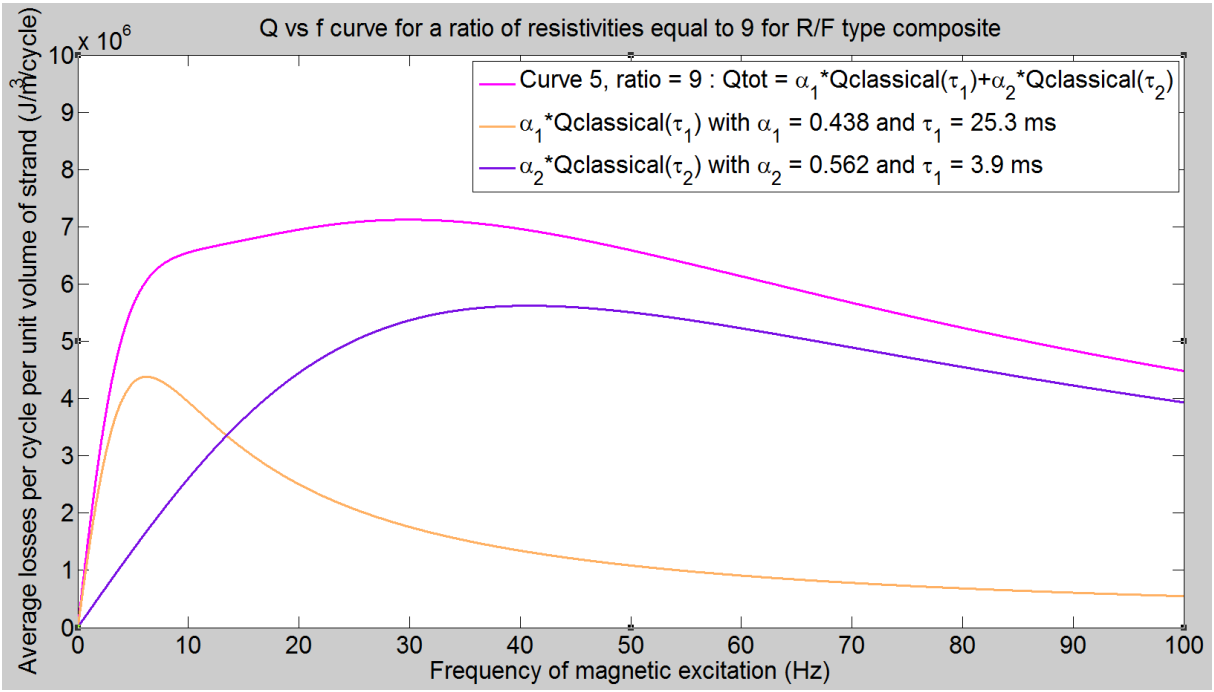

Figure 24 : Q vs f curve of R/F type composite with $\rho_{t_2}/\rho_{t_1} = 9$ (curve 5) and its decomposition into two classical curves for $B_a = B_p sin(\omega t)$, $B_p = 2T$

This observation can have very practical consequences: measurements of Q vs f curves are usually carried out up to a certain frequency range which sometimes imposes to stay within the linear part of the Q vs f curve (i.e. for $\omega\tau \ll 1$). If the measured strand features more than one time constant, as shown in this particular case, the extrapolation of its behavior at high frequencies upon the fitting with classical formula (126) of the measurements made in the linear part of the Q vs f curve would result in substantial gaps.

In order to quantify this consideration, we will extrapolate curve 5 at high frequencies from its linear part and using the classical formula (126).

In order to do so, we consider that the R/F type composite has only one time constant and therefore assume that its associated coupling losses per cycle per unit volume of filamentary zone can be described by formula (126) which is equivalent to

$$Q_{classical}(f,\tau) = \left(\frac{R_f}{R}\right)^2 \frac{{B_p}^2}{\mu_0} \frac{4\pi^2 f\tau}{1+(2\pi f\tau)^2}$$

per unit volume of strand.

For small values of f satisfying $2\pi f\tau \ll 1$, we can assume that the $Q_{classical}(f,\tau)$ function is well described by the following linear function

$$Q_{classical}(f \ll 1/(2\pi\tau),\tau) \simeq 4\pi^2\tau\left(\frac{R_f}{R}\right)^2 \frac{{B_p}^2}{\mu_0} f$$

And it is then possible to compute the time constant τ of the strand from the slope at origin a of curve 5 as

$$\tau = \frac{\mu_0}{4\pi^2 {B_p}^2}\left(\frac{R}{R_f}\right)^2 a$$

Using this formula and the slope at origin of curve 5, we have obtained $\tau = 13.3\ ms$ and have then extrapolated curve 5 at high frequencies using this τ; both curve 5 and the extrapolation from its linear part are displayed in Figure 25.

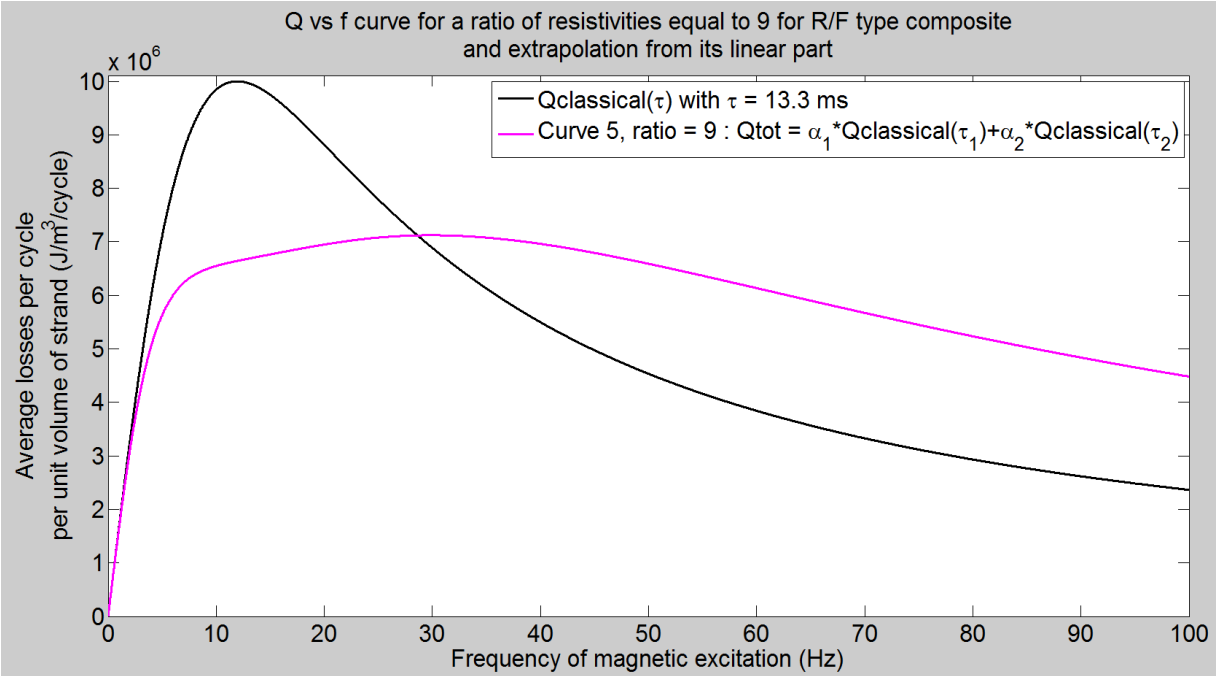

Figure 25 : Q vs f curve of R/F type composite with $\rho_{t_2}/\rho_{t_1} = 9$ (curve 5) for $B_a = B_p sin(\omega t)$, $B_p = 2T$ and corresponding curve with single time constant approach

We clearly see a disagreement between these two curves at frequencies higher than $2\ Hz$. The discrepancy between both curves is clear: it reaches a factor 1.5 for $f = 11Hz$ and generally shows that for most of the high frequencies important over-evaluations or under-evaluations are made between the two approaches. We can also note that curve 5 reaches its maximum at $f = 30Hz$ while its extrapolation reaches its maximum at $f = 12Hz$.

II.4.2 Study on the effect of the layout of a composite on coupling losses

When designing a composite, the total amount of superconductor inside the composite is a key parameter as it will ensure the ability of the strand to produce the desired current, but it is not the only one. The Cu/NonCu ratio is also an important parameter as it will ensure the stability of the composite while guaranteeing also its integrity in case of quench. The filaments diameter plays a significant role in the protection of the composite against flux jumps too and should not be too large for this reason.

With the knowledge of the main design parameters of the composite, it is possible to propose a geometry that will meet given design requirements.

There can be more than one acceptable geometry since the number and sequencing of the layers are usually not fixed. These parameters might be optimized with respect to coupling losses.

In order to draw a tentative contribution to those considerations we have carried out a study on the response of composites meeting the same design requirements, but with different layouts, to sinusoidal magnetic excitations.

We have therefore chosen the four different layouts displayed on Figure 26: F, F/R, R/F and R/F/R.

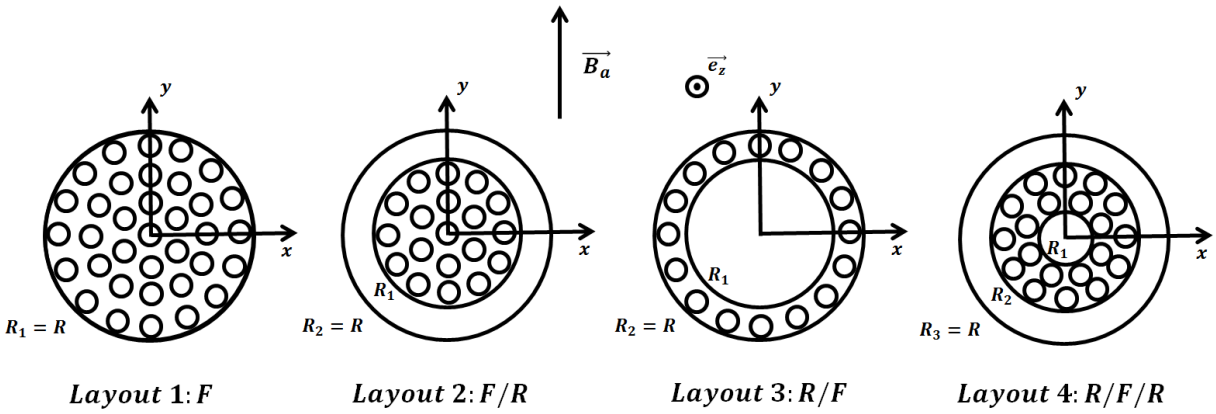

Figure 26 : The four different layouts considered in our study

We have chosen realistic design requirements (inspired from the design of JT-60SA TF conductor) and have therefore set the radius R of the composites to $R = 0.405\ mm$, the filaments diameter to $d_{fil} = 20\ \mu m$ and the Cu/NonCu ratio to 1.5. We assume that the superconductor is the only non-copper material inside the composites; the overall proportion λ of superconductor in each composite is then

$$\lambda = \frac{1}{1 + \mathrm{Cu/NonCu}} = 0.4$$

For layouts 2 to 4 which feature several layers, the radii of each of their internal zones are set as below (these assumptions are considered as examples for possible design constraints).

For layout 2, R_1 is such that the surface of layer 2 (copper) is equal to half that of layer 1 (filamentary), we then have $R_1 = R\sqrt{2/3}$.

For layout 3, we have set R_1 such that the surface of layer 1 (copper) is equal to half that of layer 2 (filamentary), therefore $R_1 = R/\sqrt{3}$.

For layout 4, we have set R_1 and R_2 such that the surface of layer 1 (copper) is equal to that of layer 3 (copper) and one fourth that of layer 2 (filamentary), thus

$$\begin{cases} R_1 = R/\sqrt{6} \\ R_2 = R\sqrt{5/6} \end{cases}$$

The resistivity of copper is set to

$$\rho_{Cu} = 1.5 \times 10^{-10} \Omega.m$$

which again corresponds to the resistivity of copper with $RRR = 150$ at $T = 4.2K$ and $B = 1T$.

We now have to compute the effective transverse resistivities of the filamentary zone of each strand. In order to do so, we will use the formula given by Ciazynski [30] which is in agreement with the two extreme values of the filament-to-matrix contact resistance given by Carr [24]. In his formula Ciazynski assumes that the filament-to-matrix contact can be represented by a small resistive barrier of thickness e_b and resistivity ρ_b surrounding the filaments; we assume this barrier to be thin enough so that his formula can be written as in [32]

$$\rho_t = \rho_m \frac{1 - \lambda_F + \chi(1 + \lambda_F)}{1 + \lambda_F + \chi(1 - \lambda_F)}$$

with

$$\chi = \frac{\rho_b e_b}{\rho_m r_{fil}}$$

r_{fil} is the radius of the filaments and ρ_m is the resistivity of the matrix in the filamentary zone, but since the matrix is supposed to be exclusively made of copper, we have here $\rho_m = \rho_{Cu}$.

Turck [33] has estimated the $\rho_b e_b$ parameter to be close to

$$\rho_b e_b = 6 \times 10^{-15} \Omega.m^2$$

which is consistent with the measurements presented in [38].

We have chosen this value for each of the four composites because since we assume this parameter is related to the fabrication process, it should be the same for every strand.

λ_F is the proportion of superconductor in the filamentary zone; it is therefore not always equal to λ depending on the layout. Let us note ${\lambda_F}^{(k)}$ the proportion of superconductor in the filamentary zone of the composite with layout k, in order to conserve the have the same amount of superconductor in each composite we must have

$$\begin{cases} {\lambda_F}^{(1)} \pi R^2 = \lambda \pi R^2 \\ {\lambda_F}^{(2)} \pi {R_1}^2 = \lambda \pi R^2 \\ {\lambda_F}^{(3)} \pi \left(R^2 - {R_1}^2\right) = \lambda \pi R^2 \\ {\lambda_F}^{(4)} \pi \left({R_2}^2 - {R_1}^2\right) = \lambda \pi R^2 \end{cases}$$

which is equivalent to

$$\begin{cases} {\lambda_F}^{(1)} = \lambda \\ {\lambda_F}^{(2)} = \lambda \left(\frac{R}{R_1}\right)^2 \\ {\lambda_F}^{(3)} = \lambda \frac{R^2}{R^2 - {R_1}^2} \\ {\lambda_F}^{(4)} = \lambda \frac{R^2}{{R_2}^2 - {R_1}^2} \end{cases}$$

We now have all the elements to compute the effective transverse resistivities of the filamentary zone of each composite.

Table 2 and Table 3 summarize the geometrical and electrical parameters of the composites computed using the previous considerations for the four different layouts.

Table 2

Common parameters					
Name	*Composite radius* R	*Proportion of superconductor* λ	*Twist pitch of filaments* l_p	*Filaments radius* r_{fil}	*Resistivities of copper* ρ_{Cu} *and matrix* ρ_m
Value	$\mathbf{0.405\ mm}$	$\mathbf{0.4}$	$\mathbf{15\ mm}$	$\mathbf{10\ \mu m}$	$\mathbf{1.5 \times 10^{-10}\ \Omega.m}$

Table 3

Specific parameters for the different layouts								
Layout number	**1**	**2**		**3**		**4**		
Type	*F*	*F/R*		*R/F*		*R/F/R*		
$\boldsymbol{\lambda_F}$	**0.4**	**0.6**		**0.6**		**0.6**		
Radii of zones	R_1	R_1	R_2	R_1	R_2	R_1	R_2	R_3
Value (μm)	**405**	**331**	**405**	**234**	**405**	**165**	**370**	**405**
Transverse resistivities of zones	ρ_{t_1}	ρ_{t_1}	ρ_{t_2}	ρ_{t_1}	ρ_{t_2}	ρ_{t_1}	ρ_{t_2}	ρ_{t_3}
Value ($\times 10^{-10}\ \Omega.m$)	**2.45**	**3.19**	**1.5**	**1.5**	**3.19**	**1.5**	**3.19**	**1.5**

Using the parameters presented in Table 2 and Table 3 we have been able to produce the Q vs f curves for the four layouts; they are plotted on Figure 27.

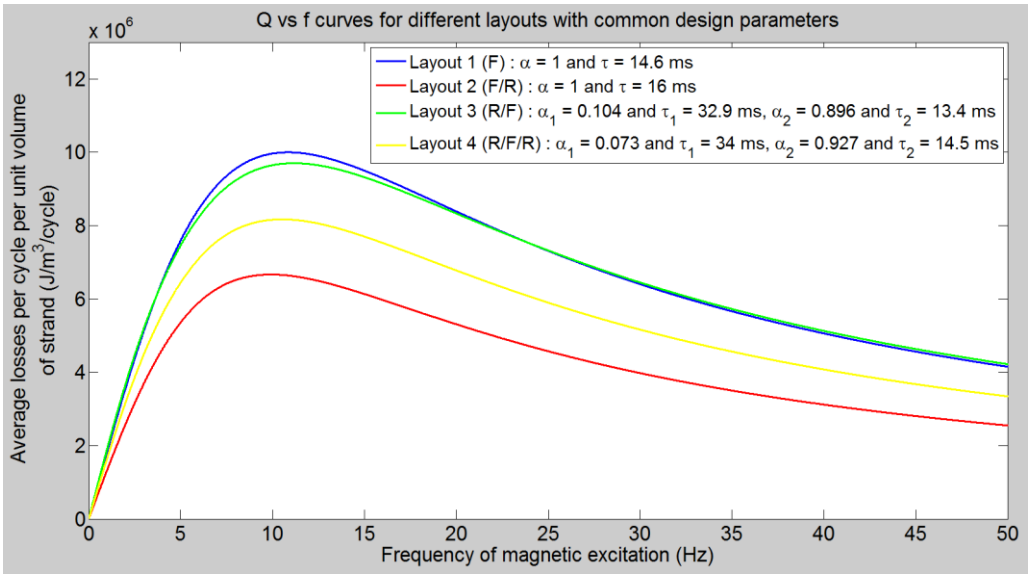

Figure 27 : Q vs f curves for composites with common design parameters and different layouts for $B_a = B_p sin(\omega t), B_p = 2T$

First of all, it is quite clear that, under our design assumptions, the F/R layout seems to be the best configuration with respect to coupling losses while the F one is the worst : there is a factor 1.5 between the maxima of the Q vs f curves of the F and F/R type composites. In between these two extremes, are the R/F/R and R/F type composites.

The obtained results are not intuitive at all and are quite difficult to predict qualitatively. Indeed, the different parameters of each strand have several effects that are competing with each other in the phenomenon of coupling losses.

Actually two antagonistic effects enter into competition. First, the radius R_f on which the outer edge filaments are located defines the volume to shield, therefore the larger the radius R_f, the larger the volume to shield and thus the larger the losses. Secondly, for a given variation of applied magnetic field B_a, the smaller the total effective transverse resistivity, the higher the induced currents and consequently the larger the losses.

If we now take a look at the parameters of the F and F/R type composites present in Table 3, we observe that the F composite has an effective transverse resistivity of $\rho_t = 2.45 \times 10^{-10}\ \Omega.m$ while the F/R one has a higher transverse resistivity in its filamentary zone ($\rho_{t_1} = 3.19 \times 10^{-10}\ \Omega.m$) and a lower one in its copper sheath ($\rho_{t_2} = 1.5 \times 10^{-10}\ \Omega.m$). The first difficulty is to compute the total effective transverse conductivity (i.e. $1/\rho_{t_{tot}}$) of the F/R type composite as it consists in a weighted sum of the effective transverse conductivities of its two layers (i.e. $1/\rho_{t_1}$ and $1/\rho_{t_2}$). The two weighting coefficients depend on the geometrical parameters of the strand but they cannot be trivially derived, therefore we will not calculate them here. However given the values of the different resistivities and the geometry of both strands we can assume that the total effective transverse resistivity of the F/R type composite should be close to that of the F strand. Knowing that the time constant of an F or an F/R type strand is inversely proportional to its total effective transverse resistivity (see section II.1.2), our previous conjecture is confirmed by the fact that the time constants of both strands are very close from one another ($14.6\,ms$ for F and $16\,ms$ for F/R). As a consequence, from considerations on the resistivities of both strands, we expect their respective coupling losses to be very similar and yet this is not what we observe.

Regarding the location of the outer edge filaments we see that the F/R type composite has an advantage on its counterpart. Indeed the ratio of the shielded volumes of both strands is here equal to $2/3$ and is in favor of layout 2 (F/R); this therefore explains the relative positions of their Q vs f curves.

Finally, in order to produce a qualitative explanation for the positions of the different Q vs f curves, we have displayed in Table 4 the ratio of the shielded volume to the strand volume for the four layouts.

Table 4

Ratio of shielded volume to strand volume for the different layouts				
Layout number	1	2	3	4
Type	*F*	*F/R*	*R/F*	*R/F/R*
$ratio$	1	2/3	1	5/6
Maximum of Q(f) ($\mathbf{10^6\ J/cm^3/cycle}$)	***10.0***	**6.67**	**9.70**	**8.17**

A posteriori we see that the shielded volume is the parameter that mainly impacts the coupling losses : the order of the ratios of Table 4 is consistent with the relative positions of the curves.

In summary, the results of our study have shown that when designing a composite, if the factor of merit includes the coupling losses, it would be better to minimize the radius on which the outer edge filaments are located.

Our study only considers coupling losses so the conclusions might differ when other parameters (critical performances, ease of assembly at manufacturing stage, stability of the composite in self-field, cost, etc…) are taken into account in the design requirements of a composite; these considerations could lead to the choice of another type of composite (different from F/R) with respect to the design constraints.

Since this section aims only at spotting the general trends among different options, we go into a more quantitative approach by studying a particular design in the following section.

II.4.3 Study on JT-60SA TF strand

In this section we will present a detailed study of the electromagnetic behavior of the strand to be integrated into the Toroidal Field Coil of JT-60SA tokamak [39] when subject to a transverse time-varying magnetic field. This strand is the K006-01C and was manufactured by Furukawa.

As shown on Figure 11, this composite features a copper core surrounded by a filamentary zone containing NbTi filaments embedded in a copper matrix. The filamentary zone is enclosed in a CuNi barrier which is surrounded by a copper shell; this strand is thus of R/F/R/R type.

II.4.3.1 Determination of the filament-to-matrix contact $\rho_b e_b$ parameter

First of all, we have to determine the effective transverse resistivity of its filamentary zone (i.e. ρ_{t_2}). In order to do so, we will use the coupling losses measurements that we have carried out on this strand in the Speedy facility at CEA; they are presented in section II.5.2.1 .

However, since we have not directly measured its effective resistivity, we have to express the coupling losses of this strand as function of ρ_{t_2} to be able to deduce its value.

The measurements were made for trapezoidal cycles consisting in a succession of rising ramps, plateaus and falling ramps; we can then consider that the measurements were made in steady state regime since the durations of the ramps and plateaus were long compared to the large time constant of the JT-60SA TF strand (see section II.5.2.1).

As a consequence we will derive the formula of coupling losses inside this strand for steady state regime.

Since the strand is of R/F/R/R type, it features $n = 4$ layers and we therefore have $2n - 1 = 7$ electric field coefficients to determine i.e. $\left(E_{0_k}\right)_{2 \leq k \leq 8}$.

The second layer being filamentary, we can use equation (37) for $k = 2$ which gives

$$\begin{cases} E_{0_3} = 0 \\ E_{0_4} = \dfrac{l_p}{2\pi}\dot{B}_a \end{cases}$$

At $r = R_1$ there is an interface of resistive/filamentary type, according to equation (40) for $k = 1$ we can thus write

$$-E_{0_1} + E_{0_2} = \frac{l_p}{2\pi}\dot{B}_a$$

which reduces to

$$E_{0_2} = \frac{l_p}{2\pi}\dot{B}_a$$

since E_{0_1} is always zero.

The ultimate layer of the composite is resistive, for $n = 4$ equation (43) indicates that

$$E_{0_8} = -E_{0_7}$$

The filamentary/resistive interface located at $r = R_2$ leads, from equation (41) for $k = 2$, to

$$-\left(\frac{R_3}{R_2}\right)^2 E_{0_5} + E_{0_6} = \frac{l_p}{2\pi}\dot{B}_a$$

Finally since there is an interface between two resistive layers at $r = R_3$, we can use equation (39) for $k = 3$ and the fact that $E_{0_8} = -E_{0_7}$ to obtain

$$\begin{cases} E_{0_5} = \dfrac{1}{2}\left(\dfrac{R_4}{R_3}\right)^2\left(\dfrac{\rho_{t_3}}{\rho_{t_4}} + 1\right)E_{0_7} + \dfrac{1}{2}\left(\dfrac{\rho_{t_3}}{\rho_{t_4}} - 1\right)E_{0_8} = s_1 E_{0_7} \\ E_{0_6} = \dfrac{1}{2}\left(\dfrac{R_4}{R_3}\right)^2\left(\dfrac{\rho_{t_3}}{\rho_{t_4}} - 1\right)E_{0_7} + \dfrac{1}{2}\left(\dfrac{\rho_{t_3}}{\rho_{t_4}} + 1\right)E_{0_8} = s_2 E_{0_7} \end{cases}$$

with

$$\begin{cases} s_1 = \dfrac{1}{2}\left[\left(\dfrac{R_4}{R_3}\right)^2\left(\dfrac{\rho_{t_3}}{\rho_{t_4}} + 1\right) + 1 - \dfrac{\rho_{t_3}}{\rho_{t_4}}\right] \\ s_2 = \dfrac{1}{2}\left[\left(\dfrac{R_4}{R_3}\right)^2\left(\dfrac{\rho_{t_3}}{\rho_{t_4}} - 1\right) - 1 - \dfrac{\rho_{t_3}}{\rho_{t_4}}\right] \end{cases}$$

The combination of these expressions with the equation on E_{0_5} and E_{0_6} above gives

$$E_{0_7} = \frac{{R_2}^2}{s_2{R_2}^2 - s_1{R_3}^2}\frac{l_p}{2\pi}\dot{B}_a$$

We can now give the expressions of the $\left(E_{0_k}\right)_{2\leq k\leq 8}$ coefficients

$$\begin{cases} E_{0_2} = \dfrac{l_p}{2\pi}\dot{B}_a \\ E_{0_3} = 0 \\ E_{0_4} = \dfrac{l_p}{2\pi}\dot{B}_a \\ E_{0_5} = \dfrac{s_1{R_2}^2}{s_2{R_2}^2 - s_1{R_3}^2}\dfrac{l_p}{2\pi}\dot{B}_a \\ E_{0_6} = \dfrac{s_2{R_2}^2}{s_2{R_2}^2 - s_1{R_3}^2}\dfrac{l_p}{2\pi}\dot{B}_a \\ E_{0_7} = \dfrac{{R_2}^2}{s_2{R_2}^2 - s_1{R_3}^2}\dfrac{l_p}{2\pi}\dot{B}_a \\ E_{0_8} = \dfrac{-{R_2}^2}{s_2{R_2}^2 - s_1{R_3}^2}\dfrac{l_p}{2\pi}\dot{B}_a \end{cases}$$

Using formula (112) we can express the instant power per unit volume of strand as

$$\bar{P}(t) = \sum_{j=2}^{8} \beta_j {E_{0_j}}^2(t) = \left[\beta_2 + \beta_4 + \frac{(s_1{}^2\beta_5 + s_2{}^2\beta_6 + \beta_7 + \beta_8){R_2}^4}{\left(s_2{R_2}^2 - s_1{R_3}^2\right)^2}\right]\left(\frac{l_p}{2\pi}\right)^2 {\dot{B}_a}^2$$

For a trapezoidal magnetic cycle falling from B_m to $-B_m$ in a time of $2\tau_a$ and rising again to B_m after a plateau of duration T_p, we can calculate the coupling losses per unit volume of strand as

$$Q = \int_0^{2\tau_a} \bar{P}(t)dt + \int_{T_p}^{T_p+2\tau_a} \bar{P}(t)dt = \left[\beta_2 + \beta_4 + \frac{(s_1{}^2\beta_5 + s_2{}^2\beta_6 + \beta_7 + \beta_8){R_2}^4}{\left(s_2{R_2}^2 - s_1{R_3}^2\right)^2}\right]\left(\frac{l_p}{2\pi}\right)^2 \frac{4{B_m}^2}{\tau_a}$$

Q is therefore a linear function of $1/\tau_a$ and can alternatively be written as

$$Q = a/\tau_a$$

With the expression of β_4 given by (113) for $j = 2$, we can now derive ρ_{t_2} as function of a

$$\rho_{t_2} = \frac{{R_2}^2 - {R_1}^2}{{R_4}^2\left[\dfrac{a}{4{B_m}^2}\left(\dfrac{2\pi}{l_p}\right)^2 - \beta_2 - \dfrac{(s_1{}^2\beta_5 + s_2{}^2\beta_6 + \beta_7 + \beta_8){R_2}^4}{\left(s_2{R_2}^2 - s_1{R_3}^2\right)^2}\right]}$$

From the measurements (see section II.5.2.1), we have determined

$$a = 6.34 \times 10^5 J.m^{-3}.s$$

for a trapezoidal cycle with a B_m of $3T$.

The average magnetic field amplitude during the $-3/+3T$ trapezoidal cycle being $1.5T$, we have set

$$\rho_{Cu} = 2.278 \times 10^{-10}\Omega.m$$

which corresponds to the resistivity of copper with $RRR = 100$ at $T = 4.2K$ and $B = 1.5T$.

The third layer of the composite is a cupronickel barrier of 13 wt% (weight percent) Ni; the resistivity values of CuNi present in [32] has led us to

$$\rho_{CuNi} = 1.730 \times 10^{-7} \Omega.m$$

We now have the transverse resistivities needed to compute ρ_{t_2}, i.e.

$$\begin{cases} \rho_{t_1} = 2.278 \times 10^{-10} \Omega.m \\ \rho_{t_3} = 1.730 \times 10^{-7} \Omega.m \\ \rho_{t_4} = 2.278 \times 10^{-10} \Omega.m \end{cases}$$

The geometrical parameters of the K006-01C JT-60SA TF strand are the following

$$\begin{cases} R_1 = 185\ \mu m \\ R_2 = 327\ \mu m \\ R_3 = 346\ \mu m \\ R_4 = 405\ \mu m \\ l_p = 15\ mm \end{cases}$$

These information, combined with the measured value of a, has led us to

$$\rho_{t_2} = 2.096 \times 10^{-10} \Omega.m$$

which is very close to the value of ρ_{Cu}, i.e. to the values of ρ_{t_1} and ρ_{t_4}.

From the formulae presented in the previous section, it is also possible to deduce $\rho_b e_b$ as function of ρ_{t_2}

$$\rho_b e_b = \rho_m r_{fil} \frac{(1-\lambda_F)\rho_m - (1+\lambda_F)\rho_{t_2}}{(1-\lambda_F)\rho_{t_2} - (1+\lambda_F)\rho_m}$$

For the considered composite, $r_{fil} = 9.5\ \mu m$, $\lambda_F = 0.86$ and $\rho_m = \rho_{Cu}$ [39] . We therefore obtain

$$\rho_b e_b = 2 \times 10^{-15} \Omega.m^2$$

II.4.3.2 Simulated Q vs f curve for JT-60SA TF strand

Knowing all the electrical and geometrical parameters of K006-01C JT-60SA TF strand, we have been able to instantly compute its Q vs f curve for $B_a = B_p \sin(2\pi f t)$ with $B_p = 3T$ using CLASS algorithm - which features analytical formula (127) - and the measurements made in the low frequency region with CEA SPEEDY facility, i.e. with $\rho_{t_2} = 2.096 \times 10^{-10}\ \Omega.m$, see section II.5.2.1 ; the curve is displayed on Figure 28.

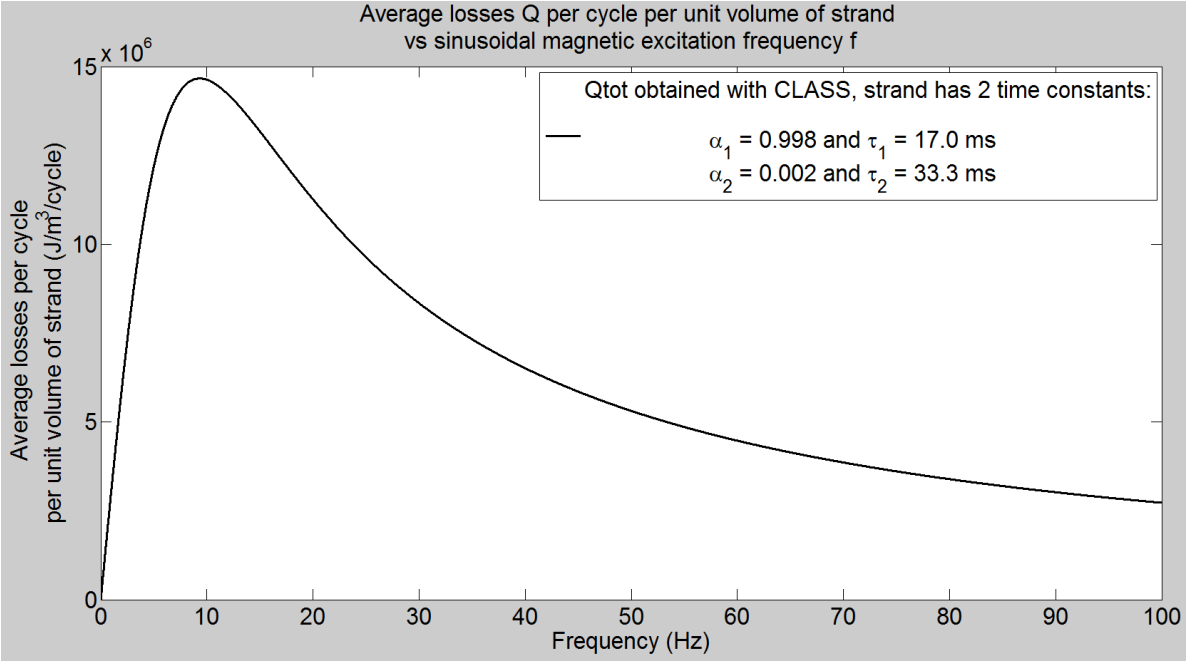

Figure 28 : Simulated Q vs f curve for K006-01C JT-60SA TF composite and $B_a = B_p sin(\omega t)$, $B_p = 3T$ from measurements made in the low frequency region with CEA SPEEDY facility (i.e. with $\rho_{t_2} = 2.096 \times 10^{-10} \Omega.m$)

Since K006-01C JT-60SA TF composite features two interfaces between filamentary and resistive zones (see Figure 11), it has two time constants. As shown on Figure 28, CLASS algorithm has obtained the following time constants τ_{c_k} and α_k coefficients for the K006-01C JT-60SA TF composite with the previous electrical and geometrical parameters:

$$\begin{cases} \tau_{c_1} = 17.0\ ms\ with\ \alpha_1 = 0.998 \\ \tau_{c_2} = 33.3\ ms\ with\ \alpha_2 = 0.002 \end{cases}$$

This clearly indicates that even if the K006-01C JT-60SA TF composite has two time constants, the first one i.e. $\tau_{c_1} = 17.0\ ms$ is largely predominant. Indeed, its weighting in the losses is worth 99.8% while the other one ($\tau_{c_2} = 33.3\ ms$) only weights 0.2%. From this information we can readily deduce that, for an average magnetic field of 1.5 T (+/- 3T cycles), the K006-01C JT-60SA TF composite behaves as if it only had one time constant : this is due to the fact that here $\rho_{t_2} \simeq \rho_{t_1}$ (see discussion in section II.3.2).

Note that the value of the average magnetic field seen by the composite is important because it has an influence on the transverse resistivities of the different zones and thus can affect the values of the time constants τ_{c_k} and α_k coefficients.

The results of CLASS algorithm on this specific case are consistent with the ones that would be classically derived from the experimental losses. Indeed the composite is subject to +/- 3T trapezoidal cycles whose ramps last $2\tau_a$ and whose plateaus last T_p (both τ_a and T_p are greater than the largest time constant of the strand), therefore the coupling losses per cycle per unit volume of strand Q can be determined from (3) assuming that for most of the cycle $\dot{B}_i = \dot{B}_a$, i.e.

$$Q = \left(\frac{R_f}{R}\right)^2 \left[\int_0^{2\tau_a} \frac{n\tau \dot{B}_i^{\,2}}{\mu_0} dt + \int_{T_p}^{T_p+2\tau_a} \frac{n\tau \dot{B}_i^{\,2}}{\mu_0} dt\right] \simeq \left(\frac{R_f}{R}\right)^2 \frac{n\tau \dot{B}_a^{\,2}}{\mu_0} 4\tau_a$$

Now, using the fact that $n = 2$ for cylindrical composites and that here $\dot{B}_a{}^2 = (B_m/\tau_a)^2$ with $B_m = 3T$, we can derive

$$Q \simeq \left(\frac{R_f}{R}\right)^2 \frac{8\tau {B_m}^2}{\mu_0} \frac{1}{\tau_a}$$

which can be expressed as

$$Q = a/\tau_a$$

with

$$a \simeq \left(\frac{R_f}{R}\right)^2 \frac{8\tau {B_m}^2}{\mu_0}$$

Therefore using $a = 6.34 \times 10^5 J.m^{-3}.s$ determined from measurements, we can deduce

$$\tau \simeq \left(\frac{R}{R_f}\right)^2 \frac{\mu_0 a}{8{B_m}^2} \simeq 17.0\ ms$$

which is fully consistent with the results obtained with CLASS.

It is very important to understand that the case of the K006-01C JT-60SA TF composite is a specific one. Indeed, although having two time constants, it here behaves exactly as if it had only one time constant, but there is no guarantee that it will keep this behavior for any magnetic field amplitude. Considering it a single time constant strand under any circumstances could lead to appreciable discrepancies.

Erratum: In [40] and [41] we have presented the same application but the associated results at the time of the publications were different than those discussed in the present manuscript; an error was made on the determination of the effective transverse resistivity. Consequently, the discrepancy between the single time constant approach and the CLASS algorithm has been significantly reduced on this particular case (JT-60SA TF strand).

In order to highlight again the difference in behavior between single time constant strands and multiple time constants ones, we have also computed another Q vs f curve assuming this composite had an arbitrary but realistic $\rho_b e_b$ value of

$$\rho_b e_b = 6 \times 10^{-15} \Omega.m^2$$

This modification of the $\rho_b e_b$ value also has an impact on the effective transverse resistivity of the second zone which is now quite different from ρ_{t_1}, i.e.

$$\rho_{t_2} = 5.367 \times 10^{-10} \Omega.m$$

The new Q vs f curve computed by CLASS ("Qtot") is displayed on Figure 29. It is interesting to note that it is no longer possible to see the K006-01C JT-60SA TF strand as a single time constant composite. Indeed the new values of time constants τ_{c_k} and α_k coefficients are :

$$\begin{cases} \tau_{c_1} = 8.3\ ms\ with\ \alpha_1 = 0.876 \\ \tau_{c_2} = 21.1\ ms\ with\ \alpha_2 = 0.124 \end{cases}$$

and here τ_{c_1} is not as predominant as before (weight of 87.6%).

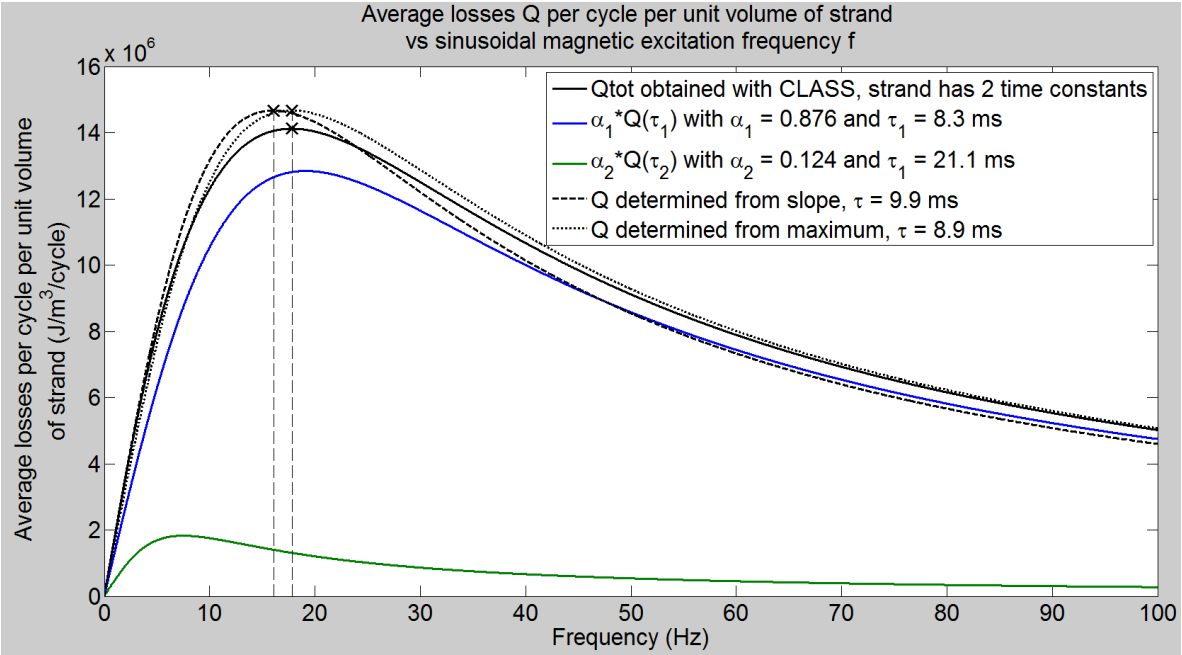

Figure 29 : Simulated Q vs f curve for K006-01C JT-60SA TF composite and $B_a = B_p sin(\omega t)$, $B_p = 3T$ with $\rho_b e_b = 6 \times 10^{-15} \Omega.m^2$ and thus $\rho_{t_2} = 5.367 \times 10^{-10} \Omega.m$

In order to visualize the error made considering a two time constant strand as a single time constant one, we have plotted two additional Q vs f curves on Figure 29. The first one "Q determined from slope" is computed assuming the strand has only one time constant : the value of the time constant is determined from the behavior of "Qtot" in the low frequency linear region (i.e. in the steady state region). The second one "Q determined from maximum" is computed assuming the strand has only one time constant : the value of the time constant is determined from the location of the maximum of "Qtot" (i.e. when $\omega\tau = 1$).

II.4.3.3 2D cartographies of main physical quantities for JT-60SA TF strand

With the knowledge of the electrical and geometrical parameters of a strand, it is also possible to simulate its time response to any magnetic signal and to produce detailed cartographies of all the physical quantities inherent to this strand in a very short computation time using CLASS algorithm issued from our analytical modeling.

Indeed, after the numerical solve of the matrix equation of the system (72), equations (103) to (111) are used to compute the time dependent solutions of the screening currents and of the spatial average of the losses as well as instant detailed cartographies of the electric field, of the transverse currents, of the magnetic field and of the coupling losses inside the composite.

We have therefore used CLASS algorithm to simulate the response of K006-01C JT-60SA TF strand to the following sinusoidal magnetic field with $B_p = 3T$ and $f = 1Hz$

$$B_a = B_p \sin(2\pi f t)$$

The computed time dependent solutions of the screening currents, of the magnetic field at the center of the strand and of the spatial averages of the losses are displayed on Figure 30. Note that in principle

for K006-01C JT-60SA TF strand there are only two screening currents located at $r = R_1$ and $r = R_2$ while on Figure 30 we see that there are four of them. In reality the two additional screening currents K_{0_3} and K_{0_4} are always zero since there are no superconducting filaments at the interfaces located at $r = R_3$ and $r = R_4$ (this point has previously been discussed).

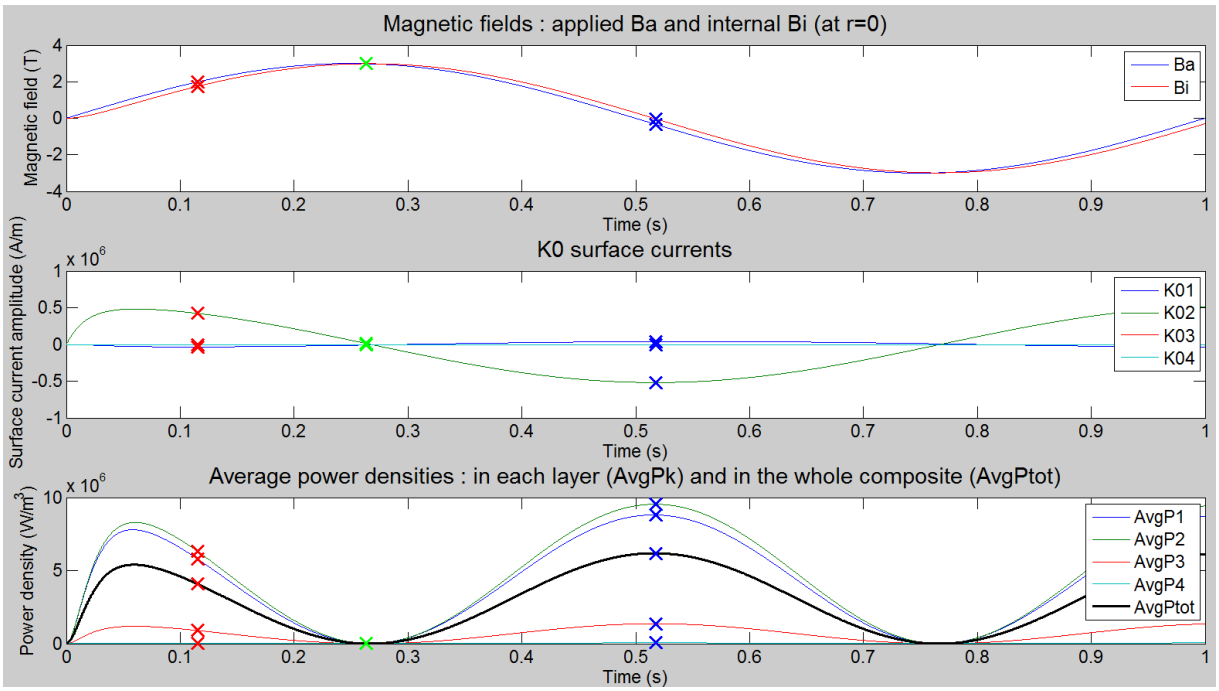

Figure 30 : Simulated time solutions of screening currents, magnetic fields and average losses for K006-01C JT-60SA TF composite and $B_a = B_p sin(2\pi ft)$ with $B_p = 3T, f = 1Hz$

Using CLASS algorithm, we have also been able to generate detailed cartographies at three different instant corresponding to the color markers displayed on Figure 30; they are shown from Figure 81 to Figure 92 in Appendix D. The objective of these figures is to show the large variations of the main physical quantities during a cycle of magnetic excitation as well as the potential of the CLASS tool.

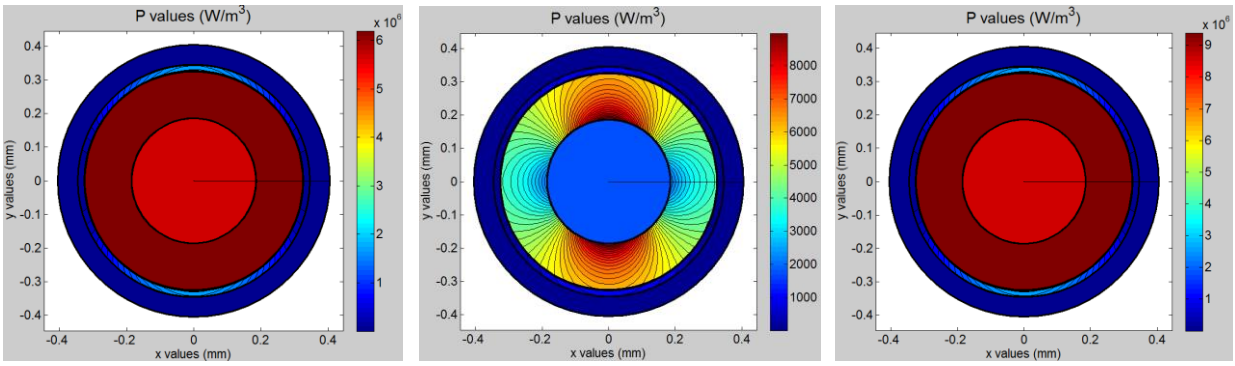

(a) : First instant (Figure 84) **(b) : Second instant (Figure 88)** **(c) : Third instant (Figure 92)**

Figure 31 : Examples of the different holders with superconducting composite and copper pick-up coils

These cartographies are interesting as they provide both time and spatial variations of the physical quantities inside the composite. In our example, we clearly see that the power density cartographies produced at three different instants of the simulation (see Figure 31) show major differences between them. We can see that the power dissipated is here higher in the filamentary zone (second layer) than in the copper core and that the power dissipated in the two outer layers (CuNi barrier and copper shell) is almost negligible because of the presence of the CuNi barrier.

Furthermore, for illustrative purposes, we have also simulated the response of K006-01C JT-60SA TF strand to a ramp going from $0T$ to $3T$ in $1s$ followed by a plateau and to the same rising ramp but this time followed by an exponential decay with a characteristic time of 0.1s (this value lies in the range of the time constant of the composite); the results are displayed through Figure 93 to Figure 96 in Appendix D.

All these cartographies exhibit a large heterogeneity of the power density spatial distribution inside the composite; they clearly differ one from another either in terms of distribution or in terms of magnitude. This fact stresses that the stability of a strand can be impacted differently according to the operating conditions and that dedicated analyses e.g. with the present tool must be conducted in order to finely assess the risk of quench in given conditions.

Conversely to the analytical approach which currently prevails in the community of superconducting magnets and which considers that the power is homogeneously dissipated inside superconducting strands, our model allows to predict the spatial variation of the power deposition at any time with very low CPU consumption thanks to its analytical nature. This characteristic makes it attractive because it can be quickly integrated in any multiphysics platforms that must scan thousands of scenario point; it would have a marginal impact on studies complexity or computation time.

Regarding stability studies, our model can provide one of the source terms of the heat equation which are essential to any thermal study. It therefore stands as a first step towards the development of an integrated model dedicated to stability diagnostics.

II.5 Experimental work

II.5.1 Presentation of Speedy facility

II.5.1.1 Speedy

The Speedy facility has existed at CEA for many years and has thoroughly been described in [42]. The Speedy facility is located at IRFM CEA Cadarache and is used for measuring the magnetization cycles of superconducting composites, which allow the determination of their hysteresis and coupling losses. It features a liquid helium bath in which the superconducting coil responsible for the application of a magnetic field on the composite to be tested is immersed (see Figure 32).

Figure 32 : Superconducting coil used for the application of a magnetic field on the tested composite

The composite is tested with the compensated pick-ups method and is therefore wound on a cylindrical sample holder. An inner pick-up copper coil called reference coil is wound on a "finger holder" and inserted inside the sample holder. An outer pick-up copper coil is used as a measurement coil and is wound on a "sheath holder" which encloses the sample holder. The different holders which are about ten centimeters high, the pick-up coils and the position of the composite to be tested are presented in Figure 33.

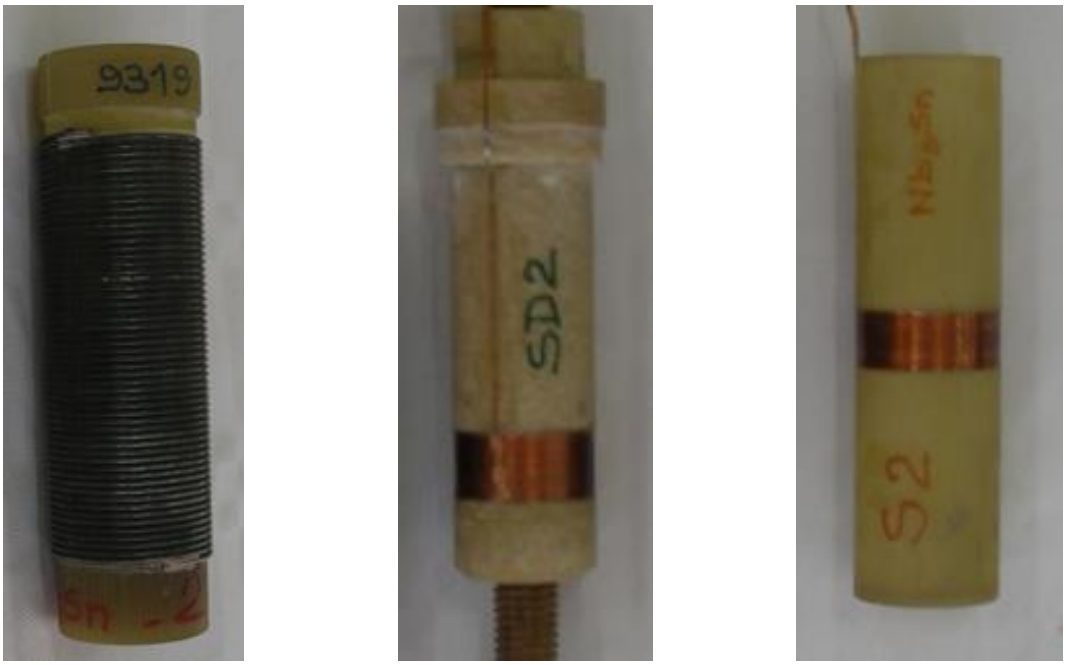

(a) : Example of a sample holder with a composite wound on it

(b) : Example of a finger holder with the inner pick-up coil wound on it

(c) : Example of a sheath holder with the outer pick-up coil wound on it

Figure 33 : Examples of the different holders with superconducting composite and copper pick-up coils

The three holders are designed in an accurate way so that they can exactly fit in each other. Their assembly is displayed on Figure 34.

(a) : The three holders dissociated

(b) : The three holders assembled

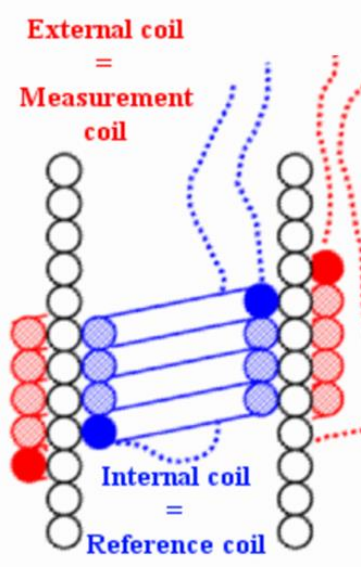

(c) : Schematic view of pick-up coils and composite for assembled holders

Figure 34 : Assembly of the different holders with their pick-up coils and the superconducting composite

Once assembled, the three holders and their coils are integrated onto a rod that will be placed in the central hole of the superconducting coil visible on Figure 32 which is immersed in a liquid helium bath.

Figure 35 displays a complete overview of the Speedy facility. We see that the superconducting coil creates a magnetic field called $\overrightarrow{B_a}$: it corresponds to the magnetic field that would exist inside the superconducting coil if its enclosed volume was empty (i.e. without the composite to be tested).

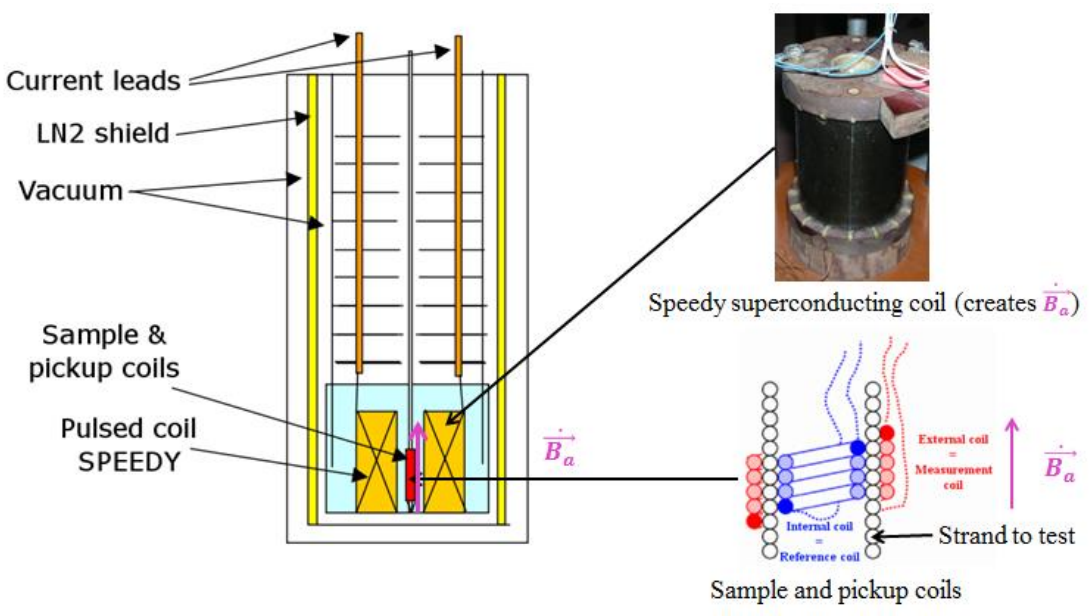

Figure 35 : Schematic overview of the Speedy facility

It is important to note that the ends of the superconducting composite to be tested are not connected to avoid it behaving as a small coil once immersed in the magnetic field generated by the superconducting coil of Figure 32. The reasons why the sample is coil shaped are that:

- it allows the measurement of the composite response to a transverse time varying magnetic field
- the different turns increase the total measured magnetization and therefore enhance the quality of the measurement

On the other hand, the ends of both the inner and outer pick-up coils are connected through a Wheatstone bridge whose electrical scheme can be seen on Figure 36.

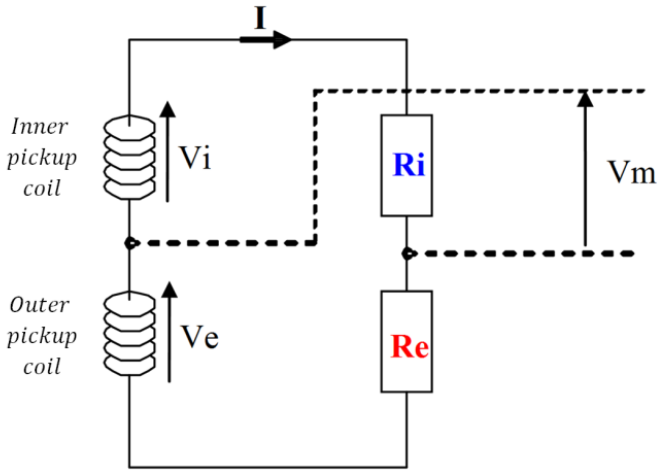

Figure 36 : Electrical scheme of the Wheatsone bridge used in Speedy facility

This bridge features two electrical resistances noted R_i and R_e and is designed so that the voltage induced in the inner coil (reference) by the time variation of the applied magnetic field $\overrightarrow{B_a}$ can compensate that induced in the outer coil (measurement). Indeed, when the bridge is balanced, these voltages cancel each other out and V_m can be directly linked to the time variation of the magnetization of the composite. According to the electric scheme of Figure 36, we have

$$V_m = \frac{R_i V_e - R_e V_i}{R_i + R_e}$$

We can now decompose the voltage induced in each pick-up coils as a sum of the voltage due to the time variation of the applied magnetic field (i.e. due to $\dot{B}_a$) and of the voltage due to the time variation of the magnetization of the composite (i.e. due to $\dot{M}$). This consideration leads to the following equations:

$$\begin{cases} V_i = V_{i_{\dot{B}_a}} + V_{i_{\dot{M}}} = n_i \pi {r_i}^2 \dot{B}_a + V_{i_{\dot{M}}} \\ V_{e_{\dot{M}_0}} = V_{e_{\dot{B}_a}} + V_{e_{\dot{M}}} = n_e \pi {r_e}^2 \dot{B}_a + V_{e_{\dot{M}}} \end{cases}$$

where n_i and n_e are the number of turns of the inner and outer pick-up coils respectively and r_i and r_e are their respective winding radii.

Now replacing V_i and V_e in the expression of V_m, we obtain

$$V_m = \frac{R_i V_{e_{\dot{M}}} - R_e V_{i_{\dot{M}}}}{R_i + R_e} + \frac{n_e \pi {r_e}^2 R_i - n_i \pi {r_i}^2 R_e}{R_i + R_e} \dot{B}_a$$

In order for the Wheatstone bridge to be balanced, the second term in V_m expression must be zero, so that the measured value of V_m only relates to the time variation of the magnetization of the composite.

Therefore the balancing condition of the Wheatstone bridge is

$$n_e \pi {r_e}^2 R_i = n_i \pi {r_i}^2 R_e$$

which can be alternatively expressed as

$$\frac{R_i}{R_e} = \frac{n_i {r_i}^2}{n_e {r_e}^2}$$

When the Wheatstone bridge is balanced, V_m only depends on the time variation of the magnetization of the composite $\dot{M}$ and is equal to

$$V_m = \frac{R_i V_{e_{\dot{M}}} - R_e V_{i_{\dot{M}}}}{R_i + R_e}$$

We will derive the expressions of $V_{i_{\dot{M}}}$ and $V_{e_{\dot{M}}}$ as functions $\dot{M}$ of in the next section.

II.5.1.2 Measurement method of magnetization

We will here derive the expression which links the energy dissipated during a magnetic cycle to the measured voltage V_m presented in the previous section.

This calculation has already been carried out by Ciazynski [30] for a composite having only one screening current (i.e. having only one interface between resistive and filamentary zones, see section II.2.3). However, in our modeling, we have considered composites with any number of screening currents (i.e. with any number of interfaces between resistive and filamentary zones), therefore we had to derive again the relation between the energy dissipated during a magnetic cycle and the measured voltage V_m for these configurations.

First of all, we know that the energy density Q_{vol} dissipated during a cycle of the external magnetic excitation is equal to

$$Q_{vol} = -\int_{cycle} \vec{M}.d\vec{B}_i$$

where $\vec{M}$ is the magnetization inside the strand and $\vec{B}_i$ the induction inside the strand.

Splitting $\vec{B}_i$ as $\vec{B}_i = \vec{B}_a + \vec{B}_{react}$ where $\vec{B}_{react}$ is the reacting magnetic field, i.e. the magnetic field due to the induced currents, we can alternatively write

$$Q_{vol} = -\int_{cycle} \vec{M}.d\vec{B}_i = -\int_{cycle} \vec{M}.d\vec{B}_a - \int_{cycle} \vec{M}.d\vec{B}_{react}$$

In addition we have

$$\vec{B}_i = \mu_0\left(\vec{H} + \vec{M}\right) = \mu_0(\vec{H}_a + \vec{H}_d + \vec{M})$$

where $\mu_0\vec{H}_a = \vec{B}_a$ is the applied field and $\vec{H}_d$ is the demagnetizing field. We can therefore express $\vec{B}_{react}$ as

$$\vec{B}_{react} = \mu_0(\vec{H}_d + \vec{M})$$

Finally, the relation between $\vec{H}_d$ and $\vec{M}$ can be written as

$$\vec{H}_d = -N_d\vec{M}$$

where N_d is known as the coefficient of demagnetization (it can also be a tensor if the relation between $\vec{H}_d$ and $\vec{M}$ is anisotropic).

Using the previous relations, it is now possible to write

$$\vec{B}_{react} = \mu_0(1 - N_d)\vec{M}$$

and thus

$$-\int_{cycle} \vec{M}.d\vec{B}_{react} = -\mu_0(1 - N_d)\int_{cycle} \vec{M}.d\vec{M} = -\mu_0(1 - N_d)\frac{1}{2}\left[{M_{end}}^2 - {M_{start}}^2\right]$$

where M_{end} is the magnetization at the end of a cycle and M_{start} is the magnetization at the beginning of the same cycle.

After the first magnetic cycle, we are sure that the magnetization is the same at the beginning and at the end of each cycle, consequently $M_{end} = M_{start}$ and

$$-\int_{cycle} \vec{M}.d\vec{B}_{react} = 0$$

As a result, Q_{vol} can be reduced to

$$Q_{vol} = -\int_{cycle} \vec{M}.d\vec{B}_a$$

We will now compute the magnetization inside a cylinder carrying a surface current $\vec{K} = K_0\cos(\theta)\overrightarrow{e_z}$ on its outer surface. In the following, this distribution of current will be referred to as a "circular dipole". According to (57), we know that the magnetic field components inside and outside the cylinder of radius R are given by

$$\begin{cases} B_{x_{int}}(r,\theta) = 0 \\ B_{x_{ext}}(r,\theta) = -\dfrac{\mu_0 K_0}{2}\left(\dfrac{R}{r}\right)^2 \sin(2\theta) \\ B_{y_{int}}(r,\theta) = -\dfrac{\mu_0 K_0}{2} \\ B_{y_{ext}}(r,\theta) = \dfrac{\mu_0 K_0}{2}\left(\dfrac{R}{r}\right)^2 \cos(2\theta) \end{cases}$$

Outside the cylinder, we have $\vec{B}_{ext} = \mu_0\vec{H}_{ext}$ and inside, we have $\vec{B}_{int} = \mu_0\left(\vec{H}_{int} + \vec{M}\right)$. Given the spatial form of the magnetic field inside the cylinder, we can assume that

$$\begin{cases} \vec{H}_{int} = H_{int_x}\overrightarrow{e_x} + H_{int_y}\overrightarrow{e_y} \\ \vec{M} = M_x\overrightarrow{e_x} + M_y\overrightarrow{e_y} \end{cases}$$

where H_{int_x}, H_{int_y}, M_x and M_y do not depend on r and θ.

The continuity equation of $\vec{H}$ at $r = R$ leads to

$$\overrightarrow{e_r} \times \left[\vec{H}_{ext}(R,\theta) - \vec{H}_{int}(R,\theta)\right] = \left[\frac{K_0}{2}\cos(\theta) + H_{int_x}\sin(\theta) - H_{int_y}\cos(\theta)\right]\overrightarrow{e_z} = \vec{0}$$

Therefore

$$\begin{cases} H_{int_x} = 0 \\ H_{int_y} = \dfrac{K_0}{2} \end{cases}$$

Using the fact that $\vec{B}_{int} = \mu_0\left(\vec{H}_{int} + \vec{M}\right)$, we can deduce

$$\begin{cases} M_x = 0 \\ M_y = -K_0 \end{cases}$$

We will now compute the magnetic flux due to a vertical row of circular dipoles of radius *R* enclosed by each pick up coil.

According to (55), the magnetic vector potential A_{z_d} at (x, y) created by a circular dipole of radius R_d located at (x_d, y_d) with a surface current amplitude K_{0_d} is equal to

$$A_{z_d}(x,y) = \frac{\mu_0 K_{0_d}}{2}\ {R_d}^2 \frac{x - x_d}{(x-x_d)^2 + (y-y_d)^2}$$

For a vertical row of $2n+1$ circular dipoles spaced $2a$ apart (see Figure 37) and centered on $y = y_{d_0}$ with $-a \le y_{d_0} \le a$, we have

$$A_{z_{d\,row}}(x,y) = \frac{\mu_0 K_{0_d}}{2}\ {R_d}^2 (x - x_d) \sum_{k=-n}^{n} \frac{1}{(x-x_d)^2 + \left(y - y_{d_0} - 2ka\right)^2}$$

The height of the wound sample in the vertical direction (i.e. $4na$ along the y-axis) being large compared to the heights of the pick-up coils (see Figure 34), we can assume that the magnetic vector potential felt by the pick-up coils at any y is constant and given by

$$\langle A_{z_{d\,row}} \rangle (x) = \frac{1}{2a} \int_{y=-a}^{a} A_{z_{d\,row}}(x,y)\,dy$$

which is equal to

$$\langle A_{z_{d\,row}} \rangle (x) = \frac{\mu_0 K_{0_d}\ {R_d}^2 (x - x_d)}{4a} \sum_{k=-n}^{n} \int_{y=-a}^{a} \frac{dy}{(x-x_d)^2 + \left(y - y_{d_0} - 2ka\right)^2}$$

The integral inside the sum being equal to

$$\frac{1}{(x-x_d)}\left[\arctan\left(\frac{y_{d_0} + (2k+1)a}{x - x_d}\right) - \arctan\left(\frac{y_{d_0} + (2k-1)a}{x - x_d}\right)\right]$$

we can simplify the sum as

$$\frac{1}{(x-x_d)}\left[\arctan\left(\frac{y_{d_0} + (2n+1)a}{x - x_d}\right) - \arctan\left(\frac{y_{d_0} - (2n+1)a}{x - x_d}\right)\right]$$

since it is a telescopic sum.

Assuming that $(2n+1)a \gg |x - x_d|$ and that $(2n+1)a \gg \left|y_{d_0}\right|$, we can deduce

$$\langle A_{z_{d\,row}}\rangle(x) = \frac{\mu_0 K_{0_d}\, {R_d}^2 \pi}{4a} sign(x - x_d)$$

For $x = -h_i$ or $x = h_e$, the assumption $(2n+1)a \gg |x - x_d|$ is valid since the half-height of the sample (several centimeters in the vertical direction, see Figure 34) is much larger than the distance between the sample and the pick-up coils in the (Oxz) plane (this distance is usually comparable to the radius of the tested composite, i.e. about half a millimeter). In addition, since the sample is wound with a large number of turns n (see Figure 34) and $|y_{d_0}| \leq a$, the assumption $(2n+1)a \gg |y_{d_0}|$ is also valid.

The magnetic flux $\Phi_{i_{d\,row}}$ due to a vertical row of circular dipoles with radius R and current K_{0_d} enclosed by the internal pick-up coil which has a winding radius r_i and n_i turns is then

$$\Phi_{i_{d\,row}} = -2\pi r_i n_i \langle A_{z_{d\,row}}\rangle(x = -h_i) = 2\pi r_i n_i \frac{\mu_0 K_{0_d} {R_d}^2 \pi}{4a}$$

Note that the flux of a magnetic field oriented along the y-axis through the inner pick-up coil is counted as positive here.

Using the fact that the magnetization inside the dipole is $M_d = -K_{0_d}$, we have

$$\Phi_{i_{d\,row}} = -2\pi r_i n_i \frac{\mu_0 M_d {R_d}^2 \pi}{4a}$$

Similarly, the magnetic flux $\Phi_{e_{d\,row}}$ enclosed by the external pick-up coil which has a winding radius r_e and n_e turns is then

$$\Phi_{e_{d\,row}} = -2\pi r_e n_e \langle A_{z_{d\,row}}\rangle(x = h_e) = -2\pi r_e n_e \frac{\mu_0 K_{0_d} {R_d}^2 \pi}{4a} = 2\pi r_e n_e \frac{\mu_0 M_d {R_d}^2 \pi}{4a}$$

Again the flux of a magnetic field oriented along the y-axis through the outer pick-up coil is counted as positive here.

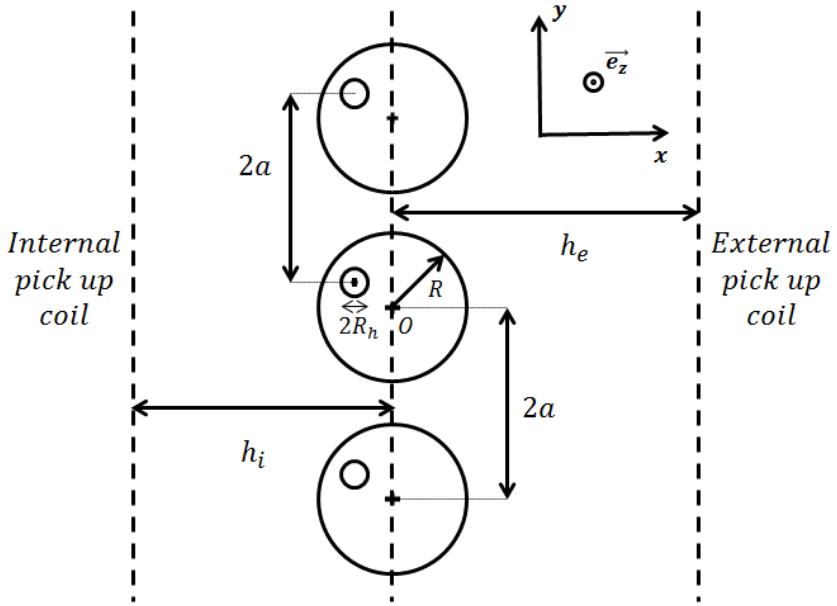

Figure 37 : Schematic cross-section of three turns of sample in Speedy facility

In a composite, there exist several circular dipoles with different internal magnetizations M_d and radii R_d. Indeed, the magnetization currents flowing through the superconducting filaments which are responsible for the hysteresis losses can be seen as dipoles with a radius equal to that of a filament ($R_h = r_{fil}$). In addition, the currents flowing through the edge filaments of each filamentary zone are also circular dipoles with a radius equal to the radial localization of the currents.

Therefore we can define an average magnetization M_0 over the whole volume of a composite of radius R as

$$M_0 = \frac{1}{R^2}\sum_d M_d {R_d}^2$$

In order to take into account the contribution of every circular dipole existing inside the composite in the magnetic flux enclosed by each pick-up coil, we have to sum the previous relations over every dipole, i.e.

$$\begin{cases} \Phi_{i_{M_0}} = \sum_d \Phi_{i_{d\,row}} = -2\pi r_i n_i \frac{\mu_0 \pi}{4a} \sum_d M_d {R_d}^2 \\ \Phi_{e_{M_0}} = \sum_d \Phi_{e_{d\,row}} = 2\pi r_e n_e \frac{\mu_0 \pi}{4a} \sum_d M_d {R_d}^2 \end{cases}$$

This leads to

$$\begin{cases} \Phi_{i_{M_0}} = -r_i n_i \frac{\mu_0 \pi^2}{2a} M_0 R^2 \\ \Phi_{e_{M_0}} = r_e n_e \frac{\mu_0 \pi^2}{2a} M_0 R^2 \end{cases}$$

It is interesting to note that, from the point of view of each pick-up coil, there is absolutely no distinction between the effects of several circular dipoles with different radii inside the composite and a circular dipole with a radius equal to that of the composite (i.e. R) and a magnetization M_0 equal to the surface weighted average of the magnetizations of every circular dipoles in the composite.

Finally we can deduce that the voltage induced in each pick-up coil by the variation of M_0 is

$$\begin{cases} V_{i_{\dot{M}_0}} = -\dot{\Phi}_{i_{M_0}} = r_i n_i \frac{\mu_0 \pi^2}{2a} \dot{M}_0 R^2 \\ V_{e_{\dot{M}_0}} = -\dot{\Phi}_{e_{M_0}} = -r_e n_e \frac{\mu_0 \pi^2}{2a} \dot{M}_0 R^2 \end{cases}$$

Now, using the relation of the Wheatstone bridge given in the previous section, we have

$$V_m = \frac{R_i V_{e_{\dot{M}_0}} - R_e V_{i_{\dot{M}_0}}}{R_i + R_e} = -\frac{\mu_0 \pi^2 R^2}{2a}\left[\frac{n_e r_e R_i + n_i r_i R_e}{R_i + R_e}\right]\dot{M}_0$$

assuming the bridge is balanced. We can now give the relation between the measured voltage V_m and the average magnetization M_0 as

$$\mu_0 M_0 = -f_{geo} \int V_m dt$$

with

$$f_{geo} = \frac{2a}{\pi^2 R^2} \left[\frac{R_i + R_e}{n_e r_e R_i + n_i r_i R_e} \right]$$

To compute the energy per unit volume of strand dissipated during a magnetic cycle, we can now replace $\vec{M}$ with $M_0 \overrightarrow{e_y}$ and $\vec{B}_a$ with $B_a \overrightarrow{e_y}$ in $Q_{vol} = -\int_{cycle} \vec{M}.d\vec{B}_a$. This leads to

$$Q_{vol} = -\int_{cycle} M_0 dB_a = \int_{cycle} \frac{f_{geo}}{\mu_0} \left(\int V_m dt \right) dB_a$$

The expression we have obtained is almost equal to that of Ciazynski [30] because the taking into account of the additional screening currents does not modify the relation between the energy and V_m (the difference is about 5% and is due to the different approaches we have used to average the magnetic vector potential felt by the pick-up coils). Indeed, we have seen that the pick-up coils make no distinction between the contributions of every circular dipoles in the composite and that of an equivalent circular dipole with radius R and magnetization M_0 equal to the surface weighted average of the magnetizations of every circular dipoles in the composite. However this calculation had to be carried out in order to assess the effect of the additional screening currents in the relation between the measured voltage V_m and the magnetization of the composite.

II.5.2 Measurements

In this section we will present the results issued from the AC losses measurements we have carried out in the Speedy facility on the two strands displayed on Figure 38.

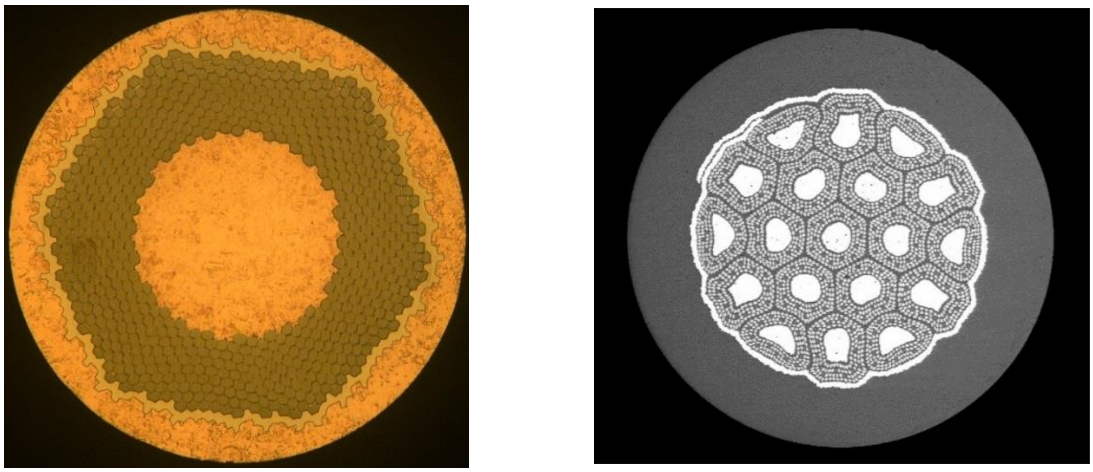

(a) : K006-01C JT-60SA TF strand (NbTi)

(b) : F 0796-1 ITER TF strand (Nb_3Sn)

Figure 38 : Strands measured in the Speedy facility

As a reminder K006-01C JT-60SA TF strand [39] has been manufactured by Furukawa and contains a copper core surrounded by a filamentary zone which consists of twisted NbTi superconducting filaments embedded in a copper matrix. The filamentary zone is enclosed in a CuNi barrier which is surrounded by a copper shell.

The F 0796-1 ITER TF strand [43] has been manufactured by Oxford Instruments Superconducting Technology (OST) by means of the Internal Tin Diffusion Process. It features 19 sub-elements each containing a tin core surrounded by twisted Nb_3Sn superconducting filaments embedded in a bronze matrix (originally the matrix is made of copper but is transformed into a bronze matrix during the tin diffusion process). The 19 sub-elements are assembled together and are surrounded by a tantalum diffusion barrier; outside the barrier is a copper shell.

The AC losses of K006-01C JT-60SA TF strand have been measured at CEA in 2011 [44] for trapezoidal cycles which were slowly time-varying. According to our analytical modeling, this strand is supposed to exhibit two time constants because it features two interfaces between filamentary and resistive zones but this behavior cannot be observed in slowly time-varying regimes. Consequently our original objective was to measure the AC losses of this strand for fast time-varying magnetic regimes in order to produce its Q vs f curve and to verify if the strand was indeed exhibiting two time constants instead of one as it is usually admitted within the community for any strand. The fast regimes were supposed to be explored using sinusoidal signal excitation, tentatively implemented for the first time in CEA Speedy facility.

However, we have encountered two difficulties which have prevented us from observing this behavior:

- The power supply used in the Speedy facility is limited to 800 A in current and 30 V in voltage; it is therefore not powerful enough to explore sufficiently fast time-varying regimes because of the complex impedance due to the self-inductance of the Speedy superconducting coil. Knowing that it would not be possible to reach frequencies high enough to overpass the maximum of the Q vs f curve of K006-01C JT-60SA TF strand, our original plan was just to measure the AC losses outside the linear region of the Q vs f curve. Unfortunately, it appeared that the sinusoidal magnetic field $B_a = B_p \sin(2\pi f t)$ that the power supply and the coil could produce was limited to $B_p = 17\ mT$ at $f = 10Hz$ and to $B_p = 1\ mT$ at $f = 20Hz$; with these amplitudes, it is not possible to have trustworthy magnetization signals (values close to H_{C1} value and complex way to discriminate coupling and hysteresis losses). Consequently it was then not possible to explore out of the linear region of the Q vs f curve.

- After having measured the AC losses of K006-01C JT-60SA TF strand for slow time-varying regimes, we have been able to deduce the effective transverse resistivity of its filamentary zone (see section II.4.3) : it appeared that this resistivity was very close to that of the copper core so that the screening current flowing at the interface between the copper core and the filamentary zone was too weak. This implies that K006-01C JT-60SA TF strand almost behaves as a single time constant strand and therefore it would have been very difficult to distinguish the contribution of a second time constant in the measurements.

Despite these difficulties we have been able to take profit of the experiments by measurements of the AC losses of K006-01C JT-60SA TF strand for trapezoidal cycles with different magnetic field amplitudes and for sinusoidal cycles until $f = 1Hz$ also with different magnetic field amplitudes; we will present these results further.

Regarding the F 0796-1 ITER TF strand, it appears that there is no record of measurement of any Nb_3Sn strand coupling losses while the hysteresis losses of ITER TF-type strands have systematically been measured [45] in the production QA flow. For this reason we have chosen to measure this strand to evaluate its time constant.

II.5.2.1 NbTi strand (JT-60SA TF)

II.5.2.1.1 Trapezoidal cycles

We have first measured the AC losses of K006-01C JT-60SA TF strand generated during symmetric magnetic trapezoidal cycles. These cycles are routinely specified for a strand fabrication and therefore accordingly used by manufacturers for the characterization of superconducting strands during manufacture.

Each trapezoidal cycle started from $+B_m$, fell to $-B_m$ in a time $2\tau_a$, then stayed at $-B_m$ for a time T_p (typically around 5s), then went back to $+B_m$ again in a time $2\tau_a$ and finally stayed at $+B_m$ for a time T_p. The pattern of the trapezoidal cycle can be seen on Figure 39. Both τ_a and T_p are long compared to the largest time constant of the strand so that we can consider the magnetic trapezoidal cycles as slow time-varying regimes.

For this strand, we have carried out several series of measurement for three different values of B_m : $1.5T$, $2.5T$ and $3T$. For each value of B_m we have also made several measurements of losses for different values of τ_a between 2s and 20s.

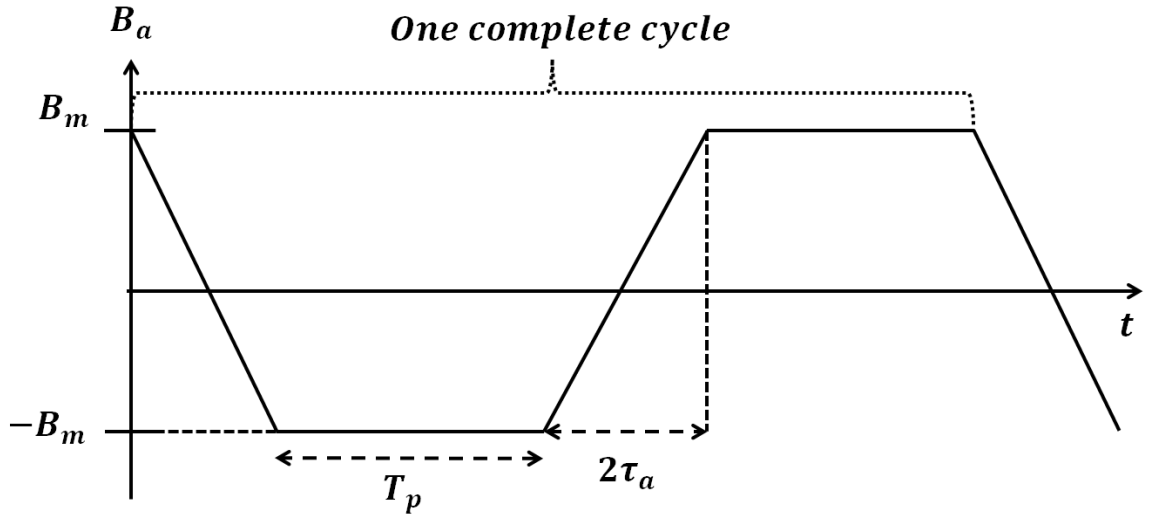

Figure 39 : Schematic pattern of a trapezoidal magnetic cycle

Finally, in order to increase the reliability of the measured losses, for each (B_m, τ_a) couple we have submitted the strand to 5 consecutive cycles and only kept the average of the losses over these 5 cycles.

For each value of B_m, we will display both the magnetization cycles we have measured in the Speedy facility and the curve of AC losses per cycle per unit volume of strand Q as function of $1/\tau_a$. This curve is important as it enables us to distinguish the hysteresis losses from the coupling losses and to deduce

the time constant of the strand. Indeed we can split the total measured losses Q as a sum of the hysteresis losses Q_{hyst} and of the coupling losses Q_{coup}

$$Q = Q_{hyst} + Q_{coup}$$

We first express the instant power per unit volume of strand P_{coup} during a ramp of a trapezoidal cycle using equation (3) and considering that $\dot{B}_a \simeq \dot{B}_i$ since the ramps are long enough (i.e. much longer that the highest time constant of the strand)

$$P_{coup} \simeq \frac{2\tau \dot{B}_a{}^2}{\mu_0}\left(\frac{R_f}{R}\right)^2 = \frac{2\tau}{\mu_0}\left(\frac{B_m}{\tau_a}\right)^2\left(\frac{R_f}{R}\right)^2$$

where R_f is the external radius of the filamentary zone, R the radius of the composite and τ is either the time constant of the strand if it is a single time constant strand or the equivalent time constant of the strand for slowly time-varying regimes if it is a multiple time constants strand (in this case the equivalent time constant will then be a linear combination of the time constants of the strand).

Consequently, since the total duration of the ramps in a trapezoidal cycle is equal to $4\tau_a$, we can deduce that

$$Q_{coup} \simeq 4\tau_a \frac{2\tau}{\mu_0}\left(\frac{B_m}{\tau_a}\right)^2\left(\frac{R_f}{R}\right)^2 = \frac{8\tau B_m{}^2}{\mu_0}\left(\frac{R_f}{R}\right)^2 \frac{1}{\tau_a}$$

The hysteresis losses are independent of the rate of variation of the applied magnetic field B_a, therefore for trapezoidal cycles with a fixed value of B_m, they will always be the same. It is then now possible to express Q as function of $1/\tau_a$

$$Q\left(\frac{1}{\tau_a}\right) = Q_{hyst} + Q_{coup} = \frac{8\tau B_m{}^2}{\mu_0}\left(\frac{R_f}{R}\right)^2 \frac{1}{\tau_a} + Q_{hyst}$$

From the expression above we immediately see that the measured curve of $Q\left(\frac{1}{\tau_a}\right)$ should be a linear function of $1/\tau_a$ that can be expressed as

$$Q\left(\frac{1}{\tau_a}\right) = a\frac{1}{\tau_a} + b$$

with

$$\begin{cases} a = \dfrac{8\tau B_m{}^2}{\mu_0}\left(\dfrac{R_f}{R}\right)^2 \\ b = Q_{hyst} \end{cases}$$

Finally, from the experimental value of a, we can compute the time constant τ as

$$\tau = \frac{\mu_0}{8B_m{}^2}\left(\frac{R}{R_f}\right)^2 a \tag{129}$$

The total losses per unit volume of strand per cycle are proportional to the areas of the measured magnetization cycles displayed on Figure 97, Figure 99 and Figure 101 in Appendix E. We clearly see that the lower τ_a the higher the area of the measured magnetization cycle and thus the higher the total losses.

In reality, for a fixed value of B_m, the area corresponding to the hysteresis losses is the same for each magnetization cycle because it does not depend on τ_a while the area of the coupling losses increases with decreasing τ_a.

This is logical as the rate of change of the applied magnetic field B_a, and thus the coupling losses, are higher if τ_a is lower.

From the different experimental values of the losses per unit volume of strand per cycle and their linear fitting, we can now deduce the hysteresis losses of K006-01C JT-60SA TF strand and its time constant for the different values of B_m using equation (129) with $R_f = 327\ \mu m$ and $R = 405\ \mu m$ (see section II.4.3.1); they are displayed on Table 5.

Table 5

Experimental hysteresis losses and time constant of K006-01C JT-60SA TF strand for trapezoidal cycles with different values of B_m			
$B_m\ (T)$	1.5	2.5	3
$Q_{hyst}(mJ/cm^3/cycle)$ per unit volume of strand	**98.9**	**134.1**	**145.3**
$\boldsymbol{\tau}\ (\boldsymbol{ms})$	**20.9**	**17.6**	**17.0**

The values of hysteresis losses and of time constant measured for a trapezoidal cycle with $B_m = 3T$ are consistent with those measured at CEA in 2011 [44].

Regarding the other values of B_m, we can clearly see that the time constant decreases with increasing B_m : this is explained by the fact that when B_m is higher, the average magnetic field felt by the strand during the cycle is also higher and thus the average magnetoresistance of copper increases. Consequently, the equivalent transverse resistivity of the whole strand increases and thus its time constant decreases (see section II.1.2).

II.5.2.1.2 Positive trapezoidal cycles

We will present here the experimental AC losses of K006-01C JT-60SA TF strand measured for positive trapezoidal cycles; these cycles are used here because they will also be used in a later section focused on the AC losses of JT-60SA TF conductor that we have measured in Josefa facility at CEA Cadarache.

The positive trapezoidal cycles are trapezoidal cycles in which the applied magnetic field B_a is always positive; their pattern is displayed on Figure 40.

Again, for each value of B_m (either $1T$ or $1.5T$), both the magnetization cycles and the curve of AC losses per cycle per unit volume of strand Q as function of $1/\tau_a$ we have measured in the Speedy facility are displayed through Figure 103 to Figure 106 in Appendix E.

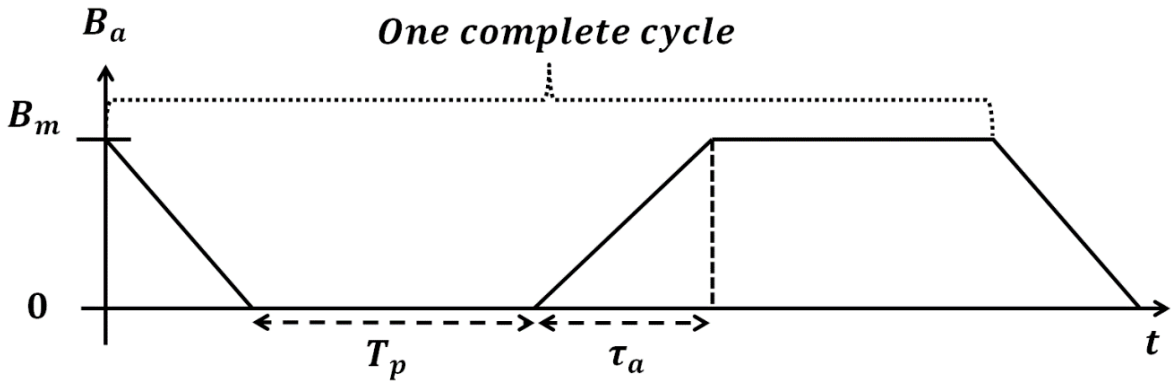

Figure 40 : Schematic pattern of a positive trapezoidal magnetic cycle

The hysteresis losses and the time constant are deduced using the same methodology; the only difference lies in the adaptation of equation (129) which becomes

$$\tau = \frac{\mu_0}{4{B_m}^2}\left(\frac{R}{R_f}\right)^2 a \qquad (130)$$

because the total duration of the ramps in a positive trapezoidal cycle is to $2\tau_a$ instead of $4\tau_a$.

As we did previously, we can deduce the hysteresis losses and time constant from the different experimental values of the losses per unit volume of strand per cycle and their linear fitting using equation (130); they are displayed on Table 6. The time constants measured here are consistent with the previous measurements made with the symmetric trapezoidal cycles.

Table 6

Experimental hysteresis losses and time constant of K006-01C JT-60SA TF strand for positive trapezoidal cycles with different values of B_m		
$B_m\ (T)$	1	1.5
$Q_{hyst}(mJ/cm^3/cycle)$ per unit volume of strand	**31.5**	**42.7**
$\boldsymbol{\tau\ (ms)}$	**20.4**	**18.8**

II.5.2.1.3 Sinusoidal cycles

We have also measured the experimental AC losses of K006-01C JT-60SA TF strand for sinusoidal cycles with frequencies up to $1Hz$. This constitutes an innovation for the Speedy facility as so far it was not able to produce sinusoidal magnetic excitations.

We have carried out four series of measurements where the sinusoidal magnetic excitations are all given by

$$B_a = B_p \sin(2\pi f t) + B_{off}$$

The first three series of measurements were made for $B_{off} = 0\ T$ and $B_p = 1.5\ T$, $B_p = 2.5\ T$, $B_p = 3\ T$ and the last series was made for $B_{off} = 1.5\ T$ and $B_p = 1.25\ T$. The experimental results (magnetization cycles and curves of losses Q vs f) are displayed though Figure 107 to Figure 114 in Appendix E.

Since the magnetic excitation is here different from ramps we have to express the instant power per unit volume of strand P_{coup} during a sinusoidal cycle using equation (3) and considering that $\dot{B}_a \simeq \dot{B}_i$ since the time periods of the sinusoids are long enough (i.e. much longer that the highest time constant of the strand)

$$P_{coup}(t) \simeq \frac{2\tau \dot{B_a}^2}{\mu_0}\left(\frac{R_f}{R}\right)^2 = \frac{2\tau}{\mu_0}\left(2\pi f B_p\right)^2\left(\frac{R_f}{R}\right)^2 \cos^2(2\pi f t)$$

Since $Q_{coup} = \int_0^T P_{coup}(t)dt$ where $T = 1/f$ is the time period of the sinusoidal magnetic excitation, we can deduce that

$$Q_{coup} \simeq \frac{2\tau}{\mu_0}\left(2\pi f B_p\right)^2\left(\frac{R_f}{R}\right)^2 \int_0^T \cos^2(2\pi f t)\, dt = \frac{2\tau}{\mu_0}\left(2\pi f B_p\right)^2\left(\frac{R_f}{R}\right)^2 \frac{T}{2} = \frac{4\pi^2 {B_p}^2 \tau}{\mu_0}\left(\frac{R_f}{R}\right)^2 f$$

We can now express Q as function of f

$$Q(f) = Q_{hyst} + Q_{coup} = \frac{4\pi^2 {B_p}^2 \tau}{\mu_0}\left(\frac{R_f}{R}\right)^2 f + Q_{hyst}$$

From the expression above we immediately see that the measured curve of $Q(f)$ should be a linear function of f that can be expressed as

$$Q(f) = af + b$$

with

$$\begin{cases} a = \dfrac{4\pi^2 {B_p}^2 \tau}{\mu_0}\left(\dfrac{R_f}{R}\right)^2 \\ b = Q_{hyst} \end{cases}$$

Finally, from the experimental value of a, we can compute the time constant τ as

$$\tau = \frac{\mu_0}{4\pi^2 {B_p}^2}\left(\frac{R}{R_f}\right)^2 a \qquad (131)$$

As we did previously, we can deduce the hysteresis losses and time constant from the different experimental values of the losses per unit volume of strand per cycle and their linear fitting using equation (131); they are displayed on Table 7.

Table 7

Experimental hysteresis losses and time constant of K006-01C JT-60SA TF strand for sinusoidal cycles with different values of B_p and B_{off}				
$B_p\ (T)\ /\ B_{off}\ (T)$	1.5 / 0	2.5 / 0	3 / 0	1.25 / 1.5
$Q_{hyst}(mJ/cm^3/cycle)$ per unit volume of strand	**101.1**	**134.5**	**150.5**	**78.5**
$\boldsymbol{\tau}\ (\boldsymbol{ms})$	**21.3**	**18.0**	**17.1**	**14.9**

The values of hysteresis losses and of time constant measured for sinusoidal cycles are fully consistent with those measured for trapezoidal cycles (displayed on Table 5).

II.5.2.2 Nb_3Sn strand (ITER TF)

We have also measured the AC losses of F 0796-1 ITER TF strand generated during magnetic trapezoidal cycles and sinusoidal cycles in order to deduce its time constant; the experimental results are displayed in the following.

II.5.2.2.1 Trapezoidal cycles

The trapezoidal cycles we have used for the measurements of the AC losses of F 0796-1 ITER TF strand are identical to these we have used for K006-01C JT-60SA TF strand.

The experimental results (magnetization cycles and AC losses per unit volume of strand per cycle) are displayed though Figure 115 to Figure 120 in Appendix F.

For each value of B_m, we can clearly see that the magnetization curves we have measured for different values of τ_a are really close from one another. This means that the hysteresis losses of F 0796-1 ITER TF strand are largely predominant over its coupling losses. As a consequence the experimental determination of its time constant is not easy since the magnetization signal of its coupling losses appears to be negligible compared to that of its hysteresis losses.

Despite this difficulty, we have deduced the hysteresis losses of F 0796-1 ITER TF strand and its time constant for the different values of B_m from the experimental values of the losses per unit volume of strand per cycle and their linear fitting using equation (129) with $R_f = 293\ \mu m$ and $R = 410\ \mu m$ [43]; they are displayed on Table 8.

Table 8

Experimental hysteresis losses and time constant of F 0796-1 ITER TF strand for trapezoidal cycles with different values of B_m			
$B_m\ (T)$	1.5	2.5	3
$Q_{hyst}(mJ/cm^3/cycle)$ per unit volume of strand	**137.7**	**190.5**	**212.7**
$\boldsymbol{\tau}\ (\boldsymbol{ms})$	**1.4**	**1.2**	**1.0**

The values of hysteresis losses of F 0796-1 ITER TF strand we have measured in Speedy facility appear to be lower than those measured for other ITER TF-type strands [45] but the ratios $Q_{hyst}(B_m = 1.5T)/Q_{hyst}(B_m = 3T)$ and $Q_{hyst}(B_m = 2.5T)/Q_{hyst}(B_m = 3T)$ are consistent with the results presented in [45].

Given the fact that the coupling losses of F 0796-1 ITER TF strand are very small compared to its hysteresis losses, the values of its time constant we have measured should only be considered as an estimate of its real value.

II.5.2.2.2 Sinusoidal cycles

We have also measured the AC losses of F 0796-1 ITER TF strand for sinusoidal cycles up to $f = 1Hz$ in order to produce a better estimate of its time constant.

The sinusoidal magnetic excitation was of the form

$$B_a = B_p \sin(2\pi f t) + B_{off}$$

with $B_{off} = 1.5\ T$ and $B_p = 1.4\ T$.

The experimental results (magnetization cycles and AC losses per unit volume of strand per cycle) are displayed on Figure 121 and Figure 122 in Appendix F.

We can see that the magnetization curves we have measured for different values of f are again close from one another but less than for the trapezoidal cycles; this means that the coupling losses have here a stronger impact on the total losses than they did for the trapezoidal cycles.

We have then deduced the hysteresis losses of F 0796-1 ITER TF strand and its time constant from the experimental values of the losses per unit volume of strand per cycle and their linear fitting using equation (131) with $R_f = 293\ \mu m$ and $R = 410\ \mu m$ [43]; they are displayed on Table 9.

Table 9

Experimental hysteresis losses and time constant of F 0796-1 ITER TF strand for sinusoidal cycles	
$B_p\ (T)\ /\ B_{off}\ (T)$	1.4 / 1.5
$Q_{hyst}(mJ/cm^3/cycle)$ per unit volume of strand	**86.5**
$\boldsymbol{\tau}\ (\boldsymbol{ms})$	**0.9**

II.6 Synthesis

In this part of our work, we have established a new and fully generalized analytical description of the magnetic response of a given axisymmetric superconducting composite subject to any time variation of transverse magnetic field. The associated developed CLASS algorithm produces, in this regard, complete 2D cartographies of the coupling currents, the electric and magnetic fields and the local power density dissipated inside the composite at any time of transient magnetic field regime. This algorithm being based on analytical formulations, it requires very low CPU resources and can thus be easily implemented into multiphysics platforms. Further to its exhaustive and innovative aspect, the present achievement represents a step towards broader modeling objectives, e.g. the evaluation of composites stability limits (associated with thermal models). Besides, the CLASS tool can quantify coupling losses vs. frequency dependence and thus possibly be of a help to design optimized composites.

Aside to the modeling activities, we have also addressed an experimental work with AC losses measurements in CEA Speedy facility on JT-60SA TF and ITER TF strands. The results found (hysteresis losses, but mainly time constants) are compatible with those found in the literature for similar superconducting composites. Additional measurements could be carried out in order to build a fairly populated database and confront our model under a statistical approach.

Finally, we have recently developed a finite element model in collaboration with Aix-Marseille University to predict the effective transverse resistivity of filamentary zones which cannot be assimilated to infinite periodic lattices (e.g. filamentary zone of ITER TF strand, see Figure 38b); the outputs of this model will be confronted to the effective transverse resistivity deduced from the AC losses measurements of ITER TF Nb_3Sn strand.

III. Analytical study of the shielding due to a single stage of a CICC

Content: This part is dedicated to the presentation of an analytical modeling of a single cabling stage conductor. Comparisons with other analytical models are also presented.

Associated publication:

A. Louzguiti, L. Zani, D. Ciazynski, B. Turck, JL. Duchateau, A. Torre, F. Topin, *AC Coupling Losses in CICCs: Analytical Modeling at Different Stages*, I.E.E.E. Trans. on App. Superconductivity, Vol. 27, June 2017, Art. No. 0600505. (reference [46])

III.1 Presentation

In the previous section, we have studied the magnetic behavior of a single straight superconducting composite subject to a transverse time-varying magnetic field. Once having comprehensively addressed the elementary scale of a CICC (strand scale) and in the aim of progressing on the building of an extensive analytical representation of a multi-stage CICC, we now consider the next step of complexification, i.e. taking the features of a CICC into account. At this stage, the simplest representation of a CICC is to consider it as composed of an assembly of its last stages (petals) interacting all together, forming then at this level, a single stage CICC. We will consequently treat the problem by taking into consideration a bundle of elements twisted together into a round cable.

The definition of "element" can either be a strand, a group of strands or a petal (i.e. multiple strands twisted in several cabling stages). Therefore, even if our strategy aims at representing the CICC scale, our present approach is also applicable to a group of any type of twisted elements regardless of the scale.

The purpose of the approach is to analyze the shielding due to a specific cabling stage as we aim at improving the physical understanding of coupling losses observed at this scale. In a group of twisted elements, the magnetic shielding established by the elements bears many similarities with what occurs with filaments in the composite. However, a major difference lies in the fact that we consider a finite number of filaments while in the composite the edge filaments are considered as having an infinitely small size (i.e. forming a continuous ring at filamentary zone edges). The extra complexity of the present step comes from the discretization of the zone which carries the shielding currents. In other words, we are here entering into the first stage of the topological decomposition of the CICC towards its real geometry (ultimately a multi-stage assembly of strands).

III.2 *N*-uplet model

III.2.1 Methodology

In order to study the magnetic response of a group of twisted elements to a time-varying transverse and uniform magnetic field (N-uplet model), we make profit of the work already addressed at the strand scale following the methodology described in section II.2.1 :

- **In section III.2.3 we first begin by formulating the fundamental equations of the system**
- **In section III.2.4 we compute the currents induced in steady-state regime, i.e. when these currents are not time-varying**
- **In section III.2.5 , knowing the spatial form of the currents induced in steady-state regime, we follow the logical chain displayed on Figure 15 until the spatial form of the currents induced for any time-varying regime is defined; these expressions will enable us to reduce the equations of the system to a simple first-order differential equation**
- **In section III.2.6 , knowing the spatial form of the currents induced for any time regime, we attempt to establish the most analytical expression of the coupling power dissipated in a group of twisted elements in any time-varying regime**
- **In section III.2.3 we address the specific case of two twisted elements (i.e. a doublet)**

During the study in time-varying regime, we put in central place of our mathematical architecture the magnetic vector potential generated by the induced currents. Along this calculation based on the use of the Biot-Savart law, we deal with complex integrals that cannot be solved analytically. Consequently, extending the resolution itself, we attempt to find a purely analytical expression of this magnetic vector potential using an alternative method while keeping a high reliability. This complement is motivated by an intention to provide a tool that can easily be integrated in usual thermo-hydraulic codes (e.g. THEA code) which are not designed to integrate intermediate calculations such as complex integrals.

III.2.2 Assumptions

The geometry we consider in our modeling features a group of N elements twisted together with a pitch equal to l_p and a cabling radius equal to R_c. Since the element can either represent a strand, a group of strands or a petal, we simply consider it as a cylinder of radius R containing a thin superconducting shell of radius R_f (see Figure 41). Regarding the resistive component of the model, we consider that in a slice of thickness dz there exists a local effective conductance between adjacent elements which is noted $dG = \sigma_l dz$ where σ_l is the transverse conductance per unit axial length (i.e. expressed in S/m) and considered constant along the N-uplet axis. The current flowing longitudinally through the superconducting shell of element k at z is noted $I_k(z)$ and the current flowing transversely in a slice dz from element $k-1$ to element k at z is noted $I_{k-1\,k}(z)$. The below list depicts the overall assumptions considered in the present modeling:

- The external magnetic field B_a is transverse (along the y-axis, see Figure 41) and spatially uniform within the group of twisted elements
- The transport current is zero
- The geometry is infinitely long along the z-axis
- The superconducting shell is not saturated and thus the electric field is zero along the trajectory of an element
- The current $I_k(z)$ carried by the superconducting shell of element k at z is uniformly distributed over its circumference

- The elements are lightly twisted, i.e. $\left(2\pi R_c/l_p\right)^2 \ll 1$ where R_c is the cabling radius of the elements and l_p their twist pitch

- The time variation of the external magnetic field B_a is slow enough to neglect the displacement current so that Kirchhoff's current law applies

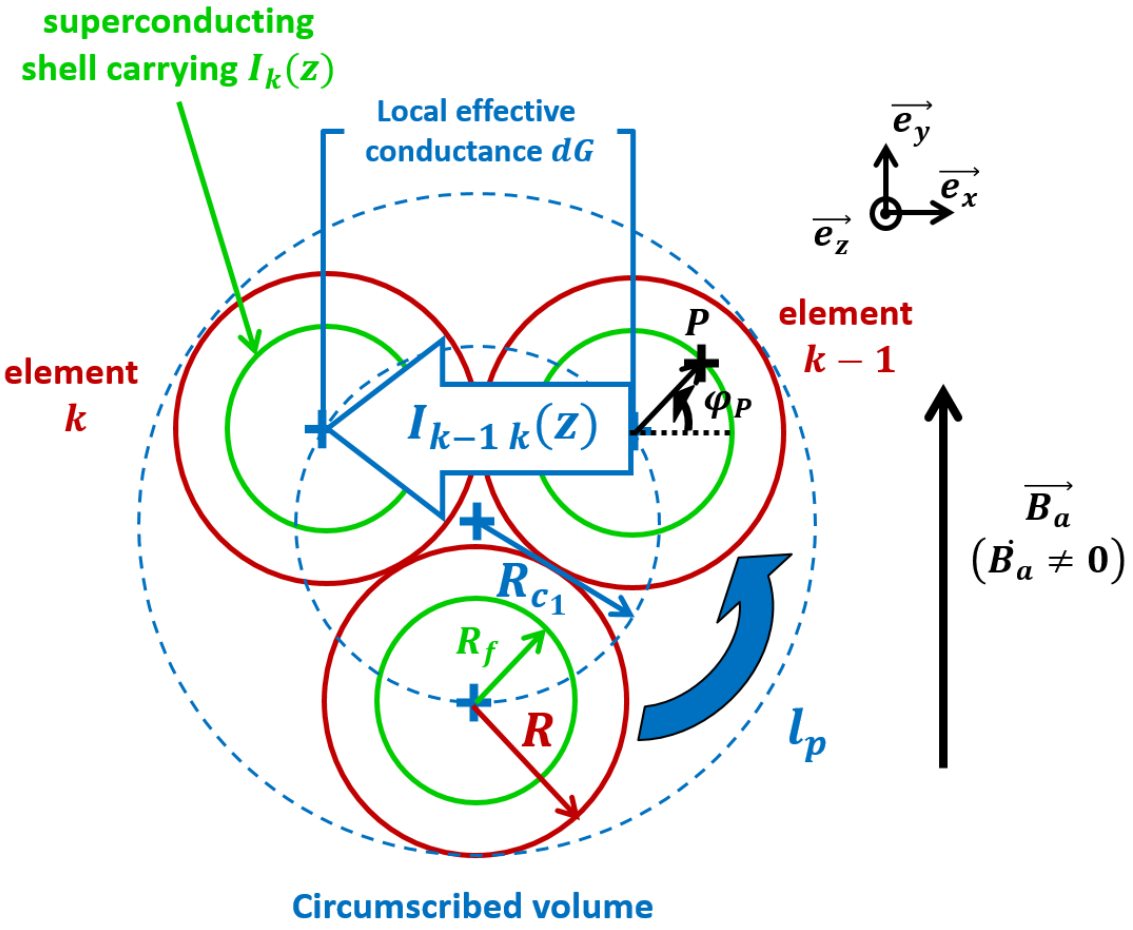

Figure 41 : Scheme showing the cross-section geometry of a triplet $(N = 3)$

Finally, the position (x_k, y_k) of the center of element k at z is given by

$$\begin{pmatrix} x_k(z) \\ y_k(z) \end{pmatrix} = \begin{pmatrix} R_C \cos\left(\frac{2\pi z}{l_p} + \frac{2\pi(k-1)}{N}\right) \\ R_C \sin\left(\frac{2\pi z}{l_p} + \frac{2\pi(k-1)}{N}\right) \end{pmatrix} \tag{132}$$

Note that we have assumed that the induced current carried by an element was located on an infinitely thin shell of superconductor. If the element is a composite this assumption is justified by the fact that the induced current is seen by the composite as a transport current and we know that the transport current does not penetrate the interior of a composite as long as the first shell of filaments is not saturated. If the element is a substage (i.e. a bundle of strands), we assume that the radius of the superconducting shell corresponds to the cabling radius of the last cabling stage of the bundle.

III.2.3 Equations of the system

❖ **We will formulate here the fundamental equations of the system using Kirchhoff's current law, Ohm's law and Faraday's law of induction.**

We will here derive the equations governing a single cabling stage conductor starting by the case $N \geq 3$. The case of the doublet (i.e. $N = 2$) - presenting some specificities - will be treated afterwards in section III.2.7 .

III.2.3.1 Electrical equations

Each element is carrying the current $I_k(z)$ in its superconducting shell along its trajectory. In addition, $I_{k-1\,k}(z)$ is the local current flowing transversely in a slice dz from element $k-1$ to k and $I_{k\,k+1}(z)$ is the local current flowing transversely in a slice dz from element k to $k+1$. Consequently, Kirchhoff's current law enables us to write

$$\frac{dI_k}{dz}(z) = \frac{1}{dz}[I_{k-1\,k}(z) - I_{k\,k+1}(z)] \tag{133}$$

In the following, we will consider that the current $I_k(z)$ flowing in the superconducting shell of element k, thus along the helicoid of element k, is exclusively oriented along the z-axis since we have assumed that the elements were lightly twisted, i.e. $\left(\frac{2\pi R_c}{l_p}\right)^2 \ll 1$. This assumption is similar to the one we have used in the composite study.

Using Ohm's law, we have

$$I_{k\,k+1}(z) = dG\; U_{k\,k+1}(z) = \sigma_l dz\; U_{k\,k+1}(z)$$

where $U_{k\,k+1}(z)$ is the local transverse voltage existing at z between the centers of elements k and $k+1$. It can alternatively be expressed as

$$\frac{1}{dz} I_{k\,k+1}(z) = \sigma_l U_{k\,k+1}(z) \tag{134}$$

III.2.3.2 Magnetic equations

Now, let us note $\Phi_{k\,k+1}(z)$ the magnetic flux enclosed between the center of element k and that of element $k+1$ from $z = 0$ to z.

It then comes

$$\Phi_{k\,k+1}(z) = \oint \vec{A}.\overrightarrow{dl} \tag{135}$$

where $\vec{A}$ has to be integrated along the red path displayed on Figure 42.

From Biot-Savart law, we know that the magnetic vector potential $\vec{A}$ is collinear to the distribution of current it is associated with if the distribution of current has a constant orientation in space. This means that the x component A_x of $\vec{A}$ is exclusively due to the x component of the current distribution, and so on for y and z. From the relation $\vec{B} = \vec{\nabla} \times \vec{A}$, we also know that the magnetic field associated with A_x will have a zero x component B_x and so on for y and z. Since we consider that the time-variation of the applied magnetic field $\overrightarrow{B_a}$ is along the y axis, we can deduce that the components of the current distribution that will actually play a role in the magnetic shielding of the conductor are the x and z ones. But since we have assumed that the elements were lightly twisted, the x component of the current carried by an element is negligible in front of its z component. As a consequence, the problem is reduced to the z component of the current distribution and thus we assume that the magnetic vector potential is given by

$$\vec{A} = A_z \overrightarrow{e_z}$$

Using this assumption, equation (135) reduces to

$$\Phi_{k\,k+1}(z) = \int_0^z \left(A_{z_{k+1}}(z') - A_{z_k}(z')\right) dz' \tag{136}$$

where $A_{z_k}(z)$ is the axial component of the magnetic vector potential at the center of element k at z.

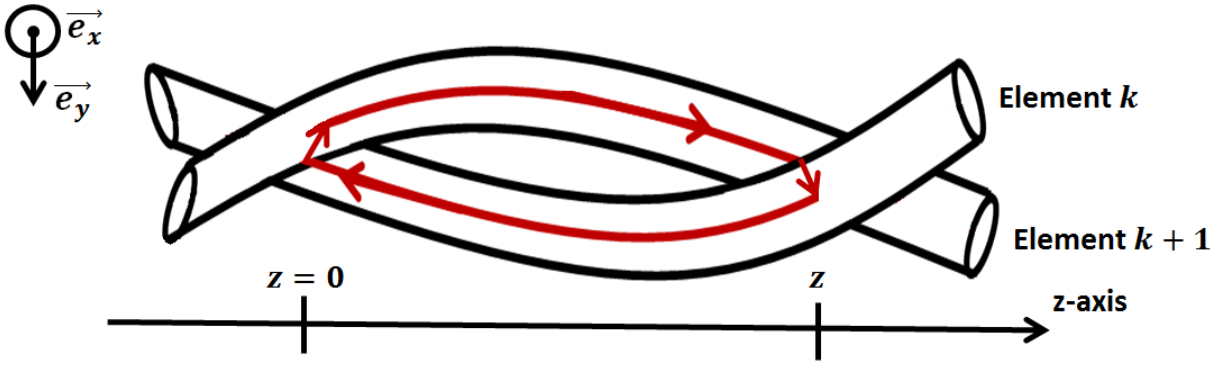

Figure 42 : Scheme showing the integration path of equation (135)

Differentiating equation (136) with respect to z and time, we now obtain

$$\frac{d}{dz}\dot{\Phi}_{k\,k+1}(z) = \dot{A}_{z_{k+1}}(z) - \dot{A}_{z_k}(z) \tag{137}$$

where the overdot notation represents differentiation with respect to time.

III.2.3.3 Electromagnetic equations

Furthermore, Faraday's law of induction enables to write

$$\oint \vec{E}.\overrightarrow{dl} = -\dot{\Phi}_{k\,k+1}(z) \tag{138}$$

where $\vec{E}$ also has to be integrated along the previous red path displayed on Figure 42.

Since we have considered that the electric field was zero along the trajectory of an element, we can reduce $\oint \vec{E}.\overrightarrow{dl}$ to

$$\oint \vec{E}.\overrightarrow{dl} = U_{k\,k+1}(z=0) - U_{k\,k+1}(z) \tag{139}$$

where $U_{k\,k+1}(z)$ is again the transverse voltage existing at z between the centers of elements k and $k+1$.

Equation (138) combined to equation (139) leads to

$$U_{k\,k+1}(z=0) - U_{k\,k+1}(z) = -\dot{\Phi}_{k\,k+1}(z)$$

The differentiation of this equation with respect to z gives

$$\frac{dU_{k\,k+1}}{dz}(z) = \frac{d}{dz}\dot{\Phi}_{k\,k+1}(z) \tag{140}$$

Once combined to equation (137), equation (140) enables us to obtain

$$\frac{dU_{k\,k+1}}{dz}(z) = \dot{A}_{z_{k+1}}(z) - \dot{A}_{z_k}(z) \tag{141}$$

III.2.3.4 Global equations

We have now written the basic equations of the system, i.e. equation (133) coming from Kirchhoff's current law, equation (134) coming from Ohm's law and equation (141) coming from Faraday's law of induction; they are recalled here

$$\begin{cases} \dfrac{dI_k}{dz}(z) = \dfrac{1}{dz}\left[I_{k-1\,k}(z) - I_{k\,k+1}(z)\right] \\ \dfrac{1}{dz}I_{k\,k+1}(z) = \sigma_l U_{k\,k+1}(z) \\ \dfrac{dU_{k\,k+1}}{dz}(z) = \dot{A}_{z_{k+1}}(z) - \dot{A}_{z_k}(z) \end{cases} \tag{142}$$

Combining the first equation of (142) to the second one enables us to write for $1 \leq k \leq N$

$$\frac{dI_k}{dz}(z) = \frac{1}{dz}\left[I_{k-1\,k}(z) - I_{k\,k+1}(z)\right] = \sigma_l\left[U_{k-1\,k}(z) - U_{k\,k+1}(z)\right]$$

Finally, differentiating this equation with respect to z and combining it to the last equation of (142) leads us to the following equation of the system

$$\frac{d^2I_k}{dz^2}(z) = \sigma_l\left[\frac{dU_{k-1\,k}}{dz}(z) - \frac{dU_{k\,k+1}}{dz}(z)\right] = \sigma_l\left[\dot{A}_{z_k}(z) - \dot{A}_{z_{k-1}}(z) - \left(\dot{A}_{z_{k+1}}(z) - \dot{A}_{z_k}(z)\right)\right]$$

which can be written as

$$\frac{d^2 I_k}{dz^2}(z) = \sigma_l\left[2\dot{A}_{z_k}(z) - \dot{A}_{z_{k-1}}(z) - \dot{A}_{z_{k+1}}(z)\right] \tag{143}$$

Similarly to what we did in the study of the magnetic shielding accomplished by a superconducting composite, we can split by superposition the magnetic vector potential present in the equation of the system, i.e. equation (143), as a sum of two terms

$$A_{z_k}(z) = A_{z_{a_k}}(z) + A_{z_{r_k}}(z)$$

where $A_{z_{a_k}}(z)$ is the axial component of the magnetic vector potential at the center of element k at z due to the applied magnetic field $\overrightarrow{B_a}$ and $A_{z_{r_k}}(z)$ is due to the currents induced in the superconducting shell of every element, i.e. due to the $(I_k)_{1\leq k\leq N}$.

We know that the magnetic vector potential $\vec{A}$ corresponding to a uniform magnetic field $\overrightarrow{B_a} = B_a\overrightarrow{e_y}$ must satisfy $\vec{\nabla} \times \vec{A} = -\overrightarrow{B_a}$; it is therefore everywhere equal to

$$\vec{A} = -xB_a\overrightarrow{e_z}$$

where x is the abscissa visible on Figure 41.

Since $A_{z_{a_k}}(z)$ is exclusively due to $\overrightarrow{B_a}$ and is felt at the center of element k at z, we can write

$$A_{z_{a_k}}(z) = -x_k(z)B_a$$

where $x_k(z)$ is the abscissa of the center of element k at z.

We have previously assumed that

$$x_k(z) = R_c\cos\left(\frac{2\pi z}{l_p} + \frac{2\pi(k-1)}{N}\right)$$

we can therefore conclude that

$$A_{z_{a_k}}(z) = -R_cB_a\cos\left(\frac{2\pi z}{l_p} + \frac{2\pi(k-1)}{N}\right) \tag{144}$$

Replacing $A_{z_k}(z)$ in the equation of the system, i.e. in equation (143), with its decomposition, we have

$$\begin{aligned}\frac{d^2 I_k}{dz^2}(z) - \sigma_l\left[2\dot{A}_{z_{r_k}}(z) - \dot{A}_{z_{r_{k-1}}}(z) - \dot{A}_{z_{r_{k+1}}}(z)\right] \\ = \sigma_l\left[2\dot{A}_{z_{a_k}}(z) - \dot{A}_{z_{a_{k-1}}}(z) - \dot{A}_{z_{a_{k+1}}}(z)\right]\end{aligned} \tag{145}$$

Injecting equation (144) in the right-hand term of equation (145), after some mathematical manipulations we have

$$\sigma_l\left[2\dot{A}_{z_{a_k}}(z) - \dot{A}_{z_{a_{k-1}}}(z) - \dot{A}_{z_{a_{k+1}}}(z)\right] = 2\sigma_l R_c\dot{B}_a\left[\cos\left(\frac{2\pi}{N}\right) - 1\right]\cos\left(\frac{2\pi z}{l_p} + \frac{2\pi(k-1)}{N}\right)$$

which simplifies to

$$\sigma_l\left[2\dot{A}_{z_{a_k}}(z)-\dot{A}_{z_{a_{k-1}}}(z)-\dot{A}_{z_{a_{k+1}}}(z)\right]=-4\sigma_l R_c\dot{B}_a\sin^2\left(\frac{\pi}{N}\right)\cos\left(\frac{2\pi z}{l_p}+\frac{2\pi(k-1)}{N}\right)$$

As a result, the equation of the system can finally be expressed as

$$\begin{cases}\dfrac{d^2I_k}{dz^2}(z)+\sigma_l\left[\dot{A}_{z_{r_{k-1}}}(z)+\dot{A}_{z_{r_{k+1}}}(z)-2\dot{A}_{z_{r_k}}(z)\right]\\ \quad=-4\sigma_l R_c\dot{B}_a\sin^2\left(\dfrac{\pi}{N}\right)\cos\left(\dfrac{2\pi z}{l_p}+\dfrac{2\pi(k-1)}{N}\right)\end{cases}\tag{146}$$

Similarly to what was done at the composite scale we will now initiate the global calculation strategy starting with the steady-state regime study.

III.2.4 Study in steady-state regime

❖ **We will calculate here the currents induced in steady-state regime. We will simply start from the system equation derived at the end of the previous section and we will solve it considering that the coupling currents are not time-varying.**

III.2.4.1 Equations of the system in steady-state regime

We here consider steady-state regimes for coupling currents, that is to say that the currents induced in the elements are, by assumption, not varying, i.e. we consider that for any z and for $1\leq k\leq N$

$$\dot{I}_k(z)=0$$

Since $A_{z_{r_k}}(z)$ is exclusively due to the induced currents, we can also conclude that for any z and for $1\leq k\leq N$

$$\dot{A}_{z_{r_k}}(z)=0$$

And therefore, from equation (146), we see that the equation of the system is, in steady-state regime, simply reduced to

$$\frac{d^2I_k}{dz^2}(z)=-4\sigma_l R_c\dot{B}_a\sin^2\left(\frac{\pi}{N}\right)\cos\left(\frac{2\pi z}{l_p}+\frac{2\pi(k-1)}{N}\right)\tag{147}$$

The double integration of equation (147) with respect to z leads to

$$I_k(z)=I_0\cos\left(\frac{2\pi z}{l_p}+\frac{2\pi(k-1)}{N}\right)+c_k z+d_k\tag{148}$$

with

$$I_0 = 4\sigma_l R_c \dot{B}_a \, sin^2\left(\frac{\pi}{N}\right)\left(\frac{l_p}{2\pi}\right)^2 \tag{149}$$

The $(c_k)_{1\le k\le N}$ and $(d_k)_{1\le k\le N}$ are integration constants that have to be determined.

III.2.4.2 Determination of the solutions for an infinitely long conductor

In a first step we start the resolution considering an infinitely long conductor, which is somehow relevant of the magnet configuration, having long lengths exposed to varying magnetic field.

We have assumed that the system was not carrying any transport current, therefore at any z, we must have

$$\sum_{k=1}^{N} I_k(z) = 0$$

Using solution (148), this implies for any z

$$\sum_{k=1}^{N}\left[4\sigma_l R_c \dot{B}_a \, sin^2\left(\frac{\pi}{N}\right)\left(\frac{l_p}{2\pi}\right)^2 \cos\left(\frac{2\pi z}{l_p} + \frac{2\pi(k-1)}{N}\right) + c_k z + d_k\right] = 0$$

Since $\sum_{k=1}^{N} \cos\left(\frac{2\pi z}{l_p} + \frac{2\pi(k-1)}{N}\right) = 0$, we can deduce that

$$\begin{cases} \sum_{k=1}^{N} c_k = 0 \\ \sum_{k=1}^{N} d_k = 0 \end{cases}$$

In addition, we can notice that the position of the center of element k at $z + l_p/N$ corresponds to that of the center of element $k+1$ at z, indeed

$$\begin{pmatrix} x_k\left(z + \frac{l_p}{N}\right) \\ y_k\left(z + \frac{l_p}{N}\right) \end{pmatrix} = \begin{pmatrix} R_c \cos\left(\frac{2\pi\left(z + \frac{l_p}{N}\right)}{l_p} + \frac{2\pi(k-1)}{N}\right) \\ R_c \sin\left(\frac{2\pi\left(z + \frac{l_p}{N}\right)}{l_p} + \frac{2\pi(k-1)}{N}\right) \end{pmatrix} = \begin{pmatrix} R_c \cos\left(\frac{2\pi z}{l_p} + \frac{2\pi k}{N}\right) \\ R_c \sin\left(\frac{2\pi z}{l_p} + \frac{2\pi k}{N}\right) \end{pmatrix} = \begin{pmatrix} x_{k+1}(z) \\ y_{k+1}(z) \end{pmatrix}$$

As a consequence, the current $I_k(z + l_p/N)$ carried by the superconducting shell of element k at $z + l_p/N$ must be equal to the current $I_{k+1}(z)$ carried by the superconducting shell of element $k+1$ at z, i.e.

$$I_k\left(z + l_p/N\right) = I_{k+1}(z)$$

Using solution (148), this implies for any z and for $1 \leq k \leq N$

$$c_k(z + l_p/N) + d_k = c_{k+1}z + d_{k+1}$$

Using this relation at $z = 0$ and at $z = -l_p/N$, we can deduce that for $1 \leq k \leq N$

$$c_{k+1} = c_k$$

Since $\sum_{k=1}^{N} c_k = 0$, we immediately conclude that for $1 \leq k \leq N$

$$c_k = 0$$

which in turn implies that for $1 \leq k \leq N$

$$d_{k+1} = d_k$$

which also gives for $1 \leq k \leq N$

$$d_k = 0$$

As a result, the integration constants $(c_k)_{1\leq k\leq N}$ and $(d_k)_{1\leq k\leq N}$ are all equal to zero and the solution of the system in steady-state regime is

$$I_k(z) = I_0 \cos\left(\frac{2\pi z}{l_p} + \frac{2\pi(k-1)}{N}\right) \tag{150}$$

with

$$I_0 = 4\sigma_l R_c \dot{B}_a \, sin^2\left(\frac{\pi}{N}\right)\left(\frac{l_p}{2\pi}\right)^2 \tag{151}$$

III.2.4.3 Determination of the solutions for a finite length of conductor

We here investigate the effect of a finite length of conductor on the induced currents. This situation is typically relevant to the configuration encountered in sample tests, where short lengths (few decimeters to meters) are exposed to varying magnetic field.

Let us consider a piece of conductor of length L so that the ends of the conductor are located at $z = -L/2$ and $z = L/2$.

For this geometry, the currents induced in each element must be zero at both ends of conductor. This implies the following boundary conditions for $1 \leq k \leq N$

$$\begin{cases} I_k(-L/2) = 0 \\ I_k(L/2) = 0 \end{cases}$$

Using solution (148), this implies for $1 \leq k \leq N$

$$\begin{cases} I_0 \cos\left(-\dfrac{\pi L}{l_p} + \dfrac{2\pi(k-1)}{N}\right) - c_k\dfrac{L}{2} + d_k = 0 \\ I_0 \cos\left(\dfrac{\pi L}{l_p} + \dfrac{2\pi(k-1)}{N}\right) + c_k\dfrac{L}{2} + d_k = 0 \end{cases}$$

The solutions of this system are for $1 \leq k \leq N$

$$\begin{cases} c_k = \frac{2}{L} I_0 \sin\left(\frac{\pi L}{l_p}\right) \sin\left(\frac{2\pi(k-1)}{N}\right) \\ d_k = -I_0 \cos\left(\frac{\pi L}{l_p}\right) \cos\left(\frac{2\pi(k-1)}{N}\right) \end{cases}$$

As a result, the solution of the system in steady-state regime for a conductor of length L is for $1 \leq k \leq N$

$$I_k(z) = I_0 \left[\cos\left(\frac{2\pi z}{l_p} + \frac{2\pi(k-1)}{N}\right) + \frac{2z}{L} \sin\left(\frac{\pi L}{l_p}\right) \sin\left(\frac{2\pi(k-1)}{N}\right) - \cos\left(\frac{\pi L}{l_p}\right) \cos\left(\frac{2\pi(k-1)}{N}\right) \right] \quad (152)$$

where I_0 is again given by equation (151).

III.2.5 Study in time-varying regime

❖ **Since we now know the spatial form of the currents induced in steady-state regime, we will follow the logical chain displayed on Figure 15 until the spatial form of the currents induced for any time-varying regime is defined (this is achieved through III.2.5.1 to III.2.5.3). These expressions will then enable us to reduce the equations of the system to a simple first-order differential equation in III.2.5.4 . Finally, we will present an alternative approach leading to a simpler expression of the system equation in III.2.5.5 .**

We are now studying the magnetic response of the conductor when the induced currents are time-varying, i.e. we now consider that for any z and for $1 \leq k \leq N$

$$\dot{I}_k(z) \neq 0$$

This also implies that for any z and for $1 \leq k \leq N$

$$\dot{A}_{z r_k}(z) \neq 0$$

Therefore we now have to take into account the contribution of the magnetic vector potential due to the induced currents in the equation of the system which is now written as

$$\frac{d^2 I_k}{dz^2}(z) + \sigma_l \left[\dot{A}_{z r_{k-1}}(z) + \dot{A}_{z r_{k+1}}(z) - 2\dot{A}_{z r_k}(z) \right] = -\left(\frac{2\pi}{l_p}\right)^2 I_{0_{ext}} \cos\left(\frac{2\pi z}{l_p} + \frac{2\pi(k-1)}{N}\right) \quad (153)$$

with

$$I_{0_{ext}} = 4\sigma_l R_c \dot{B}_a \sin^2\left(\frac{\pi}{N}\right) \left(\frac{l_p}{2\pi}\right)^2 \quad (154)$$

In order to do so, we will begin by evaluating $A_{z_{r_k}}^{(1)}(z)$ due to the spatial distribution of current found in steady-state regime and which is noted $\left(I_k^{(1)}(z)\right)_{1\leq k\leq N}$.

In doing so, we are actually following the analytical methodology we have described in section III.2.1 .

First, we have assumed that the current $I_k(z)$ carried by the superconducting shell of element k at z was uniformly distributed over its circumference, i.e. we consider that the superconducting shell of element k is in fact carrying a uniform surface current $K_k(z)$ at z with

$$K_k(z) = \frac{I_k(z)}{2\pi R_f} \tag{155}$$

where R_f is the radius of the infinitely thin superconducting shell.

The current distribution $\left(I_k^{(1)}(z) = I_0^{(1)}\cos\left(\frac{2\pi z}{l_p} + \frac{2\pi(k-1)}{N}\right)\right)_{1\leq k\leq N}$ found in steady-state regime then leads to the following distribution of surface currents $\left(K_k^{(1)}(z)\right)_{1\leq k\leq N}$

$$K_k^{(1)}(z) = \frac{I_k^{(1)}(z)}{2\pi R_f} = \frac{I_0^{(1)}}{2\pi R_f}\cos\left(\frac{2\pi z}{l_p} + \frac{2\pi(k-1)}{N}\right) \tag{156}$$

according to (155).

III.2.5.1 Calculation of the magnetic vector potential due to the current flowing in one element

Let us note $\overrightarrow{K_p^{(1)}} = K_p^{(1)}\overrightarrow{e_{s_p}}$ the surface current flowing through the superconducting shell of element p at z which has been found in steady-state regime. Using equation (156), we have

$$K_p^{(1)}(z) = \frac{I_0^{(1)}}{2\pi R_f}\cos\left(\frac{2\pi z}{l_p} + \frac{2\pi(p-1)}{N}\right) \tag{157}$$

$s_p(z)$ is the abscissa along the trajectory of the center of element p at z and $\overrightarrow{e_{s_p}}(z)$ is the unit vector tangent to the trajectory of center of element p at z.

Let us note $A_{z_{r_{(p)}}}^{(1)}(M_k)$ the axial component of the magnetic vector potential felt at the center of element k at z (the center is noted M_k) and due to $\overrightarrow{K_p^{(1)}}$. We recall that we are only interested in its axial component because we have neglected the contributions of the other components (see section III.2.3.2).

Using the Biot-Savart law, we can write

$$A^{(1)}_{z_{r(p)}}(M_k) = \frac{\mu_0}{4\pi}\iint_{P\in\Sigma} \frac{K_p^{(1)}\overrightarrow{e_{s_p}}(z_P).\overrightarrow{e_z}}{PM_k}\,d\Sigma \qquad (158)$$

where P is the source point (see Figure 41) whose axial coordinate is z_P and which has to be integrated over the area Σ corresponding to the localization of the surface current $\overrightarrow{K_p^{(1)}}$, i.e. to the external area of the hollow cylinder of radius R_f whose center follows the center of element k (see green surface on Figure 43).

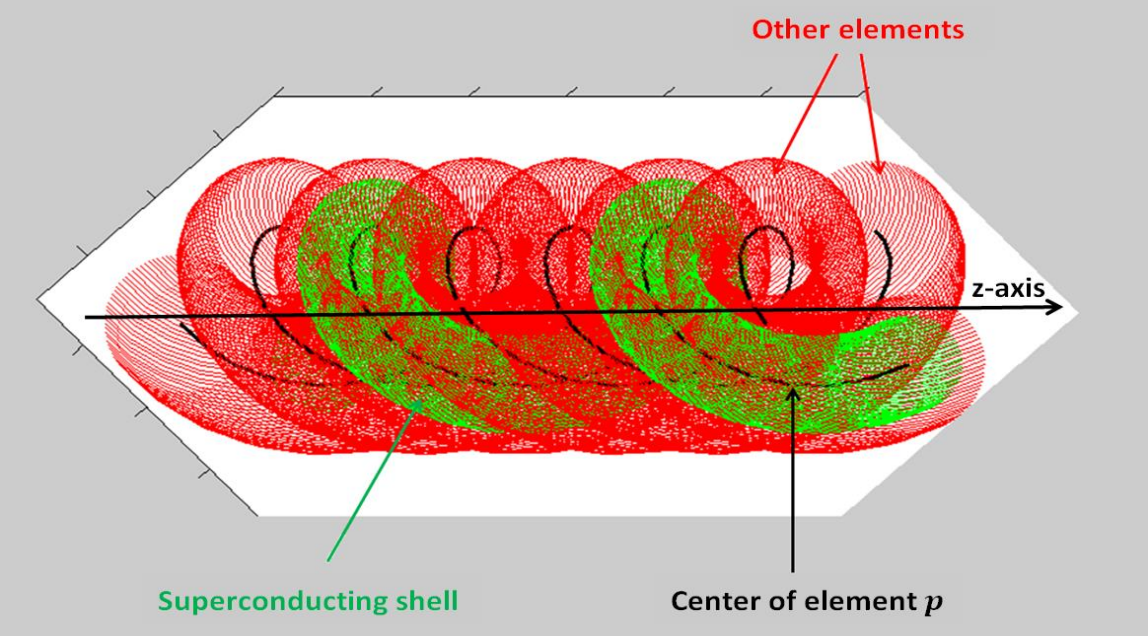

Figure 43 : Scheme showing the integration area Σ of equation (158)

The position of the center of element p at z_P noted O_p is given by (132)

$$\overrightarrow{OO_p} = \begin{pmatrix} x_p(z_P) \\ y_p(z_P) \\ z_P \end{pmatrix} = \begin{pmatrix} R_c\cos\left(\frac{2\pi z_P}{l_p} + \frac{2\pi(p-1)}{N}\right) \\ R_c\sin\left(\frac{2\pi z_P}{l_p} + \frac{2\pi(p-1)}{N}\right) \\ z_P \end{pmatrix}$$

Given the geometry, the elementary area $d\Sigma$ is equal to

$$d\Sigma = R_f d\Psi_P ds_p(z_P)$$

where Ψ_P is the angle between $\overrightarrow{e_x}$ and $\overrightarrow{O_P P}$ in the (Oxy) plane (see Figure 41) so that

$$\overrightarrow{O_P P} = R_f\cos(\Psi_P)\,\overrightarrow{e_x} + R_f\sin(\Psi_P)\,\overrightarrow{e_y}$$

assuming the elements are lightly twisted (O_P is the center of element p at z_P and P is the source point located on the superconducting shell of element p at z_P).

$s_p(z_P)$ being the abscissa corresponding to the position of O_P along the trajectory of the center of element p at z_P, we can thus write

$$ds_p(z_P) = \left\|\overrightarrow{dOO_P}\right\|$$

Since $\overrightarrow{e_{s_p}}(z_P)$ is the unit vector tangent to the trajectory of the center of element p at z_P and O_P is the center of element p at z_P, we have

$$\overrightarrow{e_{s_p}}(z_P) = \frac{\overrightarrow{dOO_P}}{\left\|\overrightarrow{dOO_P}\right\|}$$

Consequently, the term $\overrightarrow{e_{s_p}}(z_P).\overrightarrow{e_z}d\Sigma$ in equation (158) can be expressed as

$$\overrightarrow{e_{s_p}}(z_P).\overrightarrow{e_z}d\Sigma = \frac{\overrightarrow{dOO_P}}{\left\|\overrightarrow{dOO_P}\right\|}.\overrightarrow{e_z}R_f d\Psi_P\left\|\overrightarrow{dOO_P}\right\| = \overrightarrow{dOO_P}.\overrightarrow{e_z}R_f d\Psi_P = R_f d\Psi_P dz_P$$

Therefore replacing $\overrightarrow{e_{s_p}}(z_P).\overrightarrow{e_z}d\Sigma$ with the expression above and $K_p^{(1)}(P)$ with its expression given by (157) for $z = z_P$ into the formula of $A^{(1)}_{z_{r_{(p)}}}(M_k)$ given by (158), we now obtain

$$A^{(1)}_{z_{r_{(p)}}}(M_k) = \frac{\mu_0 I_0^{(1)}}{8\pi^2}\int_{z_p=-\infty}^{+\infty}\int_{\Psi_p=0}^{2\pi}\frac{\cos\left(\frac{2\pi z_P}{l_p}+\frac{2\pi(p-1)}{N}\right)}{PM_k(z,z_p,\Psi_p)}d\Psi_P dz_P \qquad (159)$$

Let us now express the distance $PM_k(z,z_P,\Psi_P)$.

Since P is the source point located on the superconducting shell of element p at z_P and M_k is the center of element k at z, their coordinates in the $(\overrightarrow{e_x},\overrightarrow{e_y},\overrightarrow{e_z})$ basis are given by

$$\begin{cases}\overrightarrow{OP} = \overrightarrow{OO_P} + \overrightarrow{O_PP} = \left[x_p(z_P) + R_f cos(\Psi_P)\right]\overrightarrow{e_x} + \left[y_p(z_P) + R_f sin(\Psi_P)\right]\overrightarrow{e_y} + z_P\,\overrightarrow{e_z} \\ \overrightarrow{OM_k} = x_k(z)\,\overrightarrow{e_x} + y_k(z)\overrightarrow{e_y} + z\,\overrightarrow{e_z}\end{cases}$$

Consequently, we have

$$PM_k(z,z_P,\Psi_P)^2 = \left[x_k(z) - x_p(z_P) - R_f cos(\Psi_P)\right]^2 + \left[y_k(z) - y_p(z_P) - R_f sin(\Psi_P)\right]^2 + [z - z_P]^2$$

After some mathematical treatment involving trigonometric simplifications, we can express $PM_k(z,z_P,\Psi_P)^2$ as

$$PM_k(z,z_P,\Psi_P)^2 = \begin{cases}4{R_c}^2\sin^2\left(\frac{\pi(z-z_P)}{l_p}+\frac{\pi(k-p)}{N}\right) \\ +4R_cR_f\sin\left(\frac{\pi(z-z_P)}{l_p}+\frac{\pi(k-p)}{N}\right)\sin\left(\frac{\pi(z+z_P)}{l_p}+\frac{\pi(k+p-2)}{N}-\Psi_P\right) \\ +{R_f}^2+(z-z_P)^2\end{cases}$$

In order to ease the mathematical treatment of integral (159), we will use the notation

$$f(z,z_P,\Psi_P) = \frac{\cos\left(\frac{2\pi z_P}{l_p}+\frac{2\pi(p-1)}{N}\right)}{PM_k(z,z_P,\Psi_P)}$$

Following this notation, integral (159) is now simply expressed as

$$A^{(1)}_{z_{r_{(p)}}}(M_k) = \frac{\mu_0 I_0^{(1)}}{8\pi^2} \int_{z_p=-\infty}^{+\infty} \int_{\Psi_p=0}^{2\pi} f\left(z, z_p, \Psi_p\right) d\Psi_P dz_P \tag{160}$$

We will now carry out the following changes of variable in integral (160)

$$\begin{cases} z' = z_P - z \\ \Psi' = \Psi_P - \left[\dfrac{\pi(z+z_P)}{l_p} + \dfrac{\pi(k+p-2)}{N}\right] \end{cases}$$

This implies

$$\begin{cases} dz' = dz_P \\ d\Psi' = d\Psi_P \end{cases}$$

The interval of integration of z_P being infinite, the new interval of integration of z' also remains infinite, i.e. from $-\infty$ to $+\infty$. In addition, $f(z, z_P, \Psi_P)$ is a 2π-periodic function of Ψ_P, thus even with the change of variable of Ψ_P into Ψ', we choose to keep the same interval of integration for Ψ' which is $[0; 2\pi]$.

As a result, it is now possible to re-express integral (160) as

$$A^{(1)}_{z_{r_{(p)}}}(M_k) = \frac{\mu_0 I_0^{(1)}}{8\pi^2} \int_{z'=-\infty}^{+\infty} \int_{\Psi'=0}^{2\pi} \frac{\cos\left(\dfrac{2\pi(z'+z)}{l_p} + \dfrac{2\pi(p-1)}{N}\right)}{g_{p\,k}(z', \Psi')} d\Psi' dz' \overrightarrow{e_z} \tag{161}$$

where $g_{p\,k}(z', \Psi')$ is given by

$$\sqrt{4{R_c}^2 \sin^2\left(\frac{\pi z'}{l_p} + \frac{\pi(p-k)}{N}\right) + 4R_c R_f \sin\left(\frac{\pi z'}{l_p} + \frac{\pi(p-k)}{N}\right) \sin(\Psi') + {R_f}^2 + {z'}^2} \tag{162}$$

The cosine term at the numerator of (161) can be expressed as

$$\cos\left(\frac{2\pi(z'+z)}{l_p} + \frac{2\pi(p-1)}{N}\right) = \cos\left(\frac{2\pi z}{l_p} + \frac{2\pi(k-1)}{N} + \frac{2\pi z'}{l_p} + \frac{2\pi(p-k)}{N}\right)$$

Developing it, we can now write $A^{(1)}_{z_{r_{(p)}}}(M_k)$ as

$$\begin{cases} \dfrac{\mu_0 I_0^{(1)}}{8\pi^2} \Bigg[\cos\left(\dfrac{2\pi z}{l_p} + \dfrac{2\pi(k-1)}{N}\right) \displaystyle\int_{z'=-\infty}^{+\infty} \int_{\Psi'=0}^{2\pi} \frac{\cos\left(\dfrac{2\pi z'}{l_p} + \dfrac{2\pi(p-k)}{N}\right)}{g_{p\,k}(z', \Psi')} d\Psi' dz' \\ \quad - \sin\left(\dfrac{2\pi z}{l_p} + \dfrac{2\pi(k-1)}{N}\right) \displaystyle\int_{z'=-\infty}^{+\infty} \int_{\Psi'=0}^{2\pi} \frac{\sin\left(\dfrac{2\pi z'}{l_p} + \dfrac{2\pi(p-k)}{N}\right)}{g_{p\,k}(z', \Psi')} d\Psi' dz' \Bigg] \end{cases} \tag{163}$$

III.2.5.2 Calculation of the magnetic vector potential due to the currents flowing in all the elements

Let us note $\left(\overrightarrow{K_p^{(1)}}(z) = K_p^{(1)}\overrightarrow{e_{s_p}}\right)_{1\leq p\leq N}$ the current distribution flowing through the superconducting shell of all the elements which has been found in steady-state regime.

Let us note $A_{z_r}^{(1)}(M_k)$ the magnetic vector potential felt at the center of element k at z (noted M_k) and due to the current distributions $\left(\overrightarrow{K_p^{(1)}}(z) = K_p^{(1)}\overrightarrow{e_{s_p}}\right)_{1\leq p\leq N}$.

Following the definition of $A_{z_{r_{(p)}}}^{(1)}(M_k)$ and $A_{z_r}^{(1)}(M_k)$, by superposition, we have

$$A_{z_r}^{(1)}(M_k) = \sum_{p=1}^{N} A_{z_{r_{(p)}}}^{(1)}(M_k) \tag{164}$$

Since $A_{z_{r_k}}^{(1)}(z)$ is by definition the axial component of the magnetic vector potential felt at the center of element k at z due to the total current distribution found in steady-state regime, we can write

$$A_{z_r}^{(1)}(M_k) = A_{z_{r_k}}^{(1)}(z)$$

in order to be consistent with the previous notations.

Making use of formula (163), we then obtain

$$A_{z_{r_k}}^{(1)}(z) = \begin{cases} \dfrac{\mu_0 I_0^{(1)}}{8\pi^2}\Bigg[\cos\left(\dfrac{2\pi z}{l_p} + \dfrac{2\pi(k-1)}{N}\right)\displaystyle\int_{z'=-\infty}^{+\infty}\int_{\Psi'=0}^{2\pi}\sum_{p=1}^{N}\frac{\cos\left(\dfrac{2\pi z'}{l_p} + \dfrac{2\pi(p-k)}{N}\right)}{g_{p\,k}(z',\Psi')}d\Psi' dz' \\ \quad -\sin\left(\dfrac{2\pi z}{l_p} + \dfrac{2\pi(k-1)}{N}\right)\displaystyle\int_{z'=-\infty}^{+\infty}\int_{\Psi'=0}^{2\pi}\sum_{p=1}^{N}\frac{\sin\left(\dfrac{2\pi z'}{l_p} + \dfrac{2\pi(p-k)}{N}\right)}{g_{p\,k}(z',\Psi')}d\Psi' dz'\Bigg] \end{cases} \tag{165}$$

where $g_{p\,k}(z',\Psi')$ is still given by (162).

Note that in the notation $g_{p\,k}(z',\Psi')$, p and k are both modulo N, i.e. for $1 \leq p \leq N$ and $1 \leq k \leq N$, we have $g_{p+N\,k}(z',\Psi') = g_{p\,k}(z',\Psi')$ and $g_{p\,k+N}(z',\Psi') = g_{p\,k}(z',\Psi')$.

We will now focus on the second integral of equation (165), i.e. on

$$\int_{z'=-\infty}^{+\infty}\int_{\Psi'=0}^{2\pi}\sum_{p=1}^{N}\frac{\sin\left(\dfrac{2\pi z'}{l_p} + \dfrac{2\pi(p-k)}{N}\right)}{g_{p\,k}(z',\Psi')}d\Psi' dz'$$

We can first split it as

$$\int_{z'=-\infty}^{0}\int_{\Psi'=0}^{2\pi}\sum_{p=1}^{N}\frac{\sin\left(\frac{2\pi z'}{l_p}+\frac{2\pi(p-k)}{N}\right)}{g_{p\,k}(z',\Psi')}d\Psi' dz' + \int_{z'=0}^{+\infty}\int_{\Psi'=0}^{2\pi}\sum_{p=1}^{N}\frac{\sin\left(\frac{2\pi z'}{l_p}+\frac{2\pi(p-k)}{N}\right)}{g_{p\,k}(z',\Psi')}d\Psi' dz'$$

In the first integral (i.e. from $z'=-\infty$ to 0), we can choose to shift Ψ' from any angle without changing the value of the integral because the function inside it is a 2π-periodic function of Ψ' which is integrated over its whole period. We then choose to shift Ψ' from π which makes the first integral now equal to

$$\int_{z'=-\infty}^{0}\int_{\Psi'=0}^{2\pi}\sum_{p=1}^{N}\frac{\sin\left(\frac{2\pi z'}{l_p}+\frac{2\pi(p-k)}{N}\right)}{g_{p\,k}(z',\Psi'+\pi)}d\Psi' dz'$$

which after changing z' in $-z'$ can alternatively be expressed as

$$\int_{z'=0}^{+\infty}\int_{\Psi'=0}^{2\pi}\sum_{p=1}^{N}\frac{\sin\left(-\frac{2\pi z'}{l_p}+\frac{2\pi(p-k)}{N}\right)}{g_{p\,k}(-z',\Psi'+\pi)}d\Psi' dz'$$

Thanks to these mathematical operations, we can now write the second integral of equation (165) as

$$\int_{z'=0}^{+\infty}\int_{\Psi'=0}^{2\pi}\sum_{p=1}^{N}h_{p\,k}(z',\Psi')\,d\Psi' dz' \tag{166}$$

with

$$h_{p\,k}(z',\Psi')=\frac{\sin\left(-\frac{2\pi z'}{l_p}+\frac{2\pi(p-k)}{N}\right)}{g_{p\,k}(-z',\Psi'+\pi)}+\frac{\sin\left(\frac{2\pi z'}{l_p}+\frac{2\pi(p-k)}{N}\right)}{g_{p\,k}(z',\Psi')} \tag{167}$$

In addition, from the expression of $g_{p\,k}(z',\Psi')$ given by equation (162), for $p=k-j$ with $j\in\mathbb{Z}$, we have

$$g_{k-j\,k}(-z',\Psi'+\pi)=g_{k+j\,k}(z',\Psi') \tag{168}$$

Therefore, using equation (167) for $p=k-j$ with $j\in\mathbb{Z}$ and equation (168), we have for any z' and any Ψ'

$$h_{k-j\,k}(z',\Psi')+h_{k+j\,k}(z',\Psi')=0 \tag{169}$$

Using equation (168) for $j=0$, we can also deduce that

$$h_{k\,k}(z',\Psi')+h_{k\,k}(z',\Psi')=0$$

which implies

$$h_{k\,k}(z',\Psi') = 0 \tag{170}$$

If N is even, using equation (168) for $j = N/2$, we can also deduce that

$$h_{k-N/2\,k}(z',\Psi') + h_{k+N/2\,k}(z',\Psi') = 0$$

and since p is modulo N in $h_{p\,k}(z',\Psi')$, we see that in reality

$$h_{k-N/2\,k}(z',\Psi') = h_{k-N/2+N\,k}(z',\Psi') = h_{k+N/2\,k}(z',\Psi') = 0 \tag{171}$$

Now let us consider the sum present in equation (166) :

- If N is odd, the sum can be expressed as

$$\sum_{p=1}^{N} h_{p\,k}(z',\Psi') = h_{k\,k}(z',\Psi') + \sum_{j=1}^{\frac{N-1}{2}} \left[h_{k+j\,k}(z',\Psi') + h_{k-j\,k}(z',\Psi')\right]$$

- If N is even, the sum can be expressed as

$$\sum_{p=1}^{N} h_{p\,k}(z',\Psi') = h_{k\,k}(z',\Psi') + h_{k+N/2\;\,k}(z',\Psi') + \sum_{j=1}^{\frac{N}{2}-1} \left[h_{k+j\,k}(z',\Psi') + h_{k-j\,k}(z',\Psi')\right]$$

In both cases, from relations (169) to (171), we see that the sum will be zero for any z' and any Ψ', therefore the second integral of equation (165) will also be zero and thus $A^{(1)}_{z_{r_k}}(z)$ is reduced to

$$A^{(1)}_{z_{r_k}}(z) = \gamma_k I_0^{(1)} \cos\left(\frac{2\pi z}{l_p} + \frac{2\pi(k-1)}{N}\right) \tag{172}$$

with

$$\gamma_k = \frac{\mu_0}{8\pi^2} \int_{z'=-\infty}^{+\infty} \int_{\Psi'=0}^{2\pi} \sum_{p=1}^{N} \frac{\cos\left(\frac{2\pi z'}{l_p} + \frac{2\pi(p-k)}{N}\right)}{g_{p\,k}(z',\Psi')} d\Psi' dz' \tag{173}$$

where $g_{p\,k}(z',\Psi')$ is still given by (162).

We will now show that in reality γ_k does not depend on k.

Indeed, according to (173), for $k \epsilon \mathbb{Z}$ we have

$$\gamma_{k+1} = \frac{\mu_0}{8\pi^2} \int_{z'=-\infty}^{+\infty} \int_{\Psi'=0}^{2\pi} \sum_{p=1}^{N} \frac{\cos\left(\frac{2\pi z'}{l_p} + \frac{2\pi(p-k-1)}{N}\right)}{g_{p\,k+1}(z',\Psi')} d\Psi' dz'$$

From the expression of $g_{p\,k}(z',\Psi')$ given by (162), we see that $g_{p\,k}(z',\Psi')$ does not directly depends on p and k but on the difference $p-k$. Therefore, since the difference between p and $k+1$ is identical to that between $p-1$ and k, we can conclude that for any z' and any Ψ'

$$g_{p\,k+1}(z',\Psi') = g_{p-1\,k}(z',\Psi') \tag{174}$$

Consequently, we can now express γ_{k+1} as

$$\gamma_{k+1} = \frac{\mu_0}{8\pi^2}\int_{z'=-\infty}^{+\infty}\int_{\Psi'=0}^{2\pi}\sum_{p=1}^{N}\frac{\cos\left(\frac{2\pi z'}{l_p}+\frac{2\pi(p-k-1)}{N}\right)}{g_{p-1\,k}(z',\Psi')}d\Psi' dz'$$

Changing the index of summation p to $p' = p-1$, we now have

$$\gamma_{k+1} = \frac{\mu_0}{8\pi^2}\int_{z'=-\infty}^{+\infty}\int_{\Psi'=0}^{2\pi}\sum_{p'=0}^{N-1}\frac{\cos\left(\frac{2\pi z'}{l_p}+\frac{2\pi(p'-k)}{N}\right)}{g_{p'\,k}(z',\Psi')}d\Psi' dz'$$

Since in both the cosine term at the numerator and $g_{p'\,k}(z',\Psi')$, the index of summation p' is modulo N, the term $p'=0$ corresponds to the term $p'=N$, and it is thus possible to write

$$\gamma_{k+1} = \frac{\mu_0}{8\pi^2}\int_{z'=-\infty}^{+\infty}\int_{\Psi'=0}^{2\pi}\sum_{p'=1}^{N}\frac{\cos\left(\frac{2\pi z'}{l_p}+\frac{2\pi(p'-k)}{N}\right)}{g_{p'\,k}(z',\Psi')}d\Psi' dz' = \gamma_k$$

As a result, since for $1 \le k \le N$ we have $\gamma_{k+1} = \gamma_k$, we can immediately conclude that for $1 \le k \le N$ $\gamma_k = \gamma_1$. Thus γ_k does not depend on k and will now simply be noted it as γ (γ is equal to γ_1).

We can finally conclude that $A^{(1)}_{z_{r_k}}(z)$ is given by

$$A^{(1)}_{z_{r_k}}(z) = \gamma I_0^{(1)}\cos\left(\frac{2\pi z}{l_p}+\frac{2\pi(k-1)}{N}\right) \tag{175}$$

with

$$\gamma = \frac{\mu_0}{8\pi^2}\int_{z'=-\infty}^{+\infty}\int_{\Psi'=0}^{2\pi}\sum_{p=1}^{N}\frac{\cos\left(\frac{2\pi z'}{l_p}+\frac{2\pi(p-1)}{N}\right)}{g_p(z',\Psi')}d\Psi' dz' \tag{176}$$

where $g_p(z',\Psi')$ is now given by

$$\sqrt{4{R_c}^2\sin^2\left(\frac{\pi z'}{l_p}+\frac{\pi(p-1)}{N}\right)+4R_cR_f\sin\left(\frac{\pi z'}{l_p}+\frac{\pi(p-1)}{N}\right)\sin(\Psi')+{R_f}^2+{z'}^2} \tag{177}$$

We recall that $A^{(1)}_{z_{r_k}}(z)$ is the axial component of the magnetic vector potential felt at the center of element k at z which is due to the current distribution induced in the system in steady-state regime.

III.2.5.3 Calculation of the new spatial form of the current induced in the elements

In the previous section we have computed the term $A_{z_{r_k}}^{(1)}(z)$ due to the current induced in the elements in steady-state regime. Following our analytical procedure described in section III.2.1 , we now have to compute the new distribution of currents induced by the time-variation of $A_{z_{r_k}}^{(1)}(z)$.

From the equation of the system given by (153), we see that the new distribution of currents $\left(I_k^{(2)}(z)\right)_{1\le k\le N}$ will satisfy for $1 \le k \le N$

$$\frac{d^2 I_k^{(2)}}{dz^2}(z) = \sigma_l \left[2\dot{A}_{z_{r_k}}^{(1)}(z) - \dot{A}_{z_{r_{k-1}}}^{(1)}(z) - \dot{A}_{z_{r_{k+1}}}^{(1)}(z)\right] \tag{178}$$

Replacing $A_{z_{r_k}}^{(1)}(z)$, $A_{z_{r_{k-1}}}^{(1)}(z)$ and $A_{z_{r_{k+1}}}^{(1)}(z)$ with their expressions given by (175) in the right-hand term of equation (178) and using trigonometric simplifications, we have

$$\sigma_l \left[2\dot{A}_{z_{r_k}}^{(1)}(z) - \dot{A}_{z_{r_{k-1}}}^{(1)}(z) - \dot{A}_{z_{r_{k+1}}}^{(1)}(z)\right] = \sigma_l \gamma \dot{I}_0^{(1)} 4 \sin^2\left(\frac{\pi}{N}\right) \cos\left(\frac{2\pi z}{l_p} + \frac{2\pi(k-1)}{N}\right) \tag{179}$$

and thus

$$\frac{d^2 I_k^{(2)}}{dz^2}(z) = \sigma_l \gamma \dot{I}_0^{(1)} 4 \sin^2\left(\frac{\pi}{N}\right) \cos\left(\frac{2\pi z}{l_p} + \frac{2\pi(k-1)}{N}\right) \tag{180}$$

This equation is almost identical to the one derived in the steady-state regime, i.e. equation (147). The only difference between these equations is that $-R_c \dot{B}_a$ has been replaced with $\gamma \dot{I}_0^{(1)}$. Consequently, to obtain the solution of (180) we just have to replace $-R_c \dot{B}_a$ with $\gamma \dot{I}_0^{(1)}$ in the solution of (147) which is given by (150) and (151), i.e.

$$I_k^{(2)}(z) = I_0^{(2)} \cos\left(\frac{2\pi z}{l_p} + \frac{2\pi(k-1)}{N}\right) \tag{181}$$

with

$$I_0^{(2)} = -4\sigma_l \gamma \dot{I}_0^{(1)} sin^2\left(\frac{\pi}{N}\right)\left(\frac{l_p}{2\pi}\right)^2 \tag{182}$$

We have demonstrated that the spatial form of the new current distribution $\left(I_k^{(2)}(z)\right)_{1\le k\le N}$ induced by the time-variation of the current distribution $\left(I_k^{(1)}(z)\right)_{1\le k\le N}$ obtained in steady-state regime exactly corresponds to that of $\left(I_k^{(1)}(z)\right)_{1\le k\le N}$. Hence, similarly to the composite methodology, we can affirm that we have reached the end of our analytical procedure and that we now know the spatial form of the current distribution $\left(I_k(z)\right)_{1\le k\le N}$ induced for any time-varying regime, which is given by $\left(I_k(z)\right)_{1\le k\le N} = \left(I_0 \cos\left(\frac{2\pi z}{l_p} + \frac{2\pi(k-1)}{N}\right)\right)_{1\le k\le N}$, where I_0 is a function of time only.

III.2.5.4 Reduction of the global equation of the system for any time-varying regime

In the global equation of the system, i.e. equation (153), we can now replace $I_k(z)$ with

$$I_0 \cos\left(\frac{2\pi z}{l_p} + \frac{2\pi(k-1)}{N}\right)$$

and from equation (179), we can also replace the term

$$\sigma_l \left[2\dot{A}_{z_{r_k}}(z) - \dot{A}_{z_{r_{k-1}}}(z) - \dot{A}_{z_{r_{k+1}}}(z)\right]$$

with

$$\sigma_l \gamma \dot{I}_0 4 \sin^2\left(\frac{\pi}{N}\right) \cos\left(\frac{2\pi z}{l_p} + \frac{2\pi(k-1)}{N}\right)$$

The new global equation of the system is thus reduced to

$$I_0 + 4\sigma_l \gamma \sin^2\left(\frac{\pi}{N}\right)\left(\frac{l_p}{2\pi}\right)^2 \dot{I}_0 = 4\sigma_l \, sin^2\left(\frac{\pi}{N}\right)\left(\frac{l_p}{2\pi}\right)^2 R_C \dot{B}_a \tag{183}$$

and can now simply be expressed as

$$I_0 + \tau \dot{I}_0 = \frac{\tau_{ext} R_C \dot{B}_a}{\mu_0} \tag{184}$$

with

$$\begin{cases} \tau = 4\sigma_l \gamma \sin^2\left(\frac{\pi}{N}\right)\left(\frac{l_p}{2\pi}\right)^2 \\ \tau_{ext} = 4\sigma_l \mu_0 \sin^2\left(\frac{\pi}{N}\right)\left(\frac{l_p}{2\pi}\right)^2 \end{cases} \tag{185}$$

and

$$\gamma = \frac{\mu_0}{8\pi^2} \int_{z'=-\infty}^{+\infty} \sum_{p=1}^{N} \cos\left(\frac{2\pi z'}{l_p} + \frac{2\pi(p-1)}{N}\right)\left[\int_{\Psi'=0}^{2\pi} \frac{1}{g_p(z', \Psi')} d\Psi'\right] dz' \tag{186}$$

where, according to equation (177), $g_p(z', \Psi')$ is equal to

$$\sqrt{4{R_c}^2 \sin^2\left(\frac{\pi z'}{l_p} + \frac{\pi(p-1)}{N}\right) + 4R_c R_f \sin\left(\frac{\pi z'}{l_p} + \frac{\pi(p-1)}{N}\right)\sin(\Psi') + {R_f}^2 + {z'}^2} \tag{187}$$

We have now reduced the global equation of the system to its simplest form. However, the γ coefficient appearing in the time constant τ of the system has a complicated expression which has to be computed numerically.

We will thus here present an alternative approach leading to an explicit analytical expression approximating the value of the γ coefficient. This approach is motivated by our will to provide expressions that can easily be integrated in already existing thermal modeling codes.

III.2.5.5 Alternative calculation of the γ coefficient

In order to provide a simpler and explicit analytical expression of the γ coefficient, we will here give another method to compute the magnetic vector potential due to the current distribution $\left(I_k(z)\right)_{1\leq k\leq N} = \left(I_0 \cos\left(\frac{2\pi z}{l_p} + \frac{2\pi(k-1)}{N}\right)\right)_{1\leq k\leq N}$.

The elements are assumed to be lightly twisted, i.e.

$$\left(\frac{2\pi R_c}{l_p}\right)^2 \ll 1$$

where R_c is the cabling radius of the elements and l_p their twist pitch and thus the current flowing along one element is also slowly varying in space.

Consequently, we can approximate the magnetic vector potential $\mathrm{A}_{\mathrm{z}_{\mathrm{r}_\mathrm{k}}}(\mathrm{z}_0)$ created by the considered current distribution at the center of element k at z_0 by the one created by a set of N straight infinite hollow tubes of current (see Figure 44), each tube being located at the position of the elements at z_0 and carrying the current $\mathrm{I}_\mathrm{k}(\mathrm{z}_0)$ constant along the z-axis. The exercise below is shown to consolidate this intuition.

The set of 3 straight infinite hollow tubes of current (in black) which are used to compute the magnetic vector potential $\mathrm{A}_{\mathrm{z}_{\mathrm{r}_\mathrm{k}}}(z_0)$ created by the current distribution (in green) of a triplet ($N = 3$) are displayed on Figure 44. The considered infinite hollow tubes (in black) are intercepting the superconducting shells (in green) of the elements at $z = z_0$. We also consider that each tube carries a current constant along the z-axis whose value corresponds to the value locally carried by the superconducting shell it intercepts.

Note that, after some bibliographic research, it appeared that this kind of approximation had already been made by Morgan in [21]. The only difference is that he originally applied it to a set of two elements instead of N elements.

The magnetic vector potential $\overrightarrow{A_{tube}}(M)$ created at a point $M(r,\theta,z)$ by an infinite hollow tube centered on $r = 0$ with radius equal to R_f and carrying a current I constant along the z-axis is given by

$$\overrightarrow{A_{tube}}(M) = A_{z_{tube}}(r,\theta,z)\overrightarrow{e_z} \tag{188}$$

with

$$A_{z_{tube}}(r,\theta,z) = \begin{cases} 0 \; if \; r \leq R_f \\ -\frac{\mu_0 I}{2\pi}\ln\left(\frac{r}{R_f}\right) if \; r > R_f \end{cases} \tag{189}$$

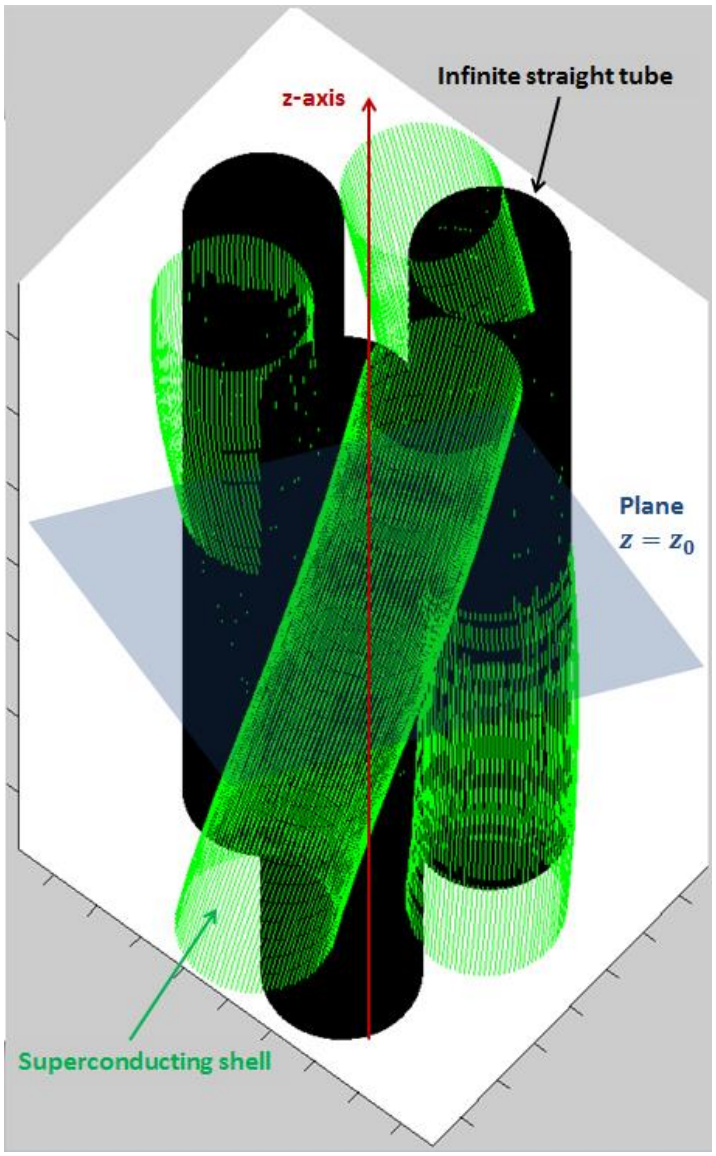

Figure 44 : Scheme showing the considered infinite tubes of current for a triplet ($N = 3$)

Now let us note $A_{z_p}(M_k)$ the magnetic vector potential felt at point M_k (center of element k at z_0) and due to the infinite hollow tube p which is centered on $(x_p(z_0), y_p(z_0))$ with radius equal to R_f and carrying a current $I_p(z_0) = I_0 \cos\left(\frac{2\pi z_0}{l_p} + \frac{2\pi(p-1)}{N}\right)$ constant along the z-axis. Using (189), we then have

$$A_{z_p}(M_k) = \begin{cases} 0 \; if \; r_{p\,k}(z_0) \leq R_f \\ -\frac{\mu_0 I_0}{2\pi} \cos\left(\frac{2\pi z_0}{l_p} + \frac{2\pi(p-1)}{N}\right) \ln\left(\frac{r_{p\,k}(z_0)}{R_f}\right) if \; r_{p\,k}(z_0) > R_f \end{cases} \quad (190)$$

where $r_{p\,k}(z_0)$ is the distance between the centers of elements p and k at $z = z_0$.

In the plane given by equation $z = z_0$, we know that the centers of elements p and k are located on a circle of radius R_c and that the angle $\theta_{p\,k}$ between the rays going from the center of the circle to the positions of the centers of elements p and k is equal to

$$\theta_{p\,k} = \frac{2\pi(p-k)}{N}$$

From this geometrical consideration, we can deduce that the distance $r_{p\,k}(z_0)$ between the centers of elements p and k at $z = z_0$ is given by

$$r_{p\,k}(z_0) = 2R_c \sin\left|\frac{\theta_{p\,k}}{2}\right| = 2R_c \sin\left|\frac{\pi(p-k)}{N}\right| \tag{191}$$

Considering that the superconducting shells of two elements cannot penetrate each other, using equations (190) and (191), we can now conclude that for any z_0 and for $1 \leq k \leq N$, $1 \leq p \leq N$

$$A_{z_p}(M_k) = \begin{cases} 0 \; if \; p = k \\ -\dfrac{\mu_0 I_0}{2\pi} \cos\left(\dfrac{2\pi z_0}{l_p} + \dfrac{2\pi(p-1)}{N}\right) \ln\left(\dfrac{2R_c}{R_f} \sin\left|\dfrac{\pi(p-k)}{N}\right|\right) \; if \; p \neq k \end{cases} \tag{192}$$

By superposition, we can now express the magnetic vector potential $A_z(M_k)$ felt at point M_k (center of element k at z_0) and due to all the tubes as

$$A_z(M_k) = \sum_{p=1}^{N} A_{z_p}(M_k) \tag{193}$$

Using equations (192) and (193), we finally obtain

$$A_z(M_k) = -\frac{\mu_0 I_0}{2\pi} \sum_{\substack{p=1 \\ p \neq k}}^{N} \cos\left(\frac{2\pi z_0}{l_p} + \frac{2\pi(p-1)}{N}\right) \ln\left(\frac{2R_c}{R_f} \sin\left|\frac{\pi(p-k)}{N}\right|\right) \tag{194}$$

Similarly to what we did previously in the calculation of γ with Biot-Savart law, we can express the cosine term of (194) as

$$\cos\left(\frac{2\pi z_0}{l_p} + \frac{2\pi(p-1)}{N}\right) = \cos\left(\frac{2\pi z_0}{l_p} + \frac{2\pi(k-1)}{N} + \frac{2\pi(p-k)}{N}\right)$$

Then (194) can be expressed as

$$A_z(M_k) = -\frac{\mu_0 I_0}{2\pi}\left[\cos\left(\frac{2\pi z_0}{l_p} + \frac{2\pi(k-1)}{N}\right) \sum_{\substack{p=1 \\ p \neq k}}^{N} a_{p\,k} - \sin\left(\frac{2\pi z_0}{l_p} + \frac{2\pi(k-1)}{N}\right) \sum_{\substack{p=1 \\ p \neq k}}^{N} b_{p\,k}\right] \tag{195}$$

with

$$\begin{cases} a_{p\,k} = \cos\left(\dfrac{2\pi(p-k)}{N}\right) \ln\left(\dfrac{2R_c}{R_f} \sin\left|\dfrac{\pi(p-k)}{N}\right|\right) \\ b_{p\,k} = \sin\left(\dfrac{2\pi(p-k)}{N}\right) \ln\left(\dfrac{2R_c}{R_f} \sin\left|\dfrac{\pi(p-k)}{N}\right|\right) \end{cases} \tag{196}$$

Now let us consider the two sums present in equation (195) :

- If N is odd, the sums can be expressed as

$$\begin{cases} \sum_{\substack{p=1 \\ p\neq k}}^{N} a_{p\,k} = \sum_{j=1}^{\frac{N-1}{2}} \left[a_{k+j\,k} + a_{k-j\,k}\right] \\ \sum_{\substack{p=1 \\ p\neq k}}^{N} b_{p\,k} = \sum_{j=1}^{\frac{N-1}{2}} \left[b_{k+j\,k} + b_{k-j\,k}\right] \end{cases}$$

- If N is even, the sums can be expressed as

$$\begin{cases} \sum_{\substack{p=1 \\ p\neq k}}^{N} a_{p\,k} = a_{k+N/2\,k} + \sum_{j=1}^{\frac{N}{2}-1} \left[a_{k+j\,k} + a_{k-j\,k}\right] \\ \sum_{\substack{p=1 \\ p\neq k}}^{N} b_{p\,k} = b_{k+N/2\,k} + \sum_{j=1}^{\frac{N}{2}-1} \left[b_{k+j\,k} + b_{k-j\,k}\right] \end{cases}$$

From equation (196), we see that

$$\begin{cases} a_{k+j\,k} + a_{k-j\,k} = 2\cos\left(\frac{2\pi j}{N}\right)\ln\left(\frac{2R_c}{R_f}\sin\left|\frac{\pi j}{N}\right|\right) \\ b_{k+j\,k} + b_{k-j\,k} = 0 \end{cases}$$

and

$$\begin{cases} a_{k+N/2\,k} = -\ln\left(\frac{2R_c}{R_f}\right) \\ b_{k+N/2\,k} = 0 \end{cases}$$

Consequently, after some mathematical operations, we obtain

$$\sum_{\substack{p=1 \\ p\neq k}}^{N} a_{p\,k} = \begin{cases} -\ln\left(\frac{2R_c}{R_f}\right)\left[1 - 2\sum_{j=1}^{\frac{N}{2}-1}\cos\left(\frac{2\pi j}{N}\right)\right] + 2\sum_{j=1}^{\frac{N}{2}-1}\cos\left(\frac{2\pi j}{N}\right)\ln\left(\sin\left|\frac{\pi j}{N}\right|\right) \;\; if\ N\ is\ even \\ \ln\left(\frac{2R_c}{R_f}\right)\left[2\sum_{j=1}^{\frac{N-1}{2}}\cos\left(\frac{2\pi j}{N}\right)\right] + 2\sum_{j=1}^{\frac{N-1}{2}}\cos\left(\frac{2\pi j}{N}\right)\ln\left(\sin\left|\frac{\pi j}{N}\right|\right) \;\; if\ N\ is\ odd \end{cases} \quad (197)$$

and

$$\sum_{\substack{p=1 \\ p\neq k}}^{N} b_{p\,k} = 0 \quad (198)$$

In addition, from some analytical calculations we have carried out, we have

$$\begin{cases} \sum_{j=1}^{\frac{N}{2}-1} \cos\left(\frac{2\pi j}{N}\right) = 0 \; if \; N \; is \; even \\ \sum_{j=1}^{\frac{N-1}{2}} \cos\left(\frac{2\pi j}{N}\right) = -1/2 \; if \; N \; is \; odd \end{cases}$$

As a result, we can simplify (197) as

$$\sum_{\substack{p=1 \\ p\neq k}}^{N} a_{p\,k} = -\ln\left(\frac{2R_c}{R_f}\right) + 2 \sum_{j=1}^{floor\left(\frac{N-1}{2}\right)} \cos\left(\frac{2\pi j}{N}\right) \ln\left(\sin\left|\frac{\pi j}{N}\right|\right) \tag{199}$$

Using equations (195) and (198), we can now express $A_z(M_k)$ as

$$A_z(M_k) = -\frac{\mu_0 I_0}{2\pi} \cos\left(\frac{2\pi z_0}{l_p} + \frac{2\pi(k-1)}{N}\right) \sum_{\substack{p=1 \\ p\neq k}}^{N} a_{p\,k} \tag{200}$$

where $\sum_{\substack{p=1 \\ p\neq k}}^{N} a_{p\,k}$ is given by (199).

We have now provided another formula for the magnetic vector potential felt at the center of element k at any z_0 and due to the current distribution $\left(I_k(z)\right)_{1\leq k\leq N} = \left(I_0 \cos\left(\frac{2\pi z}{l_p} + \frac{2\pi(k-1)}{N}\right)\right)_{1\leq k\leq N}$ using the infinite straight hollow tubes approach.

In formula (175), γ has been defined so that

$$A_{z_{r_k}}(z) = \gamma I_0 \cos\left(\frac{2\pi z}{l_p} + \frac{2\pi(k-1)}{N}\right)$$

Since $A_z(M_k)$ corresponds to $A_{z_{r_k}}(z_0)$, using equation (200) the new formula of γ obtained using the infinite straight hollow tubes approach is then

$$\gamma = -\frac{\mu_0}{2\pi} \sum_{\substack{p=1 \\ p\neq k}}^{N} a_{p\,k}$$

which using (199) leads to

$$\gamma = \frac{\mu_0}{2\pi}\left[\ln\left(\frac{2R_c}{R_f}\right) - 2 \sum_{j=1}^{floor\left(\frac{N-1}{2}\right)} \cos\left(\frac{2\pi j}{N}\right) \ln\left(\sin\left|\frac{\pi j}{N}\right|\right)\right] \tag{201}$$

III.2.5.6 Comparison between the values of γ coefficient obtained with both approaches

In order to evaluate the discrepancy between the infinite straight hollow tubes approach and the Biot-Savart one, we have chosen to compute the relative error between the values of γ obtained with equations (176) and (201) (which are also valid for $N = 2$, see section III.2.7) for two sets of realistic values of R_c (cabling radius of the elements), R_f (radius of the superconducting shell), l_p (twist pitch of the elements) and N (number of elements).

The first set of R_c, R_f and l_p values is representative of the first cabling stage of JT-60SA TF conductor: the composites (elements) have a radius of $R = 0.405\,mm$, the outer radius of their filamentary zone (superconducting shell) is $R_f = 0.327\,mm$ and their cabling twist pitch is $l_p = 45\,mm$. In addition the first cabling stage is composed of $N = 3$ strands but we will make the number of elements vary between $N = 2$ and $N = 6$ and suppose that the elements are always tangent to each other so that $Rc = R/sin(\pi/N)$. The relative errors between the values of γ computed using both approaches are displayed on Table 10.

Table 10

Relative errors on γ value for $R = 0.405\,mm$, $R_f = 0.327\,mm$ and $l_p = 45\,mm$					
Number of elements *N*	2	3	4	5	6
$R_c\ (mm)$	0.405	0.468	0.573	0.689	0.810
Relative error (%)	***1.645***	***0.248***	***0.073***	***0.022***	***0.001***

The second set of R_c, R_f and l_p values is representative of the edge filaments of K006-01C composite: the filaments (superconducting shells) have a radius of about $R_f = 10\ \mu m$, the outer radius of the filamentary zone (cabling radius of the elements) is $R_c = 0.327\ mm$ and the twist pitch of the filaments is $l_p = 15\ mm$. In this case, the relative error between the values of γ computed using both approaches is $\mathbf{0.06}$ % for $N = 50$ and $\mathbf{0.04}$ % for $N = 100$. We can now conclude that the straight hollow tubes approach is really consistent with the Biot-Savart one and that the values of γ computed using equation (201) can be trusted.

We can now conclude that the straight hollow tubes approach is a trustworthy analogy, which analytically converges with the Biot-Savart one with a marginal deviation. The values of γ computed using equation (201) can therefore be considered as fully relevant and are thus used in the following for calculation.

III.2.6 Power dissipated by coupling currents

❖ **From the knowledge of the spatial form of the currents induced for any time regime, we will establish the analytical expression of the coupling power dissipated in a group of twisted elements.**

The local transverse current flowing from element k to the adjacent element $k+1$ at z has previously been noted $I_{k\,k+1}(z)$.

The local power $dP_{k\,k+1}(z)$ dissipated in a slice of thickness dz by the flow of $I_{k\,k+1}(z)$ is expressed as

$$dP_{k\,k+1}(z) = \frac{{I_{k\,k+1}}^2(z)}{dG} = \frac{1}{\sigma_l}\left(\frac{I_{k\,k+1}(z)}{dz}\right)^2 dz \tag{202}$$

Therefore the total local power $dP(z)$ dissipated in a slice of thickness dz by the flow of all the local transverse currents $\left(I_{k\,k+1}(z)\right)_{1\le k\le N}$ is

$$dP(z) = \sum_{k=1}^{N} dP_{k\,k+1}(z) = \frac{1}{\sigma_l}\sum_{k=1}^{N}\left(\frac{I_{k\,k+1}(z)}{dz}\right)^2 dz \tag{203}$$

and the total power dissipated from $z = 0$ to z is then

$$P(z) = \int_0^z \frac{dP(z')}{dz}dz' = \frac{1}{\sigma_l}\int_0^z \sum_{k=1}^{N}\left(\frac{I_{k\,k+1}(z')}{dz}\right)^2 dz' \tag{204}$$

From our previous considerations, we know that for any time regime, the current $I_k(z)$ flowing along element k at z is given by

$$I_k(z) = I_0 \cos\left(\frac{2\pi z}{l_p} + \frac{2\pi(k-1)}{N}\right)$$

where I_0 depends on time only. Using equation (133), we can deduce that for $N \geq 3$

$$\frac{I_{k\,k+1}(z)}{dz} = \frac{I_{k-1\,k}(z)}{dz} + \frac{2\pi}{l_p} I_0 \sin\left(\frac{2\pi z}{l_p} + \frac{2\pi(k-1)}{N}\right) \tag{205}$$

which immediately gives the following relation

$$\frac{I_{k\,k+1}(z)}{dz} = \frac{I_{1\,2}(z)}{dz} + \frac{2\pi}{l_p} I_0 \sum_{j=2}^{k} \sin\left(\frac{2\pi z}{l_p} + \frac{2\pi(j-1)}{N}\right)$$

The calculation of the sum gives

$$\sum_{j=2}^{k} \sin\left(\frac{2\pi z}{l_p} + \frac{2\pi(j-1)}{N}\right) = \frac{1}{2\sin\left(\frac{\pi}{N}\right)}\left[\cos\left(\frac{2\pi z}{l_p} + \frac{\pi}{N}\right) - \cos\left(\frac{2\pi z}{l_p} + \frac{(2k-1)\pi}{N}\right)\right]$$

thus

$$\frac{I_{k\,k+1}(z)}{dz} = \frac{I_{1\,2}(z)}{dz} + \frac{2\pi}{l_p}\frac{I_0}{2\sin\left(\frac{\pi}{N}\right)}\left[\cos\left(\frac{2\pi z}{l_p}+\frac{\pi}{N}\right) - \cos\left(\frac{2\pi z}{l_p}+\frac{(2k-1)\pi}{N}\right)\right] \tag{206}$$

From Kirchhoff's voltage law, we can see that

$$\sum_{k=1}^{N} U_{k\,k+1}(z) = 0$$

combining this relation with equation (134), we can deduce that

$$\sum_{k=1}^{N} \frac{I_{k\,k+1}(z)}{dz} = 0 \tag{207}$$

since σ_l is by assumption identical between every element.

Using equations (206) and (207), we obtain

$$\frac{I_{1\,2}(z)}{dz} = -\frac{1}{N}\frac{2\pi}{l_p}\frac{I_0}{2\sin\left(\frac{\pi}{N}\right)}\sum_{k=1}^{N}\left[\cos\left(\frac{2\pi z}{l_p}+\frac{\pi}{N}\right) - \cos\left(\frac{2\pi z}{l_p}+\frac{(2k-1)\pi}{N}\right)\right]$$

and since

$$\sum_{k=1}^{N}\cos\left(\frac{2\pi z}{l_p}+\frac{(2k-1)\pi}{N}\right) = 0$$

we then have

$$\frac{I_{1\,2}(z)}{dz} = -\frac{2\pi}{l_p}\frac{I_0}{2\sin\left(\frac{\pi}{N}\right)}\cos\left(\frac{2\pi z}{l_p}+\frac{\pi}{N}\right)$$

which combined to (206) leads to

$$\frac{I_{k\,k+1}(z)}{dz} = -\frac{2\pi}{l_p}\frac{I_0}{2\sin\left(\frac{\pi}{N}\right)}\cos\left(\frac{2\pi z}{l_p}+\frac{(2k-1)\pi}{N}\right) \tag{208}$$

Now that we have determined the local transverse current $I_{k\,k+1}(z)$ flowing from element k to the adjacent element $k+1$ at z, we can compute the local power $dP(z)$ dissipated in a slice dz using (203) and (208), i.e.

$$dP(z) = \frac{1}{\sigma_l}\sum_{k=1}^{N}\left(\frac{I_{k\,k+1}(z)}{dz}\right)^2 dz = \frac{1}{\sigma_l}\left(\frac{2\pi}{l_p}\right)^2\frac{{I_0}^2}{4\sin^2\left(\frac{\pi}{N}\right)}\sum_{k=1}^{N}\cos^2\left(\frac{2\pi z}{l_p}+\frac{(2k-1)\pi}{N}\right)dz$$

Since

$$\sum_{k=1}^{N} \cos^2\left(\frac{2\pi z}{l_p} + \frac{(2k-1)\pi}{N}\right) = \frac{N}{2}$$

the local power $dP(z)$ is thus given by

$$dP(z) = \frac{1}{\sigma_l}\left(\frac{2\pi}{l_p}\right)^2 \frac{N{I_0}^2}{8\sin^2\left(\frac{\pi}{N}\right)} dz \tag{209}$$

The total power dissipated by the coupling currents in a N-uplet with $N \geq 3$ from $z = 0$ to z is then

$$P(z) = \int_0^z \frac{dP(z')}{dz} dz' = \frac{1}{\sigma_l}\left(\frac{2\pi}{l_p}\right)^2 \frac{N}{8\sin^2\left(\frac{\pi}{N}\right)} {I_0}^2 z \tag{210}$$

As a result, the power per unit length of conductor is

$$P_l(z) = \frac{P(z)}{z} = \frac{1}{\sigma_l}\left(\frac{2\pi}{l_p}\right)^2 \frac{N}{8\sin^2\left(\frac{\pi}{N}\right)} {I_0}^2 \tag{211}$$

III.2.7 Specific case of the doublet

❖ **We will address here the specific case of two twisted elements (i.e. a doublet) following the same approach than for a N-uplet with $N \geq 3$.**

Morgan has studied the magnetic response of a strand having two filaments in [21] and has expressed the time constant of the system and the average power dissipated during a sinusoidal excitation. In order to compare our model to his approach, we first have to adapt the N-uplet model to a doublet.

However it is not directly possible to replace N with 2 in the expressions we have previously derived for $N \geq 3$. Indeed, since the doublet has only one transverse current flowing from the first element to the second one, the Kirchhoff's current law we have derived in the N-uplet model is not valid anymore. As a result, we have to derive the equation governing the doublet following the methodology we have used in the N-uplet.

III.2.7.1 Global equation of the system

In the case of a doublet, there is only one local transverse current $I_{1\,2}(z)$ which flows from the first element to the second one; according to Kirchhoff's current law, it must satisfy

$$\frac{I_{1\,2}(z)}{dz} = -\frac{dI_1}{dz}(z) \tag{212}$$

instead of (133) for $N \geq 3$.

Equations (134) and (141) derived for the case $N \geq 3$ (i.e. Ohm's law and Faraday's law of induction) being still valid for $N = 2$, the set of equations of the doublet is then

$$\begin{cases} \dfrac{I_{1\,2}(z)}{dz} = -\dfrac{dI_1}{dz}(z) \\ \dfrac{1}{dz} I_{1\,2}(z) = \sigma_l U_{1\,2}(z) \\ \dfrac{dU_{1\,2}}{dz}(z) = \dot{A}_{z_2}(z) - \dot{A}_{z_1}(z) \end{cases} \tag{213}$$

Once combined, equations (213) leads to the global equation of the system

$$\frac{d^2 I_1}{dz^2}(z) = \sigma_l \left[\dot{A}_{z_1}(z) - \dot{A}_{z_2}(z)\right] \tag{214}$$

Since the doublet does not carry any transport current, we have $I_2(z) = -I_1(z)$, therefore all the equations and solutions will only be given for I_1 as I_2 is simply the opposite of I_1.

As we did it previously for $N \geq 3$, A_{z_k} can be split as $A_{z_k} = A_{z_{a_k}} + A_{z_{r_k}}$ with $A_{z_{a_k}} = -x_k B_a$.

This leads to the following equation

$$\frac{d^2 I_1}{dz^2}(z) - \sigma_l \left[\dot{A}_{z_{r_1}}(z) - \dot{A}_{z_{r_2}}(z)\right] = -2\sigma_l R_c \dot{B}_a \cos\left(\frac{2\pi z}{l_p}\right) \tag{215}$$

III.2.7.2 Study in steady-state regime

In steady-state regime, we then have

$$\frac{d^2 I_1}{dz^2}(z) = -2\sigma_l R_c \dot{B}_a \cos\left(\frac{2\pi z}{l_p}\right) \tag{216}$$

The solutions of this equation can be quickly determined from the case $N \geq 3$ as

$$I_1(z) = I_0 \cos\left(\frac{2\pi z}{l_p}\right) \tag{217}$$

for an infinitely long conductor or

$$I_1(z) = I_0 \left[\cos\left(\frac{2\pi z}{l_p}\right) - \cos\left(\frac{\pi L}{l_p}\right)\right] \tag{218}$$

for a conductor of length L. In both cases I_0 is given by

$$I_0 = 2\sigma_l R_C \dot{B}_a \left(\frac{l_p}{2\pi}\right)^2 \tag{219}$$

Note that this expression of I_0 is not equal to the one obtained replacing N with 2 in the formula of the N-uplet, i.e. equation (149).

III.2.7.3 Study in time-varying regime

The current distribution found in steady-state regime for the doublet is consistent with that found for the N-uplet, i.e. it is given by $\left(I_k(z) = I_0 \cos\left(\frac{2\pi z}{l_p} + \frac{2\pi(k-1)}{N}\right)\right)_{1\leq k\leq N}$ for $= 2$. Consequently, the formula of the magnetic vector potential due to this distribution of current is directly given by equations (175) to (177) for $N = 2$, i.e.

$$A_{z r_k}^{(1)}(z) = \gamma I_0^{(1)} \cos\left(\frac{2\pi z}{l_p} + \pi(k-1)\right) \tag{220}$$

with

$$\gamma = \frac{\mu_0}{8\pi^2} \int_{z'=-\infty}^{+\infty} \int_{\Psi'=0}^{2\pi} \sum_{p=1}^{2} \frac{\cos\left(\frac{2\pi z'}{l_p} + \pi(p-1)\right)}{g_p(z', \Psi')} d\Psi' dz' \tag{221}$$

where $g_p(z', \Psi')$ is now given by

$$\sqrt{4{R_c}^2 \sin^2\left(\frac{\pi z'}{l_p} + \frac{\pi}{2}(p-1)\right) + 4R_c R_f \sin\left(\frac{\pi z'}{l_p} + \frac{\pi}{2}(p-1)\right)\sin(\Psi') + {R_f}^2 + {z'}^2} \tag{222}$$

Using equations (215) and (220), we see that the new distribution of currents $I_1^{(2)}(z)$ induced by the time-variation of the current distribution $\left(I_k^{(1)}(z) = I_0^{(1)} \cos\left(\frac{2\pi z}{l_p} + \pi(k-1)\right)\right)_{1\leq k\leq 2}$ found in steady-state regime will satisfy

$$\frac{d^2 {I_1}^{(2)}}{dz^2}(z) = 2\sigma_l \gamma \dot{I}_0^{(1)} \cos\left(\frac{2\pi z}{l_p}\right) \tag{223}$$

Using previous considerations, the solution of this equation is

$$I_1^{(2)}(z) = I_0^{(2)} \cos\left(\frac{2\pi z}{l_p}\right) \tag{224}$$

with

$$I_0^{(2)} = -2\sigma_l \gamma \dot{I}_0^{(1)} \left(\frac{l_p}{2\pi}\right)^2 \tag{225}$$

Once again we have reached the end of our analytical procedure and we now know that the spatial form of the current distribution $I_1(z)$ induced in a doublet for any time-varying regime is given by $I_1(z) = I_0 \cos\left(\frac{2\pi z}{l_p}\right)$, where I_0 is a function of time only.

III.2.7.3.1 Reduction of the global equation of the system for any time-varying regime

Using the fact that $I_1(z) = I_0 \cos\left(\frac{2\pi z}{l_p}\right)$ and equations (215) and (220), the new global equation of the doublet can be reduced to

$$I_0 + 2\sigma_l \gamma \left(\frac{l_p}{2\pi}\right)^2 \dot{I}_0 = 2\sigma_l \left(\frac{l_p}{2\pi}\right)^2 R_C \dot{B}_a \tag{226}$$

and can now simply be expressed as

$$I_0 + \tau \dot{I}_0 = \frac{\tau_{ext} R_C \dot{B}_a}{\mu_0} \tag{227}$$

with

$$\begin{cases} \tau = 2\sigma_l \gamma \left(\frac{l_p}{2\pi}\right)^2 \\ \tau_{ext} = 2\sigma_l \mu_0 \left(\frac{l_p}{2\pi}\right)^2 \end{cases} \tag{228}$$

and

$$\gamma = \frac{\mu_0}{8\pi^2} \int_{z'=-\infty}^{+\infty} \sum_{p=1}^{2} \cos\left(\frac{2\pi z'}{l_p} + \pi(p-1)\right) \left[\int_{\Psi'=0}^{2\pi} \frac{1}{g_p(z', \Psi')} d\Psi'\right] dz' \tag{229}$$

where, according to equation (222), $g_p(z', \Psi')$ is equal to

$$\sqrt{4{R_c}^2 \sin^2\left(\frac{\pi z'}{l_p} + \frac{\pi}{2}(p-1)\right) + 4R_c R_f \sin\left(\frac{\pi z'}{l_p} + \frac{\pi}{2}(p-1)\right)\sin(\Psi') + {R_f}^2 + {z'}^2} \tag{230}$$

Note that the expressions of τ and τ_{ext} of the doublet are not equal to the one obtained replacing N with 2 in the formulae of the N-uplet, i.e. equation (185).

III.2.7.3.2 Alternative calculation of the γ coefficient

Formula (201) of the γ coefficient derived for the N-uplet using the straight infinite hollow tubes approach is still valid for the doublet but with $N = 2$, i.e.

$$\gamma = \frac{\mu_0}{2\pi} \ln\left(\frac{2R_c}{R_f}\right) \tag{231}$$

III.2.7.4 Coupling power dissipated in a doublet

Using the fact that $I_1(z) = I_0 \cos\left(\frac{2\pi z}{l_p}\right)$ and equation (212), we have

$$\frac{I_{1\,2}(z)}{dz} = \frac{2\pi}{l_p} I_0 \sin\left(\frac{2\pi z}{l_p}\right)$$

The local power $dP(z)$ dissipated in a slice of thickness dz is

$$dP(z) = \frac{{I_{1\,2}}^2(z)}{dG} = \frac{1}{\sigma_l}\left(\frac{I_{1\,2}(z)}{dz}\right)^2 dz \tag{232}$$

which combined to the previous relations leads to

$$dP(z) = \frac{1}{\sigma_l}\left(\frac{2\pi}{l_p}\right)^2 {I_0}^2 \sin^2\left(\frac{2\pi z}{l_p}\right) dz \tag{233}$$

Finally, the total power dissipated by the coupling currents in a doublet from $z = 0$ to z is then

$$P(z) = \int_0^z \frac{dP(z')}{dz} dz' = \frac{1}{\sigma_l}\left(\frac{2\pi}{l_p}\right)^2 {I_0}^2 \frac{z}{2}\left[1 - \mathrm{sinc}\left(\frac{4\pi z}{l_p}\right)\right] \tag{234}$$

where $\mathrm{sinc}(x) = \sin(x)/x$. And the power per unit length of conductor is

$$P_l(z) = \frac{P(z)}{z} = \frac{1}{\sigma_l}\left(\frac{2\pi}{l_p}\right)^2 \frac{{I_0}^2}{2}\left[1 - \mathrm{sinc}\left(\frac{4\pi z}{l_p}\right)\right] \tag{235}$$

Note that in the case of a doublet, the power dissipated by the coupling currents per unit length of conductor depends on the length of conductor considered while for a N-uplet with $N \geq 3$ it does not.

III.2.7.5 Comparison with Morgan's expressions

In [21], Morgan has derived the time constant governing a strand with two filaments and the average power per unit length dissipated during a sinusoidal excitation. In order to compare his expressions to ours, we first have to make the link between his notations and ours:

- p is the twist pitch of the filaments, we thus have $p = l_p$
- L is one fourth of the pitch, thus $L = l_p/4$
- d is the diameter of the filaments, thus $d = 2R_f$
- a is the distance between the two filaments, thus $a = 2R_c$
- ρ_e is an effective resistivity such that $d\mathcal{R} = \rho_e/dz$ is the local transverse resistance between the two filaments, we then have $\mathcal{R} = 1/dG = 1/(\sigma_l dz)$ and thus $\rho_e = 1/\sigma_l$

The time constant derived by Morgan in [21] is the following

$$\tau_{Morgan} = \frac{\mu_0}{\pi\rho_e}\left(\frac{2L}{\pi}\right)^2 \ln\left(\frac{2a-d}{d}\right) = \frac{\mu_0\sigma_l}{\pi}\left(\frac{l_p}{2\pi}\right)^2 \ln\left(\frac{2R_c - R_f}{R_f}\right)$$

The time constant we have derived is given by (228), i.e.

$$\tau = 2\sigma_l\gamma\left(\frac{l_p}{2\pi}\right)^2$$

Since Morgan has used the straight infinite tubes approach, we will replace γ with expression (231) we have found using the same approach, this leads to the following time constant

$$\tau = \frac{\mu_0\sigma_l}{\pi}\left(\frac{l_p}{2\pi}\right)^2 \ln\left(\frac{2R_c}{R_f}\right)$$

We can see that our expression is almost identical to that derived by Morgan, the only difference lies in the presence of the term $2R_c - R_f$ instead of $2R_c$ in the logarithm. This difference is simply explained by the fact that Morgan has considered filaments while we have chosen to consider elements that can be strands or groups of strands. Indeed, when computing the change of magnetic flux enclosed by the two filaments, Morgan has chosen not to take into account the part of the change of flux that was inside the volume of the filaments because of their superconducting nature (they directly shield that part developing their own screening currents, these currents correspond to the currents responsible for the hysteresis losses in superconducting filaments). In our approach, we have not made use of this assumption because the elements are not supposed to be able to instantly shield the change of magnetic flux in their own volume; this is the reason for the slight difference between both models.

Having now found an agreement between the time constants calculated by both models, we will now carry on the comparison on the average power per unit length dissipated during a sinusoidal excitation.

In [21], Morgan has also computed the following power per unit length averaged over one fourth of the twist pitch (i.e. $L = l_p/4$) and averaged over one cycle of sinusoidal magnetic excitation $B_a = B_p\sin(\omega t)$

$$P_{l_{Morgan}} = \frac{1}{4\rho_e}\left(\frac{2L}{\pi}\right)^2 {B_p}^2(a-d)^2\frac{\omega^2}{1+\omega^2{\tau_{Morgan}}^2} = \sigma_l\left(\frac{l_p}{2\pi}\right)^2 {B_p}^2\left(R_c - R_f\right)^2\frac{\omega^2}{1+\omega^2{\tau_{Morgan}}^2}$$

From equation (235), the power per unit length averaged over one fourth of the twist pitch we have computed is

$$P_l(z = l_p/4) = \frac{1}{\sigma_l}\left(\frac{2\pi}{l_p}\right)^2\frac{{I_0}^2}{2}$$

where I_0 is governed by equation (227).

In section II.2.8 , we have computed the average of $\dot{B_i}^2(t)$ governed by the equation $B_i + \tau\dot{B}_i = B_a$ over the time period $T = 1/f$ of an applied magnetic field $B_a = B_p\sin(\omega t)$ and we have found

$$\langle \dot{B_i}^2(t)\rangle_{cycle} = \frac{{B_p}^2}{2}\frac{\omega^2}{1+(\omega\tau)^2}$$

Differentiating equation $B_i + \tau\dot{B}_i = B_a$ with respect to time leads to $\dot{B}_i + \tau\ddot{B}_i = \dot{B}_a$. We can notice that this equation is very similar to the one satisfied by I_0 i.e. $I_0 + \tau\dot{I}_0 = \tau_{ext}R_C\dot{B}_a/\mu_0$.

Consequently, replacing $\dot{B}_i$ with I_0 and B_p with $B_p\tau_{ext}R_C/\mu_0$ in the expression of $\langle \dot{B_i}^2(t)\rangle_{cycle}$ above, we can directly conclude that the average of ${I_0}^2$ over the time period $T = 1/f$ of an applied magnetic field $B_a = B_p\sin(\omega t)$ is given by

$$\langle {I_0}^2(t)\rangle_{cycle} = \frac{\left(B_p\tau_{ext}R_C/\mu_0\right)^2}{2}\frac{\omega^2}{1+(\omega\tau)^2} = \frac{{B_p}^2}{2}{R_c}^2\left(\frac{\tau_{ext}}{\mu_0}\right)^2\frac{\omega^2}{1+(\omega\tau)^2}$$

Replacing τ_{ext} with its expression given by (228), we finally obtain

$$\langle {I_0}^2(t)\rangle_{cycle} = 2{B_p}^2{R_c}^2{\sigma_l}^2\left(\frac{l_p}{2\pi}\right)^4\frac{\omega^2}{1+(\omega\tau)^2}$$

Therefore, we can deduce that

$$\langle P_l(z = l_p/4)\rangle_{cycle} = \frac{1}{\sigma_l}\left(\frac{2\pi}{l_p}\right)^2\frac{\langle {I_0}^2(t)\rangle_{cycle}}{2} = \sigma_l\left(\frac{l_p}{2\pi}\right)^2{B_p}^2{R_c}^2\frac{\omega^2}{1+(\omega\tau)^2}$$

We can see that the expressions $P_{l_{Morgan}}$ and $\langle P_l(z = l_p/4)\rangle_{cycle}$ computed by both models are almost identical, again the difference lies in the presence of the term $\left(R_c - R_f\right)^2$ instead of ${R_c}^2$ which is again due to the fact that Morgan does not take into account the part of the change of magnetic flux that is inside the volume of the filaments.

III.2.8 Summary

For any time-varying regime the currents induced along the elements of the N-uplet are given by

$$I_k(z) = I_0\cos\left(\frac{2\pi z}{l_p} + \frac{2\pi(k-1)}{N}\right)$$

where I_0 is a function of time only governed by the equation

$$I_0 + \tau\dot{I}_0 = \frac{\tau_{ext}R_C\dot{B}_a}{\mu_0} \tag{236}$$

with

$$\tau = \begin{cases} 2\sigma_l \gamma \left(\frac{l_p}{2\pi}\right)^2 \; for\; N = 2 \\ 4\sigma_l \gamma \sin^2\left(\frac{\pi}{N}\right)\left(\frac{l_p}{2\pi}\right)^2 \; for\; N \geq 3 \end{cases} \tag{237}$$

and

$$\tau_{ext} = \begin{cases} 2\sigma_l \mu_0 \left(\frac{l_p}{2\pi}\right)^2 \; for\; N = 2 \\ 4\sigma_l \mu_0 \sin^2\left(\frac{\pi}{N}\right)\left(\frac{l_p}{2\pi}\right)^2 \; for\; N \geq 3 \end{cases} \tag{238}$$

For $N \geq 2$, the γ coefficient can be approximated by the following explicit formula

$$\gamma = \frac{\mu_0}{2\pi}\left[\ln\left(\frac{2R_c}{R_f}\right) - 2\sum_{j=1}^{floor\left(\frac{N-1}{2}\right)} \cos\left(\frac{2\pi j}{N}\right)\ln\left(\sin\left|\frac{\pi j}{N}\right|\right)\right] \tag{239}$$

III.3 Adaptation of the *N*-uplet model to the MPAS model

III.3.1 The MPAS model

Having derived the equation governing a conductor described by the N-uplet model, we will now express it differently as we will try to provide a physical interpretation of its behavior.

In doing so we are actually making the link with the Multizone Partial Shielding (MPAS) model [17]; this heuristic approach considers that every cabling stage of a conductor, if taken alone, can be seen as a magnetic circular dipole (see section II.5.1.2) partially screening the external magnetic field. We recall that the term “circular dipole” refers to a cosine distribution of current on the outer radius of the cross-section of a cylinder; this distribution is encountered when a composite with a central filamentary zone shields its enclosed volume from the time variation of an applied transverse magnetic field.

In the MPAS approach, each cabling stage of a CICC is considered to behave like a superconducting composite partially shielding the external magnetic excitation, this means that the isolated cabling stage j is governed by the classical equation

$$B_{int\ j} + \tau_j \dot{B}_{int\ j} = B_a \tag{240}$$

where B_a is the amplitude of the transverse applied magnetic field, $B_{int\ j}$ is the part of the induction inside cabling stage j which is collinear to B_a and τ_j is the time constant of the cabling stage j if taken alone (i.e. without considering the magnetic interactions with the other cabling stages).

The MPAS model also considers that the power density dissipated in an isolated cabling stage j is equal to

$$P_{vol} = \frac{nk_j \tau_j \dot{B}_{int\ j}^{\ 2}}{\mu_0} \tag{241}$$

where nk_j is known as the partial shielding coefficient. Note that in the case of a composite with a central filamentary zone, the nk_j coefficient is $nk_j = 2$ according to equation (3).

Finally, this model also considers that when the totality of the magnetic couplings are taken into account, the coupling losses per cycle per unit volume of cable envelope of a CICC with N cabling stages can be expressed as

$$Q_{vol} = \sum_{j=1}^{N} \frac{n\kappa_j \theta_j \dot{B}_{int\ j}^{\ 2}}{\mu_0} \tag{242}$$

where the $n\kappa_j$ and θ_j are respectively the new time constants and new partial shielding coefficients of the system which depend on the previous nk_j, τ_j and on the volume fractions in which the different stages are shielding the applied magnetic field: they reflect the magnetic coupling between the different cabling stages.

The previous equations assumed by the MPAS model seem to be in line with the experimental observations as it is possible to adjust the $n\kappa_j$ and θ_j so that the experimental losses can be described with equation (242).

However, these considerations have never been demonstrated theoretically. In the next section we will thus show that it is indeed possible to represent the magnetic behavior of single cabling stage conductor with equations (240) and (241). We will also derive the analytical formulae of its nk_j and τ_j parameters using the results of the N-uplet model.

This point is very important as it consolidates on one side, the MPAS model which is consistent with the experimental reality but which features considerations that have not been reinforced on a theoretical ground and, on the other side, the N-uplet model which is derived from purely theoretical considerations without any link -even indirect- with experimental reality.

III.3.2 Adaptation to the MPAS model

Let us start with the equation of the N-uplet, i.e. equation (184) which is

$$I_0 + \tau \dot{I}_0 = \frac{\tau_{ext} R_C \dot{B}_a}{\mu_0}$$

In steady-state regime, i.e. when the coupling currents are not time-varying, at any time t we have $\dot{I}_0(t) = 0$ and according to the equation above we have

$$I_0(t) = \frac{\tau_{ext} R_C \dot{B}_a(t)}{\mu_0}$$

From a physical point of view, this means that at any time t the time-variation of a transverse and uniform internal magnetic field $B_i(t)$ give rise to currents of the form $I_k(z) = I_0 \cos\left(\frac{2\pi z}{l_p} + \frac{2\pi(k-1)}{N}\right)$ inside the elements with

$$I_0(t) = \frac{\tau_{ext} R_C \dot{B}_i(t)}{\mu_0}$$

In time-varying regime, the internal magnetic field $\vec{B}_i$ in the volume enclosed by the elements (i.e. in the cylinder of radius R_c) corresponds to the superposition of the applied magnetic field $\vec{B}_a$ which is transverse and uniform and of the reacting magnetic field $\overrightarrow{B_{react}}$ which is the magnetic field produced by the currents flowing in the elements. We will not compute the magnetic field created by the $I_k(z) = I_0 \cos\left(\frac{2\pi z}{l_p} + \frac{2\pi(k-1)}{N}\right)$ current distribution but it is quite obvious that it is not uniform in the volume enclosed by the elements. As a result the internal magnetic field $\vec{B}_i$ cannot be uniform either and the N-uplet cannot be described by the classical equation

$$B_i + \tau \dot{B}_i = B_a$$

However, we can introduce an equivalent internal uniform magnetic field $B_{i\,eq}$ that we define as the internal uniform magnetic field collinear to $\overrightarrow{B_a}$ whose time-variation would create, at any time t, the same distribution of current $I_k(z) = I_0(t) \cos\left(\frac{2\pi z}{l_p} + \frac{2\pi(k-1)}{N}\right)$ than the one given by the N-uplet model i.e. obtained with equation (184). It would therefore satisfy the relation

$$I_0(t) = \frac{\tau_{ext} R_C \dot{B}_{i\,eq}(t)}{\mu_0} \tag{243}$$

Replacing I_0 with the expression above in equation (184) leads to

$$\frac{\tau_{ext} R_C \dot{B}_{i\,eq}}{\mu_0} + \tau \frac{\tau_{ext} R_C \ddot{B}_{i\,eq}}{\mu_0} = \frac{\tau_{ext} R_C \dot{B}_a}{\mu_0}$$

Multiplying both sides with $\mu_0/(\tau_{ext} R_C)$ and integrating in time, we obtain

$$B_{i\,eq} + \tau \dot{B}_{i\,eq} = B_a \tag{244}$$

where τ is given by (237).

This result is important as it shows that it is in fact possible to characterize the response of a single cabling stage conductor to a transverse magnetic field with an equation very similar to the one encountered in superconducting composites with a central filamentary zone. The only difference with the composite lies in the fact that we approximate the non-uniform internal magnetic field with an equivalent uniform one.

From equations (211) and (235) giving the power dissipated per unit length of conductor P_l, we can express the average power density P_{vol} inside the N-uplet dividing P_l by the circumscribed surface $\pi(R_c + R)^2$ (i.e. surface of the circumscribed circle on Figure 41) as

$$P_{vol}(z) = \begin{cases} \frac{1}{\sigma_l}\left(\frac{2\pi}{l_p}\right)^2 \frac{{I_0}^2}{2\pi(R_c+R)^2}\left[1 - \operatorname{sinc}\left(\frac{4\pi z}{l_p}\right)\right] \; for\; N = 2 \\ \frac{1}{\sigma_l}\left(\frac{2\pi}{l_p}\right)^2 \frac{N}{8\pi(R_c+R)^2 \sin^2\left(\frac{\pi}{N}\right)} {I_0}^2 \; for\; N \geq 3 \end{cases}$$

Replacing I_0 with its expression given by (243) in the equation above and using (238) giving τ_{ext}, we obtain

$$P_{vol}(z) = \begin{cases} \sigma_l \left(\frac{l_p}{2\pi}\right)^2 \frac{2}{\pi} \left(\frac{R_c}{R_c + R}\right)^2 \dot{B}_{i\,eq}{}^2 \left[1 - \mathrm{sinc}\left(\frac{4\pi z}{l_p}\right)\right] & for\ N = 2 \\ \sigma_l \left(\frac{l_p}{2\pi}\right)^2 \sin^2\left(\frac{\pi}{N}\right) \frac{2N}{\pi} \left(\frac{R_c}{R_c + R}\right)^2 \dot{B}_{i\,eq}{}^2 & for\ N \geq 3 \end{cases} \quad (245)$$

Expressing $P_{vol}(z)$ as in the MPAS model, i.e. as

$$P_{vol}(z) = \frac{nk\tau \dot{B}_{i\,eq}{}^2}{\mu_0}$$

and using the formulae of τ given by (237), we can deduce that

$$nk = \begin{cases} \frac{\mu_0}{\gamma\pi} \left(\frac{R_c}{R_c + R}\right)^2 \left[1 - \mathrm{sinc}\left(\frac{4\pi z}{l_p}\right)\right] & for\ N = 2 \\ \frac{\mu_0 N}{2\gamma\pi} \left(\frac{R_c}{R_c + R}\right)^2 & for\ N \geq 3 \end{cases}$$

where γ is given by (239).

Note that for the doublet the value of nk depends on the length of the conductor.

In addition, assuming the elements of the N-uplet being tangent to each other, we would have the following relation on R and R_c

$$R = R_c \sin\left(\frac{\pi}{N}\right)$$

Therefore, we then have

$$nk = \begin{cases} \frac{1}{2\ln\left(\frac{2R_c}{R_f}\right)} & for\ N = 2, for\ a\ length\ of\ conductor\ which\ is\ a\ multiple\ of\ l_p/4 \\ \frac{N / \left[1 + \sin\left(\frac{\pi}{N}\right)\right]^2}{\left[\ln\left(\frac{2R_c}{R_f}\right) - 2\sum_{j=1}^{floor\left(\frac{N-1}{2}\right)} \cos\left(\frac{2\pi j}{N}\right) \ln\left(\sin\left|\frac{\pi j}{N}\right|\right)\right]} & for\ N \geq 3 \end{cases} \quad (246)$$

III.3.3 Discussion about the values of nk

We have plotted on Figure 45 the values of nk as function of the superconducting shell radius to element radius ratio R_f/R and of the number of elements N.

First it can be seen that nk values are always lower than 2, which is one of the basic hypotheses of MPAS model in an axisymmetric configuration.

Furthermore, it is also very interesting to notice that $nk = 2$ for a large number of elements (for $N = 1000$ on Figure 45). Indeed when N is large, the elements are actually arranged like edge filaments

in a composite and we have previously mentioned that for a composite, the partial shielding coefficient nk was equal to 2.

The last two points, established for the configuration with single stage CICC, assess the robustness of the analytical model we have built. It ensures in fact that the assumptions considered (e.g. the distribution of currents in elements) do not degrade the relevance of our model as it aligns with the already existing approaches which are experimentally validated.

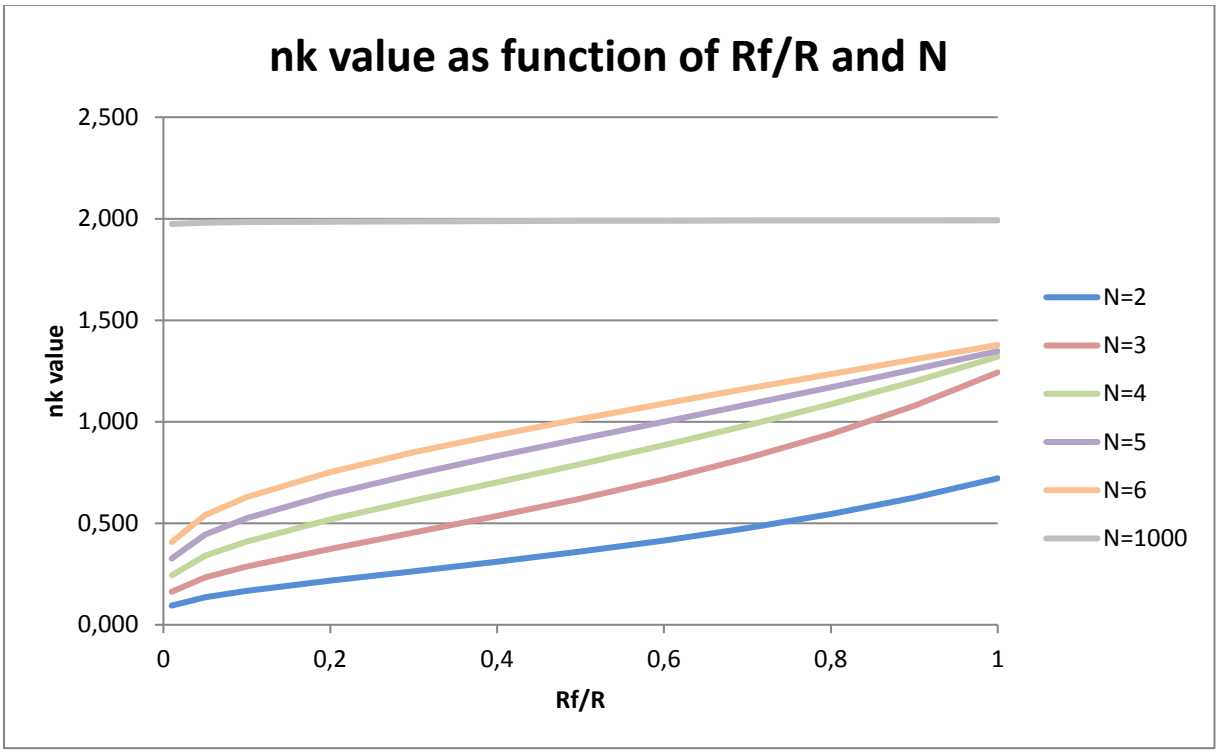

Figure 45 : nk values as function of R_f/R ratio and of N

III.4 Comparison with another analytical model

Another analytical model [18] (introduced in section I.5) considers the following average instant power per unit volume of composite $\bar{P}$ in a N-uplet of composite (one stage cable) under constant magnetic excitation (i.e. constant $\dot{B}_a$)

$$\bar{P} = \frac{2\Psi R}{\rho_b e_b \pi}\left(\frac{p_1}{2\pi}\right)^2 \dot{B}_a{}^2 \left[1 - \frac{R_f p^*}{R p_1}\right]^2 \tag{247}$$

where p_1 is the twist pitch of the first stage, p^* the effective twist pitch of filaments in the composite, Ψ is the average angular thickness of contacts between two strands, e_b is the thickness of the resistive barrier surrounding each composite and ρ_b is its resistivity.

It is then interesting to compare our expression of the power to that of this model. But first, we have to express the power per unit axial length of conductor for a constant magnetic excitation from equations (149) and (256). This gives

$$P_l(z) = 2\sigma_l \left(\frac{l_p}{2\pi}\right)^2 N R_c{}^2 \sin^2\left(\frac{\pi}{N}\right) \dot{B}_a{}^2$$

Then, in order to obtain the power per unit volume of composite, we have to divide this expression by the area of composites $N\pi R^2$, therefore we obtain

$$\bar{P} = \frac{2}{\pi}\sigma_l \left(\frac{l_p}{2\pi}\right)^2 \left(\frac{R_c \sin\left(\frac{\pi}{N}\right)}{R}\right)^2 \dot{B}_a{}^2$$

Since, the composites are considered tangent in [18], we have the relation $R_c \sin(\pi/N) = R$, and thus

$$\bar{P} = \frac{2}{\pi}\sigma_l \left(\frac{l_p}{2\pi}\right)^2 \dot{B}_a{}^2 \tag{248}$$

We now have to convert the parameters of [18] into ours. Since in [18], the interstrand resistance is assumed to be exclusively due to the resistive barrier surrounding the filaments, the transverse conductance dG between adjacent elements considered by our model corresponds to

$$dG = \frac{\Psi R}{\rho_b e_b} dz$$

In our model, we have $dG = \sigma_l dz$, therefore

$$\frac{\Psi R}{\rho_b e_b} = \sigma_l$$

Consequently, the power per unit volume of composite $\bar{P}$ derived in [18] and given by (247), is expressed in our notations, as

$$\bar{P} = \frac{2}{\pi}\sigma_l \left(\frac{l_p}{2\pi}\right)^2 \dot{B}_a{}^2 \left[1 - \frac{R_f p^*}{R l_p}\right]^2 \tag{249}$$

which is very similar to our expression given by (248), except that in (249), an additional factor is included.

In fact, in our model, we consider the N-uplet at the element scale (here composites) while [18] considers it down to the filament scale. Therefore, the additional factor in (249) is due to the fact that [18] only considers the magnetic flux variation enclosed between the closest filaments of adjacent composites (i.e. filaments of adjacent composites directly facing each other) while we consider the magnetic flux variation between the centers of adjacent composites.

Note that we have already discussed this point in section III.2.7.5 . In reality, the expression of the power must be somewhere in between these two expressions because:

- [18] has an optimistic approach considering that only the closest filaments of adjacent composites contributes to the shielding and thus to the losses (the transverse conductances between filaments of adjacent composites that are not directly facing each other are neglected, and so is their contribution in the losses)

- Our model has a conservative approach considering that the transverse conductances between filaments of adjacent composites are all identical and set to the average one (we will discuss in further detail the effect of this consideration in section IV.4.3)

III.5 Synthesis

In this section, we have established the N-uplet model which is relevant to the analytical representation of the magnetic shielding occurring in a single cabling stage of a conductor. We have shown that it can be described, as in the simplest approach at strand scale, by a single time equation with a single time constant τ and that its associated coupling power could be expressed considering a partial shielding due to coupling (in analogy with MPAS model). The partial shielding coefficient nk was expressed together with analytical expressions of τ. The comparison of the N-uplet model with other analytical models issued from the literature [18],[21] have shown a good consistency, thus consolidating our approach.

This achievement constitutes a significant step towards the modeling of coupling losses in CICCs as it shows that the losses are mainly driven by a very few number of parameters and its dependence on these parameters have now been identified. Furthermore the fact that the assumption of the MPAS model is in agreement with the analytical output of the N-uplet model is substantial because, at the same time, it provides a theoretical background to the MPAS model and it reinforces the consistency of our model since the MPAS approach has proved its ability to describe the experimental reality.

As previously mentioned at strand scale, the single-stage CICC scale stands as a step towards a more elaborated representation of a cable, i.e. the integration of complexity due to the multiple stages. In this objective, we up scale this model in the next section, addressing a two-stage cable.

IV. Analytical study of the shielding due to two stages of a CICC

Content: This part is dedicated to the presentation of an analytical modeling of a two cabling stages conductor. Experimental work (AC losses measurements and X-ray tomography) on conductors is also presented as well as comparisons with other models (analytical and numerical).

Associated publication:

A. Louzguiti, L. Zani, D. Ciazynski, B. Turck, JL. Duchateau, A. Torre, F. Topin, M. Bianchi, AC. Ricchiuto, T. Bagni, V.A. Anvar, A. Nijhuis and I. Tiseanu, *Development of a new generic analytical modeling of AC coupling losses in cable-in-conduit conductors*, I.E.E.E. Trans. on App. Superconductivity, Vol. 28, April 2018, Art. No. 4700405.

IV.1 Presentation

In the previous section, we have studied the magnetic behavior of a single cabling stage subject to a transverse time-varying magnetic field. In order to further investigate the dynamics of magnetic coupling occurring in a CICC, we now reach a higher level of complexity by considering the coupling effects occurring between different cabling stages of the CICC. We will therefore address the magnetic shielding in a two cabling stages conductor as it reveals the magnetic coupling between two consecutive cabling stages of a CICC.

The geometry we will consider here is a twisted group of twisted elements. Again the "element" can either be a strand, a group of strands or even a petal (i.e. multiple strands twisted in several cabling stages) because our approach aims at modeling the magnetic coupling between two consecutive cabling stages regardless of the scale.

In this section we will derive the equation governing the conductor as well as the power generated inside it and compare the outputs of our modeling to those of two reference numerical models (THELMA and JackPot) on two simplified geometries representative of ITER CS and JT-60SA TF conductors.

In addition, we will present the experimental losses of a sample of JT-60SA TF conductor we have measured in JOSEFA facility at CEA and its effective geometrical parameters (i.e. cabling radii and twist pitches) extracted via X-ray tomography from other samples of the same conductor.

The objective is then to investigate the possibility of representing the experimental losses with those predicted by our N_2-uplet of N_1-uplets model using the effective geometrical parameters of the conductor and adjusting the effective transverse conductances considered in our approach.

IV.2 N_2-uplet of N_1-uplets model

IV.2.1 Methodology

In order to study the magnetic response of a group of groups of twisted elements to a time-varying transverse and uniform magnetic field (N_2-uplet of N_1-uplets model), we will follow the methodology we have presented in the study of a one cabling stage conductor (see section III.2.1):

- **In section IV.2.3 we first begin by formulating the fundamental equations of the system at each scale**
- **In section IV.2.4 we compute the currents induced in steady-state regime, i.e. when these currents are not time-varying**
- **In section IV.2.5, knowing the spatial form of the currents induced in steady-state regime, we follow the logical chain displayed on Figure 15 until the spatial form of the currents induced for any time-varying regime is defined; these expressions will enable us to reduce the equations of the system to a simple first-order differential equation**
- **In section IV.2.6, knowing the spatial form of the currents induced for any time regime, we express the coupling power dissipated in a group of groups of twisted elements as a function of the currents**
- **In section IV.2.7 we assess the relevance of the inductive part of our model through a study in purely inductive regime**

IV.2.2 Assumptions

The geometry we consider in our modeling features N_2 twisted groups (with a pitch equal to l_{p_2} and a cabling radius equal to R_{c_2}) of N_1 twisted elements (with a pitch equal to l_{p_1} and a cabling radius equal to R_{c_1}). As in the N-uplet model, the element can either represent a strand, a group of strands or a petal, we simply consider it as a cylinder of radius R containing a thin superconducting shell of radius R_f (see Figure 46).

In addition, we consider that in a slice of thickness dz there exists a local effective conductance between adjacent substages which is noted $dG_2 = \sigma_{l_2} dz$ where σ_{l_2} is the transverse conductance of the superstage per unit axial length (i.e. expressed in S/m). We also consider that in a slice of thickness dz there exists a local effective conductance between adjacent elements of a substage which is noted $dG_1 = \sigma_{l_1} dz$ where σ_{l_1} is the transverse conductance per unit axial length (i.e. expressed in S/m). Both σ_{l_1} and σ_{l_2} are considered constant along the axis of the conductor. The current flowing through the superconducting shell of element k_1 of substage k_2 at z is noted $I_{k_1 k_2}(z)$, the current flowing transversely in a slice dz from substage k_2 to substage $k_2 + 1$ at z is noted $I_{k_2\, k_2+1}(z)$ and the current flowing transversely in a slice dz from element k_1 of substage k_2 to element $k_1 + 1$ of substage k_2 at z is noted $I^{\langle k_2 \rangle}_{k_1\, k_1+1}(z)$. Furthermore, we consider that:

- The external magnetic field B_a is transverse (along the y-axis, see Figure 46) and spatially uniform within the conductor

- The transport current is zero
- The geometry is infinitely long along the z-axis
- The superconducting shell is not saturated and thus the electric field is zero along the trajectory of an element
- The current $I_{k_1 k_2}(z)$ carried by the superconducting shell of element k_1 of substage k_2 at z is uniformly distributed over its circumference
- The substages and elements are lightly twisted, i.e. $\left(\frac{2\pi R_{c_2}}{l_{p_2}}\right)^2 \ll 1$ and $\left(\frac{2\pi R_{c_1}}{l_{p_1}}\right)^2 \ll 1$
- The time variation of the external magnetic field B_a is slow enough to neglect the displacement current so that Kirchhoff's current law applies
- The number of elements in each substage is at least 3, i.e. $N_1 \geq 3$ and the number of substages is at least 3, i.e. $N_2 \geq 3$. These assumptions are made here because of the specificity of the doublet case (see section III.2.7).

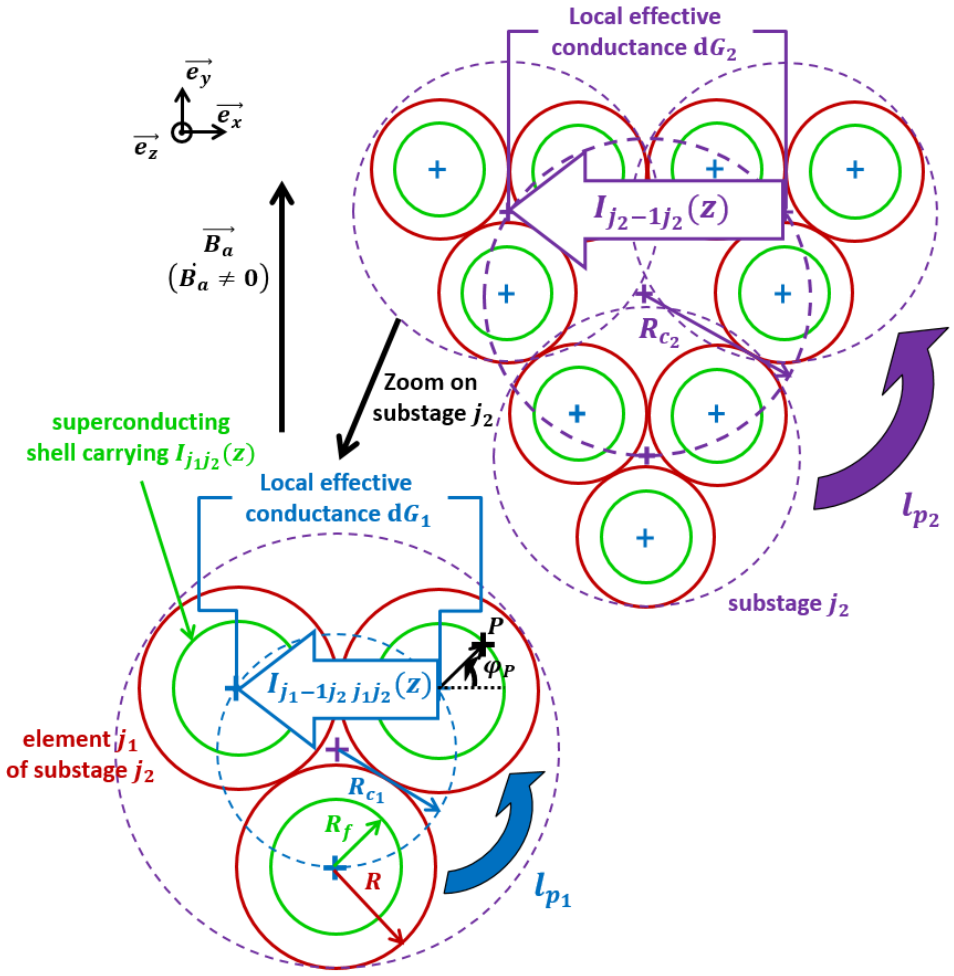

Figure 46 : Scheme showing the cross-section geometry of a triplet of triplets $(N_2 = 3, N_1 = 3)$

Finally, the position $(x_{k_1k_2}, y_{k_1k_2})$ of the center of element k_1 of substage k_2 at z is given by

$$\begin{pmatrix} x_{k_1k_2}(z) \\ y_{k_1k_2}(z) \end{pmatrix} = \begin{pmatrix} x_{k_2}^{(super)}(z) \\ y_{k_2}^{(super)}(z) \end{pmatrix} + \begin{pmatrix} x_{k_1}^{(sub)}(z) \\ y_{k_1}^{(sub)}(z) \end{pmatrix} \tag{250}$$

with

$$\begin{pmatrix} x_{k_2}^{(super)}(z) \\ y_{k_2}^{(super)}(z) \end{pmatrix} = \begin{pmatrix} R_{C_2} \cos\left(\frac{2\pi z}{l_{p_2}} + \frac{2\pi(k_2-1)}{N_2}\right) \\ R_{C_2} \sin\left(\frac{2\pi z}{l_{p_2}} + \frac{2\pi(k_2-1)}{N_2}\right) \end{pmatrix} \tag{251}$$

and

$$\begin{pmatrix} x_{k_1}^{(sub)}(z) \\ y_{k_1}^{(sub)}(z) \end{pmatrix} = \begin{pmatrix} R_{C_1} \cos\left(\frac{2\pi z}{l_{p_1}} + \frac{2\pi(k_1-1)}{N_1}\right) \\ R_{C_1} \sin\left(\frac{2\pi z}{l_{p_1}} + \frac{2\pi(k_1-1)}{N_1}\right) \end{pmatrix} \tag{252}$$

Note that Figure 46 shows a scheme which is representative of a two cabling stages conductor before compaction, but note that our approach can also be used to model the magnetic behavior of a compacted two cabling stages conductor whose scheme is displayed in Figure 47.

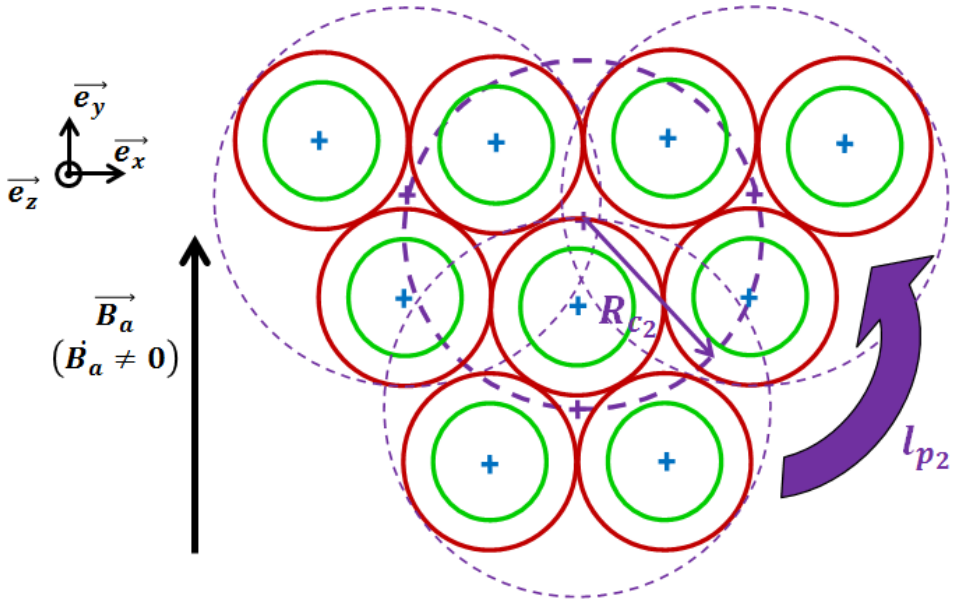

Figure 47 : Scheme showing the cross-section geometry of a compacted triplet of triplets $(N_2 = 3, N_1 = 3)$

IV.2.3 Equations of the system

❖ **We will formulate here the fundamental equations of the system at each scale using Kirchhoff's current law, Ohm's law, Faraday's law of induction. We will then combine them to express the global equation of the system.**

We will here derive the equations governing a two cabling stages conductor. The main difficulty with respect to the development of the N-uplet model, is that the geometry considered in the N_2-uplet of N_1-uplets is not necessarily periodic because l_{p_2} is not necessarily an integer multiple of l_{p_1}.

We assume that the current $I_{k_1 k_2}(z)$ flowing along each element can be decomposed as

$$I_{k_1 k_2}(z) = I_{k_2}(z)/N_1 + I_{k_1}^{\langle k_2 \rangle}(z) \tag{253}$$

where $I_{k_2}(z)$ is the current induced in substage k_2 to shield the superstage and $I_{k_1}^{\langle k_2 \rangle}(z)$ is the current induced in element k_1 of substage k_2 to shield substage k_2.

Again we assume that the magnetic vector potential $\vec{A}$ can be reduced to its axial component A_z only for the same reasons than those mentioned in section III.2.3 . We now have

$$\vec{A} = A_z \overrightarrow{e_z}$$

and the notation $A_{z_{k_1 k_2}}(z)$ will refer to the value of the axial component of the magnetic vector potential at the center of element k_1 of substage k_2 at z.

IV.2.3.1 Equations at the substage scale

Regarding the substage scale, we can directly adapt the equations of the N-uplet model for $1 \leq k_2 \leq N_2$ and $1 \leq k_1 \leq N_1$ as

$$\begin{cases} \dfrac{dI_{k_1}^{\langle k_2 \rangle}}{dz}(z) = \dfrac{1}{dz}\left[I_{k_1-1\,k_1}^{\langle k_2 \rangle}(z) - I_{k_1\,k_1+1}^{\langle k_2 \rangle}(z)\right] \\ \dfrac{1}{dz} I_{k_1\,k_1+1}^{\langle k_2 \rangle}(z) = \sigma_{l_1} U_{k_1\,k_1+1}^{\langle k_2 \rangle}(z) \\ \dfrac{dU_{k_1\,k_1+1}^{\langle k_2 \rangle}}{dz}(z) = \dot{A}_{z_{k_1+1\,k_2}}(z) - \dot{A}_{z_{k_1\,k_2}}(z) \end{cases} \tag{254}$$

Once combined, the equations of (254) enable us to write for $1 \leq k_2 \leq N_2$ and $1 \leq k_1 \leq N_1$

$$\frac{d^2 I_{k_1}^{\langle k_2 \rangle}}{dz^2}(z) = \sigma_{l_1}\left[2\dot{A}_{z_{k_1\,k_2}}(z) - \dot{A}_{z_{k_1-1\,k_2}}(z) - \dot{A}_{z_{k_1+1\,k_2}}\right] \tag{255}$$

IV.2.3.2 Equations at the superstage scale

Regarding the superstage scale, we first consider that the average voltage $U_{k_2\,k_2+1}(z)$ between substages k_2 and k_2+1 at z is equal to the difference between the average electric potential of the elements of substage k_2 $V_{k_2}(z)$ and that of the elements of substage k_2+1 $V_{k_2+1}(z)$ at z, i.e.

$$U_{k_2\,k_2+1}(z) = V_{k_2}(z) - V_{k_2+1}(z)$$

with

$$V_{k_2}(z) = \frac{1}{N_1}\sum_{k_1=1}^{N_1} V_{k_1 k_2}(z)$$

where $V_{k_1 k_2}(z)$ is the electric potential of element k_1 of substage k_2 at z.

These considerations lead to the following relation

$$U_{k_2\, k_2+1}(z) = \frac{1}{{N_1}^2}\sum_{k_1=1}^{N_1}\sum_{j_1=1}^{N_1} U_{k_1 k_2\, j_1 k_2+1}(z)$$

where $U_{k_1 k_2\, j_1 k_2+1}(z)$ is the local transverse voltage between element k_1 of substage k_2 and element j_1 of substage k_2+1 at z, which, according to equation (141) of the N-uplet model, must satisfy the equation

$$\frac{dU_{k_1 k_2\, j_1 k_2+1}}{dz}(z) = \dot{A}_{z_{j_1\, k_2+1}}(z) - \dot{A}_{z_{k_1 k_2}}(z)$$

The combination of the previous relations leads to

$$\frac{dU_{k_2\, k_2+1}}{dz}(z) = \frac{1}{N_1}\sum_{k_1=1}^{N_1}\left[\dot{A}_{z_{k_1\, k_2+1}}(z) - \dot{A}_{z_{k_1 k_2}}(z)\right]$$

We can now adapt the equations of the N-uplet model to the write the equations of the superstage scale for $1 \leq k_2 \leq N_2$ as

$$\begin{cases} \dfrac{dI_{k_2}}{dz}(z) = \dfrac{1}{dz}\left[I_{k_2-1\, k_2}(z) - I_{k_2\, k_2+1}(z)\right] \\ \dfrac{1}{dz} I_{k_2\, k_2+1}(z) = \sigma_{l_2} U_{k_2\, k_2+1}(z) \\ \dfrac{dU_{k_2\, k_2+1}}{dz}(z) = \dfrac{1}{N_1}\displaystyle\sum_{k_1=1}^{N_1}\left[\dot{A}_{z_{k_1\, k_2+1}}(z) - \dot{A}_{z_{k_1 k_2}}(z)\right] \end{cases} \tag{256}$$

Once combined, the equations of (256) enable us to write for $1 \leq k_2 \leq N_2$

$$\frac{d^2 I_{k_2}}{dz^2}(z) = \sigma_{l_2}\frac{1}{N_1}\sum_{k_1=1}^{N_1}\left[2\dot{A}_{z_{k_1\, k_2}}(z) - \dot{A}_{z_{k_1\, k_2-1}}(z) - \dot{A}_{z_{k_1\, k_2+1}}(z)\right] \tag{257}$$

IV.2.3.3 Global equations

Using equations (253), (255) and (257), we can derive the global equations of the system for $1 \leq k_2 \leq N_2$ and $1 \leq k_1 \leq N_1$ as

$$\frac{d^2 I_{k_1 k_2}}{dz^2}(z) = \begin{cases} \sigma_{l_1}\left[2\dot{A}_{z_{k_1 k_2}}(z) - \dot{A}_{z_{k_1-1\, k_2}}(z) - \dot{A}_{z_{k_1+1\, k_2}}(z)\right] \\ +\dfrac{\sigma_{l_2}}{{N_1}^2}\displaystyle\sum_{j_1=1}^{N_1}\left[2\dot{A}_{z_{j_1 k_2}}(z) - \dot{A}_{z_{j_1 k_2-1}}(z) - \dot{A}_{z_{j_1 k_2+1}}(z)\right] \end{cases} \tag{258}$$

As we did previously, we can split the magnetic vector potential $A_{z_{k_1 k_2}}(z)$ felt at the center of element k_1 of substage k_2 at z by superposition as

$$A_{z_{k_1 k_2}}(z) = A_{z_{a_{k_1 k_2}}}(z) + A_{z_{r_{k_1 k_2}}}(z)$$

where $A_{z_{a_{k_1 k_2}}}(z)$ is the part of the magnetic vector potential $A_{z_{k_1 k_2}}(z)$ which is due to the applied magnetic field B_a and $A_{z_{r_{k_1 k_2}}}(z)$ is the other part which is due to the currents $\left(I_{k_1 k_2}\right)_{1\le k_1\le N_1, 1\le k_2\le N_2}$ induced in all the elements.

With this decomposition, equations (258) now become for $1 \le k_2 \le N_2$ and $1 \le k_1 \le N_1$

$$\begin{cases} \dfrac{d^2 I_{k_1 k_2}}{dz^2}(z) - \sigma_{l_1}\left[2\dot{A}_{z_{r_{k_1 k_2}}}(z) - \dot{A}_{z_{r_{k_1-1\, k_2}}}(z) - \dot{A}_{z_{r_{k_1+1\, k_2}}}(z)\right] \\ -\dfrac{\sigma_{l_2}}{{N_1}^2}\displaystyle\sum_{j_1=1}^{N_1}\left[2\dot{A}_{z_{r_{j_1 k_2}}}(z) - \dot{A}_{z_{r_{j_1 k_2-1}}}(z) - \dot{A}_{z_{r_{j_1 k_2+1}}}(z)\right] = \\ \sigma_{l_1}\left[2\dot{A}_{z_{a_{k_1 k_2}}}(z) - \dot{A}_{z_{a_{k_1-1\, k_2}}}(z) - \dot{A}_{z_{a_{k_1+1\, k_2}}}(z)\right] \\ +\dfrac{\sigma_{l_2}}{{N_1}^2}\displaystyle\sum_{j_1=1}^{N_1}\left[\dot{A}_{z_{a_{j_1 k_2}}}(z) - \dot{A}_{z_{a_{j_1 k_2-1}}}(z) - \dot{A}_{z_{a_{j_1 k_2+1}}}(z)\right] \end{cases} \tag{259}$$

From previous considerations, we now that the magnetic vector potential $\overrightarrow{A_a}$ associated with the applied magnetic field B_a is given everywhere in space by

$$\overrightarrow{A_a} = -xB_a\overrightarrow{e_z}$$

Using (250) we can thus deduce that

$$A_{z_{a_{k_1 k_2}}}(z) = -x_{k_1 k_2}(z)B_a = -\left[x_{k_2}^{(super)}(z) + x_{k_1}^{(sub)}(z)\right]B_a$$

where $x_{k_2}^{(super)}(z)$ and $x_{k_1}^{(sub)}(z)$ are given by (251) and (252).

Consequently we have

$$2\dot{A}_{z_{a_{k_1 k_2}}}(z) - \dot{A}_{z_{a_{k_1-1\, k_2}}}(z) - \dot{A}_{z_{a_{k_1+1\, k_2}}}(z) = \left[-2x_{k_1}^{(sub)}(z) + x_{k_1-1}^{(sub)}(z) + x_{k_1+1}^{(sub)}(z)\right]\dot{B}_a$$

Using (252) and after some mathematical manipulations, we can write

$$2\dot{A}_{z_{a_{k_1 k_2}}}(z) - \dot{A}_{z_{a_{k_1-1\, k_2}}}(z) - \dot{A}_{z_{a_{k_1+1\, k_2}}}(z) = -4R_{c_1}\dot{B}_a \sin^2\left(\frac{\pi}{N_1}\right)\cos\left(\frac{2\pi z}{l_{p_1}} + \frac{2\pi(k_1-1)}{N_1}\right)$$

Using the same methodology and (251), we can also write

$$\sum_{j_1=1}^{N_1}\left[\dot{A}_{z_{a_{j_1 k_2}}}(z)-\dot{A}_{z_{a_{j_1 k_2-1}}}(z)-\dot{A}_{z_{a_{j_1 k_2+1}}}(z)\right]=-4N_1R_{c_2}\dot{B}_a\sin^2\left(\frac{\pi}{N_2}\right)\cos\left(\frac{2\pi z}{l_{p_2}}+\frac{2\pi(k_2-1)}{N_2}\right)$$

From equations (259), we can now express the global equations of the system for $1\leq k_2\leq N_2$ and $1\leq k_1\leq N_1$ as

$$\begin{cases}\dfrac{d^2I_{k_1k_2}}{dz^2}(z)-\sigma_{l_1}\left[2\dot{A}_{z_{r_{k_1 k_2}}}(z)-\dot{A}_{z_{r_{k_1-1\,k_2}}}(z)-\dot{A}_{z_{r_{k_1+1\,k_2}}}(z)\right]\\ \quad-\dfrac{\sigma_{l_2}}{{N_1}^2}\displaystyle\sum_{j_1=1}^{N_1}\left[2\dot{A}_{z_{r_{j_1 k_2}}}(z)-\dot{A}_{z_{r_{j_1 k_2-1}}}(z)-\dot{A}_{z_{r_{j_1 k_2+1}}}(z)\right]=\\ \qquad-4\sigma_{l_1}R_{c_1}\dot{B}_a\sin^2\left(\dfrac{\pi}{N_1}\right)\cos\left(\dfrac{2\pi z}{l_{p_1}}+\dfrac{2\pi(k_1-1)}{N_1}\right)\\ \qquad-4\dfrac{\sigma_{l_2}}{N_1}R_{c_2}\dot{B}_a\sin^2\left(\dfrac{\pi}{N_2}\right)\cos\left(\dfrac{2\pi z}{l_{p_2}}+\dfrac{2\pi(k_2-1)}{N_2}\right)\end{cases}\tag{260}$$

IV.2.4 Study in steady-state regime

❖ **We will calculate here the currents induced in steady-state regime. We will simply start from the system equations derived at the end of the previous section and we will solve them considering that the coupling currents are not time-varying.**

IV.2.4.1 Equations of the system in steady-state regime

In steady-state regimes for coupling currents, the currents induced in the elements are, by assumption, not time varying, i.e. we consider that for any z and for $1\leq k_2\leq N_2$ and $1\leq k_1\leq N_1$

$$\dot{I}_{k_1k_2}(z)=0$$

Since $A_{z_{r_{k_1 k_2}}}(z)$ is exclusively due to the induced currents, we can also conclude that for any z and for $1\leq k_2\leq N_2$ and $1\leq k_1\leq N_1$

$$\dot{A}_{z_{r_{k_1 k_2}}}(z)=0$$

And therefore, from equation (260), we see that the equation of the system is, in steady-state regime, simply reduced to

$$\frac{d^2I_{k_1k_2}}{dz^2}(z)=\begin{cases}-4\sigma_{l_1}R_{c_1}\dot{B}_a\sin^2\left(\dfrac{\pi}{N_1}\right)\cos\left(\dfrac{2\pi z}{l_{p_1}}+\dfrac{2\pi(k_1-1)}{N_1}\right)\\ -4\dfrac{\sigma_{l_2}}{N_1}R_{c_2}\dot{B}_a\sin^2\left(\dfrac{\pi}{N_2}\right)\cos\left(\dfrac{2\pi z}{l_{p_2}}+\dfrac{2\pi(k_2-1)}{N_2}\right)\end{cases}\tag{261}$$

Splitting again $I_{k_1k_2}(z)$ as in (253), i.e. as $I_{k_1k_2}(z) = I_{k_2}(z)/N_1 + I_{k_1}^{\langle k_2 \rangle}(z)$, we have

$$\begin{cases} \dfrac{d^2 I_{k_1}^{\langle k_2 \rangle}}{dz^2}(z) = -4\sigma_{l_1} R_{c_1} \dot{B}_a \sin^2\left(\dfrac{\pi}{N_1}\right) \cos\left(\dfrac{2\pi z}{l_{p_1}} + \dfrac{2\pi(k_1-1)}{N_1}\right) \\ \dfrac{d^2 I_{k_2}}{dz^2}(z) = -4\sigma_{l_2} R_{c_2} \dot{B}_a \sin^2\left(\dfrac{\pi}{N_2}\right) \cos\left(\dfrac{2\pi z}{l_{p_2}} + \dfrac{2\pi(k_2-1)}{N_2}\right) \end{cases} \tag{262}$$

IV.2.4.2 Determination of the solutions for an infinitely long conductor (assumption of the model)

Equations (262) being identical to equations (147) of N-uplet model, we can directly adapt the solutions given by (150) and (151) as

$$\begin{cases} I_{k_1}^{\langle k_2 \rangle}(z) = I_{0_1} \cos\left(\dfrac{2\pi z}{l_{p_1}} + \dfrac{2\pi(k_1-1)}{N_1}\right) \\ I_{k_2}(z) = I_{0_2} \cos\left(\dfrac{2\pi z}{l_{p_2}} + \dfrac{2\pi(k_2-1)}{N_2}\right) \end{cases}$$

with

$$\begin{cases} I_{0_1} = 4\sigma_{l_1} R_{c_1} \dot{B}_a \sin^2\left(\dfrac{\pi}{N_1}\right) \left(\dfrac{l_{p_1}}{2\pi}\right)^2 \\ I_{0_2} = 4\sigma_{l_2} R_{c_2} \dot{B}_a \sin^2\left(\dfrac{\pi}{N_2}\right) \left(\dfrac{l_{p_2}}{2\pi}\right)^2 \end{cases}$$

As a result, for an infinitely long conductor the solutions of equations (261) are for $1 \leq k_2 \leq N_2$ and $1 \leq k_1 \leq N_1$

$$I_{k_1k_2}(z) = I_{0_1} \cos\left(\frac{2\pi z}{l_{p_1}} + \frac{2\pi(k_1-1)}{N_1}\right) + \frac{I_{0_2}}{N_1} \cos\left(\frac{2\pi z}{l_{p_2}} + \frac{2\pi(k_2-1)}{N_2}\right) \tag{263}$$

with

$$\begin{cases} I_{0_1} = 4\sigma_{l_1} R_{c_1} \dot{B}_a \sin^2\left(\dfrac{\pi}{N_1}\right) \left(\dfrac{l_{p_1}}{2\pi}\right)^2 \\ I_{0_2} = 4\sigma_{l_2} R_{c_2} \dot{B}_a \sin^2\left(\dfrac{\pi}{N_2}\right) \left(\dfrac{l_{p_2}}{2\pi}\right)^2 \end{cases} \tag{264}$$

IV.2.4.3 Determination of the solutions for a finite length of conductor

Let us consider a piece of conductor of length L so that the ends of the conductor are located at $z = -L/2$ and $z = L/2$.

Again, equations (262) being identical to equations (147) of N-uplet model, we can directly adapt the solutions given by (151) and (152) as

$$\begin{cases} I_{k_1}^{\langle k_2 \rangle}(z) = I_{0_1}\left[\cos\left(\frac{2\pi z}{l_{p_1}} + \frac{2\pi(k_1-1)}{N_1}\right) + \frac{2z}{L}\sin\left(\frac{\pi L}{l_{p_1}}\right)\sin\left(\frac{2\pi(k_1-1)}{N_1}\right) - \cos\left(\frac{\pi L}{l_{p_1}}\right)\cos\left(\frac{2\pi(k_1-1)}{N_1}\right)\right] \\ I_{k_2}(z) = I_{0_2}\left[\cos\left(\frac{2\pi z}{l_{p_2}} + \frac{2\pi(k_2-1)}{N_2}\right) + \frac{2z}{L}\sin\left(\frac{\pi L}{l_{p_2}}\right)\sin\left(\frac{2\pi(k_2-1)}{N_2}\right) - \cos\left(\frac{\pi L}{l_{p_2}}\right)\cos\left(\frac{2\pi(k_2-1)}{N_2}\right)\right] \end{cases}$$

where I_{0_1} and I_{0_2} are given in (264).

As a result, the solutions $I_{k_1k_2}(z)$ of equations (261) for a conductor of length L are for $1 \leq k_2 \leq N_2$ and $1 \leq k_1 \leq N_1$

$$\begin{cases} I_{0_1}\left[\cos\left(\frac{2\pi z}{l_{p_1}} + \frac{2\pi(k_1-1)}{N_1}\right) + \frac{2z}{L}\sin\left(\frac{\pi L}{l_{p_1}}\right)\sin\left(\frac{2\pi(k_1-1)}{N_1}\right) - \cos\left(\frac{\pi L}{l_{p_1}}\right)\cos\left(\frac{2\pi(k_1-1)}{N_1}\right)\right] \\ + \frac{I_{0_2}}{N_1}\left[\cos\left(\frac{2\pi z}{l_{p_2}} + \frac{2\pi(k_2-1)}{N_2}\right) + \frac{2z}{L}\sin\left(\frac{\pi L}{l_{p_2}}\right)\sin\left(\frac{2\pi(k_2-1)}{N_2}\right) - \cos\left(\frac{\pi L}{l_{p_2}}\right)\cos\left(\frac{2\pi(k_2-1)}{N_2}\right)\right] \end{cases} \quad (265)$$

where I_{0_1} and I_{0_2} are still given by (264).

IV.2.5 Study in time-varying regime

❖ **Since we now know the spatial form of the currents induced in steady-state regime, we will follow the logical chain displayed on Figure 15 until the spatial form of the currents induced for any time-varying regime is defined (this is achieved through IV.2.5.1 to IV.2.5.3). These expressions will then enable us to reduce the equations of the system to a first-order differential equation in IV.2.5.4 .**

We are now studying the magnetic response of the conductor when the induced currents are time-varying, i.e. we now consider that for any z and for $1 \leq k_2 \leq N_2$ and $1 \leq k_1 \leq N_1$

$$\dot{I}_{k_1k_2}(z) \neq 0$$

This also implies that for any z and for $1 \leq k_2 \leq N_2$ and $1 \leq k_1 \leq N_1$

$$\dot{A}_{z r_{k_1k_2}}(z) \neq 0$$

Therefore we now have to take into account the contribution of the magnetic vector potential due to the induced currents in the equations of the system which are now written for $1 \leq k_2 \leq N_2$ and $1 \leq k_1 \leq N_1$ as

$$\begin{cases} \frac{d^2 I_{k_1k_2}}{dz^2}(z) - \sigma_{l_1}\left[2\dot{A}_{z r_{k_1 k_2}}(z) - \dot{A}_{z r_{k_1-1\, k_2}}(z) - \dot{A}_{z r_{k_1+1\, k_2}}(z)\right] \\ \quad - \frac{\sigma_{l_2}}{{N_1}^2}\sum_{j_1=1}^{N_1}\left[2\dot{A}_{z r_{j_1 k_2}}(z) - \dot{A}_{z r_{j_1 k_2-1}}(z) - \dot{A}_{z r_{j_1 k_2+1}}(z)\right] = \\ \qquad -\left(\frac{2\pi}{l_{p_1}}\right)^2 I_{0_1\, ext}\cos\left(\frac{2\pi z}{l_{p_1}} + \frac{2\pi(k_1-1)}{N_1}\right) \\ \qquad -\left(\frac{2\pi}{l_{p_2}}\right)^2 \frac{I_{0_2\, ext}}{N_1}\cos\left(\frac{2\pi z}{l_{p_2}} + \frac{2\pi(k_2-1)}{N_2}\right) \end{cases} \quad (266)$$

with

$$\begin{cases} I_{0_{1\,ext}} = 4\sigma_{l_1} R_{c_1} \dot{B}_a \sin^2\left(\frac{\pi}{N_1}\right)\left(\frac{l_{p_1}}{2\pi}\right)^2 \\ I_{0_{2\,ext}} = 4\sigma_{l_2} R_{c_2} \dot{B}_a \sin^2\left(\frac{\pi}{N_2}\right)\left(\frac{l_{p_2}}{2\pi}\right)^2 \end{cases} \quad (267)$$

In order to follow our analytical methodology (described in section IV.2.1), we now have to calculate the effect of the time-variation of the current distribution we have found in steady-state regime. But we see that this time, conversely to the N-uplet model, we have to take into account, by superposition, the contributions of two different current distributions instead of one, which are $\left(I_{k_1}^{\langle k_2\rangle}(z) = I_{0_{1\,ext}}\cos\left(\frac{2\pi z}{l_{p_1}} + \frac{2\pi(k_1-1)}{N_1}\right)\right)_{1\le k_1\le N_1}$ and $\left(I_{k_2}(z) = \frac{I_{0_{2\,ext}}}{N_1}\cos\left(\frac{2\pi z}{l_{p_2}} + \frac{2\pi(k_2-1)}{N_2}\right)\right)_{1\le k_2\le N_2}$.

To carry out this operation in an efficient way, we will first calculate the magnetic vector potential due to a current distribution of the following general form

$$\left(I_{k_1k_2}(z) = {I_0}^{(\alpha)}\cos\left(\alpha z + \varphi_{k_1k_2}\right)\right)_{1\le k_1\le N_1, 1\le k_2\le N_2}$$

where I_0 is a function of time only, α is a spatial frequency (corresponding to $2\pi/l_{p_1}$ and $2\pi/l_{p_2}$ in the previous current distributions) and $\varphi_{k_1k_2}$ is an initial phase shift (corresponding to $2\pi(k_1-1)/N_1$ or $2\pi(k_2-1)/N_2$ in the previous current distributions).

IV.2.5.1 Calculation of the magnetic vector potential due to the current flowing in one element

Let us note $\overrightarrow{K_{p_1p_2}^{(\alpha)}} = K_{p_1p_2}^{(\alpha)}\overrightarrow{e_{s_{p_1p_2}}}$ the surface current flowing through the superconducting shell of element p_1 of substage p_2 having the general form $K_{p_1p_2}^{(\alpha)}(z) = K_0^{(\alpha)}\cos\left(\alpha z + \varphi_{p_1p_2}\right)$ with

$$K_0^{(\alpha)} = \frac{I_0^{(\alpha)}}{2\pi R_f}$$

$s_{p_1p_2}(z)$ is the abscissa along the center of element p_1 of substage p_2 at z and $\overrightarrow{e_{s_{p_1p_2}}}(z)$ is the unit vector tangent to the trajectory of the center of element p_1 of substage p_2 at z).

Let us note $A_{z_{r_{(p_1p_2)}}}^{(\alpha)}\left(M_{k_1k_2}\right)$ the axial component of the magnetic vector potential felt at the center of element k_1 of substage k_2 at z (the center is noted $M_{k_1k_2}$) and due to $\overrightarrow{K_{p_1p_2}^{(\alpha)}}$. We recall that we are only interested in its axial component because we have neglected the contributions of the other components (see section IV.2.3).

Using the Biot-Savart law, we can write

$$A_{z_{r_{(p_1p_2)}}}^{(\alpha)}\left(M_{k_1k_2}\right) = \frac{\mu_0}{4\pi}\iint_{P\in\Sigma}\frac{K_{p_1p_2}^{(\alpha)}(P)\overrightarrow{e_{s_{p_1p_2}}}(z_P).\overrightarrow{e_z}}{PM_{k_1k_2}}d\Sigma \quad (268)$$

where P is the source point (see Figure 46) whose axial coordinate is z_P and which has to be integrated over the area Σ corresponding to the localization of the surface current $\overrightarrow{K_{p_1p_2}^{(\alpha)}}$, i.e. to the external area of the hollow cylinder of radius R_f whose center follows the center of element p_1 of substage p_2 (see green surface on Figure 48).

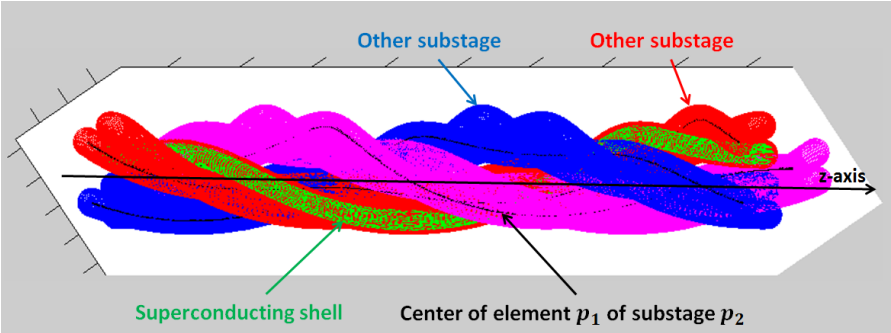

Figure 48 : Scheme showing the integration area Σ of equation (268)

The position of the center of element p_1 of substage p_2 at z_P noted O_P is given by equations (250) to (252)

$$\overrightarrow{OO_P} = \begin{pmatrix} x_{p_1p_2}(z_P) \\ y_{p_1p_2}(z_P) \\ z_P \end{pmatrix} = \begin{pmatrix} R_{c_2}\cos\left(\frac{2\pi z_P}{l_{p_2}} + \frac{2\pi(p_2-1)}{N_2}\right) + R_{c_1}\cos\left(\frac{2\pi z_P}{l_{p_1}} + \frac{2\pi(p_1-1)}{N_1}\right) \\ R_{c_2}\sin\left(\frac{2\pi z_P}{l_{p_2}} + \frac{2\pi(p_2-1)}{N_2}\right) + R_{c_1}\sin\left(\frac{2\pi z_P}{l_{p_1}} + \frac{2\pi(p_1-1)}{N_1}\right) \\ z_P \end{pmatrix}$$

Given the geometry, the elementary area $d\Sigma$ is equal to

$$d\Sigma = R_f d\Psi_P ds_{p_1p_2}(z_P)$$

where Ψ_P is the angle between $\overrightarrow{e_x}$ and $\overrightarrow{O_PP}$ in the (Oxy) plane (see Figure 46) so that

$$\overrightarrow{O_PP} = R_f\cos(\Psi_P)\,\overrightarrow{e_x} + R_f\sin(\Psi_P)\,\overrightarrow{e_y}$$

assuming the elements are lightly twisted (O_P is the center of element p_1 of substage p_2 at z_P and P is the source point located on the superconducting shell of element p_1 of substage p_2 at z_P).

$s_{p_1p_2}(z_P)$ being the abscissa corresponding to the position of O_P along the trajectory of the center of element p_1 of substage p_2 at z_P, we can thus write

$$ds_{p_1p_2}(z_P) = \left\|\overrightarrow{dOO_P}\right\|$$

Since $\overrightarrow{e_{s_{p_1p_2}}}(z_P)$ is the unit vector tangent to the trajectory of the center of element p_1 of substage p_2 at z_P and O_P is the center of element p_1 of substage p_2 at z_P, we have

$$\overrightarrow{e_{s_{p_1p_2}}}(z_P) = \frac{\overrightarrow{dOO_P}}{\left\|\overrightarrow{dOO_P}\right\|}$$

Consequently, the term $\overrightarrow{e_{s_{p_1p_2}}}(z_P).\overrightarrow{e_z}d\Sigma$ in equation (268) can be expressed as

$$\overrightarrow{e_{s_{p_1p_2}}}(z_P).\overrightarrow{e_z}d\Sigma = \frac{\overrightarrow{dOO_P}}{\left\|\overrightarrow{dOO_P}\right\|}.\overrightarrow{e_z}R_f d\Psi_P\left\|\overrightarrow{dOO_P}\right\| = \overrightarrow{dOO_P}.\overrightarrow{e_z}R_f d\Psi_P = R_f d\Psi_P dz_P$$

Therefore replacing $\overrightarrow{e_{s_{p_1p_2}}}(z_P).\overrightarrow{e_z}d\Sigma$ with the expression above and $K^{(\alpha)}_{p_1p_2}(P)$ with $K_0^{(\alpha)}\cos\left(\alpha z_P + \varphi_{p_1p_2}\right)$ into the formula of $A^{(\alpha)}_{z_{r_{(p_1p_2)}}}\left(M_{k_1k_2}\right)$ given by (268), we now obtain

$$A^{(\alpha)}_{z_{r_{(p_1p_2)}}}\left(M_{k_1k_2}\right) = \frac{\mu_0 I_0^{(\alpha)}}{8\pi^2}\int_{z_p=-\infty}^{+\infty}\int_{\Psi_p=0}^{2\pi}\frac{\cos\left(\alpha z_P + \varphi_{p_1p_2}\right)}{PM_{k_1k_2}(z, z_p, \Psi_p)}d\Psi_P dz_P \tag{269}$$

Let us now express the distance $PM_{k_1k_2}(z, z_P, \Psi_P)$.

Since P is the source point located on the superconducting shell of element p_1 of substage p_2 at z_P and $M_{k_1k_2}$ is the center of element k_1 of substage k_2 at z, their coordinates in the $(\overrightarrow{e_x}, \overrightarrow{e_y}, \overrightarrow{e_z})$ basis are given by

$$\begin{cases}\overrightarrow{OP} = \overrightarrow{OO_P} + \overrightarrow{O_PP} = \left[x_{p_1p_2}(z_P) + R_f cos(\Psi_P)\right]\overrightarrow{e_x} + \left[y_{p_1p_2}(z_P) + R_f sin(\Psi_P)\right]\overrightarrow{e_y} + z_P\,\overrightarrow{e_z} \\ \overrightarrow{OM_{k_1k_2}} = x_{k_1k_2}(z)\,\overrightarrow{e_x} + y_{k_1k_2}(z)\overrightarrow{e_y} + z\,\overrightarrow{e_z}\end{cases}$$

In order to ease the expression and the manipulation of $PM_{k_1k_2}(z, z_P, \Psi_P)$, let us note $w(z)$ the complex affix of a point with coordinates (x, y, z) in the plane orthogonal to the z-axis such that

$$w = x + iy$$

where i is the imaginary unit.

Consequently, using equations (250) to (252), the complex affix $w_{M_{k_1k_2}}(z)$ of the point $M_{k_1k_2}$ is

$$w_{k_1k_2}(z) = x_{k_1k_2}(z) + iy_{k_1k_2}(z) = R_{c_2}e^{i\left[\frac{2\pi z}{l_{p_2}} + \frac{2\pi(k_2-1)}{N_2}\right]} + R_{c_1}e^{i\left[\frac{2\pi z}{l_{p_1}} + \frac{2\pi(k_1-1)}{N_1}\right]} \tag{270}$$

and the complex affix $w_P(z_P, \Psi_P)$ of the source point P is

$$\begin{aligned} w_P(z_P, \Psi_P) &= \left[x_{p_1p_2}(z) + R_f cos(\Psi_P)\right] + i\left[y_{p_1p_2}(z) + R_f sin(\Psi_P)\right] \\ &= R_{c_2}e^{i\left[\frac{2\pi z_P}{l_{p_2}} + \frac{2\pi(p_2-1)}{N_2}\right]} + R_{c_1}e^{i\left[\frac{2\pi z_P}{l_{p_1}} + \frac{2\pi(p_1-1)}{N_1}\right]} + R_f e^{i\Psi_P}\end{aligned}$$

Making use of this notation, we can now write

$$PM_{k_1k_2}(z, z_P, \Psi_P)^2 = \left|w_{k_1k_2}(z) - w_P(z_P, \Psi_P)\right|^2 + [z - z_P]^2$$

where the notation $|X|$ refers to the modulus of X.

Replacing $w_{k_1k_2}(z)$ and $w_P(z_P, \Psi_P)$ with their expressions, after some manipulations, $PM_{k_1k_2}(z, z_P, \Psi_P)^2$ can be expressed as

$$PM_{k_1k_2}(z,z_P,\Psi_P)^2 = \begin{cases} [z-z_P]^2 + {R_{c_2}}^2 \left| \left(1 - e^{i\left[\frac{2\pi(z_P-z)}{l_{p_2}} + \frac{2\pi(p_2-k_2)}{N_2}\right]} - \frac{R_f}{R_{c_2}} e^{i\left[\Psi_P - \frac{2\pi z}{l_{p_2}} - \frac{2\pi(k_2-1)}{N_2}\right]} \right.\right. \\ \left.\left. + \frac{R_{c_1}}{R_{c_2}} e^{i\left[2\pi z\left(\frac{1}{l_{p_1}} - \frac{1}{l_{p_2}}\right) + 2\pi\left(\frac{k_1-1}{N_1} - \frac{k_2-1}{N_2}\right)\right]} \left(1 - e^{i\left[\frac{2\pi(z_P-z)}{l_{p_1}} + \frac{2\pi(p_1-k_1)}{N_1}\right]}\right)\right)\right|^2 \end{cases}$$

We will now carry out the following changes of variable in integral (269)

$$\begin{cases} z' = z_P - z \\ \Psi' = \Psi_P - \left[\frac{2\pi z}{l_{p_2}} + \frac{2\pi(k_2-1)}{N_2}\right] \end{cases}$$

This implies

$$\begin{cases} dz' = dz_P \\ d\Psi' = d\Psi_P \end{cases}$$

The interval of integration of z_P being infinite, the new interval of integration of z' also remains infinite, i.e. from $-\infty$ to $+\infty$. In addition, $PM_{k_1k_2}(z,z_p,\Psi_p)$ is a 2π-periodic function of Ψ_P, thus even with the change of variable of Ψ_P into Ψ', we choose to keep the same interval of integration for Ψ' which is $[0;2\pi]$.

As a result, it is now possible to re-express integral (269) as

$$A^{(\alpha)}_{z_{r_{(p_1p_2)}}}\left(M_{k_1k_2}\right) = \frac{\mu_0 I_0^{(\alpha)}}{8\pi^2} Re\left(\int_{z'=-\infty}^{+\infty}\int_{\Psi'=0}^{2\pi} \frac{e^{i\alpha(z'+z)+\varphi_{p_1p_2}}}{g_{p_1p_2\,k_1k_2}(z,z',\Psi')} d\Psi' dz'\right) \tag{271}$$

where $Re(X)$ refers to the real part of complex number X and $g_{p_1p_2\,k_1k_2}(z,z',\Psi')$ is given by

$$\begin{aligned} {g_{p_1p_2\,k_1k_2}}^2(z,z',\Psi') \\ = \begin{cases} {z'}^2 + {R_{c_2}}^2 \left| \left(1 - e^{i\left[\frac{2\pi z'}{l_{p_2}} + \frac{2\pi(p_2-k_2)}{N_2}\right]} - \frac{R_f}{R_{c_2}} e^{i\Psi'} \right.\right. \\ \left.\left. + \frac{R_{c_1}}{R_{c_2}} e^{i\left[2\pi z\left(\frac{1}{l_{p_1}} - \frac{1}{l_{p_2}}\right) + 2\pi\left(\frac{k_1-1}{N_1} - \frac{k_2-1}{N_2}\right)\right]} \left(1 - e^{i\left[\frac{2\pi z'}{l_{p_1}} + \frac{2\pi(p_1-k_1)}{N_1}\right]}\right)\right)\right|^2 \end{cases} \end{aligned} \tag{272}$$

From the expression of $g_{p_1p_2\,k_1k_2}(z,z',\Psi')$ given by equation (272), we can see that it is a l-periodic function of z with

$$l = \frac{1}{l_{p_1}} - \frac{1}{l_{p_2}} \tag{273}$$

Note that l actually corresponds to the distance that separates two consecutive contacts between elements of adjacent substages.

We can therefore conclude that the function $1/g_{p_1p_2\,k_1k_2}(z,z',\Psi')$ inside integral (271) is also a l-periodic function of z and can thus be expanded in Fourier series as

$$\frac{1}{g_{p_1p_2\,k_1k_2}(z,z',\Psi')}=\sum_{n=-\infty}^{+\infty}c_n(z',\Psi')e^{i\frac{2\pi nz}{l}} \tag{274}$$

with

$$c_n(z',\Psi')=\frac{1}{l}\int_{z''=-l/2}^{l/2}\frac{e^{-i\frac{2\pi nz''}{l}}}{g_{p_1p_2\,k_1k_2}(z'',z',\Psi')}dz'' \tag{275}$$

In order to lighten the formulae, we will now use the complex notation $\overline{A^{(\alpha)}_{z_{r(p_1p_2)}}}\left(M_{k_1k_2}\right)$ such that

$$A^{(\alpha)}_{z_{r(p_1p_2)}}\left(M_{k_1k_2}\right)=Re\left(\overline{A^{(\alpha)}_{z_{r(p_1p_2)}}}\left(M_{k_1k_2}\right)\right) \tag{276}$$

As a result, using integral (271) and equations (274) and (276), we have

$$\overline{A^{(\alpha)}_{z_{r(p_1p_2)}}}\left(M_{k_1k_2}\right)=\frac{\mu_0 I_0^{(\alpha)}}{8\pi^2}\sum_{n=-\infty}^{+\infty}e^{i\left[\left(\alpha+\frac{2\pi n}{l}\right)z+\varphi_{p_1p_2}\right]}X^{(\alpha)}_{n_{p_1p_2\,k_1k_2}} \tag{277}$$

with

$$\begin{aligned}&X^{(\alpha)}_{n_{p_1p_2\,k_1k_2}}\\&=\frac{1}{l}\int_{z'=-\infty}^{+\infty}e^{i\alpha z'}\int_{z''=-l/2}^{l/2}e^{-i\frac{2\pi nz''}{l}}\int_{\Psi'=0}^{2\pi}\frac{1}{g_{p_1p_2\,k_1k_2}(z'',z',\Psi')}d\Psi'\,dz''\,dz'\end{aligned} \tag{278}$$

where l is given by (273) and $g_{p_1p_2\,k_1k_2}(z'',z',\Psi')$ is given by

$$g_{p_1p_2\,k_1k_2}(z'',z',\Psi')=\left\{\begin{array}{l}\left[{z'}^2+{R_{c_2}}^2\left|1-e^{i\left[\frac{2\pi z'}{l_{p_2}}+\frac{2\pi(p_2-k_2)}{N_2}\right]}-\frac{R_f}{R_{c_2}}e^{i\Psi'}\right.\right.\\\left.\left.+\frac{R_{c_1}}{R_{c_2}}e^{i\left[\frac{2\pi z''}{l}+2\pi\left(\frac{k_1-1}{N_1}-\frac{k_2-1}{N_2}\right)\right]}\left(1-e^{i\left[\frac{2\pi z'}{l_{p_1}}+\frac{2\pi(p_1-k_1)}{N_1}\right]}\right)\right|^2\right]^{1/2}\end{array}\right. \tag{279}$$

This result is important as we have shown that the magnetic vector potential generated by a current with any spatial frequency α flowing in an element of the conductor contains the following spatial frequencies

$$\left(\alpha+2\pi n\left(\frac{1}{l_{p_1}}-\frac{1}{l_{p_2}}\right)\right)_{n\in\mathbb{Z}}$$

Indeed, without this knowledge, we would not be able to solve the equations of the system, i.e. equations (266).

IV.2.5.2 Calculation of the magnetic vector potential due to the currents flowing in all the elements

Let us note $\left(\overrightarrow{K_{p_1p_2}^{(\alpha)}} = K_{p_1p_2}^{(\alpha)}\overrightarrow{e_{s_{p_1p_2}}}\right)_{1\le p_1\le N_1, 1\le p_2\le N_2}$ the surface currents flowing through the superconducting shells of all the elements having the general form $K_{p_1p_2}^{(\alpha)}(z) = K_0^{(\alpha)}\cos\left(\alpha z + \varphi_{p_1p_2}\right)$ with

$$K_0^{(\alpha)} = \frac{I_0^{(\alpha)}}{2\pi R_f}$$

Let us note $A_{z_r}^{(\alpha)}\left(M_{k_1k_2}\right)$ the magnetic vector potential felt at the center of element k_1 of substage k_2 at z (noted $M_{k_1k_2}$) and due to the current distributions $\left(\overrightarrow{K_{p_1p_2}^{(\alpha)}} = K_{p_1p_2}^{(\alpha)}\overrightarrow{e_{s_{p_1p_2}}}\right)_{1\le p_1\le N_1, 1\le p_2\le N_2}$.

Following the definition of $A_{z_{r_{(p_1p_2)}}}^{(\alpha)}\left(M_{k_1k_2}\right)$ and $A_{z_r}^{(\alpha)}\left(M_{k_1k_2}\right)$, by superposition, we have

$$A_{z_r}^{(\alpha)}\left(M_{k_1k_2}\right) = \sum_{p_2=1}^{N_2}\sum_{p_1=1}^{N_1} A_{z_{r_{(p_1p_2)}}}^{(\alpha)}\left(M_{k_1k_2}\right)$$

Again using the complex notation $\overline{A_{z_r}^{(\alpha)}}\left(M_{k_1k_2}\right)$ such that

$$A_{z_r}^{(\alpha)}\left(M_{k_1k_2}\right) = Re\left(\overline{A_{z_r}^{(\alpha)}}\left(M_{k_1k_2}\right)\right) \tag{280}$$

we can write

$$\overline{A_{z_r}^{(\alpha)}}\left(M_{k_1k_2}\right) = \sum_{p_2=1}^{N_2}\sum_{p_1=1}^{N_1} \overline{A_{z_{r_{(p_1p_2)}}}^{(\alpha)}}\left(M_{k_1k_2}\right)$$

Using the expression of $\overline{A_{z_{r_{(p_1p_2)}}}^{(\alpha)}}\left(M_{k_1k_2}\right)$ given by (277), we now have

$$\overline{A_{z_r}^{(\alpha)}}\left(M_{k_1k_2}\right) = \frac{\mu_0 I_0^{(\alpha)}}{8\pi^2}\sum_{n=-\infty}^{+\infty} e^{i\left(\alpha+\frac{2\pi n}{l}\right)z}\sum_{p_2=1}^{N_2}\sum_{p_1=1}^{N_1} X_{n_{p_1p_2\,k_1k_2}}^{(\alpha)} e^{i\varphi_{p_1p_2}} \tag{281}$$

In order to be consistent with the previous notations, let us note $A_{z_{r_{k_1k_2}}}^{(\alpha)}(z)$ the axial component of the magnetic vector potential felt at the center of element k_1 of substage k_2 at z and due to the current distributions $\left(\overrightarrow{K_{p_1p_2}^{(\alpha)}} = K_{p_1p_2}^{(\alpha)}\overrightarrow{e_{s_{p_1p_2}}}\right)_{1\le p_1\le N_1, 1\le p_2\le N_2}$. Using again the complex notation, we have

$$\overline{A_{z_{r_{k_1k_2}}}^{(\alpha)}}(z) = \overline{A_{z_r}^{(\alpha)}}\left(M_{k_1k_2}\right)$$

IV.2.5.3 New currents induced by the time-variation of currents flowing in all the elements

We now know the expression of the magnetic vector potential generated by surface currents flowing through the superconducting shells of all the elements and having the general form $K_{p_1p_2}^{(\alpha)}(z) = K_0^{(\alpha)}\cos(\alpha z + \varphi_{p_1p_2})$.

Using equation (281), we can then write

$$\left[2\overline{\dot{A}_{z_{r_{k_1k_2}}}^{(\alpha)}}(z) - \overline{\dot{A}_{z_{r_{k_1-1\,k_2}}}^{(\alpha)}}(z) - \overline{\dot{A}_{z_{r_{k_1+1\,k_2}}}^{(\alpha)}}(z)\right] = \frac{\mu_0 \dot{I}_0^{(\alpha)}}{8\pi^2}\sum_{n=-\infty}^{+\infty} e^{i\left(\alpha+\frac{2\pi n}{l}\right)z}\sum_{p_2=1}^{N_2}\sum_{p_1=1}^{N_1} C_{n_{p_1p_2\,k_1k_2}}^{(\alpha)} e^{i\varphi_{p_1p_2}} \tag{282}$$

with

$$C_{n_{p_1p_2\,k_1k_2}}^{(\alpha)} = 2X_{n_{p_1p_2\,k_1k_2}}^{(\alpha)} - X_{n_{p_1p_2\,k_1-1k_2}}^{(\alpha)} - X_{n_{p_1p_2\,k_1+1k_2}}^{(\alpha)} \tag{283}$$

and

$$\sum_{j_1=1}^{N_1}\left[2\overline{\dot{A}_{z_{r_{j_1\,k_2}}}^{(\alpha)}}(z) - \overline{\dot{A}_{z_{r_{j_1\,k_2-1}}}^{(\alpha)}}(z) - \overline{\dot{A}_{z_{r_{j_1\,k_2+1}}}^{(\alpha)}}(z)\right] = \frac{\mu_0 \dot{I}_0^{(\alpha)}}{8\pi^2}\sum_{n=-\infty}^{+\infty} e^{i\left(\alpha+\frac{2\pi n}{l}\right)z}\sum_{p_2=1}^{N_2}\sum_{p_1=1}^{N_1} C_{n_{p_1p_2\,k_2}}^{(\alpha)} e^{i\varphi_{p_1p_2}} \tag{284}$$

with

$$C_{n_{p_1p_2\,k_2}}^{(\alpha)} = \sum_{j_1=1}^{N_1}\left[2X_{n_{p_1p_2\,j_1k_2}}^{(\alpha)} - X_{n_{p_1p_2\,j_1k_2-1}}^{(\alpha)} - X_{n_{p_1p_2\,j_1k_2+1}}^{(\alpha)}\right] \tag{285}$$

According to the equations of the system, i.e. equations (266), and to equations (282) and (284), we see that the time-variation of surface currents of the form $\left(\overrightarrow{K_{p_1p_2}^{(\alpha)}} = K_0^{(\alpha)}\cos(\alpha z + \varphi_{p_1p_2})\,\overrightarrow{e_{s_{p_1p_2}}}\right)_{1\le p_1\le N_1, 1\le p_2\le N_2}$ will give rise to new distributions of currents $\overline{I_{k_1k_2}}(z)$ such that for $1 \le k_2 \le N_2$ and $1 \le k_1 \le N_1$

$$\frac{d^2\overline{I_{k_1k_2}}}{dz^2}(z) = \frac{\mu_0 \dot{I}_0^{(\alpha)}}{8\pi^2}\sum_{n=-\infty}^{+\infty} e^{i\left(\alpha+\frac{2\pi n}{l}\right)z}\sum_{p_2=1}^{N_2}\sum_{p_1=1}^{N_1} D_{n_{p_1p_2\,k_1k_2}}^{(\alpha)} e^{i\varphi_{p_1p_2}} \tag{286}$$

with

$$D_{n_{p_1p_2\,k_1k_2}}^{(\alpha)} = \sigma_{l_1} C_{n_{p_1p_2\,k_1k_2}}^{(\alpha)} + \frac{\sigma_{l_2}}{{N_1}^2} C_{n_{p_1p_2\,k_2}}^{(\alpha)} \tag{287}$$

where again $\overline{I_{k_1k_2}}(z)$ is the complex notation associated with $I_{k_1k_2}(z)$ such that

$$I_{k_1k_2}(z) = Re\left(\overline{I_{k_1k_2}}(z)\right)$$

The double integration of equation (286) with respect to z leads to

$$\overline{I_{k_1k_2}}(z) = -\frac{\mu_0 \dot{I}_0^{(\alpha)}}{8\pi^2} \sum_{n=-\infty}^{+\infty} \frac{e^{i\left(\alpha+\frac{2\pi n}{l}\right)z}}{\left(\alpha+\frac{2\pi n}{l}\right)^2} \sum_{p_2=1}^{N_2} \sum_{p_1=1}^{N_1} D^{(\alpha)}_{n_{p_1p_2}\,k_1k_2} e^{i\varphi_{p_1p_2}} \tag{288}$$

This result is important as it shows that the time-variation of surface currents with spatial frequency α will induce new currents with the following infinity of spatial frequencies

$$\left(\alpha + 2\pi n\left(\frac{1}{l_{p_1}} - \frac{1}{l_{p_2}}\right)\right)_{n\in\mathbb{Z}}$$

Note that, according to equation (288), the amplitude associated with the spatial frequency $\alpha + 2\pi n\left(\frac{1}{l_{p_1}} - \frac{1}{l_{p_2}}\right)$ features a term in $1/\left(\alpha+\frac{2\pi n}{l}\right)^2$. Therefore the higher the order of the spatial frequency, i.e. the higher n, the smaller its amplitude.

In addition, since the currents induced in steady-state regime feature the spatial frequencies $2\pi/l_{p_1}$ and $2\pi/l_{p_2}$, their time-variation will induce currents with spatial frequencies $\left(\frac{2\pi}{l_{p_1}} + 2\pi n\left(\frac{1}{l_{p_1}} - \frac{1}{l_{p_2}}\right)\right)_{n\in\mathbb{Z}}$ and $\left(\frac{2\pi}{l_{p_2}} + 2\pi n\left(\frac{1}{l_{p_1}} - \frac{1}{l_{p_2}}\right)\right)_{n\in\mathbb{Z}}$.

In order to lighten the future expressions we will now use the following notation for any $n \in \mathbb{Z}$

$$\alpha_n = \frac{2\pi}{l_{p_1}} + 2\pi(n-1)\left(\frac{1}{l_{p_2}} - \frac{1}{l_{p_1}}\right) \tag{289}$$

so that

$$\begin{cases} \alpha_1 = \dfrac{2\pi}{l_{p_1}} \\ \alpha_2 = \dfrac{2\pi}{l_{p_2}} \end{cases}$$

Therefore the previous families are now noted as

$$\left(\frac{2\pi}{l_{p_1}} + 2\pi n\left(\frac{1}{l_{p_1}} - \frac{1}{l_{p_2}}\right)\right)_{n\in\mathbb{Z}} = (\alpha_{1-n})_{n\in\mathbb{Z}}$$

and

$$\left(\frac{2\pi}{l_{p_2}} + 2\pi n\left(\frac{1}{l_{p_1}} - \frac{1}{l_{p_2}}\right)\right)_{n\in\mathbb{Z}} = (\alpha_{-n+2})_{n\in\mathbb{Z}}$$

We can notice that these two families are actually identical and equal to $(\alpha_n)_{n\in\mathbb{Z}}$. Indeed, we have

$$(\alpha_{1-n})_{n\in\mathbb{Z}} = \left(\alpha_{1-(n'-1)}\right)_{n'\in\mathbb{Z}} = (\alpha_{2-n'})_{n'\in\mathbb{Z}} = (\alpha_{2-n})_{n\in\mathbb{Z}} = (\alpha_n)_{n\in\mathbb{Z}}$$

Therefore the time-variation of the currents induced in steady-state regime (featuring the spatial frequencies $2\pi/l_{p_1}$ and $2\pi/l_{p_2}$) will induce currents with spatial frequencies $(\alpha_n)_{n\in\mathbb{Z}}$.

Following the logical chain displayed on Figure 15 in section II.2.1 , we now have to determine the currents that will be induced by the time-variation of the currents with a spatial frequency belonging to the family $(\alpha_n)_{n\in\mathbb{Z}}$. Since we know that the time-variation of currents with any spatial frequency α will induce currents with the spatial frequencies $\left(\alpha + 2\pi n\left(\frac{1}{l_{p_1}} - \frac{1}{l_{p_2}}\right)\right)_{n\in\mathbb{Z}}$, we can deduce that the time-variation of the currents with a spatial frequency α_k, $k \in \mathbb{Z}$ will induce currents with the spatial frequencies $\left(\alpha_k + 2\pi n\left(\frac{1}{l_{p_1}} - \frac{1}{l_{p_2}}\right)\right)_{n\in\mathbb{Z}}$, $k \in \mathbb{Z}$. This family is again equal to $(\alpha_n)_{n\in\mathbb{Z}}$, because for any $k \in \mathbb{Z}$, we have

$$\left(\alpha_k + 2\pi n\left(\frac{1}{l_{p_1}} - \frac{1}{l_{p_2}}\right)\right)_{n\in\mathbb{Z}} = \left(\frac{2\pi}{l_{p_1}} + 2\pi(k-n+1)\left(\frac{1}{l_{p_2}} - \frac{1}{l_{p_1}}\right)\right)_{n\in\mathbb{Z}} = (\alpha_{k-n})_{n\in\mathbb{Z}} = (\alpha_n)_{n\in\mathbb{Z}}$$

We can now conclude that we have reached the end of our analytical procedure described in section II.2.1 because we have demonstrated that the currents that will be induced in the N_2-uplet of N_1-uplets conductor during any time varying regime will necessarily feature the spatial frequencies of the family $(\alpha_n)_{n\in\mathbb{Z}}$.

Consequently, we now know that the currents induced during any time-varying regime will be given for $1 \le k_1 \le N_1$ and $1 \le k_2 \le N_2$ by

$$\overline{I_{k_1k_2}}(z) = \sum_{n=-\infty}^{+\infty} \overline{I_{0_{k_1k_2}}^{(\alpha_n)}}\, e^{i\alpha_n z} \tag{290}$$

where the $\overline{I_{0_{k_1k_2}}^{(\alpha_n)}}$ for $n \in \mathbb{Z}$ are complex functions depending on time only.

Note that if $\alpha_1 \neq \alpha_2$ the elements of the family $(\alpha_n)_{n\in\mathbb{Z}}$ are all distinct from each other (if $\alpha_1 = \alpha_2$, the family $(\alpha_n)_{n\in\mathbb{Z}}$ is simply reduced to α_1).

Indeed, for $k \in \mathbb{Z}$ and $n \in \mathbb{Z}$, the equation $\alpha_k = \alpha_n$ leads to $(k-n)(\alpha_2 - \alpha_1) = 0$; the solution must then be $k = n$ if $\alpha_2 - \alpha_1 \neq 0$.

IV.2.5.4 Reduction of the global equations of the system for any time-varying regime

❖ **We have now established the expression of the magnetic vector potential as a function of the coupling currents; we also know the spatial form of these currents for any time-varying regime. First, we will make use of this knowledge to reformulate the global equation of the system, which will be presented at the end of IV.2.5.4.1. We will then use an invariance of the system and different considerations and approximations to finally reduce the system equation to a simple 4x4 matrix equation (this is achieved through IV.2.5.4.2 to IV.2.5.4.4).**

IV.2.5.4.1 Expression of the system equations using the determined spatial form of the induced currents

Let us now express the equations of the system in complex notations from equations (260), we have for $1 \leq k_1 \leq N_1$ and $1 \leq k_2 \leq N_2$

$$\begin{cases} \dfrac{d^2\overline{I_{k_1k_2}}}{dz^2}(z) - \sigma_{l_1}\left[2\overline{\dot{A}_{z_{r_{k_1\,k_2}}}}(z) - \overline{\dot{A}_{z_{r_{k_1-1\,k_2}}}}(z) - \overline{\dot{A}_{z_{r_{k_1+1\,k_2}}}}(z)\right] \\ \quad -\dfrac{\sigma_{l_2}}{{N_1}^2}\displaystyle\sum_{j_1=1}^{N_1}\left[2\overline{\dot{A}_{z_{r_{J_1\,k_2}}}}(z) - \overline{\dot{A}_{z_{r_{J_1\,k_2-1}}}}(z) - \overline{\dot{A}_{z_{r_{J_1\,k_2+1}}}}(z)\right] = \\ -4\sigma_{l_1}R_{c_1}\dot{B}_a\sin^2\left(\dfrac{\pi}{N_1}\right)e^{i\left[\frac{2\pi z}{l_{p_1}}+\frac{2\pi(k_1-1)}{N_1}\right]} - 4\dfrac{\sigma_{l_2}}{N_1}R_{c_2}\dot{B}_a\sin^2\left(\dfrac{\pi}{N_2}\right)e^{i\left[\frac{2\pi z}{l_{p_2}}+\frac{2\pi(k_2-1)}{N_2}\right]} \end{cases} \quad (291)$$

To simplify these equations, we will now make use of the knowledge of the spatial form of the currents induced during any time-varying regime given by (290) which is

$$\overline{I_{k_1k_2}}(z) = \sum_{k=-\infty}^{+\infty}\overline{I_{0_{k_1k_2}}^{(\alpha_k)}}e^{i\alpha_k z}$$

In order to do so, we will replace the expressions on the left-hand side of equations (291) with their new expressions. First, we have

$$\frac{d^2\overline{I_{k_1k_2}}}{dz^2}(z) = \frac{d^2}{dz^2}\left(\sum_{k=-\infty}^{+\infty}\overline{I_{0_{k_1k_2}}^{(\alpha_k)}}e^{i\alpha_k z}\right) = \sum_{k=-\infty}^{+\infty}\overline{I_{0_{k_1k_2}}^{(\alpha_k)}}\frac{d^2}{dz^2}\left(e^{i\alpha_k z}\right) = \sum_{k=-\infty}^{+\infty}-{\alpha_k}^2\overline{I_{0_{k_1k_2}}^{(\alpha_k)}}e^{i\alpha_k z}$$

Then, applying again the methodology of section IV.2.5.1 , we can adapt equation (277) to give the following expression of the magnetic vector potential $\overline{A_{z_{r_{(p_1p_2)}}}^{(\alpha_k)}}\left(M_{k_1k_2}\right)$ generated by a current flowing through element p_1 of substage p_2 of the form $\overline{I_{p_1p_2}}(z) = \overline{I_{0_{p_1p_2}}^{(\alpha_k)}}e^{i\alpha_k z}$ with $k \in \mathbb{Z}$

$$\overline{A_{z_{r_{(p_1p_2)}}}^{(\alpha_k)}}\left(M_{k_1k_2}\right) = \frac{\mu_0\overline{I_{0_{p_1p_2}}^{(\alpha_k)}}}{8\pi^2}\sum_{n=-\infty}^{+\infty}e^{i\left(\alpha_k+\frac{2\pi n}{l}\right)z}X_{n_{p_1p_2\,k_1k_2}}^{(\alpha_k)} = \frac{\mu_0\overline{I_{0_{p_1p_2}}^{(\alpha_k)}}}{8\pi^2}\sum_{n=-\infty}^{+\infty}e^{i\alpha_{k-n}z}X_{n_{p_1p_2\,k_1k_2}}^{(\alpha_k)}$$

Therefore, by superposition, the magnetic vector potential $\overline{A_{z_{r_{(p_1p_2)}}}}\left(M_{k_1k_2}\right)$ generated by a current flowing through element p_1 of substage p_2 of the form $\overline{I_{p_1p_2}}(z) = \sum_{k=-\infty}^{+\infty}\overline{I_{0_{p_1p_2}}^{(\alpha_k)}}e^{i\alpha_k z}$ is given by

$$\overline{A_{z_{r_{(p_1p_2)}}}}\left(M_{k_1k_2}\right) = \frac{\mu_0}{8\pi^2}\sum_{k=-\infty}^{+\infty}\overline{I_{0_{p_1p_2}}^{(\alpha_k)}}\sum_{n=-\infty}^{+\infty}e^{i\alpha_{k-n}z}X_{n_{p_1p_2\,k_1k_2}}^{(\alpha_k)}$$

Again by superposition, the magnetic vector potential $\overline{\overline{A_{z_{r_{k_1 k_2}}}}}(z)$ generated at the center of element k_1 of substage k_2 at z by all the currents flowing through the N_2-uplet of N_1-uplets conductor during any time varying regime is thus in complex notation

$$\overline{\overline{A_{z_{r_{k_1 k_2}}}}}(z) = \overline{\overline{A_{z_r}}}\left(M_{k_1 k_2}\right) = \frac{\mu_0}{8\pi^2} \sum_{k=-\infty}^{+\infty} \sum_{p_2=1}^{N_2} \sum_{p_1=1}^{N_1} \overline{I_{0_{p_1 p_2}}^{(\alpha_k)}} \sum_{n=-\infty}^{+\infty} e^{i\alpha_{k-n} z} X_{n_{p_1 p_2\, k_1 k_2}}^{(\alpha_k)} \tag{292}$$

The term

$$\left[2\overline{\dot{A}_{z_{r_{k_1\, k_2}}}}(z) - \overline{\dot{A}_{z_{r_{k_1-1\, k_2}}}}(z) - \overline{\dot{A}_{z_{r_{k_1+1\, k_2}}}}(z)\right]$$

present in the equations of the system, i.e. equations (291), can now be replaced with

$$\frac{\mu_0}{8\pi^2} \sum_{k=-\infty}^{+\infty} \sum_{p_2=1}^{N_2} \sum_{p_1=1}^{N_1} \overline{\dot{I}_{0_{p_1 p_2}}^{(\alpha_k)}} \sum_{n=-\infty}^{+\infty} e^{i\alpha_{k-n} z} C_{n_{p_1 p_2\, k_1 k_2}}^{(\alpha_k)}$$

where

$$C_{n_{p_1 p_2\, k_1 k_2}}^{(\alpha_k)} = 2X_{n_{p_1 p_2\, k_1 k_2}}^{(\alpha_k)} - X_{n_{p_1 p_2\, k_1-1 k_2}}^{(\alpha_k)} - X_{n_{p_1 p_2\, k_1+1 k_2}}^{(\alpha_k)} \tag{293}$$

and the term

$$\sum_{j_1=1}^{N_1} \left[2\overline{\dot{A}_{z_{r_{j_1\, k_2}}}(z)} - \overline{\dot{A}_{z_{r_{j_1\, k_2-1}}}}(z) - \overline{\dot{A}_{z_{r_{j_1\, k_2+1}}}(z)}\right]$$

also present in the equations of the system can now be replaced with

$$\frac{\mu_0}{8\pi^2} \sum_{k=-\infty}^{+\infty} \sum_{p_2=1}^{N_2} \sum_{p_1=1}^{N_1} \overline{\dot{I}_{0_{p_1 p_2}}^{(\alpha_k)}} \sum_{n=-\infty}^{+\infty} e^{i\alpha_{k-n} z} C_{n_{p_1 p_2\, k_2}}^{(\alpha_k)}$$

where

$$C_{n_{p_1 p_2\, k_2}}^{(\alpha_k)} = \sum_{j_1=1}^{N_1} \left[2X_{n_{p_1 p_2\, j_1 k_2}}^{(\alpha_k)} - X_{n_{p_1 p_2\, j_1 k_2-1}}^{(\alpha_k)} - X_{n_{p_1 p_2\, j_1 k_2+1}}^{(\alpha_k)}\right] \tag{294}$$

The $X_{n_{p_1 p_2\, k_1 k_2}}^{(\alpha_k)}$ are given by (278) with $\alpha = \alpha_k$.

As a result, we can now replace the global term

$$\begin{cases} \sigma_{l_1}\left[2\overline{\dot{A}_{z_{r_{k_1\, k_2}}}}(z) - \overline{\dot{A}_{z_{r_{k_1-1\, k_2}}}}(z) - \overline{\dot{A}_{z_{r_{k_1+1\, k_2}}}}(z)\right] \\ + \dfrac{\sigma_{l_2}}{{N_1}^2} \displaystyle\sum_{j_1=1}^{N_1} \left[2\overline{\dot{A}_{z_{r_{j_1\, k_2}}}(z)} - \overline{\dot{A}_{z_{r_{j_1\, k_2-1}}}}(z) - \overline{\dot{A}_{z_{r_{j_1\, k_2+1}}}(z)}\right] \end{cases}$$

of equations (291) with

$$\frac{\mu_0}{8\pi^2}\sum_{k=-\infty}^{+\infty}\sum_{p_2=1}^{N_2}\sum_{p_1=1}^{N_1}\overline{\dot{I}_{0_{p_1p_2}}^{(\alpha_k)}}\sum_{n=-\infty}^{+\infty}e^{i\alpha_{k-n}z}D_{n_{p_1p_2\,k_1k_2}}^{(\alpha_k)}$$

where

$$D_{n_{p_1p_2\,k_1k_2}}^{(\alpha_k)}=\sigma_{l_1}C_{n_{p_1p_2\,k_1k_2}}^{(\alpha_k)}+\frac{\sigma_{l_2}}{{N_1}^2}C_{n_{p_1p_2\,k_2}}^{(\alpha_k)} \tag{295}$$

Using these substitutions, the equations of the system can now be expressed for $1\leq k_1\leq N_1$ and $1\leq k_2\leq N_2$ as

$$\begin{cases}\displaystyle\sum_{k=-\infty}^{+\infty}{\alpha_k}^2\overline{I_{0_{k_1k_2}}^{(\alpha_k)}}e^{i\alpha_k z}+\frac{\mu_0}{8\pi^2}\sum_{k=-\infty}^{+\infty}\sum_{p_2=1}^{N_2}\sum_{p_1=1}^{N_1}\overline{\dot{I}_{0_{p_1p_2}}^{(\alpha_k)}}\sum_{n=-\infty}^{+\infty}e^{i\alpha_{k-n}z}D_{n_{p_1p_2\,k_1k_2}}^{(\alpha_k)}= \\ 4\sigma_{l_1}R_{c_1}\dot{B}_a\sin^2\left(\frac{\pi}{N_1}\right)e^{i\frac{2\pi(k_1-1)}{N_1}}e^{i\alpha_1 z}+4\frac{\sigma_{l_2}}{N_1}R_{c_2}\dot{B}_a\sin^2\left(\frac{\pi}{N_2}\right)e^{i\frac{2\pi(k_2-1)}{N_2}}e^{i\alpha_2 z}\end{cases} \tag{296}$$

IV.2.5.4.2 Invariance of the system

We will now make use of an invariance of the system to reduce equations (296). Indeed from equation (270), we know that for $1\leq k_1\leq N_1$ and $1\leq k_2\leq N_2$ the complex affix $w_{k_1k_2}(z)$ of the center of element k_1 of substage k_2 at z in the plane orthogonal to the z-axis is

$$w_{k_1k_2}(z)=R_{c_2}e^{i\frac{2\pi(k_2-1)}{N_2}}e^{i\alpha_2 z}+R_{c_1}e^{i\frac{2\pi(k_1-1)}{N_1}}e^{i\alpha_1 z}$$

The complex affix of the center of element ${k'}_1+k_1-1$ of substage ${k'}_2+k_2-1$ at z is then

$$w_{{k'}_1+k_1-1\,{k'}_2+k_2-1}(z)=R_{c_2}e^{i\frac{2\pi(k_2-1)}{N_2}}e^{i\frac{2\pi({k'}_2-1)}{N_2}}e^{i\alpha_2 z}+R_{c_1}e^{i\frac{2\pi(k_1-1)}{N_1}}e^{i\frac{2\pi({k'}_1-1)}{N_1}}e^{i\alpha_1 z}$$

Let us note

$$\begin{cases}z_{k_1k_2}=\dfrac{2\pi}{\alpha_1-\alpha_2}\left[\dfrac{k_2-1}{N_2}-\dfrac{k_1-1}{N_1}\right] \\ \theta_{k_1k_2}=\dfrac{2\pi}{\alpha_1-\alpha_2}\left[\alpha_1\left(\dfrac{k_2-1}{N_2}\right)-\alpha_2\left(\dfrac{k_1-1}{N_1}\right)\right]\end{cases} \tag{297}$$

So that

$$\begin{cases}\theta_{k_1k_2}-\alpha_1 z_{k_1k_2}=\dfrac{2\pi}{\alpha_1-\alpha_2}\left[\left(\dfrac{k_2-1}{N_2}\right)(\alpha_1-\alpha_1)-\left(\dfrac{k_1-1}{N_1}\right)(\alpha_2-\alpha_1)\right]=\dfrac{2\pi(k_1-1)}{N_1} \\ \theta_{k_1k_2}-\alpha_2 z_{k_1k_2}=\dfrac{2\pi}{\alpha_1-\alpha_2}\left[\left(\dfrac{k_2-1}{N_2}\right)(\alpha_1-\alpha_2)-\left(\dfrac{k_1-1}{N_1}\right)(\alpha_2-\alpha_2)\right]=\dfrac{2\pi(k_2-1)}{N_2}\end{cases}$$

Thus, replacing $2\pi(k_1-1)/N_1$ with $\theta_{k_1k_2}-\alpha_1 z_{k_1k_2}$ and $2\pi(k_2-1)/N_2$ with $\theta_{k_1k_2}-\alpha_2 z_{k_1k_2}$ in the expression of $w_{k'_1+k_1-1\,k'_2+k_2-1}(z)$, we can write

$$w_{k'_1+k_1-1\,k'_2+k_2-1}(z)=e^{i\theta_{k_1k_2}}\left[R_{c_2}e^{i\frac{2\pi(k'_2-1)}{N_2}}e^{i\alpha_2(z-z_{k_1k_2})}+R_{c_1}e^{i\frac{2\pi(k'_1-1)}{N_1}}e^{i\alpha_1(z-z_{k_1k_2})}\right]$$

And therefore, we have

$$w_{k'_1+k_1-1\,k'_2+k_2-1}(z)=e^{i\theta_{k_1k_2}}w_{k'_1k'_2}\left(z-z_{k_1k_2}\right) \tag{298}$$

- The term $w_{k'_1+k_1-1\,k'_2+k_2-1}(z)$ of equation (298) corresponds to the position of the center of element k'_1+k_1-1 of substage k'_2+k_2-1 at z in the plane orthogonal to the z-axis
- The term $w_{k'_1k'_2}\left(z-z_{k_1k_2}\right)$ of equation (298) corresponds to the position of the center of element k'_1 of substage k'_2 at $z-z_{k_1k_2}$ in the plane orthogonal to the z-axis
- The term $e^{i\theta_{k_1k_2}}$ of equation (298) corresponds to a rotation of $\theta_{k_1k_2}$ around the z-axis, therefore the term $e^{i\theta_{k_1k_2}}w_{k'_1k'_2}\left(z-z_{k_1k_2}\right)$ corresponds to the position of the center of element k'_1 of substage k'_2 at $z-z_{k_1k_2}$ after a rotation of the conductor of $\theta_{k_1k_2}$ around its axis

As a result, equation (298) means that the position of element k'_1+k_1-1 of substage k'_2+k_2-1 at z corresponds to the position of element k'_1 of substage k'_2 at $z-z_{k_1k_2}$ after a rotation of the conductor of $\theta_{k_1k_2}$ around its axis. If we choose $k'_1=k'_2=1$, equation (298) means that the position of element k_1 of substage k_2 at z corresponds to the position of element 1 of substage 1 at $z-z_{k_1k_2}$ rotated from $\theta_{k_1k_2}$ around the conductor axis; this example is illustrated on Figure 49.

These geometrical considerations are important as they imply that element k_1 of substage k_2 at z is in the same geometrical configuration than element 1 of substage 1 at $z-z_{k_1k_2}$ with respect to the other elements.

Furthermore, we can see on Figure 49 that if the applied magnetic field was $\overrightarrow{B'_a}$ instead of $\overrightarrow{B_a}$, element 1 of substage 1 at $z-z_{k_1k_2}$ would exactly be in the same magnetic configuration than element k_1 of substage k_2 at z with $\overrightarrow{B_a}$ and would thus carry the exact same induced current. Note that $\overrightarrow{B'_a}$ corresponds to $\overrightarrow{B_a}$ but rotated from $-\theta_{k_1k_2}$ around the z-axis (see Figure 49), therefore $B'_a=\left\|\overrightarrow{B'_a}\right\|=\left\|\overrightarrow{B_a}\right\|=B_a$. Let us note $I'_{k_1k_2}(z)$ the induced current carried by element k_1 of substage k_2 at z with $\overrightarrow{B'_a}$ instead of $\overrightarrow{B_a}$ with

$$\overline{I'_{k_1k_2}}(z)=\sum_{k=-\infty}^{+\infty}\overline{I'^{(\alpha_k)}_{0_{k_1k_2}}}e^{i\alpha_k z}$$

We then have $I_{k_1k_2}(z)=I'_{11}\left(z-z_{k_1k_2}\right)$, and more generally, from equations (298) we can deduce that $I_{k'_1+k_1-1\,k'_2+k_2-1}(z)=I'_{k'_1k'_2}\left(z-z_{k_1k_2}\right)$.

We will now establish the equation satisfied by $I'_{11}(z)$ with the applied magnetic field $\overrightarrow{B'_a}$ instead of $\overrightarrow{B_a}$. In order to do so, we consider a new geometric coordinate system $(O,\overrightarrow{e_{x'}},\overrightarrow{e_{y'}},\overrightarrow{e_z})$ corresponding to

the geometric coordinate system $(O, \overrightarrow{e_x}, \overrightarrow{e_y}, \overrightarrow{e_z})$ used so far but rotated from $-\theta_{k_1k_2}$ around the z-axis (see Figure 49). Using again the complex notations $\bar{x}$ and $\bar{x'}$ such that $x = Re(\bar{x})$ and $x' = Re(\bar{x'})$, we have

$$\bar{x'} e^{-i\theta_{k_1k_2}} = \bar{x} \Leftrightarrow \bar{x'} = \bar{x} e^{i\theta_{k_1k_2}}$$

We now have to express the axial component of the magnetic vector potential $\overrightarrow{A'_a}$ associated with $\overrightarrow{B'_a}$ in the geometric coordinate system $(O, \overrightarrow{e_x}, \overrightarrow{e_y}, \overrightarrow{e_z})$. Since, in the new geometric coordinate system $(O, \overrightarrow{e_{x'}}, \overrightarrow{e_{y'}}, \overrightarrow{e_z})$, $\overrightarrow{B'_a}$ is along the y'-axis, we know that A'_{z_a} is given in complex notation by

$$\overline{A'_{z_a}} = -\bar{x'} B'_a$$

And since $\bar{x'} = \bar{x} e^{i\theta_{k_1k_2}}$, in the previous geometric coordinate system $(O, \overrightarrow{e_x}, \overrightarrow{e_y}, \overrightarrow{e_z})$, we thus have

$$\overline{A'_{z_a}} = -\bar{x} e^{i\theta_{k_1k_2}} B'_a$$

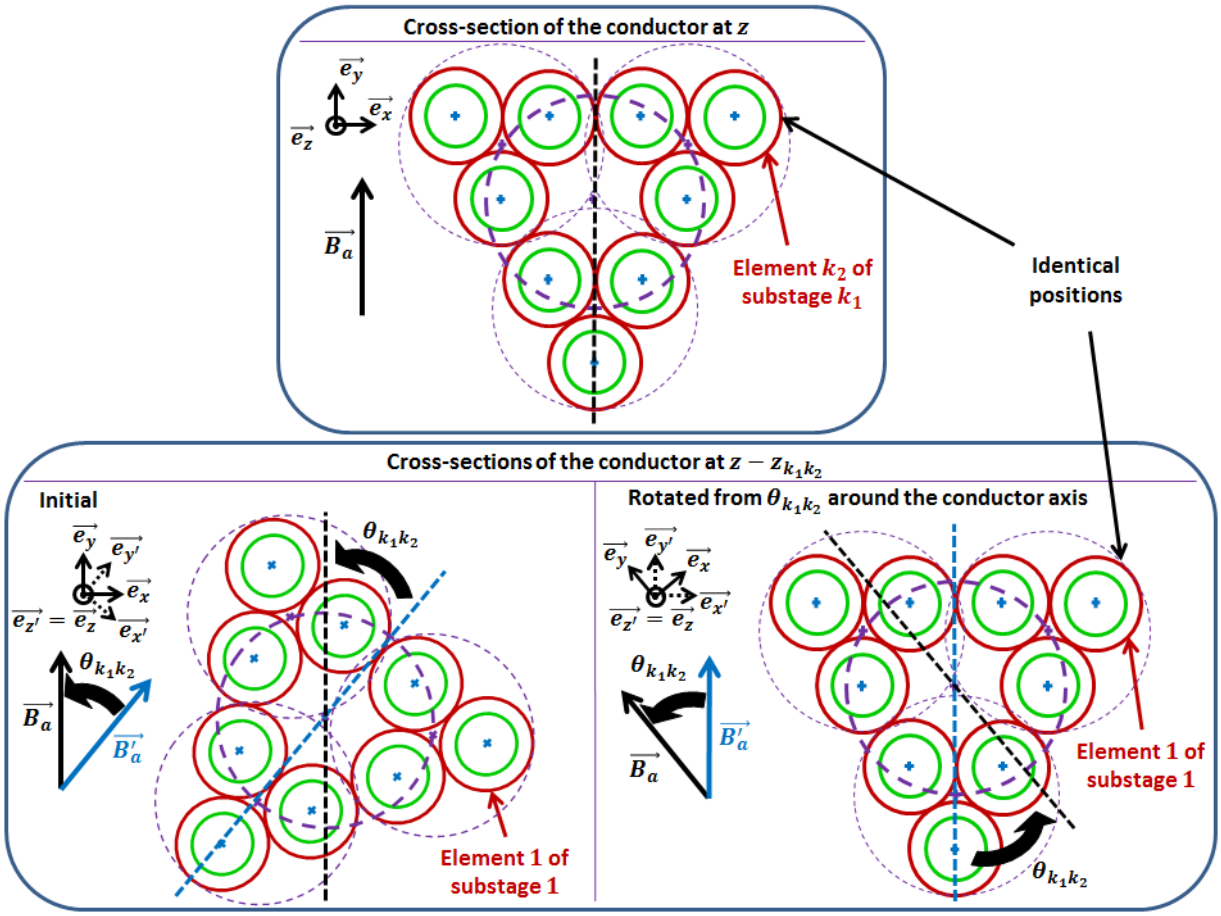

Figure 49 : Example of the geometrical meaning of equation (298) for $k'_1 = k'_2 = 1$

The equations of the system, i.e. equations (296), have been established for the applied magnetic field $\overrightarrow{B_a}$ for which we had $\overline{A_{z_a}} = -\bar{x} B_a$. Since now $\overline{A'_{z_a}} = -\bar{x} e^{i\theta_{k_1k_2}} B'_a$, we just have to replace B_a by

$B'_a e^{i\theta_{k_1k_2}}$ in the first equation of (296) (i.e. the one obtained for $k_1 = k_2 = 1$) to derive the equation governing $I'_{11}(z)$. This operation leads to

$$\begin{cases} \displaystyle\sum_{k=-\infty}^{+\infty} {\alpha_k}^2 \overline{I'^{(\alpha_k)}_{0_{11}}} e^{i\alpha_k z} + \frac{\mu_0}{8\pi^2} \sum_{k=-\infty}^{+\infty} \sum_{p_2=1}^{N_2} \sum_{p_1=1}^{N_1} \overline{\dot{I}'^{(\alpha_k)}_{0_{p_1p_2}}} \sum_{n=-\infty}^{+\infty} e^{i\alpha_{k-n} z} D^{(\alpha_k)}_{n_{p_1p_2\,11}} = \\ 4\sigma_{l_1} R_{c_1} \dot{B}_a e^{i\theta_{k_1k_2}} \sin^2\left(\frac{\pi}{N_1}\right) e^{i\alpha_1 z} + 4\frac{\sigma_{l_2}}{N_1} R_{c_2} \dot{B}_a e^{i\theta_{k_1k_2}} \sin^2\left(\frac{\pi}{N_2}\right) e^{i\alpha_2 z} \end{cases}$$

The equation verified by $I'_{11}\left(z - z_{k_1k_2}\right)$ is then

$$\begin{cases} \displaystyle\sum_{k=-\infty}^{+\infty} {\alpha_k}^2 \overline{I'^{(\alpha_k)}_{0_{11}}} e^{i\alpha_k z} e^{-i\alpha_k z_{k_1k_2}} + \frac{\mu_0}{8\pi^2} \sum_{k=-\infty}^{+\infty} \sum_{p_2=1}^{N_2} \sum_{p_1=1}^{N_1} \overline{\dot{I}'^{(\alpha_k)}_{0_{p_1p_2}}} \sum_{n=-\infty}^{+\infty} e^{i\alpha_{k-n} z} e^{-i\alpha_{k-n} z_{k_1k_2}} D^{(\alpha_k)}_{n_{p_1p_2\,11}} = \\ 4\sigma_{l_1} R_{c_1} \dot{B}_a e^{i\theta_{k_1k_2}} \sin^2\left(\frac{\pi}{N_1}\right) e^{i\alpha_1 z} e^{-i\alpha_1 z_{k_1k_2}} + 4\frac{\sigma_{l_2}}{N_1} R_{c_2} \dot{B}_a e^{i\theta_{k_1k_2}} \sin^2\left(\frac{\pi}{N_2}\right) e^{i\alpha_2 z} e^{-i\alpha_2 z_{k_1k_2}} \end{cases}$$

In addition, since we have

$$I_{k'_1+k_1-1\,k'_2+k_2-1}(z) = I'_{k'_1k'_2}\left(z - z_{k_1k_2}\right)$$

we can write for any z

$$\sum_{k=-\infty}^{+\infty} \overline{I^{(\alpha_k)}_{0_{k'_1+k_1-1\,k'_2+k_2-1}}} e^{i\alpha_k z} = \sum_{k=-\infty}^{+\infty} \overline{I'^{(\alpha_k)}_{0_{k'_1k'_2}}} e^{i\alpha_k z} e^{-i\alpha_k z_{k_1k_2}}$$

Since the elements of $(\alpha_k)_{k\in\mathbb{Z}}$ are all distinct from each other, the $\left(e^{i\alpha_k z}\right)_{k\in\mathbb{Z}}$ functions are linearly independent and we can conclude that for $k \in \mathbb{Z}$

$$\overline{I^{(\alpha_k)}_{0_{k'_1+k_1-1\,k'_2+k_2-1}}} = \overline{I'^{(\alpha_k)}_{0_{k'_1k'_2}}} e^{-i\alpha_k z_{k_1k_2}}$$

We can now use these equalities in the equation verified by $I'_{11}\left(z - z_{k_1k_2}\right)$ to finally obtain

$$\begin{cases} \displaystyle\sum_{k=-\infty}^{+\infty} {\alpha_k}^2 \overline{I^{(\alpha_k)}_{0_{k_1k_2}}} e^{i\alpha_k z} + \frac{\mu_0}{8\pi^2} \sum_{k=-\infty}^{+\infty} \sum_{p_2=1}^{N_2} \sum_{p_1=1}^{N_1} \overline{\dot{I}^{(\alpha_k)}_{0_{p_1+k_1-1\,p_2+k_2-1}}} \sum_{n=-\infty}^{+\infty} e^{i\alpha_{k-n} z} e^{in(\alpha_2-\alpha_1) z_{k_1k_2}} D^{(\alpha_k)}_{n_{p_1p_2\,11}} \\ = 4\sigma_{l_1} R_{c_1} \dot{B}_a \sin^2\left(\frac{\pi}{N_1}\right) e^{i\alpha_1 z} e^{i\frac{2\pi(k_1-1)}{N_1}} + 4\frac{\sigma_{l_2}}{N_1} R_{c_2} \dot{B}_a \sin^2\left(\frac{\pi}{N_2}\right) e^{i\alpha_2 z} e^{i\frac{2\pi(k_2-1)}{N_2}} \end{cases}$$

Because $e^{-i\alpha_{k-n} z_{k_1k_2}} = e^{-i\alpha_k z_{k_1k_2}} e^{in(\alpha_2-\alpha_1) z_{k_1k_2}}$, $e^{i\theta_{k_1k_2}} e^{-i\alpha_1 z_{k_1k_2}} = e^{i\frac{2\pi(k_1-1)}{N_1}}$ and $e^{i\theta_{k_1k_2}} e^{-i\alpha_2 z_{k_1k_2}} = e^{i\frac{2\pi(k_2-1)}{N_2}}$.

Note that the invariance of the system has enabled us to divide by $N_1 N_2$ the number of D coefficients. Indeed, the D coefficients were previously depending on k_1, k_2, p_1 and p_2 while, now, they only depend on p_1 and p_2. This reduction of coefficients has an important impact on the future computing time needed to determine them numerically.

IV.2.5.4.3 Reduction of the system equations to a first-order differential equation

For further needs, we will now express the equations of the system as

$$\begin{cases} \displaystyle\sum_{k=-\infty}^{+\infty} {\alpha_k}^2 \overline{I_{0_{k_1 k_2}}^{(\alpha_k)}} e^{i\alpha_k z} + \frac{\mu_0}{8\pi^2} \lim_{N\to\infty} \sum_{n=-N}^{N} \sum_{p=-\infty}^{+\infty} \sum_{p_2=1}^{N_2} \sum_{p_1=1}^{N_1} \overline{\dot{I}_{0_{p_1+k_1-1\, p_2+k_2-1}}^{(\alpha_p)}} e^{i\alpha_{p-n} z} e^{in(\alpha_2-\alpha_1) z_{k_1 k_2}} D_{n_{p_1 p_2\, 11}}^{(\alpha_p)} \\ \qquad = 4\sigma_{l_1} R_{c_1} \dot{B}_a \sin^2\left(\frac{\pi}{N_1}\right) e^{i\alpha_1 z} e^{i\frac{2\pi(k_1-1)}{N_1}} + 4\frac{\sigma_{l_2}}{N_1} R_{c_2} \dot{B}_a \sin^2\left(\frac{\pi}{N_2}\right) e^{i\alpha_2 z} e^{i\frac{2\pi(k_2-1)}{N_2}} \end{cases}$$

where N is the maximum order of the decomposition in Fourier series.

Again, since the $\left(e^{i\alpha_k z}\right)_{k\in\mathbb{Z}}$ functions are linearly independent, we can project the equations of the system on the basis formed by the $\left(e^{i\alpha_k z}\right)_{k\in\mathbb{Z}}$ functions. For any $k \in \mathbb{Z}$, the projection of the left-hand side of the equation on $e^{i\alpha_k z}$ leads to

$${\alpha_k}^2 \overline{I_{0_{k_1 k_2}}^{(\alpha_k)}} + \frac{\mu_0}{8\pi^2} \lim_{N\to\infty} \sum_{n=-N}^{N} \sum_{p_2=1}^{N_2} \sum_{p_1=1}^{N_1} \overline{\dot{I}_{0_{p_1+k_1-1\, p_2+k_2-1}}^{(\alpha_{k+n})}} e^{in(\alpha_2-\alpha_1) z_{k_1 k_2}} D_{n_{p_1 p_2\, 11}}^{(\alpha_{k+n})}$$

because the only index p for which we have $e^{i\alpha_{p-n} z} = e^{i\alpha_k z}$ must satisfy $p - n = k$ and is thus $p = k + n$. Therefore, we can now write the equations of the system for any $k \in \mathbb{Z}$ as

- For $k = 1$

$$\begin{cases} \overline{I_{0_{k_1 k_2}}^{(\alpha_1)}} = -\frac{\mu_0}{8\pi^2} \frac{1}{{\alpha_1}^2} \lim_{N\to\infty} \sum_{n=-N}^{N} \sum_{p_2=1}^{N_2} \sum_{p_1=1}^{N_1} \overline{\dot{I}_{0_{p_1+k_1-1\, p_2+k_2-1}}^{(\alpha_{1+n})}} e^{in(\alpha_2-\alpha_1) z_{k_1 k_2}} D_{n_{p_1 p_2\, 11}}^{(\alpha_{1+n})} \\ \qquad +4\sigma_{l_1} R_{c_1} \dot{B}_a \sin^2\left(\frac{\pi}{N_1}\right) \frac{1}{{\alpha_1}^2} e^{i\frac{2\pi(k_1-1)}{N_1}} \end{cases} \tag{299}$$

- For $k = 2$

$$\begin{cases} \overline{I_{0_{k_1 k_2}}^{(\alpha_2)}} = -\frac{\mu_0}{8\pi^2} \frac{1}{{\alpha_2}^2} \lim_{N\to\infty} \sum_{n=-N}^{N} \sum_{p_2=1}^{N_2} \sum_{p_1=1}^{N_1} \overline{\dot{I}_{0_{p_1+k_1-1\, p_2+k_2-1}}^{(\alpha_{2+n})}} e^{in(\alpha_2-\alpha_1) z_{k_1 k_2}} D_{n_{p_1 p_2\, 11}}^{(\alpha_{2+n})} \\ \qquad +4\frac{\sigma_{l_2}}{N_1} R_{c_2} \dot{B}_a \sin^2\left(\frac{\pi}{N_2}\right) \frac{1}{{\alpha_2}^2} e^{i\frac{2\pi(k_2-1)}{N_2}} \end{cases} \tag{300}$$

- For $k \in \mathbb{Z}\backslash\{1;2\}$

$$\overline{I_{0_{k_1 k_2}}^{(\alpha_k)}} = -\frac{\mu_0}{8\pi^2} \frac{1}{{\alpha_k}^2} \lim_{N\to\infty} \sum_{n=-N}^{N} \sum_{p_2=1}^{N_2} \sum_{p_1=1}^{N_1} \overline{\dot{I}_{0_{p_1+k_1-1\, p_2+k_2-1}}^{(\alpha_{k+n})}} e^{in(\alpha_2-\alpha_1) z_{k_1 k_2}} D_{n_{p_1 p_2\, 11}}^{(\alpha_{k+n})} \tag{301}$$

From equations (299), the exciting terms (featuring $\dot{B}_a$) enable us to deduce that

$$\begin{cases} \overline{I_{0_{k_1k_2}}^{(\alpha_1)}} = I_0^{(\alpha_1)} e^{i\frac{2\pi(k_1-1)}{N_1}} \\ \overline{I_{0_{k_1k_2}}^{(\alpha_2)}} = I_0^{(\alpha_2)} e^{i\frac{2\pi(k_2-1)}{N_1}} \end{cases}$$

which implies

$$\begin{cases} \overline{\dot{I}_{0_{p_1+k_1-1\ p_2+k_2-1}}^{(\alpha_1)}} = \dot{I}_0^{(\alpha_1)} e^{i\frac{2\pi(p_1-1)}{N_1}} e^{i\frac{2\pi(k_1-1)}{N_1}} \\ \overline{\dot{I}_{0_{p_1+k_1-1\ p_2+k_2-1}}^{(\alpha_2)}} = \dot{I}_0^{(\alpha_2)} e^{i\frac{2\pi(p_2-1)}{N_2}} e^{i\frac{2\pi(k_2-1)}{N_2}} \end{cases}$$

Then substituting these terms in equations (301) enables us to find the dependences of the other $\overline{I_{0_{k_1k_2}}^{(\alpha_k)}}$ amplitudes on k_1 and k_2 after several iterations. This procedure has led us for any $k \in \mathbb{Z}$ to

$$\overline{I_{0_{k_1k_2}}^{(\alpha_k)}} = I_0^{(\alpha_k)} e^{i\varphi_{k_1k_2}^{(\alpha_k)}} \tag{302}$$

where the $I_0^{(\alpha_k)}$ are real functions depending on time only and

$$\varphi_{k_1k_2}^{(\alpha_k)} = 2\pi\left(\frac{k_1-1}{N_1}\right) + (k-1)\left[2\pi\left(\frac{k_2-1}{N_2}\right) - 2\pi\left(\frac{k_1-1}{N_1}\right)\right] \tag{303}$$

Note that if we write

$$\begin{cases} \varphi_{k_1} = 2\pi\left(\frac{k_1-1}{N_1}\right) \\ \varphi_{k_2} = 2\pi\left(\frac{k_2-1}{N_2}\right) \end{cases}$$

according to (303) we have

$$\varphi_{k_1k_2}^{(\alpha_k)} = \varphi_{k_1} + (k-1)\left[\varphi_{k_2} - \varphi_{k_1}\right]$$

which is very similar to the expression of α_k given by (289).

Finally, we can now replace the $\overline{I_{0_{k_1k_2}}^{(\alpha_k)}}$ amplitudes with their expressions given by (302) in equations (299) to (301) to obtain

$$\begin{cases} I_0^{(\alpha_1)} + \frac{\mu_0}{8\pi^2}\frac{1}{{\alpha_1}^2} \lim\limits_{N\to\infty} \sum\limits_{n=-N}^{N} \dot{I}_0^{(\alpha_{1+n})} \sum\limits_{p_2=1}^{N_2} \sum\limits_{p_1=1}^{N_1} e^{i\varphi_{p_1p_2}^{(\alpha_{1+n})}} D_{n_{p_1p_2\,11}}^{(\alpha_{1+n})} = 4\sigma_{l_1} R_{c_1} \dot{B}_a \sin^2\left(\frac{\pi}{N_1}\right)\frac{1}{{\alpha_1}^2} \\ I_0^{(\alpha_2)} + \frac{\mu_0}{8\pi^2}\frac{1}{{\alpha_2}^2} \lim\limits_{N\to\infty} \sum\limits_{n=-N}^{N} \dot{I}_0^{(\alpha_{2+n})} \sum\limits_{p_2=1}^{N_2} \sum\limits_{p_1=1}^{N_1} e^{i\varphi_{p_1p_2}^{(\alpha_{2+n})}} D_{n_{p_1p_2\,11}}^{(\alpha_{2+n})} = 4\frac{\sigma_{l_2}}{N_1} R_{c_2} \dot{B}_a \sin^2\left(\frac{\pi}{N_2}\right)\frac{1}{{\alpha_2}^2} \\ I_0^{(\alpha_k)} + \frac{\mu_0}{8\pi^2}\frac{1}{{\alpha_k}^2} \lim\limits_{N\to\infty} \sum\limits_{n=-N}^{N} \dot{I}_0^{(\alpha_{k+n})} \sum\limits_{p_2=1}^{N_2} \sum\limits_{p_1=1}^{N_1} e^{i\varphi_{p_1p_2}^{(\alpha_{k+n})}} D_{n_{p_1p_2\,11}}^{(\alpha_{k+n})} = 0, for\ k \in \mathbb{Z}\backslash\{1;2\} \end{cases} \tag{304}$$

Note that equations (304) are still written in complex notation and have been derived from complex equations (291) using linear operations only. Since the real part of complex equations (291) correspond to the true equations of the system which are given by (260), we can affirm that only the real part of complex equations (291) are needed to fully describe the system. As a result, we can deduce that only the real part of complex equations (304) are governing the system.

Since the $I_0^{(\alpha_k)}$ are real functions, the equations of the system are thus reduced to

$$I_0^{(\alpha_k)} + \lim_{N\to\infty} \sum_{n=-N}^{N} \tau_{(\alpha_k)(\alpha_{k+n})} \dot{I}_0^{(\alpha_{k+n})} = I_{0_{ext}}^{(\alpha_k)} \tag{305}$$

where the $I_{0_{ext}}^{(\alpha_k)}$ are given by

$$I_{0_{ext}}^{(\alpha_k)} = \begin{cases} 4\sigma_{l_1} R_{c_1} \dot{B}_a \sin^2\left(\frac{\pi}{N_1}\right) \frac{1}{{\alpha_1}^2} \; for\; k = 1 \\ 4\frac{\sigma_{l_2}}{N_1} R_{c_2} \dot{B}_a \sin^2\left(\frac{\pi}{N_2}\right) \frac{1}{{\alpha_2}^2} \; for\; k = 2 \\ 0 \; for\; k \in \mathbb{Z}\backslash\{1;2\} \end{cases} \tag{306}$$

and the $\tau_{(\alpha_k)(\alpha_{k+n})}$ are time constants given by

$$\tau_{(\alpha_k)(\alpha_{k+n})} = \frac{\mu_0}{8\pi^2} \frac{1}{{\alpha_k}^2} Re\left(\sum_{p_2=1}^{N_2} \sum_{p_1=1}^{N_1} e^{i\varphi_{p_1p_2}^{(\alpha_{k+n})}} D_{n_{p_1p_2\,11}}^{(\alpha_{k+n})} \right) \tag{307}$$

where $Re(X)$ refers to the real part of complex number X and the expressions of α_k, $D_{n_{p_1p_2\,11}}^{(\alpha_{k+n})}$ and $\varphi_{p_1p_2}^{(\alpha_{k+n})}$ are given in (289), (295) and (303) respectively.

Using the expressions of $D_{n_{p_1p_2\;k_1k_2}}^{(\alpha_k)}$ given by (295), we can alternatively express the time constants $\tau_{(\alpha_k)(\alpha_{k+n})}$ as

$$\tau_{(\alpha_k)(\alpha_{k+n})} = \sigma_{l_1} \frac{\mu_0}{8\pi^2} \frac{1}{{\alpha_k}^2} E_{n_1}^{(\alpha_k)(\alpha_{k+n})} + \sigma_{l_2} \frac{\mu_0}{8\pi^2} \frac{1}{{\alpha_k}^2} E_{n_2}^{(\alpha_k)(\alpha_{k+n})} \tag{308}$$

From the expressions of $C_{n_{p_1p_2\;k_1k_2}}^{(\alpha_k)}$ and $C_{n_{p_1p_2\;k_2}}^{(\alpha_k)}$ given in (293) and (294) and those of $X_{n_{p_1p_2\;k_1k_2}}^{(\alpha_k)}$ given in (278), we can write

$$\begin{cases} E_{n_1}^{(\alpha_k)(\alpha_{k+n})} = Re\left(\frac{1}{l} \int_{z'=-\infty}^{+\infty} e^{i\alpha_{k+n}z'} \int_{z''=-l/2}^{l/2} e^{-i\frac{2\pi n z''}{l}} F_1(z'', z') dz'' \, dz' \right) \\ E_{n_2}^{(\alpha_k)(\alpha_{k+n})} = \frac{1}{{N_1}^2} Re\left(\frac{1}{l} \int_{z'=-\infty}^{+\infty} e^{i\alpha_{k+n}z'} \int_{z''=-l/2}^{l/2} e^{-i\frac{2\pi n z''}{l}} F_2(z'', z') dz'' \, dz' \right) \end{cases} \tag{309}$$

where $\alpha_{k+n} = \alpha_1 + (k+n-1)(\alpha_1 - \alpha_2)$, $l = 2\pi/(\alpha_1 - \alpha_2)$, $\alpha_1 = 2\pi/l_{p_1}$, $\alpha_2 = 2\pi/l_{p_2}$ and

$$\begin{cases} F_1(z'', z') = \sum_{p_2=1}^{N_2} \sum_{p_1=1}^{N_1} e^{i\varphi_{p_1p_2}^{(\alpha_{k+n})}} \int_{\Psi'=0}^{2\pi} h_{1_{p_1p_2}}(z'', z', \Psi') d\Psi' \\ F_2(z'', z') = \sum_{p_2=1}^{N_2} \sum_{p_1=1}^{N_1} e^{i\varphi_{p_1p_2}^{(\alpha_{k+n})}} \int_{\Psi'=0}^{2\pi} h_{2_{p_1p_2}}(z'', z', \Psi') d\Psi' \end{cases} \tag{310}$$

The expressions of the $h_{1_{p_1p_2}}(z'',z',\Psi')$ and $h_{2_{p_1p_2}}(z'',z',\Psi')$ functions are

$$\begin{cases} h_{1_{p_1p_2}}(z'',z',\Psi') = \dfrac{2}{g_{p_1p_2\,11}(z'',z',\Psi')} - \dfrac{1}{g_{p_1p_2\,N_1 1}(z'',z',\Psi')} - \dfrac{1}{g_{p_1p_2\,21}(z'',z',\Psi')} \\ h_{2_{p_1p_2}}(z'',z',\Psi') = \displaystyle\sum_{j_1=1}^{N_1}\left[\frac{2}{g_{p_1p_2\,j_1 1}(z'',z',\Psi')} - \frac{1}{g_{p_1p_2\,j_1 N_2}(z'',z',\Psi')} - \frac{1}{g_{p_1p_2\,j_1 2}(z'',z',\Psi')}\right] \end{cases} \tag{311}$$

where the $g_{p_1p_2\,k_1k_2}(z'',z',\Psi')$ functions are given by (279).

The current $I_{k_1k_2}(z)$ flowing though element k_1 of substage k_2 at z is, from equations (290) and (302), equal to

$$I_{k_1k_2}(z) = \sum_{k=-\infty}^{+\infty} I_0^{(\alpha_k)} \cos\left(\alpha_k z + \varphi_{k_1k_2}^{(\alpha_k)}\right) \tag{312}$$

Note that we have assumed $I_{k_1k_2}(z) = I_{k_2}(z)/N_1 + I_{k_1}^{\langle k_2\rangle}(z)$ (see equation (253) in section IV.2.3) where $I_{k_2}(z)$ is the current induced in substage k_2 to shield the superstage and $I_{k_1}^{\langle k_2\rangle}(z)$ is the current induce in element k_1 of substage k_2 to shield substage k_2. Thus we have

$$\sum_{k_1=1}^{N_1} I_{k_1}^{\langle k_2\rangle}(z) = 0$$

because all the $I_{k_1}^{\langle k_2\rangle}(z)$ currents are shielding the same substage, therefore their sum must be zero. As a result, we have

$$\sum_{k_1=1}^{N_1} I_{k_1k_2}(z) = \sum_{k_1=1}^{N_1} I_{k_1}^{\langle k_2\rangle}(z) + \sum_{k_1=1}^{N_1} \frac{I_{k_2}(z)}{N_1} = I_{k_2}(z)$$

which leads to

$$I_{k_2}(z) = \sum_{k_1=1}^{N_1}\sum_{k=-\infty}^{+\infty} I_0^{(\alpha_k)} \cos\left(\alpha_k z + \varphi_{k_1k_2}^{(\alpha_k)}\right) = \sum_{k=-\infty}^{+\infty} I_0^{(\alpha_k)} \sum_{k_1=1}^{N_1} \cos\left(\alpha_k z + \varphi_{k_1k_2}^{(\alpha_k)}\right)$$

Since, according to (303), $\varphi_{k_1k_2}^{(\alpha_k)} = (k-1)2\pi\left(\frac{k_2-1}{N_2}\right) + (2-k)2\pi\left(\frac{k_1-1}{N_1}\right)$, we can deduce that

$$\sum_{k_1=1}^{N_1} \cos\left(\alpha_k z + \varphi_{k_1k_2}^{(\alpha_k)}\right) = \begin{cases} 0 \; if \; k \neq 2 + pN_1, p \in \mathbb{Z} \\ N_1 \cos\left(\alpha_k z + (k-1)2\pi\left(\dfrac{k_2-1}{N_2}\right)\right) \; if \; k = 2 + pN_1, p \in \mathbb{Z} \end{cases}$$

So

$$I_{k_2}(z) = \sum_{p=-\infty}^{+\infty} I_0^{(\alpha_{2+pN_1})} N_1 \cos\left(\alpha_{2+pN_1} z + (1+pN_1)2\pi\left(\frac{k_2-1}{N_2}\right)\right) \tag{313}$$

The currents induced through each substage to shield the superstage are thus a combination of cosine functions of space with spatial frequencies $\left(\alpha_{2+pN_1}\right)_{p\in\mathbb{Z}}$.

We can immediately conclude that the currents induced through each element of a substage to shield it are a combination of cosine functions of space with the remaining spatial frequencies, i.e. with $(\alpha_k)_{k\neq 2+pN_1, p\in\mathbb{Z}}$. Indeed from the previous equations, we have

$$I_{k_1}^{\langle k_2\rangle}(z) = I_{k_1k_2}(z) - \frac{I_{k_2}(z)}{N_1} = \sum_{\substack{k=-\infty \\ k\neq 2+pN_1, p\in\mathbb{Z}}}^{+\infty} I_0^{(\alpha_k)} \cos\left(\alpha_k z + \varphi_{k_1k_2}^{(\alpha_k)}\right) \tag{314}$$

We have now expressed both the part of the induced currents shielding the superstage and the one shielding each substage and reduced the system equations to a first-order differential equation on the $I_0^{(\alpha_k)}$ amplitudes which depend on time only. The system equation, which is now given by (305), is an infinite matrix equation having the following form

$$\begin{bmatrix} \vdots \\ \vdots \\ \vdots \\ I_0^{(\alpha_1)} \\ I_0^{(\alpha_2)} \\ \vdots \\ \vdots \\ \vdots \end{bmatrix} + \begin{bmatrix} \ddots & \ddots & \ddots & \ddots & \ddots & \ddots & \ddots & \ddots \\ \ddots & \ddots & \ddots & \ddots & \ddots & \ddots & \ddots & \ddots \\ \ddots & \ddots & \ddots & \ddots & \ddots & \ddots & \ddots & \ddots \\ \ddots & \ddots & \tau_{(\alpha_1)(\alpha_0)} & \tau_{(\alpha_1)(\alpha_1)} & \tau_{(\alpha_1)(\alpha_2)} & \ddots & \ddots & \ddots \\ \ddots & \ddots & \ddots & \tau_{(\alpha_2)(\alpha_1)} & \tau_{(\alpha_2)(\alpha_2)} & \tau_{(\alpha_2)(\alpha_3)} & \ddots & \ddots \\ \ddots & \ddots & \ddots & \ddots & \ddots & \ddots & \ddots & \ddots \\ \ddots & \ddots & \ddots & \ddots & \ddots & \ddots & \ddots & \ddots \\ \ddots & \ddots & \ddots & \ddots & \ddots & \ddots & \ddots & \ddots \end{bmatrix} \begin{bmatrix} \vdots \\ \vdots \\ \vdots \\ \dot{I}_0^{(\alpha_1)} \\ \dot{I}_0^{(\alpha_2)} \\ \vdots \\ \vdots \\ \vdots \end{bmatrix} = \begin{bmatrix} 0 \\ \vdots \\ 0 \\ I_{0_{ext}}^{(\alpha_1)} \\ I_{0_{ext}}^{(\alpha_2)} \\ 0 \\ \vdots \\ 0 \end{bmatrix}$$

We clearly see that the two spatial modes which are directly excited by the time-variation of the applied magnetic field B_a are the spatial frequencies α_1 and α_2. The other modes are only excited by the time-variation of the currents with the spatial frequencies α_1 and α_2.

IV.2.5.4.4 Expression of the system equation for N=1

The maximum order of the Fourier series of the $1/g_{p_1p_2\,k_1k_2}(z,z',\Psi')$ function has been noted N in the previous section. Therefore the notation $N=1$ indicates that the Fourier series is stopped at the first order, i.e. we only take into account the terms obtained for $-1\leq n\leq 1$; the others are considered to be zero.

In the previous section we have shown that the system equation was described by an infinite matrix equation; it thus cannot be solved numerically.

The infinite nature of the matrix is due to two different facts:

- First, the currents induced in the elements are described by an infinity of cosine functions of space having the spatial frequencies $(\alpha_k)_{k\in\mathbb{Z}}$
- Secondly, the decomposition in Fourier series we have used in section IV.2.5.1 to express the $1/g_{p_1p_2\,k_1k_2}(z,z',\Psi')$ function (see equation (274)) is, by nature, infinite

The time constant $\tau_{(\alpha_k)(\alpha_{k+n})}$ which links the amplitude $I_0^{(\alpha_k)}$ (amplitude of the cosine function with spatial frequency α_k) to $\dot{I}_0^{(\alpha_{k+n})}$ (time variation of the amplitude of the cosine function with spatial frequency α_{k+n}) is expressed in equation (308) as

$$\tau_{(\alpha_k)(\alpha_{k+n})} = \sigma_{l_1} \frac{\mu_0}{8\pi^2} \frac{1}{{\alpha_k}^2} E_{n_1}^{(\alpha_k)(\alpha_{k+n})} + \sigma_{l_2} \frac{\mu_0}{8\pi^2} \frac{1}{{\alpha_k}^2} E_{n_2}^{(\alpha_k)(\alpha_{k+n})}$$

We can first notice that $\tau_{(\alpha_k)(\alpha_{k+n})}$ is proportional to $1/{\alpha_k}^2$ and since $\alpha_k = \alpha_1 + (k-1)(\alpha_2 - \alpha_1)$, we can conclude that for $k \gg 1$ the time constants $\tau_{(\alpha_k)(\alpha_{k+n})}$ will tend towards zero for any $n \in \mathbb{Z}$. This means that the amplitudes $I_0^{(\alpha_k)}$ with $k \gg 1$ will be decoupled from the time variation of any $I_0^{(\alpha_k)}, k \in \mathbb{Z}$, and since $I_{0_{ext}}^{(\alpha_k)} = 0$ for $k \in \mathbb{Z}\backslash\{1;2\}$, we can see that it will in fact be possible to neglect the amplitudes $I_0^{(\alpha_k)}$ for $k \gg 1$. In other words, we can consider only a finite number of spatial frequencies α_k, and thus only a finite part (in the vertical direction) of the infinite τ matrix, without changing the physical behavior of the system.

Furthermore, we have also investigated the values of the coefficients due to the decomposition in Fourier series of the $1/g_{p_1 p_2\, k_1 k_2}(z, z', \Psi')$ function, i.e. the $E_{n_1}^{(\alpha_k)(\alpha_{k+n})}$ and $E_{n_2}^{(\alpha_k)(\alpha_{k+n})}$ coefficients appearing in the expression of $\tau_{(\alpha_k)(\alpha_{k+n})}$. Indeed, we have numerically computed them for different values of k and n and for two different set of $\left(R_f, R_{c_1}, R_{c_2}, l_{p_1}, l_{p_2}, N_1, N_2\right)$ parameters which are representative of the first two and last two cabling stages of JT-60SA TF conductor; they are displayed from Figure 50 to Figure 57.

<u>First set of parameters : first two cabling stages of TF JT-60SA conductor</u>

The first set of parameters, which is representative of the first two cabling stages of JT-60SA TF conductor, is deduced from the results of section IV.5.4 :

$\left(R_f = 0.327mm, R_{c_1} = 0.49mm, R_{c_2} = 0.82mm, l_{p_1} = 45.4mm, l_{p_2} = 66.7mm, N_1 = 3, N_2 = 3\right)$

The R_f value corresponds here to the outer radius of the filamentary zone of JT-60SA TF strand (see section II.4.3).

Figure 50 displays the values of the $E_{n_1}^{(\alpha_k)(\alpha_{k+n})}$ computed numerically for $-1 \leq k \leq 4$ and $-5 \leq n \leq 5$. We can see that, for each spatial frequency α_k, the maximum absolute value of $E_{n_1}^{(\alpha_k)(\alpha_{k+n})}$ is always reached between $n = -1$ and $n = 1$. We can also observe that the $E_{n_1}^{(\alpha_k)(\alpha_{k+n})}$ coefficients are all zero for $\alpha_k = \alpha_{-1}$ and $\alpha_k = \alpha_2$.

Figure 51 displays, the values of $E_{n_1}^{(\alpha_k)(\alpha_{k+n})}$ normalized to the maximum absolute value of $E_{n_1}^{(\alpha_k)(\alpha_{k+n})}$ for each spatial frequency α_k (if the coefficients are not zero for every n).

For example, for $\alpha_k = \alpha_0$, the normalized coefficient $\left|E_{n_1\,normalized}^{(\alpha_0)(\alpha_{0+n})}\right| = \left|E_{n_1}^{(\alpha_0)(\alpha_{0+n})} / \max\left(\left|E_{n_1}^{(\alpha_0)(\alpha_{0+n})}\right|\right)_{-5\leq n\leq 5}\right|$ corresponds to the absolute value of the $E_{n_1}^{(\alpha_0)(\alpha_{0+n})}$ coefficients divided by the maximum absolute value of $E_{n_1}^{(\alpha_0)(\alpha_{0+n})}$ obtained for $-5 \leq n \leq 5$.

Therefore Figure 51 also shows that the maximum absolute value of $E_{n_1}^{(\alpha_k)(\alpha_{k+n})}$ is always reached between $n = -1$ and $n = 1$ (when the ratio is equal to 100%) and that the values of the $E_{n_1}^{(\alpha_k)(\alpha_{k+n})}$ coefficients strongly decrease with increasing n (they are all below 25% of their maximum absolute value for $|n| \geq 2$).

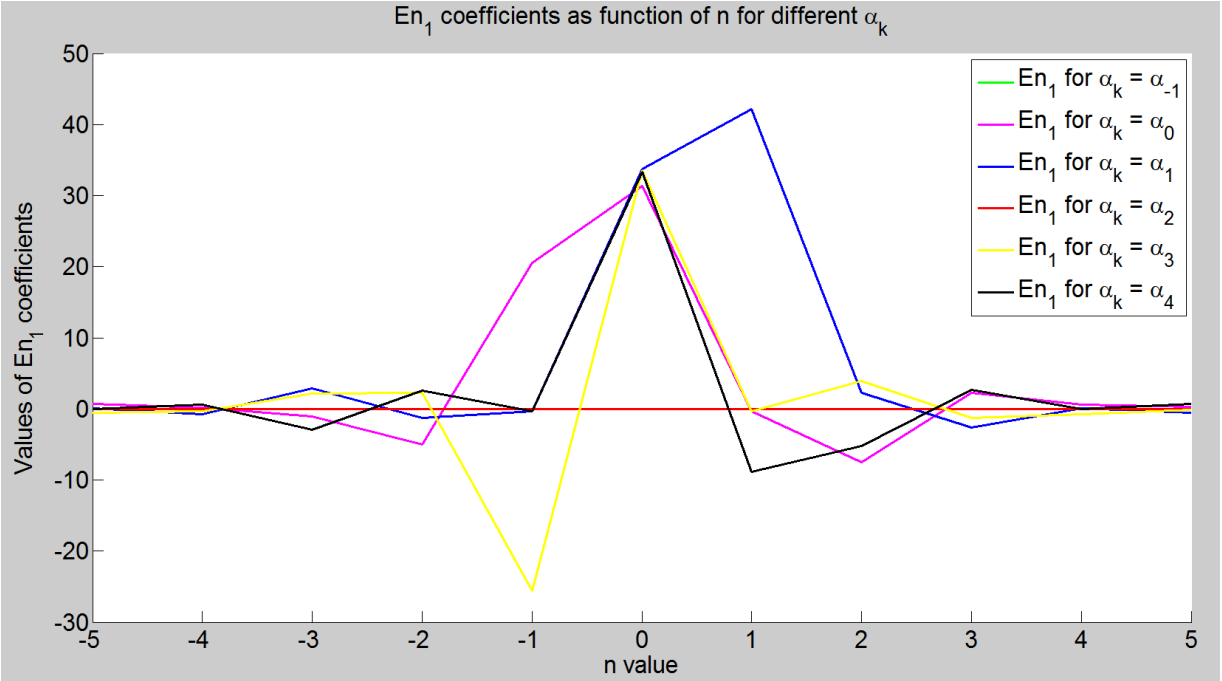

Figure 50 : $E_{n_1}^{(\alpha_k)(\alpha_{k+n})}$ coefficients for different values of k and n for the first set of parameters

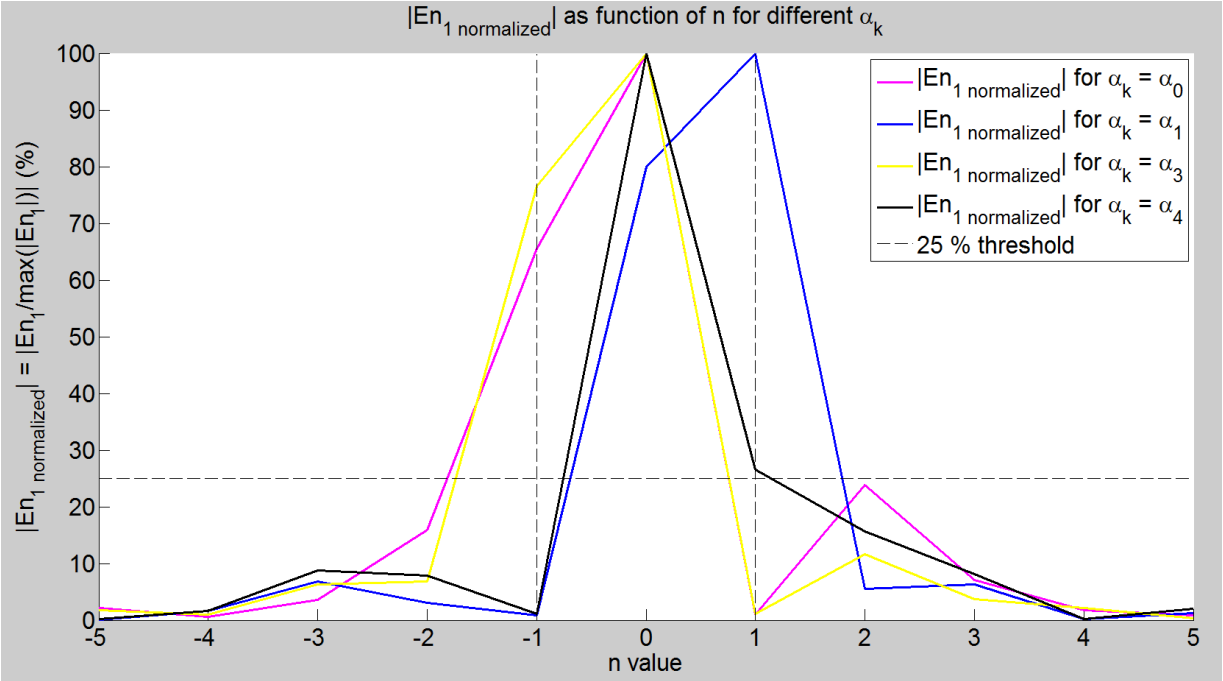

Figure 51 : $E_{n_1}^{(\alpha_k)(\alpha_{k+n})}$ normalized coefficients for different values of k and n for the first set of parameters

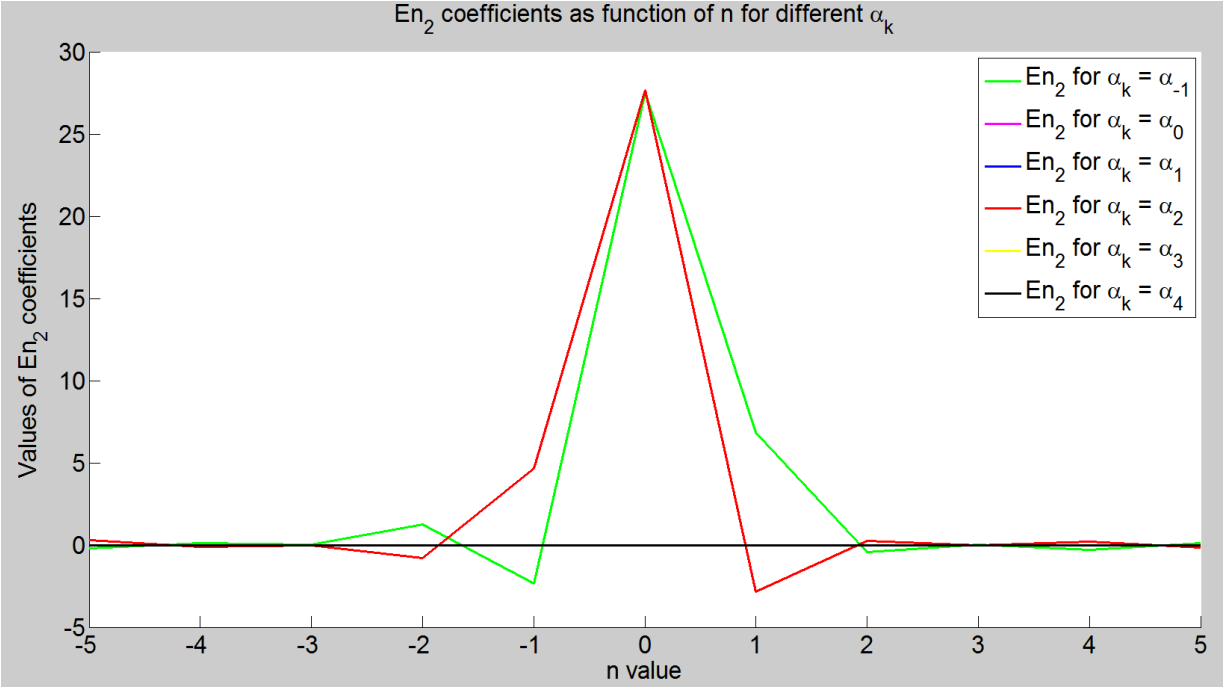

Figure 52 : $E_{n_2}^{(\alpha_k)(\alpha_{k+n})}$ coefficients for different values of k and n for the first set of parameters

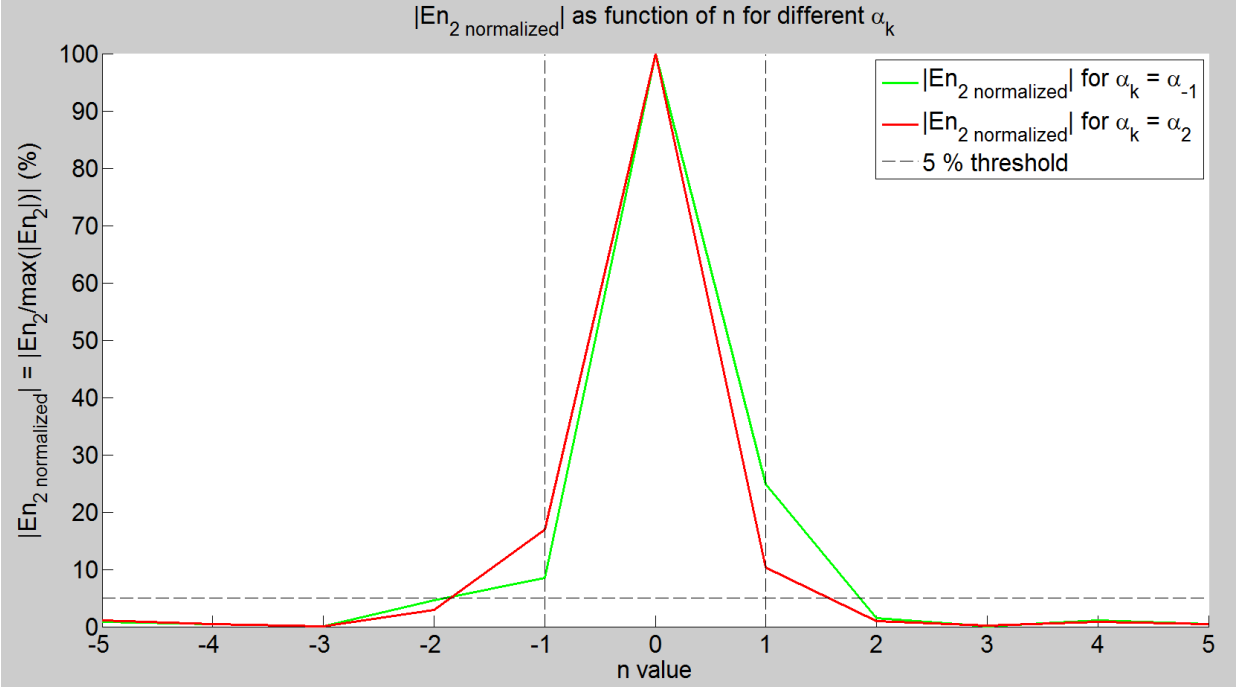

Figure 53 : $E_{n_2}^{(\alpha_k)(\alpha_{k+n})}$ normalized coefficients for different values of k and n for the first set of parameters

Figure 52 and Figure 53 are the equivalent of Figure 50 and Figure 51 but for the $E_{n_2}^{(\alpha_k)(\alpha_{k+n})}$ coefficients. We also see that the maximum absolute value of $E_{n_2}^{(\alpha_k)(\alpha_{k+n})}$ is always reached between $n = -1$ and $n = 1$ and that the absolute values of the $E_{n_2}^{(\alpha_k)(\alpha_{k+n})}$ coefficients strongly decrease with increasing n (they are all below 5% of their maximum absolute value for $|n| \geq 2$). We can observe that the $E_{n_2}^{(\alpha_k)(\alpha_{k+n})}$ coefficients are all zero for $\alpha_k = \alpha_0$, $\alpha_k = \alpha_1$, $\alpha_k = \alpha_3$ and $\alpha_k = \alpha_4$.

Second set of parameters : last two cabling stages of TF JT-60SA conductor

The second set of parameters, which is representative of the last two cabling stages of JT-60SA TF conductor, is also deduced from the results of section IV.5.4 :

$\left(R_f = 1.62mm, R_{c_1} = 2.31mm, R_{c_2} = 7.75mm, l_{p_1} = 185.2mm, l_{p_2} = 285.7mm, N_1 = 3, N_2 = 6\right)$

The R_f value corresponds here to the cabling radius of the third cabling stage of JT-60SA TF conductor because here R_{c_2} is the fifth and last cabling stage of the conductor and R_{c_1} is the fourth cabling stage of the conductor (see section IV.5.4).

Figure 54 to Figure 57 are the equivalent of Figure 50 to Figure 53 but for the second set of parameters.

As we have observed it for the first set of parameters, the maximum absolute value of $E_{n_1}^{(\alpha_k)(\alpha_{k+n})}$ and $E_{n_2}^{(\alpha_k)(\alpha_{k+n})}$ is always reached between $n = -1$ and $n = 1$ and the absolute values of the $E_{n_1}^{(\alpha_k)(\alpha_{k+n})}$ and $E_{n_2}^{(\alpha_k)(\alpha_{k+n})}$ coefficients strongly decrease with increasing n. Indeed for $|n| \geq 2$, they are all below 25% of their maximum absolute value for $E_{n_1}^{(\alpha_k)(\alpha_{k+n})}$ and below 10% for $E_{n_2}^{(\alpha_k)(\alpha_{k+n})}$).

Again we can notice on Figure 54 that the $E_{n_1}^{(\alpha_k)(\alpha_{k+n})}$ coefficients are all zero for $\alpha_k = \alpha_{-1}$ and $\alpha_k = \alpha_2$, and on Figure 56 that the $E_{n_2}^{(\alpha_k)(\alpha_{k+n})}$ coefficients are all zero for $\alpha_k = \alpha_0$, $\alpha_k = \alpha_1$, $\alpha_k = \alpha_3$ and $\alpha_k = \alpha_4$.

We recall that the time constant $\tau_{(\alpha_k)(\alpha_{k+n})}$ reflects the coupling between $I_0^{(\alpha_k)}$ and $\dot{I}_0^{(\alpha_{k+n})}$ and that it is a linear combination of $E_{n_1}^{(\alpha_k)(\alpha_{k+n})}$ and $E_{n_2}^{(\alpha_k)(\alpha_{k+n})}$. The $E_{n_1}^{(\alpha_k)(\alpha_{k+n})}$ coefficients are in fact giving the link between the $I_0^{(\alpha_k)}$ induced in each element of a substage to shield it from the time variation of the $I_0^{(\alpha_{k+n})}$ flowing through every element while the $E_{n_2}^{(\alpha_k)(\alpha_{k+n})}$ gives the link between the $I_0^{(\alpha_k)}$ induced in each substage to shield the superstage from the same variation. In the previous section we have seen that the currents induced in each substage to shield the superstage, i.e. the I_{k_2}, only featured the spatial frequencies $\left(\alpha_{2+pN_1}\right)_{p\in\mathbb{Z}}$ and that the currents induced in each element of a substage to shield it, i.e. the $I_{k_1}^{\langle k_2\rangle}$, only featured the spatial frequencies $(\alpha_k)_{k\neq 2+pN_1, p\in\mathbb{Z}}$. Consequently, the time variation of the $I_0^{(\alpha_{k+n})}$ does not induce currents with spatial frequencies different from $\left(\alpha_{2+pN_1}\right)_{p\in\mathbb{Z}}$ in the I_{k_2} and does not induce currents with spatial frequencies $\left(\alpha_{2+pN_1}\right)_{p\in\mathbb{Z}}$ in the $I_{k_1}^{\langle k_2\rangle}$; therefore the $\left(E_{n_1}^{(\alpha_{2+pN_1})(\alpha_{2+pN_1+n})}\right)_{p\in\mathbb{Z}}$ and the $\left(E_{n_2}^{(\alpha_k)(\alpha_{k+n})}\right)_{k\neq 2+pN_1, p\in\mathbb{Z}}$ are zero.

For the two different geometries we have chosen, we had $N_1 = 3$, thus the $E_{n_1}^{(\alpha_k)(\alpha_{k+n})}$ are zero for $k = 2 + 3p, p \in \mathbb{Z}$ and the $E_{n_2}^{(\alpha_k)(\alpha_{k+n})}$ are zero for $k \neq 2 + 3p, p \in \mathbb{Z}$. Since we have chosen k such that $-1 \leq k \leq 4$, the $E_{n_1}^{(\alpha_k)(\alpha_{k+n})}$ are zero for $k = \{-1; 2\}$ and the $E_{n_2}^{(\alpha_k)(\alpha_{k+n})}$ are zero for $k = \{0; 1; 3; 4\}$; this is exactly what we have observed on Figure 50, Figure 52, Figure 54 and Figure 56.

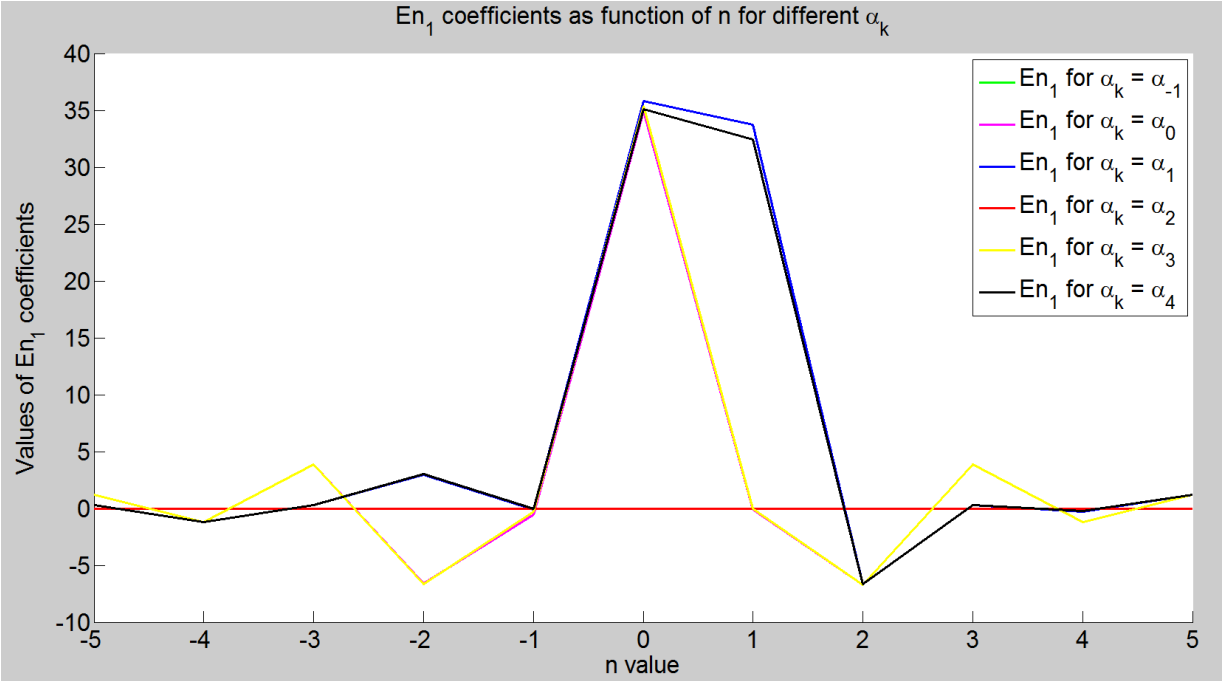

Figure 54 : $E_{n_1}^{(\alpha_k)(\alpha_{k+n})}$ coefficients for different values of k and n for the second set of parameters

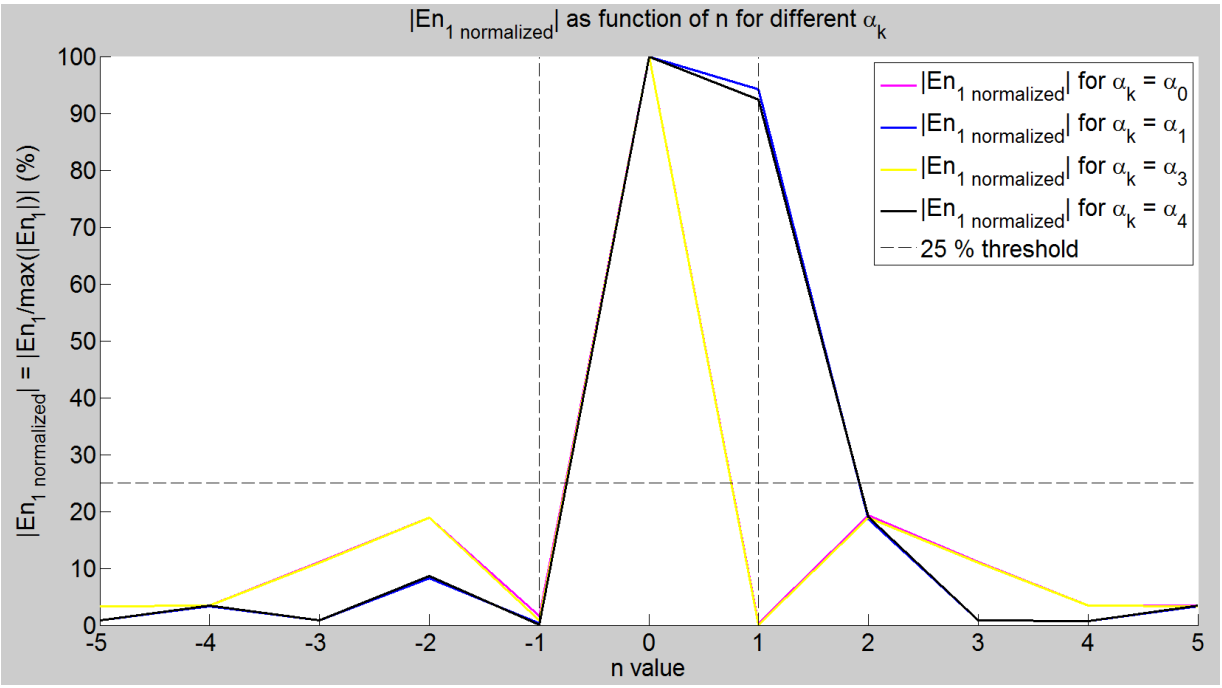

Figure 55 : $E_{n_1}^{(\alpha_k)(\alpha_{k+n})}$ normalized coefficients for different values of k and n for the second set of parameters

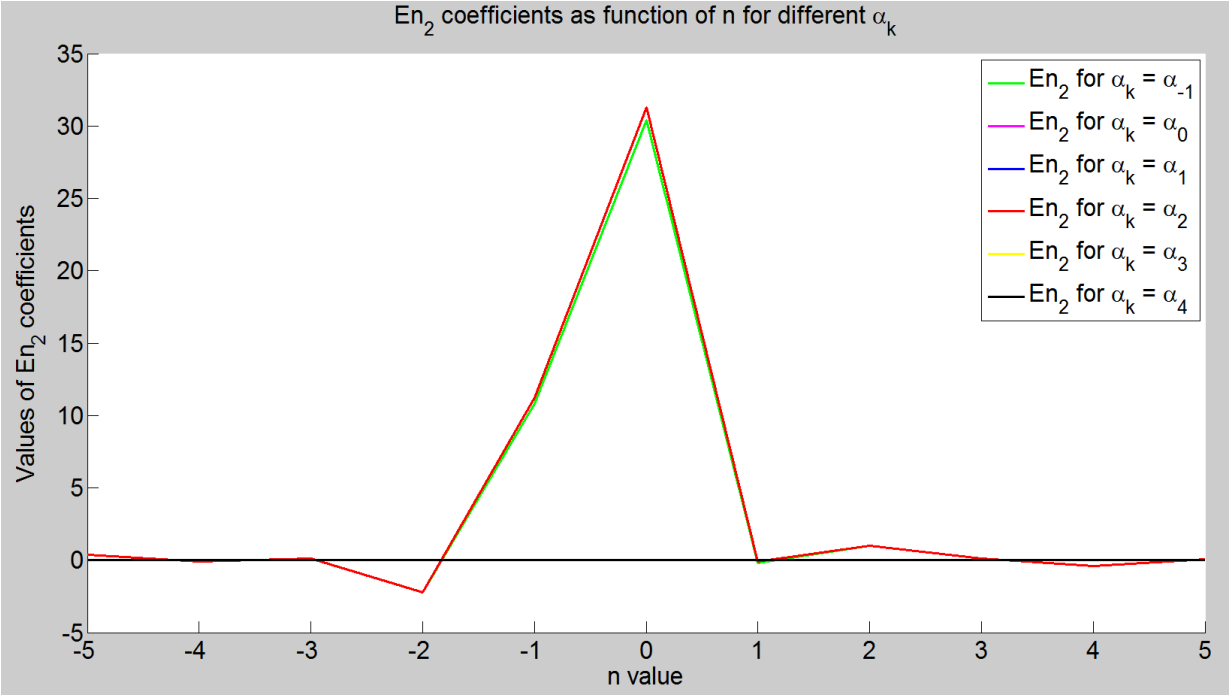

Figure 56 : $E_{n_2}^{(\alpha_k)(\alpha_{k+n})}$ coefficients for different values of k and n for the second set of parameters

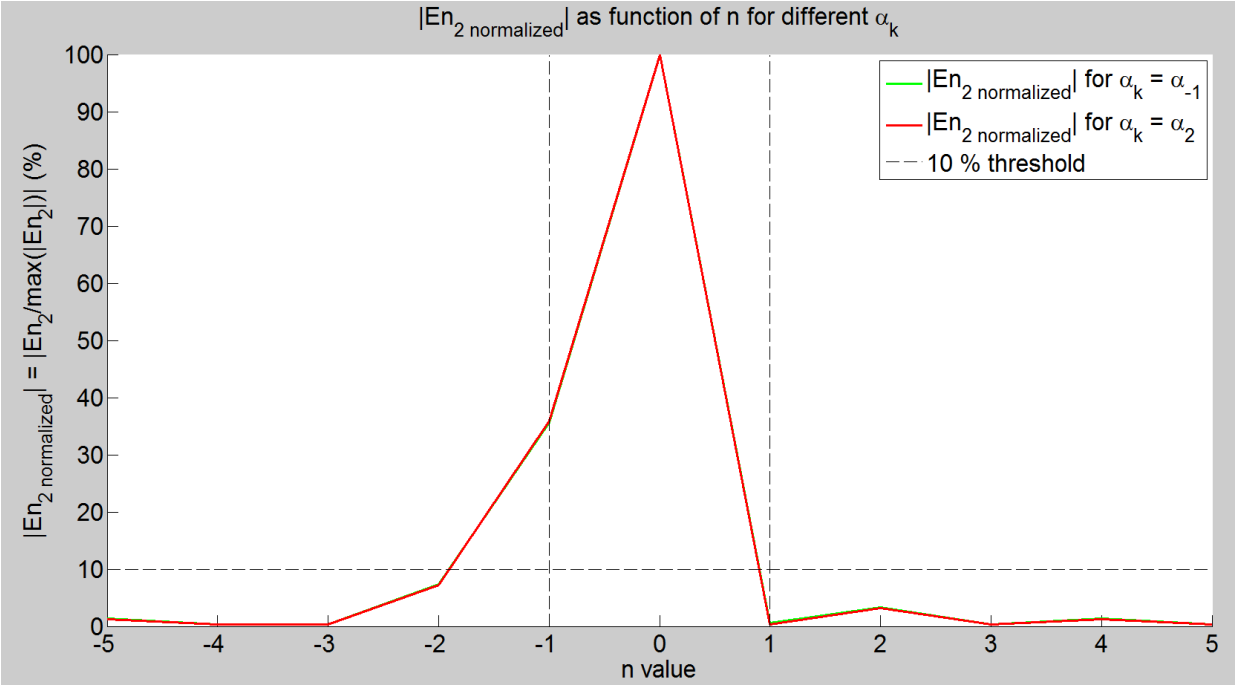

Figure 57 : $E_{n_2}^{(\alpha_k)(\alpha_{k+n})}$ normalized coefficients for different values of k and n for the second set of parameters

This numerical evaluation of the $\left(E_{n_1}^{(\alpha_k)(\alpha_{k+n})}, E_{n_2}^{(\alpha_k)(\alpha_{k+n})}\right)$ coefficients for geometries at two very different scales (one representative of the first two cabling stages and the other representative of the last two cabling stages of TF JT-60SA conductor) has shown us that the coefficients obtained for $|n| > 1$ were negligible in front of those obtained for $|n| \leq 1$.

In other words, this means that the coupling between the $I_0^{(\alpha_k)}$ and the $\dot{I}_0^{(\alpha_{k+n})}$ can be neglected when $|n| > 1$.

Therefore, we can now be confident about the fact that stopping the Fourier series of the $1/g_{p_1 p_2\, k_1 k_2}(z, z', \Psi')$ function at the first order (i.e. for $N = 1$) will not induce high differences in the modeling of the two cabling stage conductor. This step is an important one as we have assessed here that the analytical expression we have chosen along a trade-off between mathematical complexity and relevancy, finds our model still strongly reliable and stays in the guideline of our global model development strategy.

In addition, the assumption $N = 1$ implies that the τ matrix describing the coupling between the different amplitudes is tridiagonal but still infinite. In this case, the matrix equation leads to the following equations for any $k \in \mathbb{Z}$

$$I_0^{(\alpha_k)} + \sum_{n=-1}^{1} \tau_{(\alpha_k)(\alpha_{k+n})} \dot{I}_0^{(\alpha_{k+n})} = I_{0_{ext}}^{(\alpha_k)}$$

which can alternatively be expressed, using the complex notation $\overline{I_0^{(\alpha_k)}} = I_0^{(\alpha_k)} e^{i\omega t}$, as

$$\overline{I_0^{(\alpha_k)}} = \frac{1}{1 + i\omega\tau_{(\alpha_k)(\alpha_k)}} \overline{I_{0_{ext}}^{(\alpha_k)}} - \frac{\omega\tau_{(\alpha_k)(\alpha_{k-1})}}{1 + i\omega\tau_{(\alpha_k)(\alpha_k)}} \overline{I_0^{(\alpha_{k-1})}} - \frac{\omega\tau_{(\alpha_k)(\alpha_{k+1})}}{1 + i\omega\tau_{(\alpha_k)(\alpha_k)}} \overline{I_0^{(\alpha_{k+1})}} \tag{315}$$

Since the only non-zero $I_{0_{ext}}^{(\alpha_k)}$ are obtained for $k = 1$ and $k = 2$, we can deduce that $I_0^{(\alpha_1)}$ and $I_0^{(\alpha_2)}$ are the only amplitudes that are directly excited by the time variation of the applied magnetic field B_a. For a slowly time varying applied magnetic field B_a, the coupling between the $I_0^{(\alpha_k)}$ is negligible and the only non-zero $I_0^{(\alpha_k)}$ are obtained for $k = 1$ and $k = 2$. When the coupling is maximum, i.e. when $\omega\tau_{(\alpha_k)(\alpha_k)} \gg 1$ for any $k \in \mathbb{Z}$, equation (315) becomes

$$\overline{I_0^{(\alpha_k)}} \simeq \frac{-i}{\omega\tau_{(\alpha_k)(\alpha_k)}} \overline{I_{0_{ext}}^{(\alpha_k)}} + i\frac{\tau_{(\alpha_k)(\alpha_{k-1})}}{\tau_{(\alpha_k)(\alpha_k)}} \overline{I_0^{(\alpha_{k-1})}} + i\frac{\tau_{(\alpha_k)(\alpha_{k+1})}}{\tau_{(\alpha_k)(\alpha_k)}} \overline{I_0^{(\alpha_{k+1})}}$$

Using our previous considerations on the $\left(E_{n_1}^{(\alpha_k)(\alpha_{k+n})}, E_{n_2}^{(\alpha_k)(\alpha_{k+n})}\right)$ coefficients and equation (308), we have

$$\tau_{(\alpha_k)(\alpha_{k-1})}/\tau_{(\alpha_k)(\alpha_k)} = \begin{cases} E_{-1_1}^{(\alpha_k)(\alpha_{k-1})}/E_{0_1}^{(\alpha_k)(\alpha_k)} \; if \; k \neq 2 + pN_1, p \in \mathbb{Z} \\ E_{-1_2}^{(\alpha_k)(\alpha_{k-1})}/E_{0_2}^{(\alpha_k)(\alpha_k)} \; if \; k = 2 + pN_1, p \in \mathbb{Z} \end{cases}$$

According to Figure 50 and Figure 57, it appears that those terms are almost always much smaller than 1; using the complex equation above, this indicates that the main contribution to $I_0^{(\alpha_k)}$ is the source

term $I_{0_{ext}}^{(\alpha_k)}$ even when the coupling is maximum. As a result, we realize that there is no need to consider every $I_0^{(\alpha_k)}$since their amplitudes rapidly decreases for $k < 1$ and $k > 2$ even in fully coupled regimes.

Consequently, for $N = 1$, we have decided to only consider the four amplitudes $\left(I_0^{(\alpha_k)}\right)_{0\leq k\leq 3}$ and have reduced the equation to

$$\begin{bmatrix} I_0^{(\alpha_0)} \\ I_0^{(\alpha_1)} \\ I_0^{(\alpha_2)} \\ I_0^{(\alpha_3)} \end{bmatrix} + \begin{bmatrix} \tau_{(\alpha_0)(\alpha_0)} & \tau_{(\alpha_0)(\alpha_1)} & 0 & 0 \\ \tau_{(\alpha_1)(\alpha_0)} & \tau_{(\alpha_1)(\alpha_1)} & \tau_{(\alpha_1)(\alpha_2)} & 0 \\ 0 & \tau_{(\alpha_2)(\alpha_1)} & \tau_{(\alpha_2)(\alpha_2)} & \tau_{(\alpha_2)(\alpha_3)} \\ 0 & 0 & \tau_{(\alpha_3)(\alpha_2)} & \tau_{(\alpha_3)(\alpha_3)} \end{bmatrix} \begin{bmatrix} \dot{I}_0^{(\alpha_0)} \\ \dot{I}_0^{(\alpha_1)} \\ \dot{I}_0^{(\alpha_2)} \\ \dot{I}_0^{(\alpha_3)} \end{bmatrix} = \begin{bmatrix} 0 \\ I_{0_{ext}}^{(\alpha_1)} \\ I_{0_{ext}}^{(\alpha_2)} \\ 0 \end{bmatrix} \tag{316}$$

where the $\tau_{(\alpha_k)(\alpha_{k+n})}$ are given by equation (308) with $E_{n_1}^{(\alpha_k)(\alpha_{k+n})} = 0$ for $k = 2$ and $E_{n_2}^{(\alpha_k)(\alpha_{k+n})} = 0$ for $k = \{0; 1; 3\}$ and the $I_{0_{ext}}^{(\alpha_k)}$ are given by equation (306).

IV.2.6 Power dissipated by coupling currents

❖ **We will now express the coupling power dissipated in a group of groups of twisted elements as a function of the $I_0^{(\alpha_k)}$ amplitudes of the coupling currents.**

IV.2.6.1 General expression

In section IV.2.3.1 , we have noted $I_{k_1\,k_1+1}^{\langle k_2\rangle}(z)$ the local transverse current flowing in substage k_2 from element k_1 to the adjacent element $k_1 + 1$ at z. The local power $dP_{k_1\,k_1+1}^{\langle k_2\rangle}(z)$ dissipated in a slice of thickness dz by the flow of $I_{k_1\,k_1+1}^{\langle k_2\rangle}(z)$ is then given by

$$dP_{k_1\,k_1+1}^{\langle k_2\rangle}(z) = \frac{{I_{k_1\,k_1+1}^{\langle k_2\rangle}}^2(z)}{dG_1} = \frac{1}{\sigma_{l_1}}\left(\frac{I_{k_1\,k_1+1}^{\langle k_2\rangle}(z)}{dz}\right)^2 dz \tag{317}$$

In section IV.2.3.2 , we have noted $I_{k_2\,k_2+1}(z)$ the local transverse current flowing from substage k_2 to the adjacent substage $k_2 + 1$ at z.

The local power $dP_{k_2\,k_2+1}(z)$ dissipated in a slice of thickness dz by the flow of $I_{k_2\,k_2+1}(z)$ is then

$$dP_{k_2\,k_2+1}(z) = \frac{{I_{k_2\,k_2+1}}^2(z)}{dG_2} = \frac{1}{\sigma_{l_2}}\left(\frac{I_{k_2\,k_2+1}(z)}{dz}\right)^2 dz \tag{318}$$

Therefore the total local power $dP(z)$ dissipated in a slice of thickness dz by the flow of all the local transverse currents $\left(I_{k_1\,k_1+1}^{\langle k_2\rangle}(z)\right)_{\substack{1\leq k_1\leq N_1\\ 1\leq k_2\leq N_2}}$ and $\left(I_{k_2\,k_2+1}(z)\right)_{1\leq k_2\leq N_2}$ is

$$dP(z) = dP_{superstage}(z) + dP_{substage}(z) \tag{319}$$

with

$$\begin{cases} dP_{superstage}(z) = \sum_{k_2=1}^{N_2} dP_{k_2\,k_2+1}(z) \\ dP_{substage}(z) = \sum_{k_2=1}^{N_2}\sum_{k_1=1}^{N_1} dP^{\langle k_2\rangle}_{k_1\,k_1+1}(z) \end{cases} \tag{320}$$

Using equations (254) and (256), we have

$$\frac{dI_{k_1k_2}(z)}{dz} = \left[\frac{I^{\langle k_2\rangle}_{k_1-1\,k_1}(z)}{dz} - \frac{I^{\langle k_2\rangle}_{k_1\,k_1+1}(z)}{dz}\right] + \frac{1}{N_1}\left[\frac{I_{k_2-1\,k_2}(z)}{dz} - \frac{I_{k_2\,k_2+1}(z)}{dz}\right] \tag{321}$$

which enables us to write

$$\sum_{k_1=1}^{N_1}\frac{dI_{k_1k_2}(z)}{dz} = \left[\frac{I_{k_2-1\,k_2}(z)}{dz} - \frac{I_{k_2\,k_2+1}(z)}{dz}\right]$$

In addition, from equation (312), we know that for any time regime

$$\frac{dI_{k_1k_2}(z)}{dz} = \sum_{k=-\infty}^{+\infty} -\alpha_k I_0^{(\alpha_k)} \sin\left(\alpha_k z + \varphi^{(\alpha_k)}_{k_1k_2}\right)$$

Thus

$$\sum_{k_1=1}^{N_1}\frac{dI_{k_1k_2}(z)}{dz} = \sum_{k=-\infty}^{+\infty} -\alpha_k I_0^{(\alpha_k)} \sum_{k_1=1}^{N_1}\sin\left(\alpha_k z + \varphi^{(\alpha_k)}_{k_1k_2}\right)$$

Since from (303), $\varphi^{(\alpha_k)}_{k_1k_2} = (k-1)\frac{2\pi(k_2-1)}{N_2} + (2-k)\frac{2\pi(k_1-1)}{N_1}$, we can deduce that

$$\sum_{k_1=1}^{N_1}\sin\left(\alpha_k z + \varphi^{(\alpha_k)}_{k_1k_2}\right) = \begin{cases} N_1 \sin\left(\alpha_k z + (k-1)\dfrac{2\pi(k_2-1)}{N_2}\right) \; if\; k = 2 + pN_1, p \in \mathbb{Z} \\ 0 \; if \; k \neq 2 + pN_1, p \in \mathbb{Z} \end{cases}$$

Therefore

$$\left[\frac{I_{k_2-1\,k_2}(z)}{dz} - \frac{I_{k_2\,k_2+1}(z)}{dz}\right] = \sum_{\substack{k=-\infty \\ k=2+pN_1, p\in\mathbb{Z}}}^{+\infty} -\alpha_k I_0^{(\alpha_k)} N_1 \sin\left(\alpha_k z + (k-1)\frac{2\pi(k_2-1)}{N_2}\right)$$

With the method we have used in section III.2.6 to derive equation (208) and from the equation above, we can write for $1 \leq k_2 \leq N_2$

$$\frac{I_{k_2\,k_2+1}(z)}{dz} = \sum_{\substack{k=-\infty \\ k=2+pN_1, p\in\mathbb{Z}}}^{+\infty} \alpha_k I^{(\alpha_k)}_{k_2\,k_2+1}(z) \tag{322}$$

with

$$I_{k_2\,k_2+1}^{(\alpha_k)}(z)=\begin{cases} I_{t_{0_2}}^{(\alpha_k)}\cos\left[\alpha_k z+(k-1)\dfrac{\pi(2k_2-1)}{N_2}\right] \; if\; k\neq jN_2+1, j\in\mathbb{Z} \\ I_0^{(\alpha_k)}N_1\left(k_2-\dfrac{N_2+1}{2}\right)\sin(\alpha_k z)\; if\; k=jN_2+1, j\in\mathbb{Z}\end{cases} \tag{323}$$

where the $I_{t_{0_2}}^{(\alpha_k)}$ are functions depending on time only equal to

$$I_{t_{0_2}}^{(\alpha_k)}=\frac{-I_0^{(\alpha_k)}N_1}{2\sin\left((k-1)\dfrac{\pi}{N_2}\right)} \tag{324}$$

Now, going back to equation (321), for $1\leq k_2\leq N_2$, we have

$$\left[\frac{I_{k_1-1\,k_1}^{\langle k_2\rangle}(z)}{dz}-\frac{I_{k_1\,k_1+1}^{\langle k_2\rangle}(z)}{dz}\right]=\frac{dI_{k_1k_2}(z)}{dz}-\frac{1}{N_1}\left[\frac{I_{k_2-1\,k_2}(z)}{dz}-\frac{I_{k_2\,k_2+1}(z)}{dz}\right]$$

Using the previous relations, this leads to

$$\left[\frac{I_{k_1-1\,k_1}^{\langle k_2\rangle}(z)}{dz}-\frac{I_{k_1\,k_1+1}^{\langle k_2\rangle}(z)}{dz}\right]=\sum_{\substack{k=-\infty \\ k\neq 2+pN_1, p\in\mathbb{Z}}}^{+\infty}-\alpha_k I_0^{(\alpha_k)}\sin\left(\alpha_k z+\varphi_{k_1k_2}^{(\alpha_k)}\right)$$

Again, with the method we have used in section III.2.6 to derive equation (208) and from the equation above, we can write for $1\leq k_2\leq N_2$ and $1\leq k_2\leq N_2$

$$\frac{I_{k_1\,k_1+1}^{\langle k_2\rangle}}{dz}=\sum_{\substack{k=-\infty \\ k\neq 2+pN_1, p\in\mathbb{Z}}}^{+\infty}\alpha_k I_{t_{0_1}}^{(\alpha_k)}\cos\left[\alpha_k z+\varphi_{k_1k_2}^{(\alpha_k)}+(2-k)\frac{\pi}{N_1}\right] \tag{325}$$

where the $I_{t_{0_1}}^{(\alpha_k)}$ are functions depending on time only equal to

$$I_{t_{0_1}}^{(\alpha_k)}=\frac{-I_0^{(\alpha_k)}}{2\sin\left((2-k)\dfrac{\pi}{N_1}\right)} \tag{326}$$

The local power $dP_{superstage}(z)$ dissipated in a slice of thickness dz by the flow of the interbundle (between substages) currents can be expressed using equations (318), (320) and (322) as

$$dP_{superstage}(z)=\frac{1}{\sigma_{l_2}}\sum_{k_2=1}^{N_2}\left(\sum_{\substack{k=-\infty \\ k=2+pN_1, p\in\mathbb{Z}}}^{+\infty}\alpha_k I_{k_2\,k_2+1}^{(\alpha_k)}(z)\right)^2 dz \tag{327}$$

with from (323)

$$I_{k_2\,k_2+1}^{(\alpha_k)}(z)=\begin{cases} I_{t_{0_2}}^{(\alpha_k)}\cos\left[\alpha_k z+(k-1)\dfrac{\pi(2k_2-1)}{N_2}\right] \; if\; k\neq jN_2+1, j\in\mathbb{Z} \\ I_0^{(\alpha_k)}N_1\left(k_2-\dfrac{N_2+1}{2}\right)\sin(\alpha_k z)\; if\; k=jN_2+1, j\in\mathbb{Z}\end{cases} \tag{328}$$

where $I_{t_{0_2}}^{(\alpha_k)}$ is given by (324).

And the local power $dP_{substage}(z)$ dissipated in a slice of thickness dz by the flow of the intrabundle (inside each substage) currents using equations (317), (320) and (325)

$$dP_{substage}(z) = \frac{1}{\sigma_{l_1}} \sum_{k_2=1}^{N_2} \sum_{k_1=1}^{N_1} \left(\sum_{\substack{k=-\infty \\ k \neq 2+pN_1 \\ p \in \mathbb{Z}}}^{+\infty} \alpha_k I_{t_{0_1}}^{(\alpha_k)} \cos\left[\alpha_k z + \varphi_{k_1 k_2}^{(\alpha_k)} + (2-k)\frac{\pi}{N_1} \right] \right)^2 dz \qquad (329)$$

where $I_{t_{0_1}}^{(\alpha_k)}$ is given by (326).

IV.2.6.2 Expression for $N = 1$

In section IV.2.5.4.4, we have seen that it was possible to take into account only four of the $\left(I_0^{(\alpha_k)}\right)_{k \in \mathbb{Z}}$ amplitudes for $0 \leq k \leq 3$. From equation (327), we can now write

$$dP_{superstage}(z) = \frac{1}{\sigma_{l_2}} \sum_{k_2=1}^{N_2} \left(\sum_{\substack{k=0 \\ k=2+pN_1, p \in \mathbb{Z}}}^{3} \alpha_k I_{k_2\, k_2+1}^{(\alpha_k)}(z) \right)^2 dz$$

The relative integer p must satisfy $0 \leq 2 + pN_1 \leq 3$ and thus $-\frac{2}{N_1} \leq p \leq \frac{1}{N_1}$, since by assumption $N_1 \geq 3$, the only possible relative integer is $p = 0$ which corresponds to $k = 2$. Therefore, from (323) and (324), since $N_2 \geq 3$, we have

$$dP_{superstage}(z) = \frac{1}{\sigma_{l_2}} \frac{{\alpha_2}^2 {I_0^{(\alpha_2)}}^2 {N_1}^2}{4\sin^2\left(\frac{\pi}{N_2}\right)} \sum_{k_2=1}^{N_2} \cos^2\left[\alpha_2 z + \frac{\pi(2k_2-1)}{N_2} \right] dz$$

Since the sum of the squared cosines gives $N_2/2$, we finally have

$$\frac{dP_{superstage}(z)}{dz} = \frac{{\alpha_2}^2 {N_1}^2 N_2}{8\sigma_{l_2} \sin^2\left(\frac{\pi}{N_2}\right)} {I_0^{(\alpha_2)}}^2 \qquad (330)$$

Regarding the local power due to the substage scale, from equation (329), we can write

$$dP_{substage}(z) = \frac{1}{\sigma_{l_1}} \sum_{k_2=1}^{N_2} \sum_{k_1=1}^{N_1} \left(\sum_{\substack{k=0 \\ k \neq 2+pN_1, p \in \mathbb{Z}}}^{3} \alpha_k I_{t_{0_1}}^{(\alpha_k)} \cos\left[\alpha_k z + \varphi_{k_1 k_2}^{(\alpha_k)} + (2-k)\frac{\pi}{N_1} \right] \right)^2 dz$$

Since $k = 2$ was the only possible value of k with respect to the condition $k = 2 + pN_1, p \in \mathbb{Z}$, we can deduce that the values of k between 0 and 4 that satisfy the condition $k \neq 2 + pN_1, p \in \mathbb{Z}$ are $k = \{0; 1; 3\}$. Therefore, from (326), we have

$$dP_{substage}(z) = \frac{1}{4\sigma_{l_1}} \sum_{k_2=1}^{N_2} \sum_{k_1=1}^{N_1} \left(\sum_{\substack{k=0 \\ k\neq 2}}^{3} \frac{\alpha_k I_0^{(\alpha_k)}}{\sin\left((2-k)\frac{\pi}{N_1}\right)} \cos\left[\alpha_k z + \varphi_{k_1 k_2}^{(\alpha_k)} + (2-k)\frac{\pi}{N_1}\right] \right)^2 dz$$

The term inside the brackets features crossed cosines, which after the sum over k_1, leads to

$$\frac{dP_{substage}(z)}{dz} = \frac{N_2 N_1}{8\sigma_{l_1}} \sum_{\substack{k=0 \\ k\neq 2}}^{3} \frac{{\alpha_k}^2}{\sin^2\left((2-k)\frac{\pi}{N_1}\right)} {I_0^{(\alpha_k)}}^2 \tag{331}$$

Finally, from equation (319), we have

$$\frac{dP(z)}{dz} = \frac{{\alpha_2}^2 {N_1}^2 N_2}{8\sigma_{l_2} \sin^2\left(\frac{\pi}{N_2}\right)} {I_0^{(\alpha_2)}}^2 + \frac{N_2 N_1}{8\sigma_{l_1}} \sum_{\substack{k=0 \\ k\neq 2}}^{3} \frac{{\alpha_k}^2}{\sin^2\left((2-k)\frac{\pi}{N_1}\right)} {I_0^{(\alpha_k)}}^2 \tag{332}$$

and the instant power per unit axial length generated inside the N_2-uplet of N_1-uplets is

$$P_l(z) = \frac{{\alpha_2}^2 {N_1}^2 N_2}{8\sigma_{l_2} \sin^2\left(\frac{\pi}{N_2}\right)} {I_0^{(\alpha_2)}}^2 + \frac{N_2 N_1}{8\sigma_{l_1}} \sum_{\substack{k=0 \\ k\neq 2}}^{3} \frac{{\alpha_k}^2}{\sin^2\left((2-k)\frac{\pi}{N_1}\right)} {I_0^{(\alpha_k)}}^2 \tag{333}$$

IV.2.7 Study in inductive regime

❖ **We will now assess the relevance of the inductive part of our model through a study in purely inductive regime.**

In order to assess the relevance of N_2-uplet of N_1-uplets model with the assumption $N = 1$, we have carried out a comparison of the results in purely inductive regime with a simplified analytical approach.

The purely inductive regime occurs when the conductor is subject to an infinite variation of the applied magnetic field B_a, i.e. when B_a behaves as a step function.

The simplified analytical approach considers that the two cabling stages conductor can be represented, at a given position z along the z-axis, by N_2 groups of N_1 infinite straight tubes whose positions in the cross-sectional plane correspond to the positions of the elements at the same z. The geometry considered here is identical to the one displayed on Figure 44 but for N_2 groups of N_1 elements instead of N elements; its cross-section is displayed on Figure 58

The simplified analytical approach consists in computing the inductance matrix per unit axial length $[L]$ of the N_2 groups of N_1 infinite straight tubes using the analytical formulae of self and mutual inductances per unit length between tubes and in assuming that the tubes are subject to a step function of B_a.

This inductance matrix per unit axial length $[L]$ is used in the equation

$$[L][\dot{I}] = -[x]\dot{B}_a$$

where $[\dot{I}]$ is the column vector of the time variation of the currents flowing through the infinite straight tubes and $[x]$ is the column vector of the positions of the infinite straight tubes along the x-axis. Note that the left-hand term of this equation corresponds to the time variation of the magnetic flux per unit axial length felt by the tubes and due to the currents in the tubes; the right-hand term is the time variation of the magnetic flux per unit axial length felt by the tubes and due to the applied magnetic field variation.

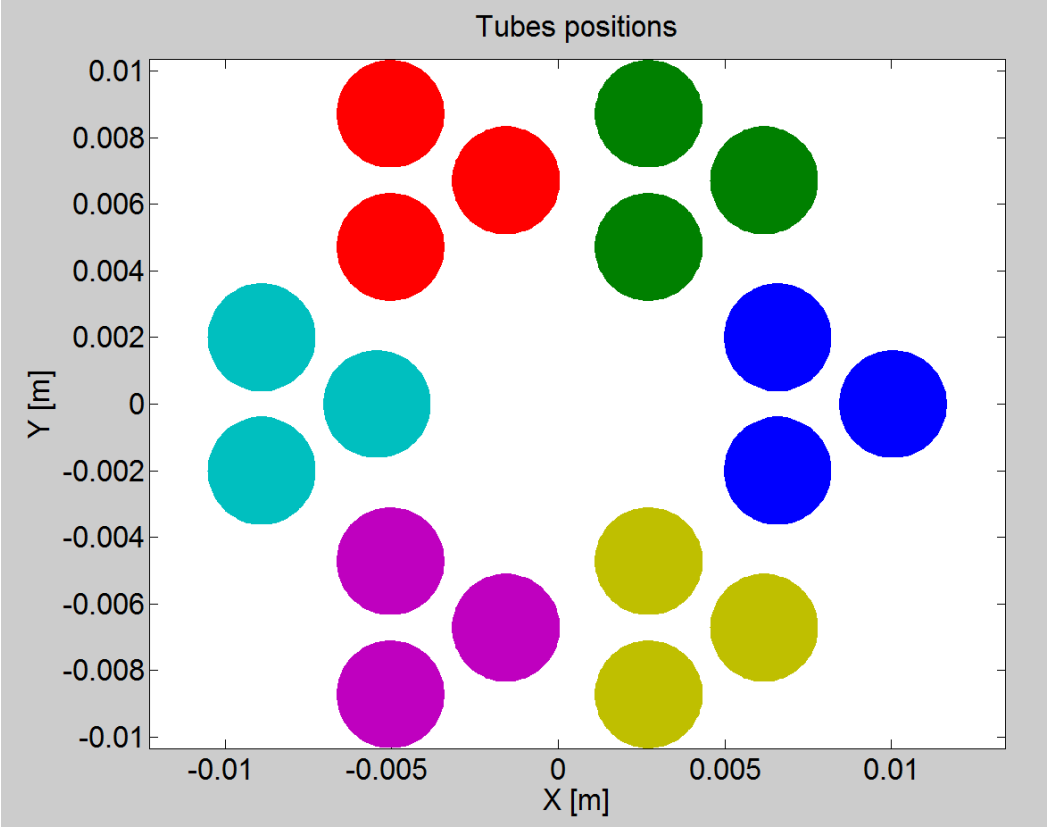

Figure 58 : Cross-section positions of the infinite straight tubes for a sextuplet of triplets

This equation enables us to compute the currents induced in the infinite straight tubes by an infinitely fast variation of B_a (step function) as

$$[dI] = -[L]^{-1}[x]dB_a$$

In our model, in purely inductive regime, the system equation, given by (316), can be reduced to

$$\begin{bmatrix} \tau_{(\alpha_0)(\alpha_0)} & \tau_{(\alpha_0)(\alpha_1)} & 0 & 0 \\ \tau_{(\alpha_1)(\alpha_0)} & \tau_{(\alpha_1)(\alpha_1)} & \tau_{(\alpha_1)(\alpha_2)} & 0 \\ 0 & \tau_{(\alpha_2)(\alpha_1)} & \tau_{(\alpha_2)(\alpha_2)} & \tau_{(\alpha_2)(\alpha_3)} \\ 0 & 0 & \tau_{(\alpha_3)(\alpha_2)} & \tau_{(\alpha_3)(\alpha_3)} \end{bmatrix} \begin{bmatrix} \dot{I}_0^{(\alpha_0)} \\ \dot{I}_0^{(\alpha_1)} \\ \dot{I}_0^{(\alpha_2)} \\ \dot{I}_0^{(\alpha_3)} \end{bmatrix} = \begin{bmatrix} 0 \\ I_{0_{ext}}^{(\alpha_1)} \\ I_{0_{ext}}^{(\alpha_2)} \\ 0 \end{bmatrix}$$

because the time-variations of B_a and of the current amplitudes $\left(I_0^{(\alpha_k)}\right)_{0\leq k\leq 3}$ are supposed to be infinitely greater than the current amplitudes $\left(I_0^{(\alpha_k)}\right)_{0\leq k\leq 3}$.

Multiplying both sides of the equation by dt and using (306), (308) and our previous considerations on the $\left(E_{n_1}^{(\alpha_k)(\alpha_{k+n})}, E_{n_2}^{(\alpha_k)(\alpha_{k+n})}\right)$ coefficients we obtain

$$\begin{bmatrix} \sigma_{l_1} M_{(\alpha_0)(\alpha_0)} & \sigma_{l_1} M_{(\alpha_0)(\alpha_1)} & 0 & 0 \\ \sigma_{l_1} M_{(\alpha_1)(\alpha_0)} & \sigma_{l_1} M_{(\alpha_1)(\alpha_1)} & \sigma_{l_1} M_{(\alpha_1)(\alpha_2)} & 0 \\ 0 & \sigma_{l_2} M_{(\alpha_2)(\alpha_1)} & \sigma_{l_2} M_{(\alpha_2)(\alpha_2)} & \sigma_{l_2} M_{(\alpha_2)(\alpha_3)} \\ 0 & 0 & \sigma_{l_1} M_{(\alpha_3)(\alpha_2)} & \sigma_{l_1} M_{(\alpha_3)(\alpha_3)} \end{bmatrix} \begin{bmatrix} dI_0^{(\alpha_0)} \\ dI_0^{(\alpha_1)} \\ dI_0^{(\alpha_2)} \\ dI_0^{(\alpha_3)} \end{bmatrix} = \begin{bmatrix} 0 \\ 4\sigma_{l_1} R_{c_1} \sin^2\left(\frac{\pi}{N_1}\right) \frac{1}{{\alpha_1}^2} \\ 4\sigma_{l_2} \frac{R_{c_2}}{N_1} \sin^2\left(\frac{\pi}{N_2}\right) \frac{1}{{\alpha_2}^2} \\ 0 \end{bmatrix} dB_a$$

with

$$M_{(\alpha_k)(\alpha_{k+n})} = \begin{cases} \frac{\mu_0}{8\pi^2} \frac{1}{{\alpha_k}^2} E_{n_1}^{(\alpha_k)(\alpha_{k+n})} \; if \; k = \{0; 1; 3\} \\ \frac{\mu_0}{8\pi^2} \frac{1}{{\alpha_k}^2} E_{n_2}^{(\alpha_k)(\alpha_{k+n})} \; if \; k = 2 \end{cases}$$

This system can simply be solved diving both sides of the first, second and fourth lines of the matrix equation by σ_{l_1}, and the third line by σ_{l_2} and then inversing the obtained matrix on the left-hand side.

The variations of currents due to the step of B_a (here chosen as $dB_a = 1T$) computed using this procedure and the straight infinite tubes approach on the sextuplet of triplets of Figure 58 are displayed on Figure 59. We can see the good agreement between the results; the inductive part of the model is then consistent for realistic geometries.

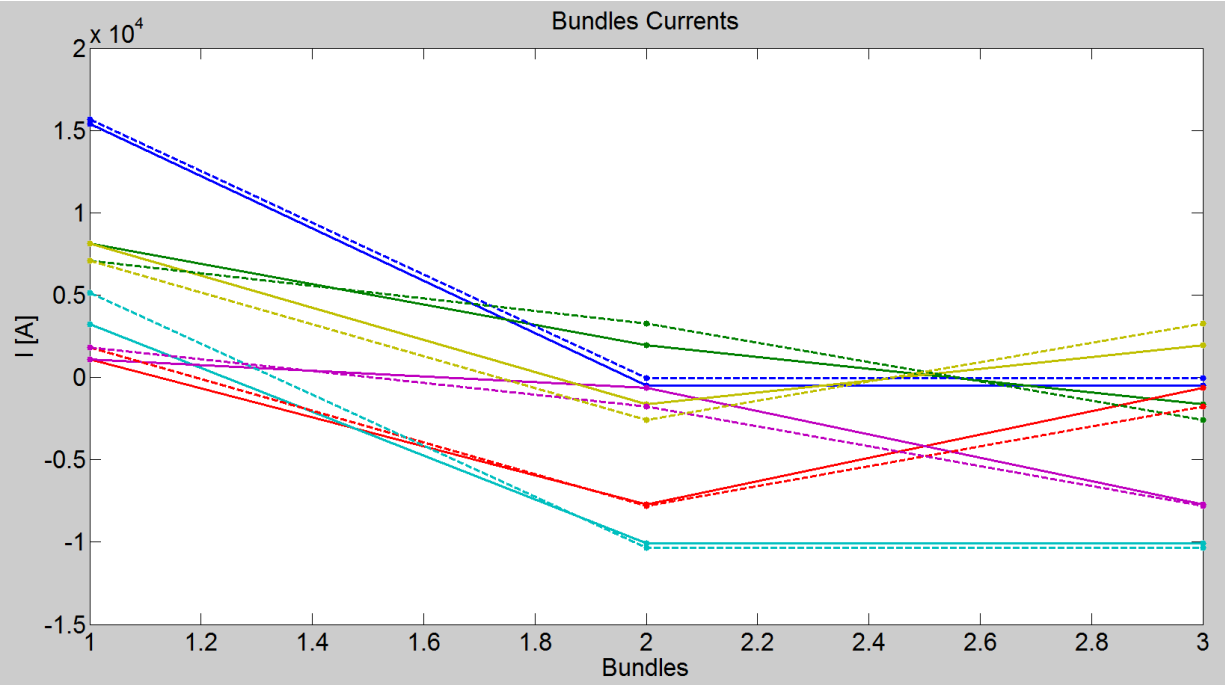

Figure 59 : Variations of currents induced in the sextuplet of triplets displayed on Figure 58 computed using the straight infinite tubes approach (solid lines) and the N_2-uplet of N_1-uplets model (dashed lines)

IV.3 Adaptation of the N_2-uplet of N_1-uplets model to the MPAS model

Having derived the equation governing a conductor described by the N_2-uplet of N_1-uplets model as well as the coupling power generated by unit length of conductor, we will show that it is possible to express the coupling losses per cycle per unit volume of conductor envelope (i.e. circumscribed volume) as in the MPAS model (see section III.3).

We first start by expressing the coupling power generated by unit volume of conductor envelope P_{vol}. In order to do so, we simply have to divide the coupling power generated by unit length of conductor - which is given by equation (333) - by the surface of the conductor envelope which is $\pi\left(R_{c_2}+R_{c_1}+R\right)^2$ where R is the radius of the elements of the N_2-uplet of N_1-uplets (see section IV.2.2).

Consequently, from equation (333), we have

$$P_{vol}=\frac{P_l}{\pi\left(R_{c_2}+R_{c_1}+R\right)^2}=\sum_{j=0}^{3}\delta_j {I_0^{(\alpha_j)}}^2 \tag{334}$$

where

$$\begin{cases}\delta_0=\dfrac{N_2N_1{\alpha_0}^2}{8\sigma_{l_1}\sin^2\left(\dfrac{2\pi}{N_1}\right)\pi\left(R_{c_2}+R_{c_1}+R\right)^2}\\ \delta_1=\dfrac{N_2N_1{\alpha_1}^2}{8\sigma_{l_1}\sin^2\left(\dfrac{\pi}{N_1}\right)\pi\left(R_{c_2}+R_{c_1}+R\right)^2}\\ \delta_2=\dfrac{N_2{N_1}^2{\alpha_2}^2}{8\sigma_{l_2}\sin^2\left(\dfrac{\pi}{N_2}\right)\pi\left(R_{c_2}+R_{c_1}+R\right)^2}\\ \delta_3=\dfrac{N_2N_1{\alpha_3}^2}{8\sigma_{l_1}\sin^2\left(\dfrac{\pi}{N_1}\right)\pi\left(R_{c_2}+R_{c_1}+R\right)^2}\end{cases} \tag{335}$$

Let us note $[I_0]$ the column vector of the $\left(I_0^{(\alpha_k)}\right)_{0\le k\le 3}$ current amplitudes such that for $1\le k\le 4$, $[I_0]_k=I_0^{(\alpha_{k-1})}$. According to equation (316), the equation governing $[I_0]$ can be written as

$$[I_0]+[\tau]\left[\dot{I}_0\right]=[Y]\dot{B}_a \tag{336}$$

with

$$[\tau]=\begin{bmatrix}\tau_{(\alpha_0)(\alpha_0)} & \tau_{(\alpha_0)(\alpha_1)} & 0 & 0\\ \tau_{(\alpha_1)(\alpha_0)} & \tau_{(\alpha_1)(\alpha_1)} & \tau_{(\alpha_1)(\alpha_2)} & 0\\ 0 & \tau_{(\alpha_2)(\alpha_1)} & \tau_{(\alpha_2)(\alpha_2)} & \tau_{(\alpha_2)(\alpha_3)}\\ 0 & 0 & \tau_{(\alpha_3)(\alpha_2)} & \tau_{(\alpha_3)(\alpha_3)}\end{bmatrix} \text{ and } [Y]=\begin{bmatrix}0\\ 4\sigma_{l_1}R_{c_1}\sin^2\left(\dfrac{\pi}{N_1}\right)/{\alpha_1}^2\\ 4\dfrac{\sigma_{l_2}}{N_1}R_{c_2}\sin^2\left(\dfrac{\pi}{N_2}\right)/{\alpha_2}^2\\ 0\end{bmatrix}\dot{B}_a$$

where the $\tau_{(\alpha_k)(\alpha_{k+n})}$ are given by equation (308).

As we did in the composite modeling in section II.2.8 , assuming that $[\tau]$ is a diagonalizable matrix, we can express it as

$$[\tau] = [V][\tau_c][V]^{-1} \tag{337}$$

where $[\tau_c]$ is the diagonal matrix containing the eigenvalues of $[\tau]$ and $[V]$ is the matrix containing the eigenvectors of $[\tau]$.

By analogy with the calculations we have carried out in section II.2.8 , we can immediately conclude that it is possible to express the coupling losses per cycle of magnetic excitation $B_p \sin(\omega t)$ per unit volume of conductor envelope Q adapting equations (126), (127) and (128) to

$$Q(\omega) = \sum_{j=1}^{4} n\kappa_j \frac{{B_p}^2}{\mu_0} \frac{\pi\omega\tau_{c_j}}{1 + \left(\omega\tau_{c_j}\right)^2} \tag{338}$$

with

$$n\kappa_j = 2\mu_0 \sum_{k=1}^{4}\sum_{l=1}^{4} \frac{\delta_{k-1}[V]_{k\,j}[V]_{k\,l}[Y_b]_l[Y_b]_j}{\tau_{c_j} + \tau_{c_l}} \tag{339}$$

where the $\left(\delta_j\right)_{0\leq j\leq 3}$ are given in (335), $[V]$ and $[\tau_c]$ are obtained diagonalizing $[\tau]$, and $[Y_b]$ is defined as

$$[Y_b] = [V]^{-1}[Y] \tag{340}$$

In addition, using the fact $[\tau] = [V][\tau_c][V]^{-1}$ and that $[Y_b] = [V]^{-1}[Y]$, we can express equation (336) as

$$[V]^{-1}[I_0] + [\tau_c][V]^{-1}\left[\dot{I}_0\right] = [Y_b]\dot{B}_a$$

which is equivalent to

$$[V_b][I_0] + [\tau_c][V_b]\left[\dot{I}_0\right] = \begin{bmatrix}1\\1\\1\\1\end{bmatrix}\dot{B}_a$$

with, for $1 \leq j \leq 4$, $[V_b]_j = [V]_j^{-1}/[Y_b]_j$; the notation $[X]_j$ refers to the j[th] line of $[X]$.

From this equation, it is legitimate to introduce a vector of magnetic fields $\left(B_{i\,eq_j}\right)_{1\leq j\leq 4}$ noted $\left[B_{i\,eq}\right]$ such that $[V_b][I_0] = \left[\dot{B}_{i\,eq}\right]$; integrating the equation with respect to time leads for $1 \leq j \leq 4$ to

$$B_{i\,eq_j} + \tau_{c_j}\dot{B}_{i\,eq_j} = B_a \tag{341}$$

where τ_{c_j} refers to the j[th] diagonal element of $[\tau_c]$, and thus to the j[th] eigenvalue of $[\tau]$.

Following the definition of $B_{i\,eq}$ we have introduced in the N-uplet model in section III.3.2 , we can say that $B_{i\,eq_j}$ is the equivalent internal uniform magnetic fields collinear to $\overrightarrow{B_a}$ whose time-variation would create, at any time t, the same distribution of current $\left(I_0^{(\alpha_{j-1})}\cos\left(\alpha_{j-1}z + \varphi_{k_1k_2}^{(\alpha_{j-1})}\right)\right)_{\substack{1\leq k_1\leq N_1\\ 1\leq k_2\leq N_2}}$ than the one given by the N_2-uplet of N_1-uplets model.

We have therefore shown that a two cabling stages conductor could be described as in the MPAS model, i.e. with a set of local internal magnetic fields $B_{i\,eq_j}$ associated with time constants τ_{c_j} (the τ_{c_j} are analogous to the θ_j of the MPAS model in section III.3).

Note that we have found here that the N_2-uplet of N_1-uplets was described by a set of four time constants instead of two considered by the MPAS model.

However the MPAS model initially also considers that there are more than two time constants for a two cabling stages conductor, it simply reduces them to only two in order to simplify the approach. We have also chosen to reduce the number of time constants of the N_2-uplet of N_1-uplets because we have previously seen that theoretically there exists an infinity of time constants.

Again, this point is important as it consolidates both the MPAS model, which is consistent with the experimental reality, and our model because our theoretical results are in agreement with the assumptions of the MPAS model.

IV.4 Comparisons with numerical models

In this section, we will compare the results of the N_2-uplet of N_1-uplets model with those of the reference numerical models THELMA and JackPot on two different simplified geometries which are respectively representative of ITER CS and JT-60SA TF conductors.

For both comparisons, we have considered geometries which consist in a group of groups of cable elements (as in the N_2-uplet of N_1-uplets model) and slowly-time varying regimes of the applied transverse magnetic field B_a so that we can assess the relevance of the resistive part of our model.

In each comparison, we will start by extracting the effective geometrical parameters of the trajectories of the cable elements generated by the code (either THELMA or JackPot); these parameters are the cabling radii and the twist pitches of the substage and superstage scales, i.e. R_{c_1}, R_{c_2}, l_{p_1} and l_{p_2}. We will then extract the effective electrical parameters of the conductor from the conductance network generated by the code; these parameters are the transverse conductances per unit axial length of the substage and superstage scales, i.e. σ_{l_1} and σ_{l_2}. Having determined the effective parameters needed in the N_2-uplet of N_1-uplets model, we will then be able to compute the losses dissipated in the conductor and to compare it to the value computed by the code.

IV.4.1 THELMA

The THELMA code was developed to analyze the electromagnetic and thermo-hydraulic transients of superconducting CICCs for fusion magnets [8], [47]. In this work, the electromagnetic part of the code [48] has been applied to the analysis of the CS ITER conductor, through the same 24-sub-cable model adopted for the analysis of AC losses in the CS Insert experiment [49].

IV.4.1.1 Assumptions of the comparison

The comparison between the outputs of our analytical modeling and those of THELMA was carried out on a simplified representation of the last two stages of ITER CS conductor subject to a cyclic transverse and uniform magnetic excitation.

The considered geometry was then a sextuplet of quadruplets, i.e. six bundles of four elements (with diameter of 6.49mm) each, and the cycles were +/- 0.2T triangles with frequency set to 0.1 Hz.

IV.4.1.2 Determination of the effective geometrical parameters

We consider that the trajectory of any element can be described by the following formula which is similar to that given by equations (250) to (252)

$$\begin{pmatrix} x(z) \\ y(z) \end{pmatrix} = \begin{pmatrix} R_{C_2} \cos\left(\frac{2\pi z}{l_{p_2}} + \varphi_2\right) + R_{C_1} \cos\left(\frac{2\pi z}{l_{p_1}} + \varphi_1\right) \\ R_{C_2} \sin\left(\frac{2\pi z}{l_{p_2}} + \varphi_2\right) + R_{C_1} \sin\left(\frac{2\pi z}{l_{p_1}} + \varphi_1\right) \end{pmatrix} \tag{342}$$

In the expression above, R_{C_2} and l_{p_2} are the cabling radius and twist pitch of the superstage while R_{C_1} and l_{p_1} are those of the substage; φ_2 and φ_1 are initial phase shifts.

In order to find the effective geometrical parameters of the trajectories generated by THELMA, we have developed an algorithm which iteratively processes a given set of trajectories of elements. It first generates complex trajectories out of the real trajectories of the elements with the relation $w(z) = x(z) + iy(z)$, where $x(z)$ and $y(z)$ are the positions of the center of the element along the x-axis and the y-axis respectively at given axial position z. It then computes the Fourier transform of each complex trajectory and processes them to extract the cabling radii R_{c_k} (from the values of the maximum amplitudes of the Fourier transform) and the twist pitches l_{p_k} (from the spatial frequencies of each of the maximum amplitudes of the Fourier transform) associated with each cabling stage k.

The effective cabling radii and twist pitches we have found with our algorithm (whose values are displayed on Table 11) were in almost perfect agreement with the trajectories generated by THELMA since they consisted in a combination of perfect helicoids.

This is shown on Figure 60 which displays the trajectory of cable element 1 (CE1) generated by THELMA and the one determined from the effective cabling radii and twist pitches we have found with our algorithm and from the fit of the initial phase shifts φ_2 and φ_1 using equation (342).

Table 11

Effective geometrical parameters extracted from THELMA trajectories				
Name	R_{c_1}	R_{c_2}	l_{p_1}	l_{p_2}
Value (*mm*)	**3.86**	**11.49**	**112.5**	**450.0**

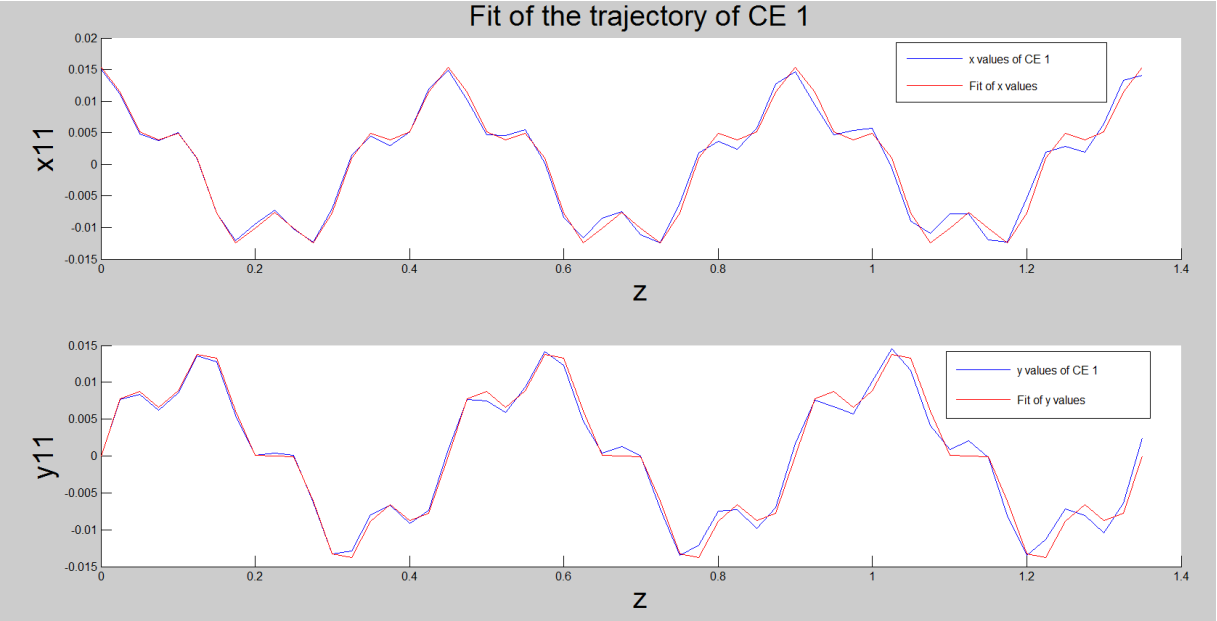

Figure 60 : Fit of the trajectory of CE 1 generated by THELMA using our effective geometrical parameters

IV.4.1.1 Determination of the effective electrical parameters

In the N_2-uplet of N_1-uplets model, we consider the following electrical scheme for each cross-section of the geometry considered in the present comparison.

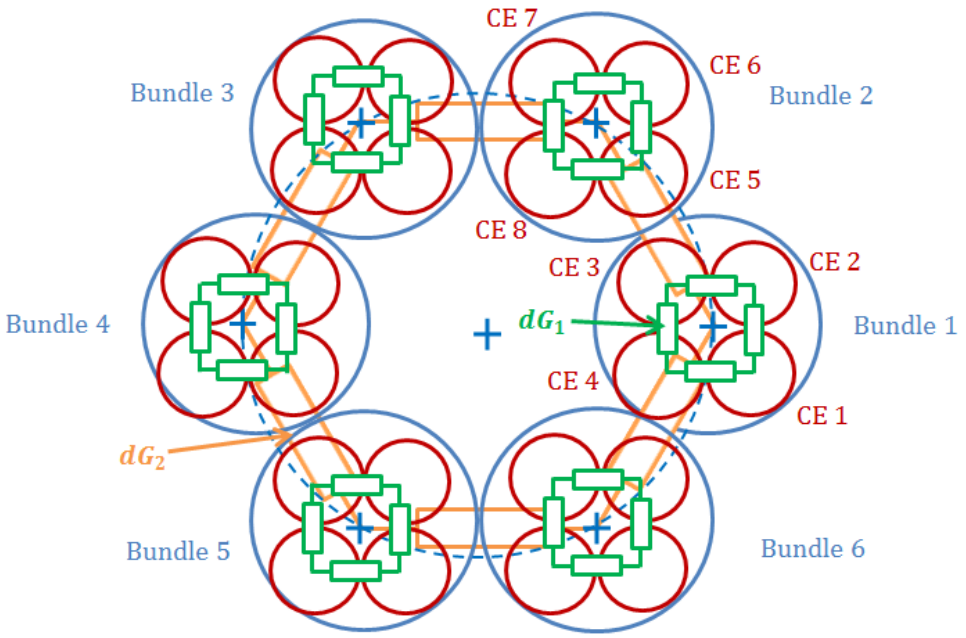

Figure 61 : Electrical scheme of a cross-section of a sextuplet of quadruplets ($N_2 = 6, N_1 = 4$)

Each element is only in electrical contact with its direct neighbors (no diagonal contacts). We recall that in the model we consider a local transverse conductance dG_1 between two adjacent elements of the substage which is given for a slice of conductor of thickness dz by

$$dG_1 = \sigma_{l_1} dz$$

where σ_{l_1} is the transverse conductance per unit axial length of the substage scale.

Similarly, the local transverse conductance dG_2 between two adjacent substages (i.e. bundles) is given for a slice of conductor of thickness dz by

$$dG_2 = \sigma_{l_2} dz$$

where σ_{l_2} is the transverse conductance per unit axial length of the superstage scale.

The conductance network generated by THELMA for the considered geometry is a 3D matrix whose $\sigma_{l_{k\,j}}(z)$ coefficients correspond to the local transverse conductance per unit axial length between Cable Elements k and j at z.

It is important to note that THELMA considers diagonal contacts between each CE of the same bundle while these contacts are considered as non-existent in the N_2-uplet of N_1-uplets model. Therefore, in order to be able to extract the effective electrical parameters of the conductor (i.e. σ_{l_1} and σ_{l_2}) from the conductance network generated by THELMA, we first have to convert the electrical circuit considered by THELMA which features adjacent and diagonal contacts inside each bundle into one with adjacent contacts only (as shown in Figure 62).

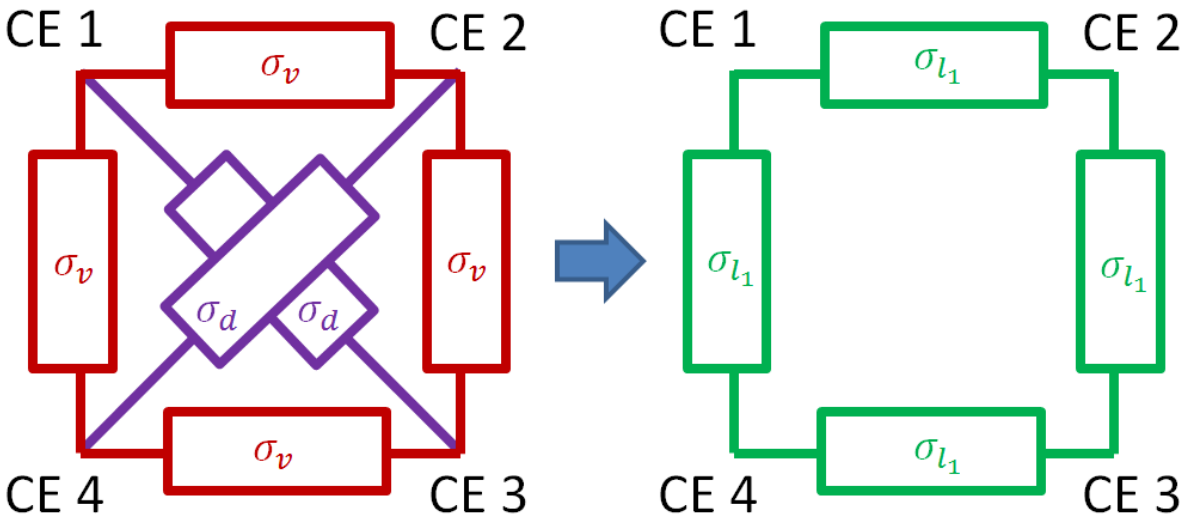

Figure 62 : Conversion of the electrical circuit considered by THELMA

The transverse conductance per unit axial length between diagonal CEs of the same bundle is noted σ_d and the one between adjacent CEs of the same bundle is noted σ_v. In the conductance network generated by THELMA, the σ_d values are identical for all the bundles and for any position along the z-

axis. The σ_v values are also identical for all the bundles and for any position along the z-axis but are different from the σ_d values.

Using electrical circuit laws we can derive

$$\sigma_{l_1} = \frac{3}{4}(\sigma_v + \sigma_d)$$

According to the data generated by THELMA we have $\sigma_v = 1.73 * 10^7\ S.m^{-1}$ and $\sigma_d = 1.41 * 10^7\ S.m^{-1}$ which using the previous formula leads to the value of σ_{l_1} displayed in Table 12.

Regarding the average transverse conductance per unit axial length between adjacent bundles, i.e. σ_{l_2}, it is computed using the following procedure: for each group of adjacent bundles, we set all CEs of the first bundle to an electric potential V and all CEs of the second bundle to a zero electrical potential, then we compute the current I flowing from the first bundle to the second one and deduce an average conductance per unit length dividing I by V and by the length of conductor. Finally we average the values of conductance per unit length obtained for each group of adjacent strands.

The procedure leads to the following relation

$$\sigma_{l_2} = \frac{1}{N_2}\left[\sum_{i=1}^{N_2-1}\sum_{k=N_1(i-1)+1}^{iN_1}\sum_{j=iN_1+1}^{N_1(i+1)}\langle\sigma_{l_{kj}}(z)\rangle_z + \sum_{k=1}^{N_1}\sum_{j=N_1(N_2-1)+1}^{N_1N_2}\langle\sigma_{l_{kj}}(z)\rangle_z\right]$$

the notation $\langle X(z)\rangle_z$ refers to the average of X over z.

Using the conductance network generated by THELMA, this formula has led us to the value of σ_{l_2} displayed in Table 12.

Table 12

Effective electrical parameters extracted from THELMA conductance network		
Name	σ_{l_1}	σ_{l_2}
Value ($10^7\ S.m^{-1}$)	**2.36**	**6.50**

IV.4.1.2 Comparison on the coupling power

In the comparison with THELMA, the conductor was subject to +/- 0.2T triangular cycles of transverse magnetic field with frequency set to 0.1 Hz. We have chosen to compare the value of the coupling stationary power generated at the end of a rising ramp computed using the N_2-uplet of N_1-uplets model with that given by THELMA.

Since we consider a stationary regime at the end of a rising ramp, the coupling currents are not time-varying and the system equation given by equation (316) is simply reduced to

$$\begin{bmatrix} I_0^{(\alpha_0)} \\ I_0^{(\alpha_1)} \\ I_0^{(\alpha_2)} \\ I_0^{(\alpha_3)} \end{bmatrix} = \begin{bmatrix} 0 \\ I_{0_{ext}}^{(\alpha_1)} \\ I_{0_{ext}}^{(\alpha_2)} \\ 0 \end{bmatrix}$$

Using the expressions of $I_{0_{ext}}^{(\alpha_1)}$ and $I_{0_{ext}}^{(\alpha_2)}$ given by (306), we have

$$\begin{cases} I_0^{(\alpha_1)} = 4\sigma_{l_1} R_{c_1} \dot{B}_a \sin^2\left(\frac{\pi}{N_1}\right) \frac{1}{{\alpha_1}^2} \\ I_0^{(\alpha_2)} = 4\frac{\sigma_{l_2}}{N_1} R_{c_2} \dot{B}_a \sin^2\left(\frac{\pi}{N_2}\right) \frac{1}{{\alpha_2}^2} \end{cases}$$

where $\alpha_1 = 2\pi/l_{p_1}$ and $\alpha_2 = 2\pi/l_{p_2}$

Since $I_0^{(\alpha_0)} = 0$ and $I_0^{(\alpha_3)} = 0$, from equation (333), the coupling power per unit axial length is

$$P_l(z) = \frac{{\alpha_1}^2 N_1 N_2}{8\sigma_{l_1} \sin^2\left(\frac{\pi}{N_1}\right)} {I_0^{(\alpha_1)}}^2 + \frac{{\alpha_2}^2 {N_1}^2 N_2}{8\sigma_{l_2} \sin^2\left(\frac{\pi}{N_2}\right)} {I_0^{(\alpha_2)}}^2$$

which combined with the expressions of $I_0^{(\alpha_1)}$ and $I_0^{(\alpha_2)}$ above leads to

$$P_l(z) = 2N_2 \left[\sigma_{l_1} N_1 {R_{c_1}}^2 \sin^2\left(\frac{\pi}{N_1}\right) \left(\frac{l_{p_1}}{2\pi}\right)^2 + \sigma_{l_2} {R_{c_2}}^2 \sin^2\left(\frac{\pi}{N_2}\right) \left(\frac{l_{p_2}}{2\pi}\right)^2 \right] {\dot{B}_a}^2$$

For a rising ramp going from 0 to 0.2T in 2.5s, the time variation of the applied magnetic field is $\dot{B}_a = 0.08\, T.s^{-1}$. Using $N_1 = 4$, $N_2 = 6$ and the values of the effective parameters given in Table 11 and Table 12, we have computed the following coupling stationary power per unit length of conductor

$$P_l = 862\, mW.m^{-1}$$

We have found this value to be about 30% higher than the one computed by THELMA which was around $667\, mW.m^{-1}$ (between $662\, mW.m^{-1}$ and $673\, mW.m^{-1}$ depending on the length of cable considered by THELMA).

IV.4.1.3 Comparison on the induced currents

In addition to the calculation of the coupling stationary power, we have also computed the longitudinal current induced in the first element of the first bundle $I_{CE\,1}(z)$ at the end of a rising ramp and compared it with the one obtained by THELMA; the results are displayed on Figure 63.

In order to compute $I_{CE\,1}(z)$, we have adapted equation (312) such that

$$I_{CE\,1}(z) = I_0^{(\alpha_1)} \cos(\alpha_1 z + \varphi_1) + I_0^{(\alpha_2)} \cos(\alpha_2 z + \varphi_2)$$

where φ_1 and φ_2 are the initial phase shifts that we have found to be $\varphi_1 = 0$ and $\varphi_2 = 0$ when we have fitted the trajectory of CE 1.

However, THELMA has considered that the applied magnetic field was along the x-axis while our formulae are valid for an applied magnetic field along the y-axis. After having applied the relevant modifications on our formulae, the expression above becomes

$$I_{CE\,1}(z) = I_0^{(\alpha_1)} \sin(\alpha_1 z) + I_0^{(\alpha_2)} \sin(\alpha_2 z)$$

Using $N_1 = 4$, $N_2 = 6$, the values of the effective parameters given in Table 11 and Table 12 and the formulae of $I_0^{(\alpha_1)}$ and $I_0^{(\alpha_2)}$ of the previous section, we have found

$$\begin{cases} I_0^{(\alpha_1)} = 4.7\ A \\ I_0^{(\alpha_2)} = 76.6\ A \end{cases}$$

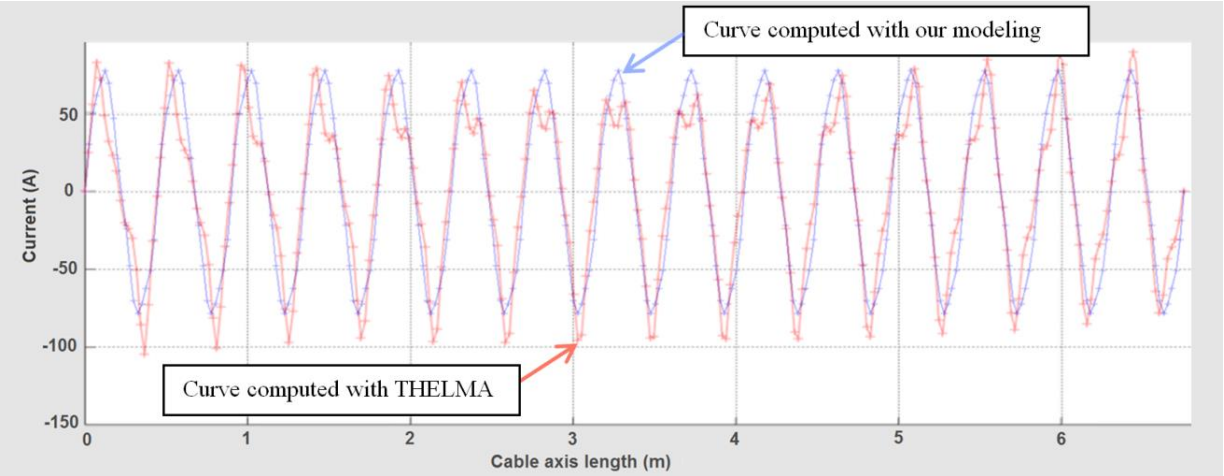

Figure 63 : Current induced in CE 1 computed by THELMA (red curve) and by our model (blue curve)

We can see on Figure 63 the good agreement between the calculations of $I_{1\,1}(z)$ by both models (the difference lies in the range of 15% maximum).

However our expression of $I_{1\,1}(z)$ only consists of two sinusoids with spatial periods l_{p_1} and l_{p_2} while the one computed by THELMA features an additional signal (smaller than the sinusoids).

This additional signal is very likely to come from the discretization of the inter-bundle (superstage scale) conductance network. Indeed, in our model we have averaged this network and, by doing this, we have also removed its local variations. The effect of the discretization of the intra-bundle (substage scale) conductance network may also play a role in the additional signal but with a smaller weight since we have seen that $I_0^{(\alpha_1)}$ was around 6% of $I_0^{(\alpha_2)}$.

IV.4.2 JackPot

JackPot AC/DC is a numerical model developed at the University of Twente [9]. It is an electromagnetic and thermal model that describes the AC/DC performance of CICCs and joints at strand level detail [50]. This model is used to study effects of current distribution non-uniformity, optimization of cable patterns and ITER and DEMO conductor and joint stability [51].

IV.4.2.1 Assumptions of the comparison

We here present the comparison we have carried out with the University of Twente on a simplified geometry of the last two stages of JT-60SA TF conductor: sextuplet of triplets of elements with diameter of 4.21mm. The conductor was subject to a +/- 1T sinusoidal transverse magnetic field with frequency set to 0.05 Hz.

IV.4.2.2 Determination of the effective geometrical parameters

Using the algorithm we have discussed in section IV.4.1.2 and the set of trajectories generated by JackPot we have determined the effective geometrical parameters displayed on Table 13.

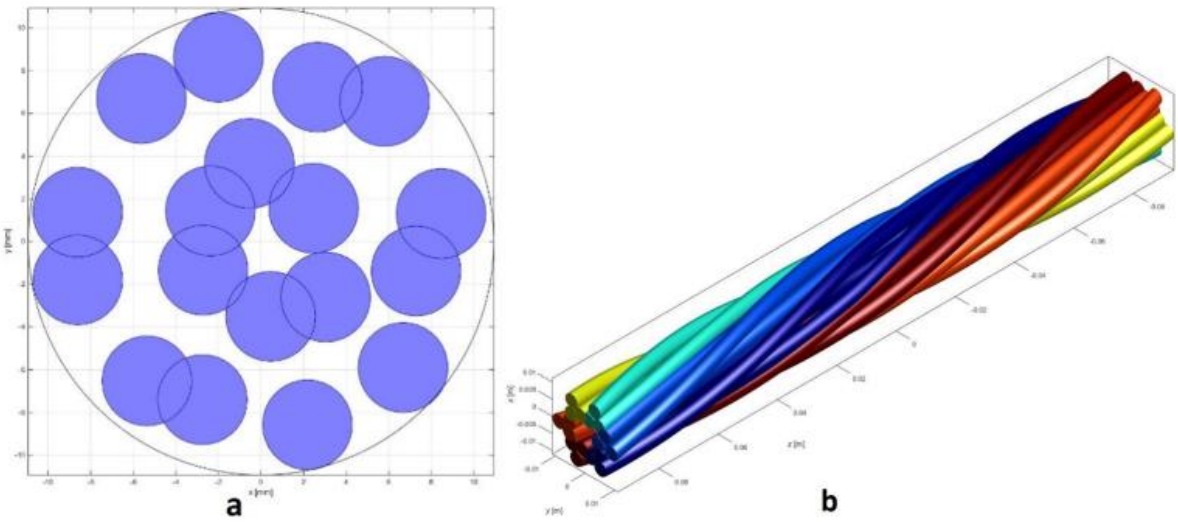

Figure 64 : Cross-section (a) and 3D geometry (b) generated by JackPot

Table 13

Effective geometrical parameters extracted from JackPot trajectories				
Name	R_{c_1}	R_{c_2}	l_{p_1}	l_{p_2}
Value (*mm*)	**3.0**	**6.6**	**187.0**	**290.2**

Using the effective cabling radii and twist pitches of Table 13, we have adjusted the initial phases of CE 1, i.e. φ_2 and φ_1 of equation (342), with respect to the trajectory of CE 1 generated by JackPot.

Both our representation of the trajectory of CE 1 and the one generated by JackPot are displayed on Figure 65.

JackPot having the ability to simulate the compaction of a cable, the trajectories it generates are not exactly combinations of perfect helicoids (see Figure 64). Therefore our representation of the trajectory of CE 1 is not exaclty the same that the one generated by JackPot though we can see on Figure 65 that it is very close to it.

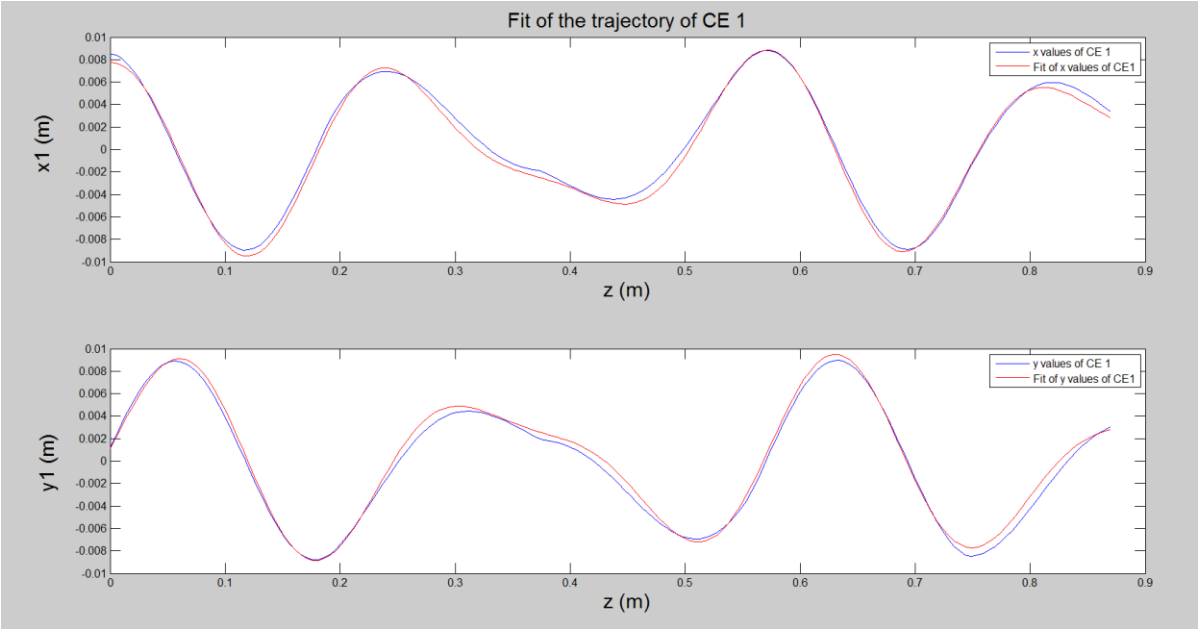

Figure 65 : Fit of the trajectory of CE1 generated by JackPot using our effective geometrical parameters

IV.4.2.3 Determination of the effective electrical parameters

The conductance network generated by JackPot for the considered geometry is a 3D matrix whose $dG_{k\,j}(z)$ coefficients correspond to the local transverse conductances between Cable Elements k and j at z. We can therefore write $dG_{k\,j}(z) = \sigma_{l_{k\,j}}(z)dz$ where $\sigma_{l_{k\,j}}(z)$ is the local transverse conductance per unit axial length between Cable Elements k and j at z.

Conversely to the conductance network generated by THELMA, there are no diagonal contacts between elements of the same bundle and the local transverse conductances between adjacent elements of the same bundle are not identical for all the bundles and for any position along the z-axis in the conductance network generated by JackPot.

We recall that the N_2-uplet of N_1-uplets model considers the electrical scheme displayed on Figure 66 for each cross-section of the geometry considered in the comparison.

In order to extract the effective electrical parameters of the conductance network generated by JackPot, i.e. σ_{l_1} and σ_{l_2}, we use the procedure described below.

We first compute the global transverse conductances between each CE by summing the $dG_{k\,j}(z)$ given by JackPot over the cable length L. This gives us the global transverse conductance matrix G between each CE whose coefficients are equal to

$$G(k,j) = \sum_{z=0}^{L} dG_{k\,j}(z)$$

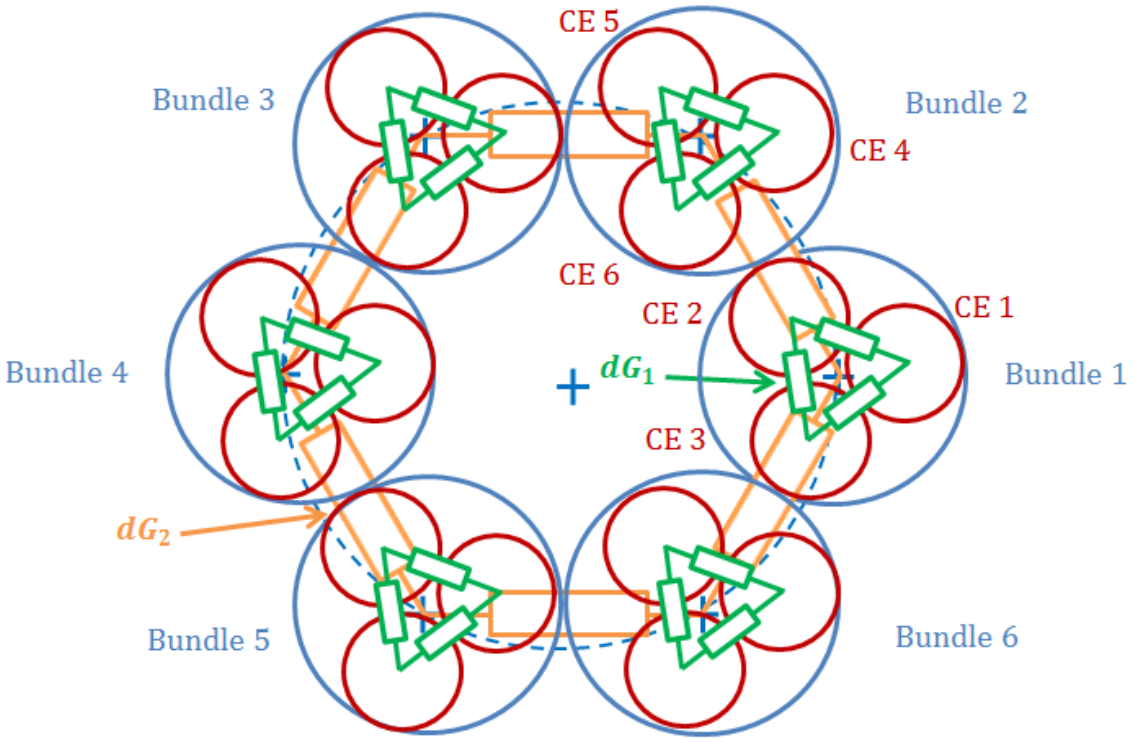

Figure 66 : Electrical scheme of a cross-section of a sextuplet of triplets ($N_2 = 6$, $N_1 = 3$)

From this G matrix, we compute the "intrabundle" average transverse conductance $\widehat{G_1}$ which corresponds to the average transverse conductance between adjacent CEs of the same bundle.

Following the definition of $\widehat{G_1}$ and σ_{l_1} we then have $\sigma_{l_1} = \widehat{G_1}/L$.

Using the conductance network generated by JackPot, the procedure has led us to the value of σ_{l_1} displayed in Table 14.

Regarding the calculation of σ_{l_2}, we first have to build an "interbundle" transverse conductance matrix G_2 ($N_2 \times N_2$ matrix) which gives the transverse conductance between every bundle.

The transverse conductance between bundle k and bundle j ("interbundle" conductance) is equal to the sum of the transverse conductances between every CE of bundle k and every CE of bundle j.

Therefore the expression of G_2 coefficients is

$$G_2(k_2, j_2) = \sum_{k_1=1}^{N_1} \sum_{j_1=1}^{N_1} G((k_2 - 1)N_1 + k_1, (j_2 - 1)N_1 + j_1)$$

From this G_2 matrix, we compute the "interbundle" transverse average conductance $\widehat{G_2}$ which corresponds to the average transverse conductance between adjacent bundles.

Following the definition of $\widehat{G_1}$ and σ_{l_1} we then have $\sigma_{l_2} = \widehat{G_2}/L$.

Using the conductance network generated by JackPot, the procedure has led us to the value of σ_{l_2} displayed in Table 14.

Table 14

Effective electrical parameters extracted from JackPot conductance network		
Name	σ_{l_1}	σ_{l_2}
Value ($10^7\ S.m^{-1}$)	**1.38**	**5.92**

IV.4.2.4 Comparison on the coupling power

In the comparison with JackPot, the conductor was subject to +/- 1T sinusoidal cycles of transverse magnetic field with frequency set to 0.05 Hz. We have chosen to compare the value of the coupling losses per sinusoidal cycle computed using the N_2-uplet of N_1-uplets model with that given by JackPot.

In order to do so, we first assume that the frequency of 0.05 Hz is small enough to neglect the magnetic coupling between the currents induced in all the elements. This implies that the $\left(\tau_{(\alpha_k)(\alpha_{k'})} I_0^{(\alpha_{k'})}\right)_{\substack{0\le k\le 4\\ 0\le k'\le 4}}$ terms of system equation (316) can be neglected so that we again have

$$\begin{cases} I_0^{(\alpha_1)} = 4\sigma_{l_1} R_{c_1} \dot{B}_a \sin^2\left(\frac{\pi}{N_1}\right)\frac{1}{{\alpha_1}^2} \\ I_0^{(\alpha_2)} = 4\frac{\sigma_{l_2}}{N_1} R_{c_2} \dot{B}_a \sin^2\left(\frac{\pi}{N_2}\right)\frac{1}{{\alpha_2}^2} \end{cases}$$

and $I_0^{(\alpha_0)} = I_0^{(\alpha_3)} = 0$.

Therefore, the instant coupling power per unit axial length is also given by

$$P_l(z) = 2N_2\left[\sigma_{l_1} N_1 {R_{c_1}}^2 \sin^2\left(\frac{\pi}{N_1}\right)\left(\frac{l_{p_1}}{2\pi}\right)^2 + \sigma_{l_2} {R_{c_2}}^2 \sin^2\left(\frac{\pi}{N_2}\right)\left(\frac{l_{p_2}}{2\pi}\right)^2\right]{\dot{B}_a}^2$$

Since we have agreed with the University of Twente to compare the results of the N_2-uplet of N_1-uplets model and of JackPot on the coupling losses per sinusoidal cycle per unit axial length Q_l, we have to make use of the relation

$$Q_l(z) = \int_0^T P_l dt$$

where T is the time period of the sinusoidal cycles ($T = 1/f$ with $f = 0.05Hz$).

Since

$$\int_0^T {\dot{B}_a}^2 dt = 2{B_p}^2 \pi^2 f$$

where $B_p = 1T$ is the amplitude of the sinusoidal cycles, from the expression of P_l above we have

$$Q_l = 4{B_p}^2\pi^2 f N_2 \left[\sigma_{l_1} N_1 {R_{c_1}}^2 \sin^2\left(\frac{\pi}{N_1}\right)\left(\frac{l_{p_1}}{2\pi}\right)^2 + \sigma_{l_2}{R_{c_2}}^2 \sin^2\left(\frac{\pi}{N_2}\right)\left(\frac{l_{p_2}}{2\pi}\right)^2\right]$$

Using $N_1 = 3$, $N_2 = 6$ and the values of the effective parameters given in Table 13 and Table 14, we have computed the following coupling losses per sinusoidal cycle per unit axial length

$$Q_l = \ 19.22\, J.m^{-1}/cycle$$

We have found this value to be about 40% higher than the one computed by JackPot which was $13.35\, J.m^{-1}/cycle$.

IV.4.3 Discussions

In order to understand the origin of the differences between the results of the N_2-uplet of N_1-uplets model and those of the numerical codes, several numerical effects have been investigated (changes of spatial discretization, length of conductor and initial phase shifts between elements) but none of them were responsible for the 30-40% discrepancy.

As a matter of fact, it appears that, for both geometries, the coupling power is almost exclusively due to the inter-bundle currents (i.e. superstage); the difference is then bound to come from considerations made at the superstage scale.

In our approach, the local transverse voltages and conductances between any element of a bundle and any element of an adjacent bundle are all set to their respective average U_{avg} and σ_{avg}. We then tend to underestimate the local transverse conductance σ_{loc} (compared to the one of JackPot or THELMA) and overestimate the local transverse voltage U_{loc} between close elements of adjacent bundles and vice versa for distant elements. The local power dissipated between elements of adjacent bundles being equal to $P_{loc} = \sigma_{loc}{U_{loc}}^2$, it is legitimate to expect that the antagonistic effects cancel each other out so that the average power dissipated between adjacent bundles would be close to $P_{avg} = \sigma_{avg}{U_{avg}}^2$. However σ_{loc}, and thus P_{loc}, are always zero between distant elements in THELMA and JACKPOT but this is not the case in our model. Consequently, we slightly overestimate the total coupling power computed by the numerical codes.

Therefore, our model turns out to be a conservative one and, although probably systematically overestimating the overall heat load deposited in the conductor as compared to the numerical prediction, it will rather lead to an over-dimensioning of the magnets, which, on the point of view of their operability, remains on the safe side.

Furthermore, since we have compared our analytical model on two different geometries with two different reference numerical codes, we can be fairly confident about the fact that the overestimation of our model is very likely to remain in the range found, i.e. about 30-50% more than the values computed by the numerical codes.

Knowing this characteristic of the model is precious and consistent with our objective of providing a rational analytical tool of conductor design with respect to coupling losses.

In addition, in the comparison with THELMA, we have also seen that the agreement on the induced currents lies in the range of 15%; this is also an important point as it shows that our analytical model is also legitimate for the study of the stability of a conductor.

To make an overall comment, at this stage of development, we have established an analytical model which possesses the expected features on the point of view of mathematical expression simplicity and ease of implementation. The present benchmarking exercise has shown that, when compared to the numerical approaches currently available, it still keeps its relevancy at the expense of some conservativeness. Therefore, the model can actually be trusted and, to a large extent, used for calculations when a two-stage cable description is adapted.

The future improvements remaining would aim at reducing the gap of our model with the numeric approaches, for example by considering correction factors for the potential map, depending on the stage considered. In this regard model refinements will be interesting to conduct.

IV.5 Experimental work

IV.5.1 Presentation of Josefa facility

The Josefa facility is located at IRFM CEA Cadarache and is used both for characterizing the critical current of a conductor with respect to the magnetic field and to the temperature to which it is subject, and for measuring the magnetization cycles of the conductor, which allow the determination of its hysteresis and coupling losses.

It features two liquid helium baths: one in which the superconducting dipole coil responsible for the application of a magnetic field on the conductor is immersed (its temperature is fixed to 4.2K), and one in which the conductor to be tested is immersed (its temperature can be adjusted for the characterization of the critical current of the conductor).

In the following we will focus the presentation of the Josefa facility on its configuration for AC losses measurement. In this configuration, the temperature of the liquid helium bath in which the conductor to be tested is immersed, is fixed to 4.2K.

The length of conductor that can be tested in Josefa facility is limited to 300mm. It is integrated into a sample holder as shown through Figure 67. The sample holder is then immersed in a liquid helium bath in the middle of the dipole coil.

We can see on Figure 67 (a) that a replica in epoxy resin of the conductor is also integrated into the sample holder and that magnetization pick-up coils are wound both on the conductor and on its replica. The replica is used to ensure that the voltage induced in its magnetization pick-up coil by the time variation of a uniform magnetic field is the same than the one induced in the magnetization pick-up coil wound on the conductor. The difference between the voltages induced in both pick-up coils is then proportional to the magnetization of the conductor when subject to a time-varying applied magnetic field.

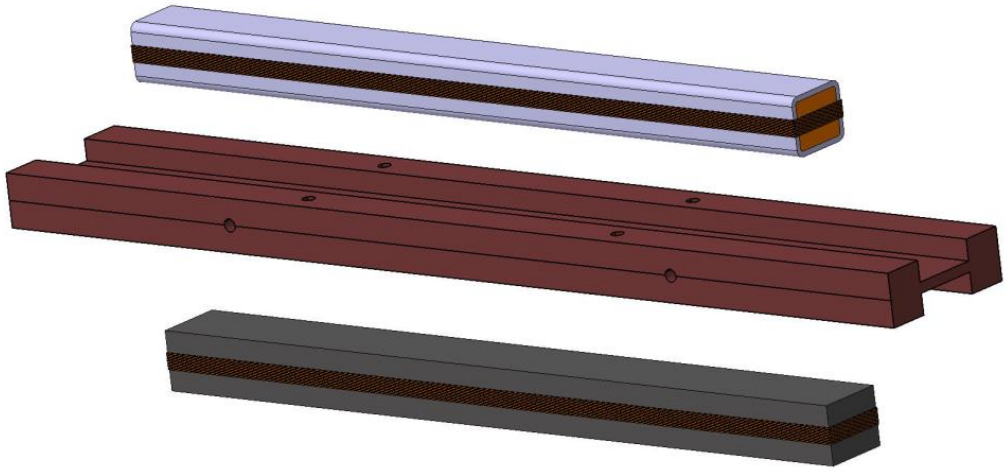

(a) : Conductor to be tested (above) and its replica in epoxy resin (below) together with their magnetization pick-up coils

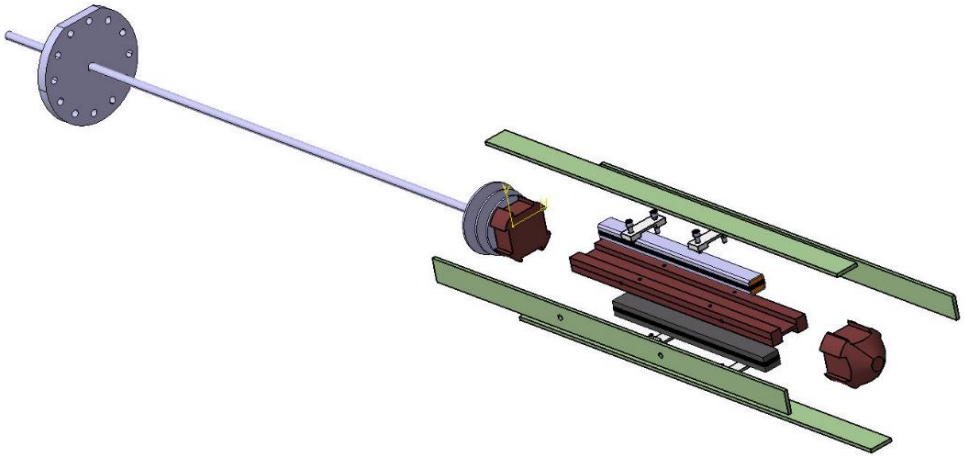

(b) : Integration of the conductor to be tested and its replica in epoxy resin into the sample holder

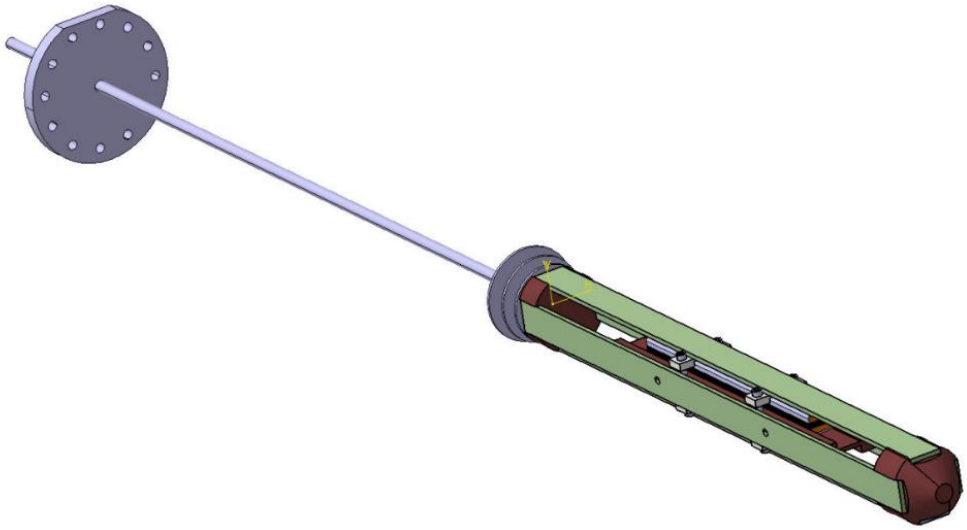

(c) : Conductor to be tested and its replica in epoxy resin fully integrated into the sample holder

Figure 67 : Scheme of the assembly of the conductor and of its replica in epoxy resin into the sample holder

IV.5.2 Measurement method of magnetization

First of all, we have seen in section II.5.1.2 that the energy density Q_{vol} dissipated during a cycle of the external magnetic excitation is equal to

$$Q_{vol} = -\int_{cycle} \vec{M}.d\vec{B}_a$$

where $\vec{M}$ is here the magnetization inside the conductor and $\vec{B}_a$ is the magnetic field applied on the conductor.

We note V_i the voltage induced in the magnetization pick-up coil wound on the conductor and V_e the voltage induced in the magnetization pick-up coil wound on the replica in epoxy resin of the conductor.

Again, by superposition, we can split V_i and V_e as

$$\begin{cases} V_i = V_{i_{\dot{B}_a}} + V_{i_{\dot{M}_0}} \\ V_e = V_{e_{\dot{B}_a}} + V_{e_{\dot{M}_0}} \end{cases}$$

where $V_{i_{\dot{B}_a}}$ is the voltage in the pick-up coil of the conductor due to the time variation of the applied magnetic field B_a and $V_{i_{\dot{M}_0}}$ is the voltage (in the same pick-up coil) due to the time variation of the magnetization M_0 of the conductor. $V_{e_{\dot{B}_a}}$ and $V_{e_{\dot{M}_0}}$ follow the same definition than $V_{i_{\dot{B}_a}}$ and $V_{i_{\dot{M}_0}}$ but for the pick-up coil of the replica.

Since the pick-up coil wound on the replica has the same characteristics that the one wound on the conductor, we have

$$V_{e_{\dot{B}_a}} = V_{i_{\dot{B}_a}}$$

As in the Speedy facility, the magnetization pick-up coils are also connected via a Wheatstone bridge such that the measured voltage V_m is equal to

$$V_m = \frac{R_i V_e - R_e V_i}{R_i + R_e}$$

where R_i and R_e are the electrical resistances of the Wheatstone bridge (see Figure 36).

Given the fact that we have $V_{e_{\dot{B}_a}} = V_{i_{\dot{B}_a}}$, we have set R_i and R_e such that $R_i = R_e = R_0 = 981\ \Omega$.

Consequently

$$V_m = \frac{V_{e_{\dot{M}_0}} - V_{i_{\dot{M}_0}}}{2}$$

In order to determine the links between $V_{e_{\dot{M}_0}}$ and $\dot{M}_0$ and $V_{i_{\dot{M}_0}}$ and $\dot{M}_0$, we have developed an algorithm whose principle is described below.

We first represent the conductor with a large number of infinite straight tubes located on its most outer surface. We then compute the inductance matrix per unit axial length $[L]$ of these infinite straight

tubes using the analytical formulae of self and mutual inductance between infinite straight tubes (as in section IV.2.7).

This inductance matrix per unit axial length $[L]$ is used in the equation

$$[L]\left[\dot{I}\right] = -[x]\dot{B}_a$$

where $\left[\dot{I}\right]$ is the column vector of the time variation of the currents flowing through the infinite straight tubes and $[x]$ is the column vector of the positions of the infinite straight tubes along the x-axis.

This equation enables us to compute the currents induced in the infinite straight tubes by an infinitely fast variation of B_a (step function) as

$$[dI] = -[L]^{-1}[x]dB_a$$

Assuming the initial currents flowing through the infinite straight tubes to be zero, we can compute the energy E_l stored in the system per unit axial length after the step variation dB_a of B_a as

$$E_l = {}^T[dI][L][dI]$$

where the notation ${}^T[dI]$ refers to the transposition of the column vector $[dI]$ into a line vector.

At the same time we can write

$$E_l = -\frac{dM_0 dB_a}{2} S$$

where S is the area of superconducting composites in the conductor and dM_0 is the step variation of the magnetization per unit area S.

From the relation above, we can determine dM_0 as

$$dM_0 = -\frac{2E_l}{dB_a S}$$

In parallel, we compute the flux changes $d\Phi_i = V_i dt$ and $d\Phi_e = V_e dt$ in each of the pick-up coils due to the variations $[dI]$ of the currents flowing through the infinite straight tubes and deduce the value of $V_m dt$.

Finally, diving the value of $V_m dt$ by that of dM_0, we determine the coefficient linking V_m to $\dot{M}_0$.

IV.5.3 Measurements on JT-60SA TF conductor

In this section we will present the results issued from the AC losses measurements we have carried out in the Josefa facility on a sample of JT-60SA TF conductor whose photograph is displayed on Figure 68. This conductor is made of 486 strands : 324 NbTi superconducting composites and 162 copper strands [39].

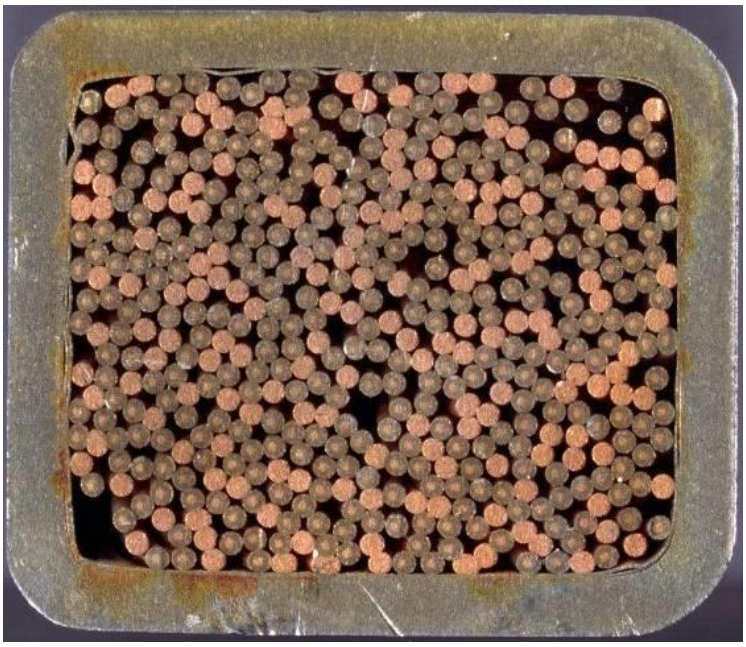

Figure 68 : Photograph of a cross-section of a sample of JT-60SA TF conductor

The magnetic system of Josefa facility composed of the power supply and of the dipole coil can only generate a magnetic field on the conductor in one direction; we have therefore measured the AC losses dissipated in a sample of JT-60SA TF conductor during positive trapezoidal cycles.

We recall that a positive trapezoidal cycle starts from 0 T, rises to $+B_m$ in a time τ_a, then stays at $+B_m$ for a time T_p (typically around 5s), and finally goes back to 0 T again in a time τ_a; the pattern is displayed again on Figure 69. We have carried out two series of measurements for $B_m = 1T$ and $B_m = 1.5T$ and for each series we have used 12 different values of τ_a, between $1.58s$ and $25s$. Again, in order, to increase the reliability of the measured AC losses, for each (B_m, τ_a) couple we have submitted the conductor to 5 consecutive cycles and only kept the average of the AC losses over these 5 cycles.

The curves of AC losses per cycle per unit volume of conductor Q as function of $1/\tau_a$ we have measured in Josefa facility are displayed through Figure 70 to Figure 73.

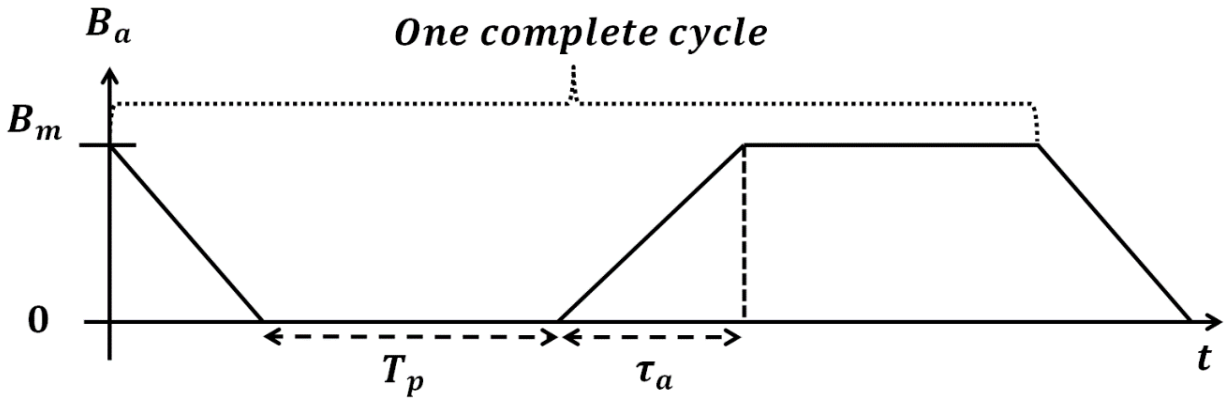

Figure 69 : Schematic pattern of a positive trapezoidal magnetic cycle

IV.5.3.1 Measurement series for $B_m = 1\ T$

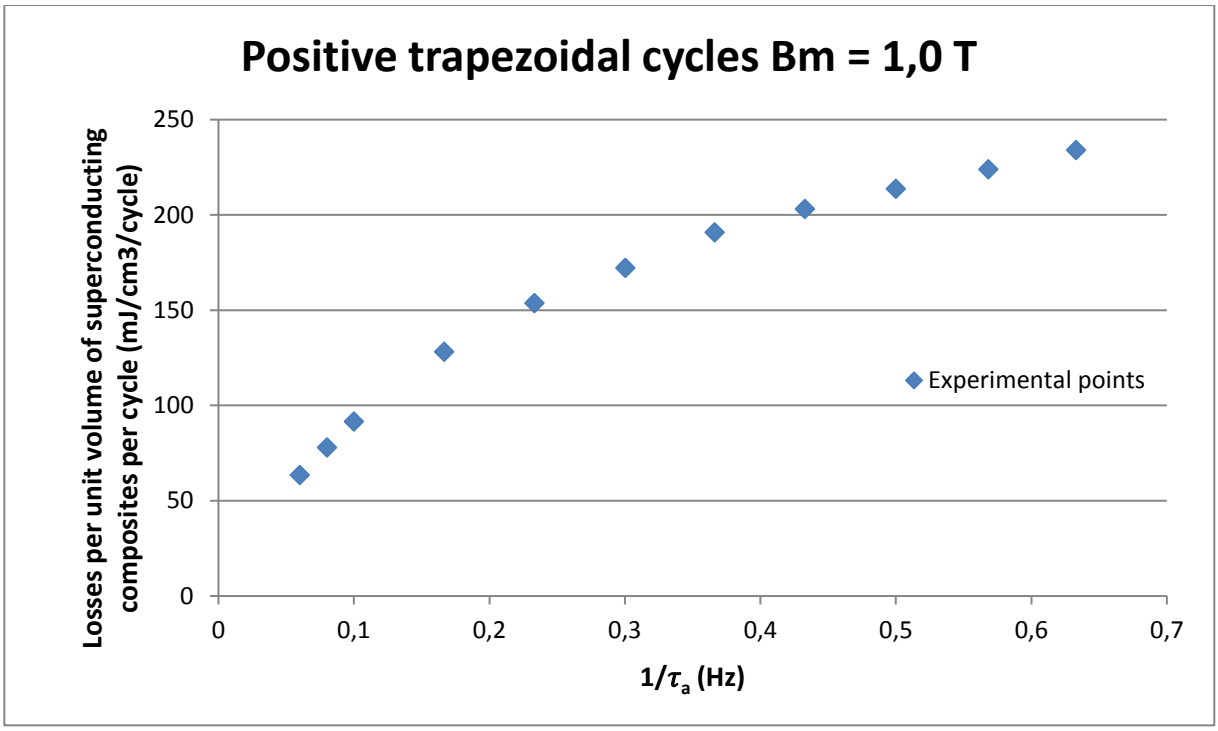

Figure 70 : AC losses of JT-60SA TF conductor per unit volume of superconducting composites per cycle measured in Josefa facility for positive trapezoidal cycles with $B_m = 1T$

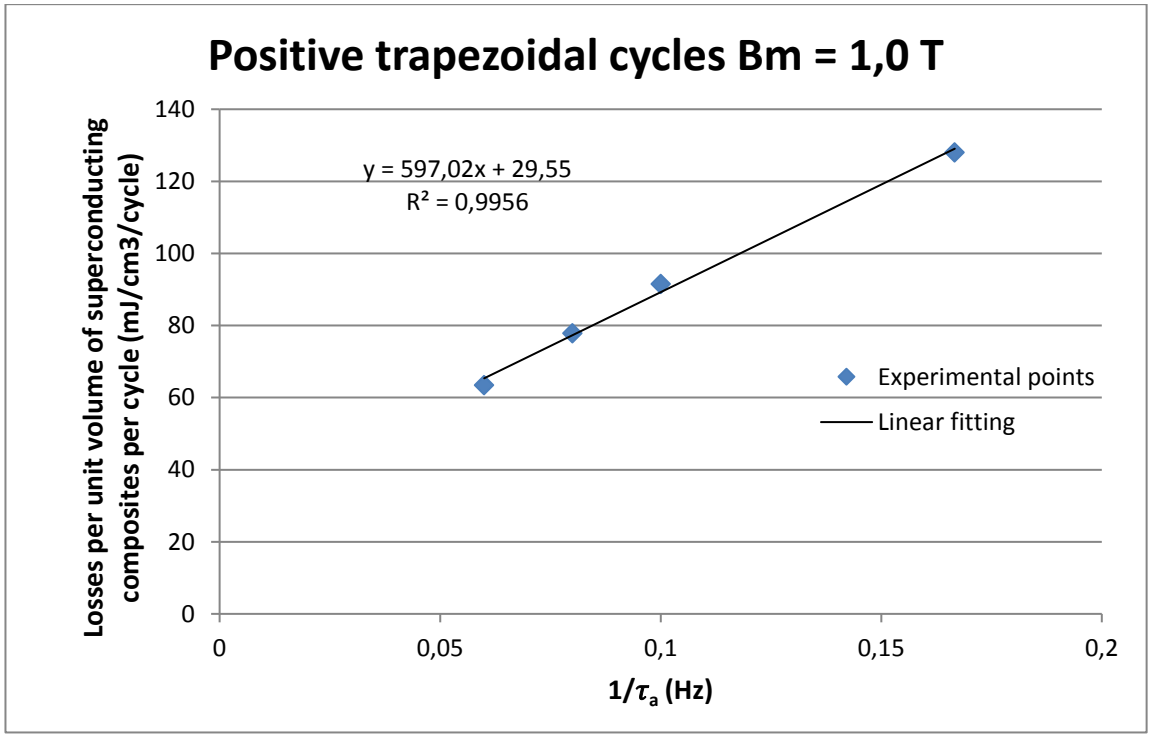

Figure 71 : Zoom on the low frequency region of Figure 70

IV.5.3.2 Measurement series for $B_m = 1.5\ T$

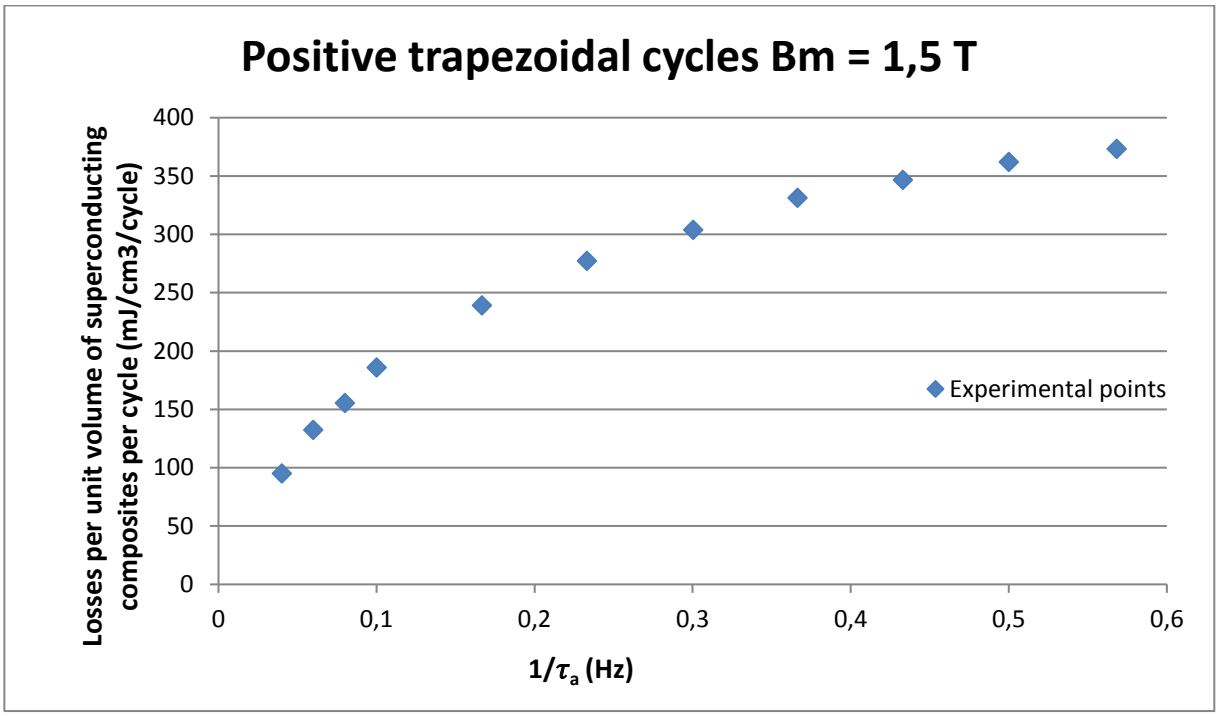

Figure 72 : AC losses of JT-60SA TF conductor per unit volume of superconducting composites per cycle measured in Josefa facility for positive trapezoidal cycles with $B_m = 1.5T$

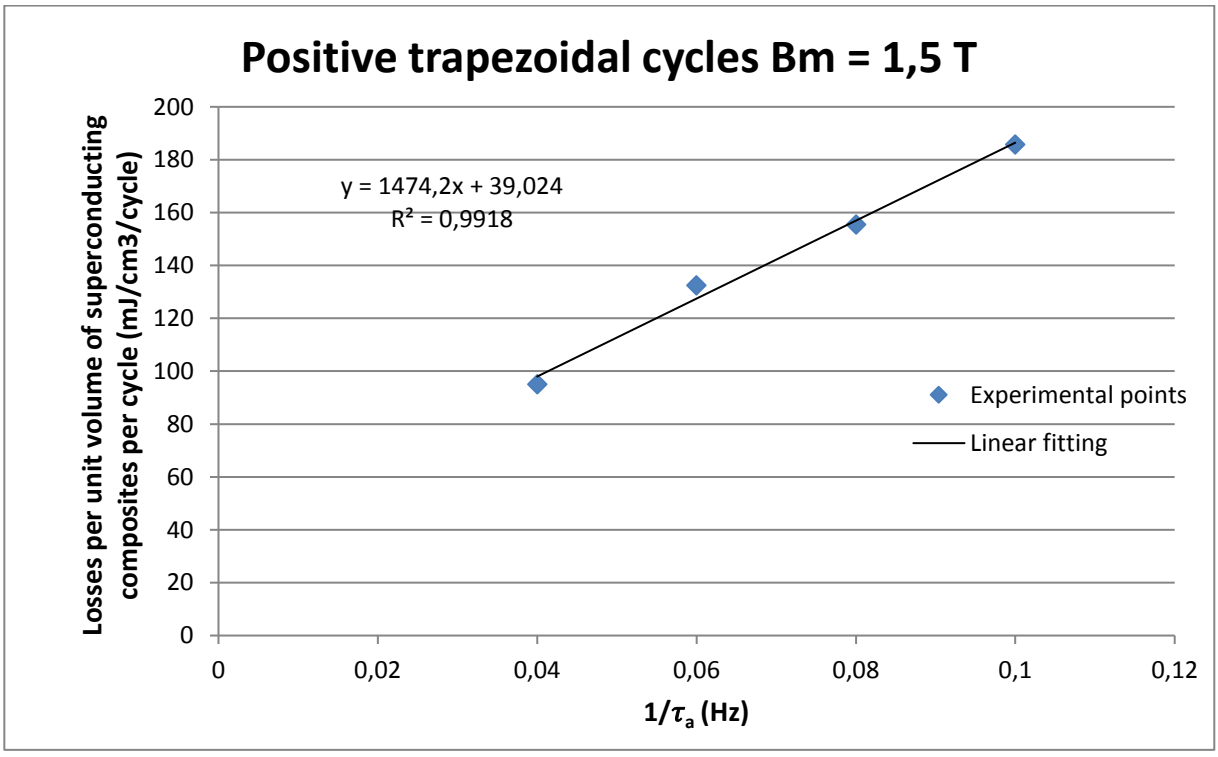

Figure 73 : Zoom on the low frequency region of Figure 72

IV.5.3.3 Hysteresis losses and apparent time constant $n\tau$

It is usually admitted in the community that the instant coupling power per unit volume of superconducting composites P_{coup} generated in a conductor is given by

$$P_{coup} = \frac{n\tau \dot{B}_a{}^2}{\mu_0}$$

where $n\tau$ is the apparent time constant in the system.

Note that this approach is only valid when the applied magnetic field B_a is slowly time varying so that the coupling between the screening currents is negligible.

For these regimes, the hysteresis losses per unit volume of superconducting composites Q_{hyst} per cycle do not depend on the rate of change of the applied magnetic field B_a; it therefore does not depend on τ_a.

The total AC losses Q dissipated in the conductor per unit volume of superconducting composites during a cycle of applied magnetic field B_a are then given by

$$Q = \int_0^T P_{coup}(t)\, dt + Q_{hyst}$$

where T is the time period of a cycle.

For a positive trapezoidal cycle, $\dot{B}_a{}^2$ is constant during the rising and falling ramps and equal to

$$\dot{B}_a{}^2 = \left(\frac{B_m}{\tau_a}\right)^2$$

The total duration of the ramps being $2\tau_a$, we can write

$$\int_0^T P_{coup}(t)\, dt = 2\tau_a \frac{n\tau}{\mu_0}\left(\frac{B_m}{\tau_a}\right)^2 = \frac{2n\tau B_m{}^2}{\mu_0}\frac{1}{\tau_a}$$

Therefore, we can deduce that Q is a linear function of $1/\tau_a$

$$Q\left(\frac{1}{\tau_a}\right) = a\frac{1}{\tau_a} + b$$

with

$$\begin{cases} a = \dfrac{2n\tau B_m{}^2}{\mu_0} \\ b = Q_{hyst} \end{cases}$$

Using the experimental values of a and b given in Figure 71 and Figure 73, we have determined the hysteresis losses and the apparent time constant $n\tau$ of the sample of JT-60SA TF conductor we have measured in Josefa facility; the results are displayed in Table 15.

Table 15

Experimental hysteresis losses and apparent time constant $n\tau$ of a sample of JT-60SA TF conductor for positive trapezoidal cycles with different values of B_m		
$B_m\ (T)$	1.0	1.5
$Q_{hyst}(mJ/cm^3/cycle)$ per unit volume of superconducting composites	**29.6**	**39.0**
$\boldsymbol{n\tau\ (ms)}$	**375**	**412**

Note that the hysteresis losses of the sample of JT-60SA TF conductor are consistent with those of K006-01C JT-60SA TF strand measured in Speedy facility for the same trapezoidal cycles.

IV.5.3.4 Determination of the average transverse conductance

In this part, we assume that the sample of JT-60SA TF conductor can be modeled with the N_2-uplet of N_1-uplets model and we will determine the average transverse conductance per unit axial length of the superstage scale, i.e. σ_{l_2}, using

- the value of the average transverse conductance per unit axial length of the substage scale, i.e. σ_{l_1}, we have extracted from the JackPot conductance network
- the effective geometrical parameters of the last two cabling stages of a sample of JT-60SA TF conductor which are issued from the results of section IV.5.4
- the coupling losses of the sample of JT-60SA TF conductor we have measured in Josefa facility

In section IV.4.2.4 , we have given the analytical formula of the instant coupling power per unit axial length generated by a slowly time variation of the applied magnetic field B_a as

$$P_l = 2N_2\left[\sigma_{l_1} N_1 {R_{c_1}}^2 \sin^2\left(\frac{\pi}{N_1}\right)\left(\frac{l_{p_1}}{2\pi}\right)^2 + \sigma_{l_2} {R_{c_2}}^2 \sin^2\left(\frac{\pi}{N_2}\right)\left(\frac{l_{p_2}}{2\pi}\right)^2\right]{\dot{B}_a}^2$$

Since P_{coup} is the instant coupling power per unit volume of superconducting composites, we have the following relation

$$P_l = P_{coup} S$$

where $S = N_{sc} \pi R^2$ is the area of superconducting composites in the conductor. N_{sc} is the number of superconducting composites inside the conductor which is equal to $N_{sc} = 324$, and R is the radius of the superconducting composites which is equal to $R = 0.405mm$.

In addition, we have

$$P_{coup} = \frac{n\tau \dot{B}_a{}^2}{\mu_0}$$

Therefore, we can write

$$\sigma_{l_2} = \frac{n\tau S}{\mu_0} \frac{1}{2N_2 R_{c_2}{}^2 \sin^2(\pi/N_2)} - \sigma_{l_1} N_1 \left(\frac{R_{c_1}}{R_{c_2}}\right)^2 \left[\frac{\sin(\pi/N_1)}{\sin(\pi/N_2)}\right]^2 \left(\frac{l_{p_1}}{l_{p_2}}\right)^2$$

Using the following values

$$\begin{cases} \sigma_{l_1} = 1.38 * 10^7\ S/m \\ S = 167\ mm^2 \\ n\tau = 412\ ms \\ R_{c_1} = 2.31\ mm \\ R_{c_2} = 7.75\ mm \\ l_{p_1} = 185.2\ mm \\ l_{p_2} = 285.7\ mm \\ N_1 = 3 \\ N_2 = 6 \end{cases}$$

we find

$$\sigma_{l_2} = 1.42 * 10^8\ S/m$$

Note that the order of magnitude of the computed value of σ_{l_2} is consistent with those extracted from the conductance networks of THELMA and JackPot (see sections IV.4.1.1 and IV.4.2.3).

In addition, in the computation of σ_{l_2} we have considered that the coupling power generated inside JT-60SA TF conductor was exclusively due to the last two cabling stages, while in reality it is due to the five cabling stages and to the composite stage of JT-60SA TF conductor. Therefore, the value of σ_{l_2} we have computed using the N_2-uplet of N_1-uplets model is bound to be higher than the real one because the coupling power of the superstage scale also includes here the coupling power of the first three cabling stages and of the composite stage.

This comparison is the first one, actually not too much developed for reason of time. However, it opens towards a broad analysis with free parameters for both conductances, in order to check the reliability of a two-stage cable description. Furthermore, the actual modeling and conductances sizing would be substantially consolidated by experimental data coming from interbundle resistance measurements. Such extensions are left for future investigations.

IV.5.4 X-ray tomography

The knowledge of the internal architecture of a Cable-In-Conduit Conductor is of precious use since its geometrical characteristics largely influence the electromagnetic behavior of the conductor. However, the strong compaction of the CICCs prevents any mechanical method from revealing its inner structure without modifying the initial strands configuration. There is then a need for a non-destructive analysis; one method particularly adapted to this problematic is the X-ray microtomography [52].

In the framework of a collaboration with the INFLPR Bucharest, several samples of JT-60SA TF conductor have been scanned by 2D X-ray microtomography. To reconstruct the internal architecture of each conductor, the following procedure has been implemented:

- several 2D transverse images are generated along the axis of the sample using the data issued from the X-ray microtomography
- these images are automatically processed to identify the positions of the strands in each slice of the conductor
- from this set of strand positions along the conductor axis, the strand trajectories are reconstructed

Even though the procedure seems to be achievable without any difficulty, several facts have to be pointed out. Indeed, the CICCs exhibit a thick steel sheath which strongly attenuates the X-rays and thus prevents the 2D images of the transverse plane of the conductor from having an optimal contrast (see Figure 74); this makes the automatic strand detection quite challenging. In addition, the X-ray microtomography of a slice of conductor being quite time consuming, the 2D transverse images are only obtained every millimeter along the conductor axis; this implies a substantial displacement of each strand from a slice to the next one and thus the covering between its positions in two consecutive slices is weak.

The INFLPR Bucharest has worked both on the automatic detection of the strand positions in each slice of the sample and on the trajectories reconstruction while we have mainly focused on the second point; because of the specificities of the problem, we had to develop our own reconstruction method: the Iterative Velocity-Oriented Reconstruction Algorithm (IVORA).

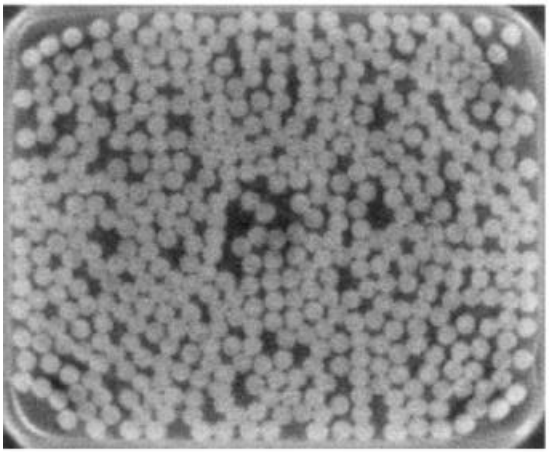

Figure 74 : Slice of JT-60SA TF conductor obtained by X-ray tomography

IV.5.4.1 Strategy of the IVORA algorithm

Initially, because of the low contrast of the 2D images obtained via X-ray tomography, the automatic strand detection in each slice of the sample was not 100% reliable even though it had a very good success rate (more than 98%). An example of strand detection in a slice of JT-60SA TF conductor is displayed on Figure 75; we can see a false strand detection on the bottom right-hand corner (red circle on the conductor wrapping) and a missing one the bottom left-hand corner.

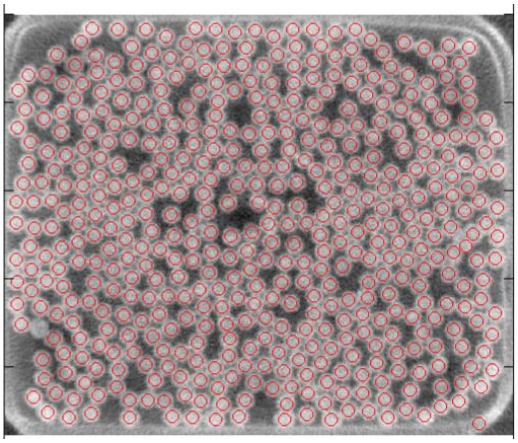

Figure 75 : Slice of JT-60SA TF conductor obtained by X-ray tomography with detected strand positions

As a result, our first objective was to develop an algorithm able to reconstruct the strand trajectories with a set of strand positions featuring a very small number of missing positions or false detections. In order to do so, we have developed a strategy based on the global consistency of the strands displacement from one slice to the next one. It is sequenced as follows:

- Between strand positions of slice n and those of slice n+1, we apply a first restrictive logical rule mainly based on the closest neighbor approach: this creates a first set of associations between positions of slice n and slice n+1 which does not include the totality of the strands

- From this set we create a 2D displacement field (that we call velocity field) between slice n and n+1, we then use it as a tool to associate the strands left aside by the first rule; we use the new complete set of associations to create a new velocity field

- We then average the different velocity fields associated with each group of two consecutive slices to generate an average velocity field which constitutes our global association tool

- The previous sets of associations are then cleared and we start over the association process but this time using the average velocity field

- Every trajectory which is complete (i.e. continuous) after these new associations, are saved and removed from the pool of strand positions so that we are left with the strands that have disappeared (missing or not associated) for at least one slice

- To deal with these strands we create a new average velocity field between slices n and n+2 using the set of associations which are both validated between slices n and n+1 and between slices n+1 and n+2

- After the new associations between slices n and n+2, we are left with the strands that have disappeared (missing or not associated) for at least two consecutive slices

- We then repeat the process until we have created the average velocity field between slices n and n+5 as we have observed that beyond, we do not get any extra complete trajectory

An example of velocity field generated between slice 1 and slice 2 of a sample of JT-60SA TF conductor is displayed on Figure 76.

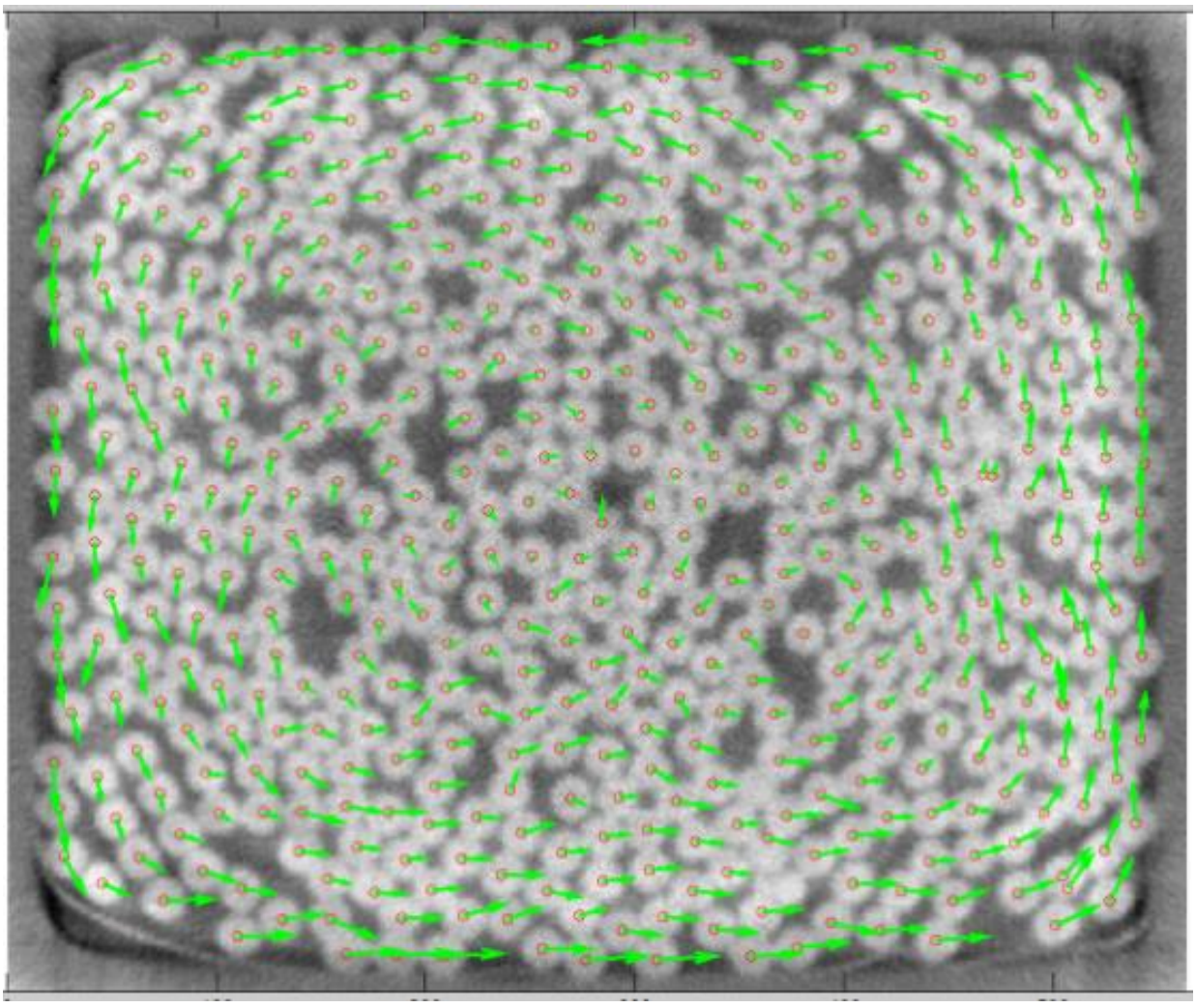

Figure 76 : Velocity field between slice 1 and slice 2 of a sample of JT-60SA TF conductor

IV.5.4.2 Results of the IVORA algorithm

On a 56mm long sample, the IVORA algorithm has been able to reconstruct 100% of the trajectories using 100% complete strand detection while on a 292mm long one it has led to 80% of complete trajectories using also 100% complete strand detection; note that the remaining strand positions are part of fragments of trajectories which are not 292mm long. An example of the reconstruction of strand trajectories is displayed on Figure 77.

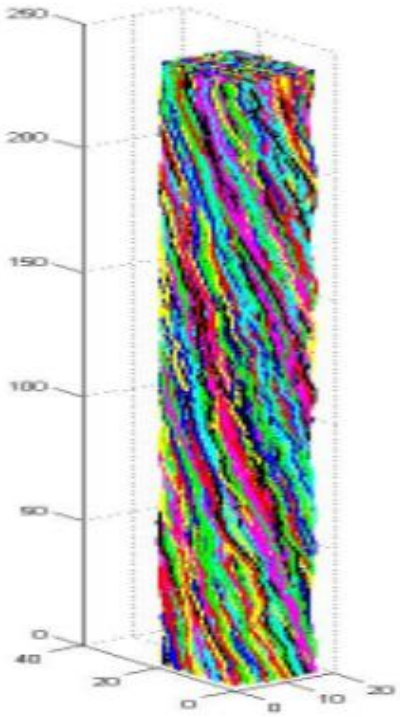

Figure 77 : Reconstructed strand trajectories of a sample of JT-60SA TF conductor

Using the iterative Fourier transform algorithm described in section IV.4.1.2 and the 80% of complete trajectories of the 292mm long sample, we have been able to extract the effective geometrical parameters of JT-60SA TF conductor (i.e. cabling radii and twist pitches of the different cabling stages); they are displayed on Table 16 together with the cable specifications [39].

Table 16

Cabling radii and twist pitches of JT-60SA TF conductor extracted from X-ray tomography					
Cabling stage	*1*	*2*	*3*	*4*	*5*
Cabling radii (mm)	**0.49**	**0.82**	**1.62**	**2.31**	**7.75**
Twist pitches (mm)	**45.4**	**66.7**	**120.2**	**185.2**	**285.7**
Twist pitches specifications [39] (mm)	**45**	**70**	**120**	**190**	**290**

We can notice on Table 16 the good consistency between the twist pitches issued from our treatment of the X-ray tomography of a sample of JT-60SA TF conductor and their specifications. In addition, the first cabling stage of JT-60SA TF conductor being a triplet of strands having a radius of 0.405mm, we expect its cabling radius to be near $0.405mm/\sin(\pi/3) \simeq 0.47mm$, which is close to the radius issued from our treatment (0.49mm).

Furthermore, we have also initiated a comparison with the INFLPR algorithm which is based on the minimization of the total length of the strand trajectories. We have observed a global consistency between the two approaches but with some local disagreements; this comparison will be continued.

IV.6 Synthesis

In this third and last part of our work, we have established the N_2-uplet of N_1-uplets model which represents the behavior of a two cabling stages conductor when subject to any transverse time varying magnetic field. We have seen that the inductive part of our model was consistent as it provides results close to the response of a set of straight infinite tubes (representative of the behavior of the cable in purely inductive regime).

Our work has shown that the currents induced in a two cabling stages conductor can be reduced from an infinite basis of cosine spatial functions (impossible to handle simply) to only four elements (i.e. four cosine functions with four different spatial frequencies, simple to possibly handle for evaluation). This was assessed on two different geometries representative of the first and last cabling stages of JT-60SA TF conductor. In addition, we have analytically defined the expression of coupling losses per cycle in analogy with the MPAS model approach. The difference lies in the number of time constants needed to represent the conductor: two in the MPAS model and four in ours. This point is important as it shows both the consistency of the MPAS model, which is in line with the experimental reality (i.e. the losses of conductor can be represented with a reduced set of time constants), and of our model, whose outputs are dependent upon the cable features, and finally found in line with the assumptions of the MPAS model.

Moreover the comparison of the results of the N_2-uplet of N_1-uplets model with those of two reference numerical models (THELMA and JackPot) on two different geometries has shown a fair agreement (30-40% range for losses and 15% for induced currents) and assessed that our model is slightly conservative.

For all the above-mentioned reasons, we can remain confident in the capacity of our N_2-uplet of N_1-uplets model to represent the magnetic behavior of a cable subject to transient magnetic field. Although surely bearing improvement margins, the present analytical model is sufficiently advanced to form a robust basis for further developments.

Besides, on the experimental side, the AC losses measurements we have carried out in CEA Josefa facility on a sample of JT-60SA TF conductor have led to hysteresis losses consistent with those of its composite measured in Speedy and to an apparent time constant ($n\tau$ parameter) which is in a realistic range. We have also developed an algorithm (IVORA) to reconstruct the strand trajectories of a conductor from the data of its X-ray tomography. It has shown interesting abilities which have allowed the extraction of the effective geometrical parameters of JT-60SA TF conductor; these parameters were consistent with the cable specifications.

V. Conclusions and prospects

In the overall work described in this document, we attempted to address the representation of the coupling losses in a multistage cable with two strategy elements kept along the whole work: encompassing the model expression under the most advanced possible analytical approach and establishing models with a "generic" validity (i.e. for any transient magnetic field regime). In this regard the cable modeling was built increasing step by step the representation scale (strand to CICC) and the cable geometry complexity (single to dual-staged CICC). Although the theoretical way to the development of the CICC analytical model in a sort of ab-initio approach constitutes the major part of the work outcome, other thematic extensions were investigated: the purely numerical way (applicative scripts for the models developed, benchmarking with EU numerical codes, strands trajectories reconstruction out of tomography database) and the purely experimental way (coupling losses measurements at strand scale and at CICC scale). This variety of approaches gives a broader view to the scientific research outcomes obtained in this doctoral project and furthermore allows to more widely open possible paths for the future investigations complementing the present achievements.

During this thesis, we tried to develop our work from the theoretical/analytical side up to the development and implementation of actual working tools directly usable for integration in wider framework (CLASS, IVORA). In the following paragraphs, a complete summary of the present work along with concluding remarks is given. It is reorganized along three main lines: analytical/theoretical works, 3D imaging tools, experimental investigations. An additional specific emphasis is put on numerical models lately developed during this thesis.

V.1 Analytical modeling

V.1.1 Composite strand model development and implementation into CLASS

We have established an original fully generalized analytical representation of the magnetic behavior of a given axisymmetric superconducting composite subject to any time variation of transverse magnetic field. This achievement makes available for the first time a comprehensive analytical model representing composite strands valid for any geometry and any field transient. The associated ad-hoc developed CLASS algorithm produces in this regard complete 2D cartographies of the coupling currents, the electric and magnetic fields and the local power density dissipated inside the composite at any time of transient magnetic field regime. This algorithm being based on analytical formulations, it is easily implementable in multiphysics codes and requires very low CPU resources to be run. Further to its exhaustive and innovative aspect, the present achievement represents a step towards broader modeling objectives, e.g. the evaluation of composites stability limits (associated with thermal models). Besides, the CLASS tool can quantify coupling losses vs. frequency dependence and thus possibly be of a help to design optimized composites.

V.1.2 "Basic" CICC modeling and comparison

We have established and implemented the N-uplet model which is relevant to the analytical representation of the magnetic shielding occurring in a single cabling stage of a conductor. This configuration is the lowest level of complexity in the CICC representation besides the composite analogy.

The achievement of the modeling at this scale constitutes a significant step towards the modeling of coupling losses in CICCs as it shows that the coupling losses are mainly driven by a very few number of cable parameters and their dependence on these parameters has been identified. Furthermore, the fact that the assumption of the MPAS model is in agreement with the analytical output of the N-uplet model is central since, at the same time, it provides a theoretical background to the MPAS model and it reinforces the consistency of our model since the MPAS approach has proved its ability to describe the experimental reality.

V.1.3 Entering into the multistage cable configuration

We have established and implemented the N_2-uplet of N_1-uplets model which represents the behavior of a two cabling stages conductor when subject to any transverse time varying magnetic field. Although surely bearing improvement margins, our model is, in its current version, sufficiently advanced to form a robust basis for further developments, still keeping in line its analytical nature.

We have analytically defined the expression of coupling losses per cycle in analogy with the MPAS model approach. The difference lies in the number of time constants needed to represent the conductor: two in the MPAS model and four in ours. This point is important as it shows both the consistency of the MPAS model, which is in line with the experimental reality (i.e. the losses of conductor can be represented with a reduced set of time constants), and of our model, whose outputs are dependent upon the cable features, and finally found in line with the assumptions of the MPAS model. Moreover the comparison of the results of the N_2-uplet of N_1-uplets model with those of two reference numerical models (THELMA and JackPot) on two different geometries has shown a fair agreement (30-40% range for losses and 15% for induced currents) and assessed that our model is slightly conservative.

V.2 Experimental validations

Several attempts have been carried out in order to obtain reference values of several strand and cable properties and consolidate our model validity. Unfortunately, technical limitations of the existing facility used during this thesis, have prevented the use of the output data for our models validation.

Nevertheless, AC losses measurements have been carried out in CEA Speedy facility on JT-60SA TF and ITER TF strands and the results found (hysteresis losses but mainly time constants) are finally compatible with those found in the literature for similar superconducting composites. More tests could be conducted to build a fairly populated database and confront our model along a statistical approach.

AC losses measurements have also been carried out in CEA Josefa facility on a sample of JT-60SA TF conductor; they have led to hysteresis losses consistent with those of its strand measured in Speedy and to an apparent time constant ($n\tau$ parameter) which lies in a realistic range.

V.3 Numerical approach

V.3.1 3D CICC morphology and effective properties

We have also developed and implemented an ad-hoc algorithm (IVORA) to reconstruct the strand trajectories of a conductor from the data of its X-ray tomography.

Results obtained from the tomography of real samples have been validated. A satisfying agreement between the effective geometrical parameters of JT-60SA TF conductor extracted from the reconstructed trajectories and the specifications of this cable has been obtained.

This algorithm needs to keep being improved to reach a systematic 100% reconstruction rate in order to generate the real 3D conductance and inductance network of any conductor from its X-ray tomography. This will then open the path for highly representative numerical simulations and will also provide information about pending questions such as the evolution of AC losses in a conductor along mechanical cycles (with insights on modification of its inner geometry).

V.3.2 Numerical simulation

In the view of future investigations of the AC losses measurements, a finite element model was recently developed to quantify the effective transverse resistivity of macroscopic filamentary zones from actual geometries which deviate from the periodic representation (e.g. filamentary zone of ITER TF strands). This complementary approach to the CLASS development provides insight to further extend the strand analytical model and its applicability to other geometries. A first step will be the prediction of effective transverse resistivity, to be further confronted to the one deduced from the AC losses measurements of ITER TF Nb_3Sn strand.

V.4 Summary and recommendations

As an overall synthesis, we have established at the conductor scale an analytical model representing the coupling currents and coupling losses inside two types of cable: single-staged and double-staged ones. Their comparisons with various models (analytical, numerical and heuristic) for different geometries and different time regimes have robustly assessed the global consistency of our approach and exhibited its conservative tendency which is fully compatible with the requirements associated with conductor design and risk assessments. In addition, the analytical nature of the achieved studies exhibits a simple form which enhances the physical understanding of the coupling losses phenomenon.

In a more general view, the integration of tailored designed superconducting magnets is essential for the safe and efficient operation of fusion reactors. Optimization of their design (e.g. conductor shape, size and architecture) regarding factors of merit such as electromagnetic or thermo-hydraulic performances is of major importance. The work presented here is included in this long-term framework and, based on the outcomes previously discussed and in complement of the actual state of the art, some prospective remarks can be drawn.

First, our development and implementations could easily be integrated into multiphysics platforms and constitute first rational design tools of conductors with respect to their AC losses.

Secondly, these models can also be considered as a strong building material for the study of conductor stability since they are dealing with all the elements of the elaborated modeling (thermal, currents).

And thirdly, our work would be the keystone of the up scale approach on CICC modeling. As a matter of fact, since CICCs feature more than two cabling stages, the sophistication of the representation of their magnetic shielding behavior considering number of stages beyond the N_2-uplet of N_1-uplets geometry, is to be explored. Due to the complexity of the analytical calculations involved in the development of the N_2-uplet of N_1-uplets model, a strict replication of the presented approach on a three cabling stages conductor might reveal high difficulties. As tentative suggestion, two options could be considered:

- condense the magnetic shielding effects of two consecutive cabling stages into a single "effective" one with the appropriate partial shielding coefficient and then consider the third stage contribution

- consider only the magnetic coupling between consecutive cabling stages assuming/checking low coupling effect between non-consecutive cabling stages.

Another way to use the outputs of the N_2-uplet of N_1-uplets model would consist in extrapolating the electrical potential at the positions of each strand from the one given by the N_2-uplet of N_1-uplets model at the center of gravity of the last but one cabling stage of a conductor.

Finally, we have contributed, at our level, to improve knowledge and representation of coupling losses in superconducting cables, providing to the community analytical concepts as well as various tools on this subject. Considering the importance of this phenomenon in the fusion magnet operation, which is, among others, linked to tokamaks safety aspects, this investigation domain should keep the attention of the fusion community. Hopefully further investigations will be carried out on coupling losses, in the aim to consolidate the future fusion reactor operation.

References

[1] L.A. Artsimovich, S.V. Mirnov and V.S. Strelkov, Plasma Physics, Journal of Nuclear Energy, Part C7, 1965, pp. 305

[2] J. Bardeen, L.N. Cooper and J.R. Schrieffer, *Theory of Superconductivity*, Physical Review, Vol. 108, No. 5, 1957, pp. 1175-1204.

[3] M.N. Wilson, "Introduction" in *Superconducting Magnets*, New York: Oxford University Press Inc., 1983, p. 2.

[4] JL. Duchateau, D. Ciazynski, O. Guerber, S. H. Park, W.H. Fietz, A. Ulbricht, G. Zahn and L. Zani, *Exploring the limits of a very large Nb_3Sn conductor : the 80 kA conductor of the ITER Toroidal Field Model Coil*, Supercond. Sci. Technol., Vol. 17, No. 5, 2005, S241

[5] R.K. Maix et al., *Design, Production and QA Test Results of the NbTi CIC Conductors for the W7-X Magnet System*, J. Phys.: Conf. Ser. 43, 2006, p. 753

[6] Yamamoto et al., *Helical and poloidal coil R&D in LHD*, Fusion Engineering and Design, Vol. 41, Issues 1–4, 1998, pp. 231-239.

[7] Y. Koide et al., *JT-60SA superconducting magnet system*, Nucl. Fusion, Vol. 55, No. 8, 2015, 086001

[8] M. Ciotti, A. Nijhuis, P. L. Ribani, L. Savoldi Richard, R. Zanino, *THELMA code electromagnetic model of ITER superconducting cables and application to the ENEA stability experiment*, Supercond. Sci. Technol., Vol. 19, Oct. 2006, pp. 987–997.

[9] E.P. van Lanen, A. Nijhuis, *JackPot: A novel model to study the influence of current non-uniformity and cabling patterns in cable-in-conduit conductor*, Cryogenics, Vol. 50, 2010, pp. 139-148.

[10] M.N. Wilson, "Time-vaying fields and A.C. losses" in *Superconducting Magnets*, New York: Oxford University Press Inc., 1983, pp. 176–180.

[11] P. Tixador, "Supraconductivité" in *Les supraconducteurs*, Paris, France: Editions Hermès, 1995, pp. 53–58.

[12] D. Ciazynski, B. Turck, JL. Duchateau, C. Meuris, *AC losses and current distribution in 40 kA NbTi and NbSn conductors for NET / ITER*, I.E.E.E. Trans. on App. Superconductivity, Vol 3, No. 1, 1993, p. 594

[13] P. Bruzzone, *AC losses and stability on large cable-in-conduit superconductors*, Physica C: Superconductivity, Vol. 310, Issues 1–4, 1998, pp. 240-246.

[14] Y. Takahashi et al., *AC Loss Measurement of 46 kA-13T Nb_3Sn Conductor for ITER*, I.E.E.E. Trans. on App. Superconductivity, Vol.11, No. 1, 2001, p. 1546

[15] A. Nijhuis, Y. Ilyin, W. Abbas, H.H.J. ten Kate, *Evolution of contact resistance and coupling loss in prototype ITER PF NbTi conductors under transverse cyclic load*, I.E.E.E. Trans. on App. Superconductivity, Vol.13, No. 2, 2003, p. 2388

[16] A. Nijhuis, Yu. Ilyin, W. Abbas, B. ten Haken, H.H.J. ten Kate, *Change of interstrand contact resistance and coupling loss in various prototype ITER NbTi conductors with transverse loading in the Twente Cryogenic Cable Press up to 40,000 cycles*, Cryogenics, Vol. 44, 2004, pp. 319–339

[17] B. Turck, L. Zani, *A macroscopic model for coupling current losses in cables made of multistages of superconducting strands and its experimental validation*, Cryogenics, Vol. 50, 2010, pp. 443-449.

[18] T. Schild, D. Ciazynski, *A model for calculating AC losses in multistage superconducting cables*, Cryogenics, vol. 36, pp. 1039–1049, 1996.

[19] T. Schild, JL. Duchateau, *AC losses dependence on a CuNi layer location in NbTi CICC*, Physica C, Vol. 310, 1998, pp. 247-252.

[20] M.N. Wilson, C.R. Walters, J.D. Lewin, P.F. Smith, A.H. Spurway, *Experimental and Theoretical Studies of Filamentary Superconducting Composites*, J. Phys. D : Appl. Phys., Vol. 3, No. 11, November 1970, pp. 1517-1585.

[21] G.H. Morgan, *Theoretical Behavior of Twisted Multicore Superconducting Wire in a Time-Varying Uniform Magnetic Field*, J. Appl. Phys., Vol. 41, No. 9, March 1970, pp. 3673-3679.

[22] W.J. Carr, Jr., *Longitudinal and transverse field losses in multifilament superconductors*, I.E.E.E. Trans. on Magnetics, MAG-13, No. 1, January 1977, pp. 129–136.

[23] G. Ries, *AC-losses in multifilamentary superconductors at technical frequencies*, I.E.E.E. Trans. on Magnetics, MAG-13, No. 1, January 1977, pp. 524–526.

[24] W.J. Carr, Jr., *Conductivity, permeability, and dielectric constant in a multifilament superconductor*, J. Appl. Phys., Vol. 41, No. 9, March 1970, pp. 3673-3679.

[25] B. Turck, *Coupling losses in various outer normal layers surrounding the filament bundle of a superconducting composite*, J. Appl. Phys., Vol. 50, No. 8, August 1979, pp. 5397-5401.

[26] T. Ogasawara, Y. Takahashi, K. Kanbara, Y. Kubota, K. Yasohama, K. Yasukochi, *Transient field losses in multifilamentary composite conductors carrying dc transport currents*, Cryogenics, Vol. 20, 1980, pp. 216-222.

[27] T. Ogasawara, Y. Takahashi, K. Kanbara, Y. Kubota, K. Yasohama, K. Yasukochi, *Alternating field losses in superconducting wires carrying dc transport currents. Part 2: multifilamentary composite conductors*, Cryogenics, Vol. 21, 1981, pp. 97-101.

[28] D.R. Salmon, J.A. Catterall, *AC losses in composite superconducting wires*, J. Phys. D : Appl. Phys., Vol. 3, No. 7, January 1970, pp. 1023-1032.

[29] K. Kwasnitza, *Scaling law for the ac losses of multifilament superconductors*, Cryogenics, Vol. 17, 1977, pp. 616-620.

[30] D. Ciazynski, *Distributions de courant et pertes à l'intérieur d'un composite multifilamentaire supraconducteur soumis à un champ magnétique variable*, Thèse de doctorat d'état, Paris VI : Université de Pierre et Marie Curie, 1985, pp. 129–136.

[31] T.J.E. Miller, P.J. Lawrenson, Penetration of transient magnetic fields through conducting cylindrical structures with particular reference to superconducting a.c. machines, Proceedings I.E.E., Vol. 123, Issue 5, May 1976, pp. 437-443.

[32] JL. Duchateau, B. Turck, D. Ciazynski, *Coupling-current losses in composites and cables: analytical calculations* in Handbook of Applied Superconductivity, Vol. 1, ed. B. Seeber (Bristol: IOP Publishing), 1998, p. 212.

[33] B. Turck, *Effective transverse resistivity in multifilamentary superconducting composite*, 9th International Cryogenic Engineering Conference, Kobe, ICEC-ICMC, 1982

[34] F. Sumiyoshi, F. Irie1, K. Yoshida, H. Funakoshi, *AC loss of a multifilamentary superconducting composite in a transverse ac magnetic field with large amplitude*, J. Appl. Phys., Vol. 50, No. 11, December 1979, pp. 7044-7050.

[35] A.M. Campbell, *A general treatment of losses in multifilamentary superconductors*, Cryogenics, Vol. 22, 1982, pp. 3-16.

[36] L.J.M. van de Klundert, *A.c. stability and a.c. loss in composite superconductors*, Cryogenics, Vol. 31, 1991, pp. 612-617.

[37] A. Nijhuis, H.G. Knoopers, H.H.J. ten Kate, *The influence of the diffusion barrier on the AC loss of Nb_3Sn superconductors*, Cryogenics, Vol. 34, Supp. 1, 1994, p. 548.

[38] C. Zhou, Y. Miyoshi, E.P.A. van Lanen, M. Dhallé, A. Nijhuis, *Inter-filament resistance, effective transverse resistivity and coupling loss in superconducting multi-filamentary NbTi and Nb_3Sn strands*, Superconductor Science and Technology, Vol. 25, No 6, April 2012

[39] L. Zani, P. Barabaschi,, M. Peyrot, *Starting EU Production of Strand and Conductor for JT-60SA Toroidal Field Coils*, I.E.E.E. Trans. on App. Superconductivity, Vol. 22, No. 3, June 2012, Art. No. 4801804

[40] A. Louzguiti, L. Zani, D. Ciazynski, B. Turck, F. Topin, *Development of an Analytical-Oriented Extensive Model for AC Coupling Losses in Multilayer Superconducting Composite*, I.E.E.E. Trans. on App. Superconductivity, Vol. 26, April 2016, Art. No. 4700905

[41] A. Louzguiti, L. Zani, D. Ciazynski, B. Turck, F. Topin, *Modélisation analytique de la puissance thermique générée par les courants de couplage à l'intérieur d'un composite supraconducteur*, Actes du Congrès de la Société Française de Thermique (SFT), Mars 2017, 8 p.

[42] A. Torre, CEA Working Note, AIM/NTT-2010.003, 15/02/10

[43] T. Boutboul, V. Abaecherli, G. Berger, D. Hampshire, J. Parrell, M. Raine, P. Readman, B. Sailer, K. Schlenga, M. Thoener, E. Viladiu, Y. Zhang, *European Nb_3Sn Superconducting Strand Production and Characterization for ITER TF Coil Conductor*, I.E.E.E. Trans. on App. Superconductivity, Vol. 26, No. 4, June 2016, Art. No. 6000604

[44] A. Torre, H. Cloez, C. Roux, M. Tena, *AC losses measurement on strand K006-01C*, CEA Working Note, DRF/IRFM/STEP/GCRY, 2011, 9 p.

[45] E. Seiler, D. Richter, B. Bordini, L. Bottura, D. Bessette, A. Vostner, A. Devred, *Hysteresis Losses and Effective Jc(B) Scaling Law for ITER Nb_3Sn Strands*, I.E.E.E. Trans. on App. Superconductivity, Vol. 26, No. 2, March 2016, Art. No. 8200307

[46] A. Louzguiti, L. Zani, D. Ciazynski, B. Turck, JL. Duchateau, A. Torre, F. Topin, *AC Coupling Losses in CICCs: Analytical Modeling at Different Stages*, I.E.E.E. Trans. on App. Superconductivity, Vol. 27, June 2017, Art. No. 0600505

[47] F. Bellina, D. Bessette, M. Breschi, A. Di Zenobio, P.L. Ribani, L.S. Richard, R. Zanino, *Numerical Analysis of the ITER TF Conductor Samples in SULTAN With the THELMA Code*, IEEE Transactions on Applied Superconductivity, Vol. 19, No. 3, 2009, pp.1457 – 1461.

[48] M. Breschi, P.L. Ribani, *Electromagnetic Modeling of the Jacket in Cable-in-Conduit Conductors*, IEEE Transactions on Applied Superconductivity, Vol. 18, No. 1, 2008, pp. 18 – 28.

[49] M. Breschi, M. Bianchi, R. Bonifetto, S. Carli, A. Devred, N. Martovetsky, P.L. Ribani, L. Savoldi, I. Takaaki, R. Zanino, *Analysis of AC Losses in the ITER Central Solenoid Insert Coil*, IEEE Transactions on Applied Superconductivity, Vol. 27, No. 4, 2017, Art. No. 7762085.

[50] E.P.A. van Lanen, J. van Nugteren, A. Nijhuis, *Validation of a strand level CICC-joint coupling loss model*, Supercond. Sci. Technol., Vol. 25, No. 2, 2012.

[51] T. Bagni, M. Breschi, J. Duchateau, A. Devred and A. Nijhuis, *Analysis of ITER Nb-Ti and Nb_3Sn CICCs experimental Minimum Quench Energy with JackPot, MCM and THEA models*, Supercond. Sci. Technol., Vol. 30, No. 9, 2017, p. 10.

[52] I. Tiseanu, L. Zani, C. Tiseanu, T. Craciunescu, C. Dobrea, *Accurate 3D modeling of Cable in Conduit Conductor type superconductors by X-ray microtomography*, Fusion Engineering and Design, Vol. 98–99, 2015, pp. 1176–1180.

Appendices

A. Method for the analytical solving of the E_0 coefficients in steady-state regimes

We can express the $E_{0_{2k-1}}$ and $E_{0_{2k}}$ coefficients of each filamentary zone with equation (37) and then use equations (38) to (43) to iteratively calculate the $E_{0_{2k-1}}$ and $E_{0_{2k}}$ coefficients of every resistive layers by substitution. Indeed, let us consider a subsequence of consecutive resistive layers inside the composite, only three different cases are actually possible:

- Case 1 : The subsequence goes from the first layer of the strand to the first filamentary zone

  Let f be the number of the first filamentary zone inside the strand (e.g. if the first filamentary zone of the strand is the 5th layer then $f = 5$); the subsequence of resistive layers goes then from $k = 1$ to $k = f - 1$, and therefore consists of $f - 1$ layers. There are two coefficients per layer so $2f - 2$ coefficients have to be determined. As mentioned above, we have $E_{0_1} = 0$ so we now have only $2f - 3$ coefficients left to compute. The considered subsequence features $f - 2$ interfaces between resistive layers and one interface of resistive/filamentary type, which makes $2(f - 2) + 1 = 2f - 3$ boundary equations. There are as many unknowns as equations; the subsystem can then be solved.

  From (42) we know that $E_{0_1} = 0$, using equation (38) iteratively from $k = 1$ to $k = f - 1$, we can express all the $\left(E_{0_i}\right)_{3 \le i \le 2f-2}$ as a function of E_{0_2}. Then, replacing $E_{0_{2f-3}}$ and $E_{0_{2f-2}}$ with their expressions as a function of E_{0_2} in equation (40) for $k = f - 1$, we can easily calculate E_{0_2} and thus all the $\left(E_{0_i}\right)_{3 \le i \le 2f-2}$ coefficients.

- Case 2 : The subsequence is located between two filamentary zones

  Let f_1 be the number of a filamentary zone inside the strand and f_2 the number of the next filamentary zone; the subsequence of resistive layers goes then from $k = f_1 + 1$ to $k = f_2 - 1$, so there are $2(f_2 - f_1 - 1)$ coefficients to determine. The considered subsequence features $f_2 - f_1 - 2$ interfaces between resistive layers and 2 interfaces of resistive/filamentary type, which makes $2(f_2 - f_1 - 2) + 2 = 2(f_2 - f_1 - 1)$ boundary equations. There are as many unknowns as equations; the subsystem can then be solved.

  Using system (38) iteratively from $k = f_1 + 1$ to $k = f_2 - 1$, we can express all the $\left(E_{0_i}\right)_{2f_1+3 \le i \le 2f_2-2}$ as a function of $E_{0_{2f_1+1}}$ and $E_{0_{2f_1+2}}$. Then, replacing $E_{0_{2f_2-3}}$ and $E_{0_{2f-2}}$ with their expressions as a function of $E_{0_{2f_1+1}}$ and $E_{0_{2f_1+2}}$ in equation (40) for $k = f_2 - 1$, we can easily calculate $E_{0_{2f_1+1}}$ and $E_{0_{2f_1+2}}$ with the use of equation (41) for $k = f_1$, and thus all the $\left(E_{0_i}\right)_{2f_1+3 \le i \le 2f_2-2}$ coefficients.

- Case 3 : The subsequence starts after the last filamentary zone

  Let f be the number of the last filamentary zone inside the strand; the subsequence of resistive layers goes then from $k = f + 1$ to $k = n$, and therefore consists of $n - f$ layers, so there are $2(n - f)$ coefficients to determine. The considered subsequence features $n - f - 1$ interfaces between resistive layers, one interface of resistive/filamentary type and one interface with the outer region, which makes $2(n - f - 1) + 1 + 1 = 2(n - f)$ boundary equations. There are as many unknowns as equations; the subsystem can then be solved.

Using equation (39) iteratively from $k = n - 1$ to $k = f + 1$ and equation (43), we can express all the $\left(E_{0_i}\right)_{2f+1 \leq i \leq 2n-1}$ as a function of $E_{0_{2n}}$. Then, replacing $E_{0_{2f+1}}$ and $E_{0_{2f+2}}$ with their expressions as a function of $E_{0_{2n}}$ in equation (41) for $k = f$, we can easily calculate $E_{0_{2n}}$ and thus all the $\left(E_{0_i}\right)_{2f+1 \leq i \leq 2n-1}$ coefficients.

B. Method for the automatic generation of [A] and [Y]

Equation (30) which represents the continuity of the azimuthal component E_θ of the electric field at $r = R_k$, i.e. $E_{\theta_k}(R_k) = E_{\theta_{k+1}}(R_k)$, can be rewritten, using the general expression of E_{θ_k} given by (36), as

$$E_{0_{2k-1}} - E_{0_{2k}} - \left(\frac{R_{k+1}}{R_k}\right)^2 E_{0_{2k+1}} + E_{0_{2k+2}} = 0, for\ 1 \leq k < n \tag{343}$$

Similarly, equation (31) which represents the continuity of the radial current density J_r of the electric field at an interface between two resistive layers located at $r = R_k$, i.e. $\frac{E_{r_k}(R_k)}{\rho_{t_k}} = \frac{E_{r_{k+1}}(R_k)}{\rho_{t_{k+1}}}$, can be rewritten, using the general expression of E_{r_k} given by (36), as

$$E_{0_{2k-1}} + E_{0_{2k}} - \frac{\rho_{t_k}}{\rho_{t_{k+1}}}\left(\frac{R_{k+1}}{R_k}\right)^2 E_{0_{2k+1}} - \frac{\rho_{t_k}}{\rho_{t_{k+1}}} E_{0_{2k+2}} = 0, for\ 1 \leq k < n \tag{344}$$

If the ultimate layer (layer n) is resistive, the additional condition given by equation (43) implies

$$E_{0_{2n-1}} + E_{0_{2n}} = 0 \tag{345}$$

Finally, equations (37) state that for a layer k which is filamentary, we have

$$E_{0_{2k-1}} = 0 \tag{346}$$

$$E_{0_{2k}} = \frac{l_p}{2\pi}\dot{B}_a \tag{347}$$

According to equation (42), the first coefficient E_{0_1} is always zero, we are then now able to express the system under the form

$$[A][E_0] = \frac{l_p}{2\pi}\dot{B_a}[Y] \tag{348}$$

with $[E_0]$ the column vector of the $2n-1$ $\left(E_{0_i}\right)_{2 \leq i \leq 2n}$ coefficients, $[A]$ a $(2n-1) \times (2n-1)$ square matrix and $[Y]$ a column vector whose $2n-1$ components are either 0 or 1, using exclusively equations (343) to (347).

The logical tree to build [A] and [Y] is schematically described through Figure 78; the $[A]_i$ and $[Y]_i$ notations respectively represent lines i of $[A]$ and $[Y]$.

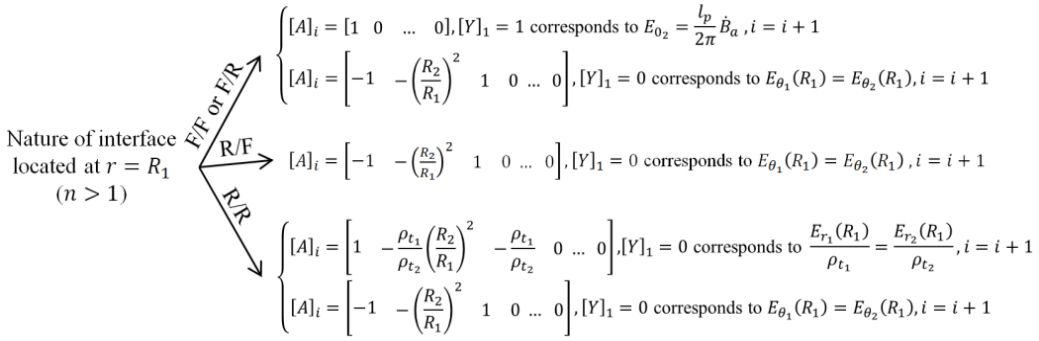

$$\begin{cases} [A]_i = [1 \quad 0 \quad \dots \quad 0], [Y]_1 = 1 \text{ corresponds to } E_{0_2} = \frac{l_p}{2\pi}\dot{B}_a, i = i+1 \\ [A]_i = \left[-1 \quad -\left(\frac{R_2}{R_1}\right)^2 \quad 1 \quad 0 \dots 0\right], [Y]_1 = 0 \text{ corresponds to } E_{\theta_1}(R_1) = E_{\theta_2}(R_1), i = i+1 \end{cases}$$

$$[A]_i = \left[-1 \quad -\left(\frac{R_2}{R_1}\right)^2 \quad 1 \quad 0 \dots 0\right], [Y]_1 = 0 \text{ corresponds to } E_{\theta_1}(R_1) = E_{\theta_2}(R_1), i = i+1$$

$$\begin{cases} [A]_i = \left[1 \quad -\frac{\rho_{t_1}}{\rho_{t_2}}\left(\frac{R_2}{R_1}\right)^2 \quad -\frac{\rho_{t_1}}{\rho_{t_2}} \quad 0 \dots 0\right], [Y]_1 = 0 \text{ corresponds to } \frac{E_{r_1}(R_1)}{\rho_{t_1}} = \frac{E_{r_2}(R_1)}{\rho_{t_2}}, i = i+1 \\ [A]_i = \left[-1 \quad -\left(\frac{R_2}{R_1}\right)^2 \quad 1 \quad 0 \dots 0\right], [Y]_1 = 0 \text{ corresponds to } E_{\theta_1}(R_1) = E_{\theta_2}(R_1), i = i+1 \end{cases}$$

(a) : Expressions of the first line of $[A]$ and $[Y]$ if n>1, the counter i is initialized to one

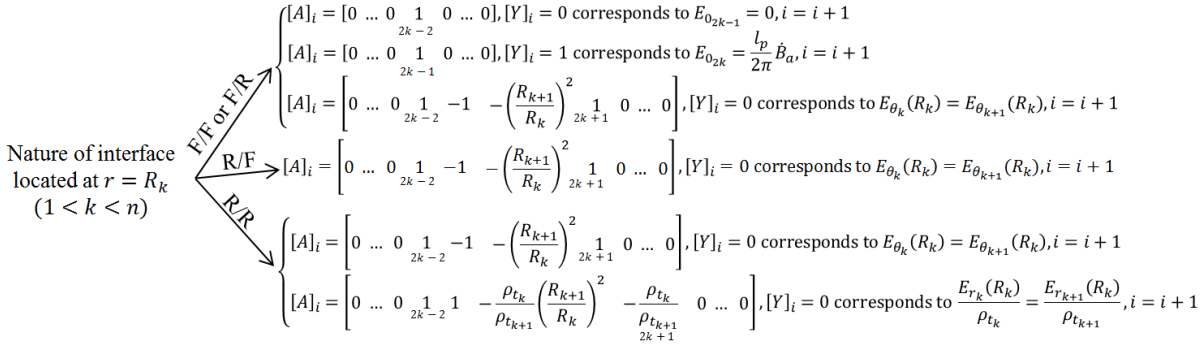

$$\begin{cases} [A]_i = [0 \dots 0 \quad \underset{2k-2}{1} \quad 0 \dots 0], [Y]_i = 0 \text{ corresponds to } E_{0_{2k-1}} = 0, i = i+1 \\ [A]_i = [0 \dots 0 \quad \underset{2k-1}{1} \quad 0 \dots 0], [Y]_i = 1 \text{ corresponds to } E_{0_{2k}} = \frac{l_p}{2\pi}\dot{B}_a, i = i+1 \\ [A]_i = \left[0 \dots 0 \quad \underset{2k-2}{1} \quad -1 \quad -\left(\frac{R_{k+1}}{R_k}\right)^2 \quad \underset{2k+1}{1} \quad 0 \dots 0\right], [Y]_i = 0 \text{ corresponds to } E_{\theta_k}(R_k) = E_{\theta_{k+1}}(R_k), i = i+1 \end{cases}$$

$$[A]_i = \left[0 \dots 0 \quad \underset{2k-2}{1} \quad -1 \quad -\left(\frac{R_{k+1}}{R_k}\right)^2 \quad \underset{2k+1}{1} \quad 0 \dots 0\right], [Y]_i = 0 \text{ corresponds to } E_{\theta_k}(R_k) = E_{\theta_{k+1}}(R_k), i = i+1$$

$$\begin{cases} [A]_i = \left[0 \dots 0 \quad \underset{2k-2}{1} \quad -1 \quad -\left(\frac{R_{k+1}}{R_k}\right)^2 \quad \underset{2k+1}{1} \quad 0 \dots 0\right], [Y]_i = 0 \text{ corresponds to } E_{\theta_k}(R_k) = E_{\theta_{k+1}}(R_k), i = i+1 \\ [A]_i = \left[0 \dots 0 \quad \underset{2k-2}{1} \quad 1 \quad -\frac{\rho_{t_k}}{\rho_{t_{k+1}}}\left(\frac{R_{k+1}}{R_k}\right)^2 \quad \underset{2k+1}{-\frac{\rho_{t_k}}{\rho_{t_{k+1}}}} \quad 0 \dots 0\right], [Y]_i = 0 \text{ corresponds to } \frac{E_{r_k}(R_k)}{\rho_{t_k}} = \frac{E_{r_{k+1}}(R_k)}{\rho_{t_{k+1}}}, i = i+1 \end{cases}$$

(b) : Iterative expressions of the lines of $[A]$ and $[Y]$, the "$2k-2$" or "$2k+1$" notations give the position of the coefficients inside the line vector $[A]_i$

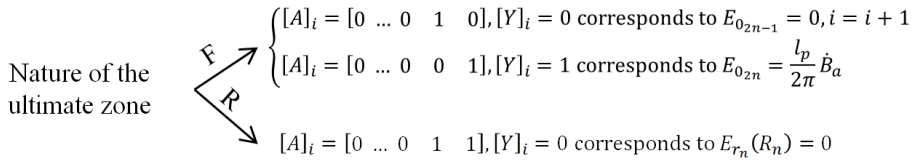

$$\begin{cases} [A]_i = [0 \quad \dots \quad 0 \quad 1 \quad 0], [Y]_i = 0 \text{ corresponds to } E_{0_{2n-1}} = 0, i = i+1 \\ [A]_i = [0 \quad \dots \quad 0 \quad 0 \quad 1], [Y]_i = 1 \text{ corresponds to } E_{0_{2n}} = \frac{l_p}{2\pi}\dot{B}_a \end{cases}$$

$$[A]_i = [0 \quad \dots \quad 0 \quad 1 \quad 1], [Y]_i = 0 \text{ corresponds to } E_{r_n}(R_n) = 0$$

(c) : Expressions of the last line(s) of $[A]$ and $[Y]$

Figure 78 : Logical trees used to build $[A]$ and $[Y]$

We will give an example of application of the logical tree to build [A] and [Y]. Let us choose a "R/F/R" composite; this means that the composite is composed of a resistive core, then of a filamentary zone and finally of another resistive layer.

For this type of geometry, we have $n = 3$ and thus have to determine the $2n - 1 = 5$ $\left(E_{0_i}\right)_{2 \le i \le 6}$ coefficients, therefore $[A]$ will be a 5×5 matrix and $[Y]$ will be a column vector with 5 lines.

To build $[A]$ and $[Y]$ we start with $i = 1$ and since $n > 1$ we use Figure 78 (a): the first interface is of "R/F" type, thus $[A]_1 = \left[-1 \quad -\left(\frac{R_2}{R_1}\right)^2 \quad 1 \quad 0 \quad 0\right], [Y]_1 = 0$ and $i = 2$.

The second interface (i.e. for $k = 2$) is of "F/R" type, using Figure 78 (b), we can deduce that $[A]_2 = [0 \quad 1 \quad 0 \quad 0 \quad 0], [Y]_2 = 0$ and $i = 3$ because here $2k - 2 = 2 * 2 - 2 = 2$, then we have $[A]_3 = [0 \quad 0 \quad 1 \quad 0 \quad 0], [Y]_3 = 1$ and $i = 4$ because $2k - 1 = 3$, and $[A]_4 = \left[0 \quad 1 \quad -1 \quad -\left(\frac{R_3}{R_2}\right)^2 \quad 1\right], [Y]_4 = 0$ and $i = 5$.

The ultimate layer is of "R" type therefore, using Figure 78 (c), we finally conclude that $[A]_5 = [0 \quad 0 \quad 0 \quad 1 \quad 1], [Y]_5 = 0$.

For a "R/F/R" composite, we obtain the following $[A]$ matrix and $[Y]$ column vector

$$[A] = \begin{bmatrix} -1 & -\left(\frac{R_2}{R_1}\right)^2 & 1 & 0 & 0 \\ 0 & 1 & 0 & 0 & 0 \\ 0 & 0 & 1 & 0 & 0 \\ 0 & 1 & -1 & -\left(\frac{R_3}{R_2}\right)^2 & 1 \\ 0 & 0 & 0 & 1 & 1 \end{bmatrix}, [Y] = \begin{bmatrix} 0 \\ 0 \\ 1 \\ 0 \\ 0 \end{bmatrix}$$

Using equation (348), we can finally give the matrix equation governing the "R/F/R" composite in steady-state regime

$$\begin{bmatrix} -1 & -\left(\frac{R_2}{R_1}\right)^2 & 1 & 0 & 0 \\ 0 & 1 & 0 & 0 & 0 \\ 0 & 0 & 1 & 0 & 0 \\ 0 & 1 & -1 & -\left(\frac{R_3}{R_2}\right)^2 & 1 \\ 0 & 0 & 0 & 1 & 1 \end{bmatrix} \begin{bmatrix} E_{0_2} \\ E_{0_3} \\ E_{0_4} \\ E_{0_5} \\ E_{0_6} \end{bmatrix} = \frac{l_p}{2\pi} \dot{B_a} \begin{bmatrix} 0 \\ 0 \\ 1 \\ 0 \\ 0 \end{bmatrix}$$

which can be solved for the $\left(E_{0_i}\right)_{2 \le i \le 6}$ coefficients.

Note that if $n = 1$, that is to say if the composite considered consists in a unique zone, it will necessarily be of "F" type since the composite must feature at least one filamentary zone. In this case there will be only one coefficient to determine which is E_{0_2} and using Figure 78 (c) we have $[A] = 1$ and $[Y] = 1$. The first equation given by the "F" branch of Figure 78 (c) is out of interest here since it would give an equation on E_{0_1} which, by assumption, is always zero.

C. Method for the automatic generation of [B]

In order to provide the logical tree needed to build the $[B]$ matrix, we first have to express the amplitudes of the surface currents located on the edges of each filamentary zones - thus these contained in $\left(K_{0_f}\right)$ - using the formulae given by equations (44) and (45). In addition, to simplify the construction of the $[B]$ matrix, we consider that there also exist surface currents at every other interface but with zero amplitudes if there are no superconducting filaments to transport them. It is therefore possible to express the relation between the $\left(K_{0_i}\right)_{1 \le i \le n}$ amplitudes and the $\left(E_{0_k}\right)_{2 \le k \le 2n}$ coefficients as

$$[K_0] = \frac{1}{\rho_{t_1}} \frac{l_p}{2\pi} [M][E_0] \tag{349}$$

where $[K_0]$ is the column vector of the n amplitudes of surface currents located at each interface and $[M]$ is then a $n \times (2n-1)$ matrix whose coefficients are dimensionless.

Using equations (44) and (45) and the previous considerations, we can derive the expressions of lines i of $[M]$ matrix which are given in Figure 79; the $[\mathrm{M}]_{\mathrm{i}}$ notation represents line i of $[M]$.

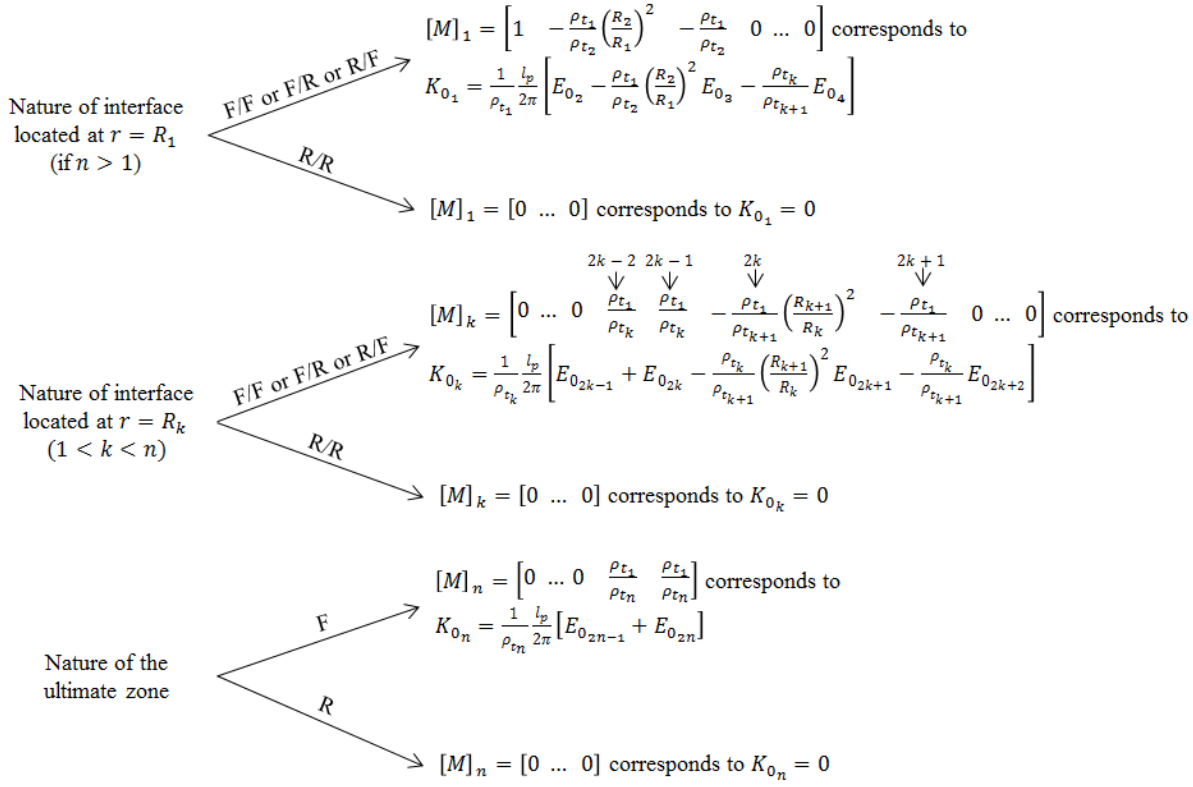

Figure 79 : Logical tree used to build $[M]$

We will give an example of application of the logical tree to build $[M]$ as we have done it previously for $[A]$ and $[Y]$; we choose the same "R/F/R" composite.

In our example $n = 3$ and thus $[M]$ will be a $(2n-1) \times n = 5 \times 3$ matrix. We start with $k = 1$ and since $n > 1$ we use Figure 79 (a): the first interface is of "R/F" type, thus $[M]_1 = \left[1 \quad -\frac{\rho_{t_1}}{\rho_{t_2}}\left(\frac{R_2}{R_1}\right)^2 \quad -\frac{\rho_{t_1}}{\rho_{t_2}} \quad 0 \quad 0\right]$. Then for $k = 2$, we have an interface of "F/R" type, using Figure 79 (b) we have $[M]_2 = \left[0 \quad \frac{\rho_{t_1}}{\rho_{t_2}} \quad \frac{\rho_{t_1}}{\rho_{t_2}} \quad -\frac{\rho_{t_1}}{\rho_{t_2}}\left(\frac{R_2}{R_1}\right)^2 \quad -\frac{\rho_{t_1}}{\rho_{t_2}}\right]$ because here $2k - 2 = 2 * 2 - 2 = 2$ and $2k + 1 = 2 * 2 + 1 = 5$. The ultimate layer is of "R" type therefore, using Figure 79 (c), we finally conclude that $[M]_3 = [0 \quad 0 \quad 0 \quad 0 \quad 0]$ and that

$$[M] = \begin{bmatrix} 1 & -\frac{\rho_{t_1}}{\rho_{t_2}}\left(\frac{R_2}{R_1}\right)^2 & -\frac{\rho_{t_1}}{\rho_{t_2}} & 0 & 0 \\ 0 & \frac{\rho_{t_1}}{\rho_{t_2}} & \frac{\rho_{t_1}}{\rho_{t_2}} & -\frac{\rho_{t_1}}{\rho_{t_2}}\left(\frac{R_2}{R_1}\right)^2 & -\frac{\rho_{t_1}}{\rho_{t_2}} \\ 0 & 0 & 0 & 0 & 0 \end{bmatrix}$$

Note that if $n = 1$, there will be only one coefficient (E_{0_2}) as mentioned previously, therefore we have to take only the last coefficient of $[M]_n$ given by the "F" branch of Figure 79 (c) and obtain $[M] = 1$ because the next-to-last one is multiplying E_{0_1} which, by assumption, is always zero.

We now need to express the sums $-\frac{\mu_0}{2}\frac{l_p}{2\pi}\sum_{i=1}^{k-1}\dot{K}_{0_i}\left(\frac{R_i}{R_k}\right)^2$ and $\frac{\mu_0}{2}\frac{l_p}{2\pi}\sum_{i=k}^{n}\dot{K}_{0_i}$ present in equation (68) as scalar products. In order to do so, we also need to build line vectors $[S]_{2k-1}$ and $[S]_{2k}$ of length n to account for these terms. Indeed, we can write $-\frac{\mu_0}{2}\frac{l_p}{2\pi}\sum_{i=1}^{k-1}\dot{K}_{0_i}\left(\frac{R_i}{R_k}\right)^2$ under the form

$$-\frac{\mu_0}{2}\frac{l_p}{2\pi}\sum_{i=1}^{k-1}\dot{K}_{0_i}\left(\frac{R_i}{R_k}\right)^2 = \frac{\mu_0}{2}\frac{l_p}{2\pi}[S]_{2k-1}[\dot{K}_0] \tag{350}$$

with

$$\begin{cases}[S]_1 = 0 \; if \; n = 1 \\ [S]_{2k-1} = -\left[\left(\frac{R_1}{R_k}\right)^2 \; \left(\frac{R_2}{R_k}\right)^2 \quad ... \quad \left(\frac{R_{k-1}}{R_k}\right)^2 \quad 0 \; ... \; 0\right] \; if \; n > 1, \; 1 \le k \le n \\ \qquad\qquad\qquad\qquad\quad \uparrow \quad \uparrow \qquad\qquad\quad \uparrow \quad \uparrow \quad \uparrow \\ \qquad\qquad\qquad\qquad\quad 1 \quad 2 \qquad\qquad k-1 \quad k \quad n \end{cases} \tag{351}$$

and $\frac{\mu_0}{2}\frac{l_p}{2\pi}\sum_{i=k}^{n}\dot{K}_{0_i}$ under the form

$$\frac{\mu_0}{2}\frac{l_p}{2\pi}\sum_{i=k}^{n}\dot{K}_{0_i} = \frac{\mu_0}{2}\frac{l_p}{2\pi}[S]_{2k}[\dot{K}_0] \tag{352}$$

with

$$\begin{cases}[S]_2 = 1 \; if \; n = 1 \\ [S]_{2k} = [0 \; ... \; 0 \quad 1 \; ... \; 1] \; if \; n > 1, \; 1 \le k \le n \\ \qquad\qquad\quad \uparrow \quad \uparrow \; \uparrow \quad \uparrow \\ \qquad\qquad\quad 1 \quad k-1 \; k \quad n \end{cases} \tag{353}$$

If we now make use of the derivative with respect to time of equation (349) which links the $(K_{0_i})_{1\le i\le n}$ amplitudes to the $(E_{0_k})_{2\le k\le 2n}$ coefficients, and of equations (350) and (352), we can finally rewrite equation (68) as

$$\begin{cases} E_{0_{2k-1}} + \frac{\mu_0}{2}\left(\frac{l_p}{2\pi}\right)^2\frac{1}{\rho_{t_1}}[S]_{2k-1}[M][\dot{E}_0] = 0 \\ E_{0_{2k}} + \frac{\mu_0}{2}\left(\frac{l_p}{2\pi}\right)^2\frac{1}{\rho_{t_1}}[S]_{2k}[M][\dot{E}_0] = \frac{l_p}{2\pi}\dot{B}_a \end{cases} \tag{354}$$

We must keep in mind that these equations are only valid if layer k is a filamentary zone; the other equations needed to complete the system are the time-derivatives of continuity equations (343), (344) and (345) multiplied by $\frac{\mu_0}{2}\left(\frac{l_p}{2\pi}\right)^2\frac{1}{\rho_{t_1}}$ (in order for all coefficients of $[B]$ to be dimensionless), i.e.

$$\frac{\mu_0}{2}\left(\frac{l_p}{2\pi}\right)^2\frac{1}{\rho_{t_1}}\left[\dot{E}_{0_{2k-1}} - \dot{E}_{0_{2k}} - \left(\frac{R_{k+1}}{R_k}\right)^2\dot{E}_{0_{2k+1}} + \dot{E}_{0_{2k+2}}\right] = 0, for \; 1 \le k < n \tag{355}$$

$$\frac{\mu_0}{2}\left(\frac{l_p}{2\pi}\right)^2\frac{1}{\rho_{t_1}}\left[\dot{E}_{0_{2k-1}} + \dot{E}_{0_{2k}} - \frac{\rho_{t_k}}{\rho_{t_{k+1}}}\left(\frac{R_{k+1}}{R_k}\right)^2\dot{E}_{0_{2k+1}} - \frac{\rho_{t_k}}{\rho_{t_{k+1}}}\dot{E}_{0_{2k+2}}\right] = 0, for \; 1 \le k < n \tag{356}$$

$$\frac{\mu_0}{2}\left(\frac{l_p}{2\pi}\right)^2\frac{1}{\rho_{t_1}}\left[\dot{E}_{0_{2n-1}}+\dot{E}_{0_{2n}}\right]=0 \tag{357}$$

We now possess all the elements required, i.e. equations (354) to (357), to give the expression of the $[B]$ matrix appearing in the equation of the system (72). The logical tree used to build $[B]$ (consistent with the construction of $[A]$ and $[Y]$ provided in Figure 78) is schematically described through Figure 80; once again, the $[B]_i$ notation represents lines i of $[B]$.

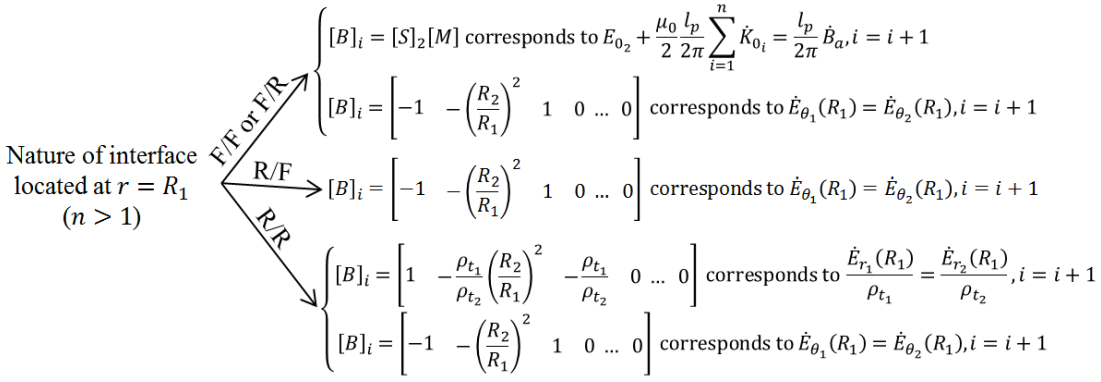

$$[B]_i=[S]_2[M] \text{ corresponds to } E_{0_2}+\frac{\mu_0}{2}\frac{l_p}{2\pi}\sum_{i=1}^{n}\dot{K}_{0_i}=\frac{l_p}{2\pi}\dot{B}_a, i=i+1$$

$$[B]_i=\begin{bmatrix}-1 & -\left(\frac{R_2}{R_1}\right)^2 & 1 & 0 & \dots & 0\end{bmatrix} \text{ corresponds to } \dot{E}_{\theta_1}(R_1)=\dot{E}_{\theta_2}(R_1), i=i+1$$

$$[B]_i=\begin{bmatrix}-1 & -\left(\frac{R_2}{R_1}\right)^2 & 1 & 0 & \dots & 0\end{bmatrix} \text{ corresponds to } \dot{E}_{\theta_1}(R_1)=\dot{E}_{\theta_2}(R_1), i=i+1$$

$$[B]_i=\begin{bmatrix}1 & -\frac{\rho_{t_1}}{\rho_{t_2}}\left(\frac{R_2}{R_1}\right)^2 & -\frac{\rho_{t_1}}{\rho_{t_2}} & 0 & \dots & 0\end{bmatrix} \text{ corresponds to } \frac{\dot{E}_{r_1}(R_1)}{\rho_{t_1}}=\frac{\dot{E}_{r_2}(R_1)}{\rho_{t_2}}, i=i+1$$

$$[B]_i=\begin{bmatrix}-1 & -\left(\frac{R_2}{R_1}\right)^2 & 1 & 0 & \dots & 0\end{bmatrix} \text{ corresponds to } \dot{E}_{\theta_1}(R_1)=\dot{E}_{\theta_2}(R_1), i=i+1$$

(a) : Expression(s) of the first line(s) of $[B]$ if n>1, the counter i is initialized to one

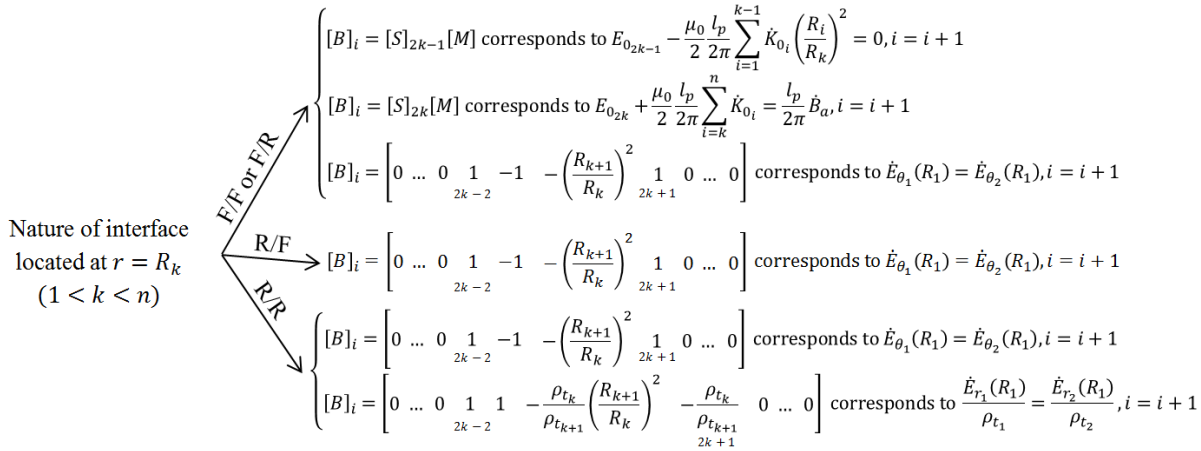

$$[B]_i=[S]_{2k-1}[M] \text{ corresponds to } E_{0_{2k-1}}-\frac{\mu_0}{2}\frac{l_p}{2\pi}\sum_{i=1}^{k-1}\dot{K}_{0_i}\left(\frac{R_i}{R_k}\right)^2=0, i=i+1$$

$$[B]_i=[S]_{2k}[M] \text{ corresponds to } E_{0_{2k}}+\frac{\mu_0}{2}\frac{l_p}{2\pi}\sum_{i=k}^{n}\dot{K}_{0_i}=\frac{l_p}{2\pi}\dot{B}_a, i=i+1$$

$$[B]_i=\begin{bmatrix}0 & \dots & 0 & \underset{2k-2}{1} & -1 & -\left(\frac{R_{k+1}}{R_k}\right)^2 & \underset{2k+1}{1} & 0 & \dots & 0\end{bmatrix} \text{ corresponds to } \dot{E}_{\theta_1}(R_1)=\dot{E}_{\theta_2}(R_1), i=i+1$$

$$[B]_i=\begin{bmatrix}0 & \dots & 0 & \underset{2k-2}{1} & -1 & -\left(\frac{R_{k+1}}{R_k}\right)^2 & \underset{2k+1}{1} & 0 & \dots & 0\end{bmatrix} \text{ corresponds to } \dot{E}_{\theta_1}(R_1)=\dot{E}_{\theta_2}(R_1), i=i+1$$

$$[B]_i=\begin{bmatrix}0 & \dots & 0 & \underset{2k-2}{1} & -1 & -\left(\frac{R_{k+1}}{R_k}\right)^2 & \underset{2k+1}{1} & 0 & \dots & 0\end{bmatrix} \text{ corresponds to } \dot{E}_{\theta_1}(R_1)=\dot{E}_{\theta_2}(R_1), i=i+1$$

$$[B]_i=\begin{bmatrix}0 & \dots & 0 & \underset{2k-2}{1} & 1 & -\frac{\rho_{t_k}}{\rho_{t_{k+1}}}\left(\frac{R_{k+1}}{R_k}\right)^2 & \underset{2k+1}{-\frac{\rho_{t_k}}{\rho_{t_{k+1}}}} & 0 & \dots & 0\end{bmatrix} \text{ corresponds to } \frac{\dot{E}_{r_1}(R_1)}{\rho_{t_1}}=\frac{\dot{E}_{r_2}(R_1)}{\rho_{t_2}}, i=i+1$$

(b) : Iterative expressions of the lines of $[B]$, the “$2k-2$” or “$2k+1$” notations give the position of the coefficient inside the line vector $[B]_i$

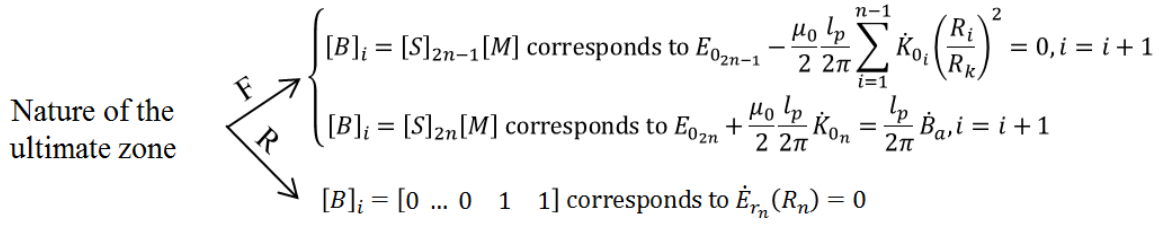

$$[B]_i=[S]_{2n-1}[M] \text{ corresponds to } E_{0_{2n-1}}-\frac{\mu_0}{2}\frac{l_p}{2\pi}\sum_{i=1}^{n-1}\dot{K}_{0_i}\left(\frac{R_i}{R_k}\right)^2=0, i=i+1$$

$$[B]_i=[S]_{2n}[M] \text{ corresponds to } E_{0_{2n}}+\frac{\mu_0}{2}\frac{l_p}{2\pi}\dot{K}_{0_n}=\frac{l_p}{2\pi}\dot{B}_a, i=i+1$$

$$[B]_i=\begin{bmatrix}0 & \dots & 0 & 1 & 1\end{bmatrix} \text{ corresponds to } \dot{E}_{r_n}(R_n)=0$$

(c) : Expression(s) of the last line(s) of $[B]$

Figure 80 : Logical tree used to build $[B]$

We will now give an example of application of the logical tree to build $[B]$ as we have done it previsouly for $[A]$, $[Y]$ and $[M]$; we continue with the same “R/F/R” composite.

The $[M]$ matrix has been built following the procedure given in Figure 79 and we can now build $[B]$: we start with $i = 1$ and since $n > 1$ we use Figure 80 (a), the first interface is of "R/F" type, thus $[B]_1 = \begin{bmatrix} -1 & -\left(\frac{R_2}{R_1}\right)^2 & 1 & 0 & 0 \end{bmatrix}$ and $i = 2$.

The second interface (i.e. for $k = 2$) is of "F/R" type, using Figure 80 (b), we can deduce that $[B]_2 = [S]_3[M]$ and $i = 3$ because here $2k - 1 = 2 * 2 - 1 = 3$, then we have $[B]_3 = [S]_4[M]$ and $i = 4$ because $2k = 2 * 2 = 4$, and $[B]_4 = \begin{bmatrix} 0 & 1 & -1 & -\left(\frac{R_3}{R_2}\right)^2 & 1 \end{bmatrix}$ and $i = 5$.

The ultimate layer is of "R" type therefore, using Figure 80 (c), we finally conclude that $[B]_5 = [0 \quad 0 \quad 0 \quad 1 \quad 1]$. According to expression (351) with $k = 2$, we have $[S]_3 = -\begin{bmatrix} \left(\frac{R_1}{R_2}\right)^2 & 0 & 0 \end{bmatrix}$ and according to expression (353) with $k = 2$, we have $[S]_4 = [0 \quad 1 \quad 1]$.

Using the expressions of $[M]$, $[S]_3$ and $[S]_4$, we can now give the explicit expressions of $[B]_2 = [S]_3[M]$ and $[B]_3 = [S]_4[M]$: $[B]_2 = \begin{bmatrix} -\left(\frac{R_1}{R_2}\right)^2 & \frac{\rho_{t_1}}{\rho_{t_2}} & \frac{\rho_{t_1}}{\rho_{t_2}}\left(\frac{R_1}{R_2}\right)^2 & 0 & 0 \end{bmatrix}$ and $[B]_3 = \begin{bmatrix} 0 & \frac{\rho_{t_1}}{\rho_{t_2}} & \frac{\rho_{t_1}}{\rho_{t_2}} & -\frac{\rho_{t_1}}{\rho_{t_2}}\left(\frac{R_2}{R_1}\right)^2 & -\frac{\rho_{t_1}}{\rho_{t_2}} \end{bmatrix}$.

For a "R/F/R" composite, we can then give the following $[B]$ matrix

$$[B] = \begin{bmatrix} -1 & -\left(\frac{R_2}{R_1}\right)^2 & 1 & 0 & 0 \\ -\left(\frac{R_1}{R_2}\right)^2 & \frac{\rho_{t_1}}{\rho_{t_2}} & \frac{\rho_{t_1}}{\rho_{t_2}}\left(\frac{R_1}{R_2}\right)^2 & 0 & 0 \\ 0 & \frac{\rho_{t_1}}{\rho_{t_2}} & \frac{\rho_{t_1}}{\rho_{t_2}} & -\frac{\rho_{t_1}}{\rho_{t_2}}\left(\frac{R_2}{R_1}\right)^2 & -\frac{\rho_{t_1}}{\rho_{t_2}} \\ 0 & 1 & -1 & -\left(\frac{R_3}{R_2}\right)^2 & 1 \\ 0 & 0 & 0 & 1 & 1 \end{bmatrix}$$

Using equation (72), we can finally express the matrix equation governing the "R/F/R" composite for any time-varying regime

$$\begin{bmatrix} -1 & -\left(\frac{R_2}{R_1}\right)^2 & 1 & 0 & 0 \\ 0 & 1 & 0 & 0 & 0 \\ 0 & 0 & 1 & 0 & 0 \\ 0 & 1 & -1 & -\left(\frac{R_3}{R_2}\right)^2 & 1 \\ 0 & 0 & 0 & 1 & 1 \end{bmatrix} \begin{bmatrix} E_{0_2} \\ E_{0_3} \\ E_{0_4} \\ E_{0_5} \\ E_{0_6} \end{bmatrix} + \frac{\mu_0}{2}\left(\frac{l_p}{2\pi}\right)^2 \frac{1}{\rho_{t_1}} \begin{bmatrix} -1 & -\left(\frac{R_2}{R_1}\right)^2 & 1 & 0 & 0 \\ -\left(\frac{R_1}{R_2}\right)^2 & \frac{\rho_{t_1}}{\rho_{t_2}} & \frac{\rho_{t_1}}{\rho_{t_2}}\left(\frac{R_1}{R_2}\right)^2 & 0 & 0 \\ 0 & \frac{\rho_{t_1}}{\rho_{t_2}} & \frac{\rho_{t_1}}{\rho_{t_2}} & -\frac{\rho_{t_1}}{\rho_{t_2}}\left(\frac{R_2}{R_1}\right)^2 & -\frac{\rho_{t_1}}{\rho_{t_2}} \\ 0 & 1 & -1 & -\left(\frac{R_3}{R_2}\right)^2 & 1 \\ 0 & 0 & 0 & 1 & 1 \end{bmatrix} \begin{bmatrix} \dot{E}_{0_2} \\ \dot{E}_{0_3} \\ \dot{E}_{0_4} \\ \dot{E}_{0_5} \\ \dot{E}_{0_6} \end{bmatrix} = \frac{l_p}{2\pi}\dot{B}_a \begin{bmatrix} 0 \\ 0 \\ 1 \\ 0 \\ 0 \end{bmatrix}$$

which can be numerically solved for the time dependency of the $\left(E_{0_i}\right)_{2 \le i \le 6}$ coefficients.

Once again, note that if $n = 1$, the only coefficient to determine will be E_{0_2}. Using Figure 80 (c) we have $[B] = [S]_2[M]$ and since in this case we have seen that $[M] = 1$, we have $[B] = 1$ because $[S]_2 = 1$ when $n = 1$ according to (353). The first equation given by the "F" branch of Figure 80 (c) is out of interest here since it would give an equation on $\dot{E}_{0_1}$ which, by assumption, is always zero.

D. Examples of 2D cartographies generated with CLASS

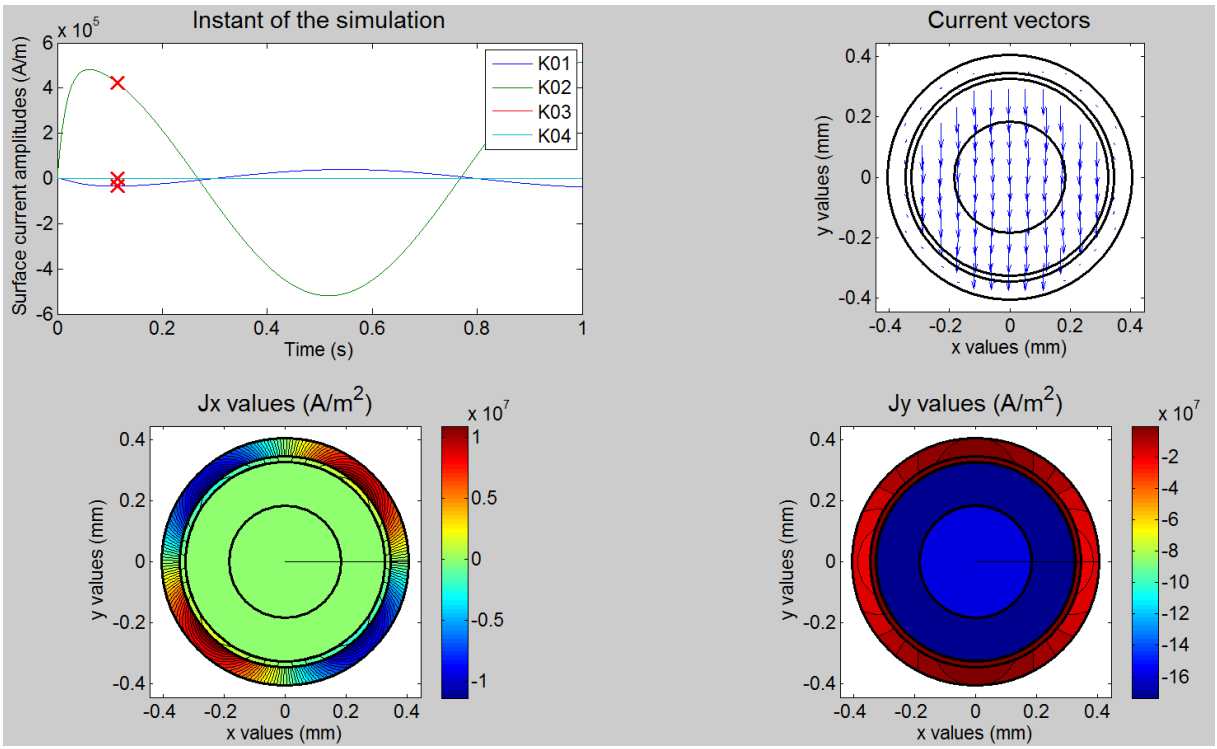

Figure 81 : Simulated cartography of transverse currents at the first instant of Figure 30 for K006-01C JT-60SA TF composite and $B_a = B_p sin(2\pi ft)$ with $B_p = 3T, f = 1Hz$

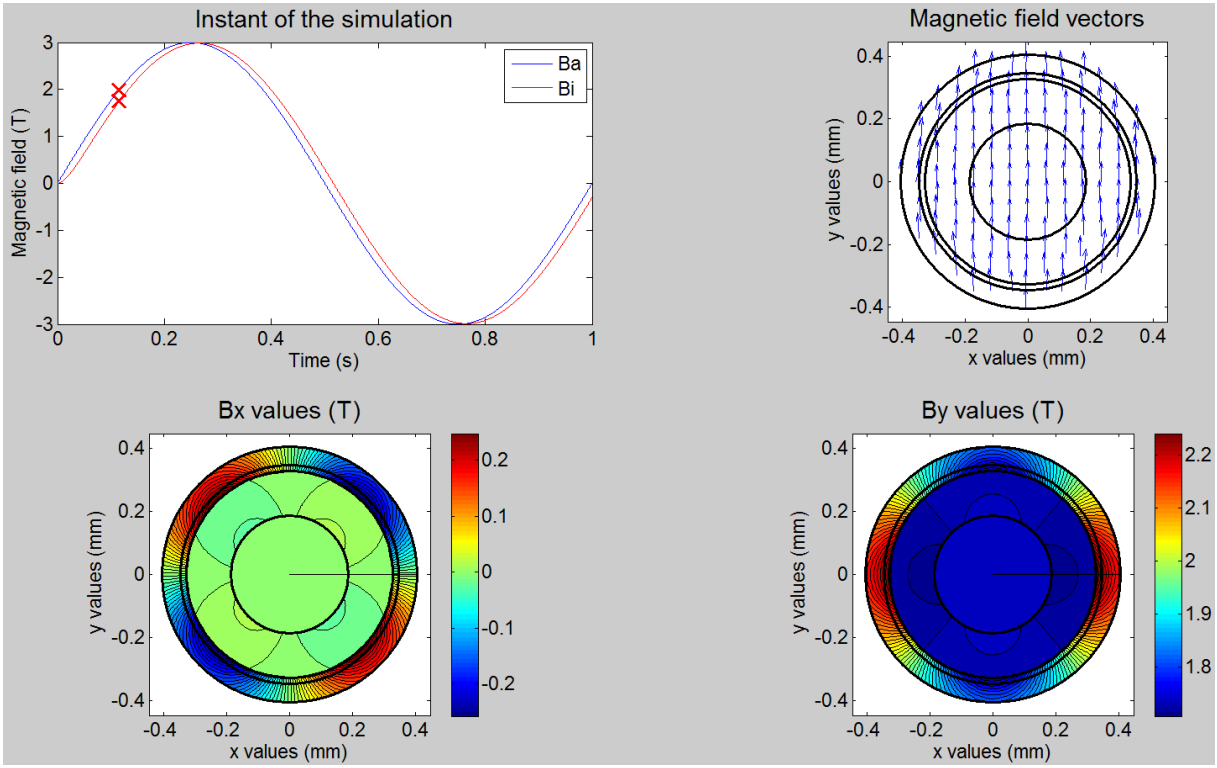

Figure 82 : Simulated cartography of magnetic field at the first instant of Figure 30 for K006-01C JT-60SA TF composite and $B_a = B_p sin(2\pi ft)$ with $B_p = 3T, f = 1Hz$

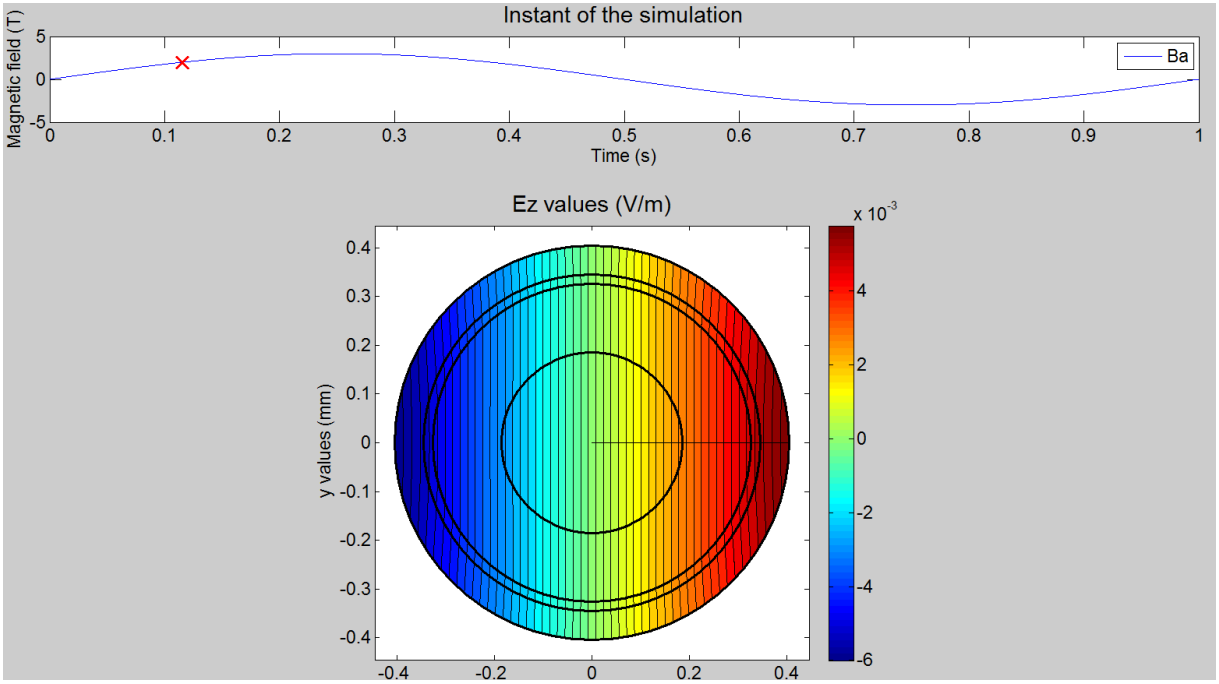

Figure 83 : Simulated cartography of axial electric field at the first instant of Figure 30 for K006-01C JT-60SA TF composite and $B_a = B_p sin(2\pi ft)$ with $B_p = 3T, f = 1Hz$

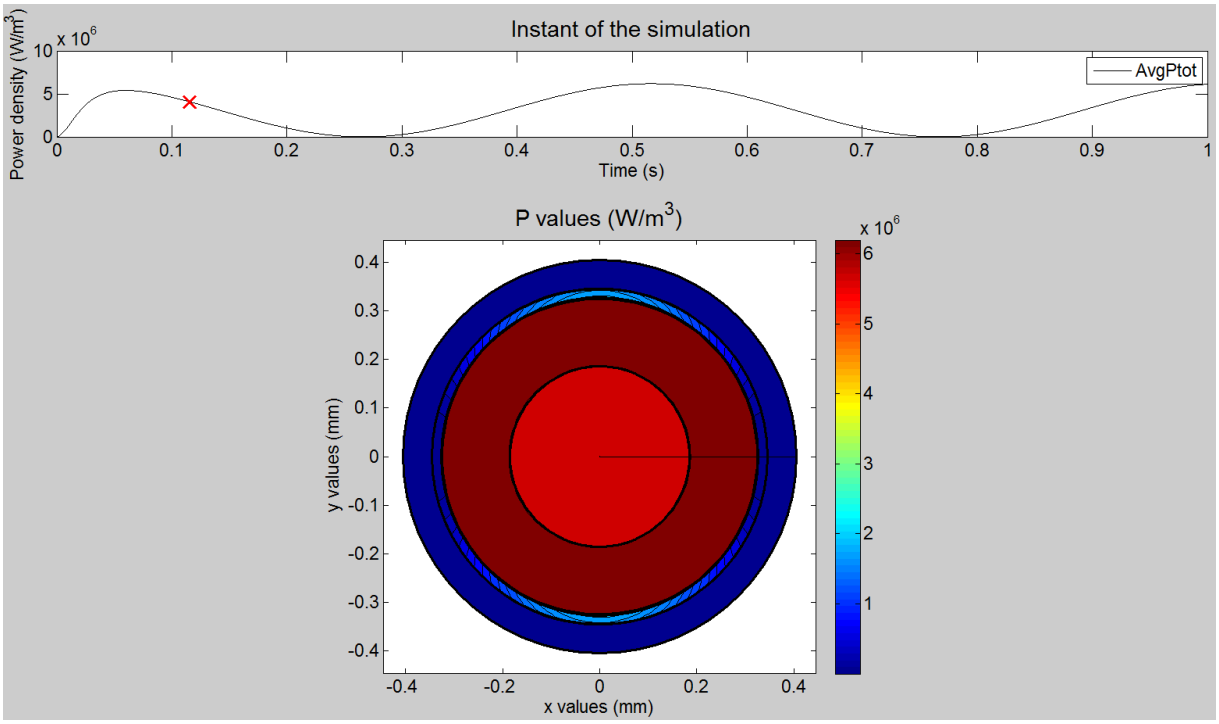

Figure 84 : Simulated cartography of power density at the first instant of Figure 30 for K006-01C JT-60SA TF composite and $B_a = B_p sin(2\pi ft)$ with $B_p = 3T, f = 1Hz$

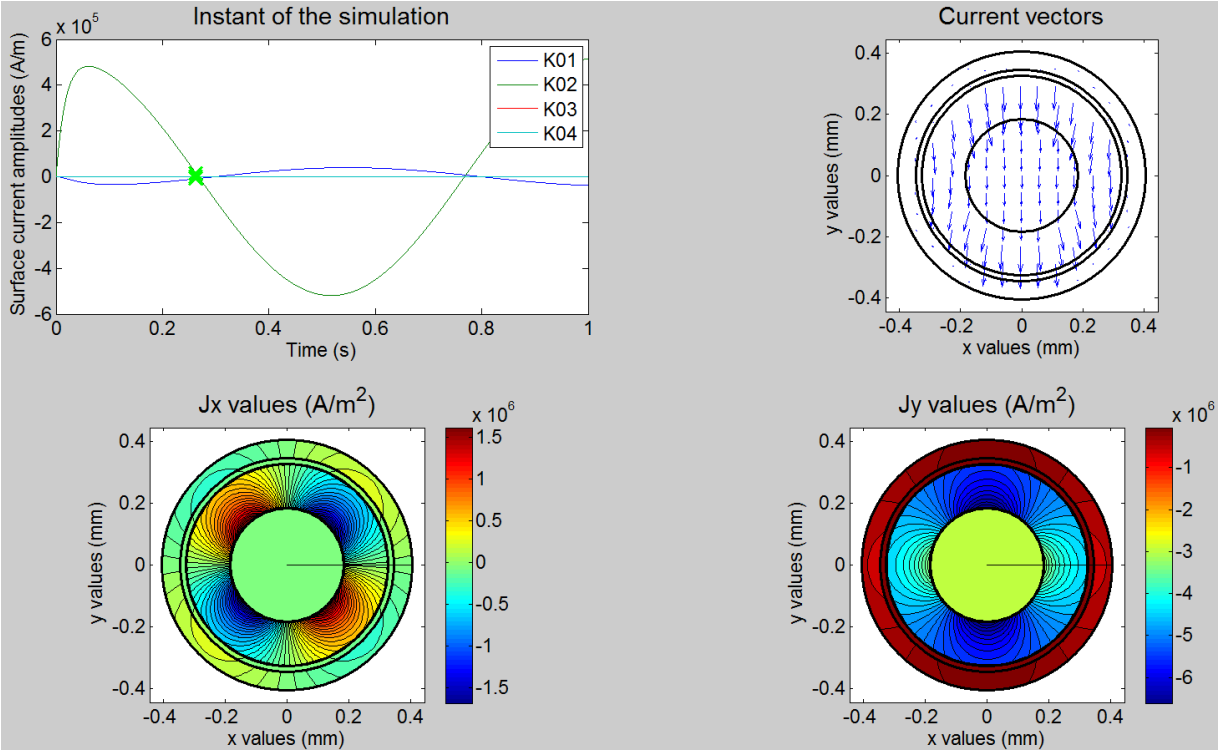

Figure 85 : Simulated cartography of transverse currents at the second instant of Figure 30 for K006-01C JT-60SA TF composite and $B_a = B_p sin(2\pi ft)$ with $B_p = 3T, f = 1Hz$

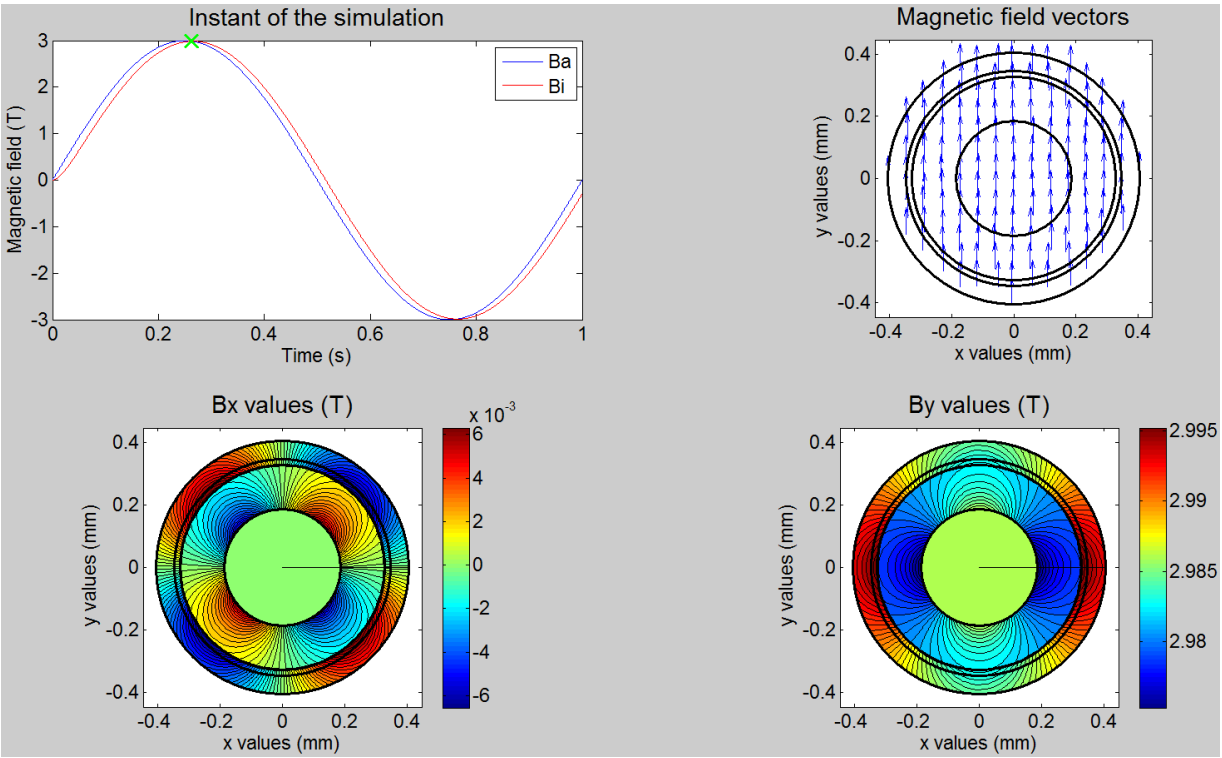

Figure 86 : Simulated cartography of magnetic field at the second instant of Figure 30 for K006-01C JT-60SA TF composite and $B_a = B_p sin(2\pi ft)$ with $B_p = 3T, f = 1Hz$

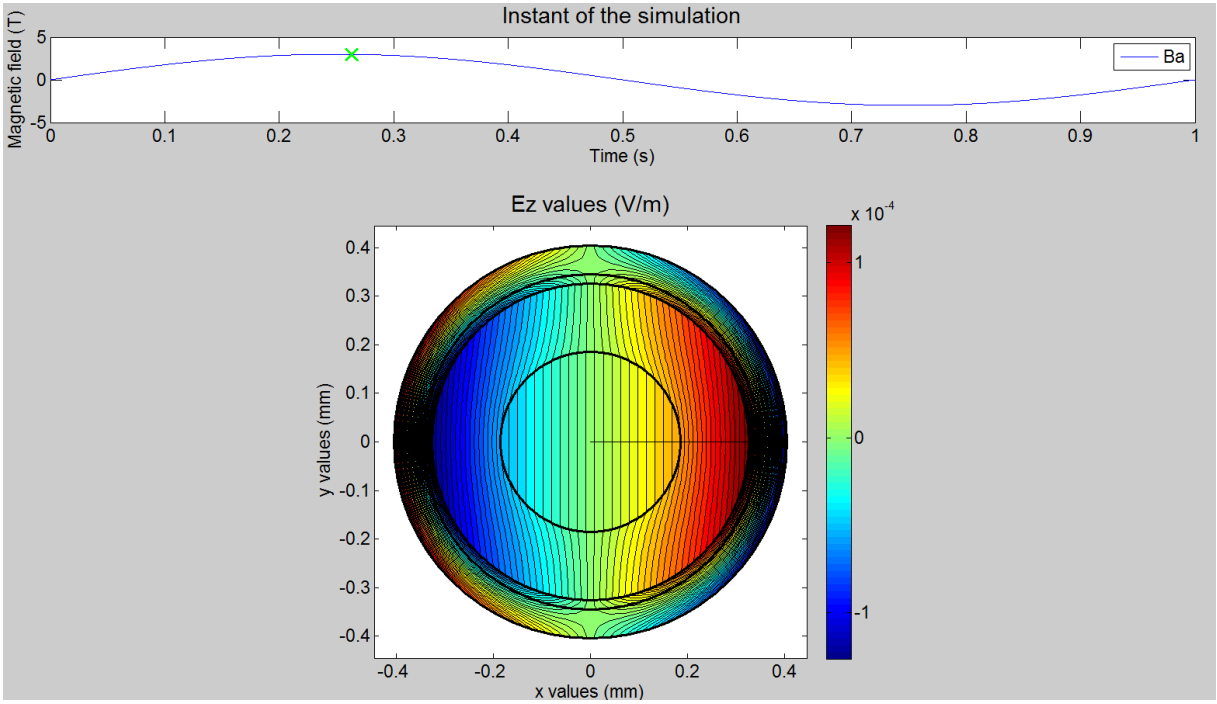

Figure 87 : Simulated cartography of axial electric field at the second instant of Figure 30 for K006-01C JT-60SA TF composite and $B_a = B_p sin(2\pi ft)$ with $B_p = 3T, f = 1Hz$

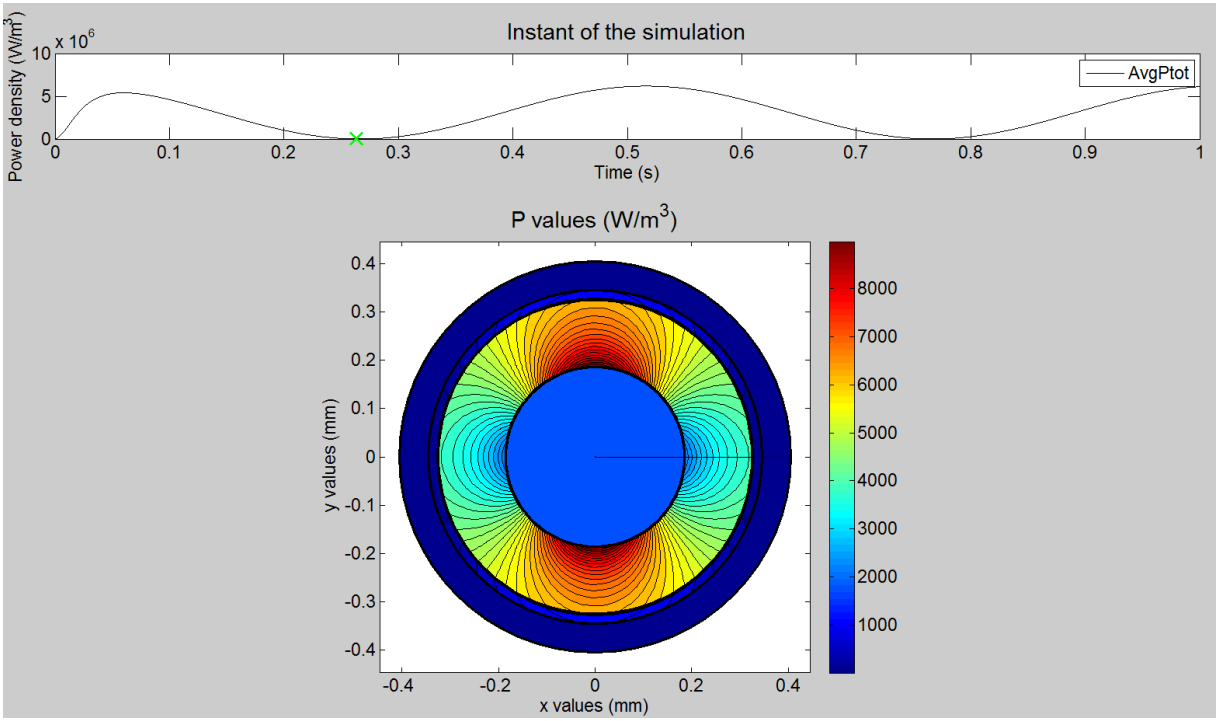

Figure 88 : Simulated cartography of power density at the second instant of Figure 30 for K006-01C JT-60SA TF composite and $B_a = B_p sin(2\pi ft)$ with $B_p = 3T, f = 1Hz$

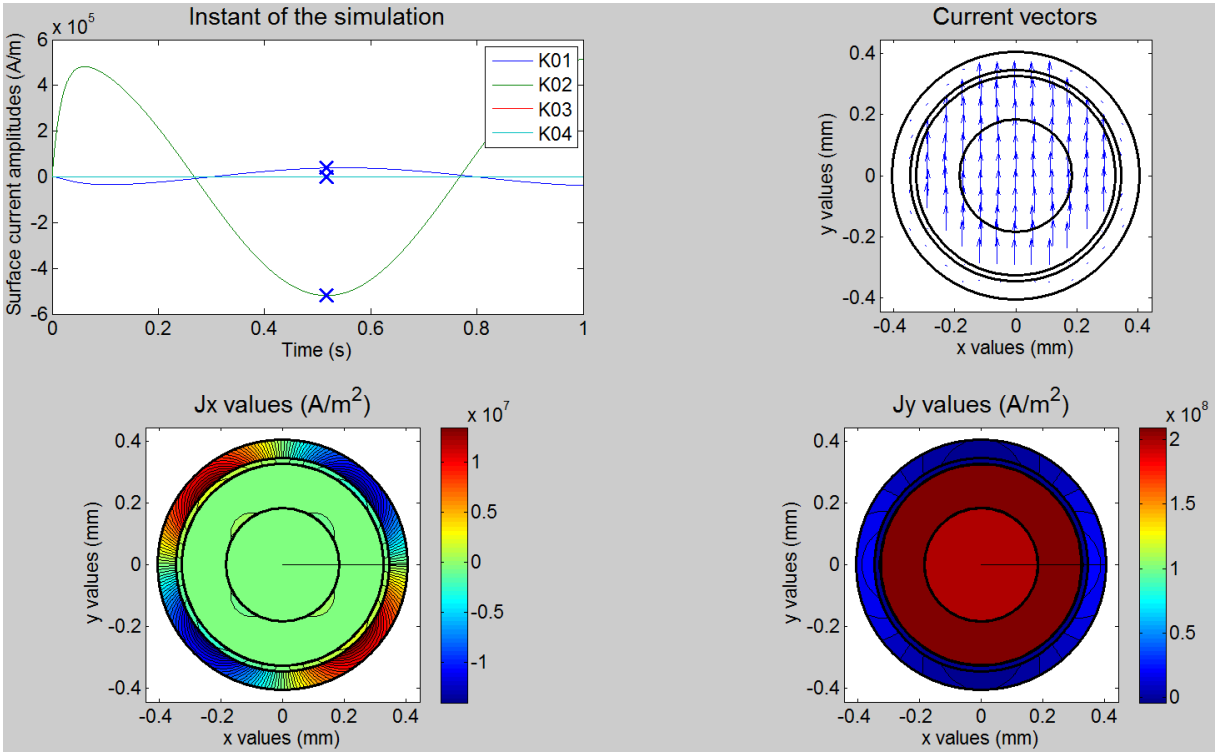

Figure 89 : Simulated cartography of transverse currents at the third instant of Figure 30 for K006-01C JT-60SA TF composite and $B_a = B_p sin(2\pi ft)$ with $B_p = 3T, f = 1Hz$

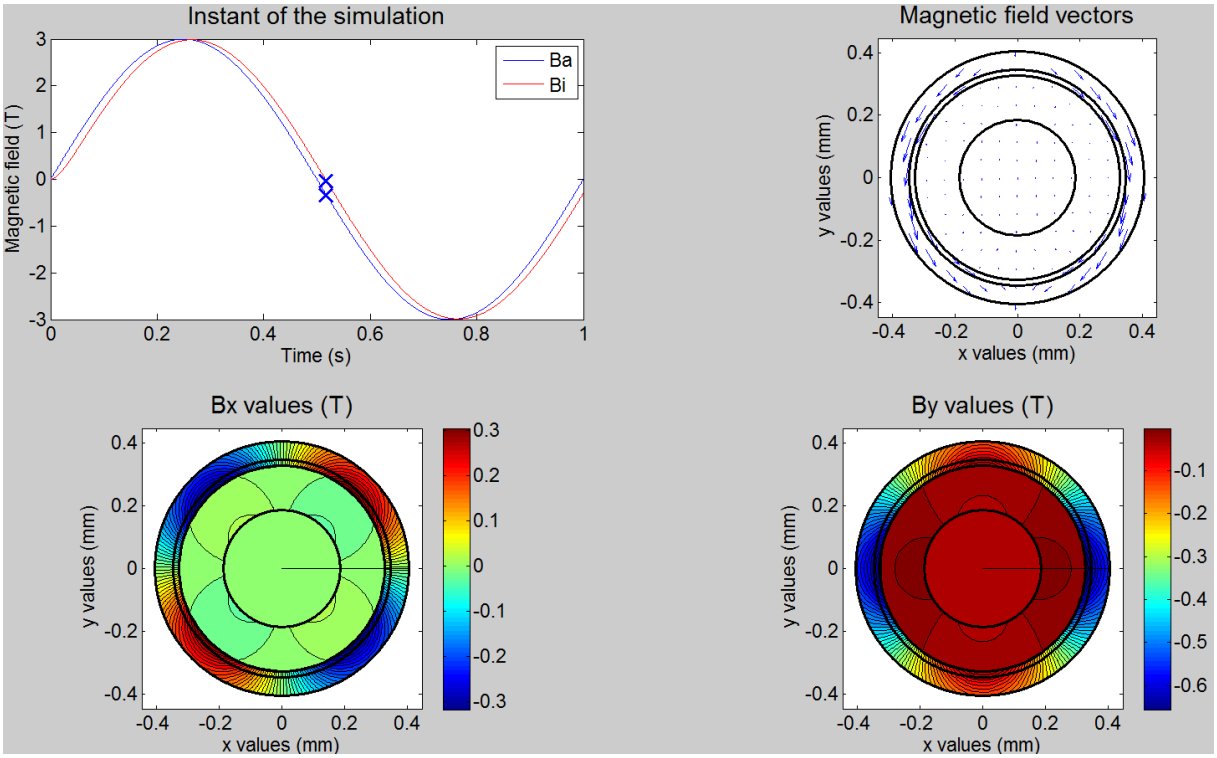

Figure 90 : Simulated cartography of magnetic field at the third instant of Figure 30 for K006-01C JT-60SA TF composite and $B_a = B_p sin(2\pi ft)$ with $B_p = 3T, f = 1Hz$

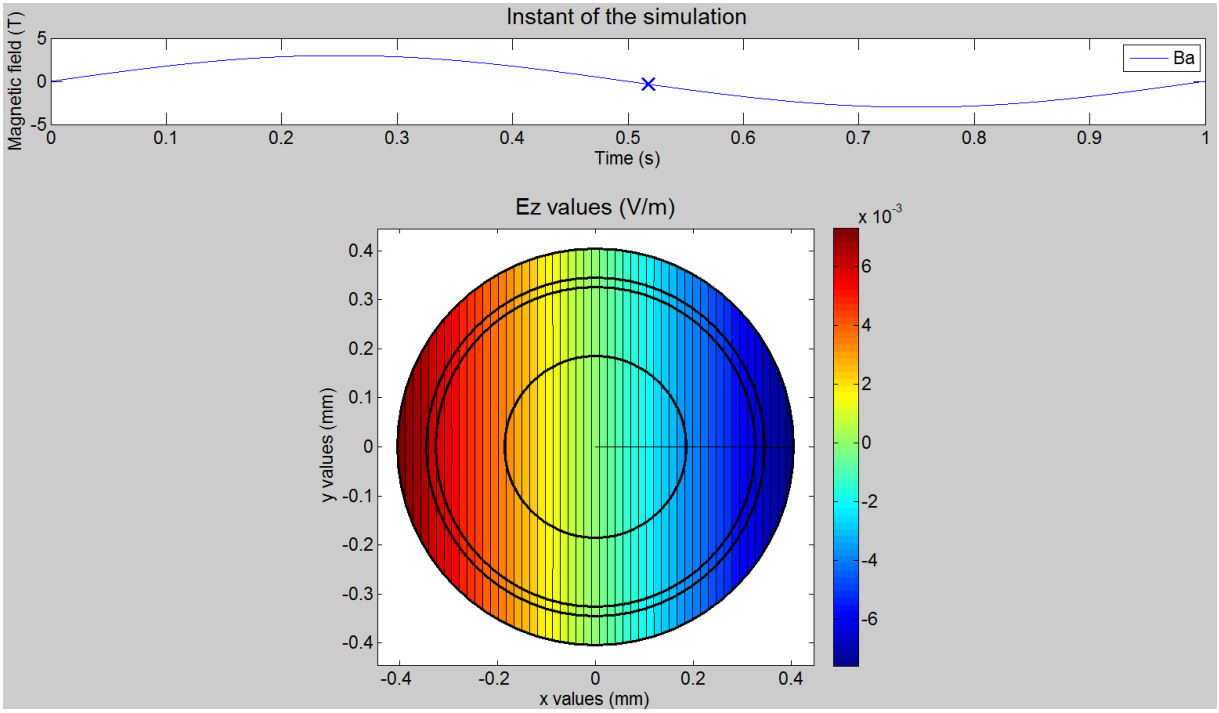

Figure 91 : Simulated cartography of axial electric field at the third instant of Figure 30 for K006-01C JT-60SA TF composite and $B_a = B_p sin(2\pi ft)$ with $B_p = 3T, f = 1Hz$

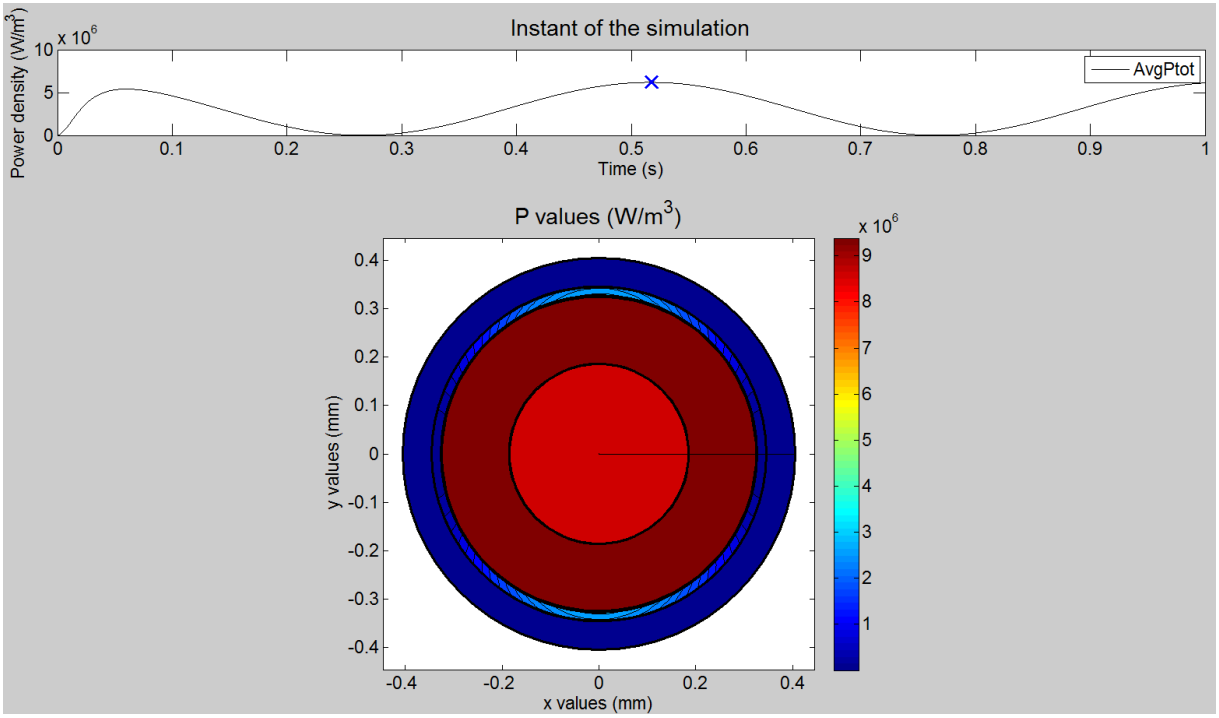

Figure 92 : Simulated cartography of power density at the third instant of Figure 30 for K006-01C JT-60SA TF composite and $B_a = B_p sin(2\pi ft)$ with $B_p = 3T, f = 1Hz$

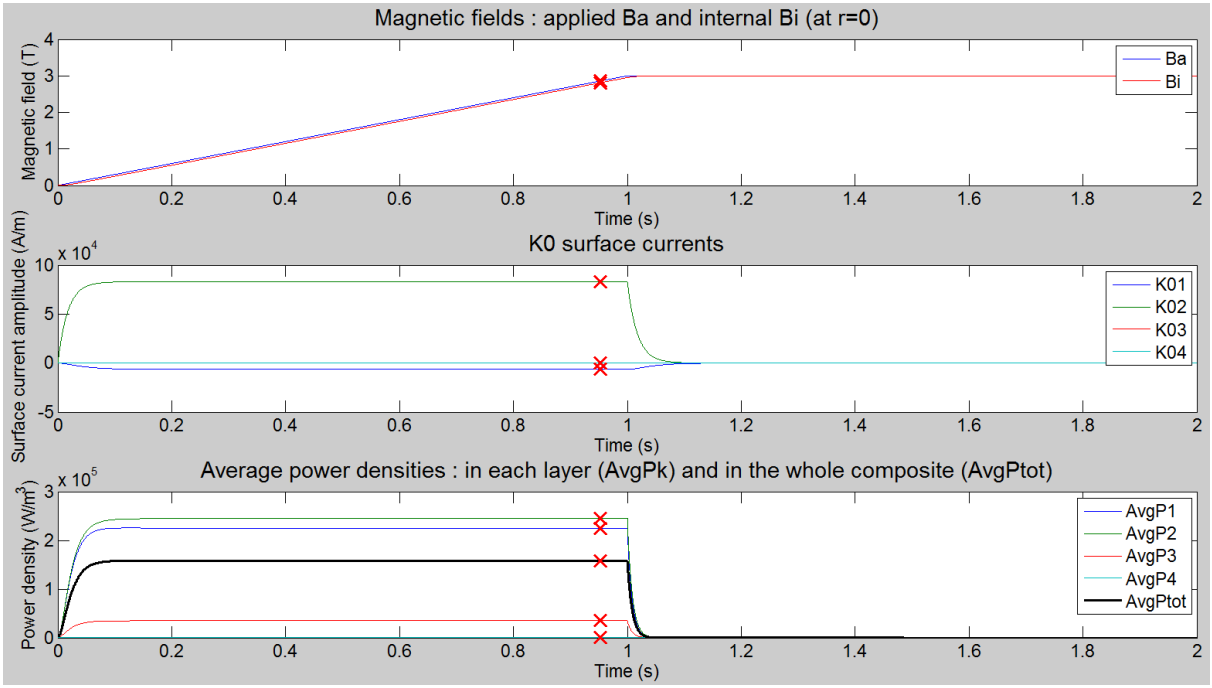

Figure 93 : Simulated time solutions of screening currents, magnetic fields and average losses for K006-01C JT-60SA TF composite for a ramp going from $0T$ to $3T$ in $1s$ followed by a plateau at $3T$

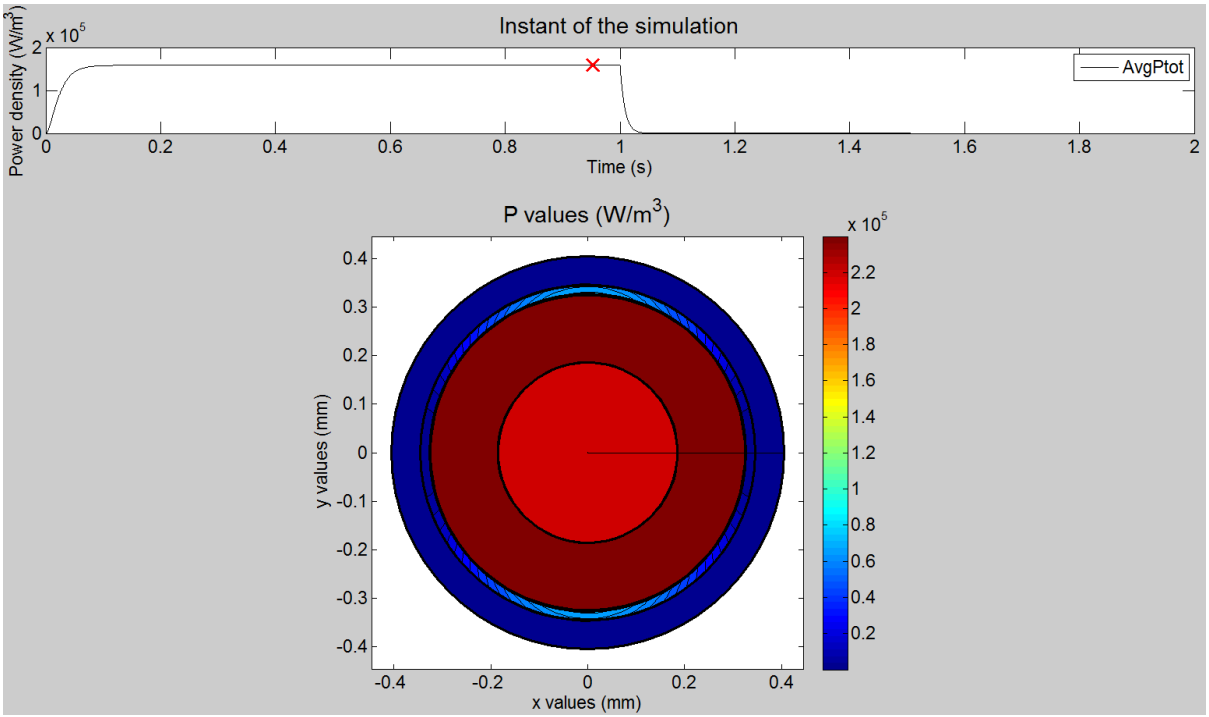

Figure 94 : Simulated cartography of power density at the instant corresponding to the marker displayed on Figure 93 for K006-01C JT-60SA TF composite for a ramp going from $0T$ to $3T$ in $1s$ followed by a plateau at $3T$

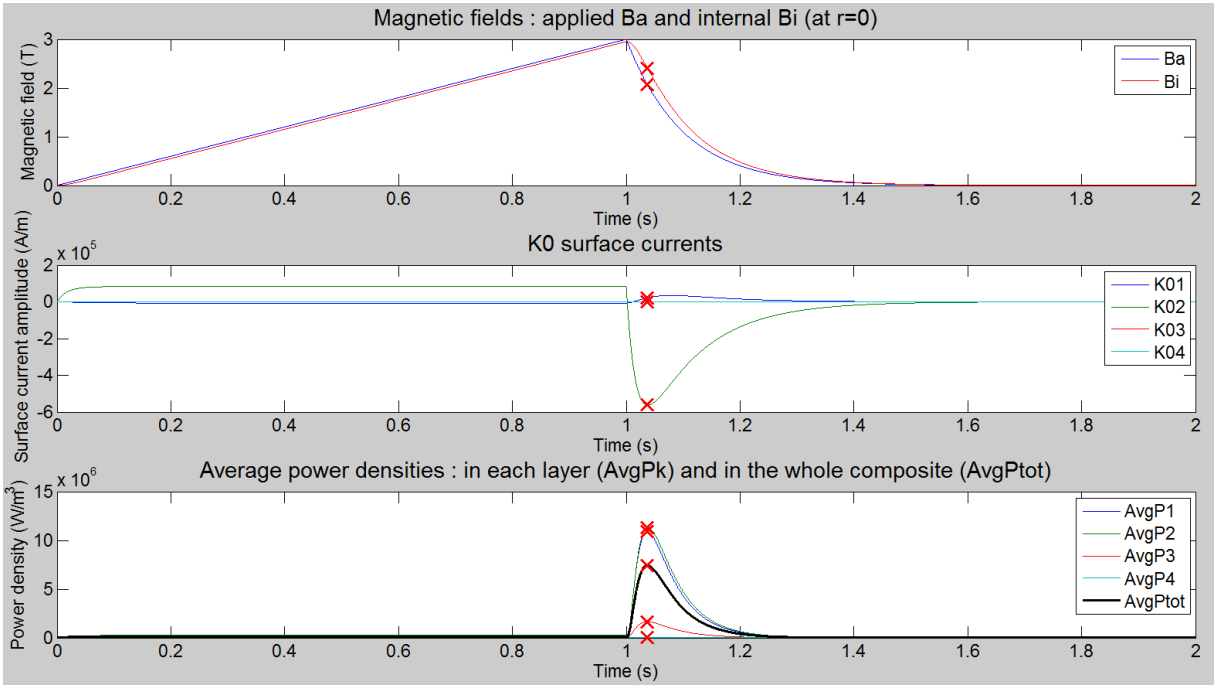

Figure 95 : Simulated time solutions of screening currents, magnetic fields and average losses for K006-01C JT-60SA TF composite for a ramp going from $0T$ to $3T$ in $1s$ followed by an exponential decay with a characteristic time of $0.1s$

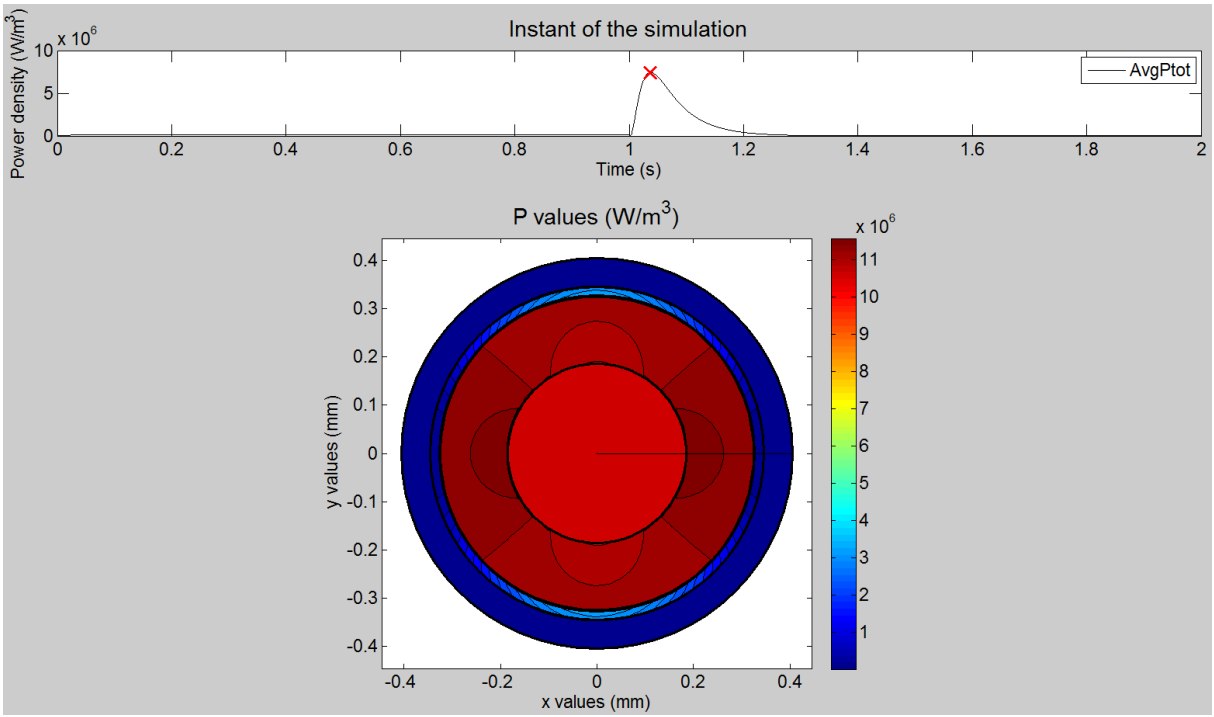

Figure 96 : Simulated cartography of power density at the instant corresponding to the marker displayed on Figure 95 for K006-01C JT-60SA TF composite for a ramp going from $0T$ to $3T$ in $1s$ followed by an exponential decay with a characteristic time of $0.1s$

E. Magnetization and AC losses measurements in JT-60SA NbTi strand

Experimental results for trapezoidal cycles with $B_m = 1.5T$

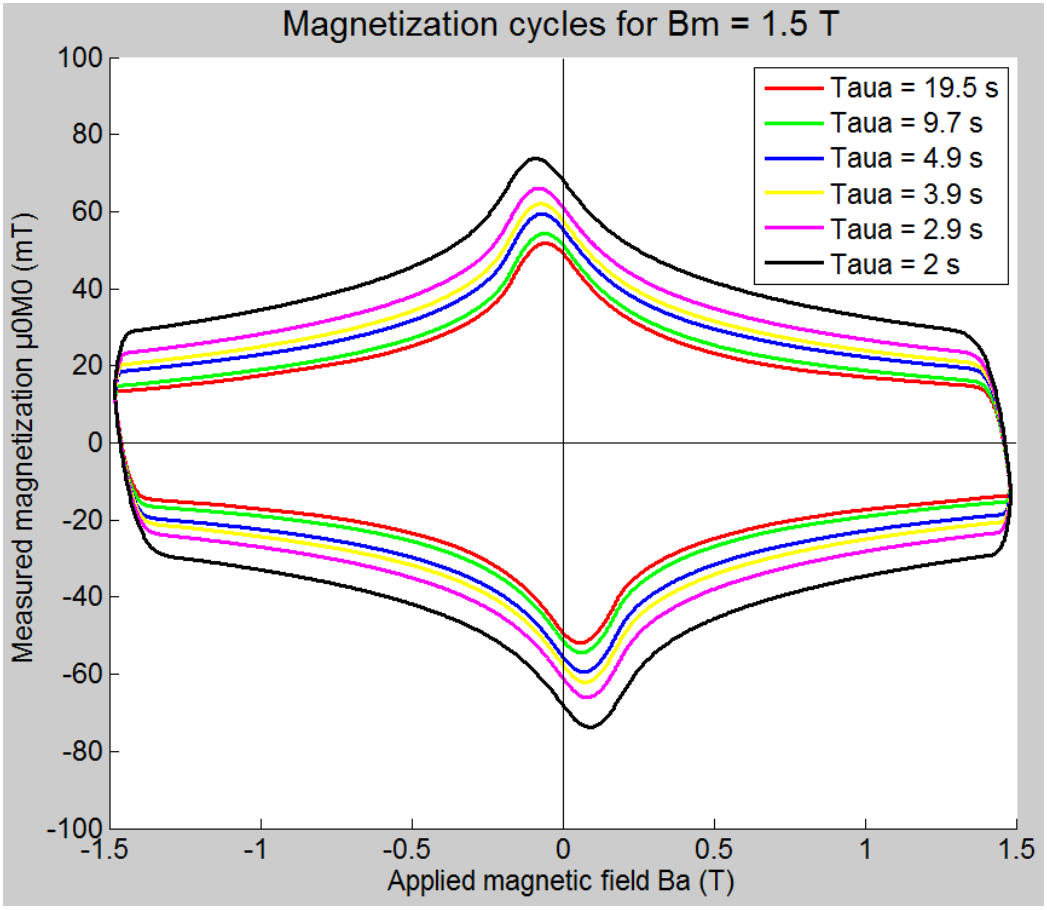

Figure 97 : Magnetization cycles of K006-01C JT-60SA TF strand measured in Speedy facility for trapezoidal cycles with $B_m = 1.5T$

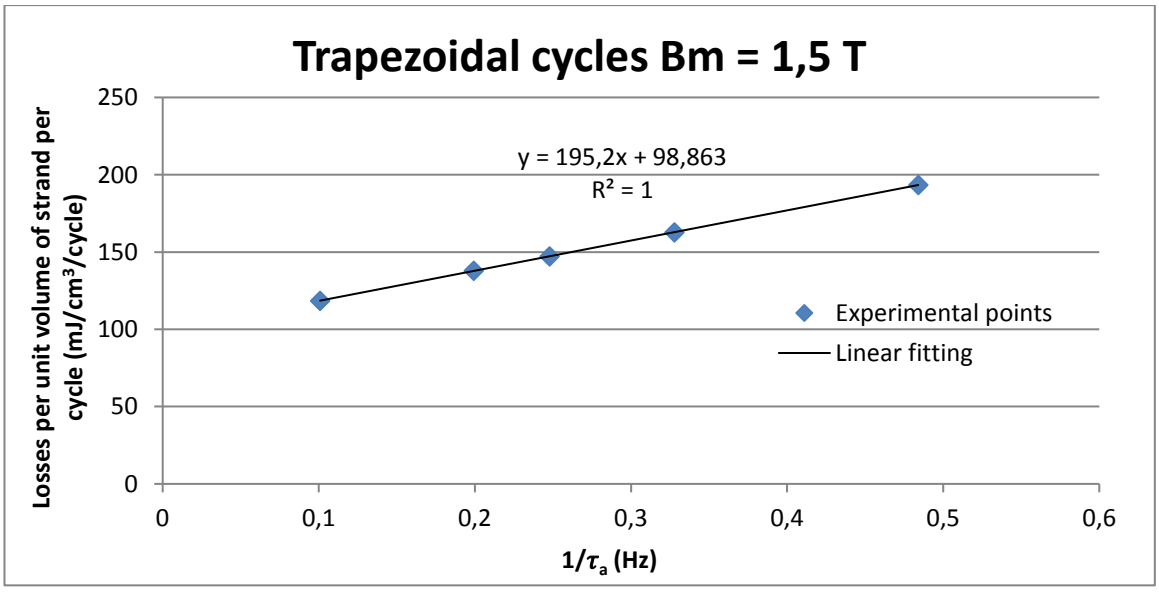

Figure 98 : Losses of K006-01C JT-60SA TF strand per unit volume of strand per cycle measured in Speedy facility for trapezoidal cycles with $B_m = 1.5T$

Experimental results for trapezoidal cycles with $B_m = 2.5T$

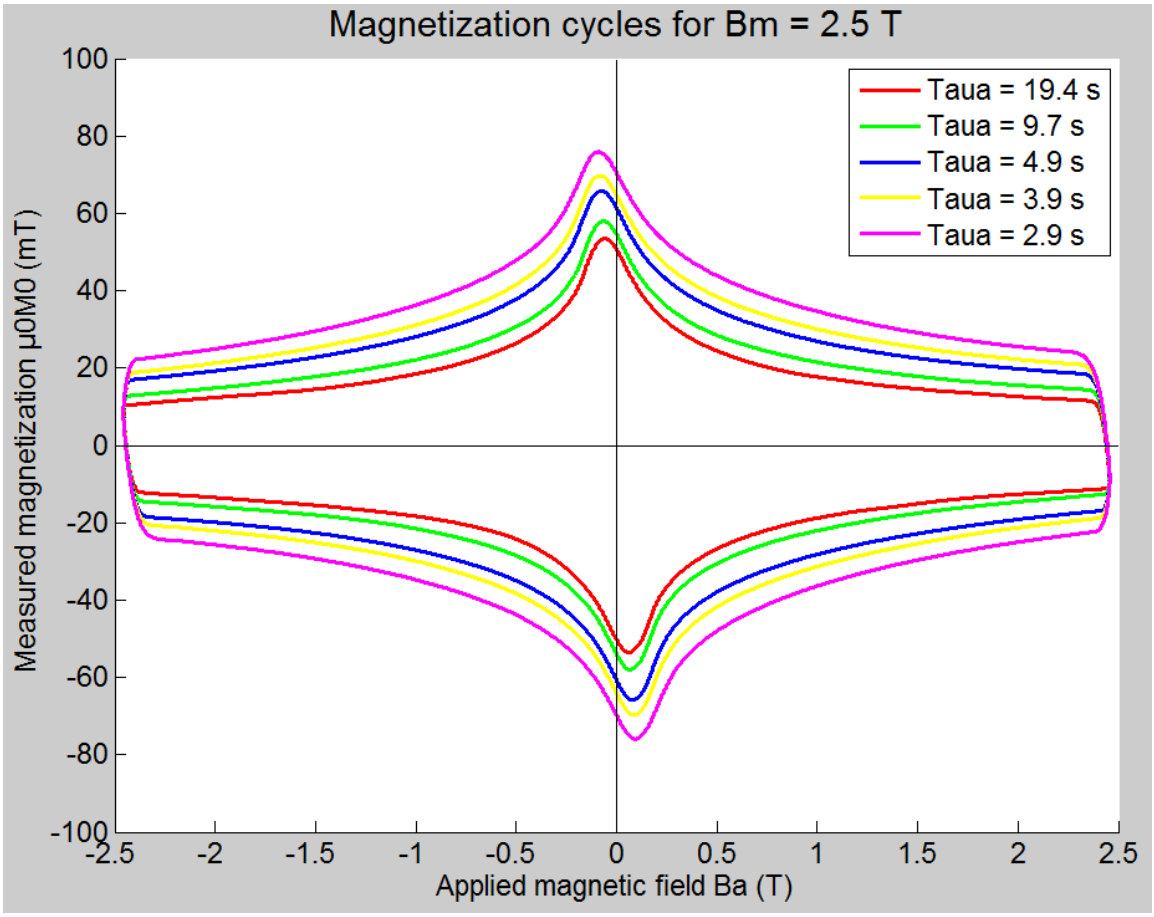

Figure 99 : Magnetization cycles of K006-01C JT-60SA TF strand measured in Speedy facility for trapezoidal cycles with $B_m = 2.5T$

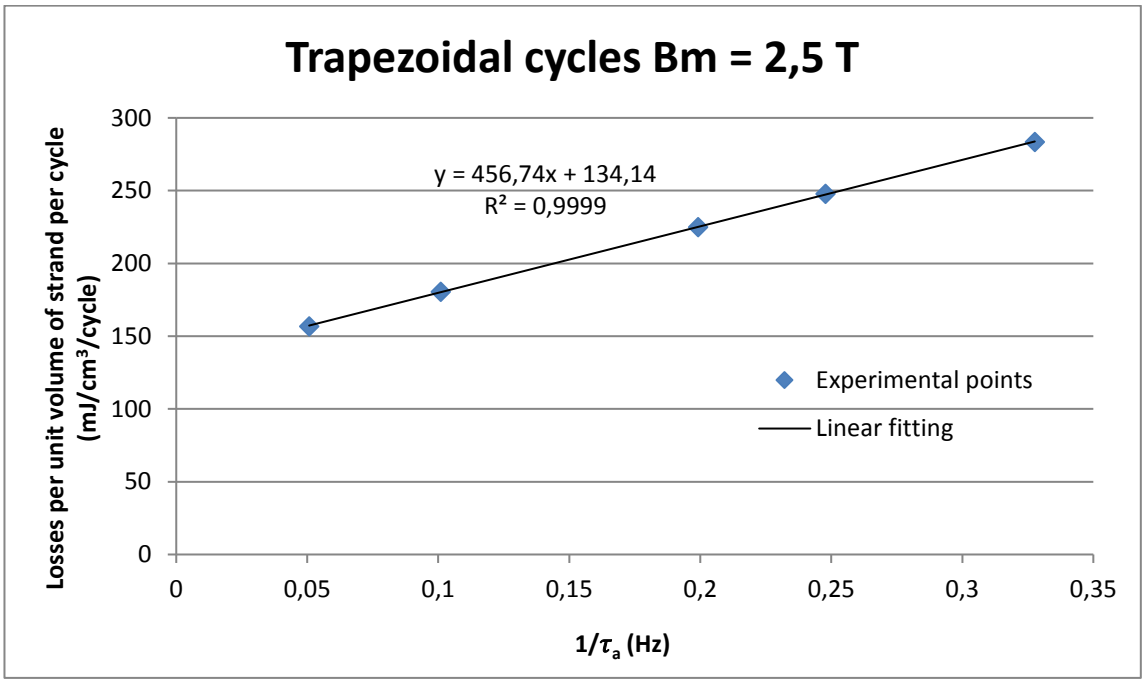

Figure 100 : Losses of K006-01C JT-60SA TF strand per unit volume of strand per cycle measured in Speedy facility for trapezoidal cycles with $B_m = 2.5T$

Experimental results for trapezoidal cycles with $B_m = 3T$

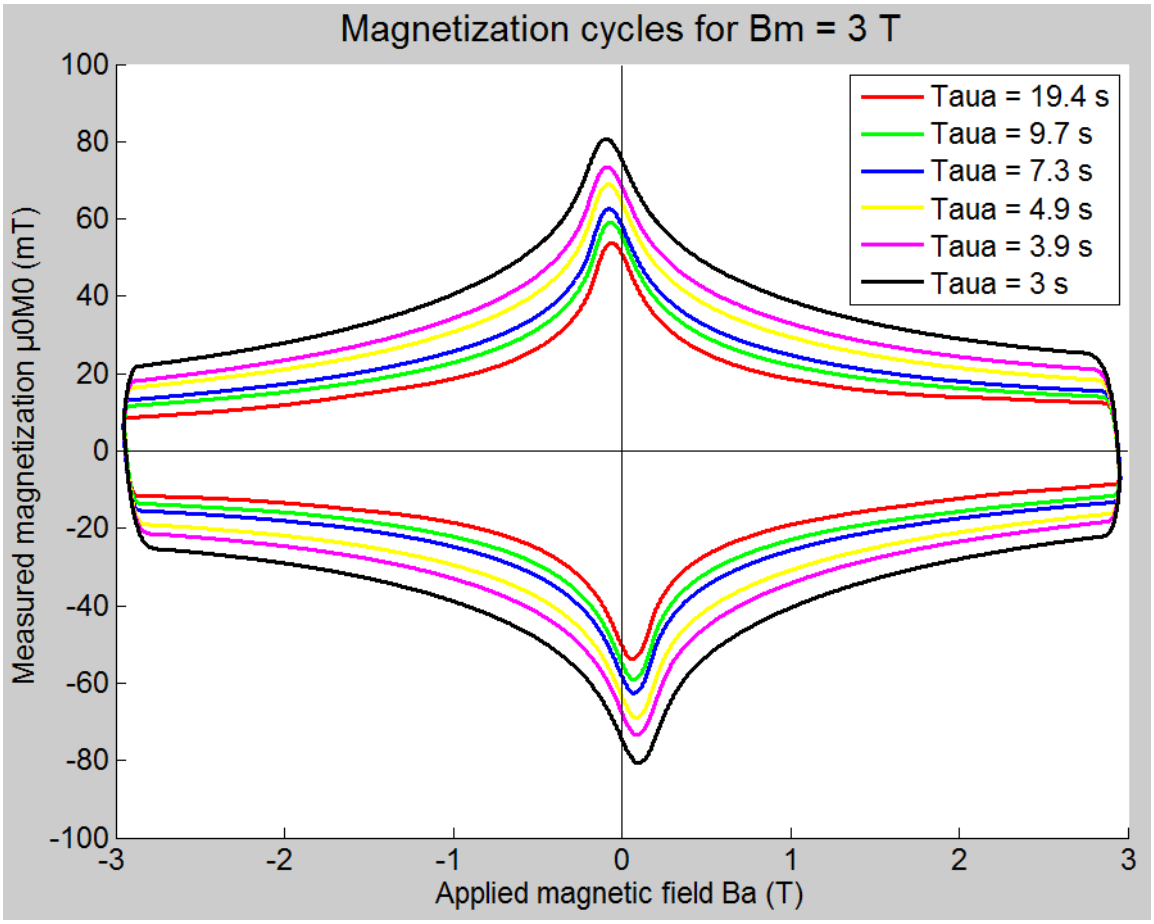

Figure 101 : Magnetization cycles of K006-01C JT-60SA TF strand measured in Speedy facility for trapezoidal cycles with $B_m = 3T$

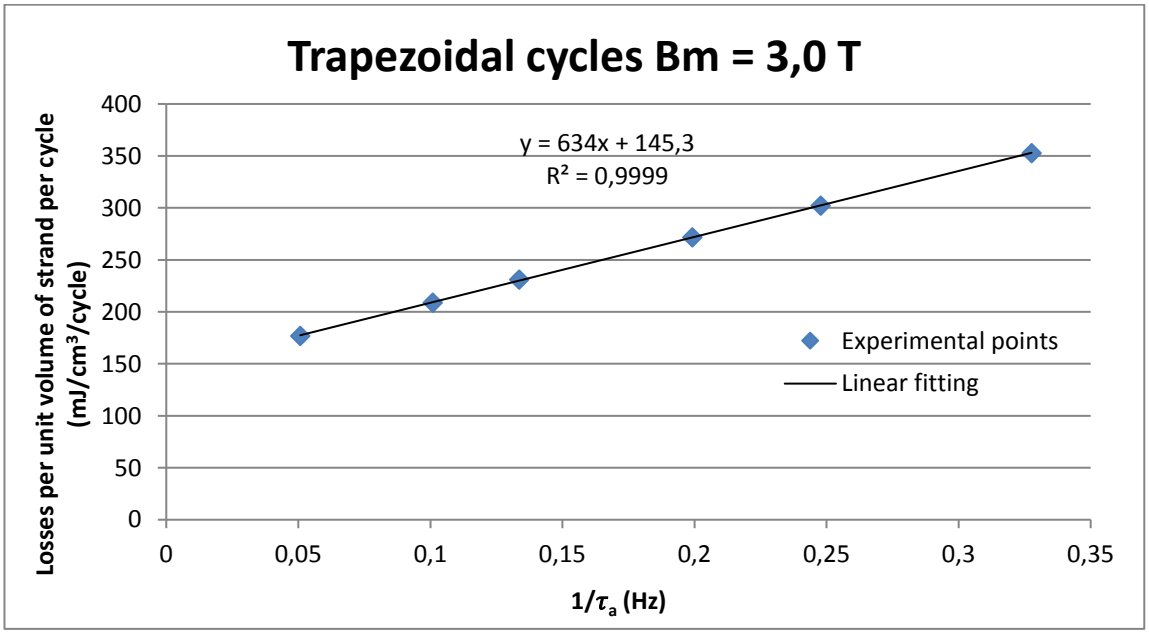

Figure 102 : Losses of K006-01C JT-60SA TF strand per unit volume of strand per cycle measured in Speedy facility for trapezoidal cycles with $B_m = 3T$

Experimental results for positive trapezoidal cycles with $B_m = 1T$

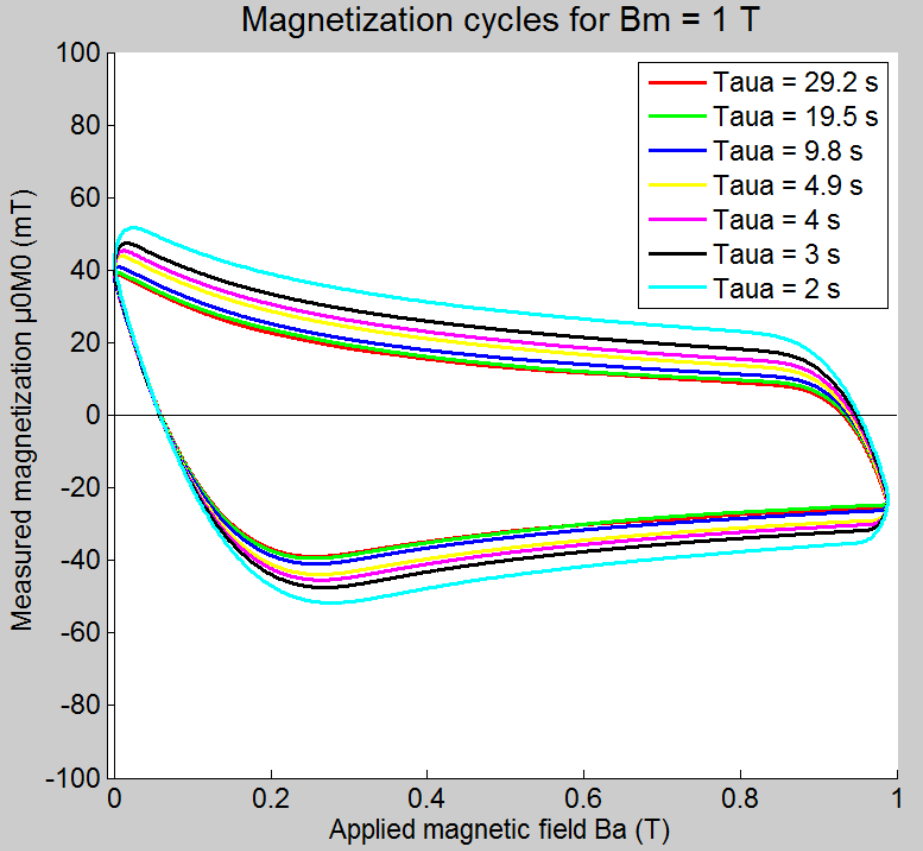

Figure 103 : Magnetization cycles of K006-01C JT-60SA TF strand measured in Speedy facility for positive trapezoidal cycles with $B_m = 1T$

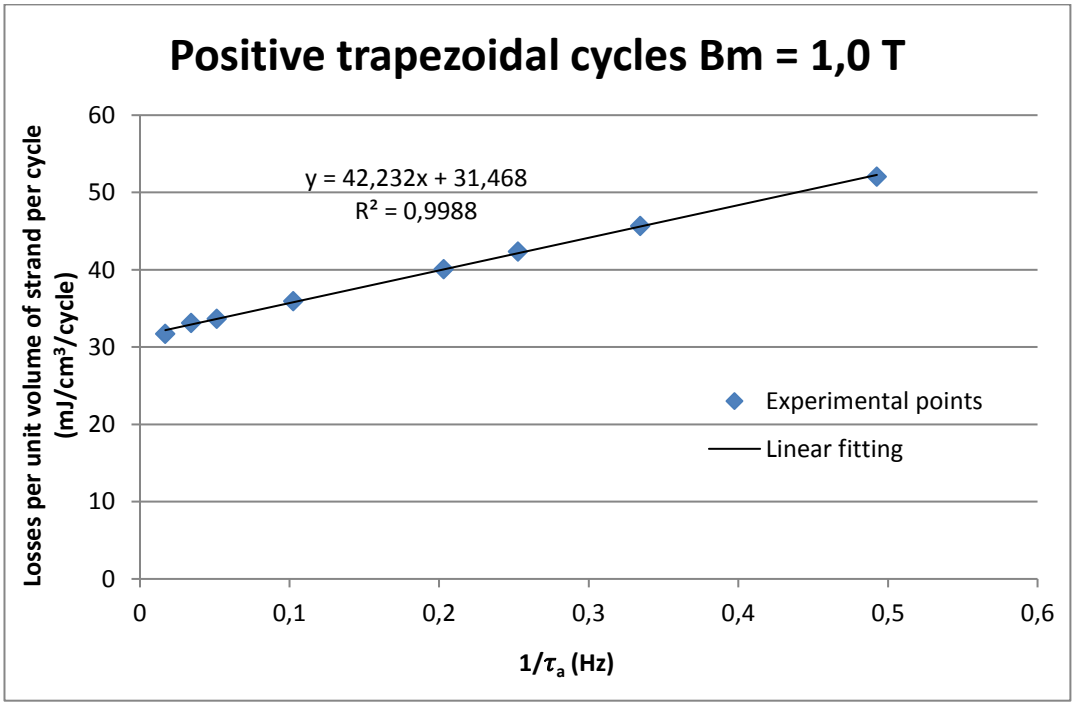

Figure 104 : Losses of K006-01C JT-60SA TF strand per unit volume of strand per cycle measured in Speedy facility for positive trapezoidal cycles with $B_m = 1T$

Experimental results for trapezoidal cycles with $B_m = 1.5T$

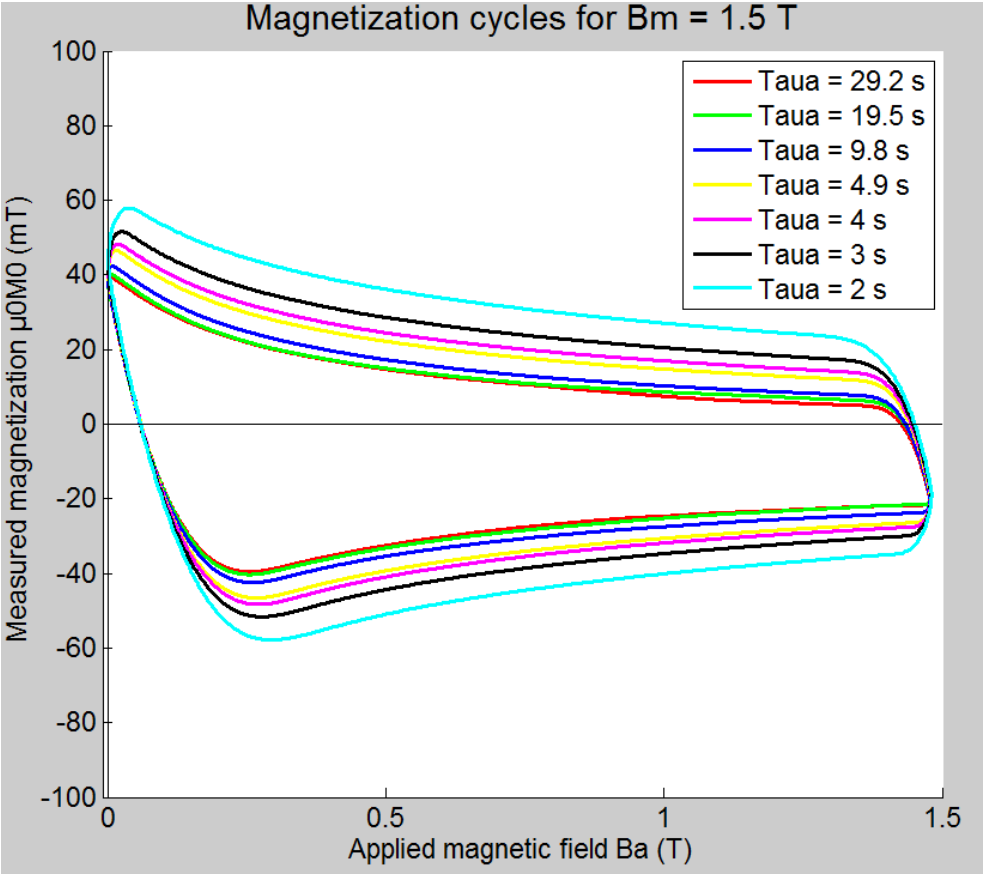

Figure 105 : Magnetization cycles of K006-01C JT-60SA TF strand measured in Speedy facility for positive trapezoidal cycles with $B_m = 1.5T$

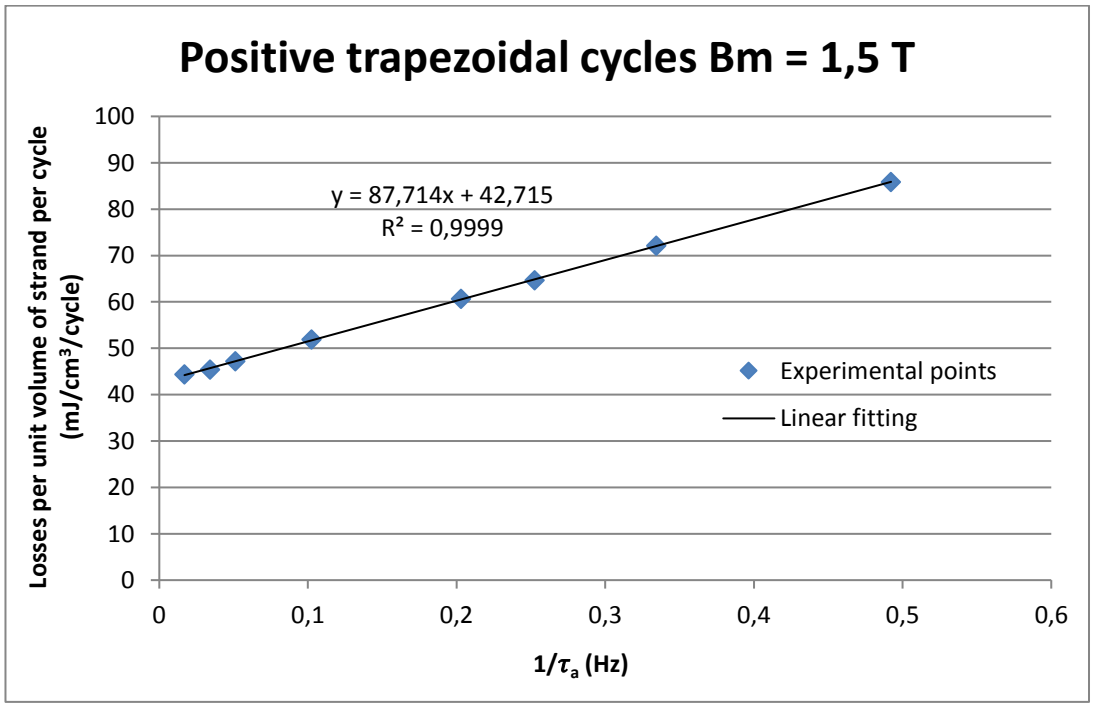

Figure 106 : Losses of K006-01C JT-60SA TF strand per unit volume of strand per cycle measured in Speedy facility for positive trapezoidal cycles with $B_m = 1.5T$

Experimental results for sinusoidal cycles with $B_p = 1.5T$ and $B_{off} = 0T$

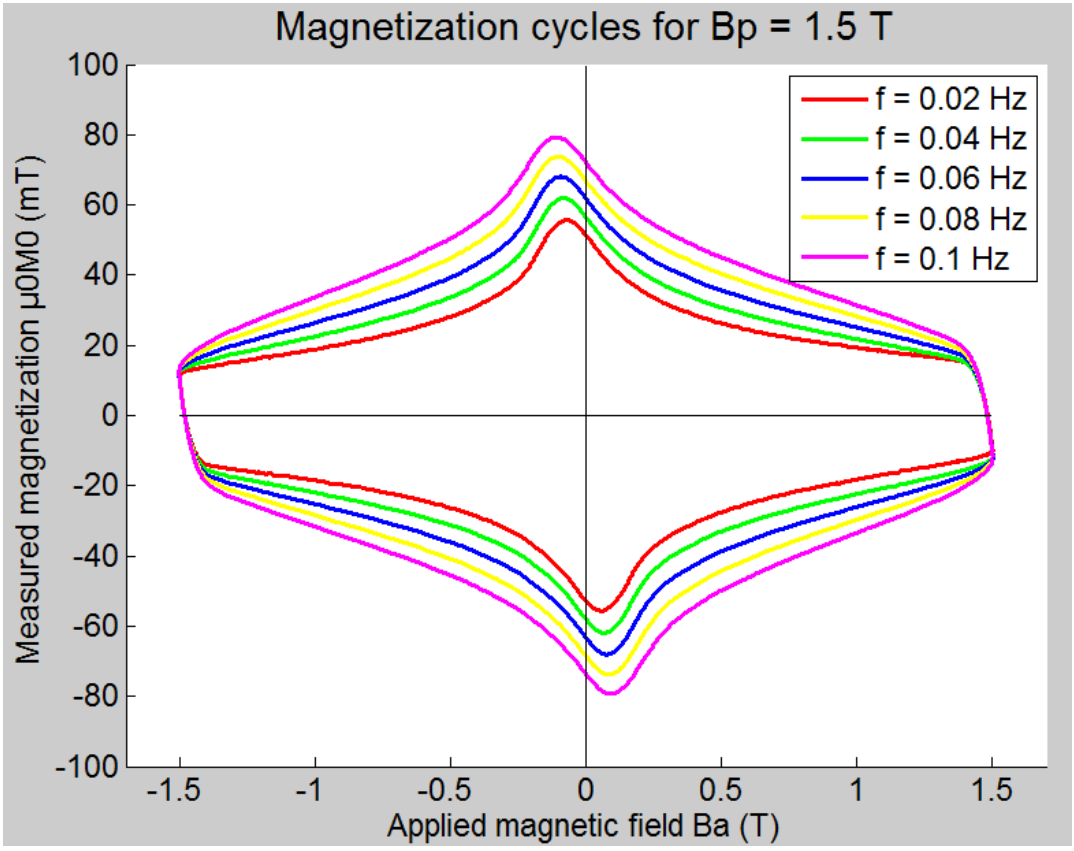

Figure 107 : Magnetization cycles of K006-01C JT-60SA TF strand measured in Speedy facility for sinusoidal cycles with $B_p = 1.5T$ and $B_{off} = 0T$

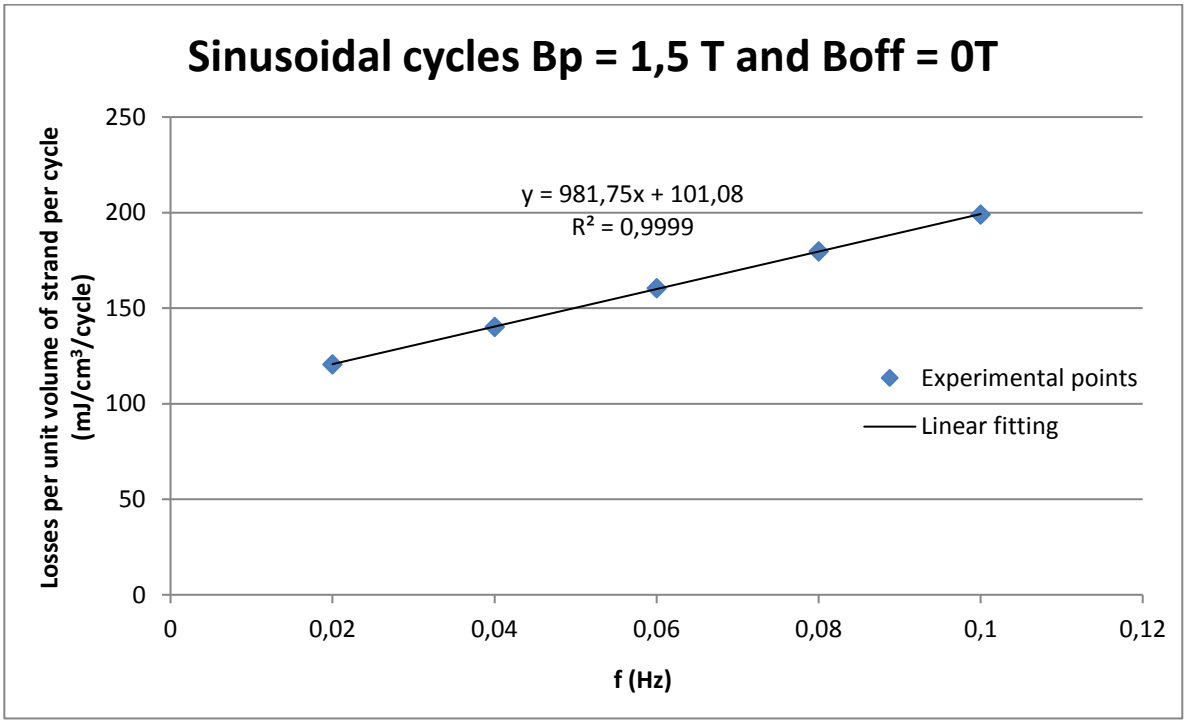

Figure 108 : Losses of K006-01C JT-60SA TF strand per unit volume of strand per cycle measured in Speedy facility for sinusoidal cycles with $B_p = 1.5T$ and $B_{off} = 0T$

Experimental results for sinusoidal cycles with $B_p = 2.5T$ and $B_{off} = 0T$

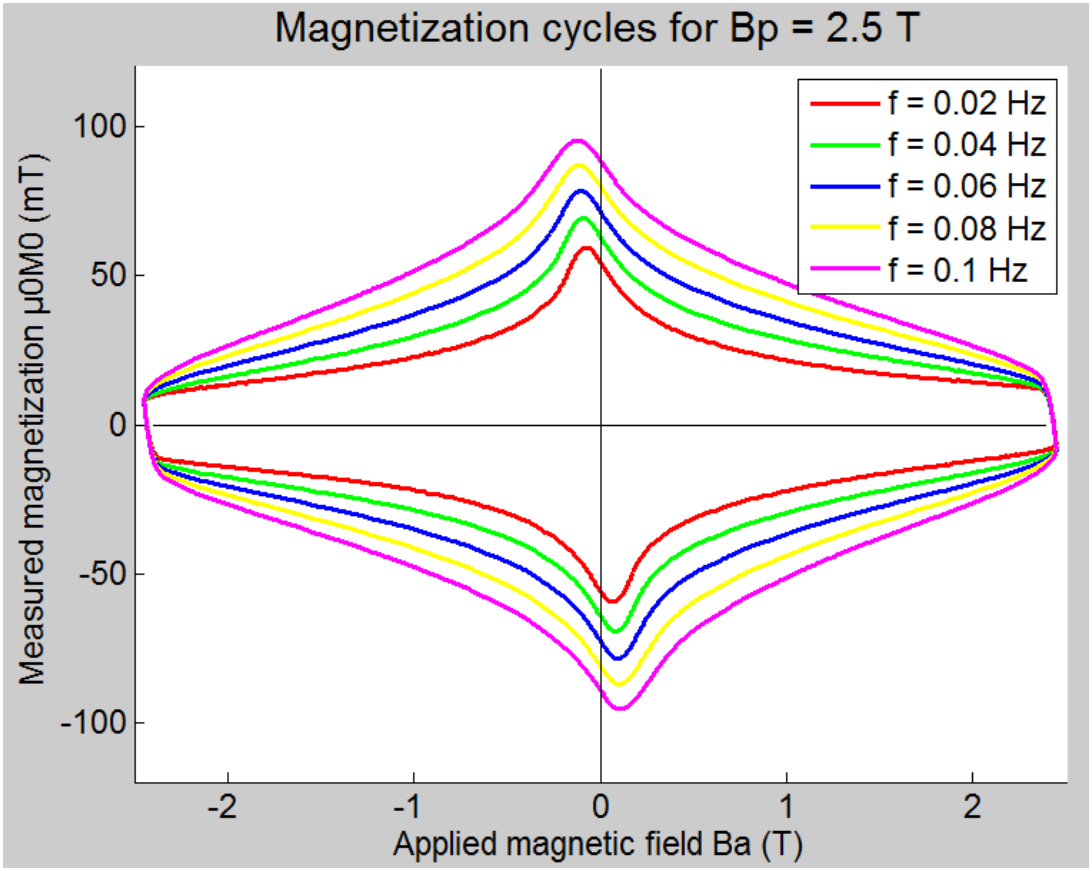

Figure 109 : Magnetization cycles of K006-01C JT-60SA TF strand measured in Speedy facility for sinusoidal cycles with $B_p = 2.5T$ and $B_{off} = 0T$

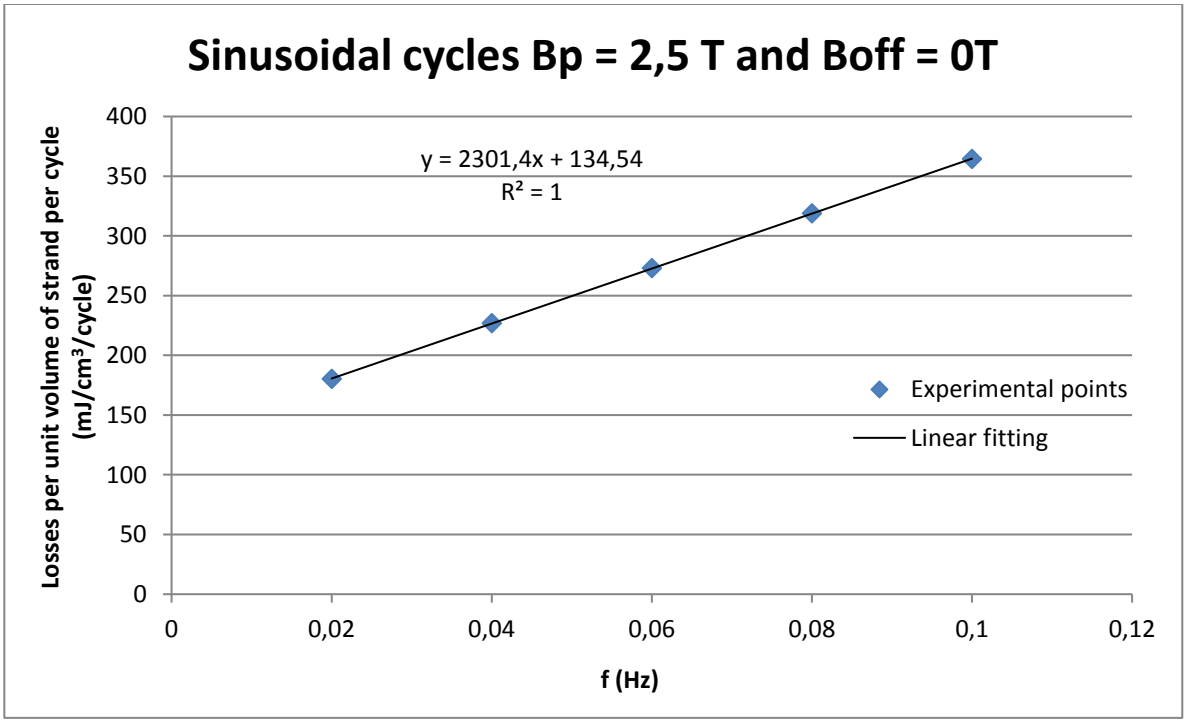

Figure 110 : Losses of K006-01C JT-60SA TF strand per unit volume of strand per cycle measured in Speedy facility for sinusoidal cycles with $B_p = 2.5T$ and $B_{off} = 0T$

Experimental results for sinusoidal cycles with $B_p = 3T$ and $B_{off} = 0T$

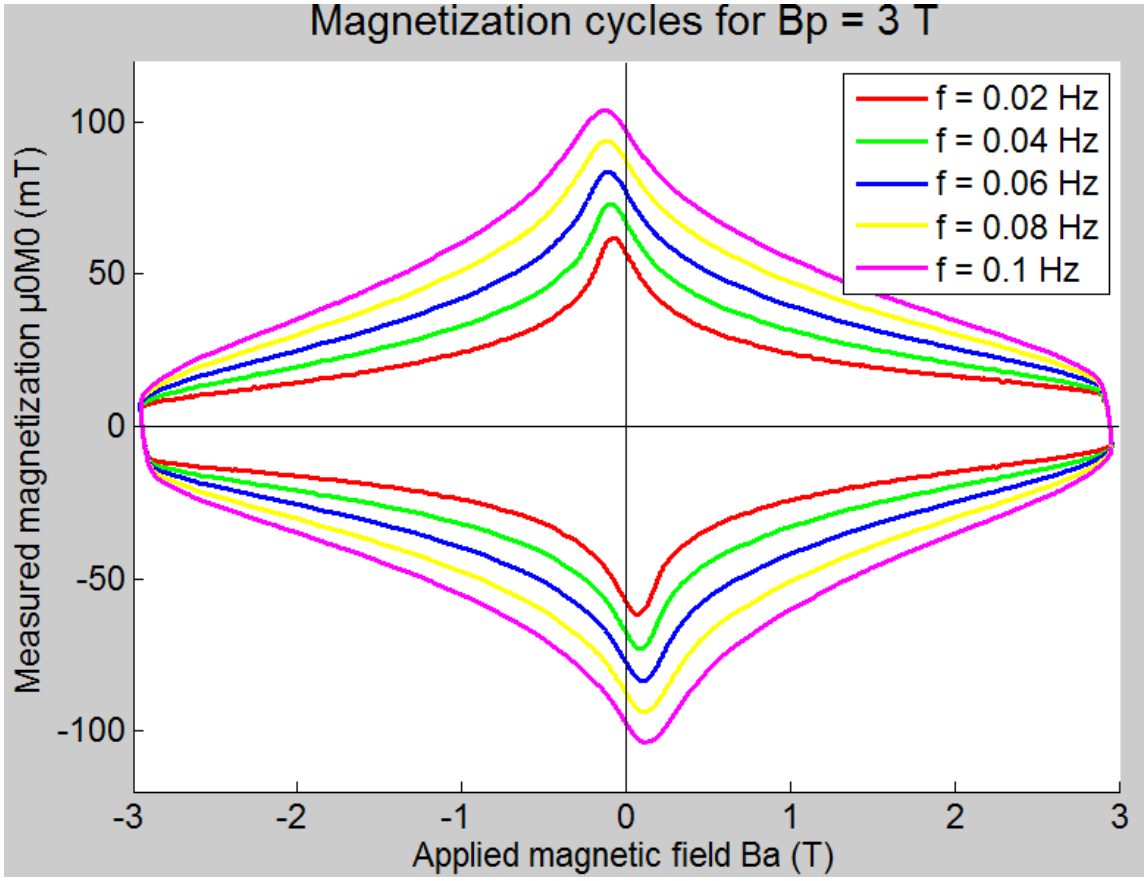

Figure 111 : Magnetization cycles of K006-01C JT-60SA TF strand measured in Speedy facility for sinusoidal cycles with $B_p = 3T$ and $B_{off} = 0T$

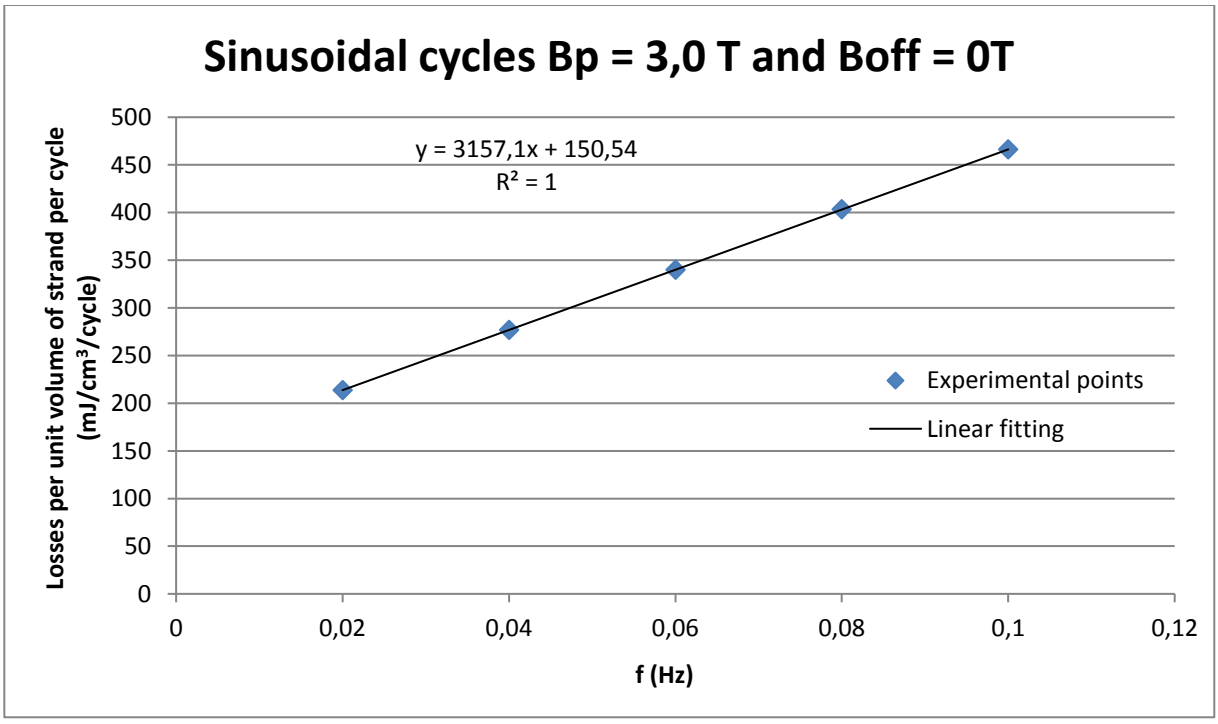

Figure 112 : Losses of K006-01C JT-60SA TF strand per unit volume of strand per cycle measured in Speedy facility for sinusoidal cycles with $B_p = 3T$ and $B_{off} = 0T$

Experimental results for sinusoidal cycles with $B_p = 1.25T$ and $B_{off} = 1.5T$

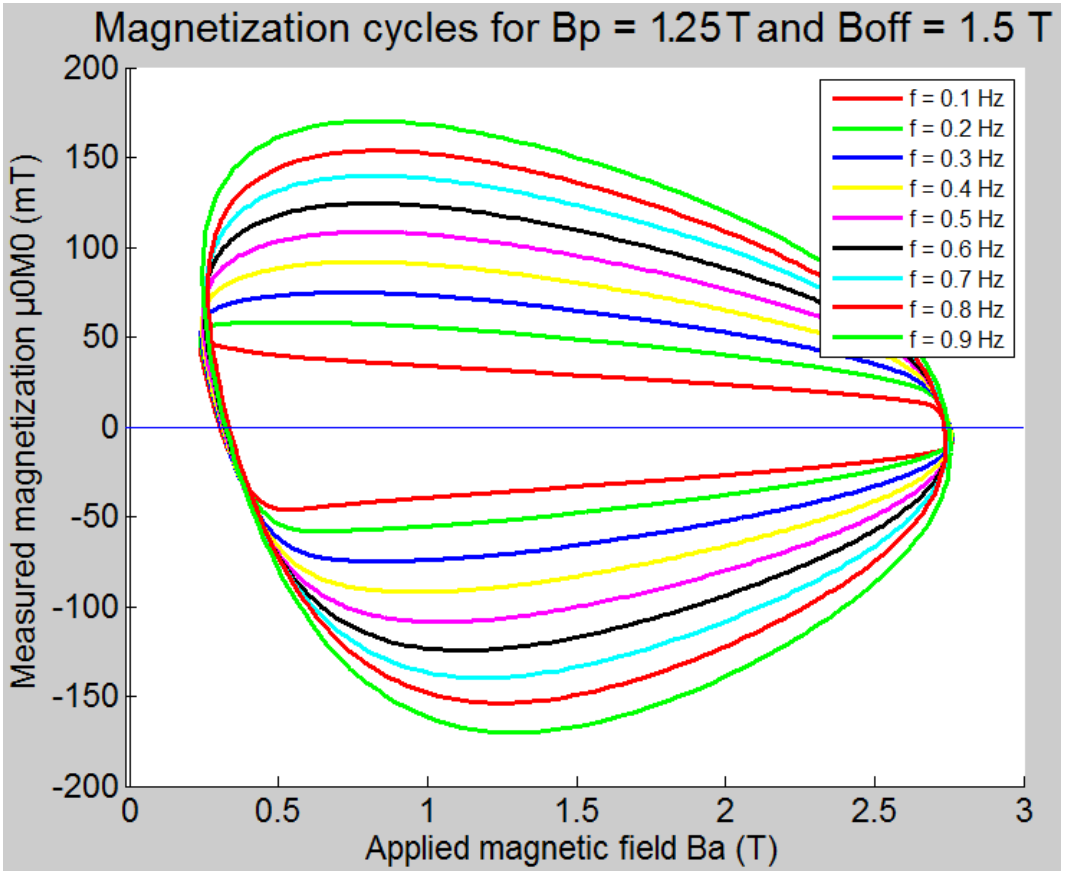

Figure 113 : Magnetization cycles of K006-01C JT-60SA TF strand measured in Speedy facility for sinusoidal cycles with $B_p = 1.25T$ and $B_{off} = 1.5T$

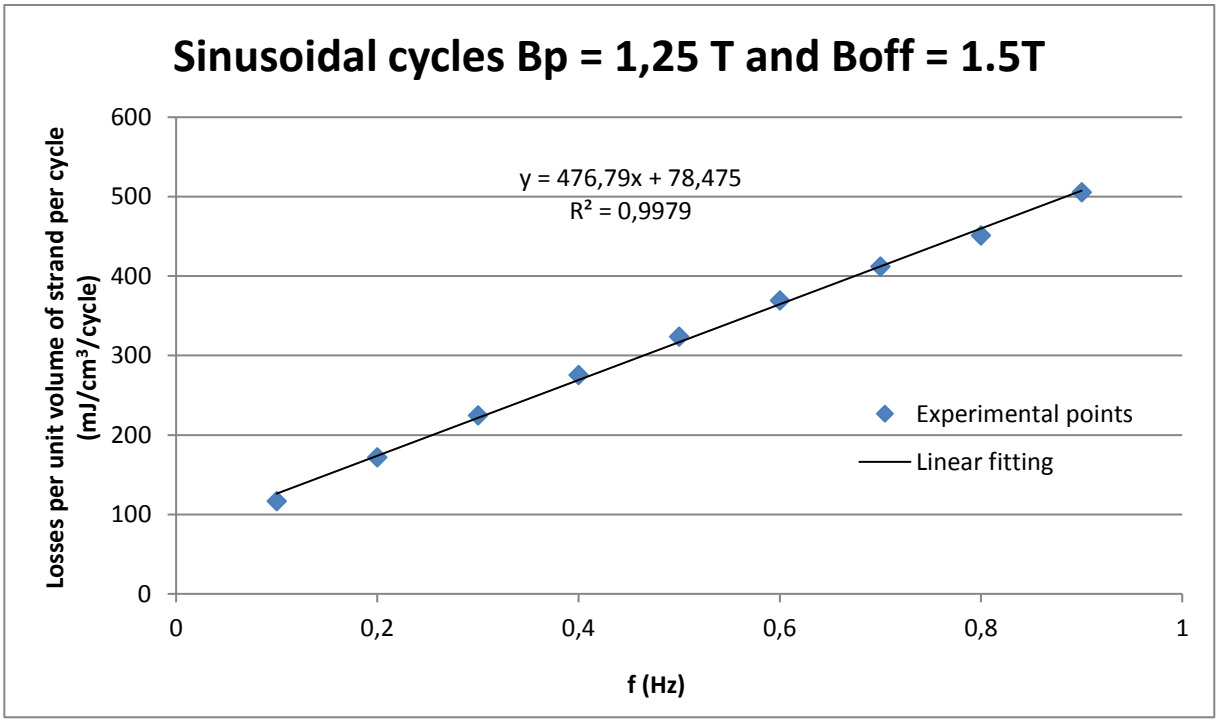

Figure 114 : Losses of K006-01C JT-60SA TF strand per unit volume of strand per cycle measured in Speedy facility for sinusoidal cycles with $B_p = 1.25T$ and $B_{off} = 1.5T$

F. Magnetization and AC losses measurements in ITER Nb_3Sn strand

Experimental results for trapezoidal cycles with $B_m = 1.5T$

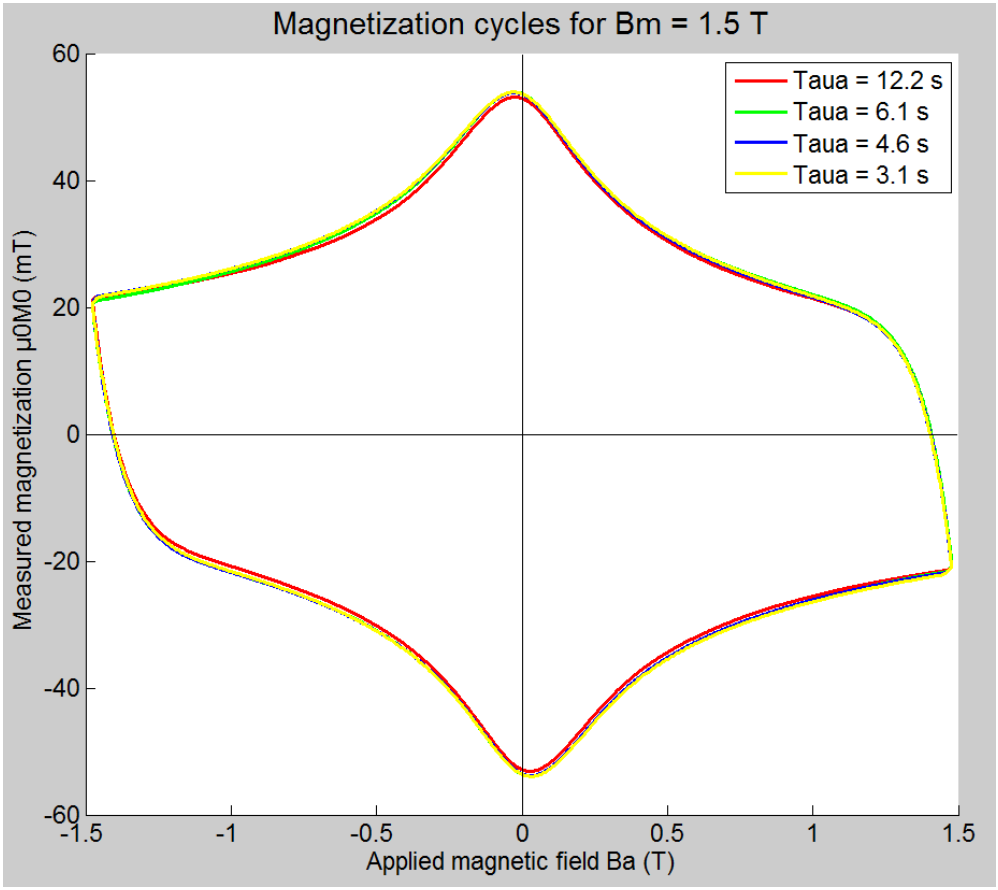

Figure 115 : Magnetization cycles of F 0796-1 ITER TF strand measured in Speedy facility for trapezoidal cycles with $B_m = 1.5T$

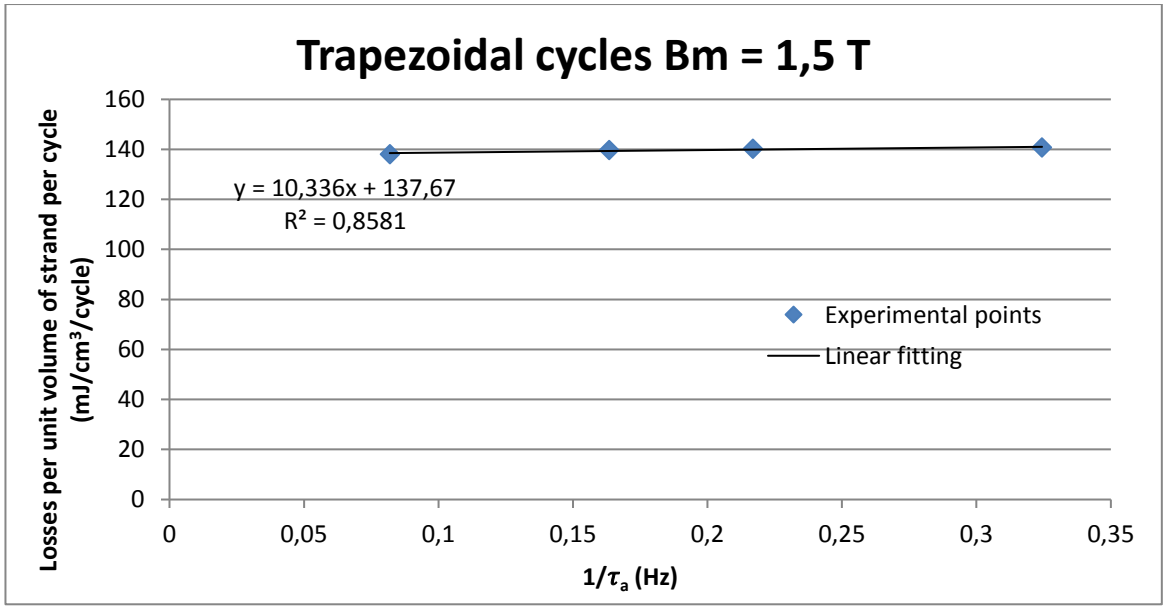

Figure 116 : Losses of F 0796-1 ITER TF strand per unit volume of strand per cycle measured in Speedy facility for trapezoidal cycles with $B_m = 1.5T$

Experimental results for trapezoidal cycles with $B_m = 2.5T$

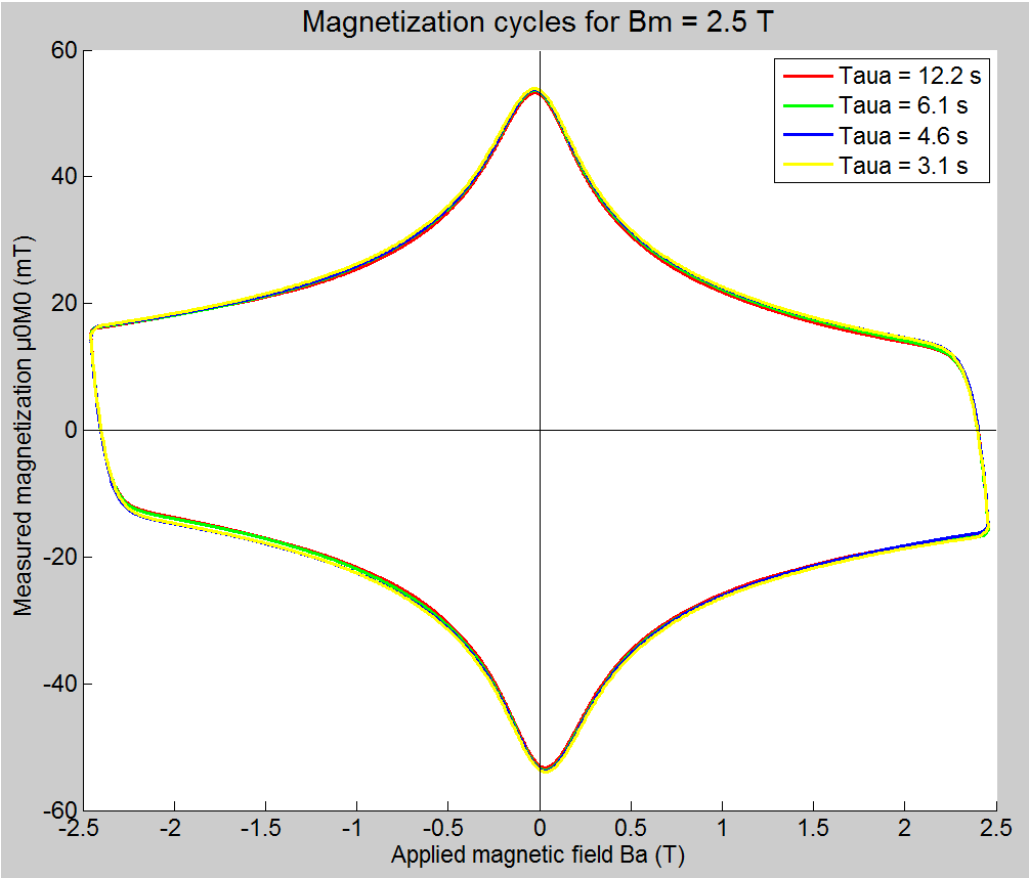

Figure 117 : Magnetization cycles of F 0796-1 ITER TF strand measured in Speedy facility for trapezoidal cycles with $B_m = 2.5T$

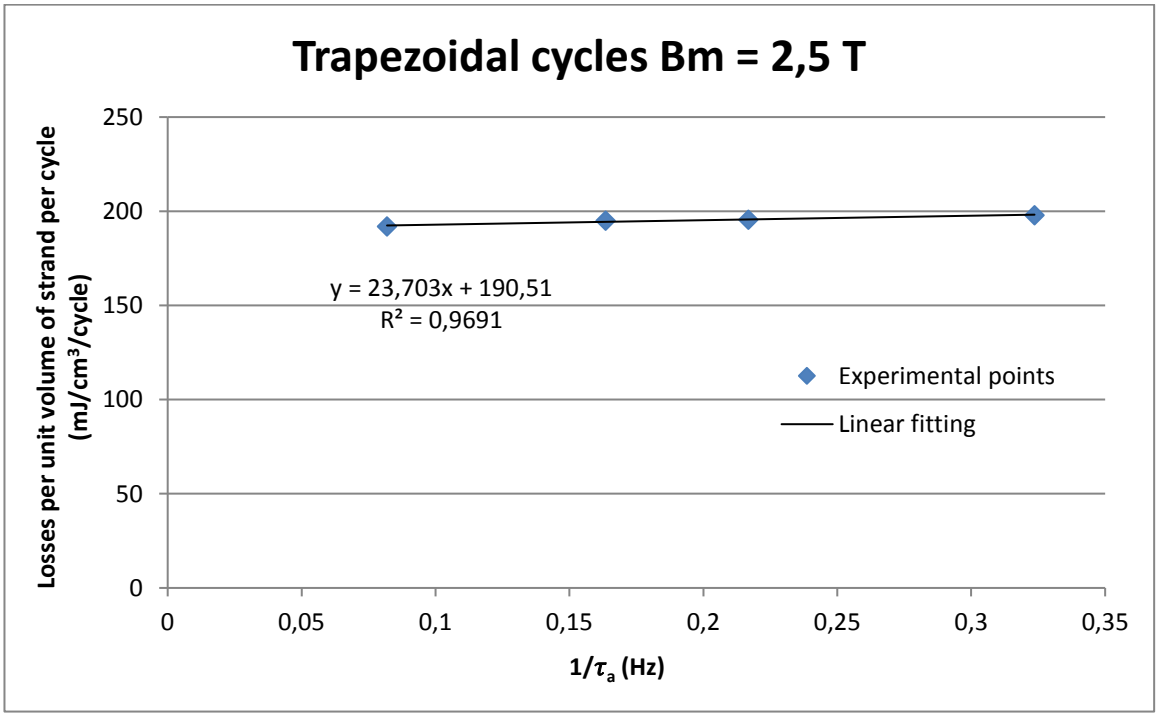

Figure 118 : Losses of F 0796-1 ITER TF strand per unit volume of strand per cycle measured in Speedy facility for trapezoidal cycles with $B_m = 2.5T$

Experimental results for trapezoidal cycles with $B_m = 3T$

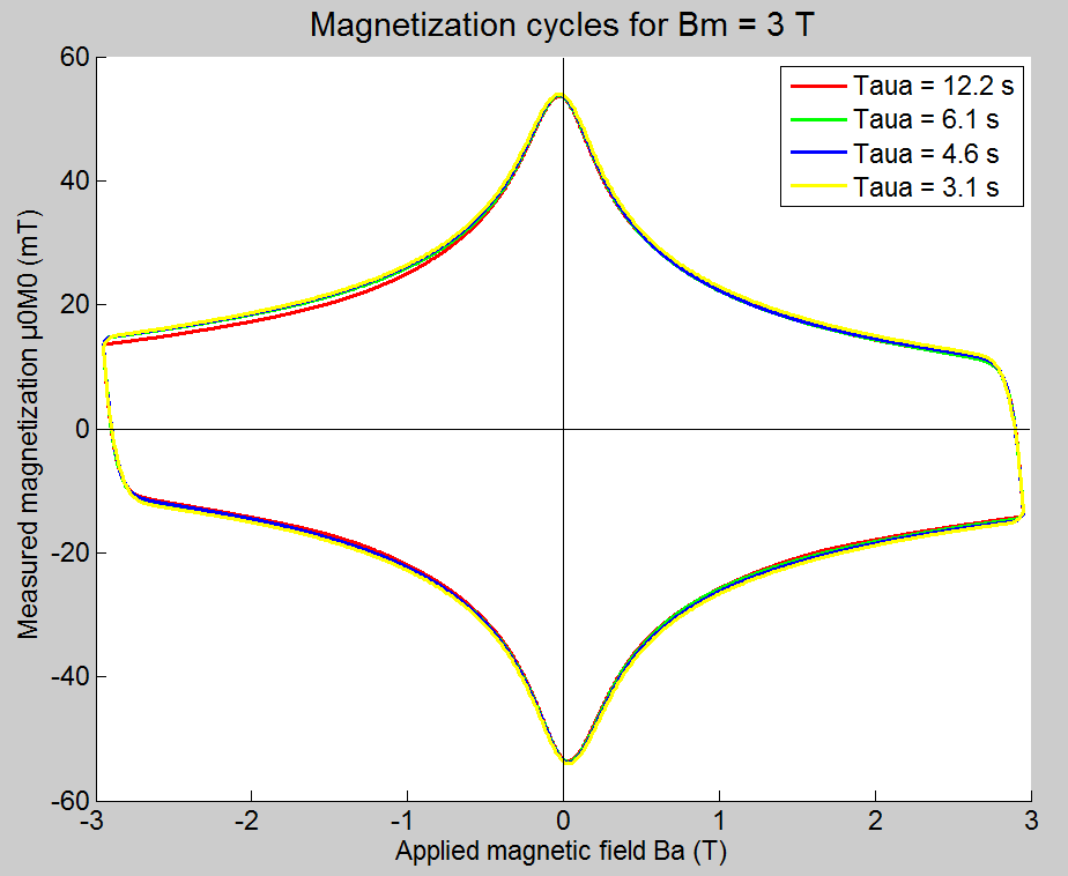

Figure 119 : Magnetization cycles of F 0796-1 ITER TF strand measured in Speedy facility for trapezoidal cycles with $B_m = 3T$

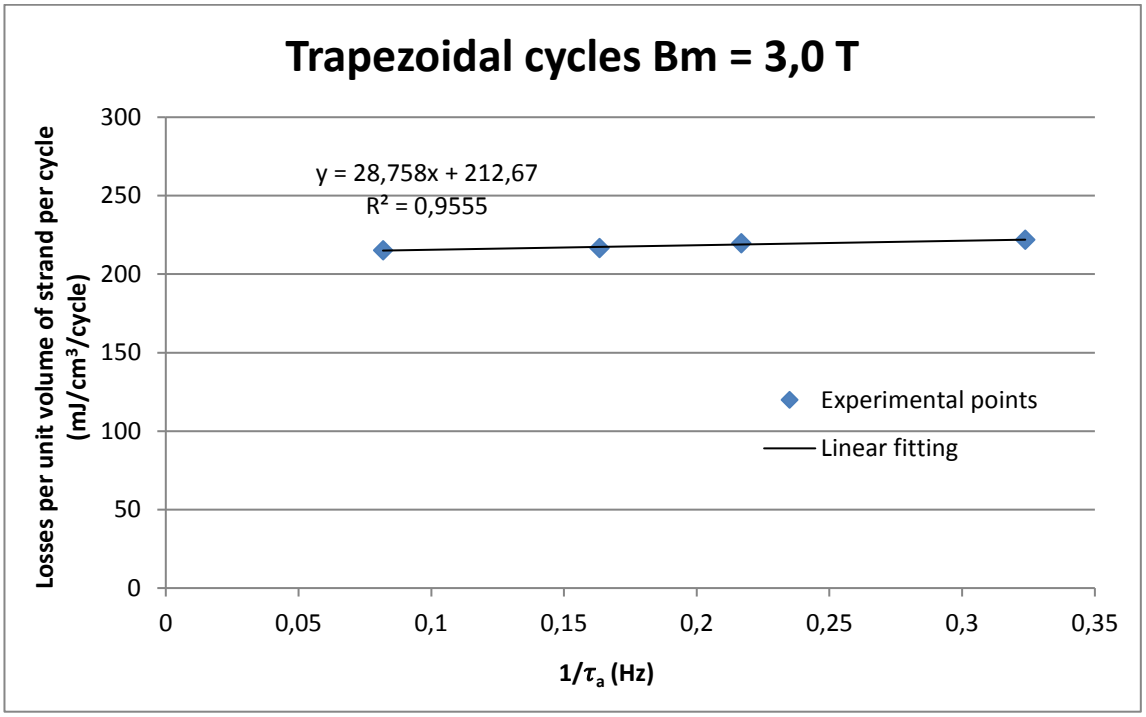

Figure 120 : Losses of F 0796-1 ITER TF strand per unit volume of strand per cycle measured in Speedy facility for trapezoidal cycles with $B_m = 3T$

Experimental results for sinusoidal cycles with $B_p = 1.4T$ and $B_{off} = 1.5T$

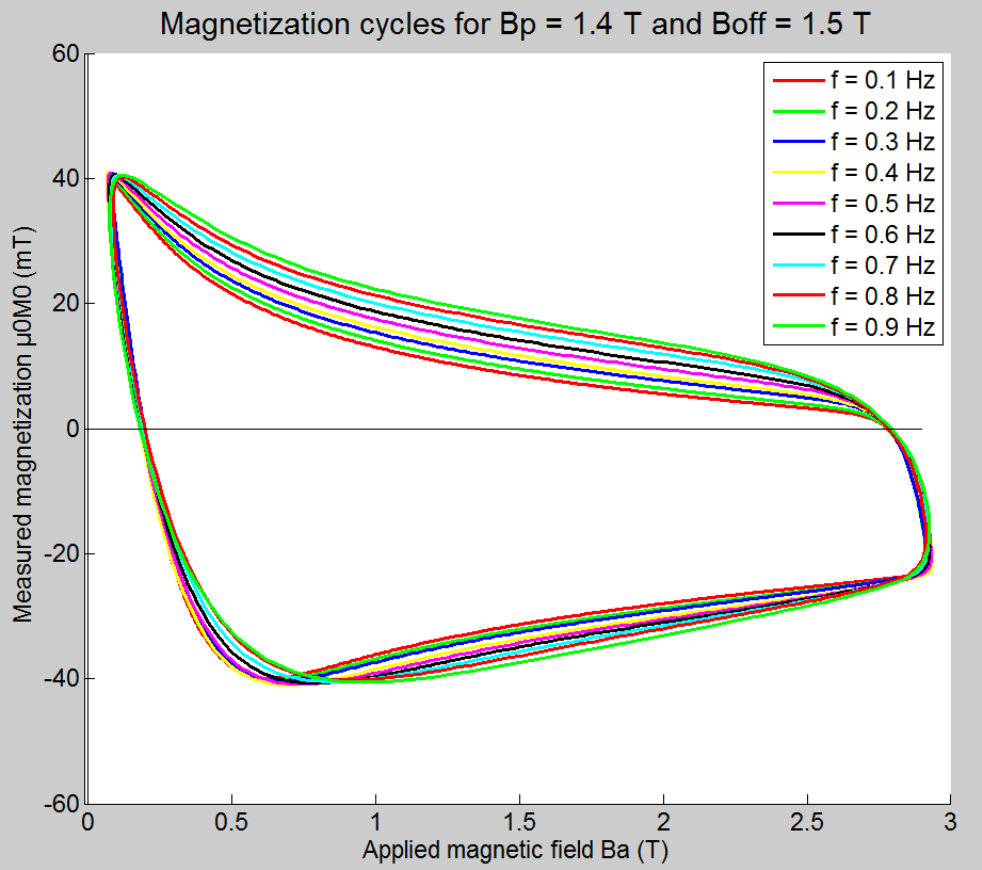

Figure 121 : Magnetization cycles of F 0796-1 ITER TF strand measured in Speedy facility for sinusoidal cycles with $B_p = 1.4T$ and $B_{off} = 1.5T$

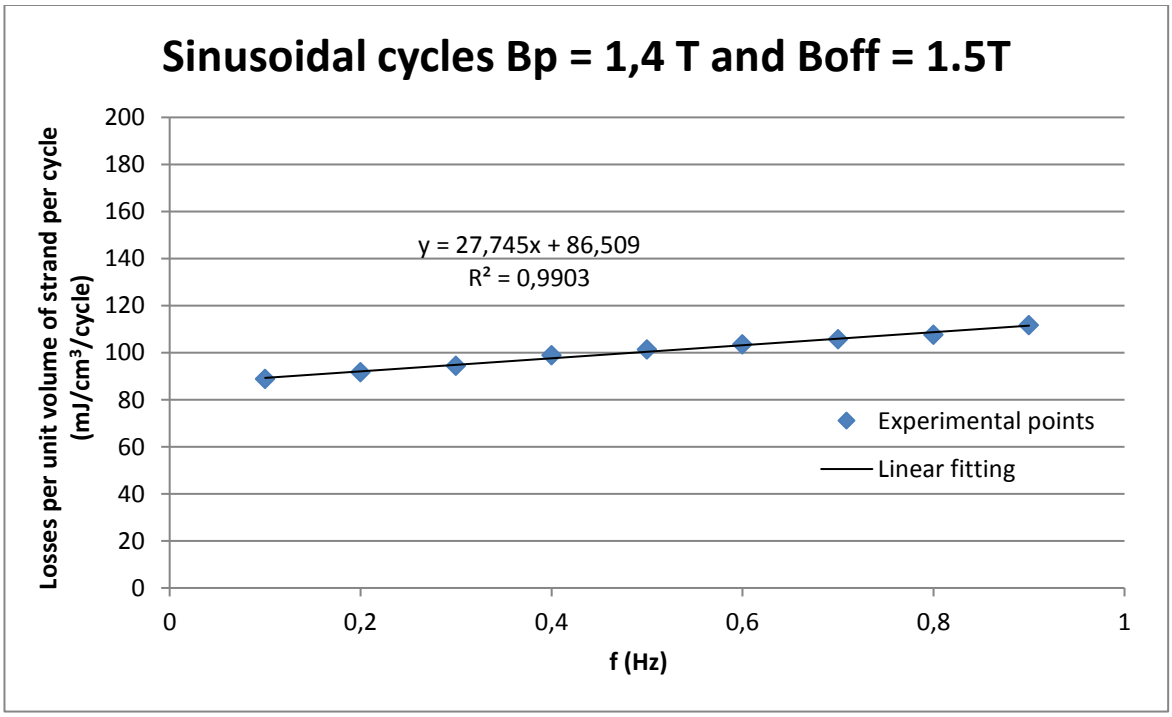

Figure 122 : Losses of F 0796-1 ITER TF strand per unit volume of strand per cycle measured in Speedy facility for sinusoidal cycles with $B_p = 1.4T$ and $B_{off} = 1.5T$